NATO Science for Peace and Security Series - B:
Physics and Biophysics

Advanced Nanotechnologies for Detection and Defence against CBRN Agents

Edited by
Plamen Petkov
Dumitru Tsiulyanu
Cyril Popov
Wilhelm Kulisch

Springer

NATO OTAN

This publication is supported by:

The NATO Science for Peace and Security Programme

Advanced Nanotechnologies for Detection and Defence against CBRN Agents

NATO Science for Peace and Security Series

This Series presents the results of scientific meetings supported under the NATO Programme: Science for Peace and Security (SPS).

The NATO SPS Programme supports meetings in the following Key Priority areas: (1) Defence Against Terrorism; (2) Countering other Threats to Security and (3) NATO, Partner and Mediterranean Dialogue Country Priorities. The types of meetings supported are generally "Advanced Study Institutes" and "Advanced Research Workshops". The NATO SPS Series collects together the results of these meetings. The meetings are co-organized by scientists from NATO countries and scientists from NATO's "Partner" or "Mediterranean Dialogue" countries. The observations and recommendations made at the meetings, as well as the contents of the volumes in the Series, reflect those of participants and contributors only; they should not necessarily be regarded as reflecting NATO views or policy.

Advanced Study Institutes (ASI) are high-level tutorial courses to convey the latest developments in a subject to an advanced-level audience.

Advanced Research Workshops (ARW) are expert meetings where an intense but informal exchange of views at the frontiers of a subject aims at identifying directions for future action.

Following a transformation of the programme in 2006, the Series has been re-named and re-organised. Recent volumes on topics not related to security, which result from meetings supported under the programme earlier, may be found in the NATO Science Series.

The Series is published by IOS Press, Amsterdam, and Springer, Dordrecht, in conjunction with the NATO Emerging Security Challenges Division.

Sub-Series

A.	Chemistry and Biology	Springer
B.	Physics and Biophysics	Springer
C.	Environmental Security	Springer
D.	Information and Communication Security	IOS Press
E.	Human and Societal Dynamics	IOS Press

http://www.nato.int/science
http://www.springer.com
http://www.iospress.nl

Series B: Physics and Biophysics

Advanced Nanotechnologies for Detection and Defence against CBRN Agents

edited by

Plamen Petkov
Department of Physics
University of Chemical Technology &
Metallurgy
Sofia, Bulgaria

Dumitru Tsiulyanu
Department of Physics
Technical University of Moldova
Chisinau, Moldova

Cyril Popov
Institute of Nanostructure Technologies and Analytics
University of Kassel
Kassel, Germany

and

Wilhelm Kulisch
Department of Mathematics and Natural Sciences
University of Kassel
Kassel, Germany

Published in Cooperation with NATO Emerging Security Challenges Division

Proceedings of the NATO Advanced Study Institute on
Advanced Nanotechnologies for Detection and Defence
against CBRN Agents
Sozopol, Bulgaria
12–20 September 2017

Library of Congress Control Number: 2018941543

ISBN 978-94-024-1516-2 (PB)
ISBN 978-94-024-1297-0 (HB)
ISBN 978-94-024-1298-7 (eBook)
https://doi.org/10.1007/978-94-024-1298-7

Published by Springer,
P.O. Box 17, 3300 AA Dordrecht, The Netherlands.

www.springer.com

Printed on acid-free paper

Preface

The ever-increasing requirements towards different aspects of security, for example, in information technology and cyber defence, in biotechnology, in management and in the early detection and defence against chemical, biological, radiological and nuclear (CBRN) agents, demand the latest achievements of nanoscience and nanotechnology. Novel functional materials, devices and systems allowing the control of matter on atomic and molecular levels, that is, at the level of the matter building blocks, have to face the challenges of the security of the modern society. The nanostructured materials possess unique mechanical, electrical, optical, magnetic and biological properties, which are entirely different from those of the conventional micro- or millimeter-sized materials, due to their distinctive sizes and shapes, and predominant surface and quantum effects determining their behaviour. In such a sense, nanomaterials and nanotechnologies have a strong potential to be the main driving forces in the development of new concepts for security and safety. It concerns not only the preparation and investigation of smart nanosized materials for different applications, like quantum dots, nanotubes, graphene, nanowires, nanoparticles and nanocomposites, but also the combination of their performance with ICs, micro- and nanooptics, MEMS and NEMS, leading to higher level of integration and effective processing and transmission. Only the common efforts of scientists from different fields of research – chemistry, physics, biology, materials science and engineering – and from different countries can bring the complementary expertise in the development of reliable conceptions in the defence against CBRN agents taking the advantages of nanomaterials and nanotechnologies.

The first objective of the ***NATO ASI on Advanced Nanotechnologies for Detection and Defence against CBRN Agents*** held between 12th and 20th September 2017 in Sozopol, Bulgaria, was to present to the participants the up-to-date achievements for applications of nanomaterials and nanotechnologies in different fields related to the diagnostics and defence against CBRN agents and the future perspectives and trends. The second objective was the teaching and training of the participants in the scientific and technological background of nanostructured materials used in fields, like new generation of advanced sensors and systems for early

detection of CBRN agents, efficient defence against these agents and so on. The third objective addressed the initiation of transborder and interdisciplinary collaborations between young scientists towards the implementation of the recent nanotechnological achievements to meet the emerging security challenges. The overall objective of the ASI was the transfer of competence in the nanomaterials and nanotechnological advances in different fields of security and networking between young scientists from NATO and partner countries in order to meet one of the key priorities of the ***NATO Science for Peace and Security Programme***.

The ASI covered topics connected with the recent achievements in different fields of security related to defence against CBRN agents taking the advantages of nanotechnology and nanomaterials. The ***lectures*** were given by outstanding scientists from universities and research institutes who are experts in nanoscience-related security fields. Eleven ***thematic seminars*** on specific topics, not covered by the lectures, were also included in the programme. Three open-air ***poster sessions*** were held in the afternoons, during which the participants could present their results, established closer contacts and discussed in less formal atmosphere.

Seventy-seven participants from 12 NATO countries (Bulgaria, Canada, Czech Republic, Germany, Hungary, Italy, Poland, Portugal, Romania, Spain, Turkey and USA) and 5 partner countries (Egypt, FYR Macedonia, Moldova, Morocco and Ukraine) ensured that the overall objective of transfer of competence and technology in the field of nanostructured materials and nanotechnologies was reached on a high level. Such events contribute to the scientific collaborations in these advanced fields of research between NATO and partner countries as well as to the promotion of nanoscience and nanotechnology in the partner countries. The latter objective was successfully reached by the participation of 25 scientists from partner countries. About half of 77 attendees were female reflecting the increased role of the women in these fields of research.

The ASI demonstrated once again the commitment of NATO to the peace and the security by facilitating the scientific dialog and cooperation, which was the major outcome of the meeting. It revealed that the top-leading fields of civil science are currently playing and will play also in the future a strategic role to address all emerging security challenges. Furthermore, the ASI exhibited the strength and effectiveness of modern science as a tool for international dialogue and supported the exchange of information and ideas on the recent development of nanoscience and nanotechnology directed to different security challenges. This major message of the event attracted the media, which covered the event in newspapers, on information web pages and on the TV.

We, the members of the Organizing Committee, would like to thank the NATO Science Committee for the financial support for the organisation of the ASI. The local organisation and the publicity of the ASI in the media were actively supported by Mr. Panayot Reyzi, Mayor of Sozopol, whom we gratefully acknowledge.

Group photo of NATO Advanced Study Institute on Advanced Nanotechnologies for Detection and Defence against CBRN Agents

Sofia, Bulgaria — Plamen Petkov
Chisinau, Moldova — Dumitru Tsiulyanu
Kassel, Germany — Cyril Popov
Kassel, Germany — Wilhelm Kulisch
November 2017

Contents

Part I
General Topics

Chapter 1
Roadmapping the Future in Defense and Security: Innovations in Technology Using Multidisciplinary Convergence

Ashok Vaseashta

Abstract Setting priorities in a complex defence environment requires technology assessment, data driven decision support tools, foresight, and roadmapping the future pathways. There are several procedures to deliver a balanced, yet strategic assessment. This report posits roadmapping of revolutionary scientific breakthroughs based on advanced sciences convergence (ASC) in multidisciplinary environments and data analytics platforms. Innovations lead to mapping technology roadmaps which are cautiously formulated based on extensive research, expert elicitation and networking approaches to project "future scenarios" realistically and epistemologically. Such roadmaps enable the development of transformative tools and methodologies that fill fundamental knowledge gaps. Synergy arising from converging technologies and research methodologies will leverage emerging and potentially transformative studies. A "framework by design" of emerging scientific and technological advances and trends is developed through a systematic and strategic planning process to deepen the understanding of current, future, and varying challenges and opportunities and create fully integrated solution pathways to address current and future global issues. Through a systematic introduction of ASC, the methodology exploits future-oriented analytical methodologies, including heuristics, data-mining, scientometrics, modelling and simulation, and scenario development to provide solutions and their potential for integrated, novel and unconventional manifestations.

Keywords Data analytics · Convergence · Roadmap · Defence · Security

A. Vaseashta (✉)
Institute for Advanced Sciences Convergence, and Int'l Clean Water Institute, Herndon, VA, USA

NJCU – State University of New Jersey, NJ, USA
e-mail: prof.vaseashta@ieee.org; prof.vaseashta@nanoknowledge.info

P. Petkov et al. (eds.), *Advanced Nanotechnologies for Detection and Defence against CBRN Agents*, NATO Science for Peace and Security Series B: Physics and Biophysics, https://doi.org/10.1007/978-94-024-1298-7_1

1.1 Introduction

In a conventional defence scenario, the outcome can be predicted by estimating the quantity of the opposing forces and/or by their quality. In the current asymmetric environment, the assumption is not valid. To gain a tactical advantage over the adversaries, it is critical to assess capability, develop scenario planning, learn gaps in capabilities and develop technological capabilities to bridge such gaps. The study presented here outlines systematic and forward-looking methodologies on intelligent ways to support policy makers by using decision support tools, developed using comprehensive analysis. The methodology offers a plausible "designed" future based on sound decisions involving the latest technologies, social dynamics, and foresight that support investment recommendations and implementation of policies that will have significant benefit to the public at large.

Employing emerging scientific and technological advances and trends, a "framework by design" is developed through a systematic and strategic foresight process to extend the understanding of current, future, and varying challenges and opportunities. Technology assessment and data analytics provide fully integrated solution pathways, or roadmaps, to address current and future global issues. Through a systematic introduction of the advanced sciences convergence (ASC), the methodology exploits future-oriented data analytical methodologies, including heuristics, data-mining, scientometrics, modelling and simulation, and scenario development to provide novel solutions in support of the mission. The synergy arising from the convergence of multiple disciplines offers boundless potential for transformational, revolutionary, and embryonic opportunities.

For sake of clarity and continuity, it is instructive to define key terminologies. **Predictive analytics** is an area of statistics that deals with extracting information from data and using it to predict trends and behaviour patterns. Often the unknown event of interest is in the future, but predictive analytics can be applied to any type of unknown whether it is in the present or future. **Technology assessment** is a scientific, interactive, and communicative process that aims to contribute to the formation of public and political opinion on societal aspects of science and technology. **Roadmapping** is creating and delivering strategy and innovation by strategic alignment and dialogue between functions. The power of roadmapping lies in its flexibility, which can provide clarity and alignment of specific needs at all levels, including functional, organization-wide and even collaboration between organizations. **Advanced Sciences Convergence** (ASC) is to understand how advances in different disciplines, and focusing on diverse and discrete problems and applications, can coalesce into an integrated system to solve a seemingly intractable problem. ASC in research methodologies transforms the way research is conducted by overcoming specific barriers or filling existing knowledge gaps.

Moore's law has made the storage and analysis of data scalable, creating opportunities for fine-grained data analytics. New data gathering tools have fostered

precise and customized data management and analysis practical. Multidisciplinary convergence and data analytics have exceptionally high potential for transforming the way state-of-the-art information is gathered, analysed, and leveraged to enable future advances and applications. The idea of "Converging Technologies" in conjunction with data analytics has considerably influenced scientific and social thinking about technological innovation space.

The objective of this investigation was aimed at the use of ASC methodologies to develop automated data mining tools and decision support tools. Three of such decision support tools were developed, viz. automated data analysis, mining and surveillance (ADAMS™), technology foresight and road-mapping (TechFARM™) and New and Emerging Science and Technology Trends and Surveillance (NESTTS™) to provide additional knowledge and databases; they are described in the next section. The objective of such data mining tools is learning technological capabilities and gaps, to provide tactical advantage. A brief overview of these decision support tools is provided later in this contribution.

1.2 Advanced Sciences Convergence and Foresight Modality

Recent advances in science and technology (S&T) have provided the means to study, recognise, control, and even "change by design" transitional characteristics between isolated atoms and molecules, and bulk materials. Various novel materials with remarkable and desired properties have recently been fabricated [1]. Such innovations have occurred in multidisciplinary environments. These advances in conjunction with advances in biotechnology, information technology, cognitive sciences, genetics, and artificial intelligence are employed to develop future-oriented analytical methodologies to provide systematic recognition and evaluation of new or existing S&T solutions and their potential for integrated, novel and/or unconventional approaches to solve new challenges.

The procedure of ASC occurs at the intersection of multiple fields and by persistent monitoring of new and emerging S&T developments. Its outcomes can be described in terms of desired actions or qualities of the eventual system. Multiple approaches, some of which may be high-yield and high-risk research, can be pursued simultaneously to create integral components of the system. Several convergence models employing nanotechnology, biotechnology, information technology, cognitive sciences; along with other fields such as artificial intelligence, genetics and robotics, are evaluated by the scientific community. Innovations occur, in part due to due to reduced dimensionality of nanomaterials, producing unique characteristics [2]. Figure 1.1a maps intersecting trajectories of different disciplines, Fig. 1.1b shows a projection metaphor to show emergence of new and unique applications [3].

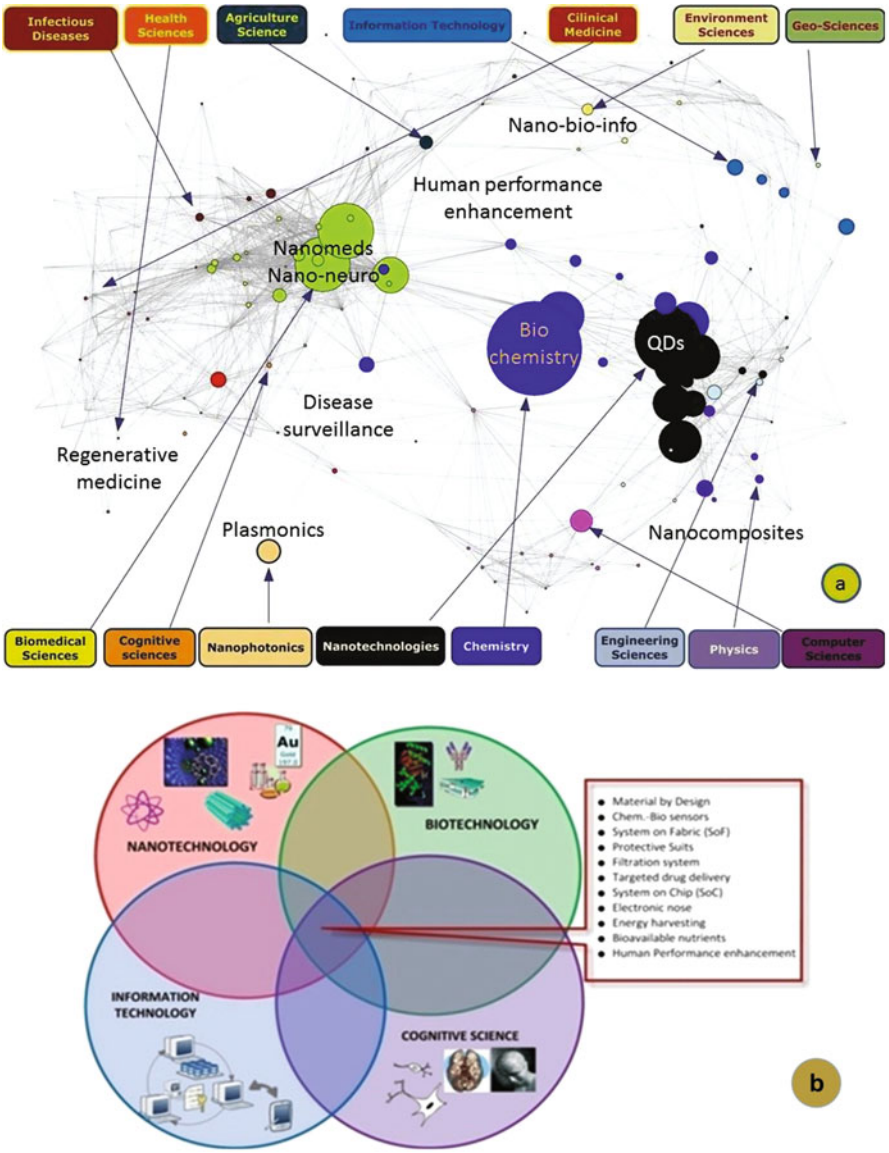

Fig. 1.1 (**a**) Intersecting trajectories of different disciplines; (**b**) projection metaphor showing the emergence of new and unique applications [3]

1.3 Foresight Innovation Pathways Methodology: Data Mining and Predictive Analytics

During the last decade alone, new digital learning technologies have fundamentally altered the practice of conducting research, articulating the path forward for future investments. Notwithstanding this tremendous progress, the synergy arising from ASC offers boundless potential for transformational, revolutionary, and embryonic opportunities. Convergence in research methodologies provide far-sightedness by highlighting the options and existing knowledge gaps. New data gathering tools have fostered precise and customized data management and analysis practices.

To provide strategic assessment of revolutionary scientific breakthroughs in multidisciplinary environments, several data analytics algorithms and their relative applicability are used in literature which are listed in Table 1.1. The objective of an independent investigation was to develop automated data mining tools – such as automated data analysis, mining and surveillance (ADAMS™), technology foresight and road-mapping (TechFARM™) and New and Emerging Science and Technology Trends and Surveillance (NESTTS™) to provide an independent confirmation. A set of specific methodologies used to develop such decision support tools along with specific tools used for this investigation, is briefly described here. It should be noted that such data mining tools, in addition to providing technological capabilities, also unveil technological gaps, allowing us to focus on gaps to achieve desired capabilities.

To explore this modality, a multi-dimensional futures-oriented methodology that identifies and manages emerging and/or disruptive S&T trends has been articulated. The TechFARM™ methodology consists of team brainstorming, expert elicitations, and creating concept maps of potential solution paths. The recommended system evolves through three stages, as shown in Fig. 1.2; it can be described as follows. Stage I: Define topic and review current situation. The preliminary activity begins with extensive environmental scanning coupled with bibliometrics of scientific publications, news and media, books, interviews, and conferences. An assessment of the strengths and weaknesses of the internal capabilities, as well as the threats and opportunities of the external environment, is critical to explore uncertainties rather than repressing them. Stage II: Identify change drivers and select critical drivers. This stage includes strengths and weaknesses of internal capabilities, as well as threats and opportunities of the external environment that cannot be ignored. A comprehensive and systematic assessment, including identification of strategic trends, critical drivers and uncertainties, possible shocks and scenario building, provides legitimacy to the envisioned ideal system. Stage III: Synthesis and recommendation. Specific methods used to develop roadmaps are listed in Table 1.2.

The primary objective of the trend forecasting is to monitor a field of activity to be able to plan the variations that will occur in short or long term. The trend monitoring through competitive intelligence is collecting data. Even more it is watching the environment persistently. When trend monitoring is done, those data must be analysed so that the environment is perfectly known, to be able to forecast the

Table 1.1 Data analytic tools developed and scope [3]

Method	Applicability environment	Rating 1–10[a]
Multiple regression analysis	When two or more independent factors are involved. Widely used for intermediate term forecasting. Assesses which factors to include; can be used to develop alternate models	8
Nonlinear regression	Used for non-linear relationships between variables. Frequently used when time is the independent variable	7
Trend analysis	Uses linear and nonlinear regression with time as the explanatory variable. Used to determine patterns over time	9
Moving average analysis	Forecasts future values based on a weighted average of past values. Easy to update due to simple averages	7
Weighted moving averages	Widely used where repeated forecasts are required. Uses methods like sum-of-the-digits and trend adjustment methods. Very powerful and economical	8
Adaptive filtering	Used for moving averages, this includes a method of learning from past errors. Responds to changes in the relative importance of trend, seasonal, and random factors	7
Exponential smoothing	A moving average form of time series forecasting. Used with seasonal patterns, relatively easy to adjust for past errors. Several different forms are used, depending on presence of trend or cyclical variations. Used to prepare follow-on forecasts and where many forecasts must be prepared	7
Hodrick-Prescott filter	Uses filter mechanism to obtain a long-term trend component in a time series. Reduces a given series into stationary and non-stationary components such that the sum of squares of the series from the non-stationary component is minimal, with a penalty on changes to the derivatives of the non-stationary component	6
Multi criteria decision analysis	Used for providing decision support with numerous and sometimes conflicting evaluations. Provides a compromise in conflicting data. Used for risk assessment and forecasting	6
COTS modeling and simulation	Modeling describes a situation through a series of equations. Allows testing of impact of changes in various factors otherwise time-consuming to construct. Requires user programming or purchase of packages such as SIMSCRIPT. Powerful in developing and testing strategies not otherwise evident	7
Certainty models	Used to predict only the most likely outcome. Used as "what if" analysis – often done with computer-based spreadsheets	6
Probabilistic models	Use Monte Carlo simulation techniques to deal with uncertainty. Provides a range of possible outcomes for each set of events	7

[a]Subjective

trends. Early warning and weak signal detection are parts of a trend forecast. This methodology is used in conjunction with the Thomson Reuters Research Analytics (TRRA) tools to identify significant trends in sciences and to determine research

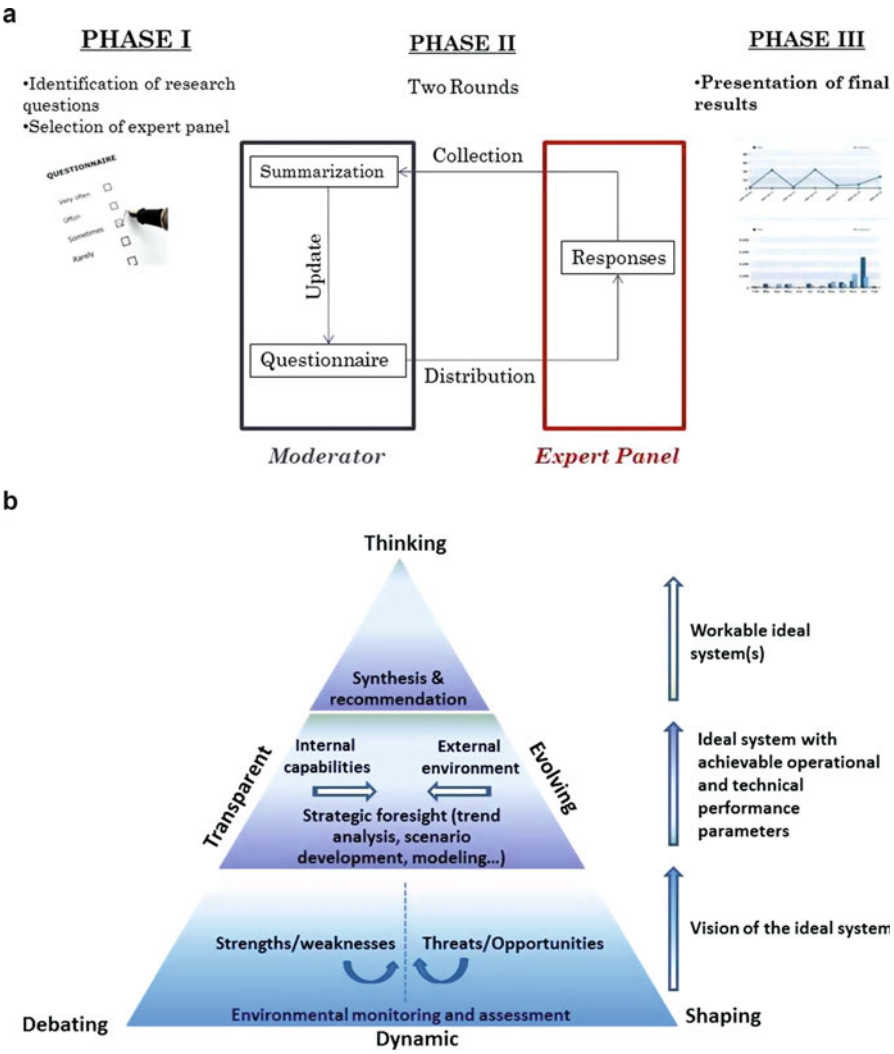

Fig. 1.2 (**a**) Overview of the Delphi expert elicitation process, and (**b**) TechFARM framework

impact in specific fields of research. Bibliometrics (aka scientometrics) applies quantitative evaluation of publication and citation data used in research performance evaluation by different organizations. A series of tools such as InCites, Essential Science Indicators, ResearcherID, ISI Web of Knowledge, and Web of Science® would accelerate the process of identifying leading edge advances in different disciplines [4–7].

Table 1.2 Specific methods used for roadmapping using ASC

NBIC convergence – environmental scanning (current trends/monitor weak signals)
Delphi survey method – expert elicitation/expert technical panels
Robust factor analysis and strategic development
Computerized modelling and dynamic simulation
Technology foresight method
Extrapolation method
Scenarios planning
Social networking – monitor trends and methodologies/virtual meetings
Predictive intelligence

1.4 Monitoring, Surveillance, Roadmapping: Metrics and Indicators

A scientific landscape in conjunction with future studies methodologies would allow metrics-based projections on the direction and pace of scientific innovation and a list of plausible scenarios for the probability of success of such technologies. Explorative methods project future analyses forward from the past or present situation, identifying the past development and status of a given science or technology to postulate its future. In contrast, a normative approach traces backward from a hypothetical future situation to assess likelihood, timing and consequences of a science or technology, thereby identifying a future desired state and determining developments and innovations necessary to reach that future. The full potential of S&T future analysis is realized only where exploratory and normative components are combined in an iterative cycle. Technology road-mapping is an important tool for planning and coordination for governments, organizations, and corporations. It is a specific technique for technology planning, which fits within a more general set of planning activities. Because of technology road-mapping, an organization can make better decisions because it has better information to (a) identify critical needs, (b) determine the technology alternatives, (c) select the appropriate technology alternatives, and (d) generate and implement a plan to develop and deploy appropriate technology alternatives. Technology roadmap (TRM) is driven by a need, not a solution, and hence must have metrics and indicators. Roadmaps are usually visionary and thus make it very difficult to develop goals; however, some of the common metrics and indicators for developing a roadmap are: identifying key problems and the metrics that reflect those outcomes; diagnosing performance issues using metrics; identifying deviations, trends and dynamic changes; preventative and corrective approaches; and goal-setting. The roadmap provided in this report is guided by most of the tools discussed above and conforms to metrics and indicators (Table 1.3).

Table 1.3 Data analytic tools developed and scope [8]

TECH FARM Application No.: 85/287,943 – Research and development of new products of others by providing technology foresight, assessment and forecasting services that apply a future-oriented approach that exploits analytical methodologies, including heuristics, data-mining, scientometrics, modeling and simulation, and scenario development to provide systematic recognition and evaluation of new or existing science and technology solutions for the development of new products and written reports supplied in connection therewith in International Class 42
NESTTS Application No.: 85/287,940 – Research services, namely, providing, tracking, analyzing and projecting new and emerging trends to provide awareness and means to mitigate threats and risks posed by chemical, biological, nuclear, radiological, high-yield explosive materials, and internet and intranet based communications for governments, non-governmental organizations, industries, and academic institutions for defense and security applications in International Class 42
ADAMS: Application No. 85/287846 – The mark ADAMS is an interactive tool that utilizes several data mining tools to analyze, evaluate, and determine emerging S&T trends based on quality of journals, recognition of individual authors and their international stature recognition, validation by heuristics, and other scientific databases to provide normalized and scientifically validated information on emerging trends in science and technologies

Within the framework of the recommendations of data analytics and anticipated characteristics of loading in nanofibers, a spectrum of potential applications was mapped and is represented in Fig. 1.3. The scope of applications considered here are textile for chem.-biological sensing/detection/protection and on-site and on-demand delivery of drugs from the uniform of soldiers in combat theatre. Furthermore, the three tools as described above were used to forecast trends in three specific disciples, viz: nanotechnology, biotechnology, and information technology (Tables 1.4, 1.5, and 1.6).

1.5 Discussion and Path Forward

Using advanced sciences convergence, three such tools are reported here – TechFARM™, ADAMS™ and NESTTS™. These tools have been applied for a specific application – defence and security. Based on a specific set of criteria, the outcome of expectation can be modified by input datasets. The tools were used to identify the evolving asymmetric threat. Implementation of effective counter-measures demands an understanding of transformational emerging sciences, concepts and theories, and their potential applications. Development of integrated solution paths through a revolutionary approach using ASC, presents unique and novel opportunities of identifying effective counter-measures to emerging unconventional threats. While ASC research has much potential in addressing the grand challenges of this century, we must also take a more proactive approach in developing ethical research guidelines and engaging social and legislative experts in ASC research dialogues in the formative years of ASC advancement.

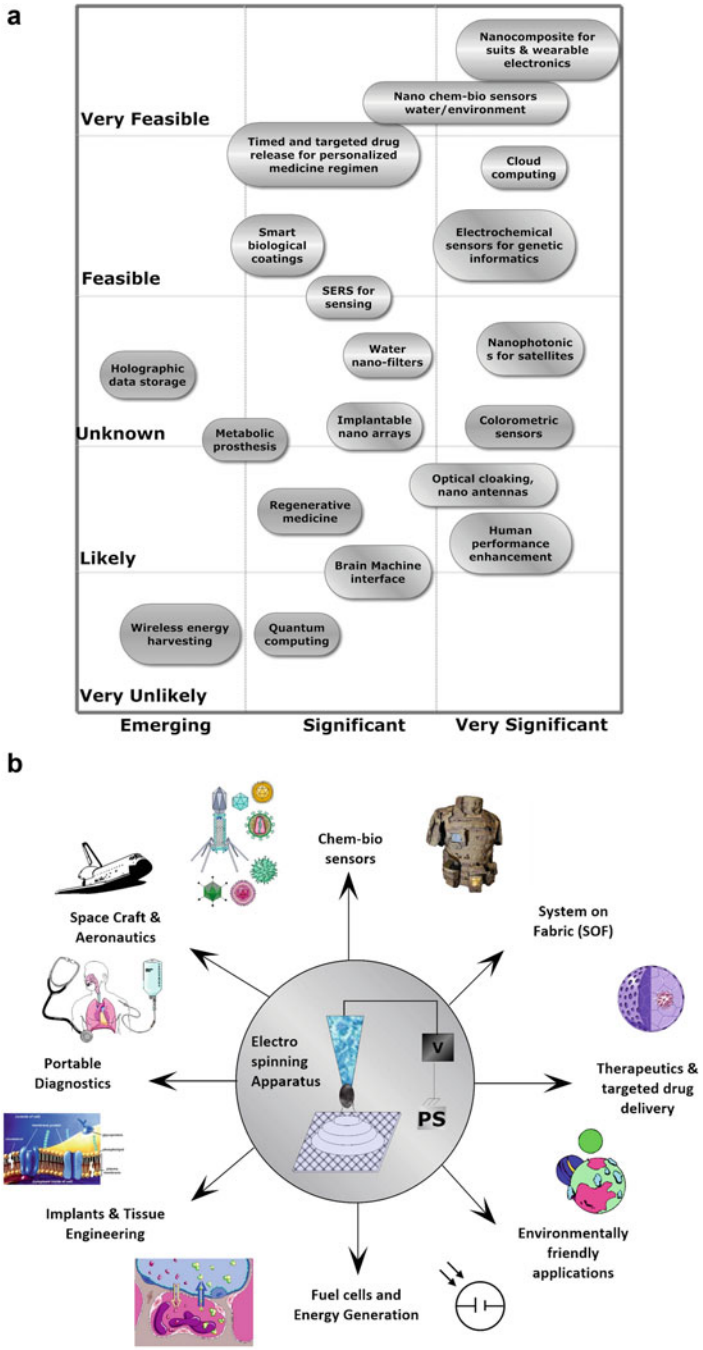

Fig. 1.3 (**a**) Use of nanofibers in information and communications technology; (**b**) spectrum of potential applications [9]

Table 1.4 Trends in nanotechnology

Smart materials with nano films/fibers and structures
Integration of functions and structure in membranes, fabrics, fibers, self-powered biomimetic materials
New environmental leaps in performance: e.g. water filtration and purification, biocidal, bioremediation and decontamination
Nano sensor networks, tracking capacities – nano-electro-mechanical systems
Wearable personalized nano sensors with data and communications capabilities
Energy and power efficiencies improvements, battery power management
Smart dust capability for widespread surveillance capability
Computational devices embedded in consumer and commercial goods
Functional, programmable nanostructures for controlled drug delivery, performance of implants and protheses
New devices, building materials and fabrics that incorporate nano materials based solar power generation and are climate responsive

Table 1.5 Trends in biotechnology

Control, improvements in living organisms
Bio-sensing at the micro and nano level, micro and nano electromechanical systems
Integration with wireless, RFID (radio frequency identification), photonics-molecular level cameras
Tissue engineering, artificial organs, implants and protheses
Targeted drug delivery and use of in vitro capacities
Rapid scalable bio-assays for molecule ID, medical diagnosis and forensics
Personalized medicine using large data sets of patient information, disease statistics, gene sequences and genotypes
Genetically modified insects to counter pathogen carriers
In silico- computer testing and comprehensive modelling for drug characteristics, side effects and receptor simulation – lab on a chip
Molecular recognition – targeted drug delivery to organs, tumours

Table 1.6 Trends in information technology and ambient intelligence

Progress toward ubiquitous information access and integrative ability
Open source collaborative tools and higher peer- to peer functionality, pervasive social networks
Continued migration towards device and functional convergence
Information based 3D models – disease surveillance
Broader object based nodes and networks, Internet of everything (IoT)
Pervasive sensor networks with powerful, dynamic simulation and modelling
Gaming for personal and organizational decisions, risk abatement and learning
Emerging horizons for faster, exponentially more powerful encryption, quantum information
Sustained information markets growth for surveillance, sensor networks, tracking capacities, nano-electromechanical systems
Wearable, implantable personalized micro-nano-bio info sensors with data and communications capabilities

References

1. Vaseashta A, Dimova-Malinovska D, Marshall JM (eds) (2005) Nanostructured & advanced materials. Springer, Dordrecht
2. Vaseashta A (2005) In: Vaseashta A, Dimova-Malinovska D, Marshall JM (eds) Nanostructured materials based next generation devices and sensors, nanostructured and advanced materials. Springer, Dordrecht, pp 1–30
3. Vaseashta A (2010) NUARI annual report (FOUO) – Technology Foresight and Road Mapping (TechFARM), year 1 report of scientific roadmap development – submitted in partial fulfilment of the Advanced Sciences Convergence Study (ASCS), authorized under Contract W911NF-07-D-0001. Delivery Order, Scientific Services Program (SSP) Subcontract Agreement – TCN 09003Defense Threat Reduction Agency
4. Nordmann A (2004) The EU-HLEG report: converging technologies – shaping the future of European societies. http://europa.eu.int/comm/research/conferences/2004/ntw/index_en.html
5. Spence R, Davy B, Dufour P, Lafond R, Leppan W, Woo J (2004) IDRC, biotechnology, and emerging technologies: a basic primer. http://web.idrc.ca/uploads/user-S/1084840901101_Foreword.doc
6. Adlakha-Hutcheon G, Khaydarov R, Korenstein R, Varma R, Vaseashta A (2009) Nanomaterials, nanotechnology: applications, consumer products, and benefits, NATO science for peace and security series c: environmental security, nanomaterials: risks and benefits
7. Vaseashta A (2009) Nanomaterials nexus in environmental, human health, and sustainability, NATO science for peace and security series b: physics and biophysics, silicon vs. carbon. Springer, Dordrecht
8. https://www.uspto.gov/ TM: Application Nos.: 85/287943, 85/287940, 85/287846
9. Vaseashta A, Karagulle N (2018) Loaded nanofibers – force protection, filtration, and decontamination. In: Advanced nanotechnologies for detection and defence against CBRN agents. Springer, Dordrecht, pp 241–252

Part II
Material Preparation and Processing

Chapter 2
Crystalline Thin Layers of $BaTiO_3$ for Gas Sensors Prepared by PLD

Tomáš Kocourek, Miroslav Jelínek, Václav Studnička, and Jan Drahokoupil

Abstract The synthesis of $BaTiO_3$ thin films for gas detectors was studied. Thin layers of $BaTiO_3$ (BTO) were deposited by pulsed laser deposition (PLD) on fused silica and Si (100) substrates using various deposition conditions from a sintered $BaTiO_3$ target. The energy density of a KrF excimer laser was in the range from 2 to 6 Jcm^{-2}. Films were deposited in an O_2 ambient in the range from 10^{-3} to 10 Pa. The films were prepared at substrate temperatures ranging from 500 to 980 °C. Polycrystalline BTO was obtained at substrate temperatures above 670 °C. With increasing deposition temperature above 700 °C the formation of the unwanted rutile phase prevented the growth of perovskite ferroelectric BTO. Concurrently, with decreasing substrate temperature below 670 °C, amorphous films were formed. The layers was characterized by XRD spectroscopy and AFM microscopy. We optimized the depositions condition of the layers for chemical sensors.

Keywords $BaTiO_3$ · Thin layer · PLD · Crystallinity

2.1 Introduction

Barium titanate ($BaTiO_3$ or BTO) is a ferroelectric ceramic material, showing a photorefractive effect and piezoelectric properties. It is used in capacitors, electromechanical transducers and nonlinear optics. This titanate is the best-studied archetypical oxide ferroelectric material with perovskite-structure Ferroelectric crystals have long been employed in optical applications owing to their high transparency,

T. Kocourek (✉) · M. Jelínek
Institute of Physics of the Czech Academy of Sciences, Prague 8, Czech Republic

Faculty of Biomedical Engineering, Czech Technical University in Prague, Kladno, Czech Republic
e-mail: kocourek@fzu.cz

V. Studnička · J. Drahokoupil
Institute of Physics of the Czech Academy of Sciences, Prague 8, Czech Republic

P. Petkov et al. (eds.), *Advanced Nanotechnologies for Detection and Defence against CBRN Agents*, NATO Science for Peace and Security Series B: Physics and Biophysics, https://doi.org/10.1007/978-94-024-1298-7_2

large refraction, and strong linear and nonlinear electro-optic effects in the visible range [1–4]. Modern and future integrated photonic and optoelectronic applications require single-crystal-type epitaxial ferroelectric thin films instead of bulk ferroelectric crystals [5–9]. Although there are a number of ferroelectric oxides with large linear electro-optic coefficients, $BaTiO_3$ has been chosen as the material for thin film. The high-temperature phase is cubic, which enables the deposition of epitaxial layers with relative ease. $BaTiO_3$ also occurs in rhombohedral, orthorhombic, and tetragonal phases.

The aim of our research is the fabrication of layers sensitive to chemical agents suitable for chemical sensing. To this end, the right deposition conditions for $BaTiO_3$ layers have to be found, with the final application in mind. In this paper we focus on crystalline structure determination and on the influence of deposition conditions. The crystalline structure is the main parameter determining the layer properties. Our aim is not to find the most crystalline sample, but the most responsive crystalline structure [10–12].

2.2 Experimental

PLD The $BaTiO_3$ films were prepared by PLD, using a KrF excimer laser (COMPexProTM 205 F, $\lambda = 248$ nm, $\tau = 20$ ns), an energy density on the target of 2, 4, and 6 J/cm^2, a pulse repetition rate of 10 Hz, an oxygen pressure from 10^{-3} Pa (vacuum) to 10 Pa. Thin layers of $BaTiO_3$ were deposited on fused silica (FS) and Si (100) substrates. The substrate temperature was between $T_S = 500$ °C, and 980 °C. The target-substrate distance ($D_{T\text{-}S}$) was also varied (4, 5, 6, and 7 cm).

Morphology The thickness of the layers was measured by an Alpha-step IQ mechanical profilometer (KLA TENCOR Co.), the layer roughness was examined by AFM.

XRD We used XRD in two different arrangements and with two sources: with divergent beam (Bragg Brentano) and with parallel beam configuration. The reason was to find a wider scale of conditions to determine preferred orientations. The first one uses a parallel beam geometry, Cu radiation (0.154056 nm), a detector scan with a stationary sample (rotating around the normal to the surface), and a glazing angle of incidence (GAOI). The second one uses a Bragg-Brentano geometry with a linear X'Celerator detector, and Co radiation ($\lambda = 0.178901$ nm). The samples were inclined by 5° from the ideal position to avoid diffraction from the single crystal substrate. The diffraction patterns were evaluated by Rietveld-like program TOPAS 3 [13–15].

2.3 Results and Discussion

The influence of the following deposition parameters on $BaTiO_3$ growth was examined: substrate temperature during the deposition process, oxygen pressure, laser fluence, and target-substrate distance. The thickness of fabricated layers for X-ray diffraction and AFM was between 500 and 1000 nm.

XRD The comparison of XRD spectra of layers fabricated at different T_S are displayed in Figs. 2.1, 2.2, 2.3, and 2.4. No significant peaks of BTO are present

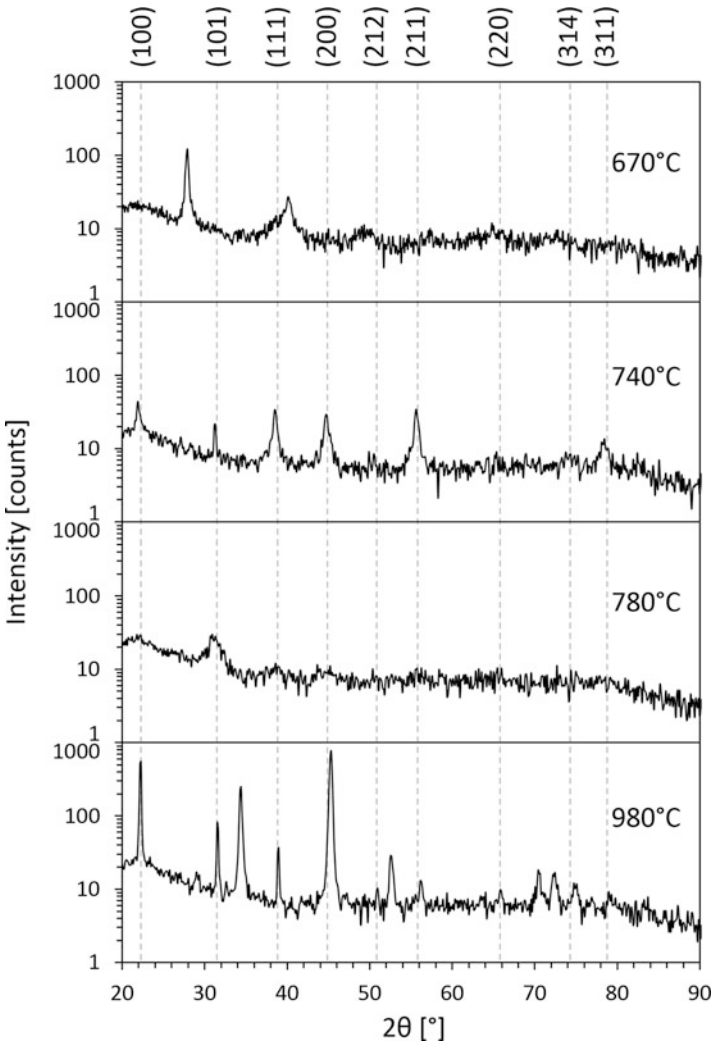

Fig. 2.1 XRD BTO spectra for different T_S for a constant laser fluence of 2 Jcm^{-2}, constant oxygen pressure of 0.5 Pa, and constant $D_{T\text{-}S}$ of 5 cm on FS substrates

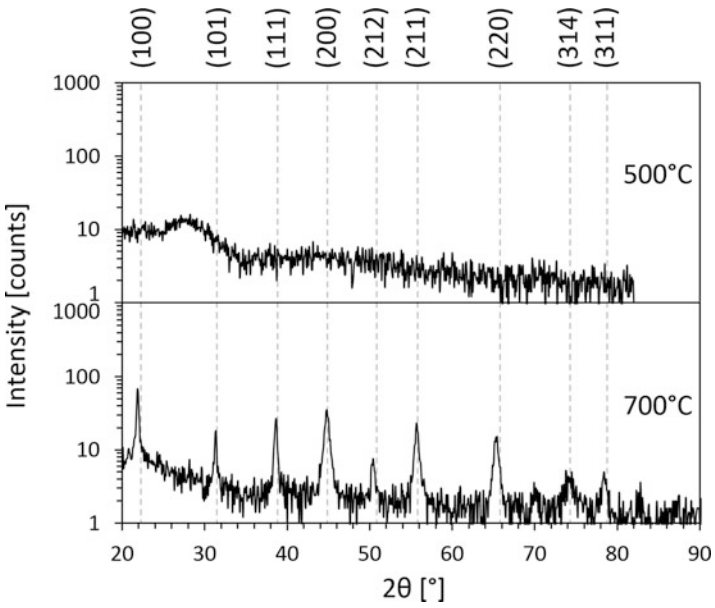

Fig. 2.2 XRD BTO spectra for different T_S for a constant laser fluence of 2 Jcm^{-2}, constant oxygen pressure of 0.1 Pa, and constant $D_{T\text{-}S}$ of 6 cm on FS substrates

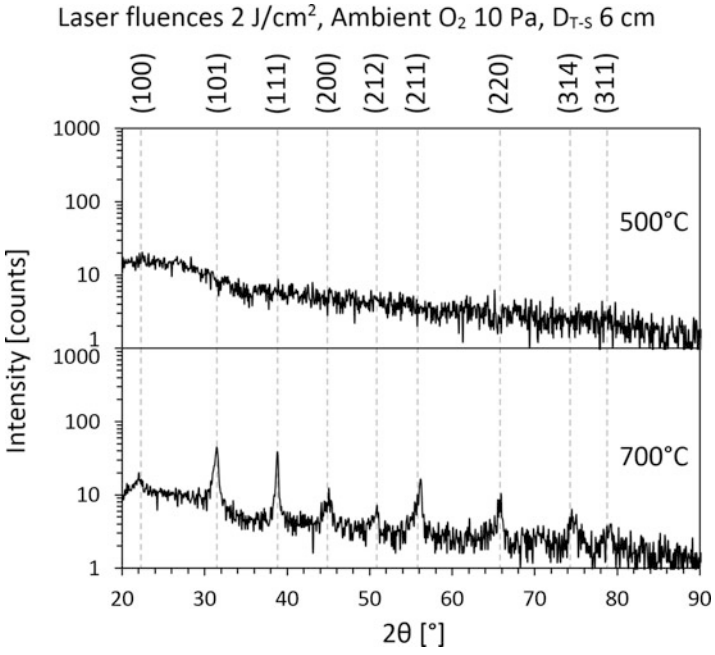

Fig. 2.3 XRD BTO spectra for different T_S for a constant laser fluence of 2 Jcm^{-2}, a constant oxygen pressure of 10 Pa, and constant $D_{T\text{-}S}$ of 6 cm on FS substrates

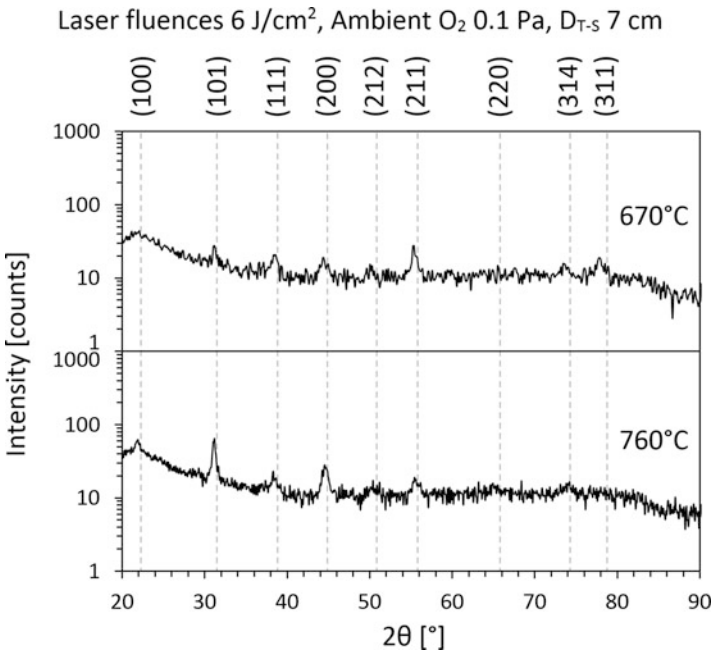

Fig. 2.4 XRD BTO spectra for different T_S for a constant laser fluence of 6 Jcm^{-2}, a constant oxygen pressure of 0.1 Pa, and constant $D_{T\text{-}S}$ of 7 cm on FS substrates

for a laser fluence of 2 Jcm^{-2}, an oxygen pressure of 0.5 Pa, $D_{T\text{-}S}$ of 5 cm, and for T_S lower than 670°. Peaks attributed to BTO start to appear at T_S of 740 °C, but disappear at 780 °C and reappear at 980 °C, but we found several more peaks that we were unable to attribute to any know BTO phase (Fig. 2.1).When the oxygen ambient was decreased to 0.1 Pa and $D_{T\text{-}S}$ increased to 6 cm, the amorphous phase at 500 °C changes to well crystalline at 700 °C. We observe all main peaks, especially the (100) orientation, which is reported to be critical for functioning sensors [10] (Fig. 2.2). With increasing pressure (10 Pa) and otherwise constant conditions (at 700 °C) the peaks still appear but their intensity is lower (Fig. 2.3). The same decrease in peak intensity is observed with the increase of the laser fluence to 6 Jcm^{-2} and $D_{T\text{-}S}$ increase to 7 cm. The signal is weak for both temperatures (Fig. 2.4).

The influence of the oxygen pressure on the XRD spectra is displayed in Figs. 2.5, 2.6, and 2.7. We tested pressure values from high vacuum (10^{-3} Pa) up to 10 Pa. For laser fluence of 2 Jcm^{-2}, T_S of 740 °C, and $D_{T\text{-}S}$ of 5 cm all layers (10^{-3}, 0.5, and 5 Pa) were polycrystalline (Fig. 2.5). With decrease of T_S to 500 °C and an increase of $D_{T\text{-}S}$ to 6 cm the layers were amorphous at 0.1 and 10 Pa (Fig. 2.6).

Well crystalline samples were prepared at T_S of 700 °C and an oxygen pressure of 0.1 Pa. The layers were textured with a strong (100) peak. At an oxygen pressure of 10 Pa the crystalline content was lower (Fig. 2.7).

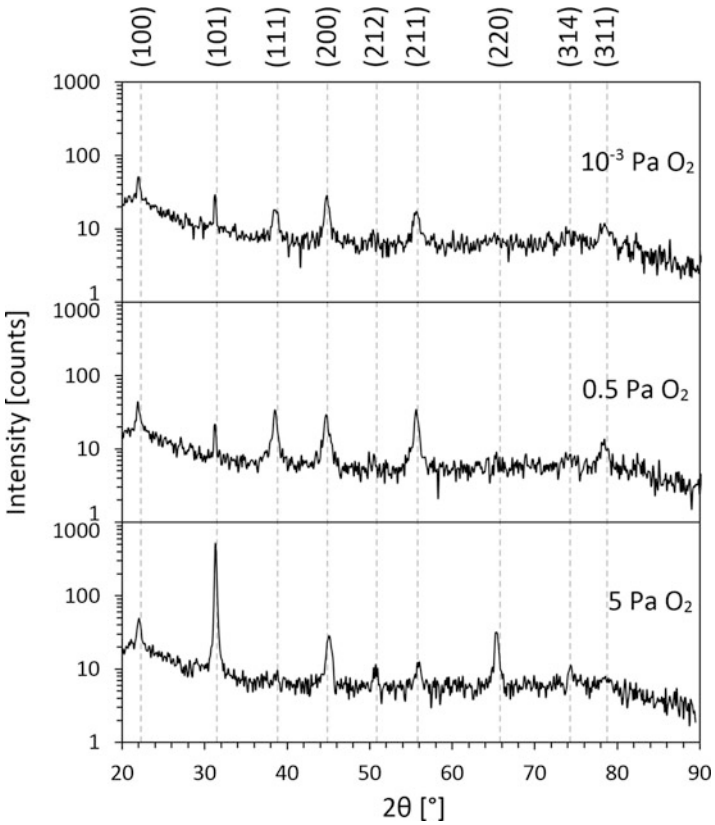

Fig. 2.5 XRD BTO spectra for different oxygen pressures, a constant laser fluence of 2 Jcm^{-2}, a constant T_S of 740 °C, and constant $D_{T\text{-}S}$ of 5 cm on FS substrates

The XRD spectra displayed in Figs. 2.8, 2.9, and 2.10 compare different laser fluences. At $T_S = 670$ °C, 0.5 Pa, and $D_{T\text{-}S} = 5$ cm, crystalline layers were obtained only for a laser fluence of 4 Jcm^{-2} (Fig. 2.8).

At T_S 700 °C, 0.1 Pa and $D_{T\text{-}S} = 6$ cm all layers are polycrystalline, but the highest crystalline content was reached for a laser fluence of 2 Jcm^{-2} (Fig. 2.9). For two best laser fluences $BaTiO_3$ layers were deposited on silicon substrates (Fig. 2.10), where the highest crystalline content was reached.

Varying $D_{T\text{-}S}$ had no significant influence on the crystalline structure for laser fluences of 2 and 4 Jcm^{-2}, at T_S of 780 °C/670 °C and an oxygen pressure of 0.5 Pa. XRD spectra for $D_{T\text{-}S}$ of 4–7 cm are displayed in Figs. 2.11 and 2.12.

From the XRD results optimal deposition conditions can be deduced for $BaTiO_3$ thin layers developed for active detection layer of chemical sensors. The optimal crystalline structure is preferably oriented in (100) and (200) directions. This orientation was reached for samples fabricated at T_S of 700 °C, a laser fluence of 2 Jcm^{-2}, an oxygen pressure of 0.1 Pa, and $D_{T\text{-}S} = 6$ cm.

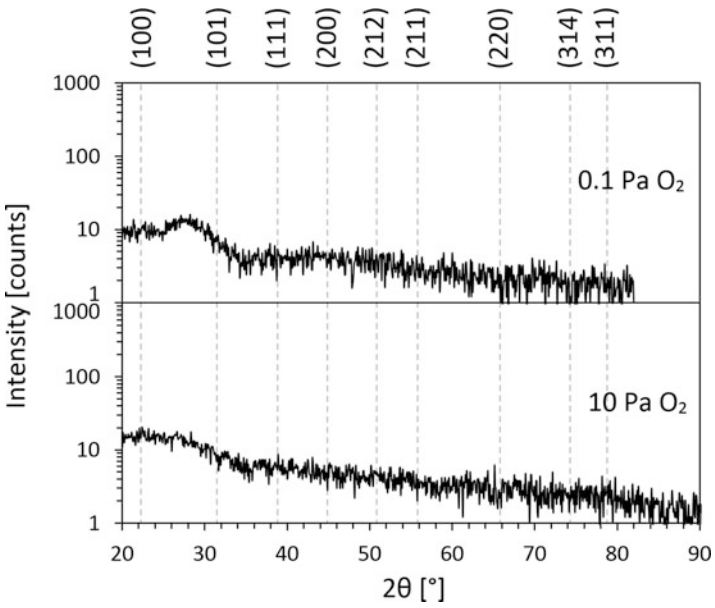

Fig. 2.6 XRD BTO spectra for different oxygen pressures, a constant laser fluence of 2 Jcm^{-2}, constant T_S of 500 °C, and constant $D_{T\text{-}S}$ of 6 cm on FS substrates

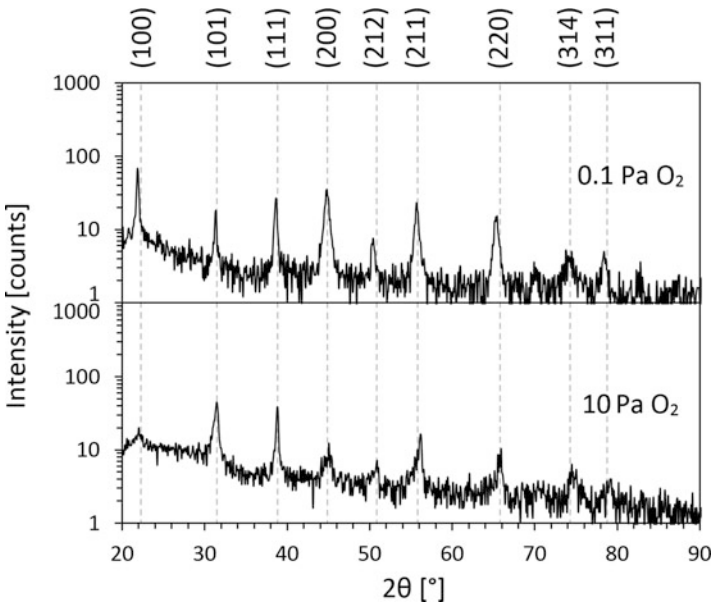

Fig. 2.7 XRD BTO spectra for different oxygen pressures, a constant laser fluence of 2 Jcm^{-2}, constant T_S of 700 °C, and constant $D_{T\text{-}S}$ of 6 cm on FS substrates

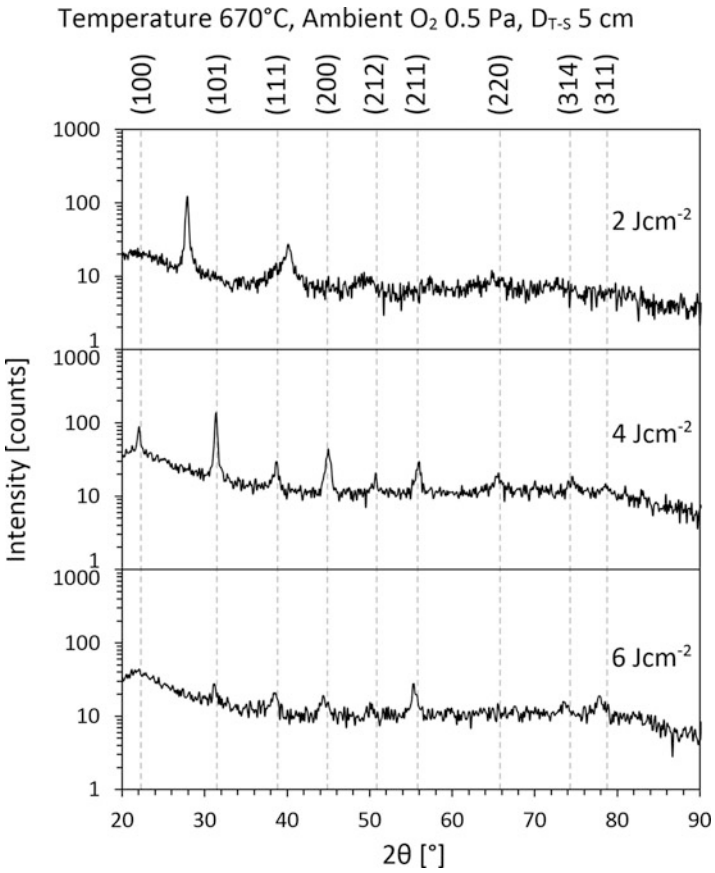

Fig. 2.8 XRD BTO spectra for different laser fluences at constant T_S of 670 °C, constant oxygen pressure of 0.5 Pa, and constant $D_{T\text{-}S}$ of 5 cm on FS substrates

Morphology The layer morphology was measured by AFM. The layer roughness rose with increasing of laser fluence. The characterized samples were fabricated on Si (100) at T_S 700 °C, 0.1 Pa, and $D_{T\text{-}S}$ of 6 cm. For a laser fluence of 2 Jcm^{-2} the layers are smooth with occasional droplets of several hundred nanometers (Fig. 2.13a). For a laser fluence of 4 Jcm^{-2} the surface is rougher with features around 40 nm (Fig. 2.13c). For the highest laser fluence of 6 Jcm^{-2} the surface irregularities reached 80 nm (Fig. 2.13b).

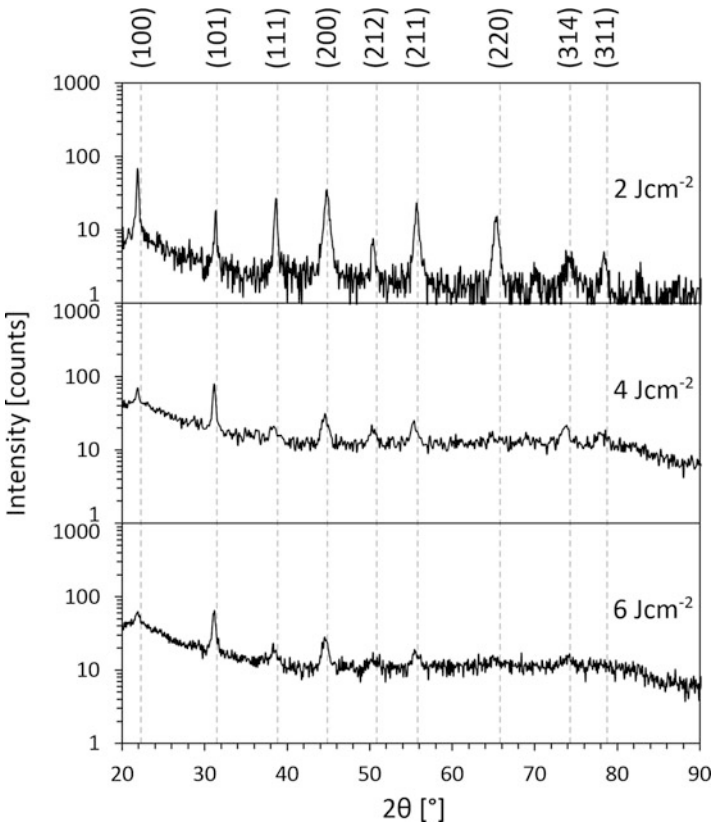

Fig. 2.9 XRD BTO spectra for different laser fluences for constant a T_S of 700 °C, a constant oxygen pressure of 0.1 Pa, and a constant $D_{T\text{-}S}$ of 6 cm on FS substrates

The surface roughness does not pose a problem for chemical sensors based on electrical resistance change, on the contrary it facilitates higher surface area, which mean higher sensitivity. For optical measurements methods it would be needed to prepare smooth and homogeneous layers.

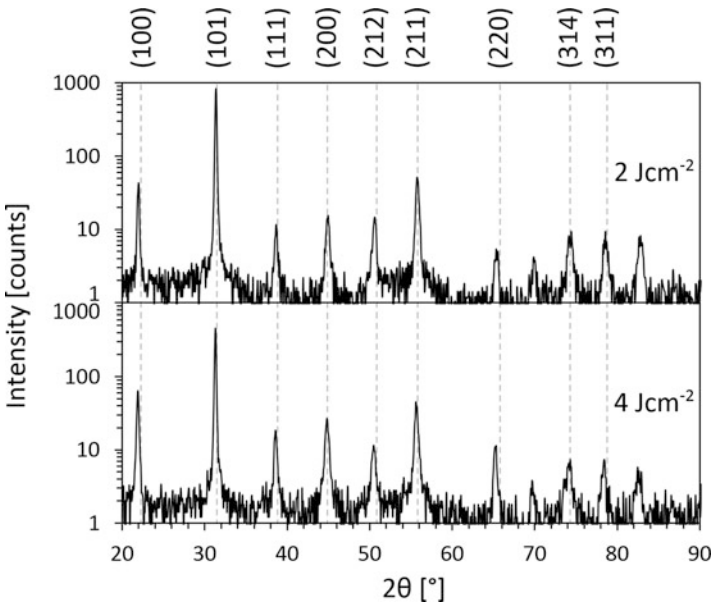

Fig. 2.10 XRD BTO spectra for different laser fluences for a constant T_S of 700 °C, a constant oxygen pressure of 0.1 Pa, and a constant $D_{T\text{-}S}$ of 6 cm on Si (100) substrates

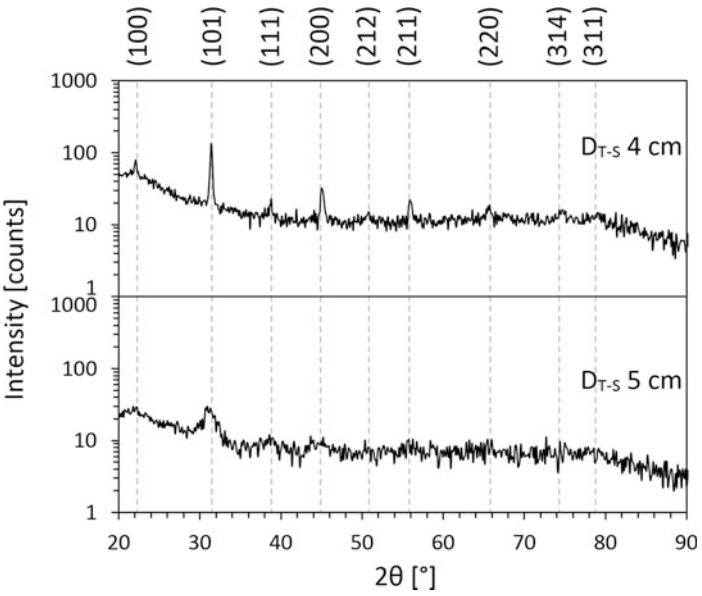

Fig. 2.11 XRD BTO spectra for different $D_{T\text{-}S}$ for a constant laser fluence of 2 Jcm^{-2}, a constant T_S of 780 °C, and a constant oxygen pressure of 0.5 Pa on FS substrates

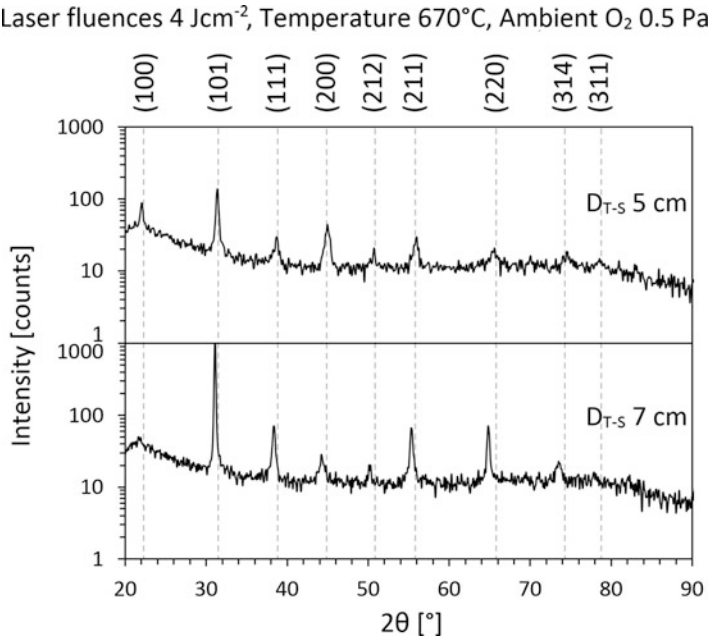

Fig. 2.12 XRD BTO spectra for different $D_{T\text{-}S}$ for constant laser fluence of 4 Jcm^{-2}, a constant T_S of 670 °C, and a constant oxygen pressure of 0.5 Pa on FS substrates

2.4 Conclusion

Our results based on XRD and our application [10, 12] indicate that we can determine the optimal crystalline structure that would be preferably oriented in (100) and (200). This crystalline structure was reached for samples prepared at T_S of 700 °C, a laser fluence of 2 Jcm^{-2}, an oxygen ambient of 0.1 Pa, and $D_{T\text{-}S}$ of 6 cm. Generally, better crystalline structures of $BaTiO_3$ were obtained at higher T_S on FS substrates. Si (100) substrates enhanced this even further. The morphology measured by AFM showed an increase of the roughness with increasing laser fluence. The higher roughness means a higher surface area which increases the sensitivity. In this case, it makes sense utilising laser fluence leading to a little deterioration of the crystalline structure of $BaTiO_3$ thin layers.

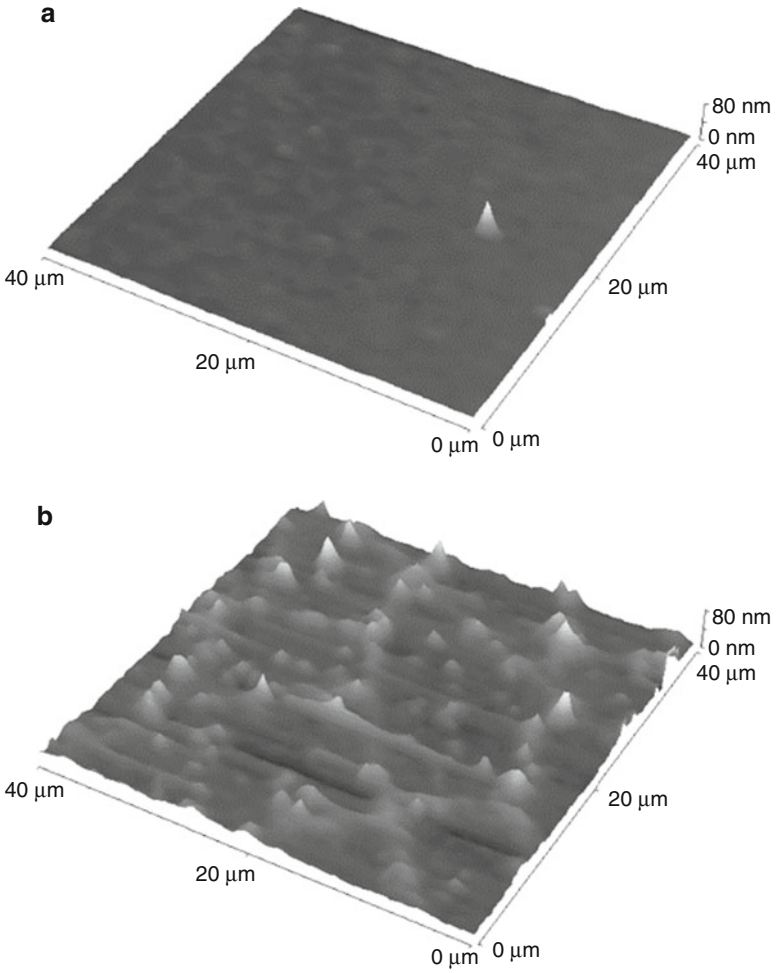

Fig. 2.13 (**a**) Surface morphology measured by AFM – laser fluence of 2 Jcm^{-2}. (**b**) Surface morphology measured by AFM – laser fluence of 6 Jcm^{-2}. All samples: T_S of 700 °C, oxygen pressure of 0.1 Pa, Si (100) substrates. (**c**) Surface morphology measured by AFM – laser fluence of 4 Jcm^{-2}

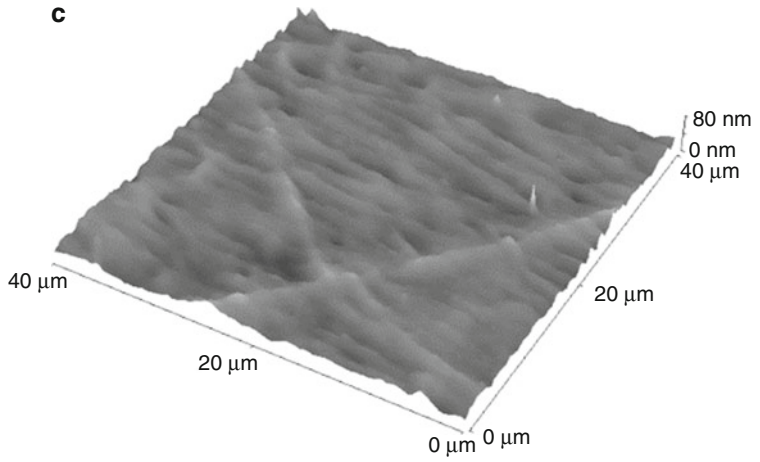

Fig. 2.13 (continued)

Acknowledgments This work has been supported by the Grant Agency of the Czech Republic (No. GA15-05864S) and the Grant Agency of the Czech Technical University in Prague (No. SGS16/190/OHK4/2T/17).

References

1. Chernova E, Pacherova O, Chvostova D, Dejneka A, Kocourek T, Jelinek M, Tyunina M (2015) Strain-controlled optical absorption in epitaxial ferroelectric $BaTiO_3$ films. Appl Phys Lett 106:192903
2. Lines ME, Glass AM (2004) Principles and applications of ferroelectrics and related materials. Clarendon Press, Oxford
3. Ferraro P, Grilli S, De Natale P (eds) (2009) Ferroelectric crystals for photonic applications: including nanoscale fabrication and characterization techniques. Springer, Berlin
4. Boyd RW (2008) Nonlinear optics. Academic, Oxford
5. Wessels BW (2007) Ferroelectric epitaxial thin films for integrated optics. Annu Rev Mater Res 37:659
6. Qin M, Yao K, Liang YC (2008) High efficient photovoltaics in nanoscaled ferroelectric thin film. Appl Phys Lett 93:122904
7. Guo R, You L, Zhou Y, Lim ZS, Zou X, Chen L, Ramesh R, Wang J (2013) Non-volatile memory based on the ferroelectric photovoltaic effect. Nat Commun 4:–1990
8. Dicken MJ, Sweatlock LA, Pacifici D, Lezec HJ, Bhattacharya K, Atwater HA (2008) Electrooptic modulation in thin film barium titanate plasmonic interferometers. Nano Lett 8:4048

9. Abel S, Stöferle T, Marchiori C, Rossel C, Rossell MD, Erni R, Caimi D, Sousa M, Chelnokov A, Offrein BJ, Fompeyrine J (2013) A strong electrooptically active lead-free ferroelectric integrated on silicon. Nat Commun 4:1671
10. Jelínek M, Kocourek T, Flory F, Escoubas L, Mazingue T, Myslík V, Vrňata M, Fryček R, Vysloužil F (2006) Laser-deposited thin films for butane detection. Laser Phys 16(2):217–222
11. Jelínek M, Vaněk P, Tolde Z, Buixaderas E, Kocourek T, Studnička V, Drahokoupil J, Petzelt J, Remsa J, Tyunina M (2017) PLD prepared bioactive BaTiO films on TiNb implants. Mater Sci Eng C 70:334–339
12. Mazingue T, Escoubas L, Spalluto L, Flory F, Jacquouton P, Perrone A, Kaminska E, Piotrowska A, Mihailescu I, Atanasov P (2006) Optical characterizations of ZnO, SnO, and TiO thin films for butane detection. Appl Opt 45(7):1425–1435
13. X.R.D. Software (2016) https://www.bruker.com/products/x-ray-diffraction-and-elemental-analysis/x-ray-diffraction/xrd-software/topas.html
14. Cheary RW, Coelho AA, Cline JP (2004) Fundamental parameters line profile fitting in laboratory diffractometers. J Res Natl Inst Stand Technol 109:1–25
15. Welzel U, Ligot J, Lamparter P, Vermeulen AC, Mittemeijer EJ (2005) Stress analysis of polycrystalline thin films and surface regions by X-ray diffraction. J Appl Crystallogr 38:1–29

Chapter 3
A Comparative Study of the Morphology of Y-Type Hexaferrite Powders Obtained by Sol-Gel Auto-Combustion and Ultrasonic Co-precipitation

Borislava Georgieva, Svetoslav Kolev, Chavdar Ghelev, Tatyana Koutzarova, Daniela Kovacheva, Benedicte Vertruyen, and Raphael Closset

Abstract In recent years, the Y-type hexaferrites have been the object of extensive research related to studying the magnetoelectric effect in the microwave frequency range that is typical for these materials and determines their potential use as microwave absorbers. The morphology of the investigated powders used as fillers in microwave absorbers considerably affects their properties. We present a study on the influence of the preparation technique on the morphology of $Ba_{0.5}Sr_{1.5}Zn_2Fe_{12}O_{22}$ and $Ba_{0.5}Sr_{1.5}Zn_2Al_{0.08}Fe_{11.92}O_{22}$ powders. The powders were synthesized by acetic-acid sol-gel auto-combustion and ultrasonic co-precipitation. The particles of the samples obtained by ultrasonic co-precipitation had an almost perfect hexagonal shape typical for hexaferrites. Al-substitution in $Ba_{0.5}Sr_{1.5}Zn_2Fe_{12}O_{22}$ ($Ba_{0.5}Sr_{1.5}Zn_2Al_{0.08}Fe_{11.92}O_{22}$) resulted in lowering the synthesis temperature.

Keywords Magnetoelectrics · Y-type hexaferrites · Al-substitution · Sol-gel auto-combustion · Ultrasonic co-precipitation

3.1 Introduction

The continuously increasing use of devices operating at microwave (MW) frequencies in our immediate environment, such as radars and wireless andmobile communication equipment, has resulted in a substantial increase in the

B. Georgieva (✉) · S. Kolev · C. Ghelev · T. Koutzarova
Institute of Electronics, Bulgarian Academy of Sciences, Sofia, Bulgaria
e-mail: b.georgiewa@abv.bg

D. Kovacheva
Institute of General and Inorganic Chemistry, Bulgarian Academy of Sciences, Sofia, Bulgaria

B. Vertruyen · R. Closset
Greenmat, Chemistry Department, University of Liege, Liege, Belgium

P. Petkov et al. (eds.), *Advanced Nanotechnologies for Detection and Defence against CBRN Agents*, NATO Science for Peace and Security Series B: Physics and Biophysics, https://doi.org/10.1007/978-94-024-1298-7_3

electromagnetic interference. This has led to the growing requirement for the development of MW absorbing materials reducing the interference, shielding sensitive equipment and minimizing the harmful effects of electromagnetic waves on biological objects [1]. The M-type hexaferrites have long been used as MW absorbers. Recently, however, the researchers' attention turned to the Y-type hexaferrites, since some of them are also magnetoelectrics, while the magnetoelectric effect in the MW frequency range has been the subject of extensive research efforts. This effect in the Y-type hexagonal ferrite $Ba_{0.5}Sr_{1.5}Zn_2Fe_{12}O_{22}$ at room temperature in a low magnetic field (0.1 T) was reported for the first time by Kimura et al. [2]. Chun et al. [3] reported a large magnetoelectric effect in $Ba_{0.5}Sr_{1.5}Zn_2Al_{0.08}Fe_{11.92}O_{22}$, which occurs in a much lower magnetic field.

Most of the studies concerning the Y-type hexaferrites focused on their magnetic and MW properties, which are determined by their microcrystalline structure. The latter is strongly dependent on the preparation technique and the chemical composition of the precursor, on the temperature and duration of the particular high-temperature synthesis, and on the type and degree of substitution. For example, in our recent studies [4] on M-type barium hexaferrites, we found that the needle-like Fe_2O_3 in the precursor leads to incomplete crystallite formation and a non-uniformity of the particles size in the samples. It was shown in [5] that the precursor's type and microstructure substantially affect the $Ba_2Co_{2-x}Zn_xFe_{12}O_{22}$ formation and, consequently, its magnetic and MW characteristics. In turn, the precursor's microstructure is strongly influenced by the method of preparation. On the other hand, the Y-type hexaferrites are complex oxides, which is reflected in the large number of difficulties encountered in the preparation of single-phase samples with homogeneous particles' size and shape. The process of synthesizing Y-type hexaferrites always involves the presence of various accompanying magnetic oxides, the main cause of this being the fact that the temperature interval for Y-phase synthesis is very narrow. Typically, the Y-type hexaferrite phase synthesis begins at 900 °C and ends at 1200 °C [6]. It is, therefore, very important to find methods for synthesis of Y-type hexaferrite particles with a high degree of homogeneity of size and shape. Bearing the above in mind, we concentrated our effort on the Y-type hexaferrites' microstructure as influenced by the preparation technique. In most of the published papers, the polycrystalline powder samples have been obtained by sol-gel auto-combustion, which is a well-known method for synthesis of complex oxides. We present here a comparative study of the microstructure of $Ba_{0.5}Sr_{1.5}Zn_2Fe_{12}O_{22}$ synthesized by citric-acid sol-gel auto-combustion and ultrasonic co-precipitation.The latter technique can be considered as a modified co-precipitation, whereby the precursor particles preparation takes place in a liquid medium under the action of a high-power ultrasound wave causing within a short period of time the formation, growth and implosive collapse of bubbles generated at a temperature of 5000 K and a pressure of 800 atm [7, 8].

Besides the preparation technique, another important factor substantially affecting the hexaferrite's magnetic and MW parameters is the substitution of the magnetic Fe^{3+}cations with non-magnetic cations. The substitution of iron cations with

aluminum ones in $Ba_{0.5}Sr_{1.5}Zn_2Fe_{12}O_{22}$ results in the appearance of a magnetic phase transition at 285 K and of a magnetoelectric effect [9]. Our earlier studies on Al-substituted M-type hexaferrite found that the Al-substitution not only affects the hexaferrite's magneto-crystalline structure, but also leads to the formation of very thin hexagonally-shaped particles [10]. We also discuss here the effect of Al-substitution in $Ba_{0.5}Sr_{1.5}Zn_2Fe_{12}O_{22}$ on the sample's microstructure.

3.2 Experiment

The $Ba_{0.5}Sr_{1.5}Zn_2Fe_{12}O_{22}$ and $Ba_{0.5}Sr_{1.5}Zn_2Al_{0.08}Fe_{11.92}O_{22}$ powders were synthesized by citric-acid sol-gel auto-combustion and ultrasonic co-precipitation.

3.2.1 Sol-Gel Auto-combustion

In this case, the corresponding metal nitrates were used as starting materials, and a citric acid solution was slowly added to the mixed nitrates as a chelator. The citric acid forms stable complexes with the metal cations and prevents their precipitation in the solution. The solution was slowly evaporated to form a gel, which was dehydrated at 120 °C to obtain barium-strontium-zinc-iron citrate or barium-strontium-zinc-aluminium-iron citrate. During the dehydration process, the gel turned into a fluffy mass and was burnt in a self-propagating combustion. The auto-combustion is accompanied by an oxidation-reduction exothermic reaction, with the heat released being sufficient to form an oxide mixture. The as-prepared auto-combusted powders were annealed at 1170 °C for 7 h.

3.2.2 Ultrasonic Co-precipitation

This technique consists in dissolving the corresponding metal nitrates in deionized water and initiating the co-precipitation of metal cations by adding NaOH at pH = 12. High-power ultrasound was applied for 15 min to assist the co-precipitation process. The ultrasonic processor used was Sonics, 750 W. The precursors produced were synthesized at 1170 °C for 7 h.

The $Ba_{0.5}Sr_{1.5}Zn_2Fe_{12}O_{22}$ and $Ba_{0.5}Sr_{1.5}Zn_2Al_{0.08}Fe_{11.92}O_{22}$ powders were characterized by X-ray diffraction with Cu-Kα radiation. Scanning electron microscopy (SEM, Philips ESEM XL30 FEG) was used to determine the size and shape of the particles and the samples' morphology.

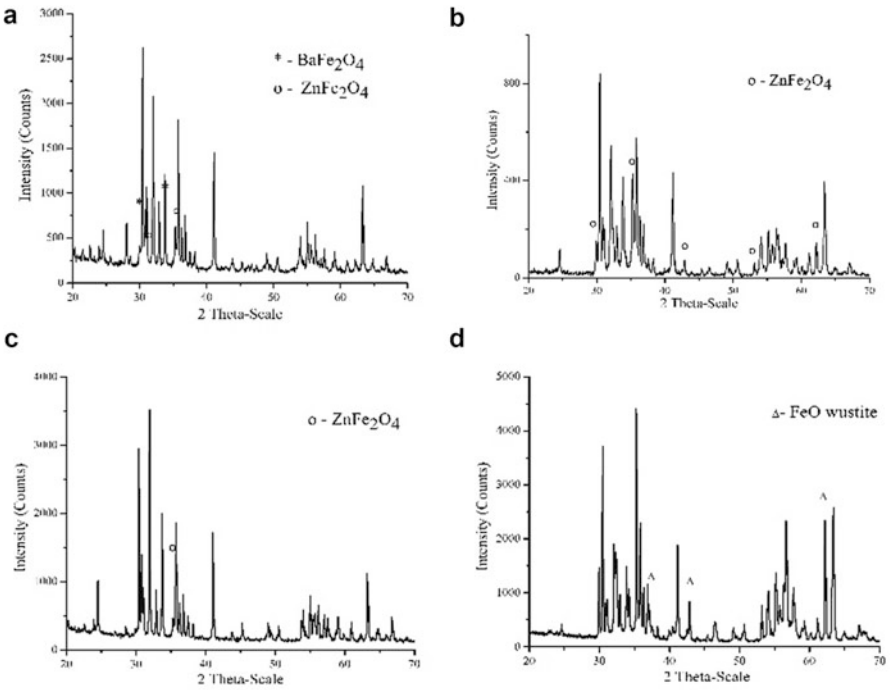

Fig. 3.1 XRD spectra of the powders obtained by sol-gel auto-combustion (**a**) $Ba_{0.5}Sr_{1.5}Zn_2Fe_{12}O_{22}$ and (**c**) $Ba_{0.5}Sr_{1.5}Zn_2Al_{0.08}Fe_{11.92}O_{22}$ and by ultrasonic co-precipitation (**b**) $Ba_{0.5}Sr_{1.5}Zn_2Fe_{12}O_{22}$ and (**d**) $Ba_{0.5}Sr_{1.5}Zn_2Al_{0.08}Fe_{11.92}O_{22}$

3.3 Results and Discussion

The XRD spectra of all synthesized powders showed the characteristic peaks corresponding to the Y-type hexaferrite structure as a main phase. The $Ba_{1.5}Sr_{0.5}Zn_2Fe_{12}O_{22}$ sample obtained by sol-gel auto-combustion contained second phases of $BaFe_2O_4$ and $ZnFe_2O_4$ (Fig. 3.1a).

The sample prepared by ultrasonic co-precipitation contained only $ZnFe_2O_4$ as a second phase (Fig. 3.1b). The XRD spectrum of the $Ba_{0.5}Sr_{1.5}Zn_2Al_{0.08}Fe_{11.92}O_{22}$ powder formed by sol-gel auto-combustion showed some impurity of $ZnFe_2O_4$ (Fig. 3.1c). Unlike all other samples, in the $Ba_{0.5}Sr_{1.5}Zn_2Al_{0.08}Fe_{11.92}O_{22}$ powder prepared by ultrasonic co-precipitation the second phase was FeO (wustite) (Fig. 3.1d).

Figure 3.2 presents the microstructure of the samples. The SEM image (Fig. 3.2a) of the $Ba_{1.5}Sr_{0.5}Zn_2Fe_{12}O_{22}$ sample obtained by auto-combustion shows that the particles were of a very non-uniform shape and well-agglomerated to form clusters of different sizes and shapes.

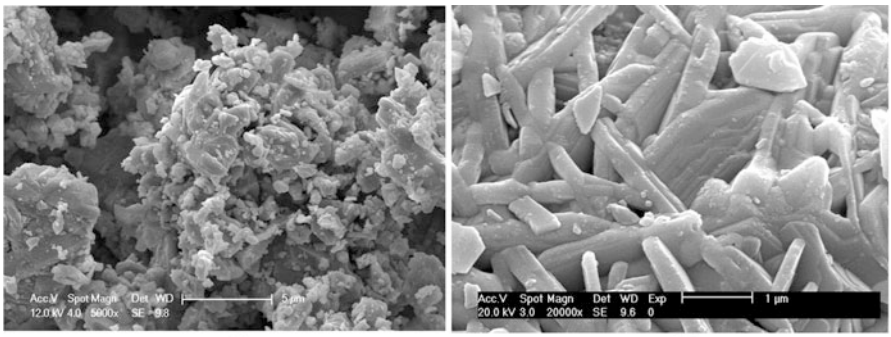

Fig. 3.2 SEM images of $Ba_{0.5}Sr_{1.5}Zn_2Fe_{12}O_{22}$ obtained by auto-combustion (**a**) and by ultrasonic co-precipitation (**b**)

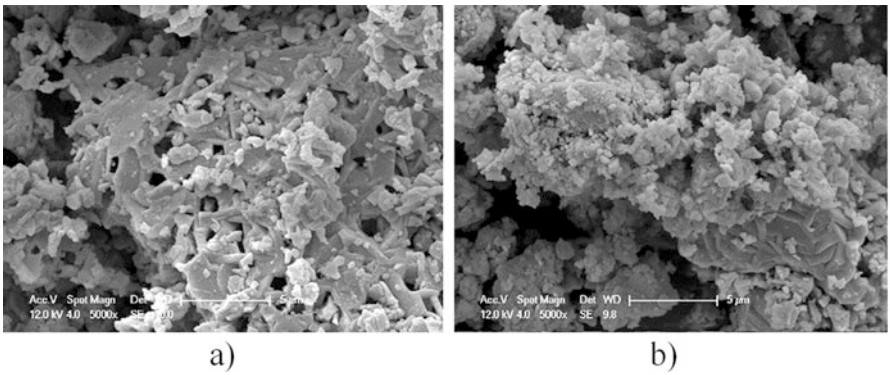

Fig. 3.3 SEM images of $Ba_{0.5}Sr_{1.5}Zn_2Al_{0.08}Fe_{11.92}O_{22}$ obtained by auto-combustion (**a**) and by ultrasonic co-precipitation (**b**)

In contrast, the particles of the sample obtained by ultrasonic co-precipitation had the perfect hexagonal shape typical for hexaferrites (Fig. 3.2b), with a size of 1.2 μm and an average thickness of 168 nm. A three-dimensional grain growth process had taken place, together with co-growth of the particles; small particles of the second phase of spinel $ZnFe_2O_4$ ferrite were also visible.

As seen in Fig. 3.3a, the Al-substitution in the $Ba_{0.5}Sr_{1.5}Zn_2Fe_{12}O_{22}$ led to a melting process at 1170 °C for the sample obtained by auto-combustion. The $Ba_{0.5}Sr_{1.5}Zn_2Al_{0.08}Fe_{11.92}O_{22}$ particles show a hexagonal shape. Small $ZnFe_2O_4$ particles with an irregular shape are again present. The $Ba_{0.5}Sr_{1.5}Zn_2Al_{0.08}Fe_{11.92}O_{22}$ powder obtained by ultrasonic co-precipitation consisted both of particles of various size and shape, and of particles with a completed hexagonal shape (Fig. 3.3b).

3.4 Conclusions

In conclusion, the Al-substitution reduces the amount of second phases in the case of auto-combustion. The different techniques of precursor preparation result in different second phases in the end-product. The SEM images of the samples' morphology demonstrate that the preparation method affects significantly the particles' shape and size, with important implications concerning the magnetic and MW absorption properties of $Ba_{0.5}Sr_{1.5}Zn_2Fe_{12}O_{22}$ and $Ba_{0.5}Sr_{1.5}Zn_2Al_{0.08}Fe_{11.92}O_{22}$.

Acknowledgments B. Georgieva was supported for the synthesis of $Ba_{0.5}Sr_{1.5}Zn_2Fe_{12}O_{22}$ by Contract DFNP-17-159 funded by the BAS under the Young Scientists and Doctoral Students Assistance Program 2017. The work was supported in part by the Bulgarian National Science Fund under contract DN 08/4 "Novel functional ferrites-based magneto-electric structures" and research agreements between WBI, Belgium, and the Bulgarian Academy of Sciences.

References

1. Xing L, Shun-kang P, Xing Z, Li-chun C (2017) Microwave-absorbing properties of strontium ferrites prepared via sol-gel method. Cryst Res Technol 52(5):1700057
2. Kimura T, Lawes G, Ramirez AP (2005) Electric polarization rotation in a hexaferrite with long-wavelength magnetic structures. Phys Rev Lett 94:137201
3. Chun SH, Chai YS, Oh YS, Jaiswal-Nagar D, Ham SY, Kim I, Lee B, Nam DH, Ko K-T, Park J-H, Chung J-H, Kim KH (2010) Realization of giant magnetoelectricity in helimagnets. Phys Rev Lett 104:037204
4. Koutzarova T, Kolev S, Grigorov K, Ghelev C, Nedkov I, Ausloos M, Cloots R, Midlarz T, Zaleski A (2008) Nanosized barium hexaferrite powders obtained by a single microemulsion technique. Solid State Phenom 140:55–60
5. Kim CM, Na E, Kim I, An SY, Wook Seo J, Hur K, Kim H (2015) The effect of precursor types on the magnetic properties of Y-type hexaferrite composite. J Appl Phys 117(17A):507
6. Pullar RC (2012) Hexagonal ferrites: a review of the synthesis, properties and applications of hexaferrite ceramics. Prog Mater Sci 57:1191–1334
7. Manickam S (2011) Sonochemical Synthesis of Oxides and Sulfides. In: Pankaj AM (ed) Theoretical and experimental sonochemistry involving inorganic systems. Springer, Heidelberg, pp 191–211
8. McNamara WB, Didenko YT, Suslick KS (1999) Sonoluminescence temperatures during multi-bubble cavitation. Nature 401:772–775
9. Georgieva BV, Koutzarova T, Kolev S, Ghelev C, Vertruyen B, Closset R, Cloots R, Zaleski A (2016) Study of quasi-monophase Y-type hexaferrite $Ba_{0.5}$ $Sr_{1.5}Zn_2$ $Al_{0.08}$ $Fe_{11.92}$ O_{22} powders. Bull Chem Comm 48(Special Issue G):141–150
10. Peneva P, Koutzarova T, Kolev S, Ghelev C, Vertruyen B, Henrist C, Closset R, Cloots R, Zaleski A (2016) Influence of the preparation methods on the structure and magnetic properties of nanosized Al-substituted barium hexaferrite powders. AIP Conf Proc 1722:220022

Chapter 4
2D Hybrid Si-, Ti-Nanocomposites for Optoelectronic Devices Manufactured by the Sol-Gel Method

G. M. Telbiz, E. Leonenko, G. Gulbinas, and P. Manoryk

Abstract Nanoscale hybrid SiO_2 and TiO_2 films manifest a set of properties beneficial for use in sensors, dye lasers, amplifiers, switching devices, solar cells, and OLEDs. With increasing minuteness of these devices, an accurate and homogeneous material structure is of primary importance. We studied factors influencing the characteristics of thin hybrid film which would help to tune the quality of mesoscale patterned surfaces and to developed a self-assemblying technology based on the sol-gel method to fabricate of high-quality hybrid nanocomposite films using network-forming oxides such as silica or titania. The results obtained are expected to promote the manufacturing of 2D mesoscale surfaces with laser dyes incorporated into host materials and to open opportunities for simpler configurations of optoelectronic and sensor device with improved performances.

Keywords Hybrid film · Rhodamine 6G · Sol-gel · Optical spectra · Luminescence

4.1 Introduction

The scientific and technological interest to mesostructured materials is connected to stable and controlled nanoscale morphologies [1]. These materials would be even more attractive and useful should it prove possible to dope them with some active components in order to produce an enhanced absorption or optical nonlinearity. The main obstacle to the realization of such hybrid materials remains the limited photostability of the confined dyes inside the solid matrix, the resulting fast degradation of the dye molecules and their luminescent properties [2]. Elaboration of such materials promises enhanced properties for their applications such as electronic,

G. M. Telbiz · E. Leonenko (✉) · P. Manoryk
L.V. Pisarzhevsky Institute of Physical Chemistry National Academy of Sciences of Ukraine, Kiev, Ukraine

G. Gulbinas
Center for Physical Sciences and Technology, Vilnius, Lithuania

P. Petkov et al. (eds.), *Advanced Nanotechnologies for Detection and Defence against CBRN Agents*, NATO Science for Peace and Security Series B: Physics and Biophysics, https://doi.org/10.1007/978-94-024-1298-7_4

optoelectronic and photovoltaic devices, chemical and biosensors. To this aim, the chromophore guest should be stable in different environments, small enough to ensure a good biocompatibility and show high fluorescence yields. Nevertheless, the preparation conditions might induce interactions between dye molecules causing their aggregation and hence the quenching of the fluorescence signal. Sometimes extreme acid or basic conditions could damage the dye causing a loss of the sensing ability of the dye. The key problem in application hybrid film as photonic materials is to fix the organic guests into the matrix in order to minimize the self-assembly aggregation process between individual dye molecules to stabilize the optical properties of the material. We studied factors strongly influencing the characteristics of thin hybrid films which would help to tune the quality of surface and bulk, developing the self-assemblying technology based on the sol-gel method to fabricate high-quality hybrid nanocomposite films using network-forming oxides such as silica or titania that allows to variate different types of inclusions [3–5].

Here we present the analysis and comparison of the optical characteristics of dye molecules self-organized in the bulk of mesostructured silica thin films. Samples with different concentration of the dye were prepared by the sol–gel method as homogeneous and transparent films deposited by spin- and dip-coating on the substrates.

4.2 Experimental

Colored mesostructured SiO_2 films were prepared by the template sol–gel technique using a precursor material composed of matrix tetraethoxysilane or titanium (IV) butoxide, ethanol, distilled water, HCl and Pluronic P123 (1:8:2:0,5:0,01 molar ratios) and dye. This sol composition has proven to yield good quality SiO_2 coatings [6]. The precursors was dissolved in the ethanol using magnetic stirring for 15 min. For preparation of the starting composition, 0,003–0,72 g of Rhodamine 6G (Rh6G) was dissolved in 10 ml sol. The dye concentration was in the range of $6 \cdot 10^{-4}$ to $1.5 \cdot 10^{-1}$ mol/l. This solution was mixed at 60 °C for 120 min to form a sol that was used in all of the following operations. The colored films were obtained on various substrates (glass, mica, silica) using a hand-made spin coating apparatus and various rotation speed (1500–2500 min^{-1}). A standard procedure of substrate processing (cleaned in hot chromic mixture), followed by a rinse with distilled water) was adopted before coating. After that the coatings films were dried at ambient temperature for a 48 h at atmospheric air conditions. The coating thickness measured by atomic force microscopy (AFM) was 200–800 nm.

The optical (absorption and transmission) spectra were measured at room temperature with a Specord PC 210 spectrophotometer. Steady state photoluminescence spectra were measured with a Hitachi MPF-4 [7]. The surface relief and thickness of the films was revealed by AFM using a NanoScope D 300.

4.3 Result and Discussion

In designing the films for optical applications, a number of factors need to be taken into account. Most important is the ability of the film matrix to effectively solubilize relatively high concentrations of the dye molecules. Such high concentrations are necessary for the films to exhibit appreciable absorbance, even when their thickness is only 150–300 nm. Under the assumption that the molecules are not effectively dispersed within the host matrix, the optical as well as the physical properties of the films tend to be negatively influenced. For example, broadening of the dye's absorption band, loss of its intensity, and a decrease of light transmission through the film are some of the adverse effects that might result. The method of production and the optical and physico-chemical quality of the resultant films are the essential factors to be considered when deciding upon the film composition. Film fabrication needs to be conducted with relative ease using proven deposition techniques such as dip-, or spin-coating. This would allow to obtain film containing a variety of dyes with different concentrations and desired optical properties.

On the Fig. 4.1 compares the absorption spectra of the mesostructured silica and titanium dioxide thin films. The spectra of the SiO_2/P123 and TiO_2/P123 films have absorption maxima at approximately 505, 537 nm and 510, 542 nm, respectively. The lower wavelength maximum between 505 and 510 nm is known to correspond to absorption by the H-form of the Rh6G dimer [8, 9]. The main absorption peak, with a maximum between 530 and 540 nm, corresponds to absorption by the free R6G monomer. Note that aggregates of Rh6G are known to suppress fluorescent emission, and are therefore undesirable in the context of amplified spontaneous emission. The spectra demonstrate that the ratio of dimer to monomer for TiO_2 is significantly lower than for a SiO_2 matrix. The results strongly suggest that the optical properties of the dye molecules in solid matrices depend on the physico-chemical properties of the matrix (i.e., polarity, refractive index, acidity, etc.), but also on host-guest interactions, affecting the distribution and orientation of the dye molecules in the host material, as well as on the dye-dye interactions, responsible for dye aggregation.

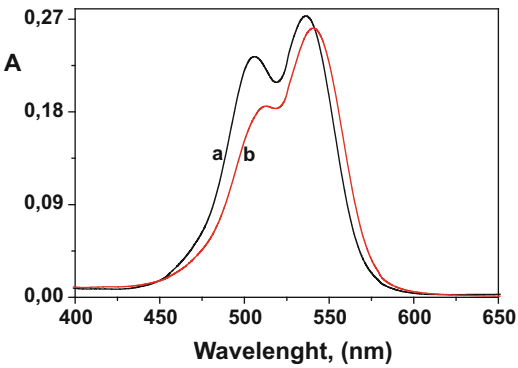

Fig. 4.1 Selected absorption spectra of (**a**) Rh6G doped P123/SiO_2 and (**b**) P123/TiO_2 sol-gel films

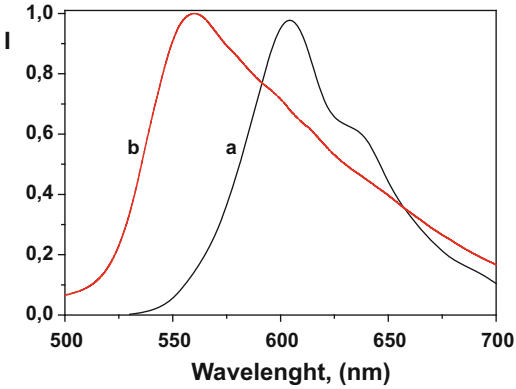

Fig. 4.2 Selected normalized fluorescence spectra of (**a**) Rh6G doped P123/SiO_2 and (**b**) P123/TiO_2 sol-gel films

Figure 4.2a, b compares the selected fluorescence spectra of Rh6G-doped mesostructured silica and titanium dioxide thin films measured by excitation at $\lambda_{ex} = 480$ nm. The spectra had been normalized to the peak emission for clarity. The fluorescence spectrum of the hybrid SiO_2 film (Fig. 4.2a) is broadened, and a shoulder in the spectrum is observed. The broadening of the band is rather due to the presence of H-type dimer aggregates, confirmed by the appearance of the shoulder in the spectrum of this film. Moreover, the appearance of a band with the maximum at ~600 nm can be interpreted as fluorescence of "sandwich"-type aggregates exclusively. This observation is in good accordance with literature data, where broadening of the emission band is characteristic for the formation of fluorescent aggregates with "head to tail" geometry. Furthermore, the asymmetric shape of the spectral band is clearly the result of a high concentration of H- and J- dimers coexisting within the mesostructured film. Since the H- and J-type aggregates possess exciton states whose energy levels lie below the monomer S1 state, they can serve to quench the fluorescence through an energy transfer process.

For Rh6G immersed in the TiO_2 matrix (Fig. 4.2b), the spectrum shows that the emission is broadened which is accompanied by a red shift of the maxima when the concentration is increased. The spectral broadening can be assigned to increased re-absorption and subsequent re-emission and at longer wavelengths interpreted as fluorescence of aggregate with high dye concentration as it was previously attributed to aggregate fluorescence at elevated RhG6 concentrations in certain solvents [10, 11]. The occurrence of an FL band at 610 nm in the spectrum was also associated by other authors [12] to Rh6G aggregates; these low-energy emissions appear at large dye concentrations. Thus, we have a distribution of dimers, corresponding to two extreme configurations, which we attribute to sandwich H-type dimers and head-to tail J-type aggregates.

In the tested regime [13], we had shown the ability of hybrid films for application as photonic layer in all-optical time-to-space converters. We have recorded the response a

dynamic grating in a single-pulse regime. A giant value of the nonlinear optical susceptibility was observed experimentally: $\chi^{(3)} = \approx 8.6 \cdot 10^{-7}$ esu $\approx 8.6 \cdot 10^{-15}$ m^2 V^{-2}.

The hybrid sol-gel films (Ti- or Si based) were studied as waveguide laser medium under transverse optical pumping. The threshold one-mode oscillation for two different configurations of planar asymmetrical waveguides has been discovered and investigated. We assumed that gain-narrowing is attributed to amplified spontaneous emission which results from the homogeneous distribution of highly doped dye molecules within the microchannels of the arrays. The pumping threshold values for the respective (Ti, Si) mesostructured waveguides are different from each other. In case of a TiO_2 matrix, a value of the pumping intensity reduced by almost two orders compared to a SiO_2 matrix is observed.

4.4 Conclusion

The development of a simple sol-gel based method for the production of high quality inorganic/organic mesostructured SiO_2 and TiO_2 composite films doped with Rh6G were studied. The comparison of the concentration dependent evolution of absorption and emission profiles of both types of matrices reveals the presence of luminescent aggregates. The observed optical and fluorescence spectra show the ability of dispersion and controlled aggregation of Rh6G molecules, owing to the time-delay of their spontaneous transformation and mesoscopic ordering during the formation of the hybrid sol-gel films. The formation of fluorescent aggregates can most probably be promoted by the presence of the amphiphilic triblock copolymers which favor the formation of hybrid micelles and by the excited state of the CT complex within hybrid micelles between dye and the surrounding Pluronic molecules. Alteration of the optical properties of the films and the exited state dynamic of Rh6G affected the exiton dynamic of H-type aggregates and makes this film a good candidate for producing photonic materials for laser action from micron-scaled devices. Variation of values of refractive index, absorption coefficient and optical conductivity can be evidence of various spatial organizations of dye molecules within the body of generated films, subject to method of deposition on substrates.

We demonstrated their possibility for use in modern optoelectronic and optical devices. It was shown that the unusually spectral-luminescence properties can be explained by the conditions of spatial organization and controlled self-organization (aggregation) of dye molecules in the formation process of the hybrid films.

Acknowledgment The authors deeply thank Dr. M. Dvoynenko (Institute of Semiconductor Physics NASU, Kiev) for kindly help in fluorescence measurements and useful discussions.

References

1. Wirnsberger G et al (2001) Mesostructured materials for optical applications: from low-k dielectrics to sensors and lasers. Spectrochim Acta Part A 57:2049
2. López Arbeloa F et al (2001) Handbook of advanced electronic and photonic materials and devices, vol 7, p 209
3. Hayward R et al (2001) The current role of mesostructures in composite materials and device fabrication. Microporous Mesoporous Mater 44–45:619
4. Wu Y et al (2004) Composite mesostructures by nanoconfinement. Nat Mater 3:816
5. Yang Y et al (2004) Laser properties and photostabilities of laser dyes doped in ORMOSILs. Opt Mater 24:621
6. Kazakevičius A et al (2015) Insight into the mechanism of enhanced rhodamine 6G dimer fluorescence in mesoscopic pluronic-silica matrixes. J Phys Chem C 119:19126
7. Telbiz G et al (2010) Effect of nanoscale confinement on fluorescence of MEH-PPV/MCM-41. Phys Status Solidi A 207:2174
8. Carbonaro C et al (2009) Light assisted dimer to monomer transformation in heavily doped rhodamine 6G-porous silica hybrids. J Phys Chem B 113:5111
9. Malfatti L et al (2008) Aggregation states of rhodamine 6G in mesostructured silica films. J Phys Chem C 112:16225
10. Lewkowicz P et al (2012) Concentration-dependent fluorescence properties of rhodamine 6G in titanium dioxide and silicon dioxide nanolayers. J Phys Chem C 116:12304
11. Vogel R et al (2002) Dimer-to-monomer transformation of rhodamine 6G in aqueous PEO-PPO-PEO block copolymer solutions. Macromolecules 35:2063
12. Palomino-Merino R et al (2007) Photoluminescence of rhodamine 6G-doped amorphous TiO_2 thin films grown by sol–gel. Vacuum 81:1480
13. Telbiz G et al (2015) Ability of dynamic holography in self-assembled hybrid nanostructured silica films for all-optical switching and multiplexing. Nanoscale Res Lett 10:196

Chapter 5
Surface Plasmon Resonance Band of Ion-Synthesized Ag Nanoparticles in High Dose Ag:PMMA Nanocomposite Films

T. S. Kavetskyy, M. M. Kravtsiv, G. M. Telbiz, V. I. Nuzhdin, V. F. Valeev, and A. L. Stepanov

Abstract Characterization of nanocomposites prepared by Ag ion implantation into polymethylmethacrylate (PMMA) at different doses (2.5×10^{16}, 1.0×10^{17}, and 1.5×10^{17} Ag^{+}/cm^{2}) with a constant energy of 30 keV and a current density of 1 μA/cm^{2} in order to prepare Ag nanoparticles (NPs) was performed by UV-Vis spectroscopy. For the first time an absorption band at a wavelength of 355 nm for the highest dose sample was observed experimentally. Changes of size and filling factor of Ag NPs in the near-surface region of ion-implanted polymers are suggested to explain this result. However, further verification is needed with more informative technique such as, for example, slow positron beam spectroscopy to probe near-surface nanometer size depth profiles.

Keywords Polymers · Ion implantation · Nanocomposite films · Surface plasmon resonance · Metal nanoparticles · Optical spectroscopy

T. S. Kavetskyy (✉)
Drohobych Ivan Franko State Pedagogical University, Drohobych, Ukraine

The John Paul II Catholic University of Lublin, Lublin, Poland

M. M. Kravtsiv
Drohobych Ivan Franko State Pedagogical University, Drohobych, Ukraine

G. M. Telbiz
L.V. Pisarzhevsky Institute of Physical Chemistry National Academy of Sciences of Ukraine, Kiev, Ukraine

V. I. Nuzhdin · V. F. Valeev
Kazan Physical-Technical Institute of RAS, Kazan, Russian Federation

A. L. Stepanov
Kazan Physical-Technical Institute of RAS, Kazan, Russian Federation

Kazan Federal University, Kazan, Russian Federation

Kazan National Research Technological University, Kazan, Russian Federation

P. Petkov et al. (eds.), *Advanced Nanotechnologies for Detection and Defence against CBRN Agents*, NATO Science for Peace and Security Series B: Physics and Biophysics, https://doi.org/10.1007/978-94-024-1298-7_5

5.1 Introduction

Understanding how the size, shape, and aggregation state of silver nanoparticles (NPs) are changed after integration into a target matrix is critical to enhance their performance in application, including molecular diagnostics, photonics and biomedical devices, and to take advantage of the novel optical properties of these nanomaterials. In particular, nanocomposites containing noble metal NPs dispersed in the polymer matrix prepared by high-dose ($>10^{16}$ ions/cm^2) implantation at low-energy ions (<100 keV) can be used for the construction of plasmonic waveguides [1] and diffraction gratings [2]. Typically, form and size of Ag NPs in optically transparent matrices are related an appearance of a surface plasmon resonance (SPR) band in the visible absorption spectra of the composite. However, synthesis of Ag NPs by ion implantation in transparent polymer matrices such as PMMA has been found [1] to be quite unusual. In the present work, characterization of nanocomposites prepared by Ag ion implantation of PMMA at different doses was performed by UV-Vis spectroscopy.

5.2 Experimental

Ion implantation into PMMA substrates was performed in vacuum under a pressure of 10^{-5} Torr at room temperature with an ILU-3 ion accelerator [1–5]. 1.2-mm-thick polymer plates with high optical quality and transparency in a wide spectral range (400–1000 nm) were used. Ion-implanted PMMA nanocomposites layers (Ag:PMMA) were fabricated with an energy of 30 keV, an ion current density of 1 μA/cm^2 and doses of 2.5×10^{16}, 1.0×10^{17}, and 1.5×10^{17} Ag$^+$/cm^2 (all doses sufficient for the formation of Ag NPs [1]). UV-Vis absorption measurements were performed with a SHIMADZU UV-2700 UV-Vis spectrophotometer.

5.3 Results and discussion

Figure 5.1 shows the absorption spectra for the high-dose Ag:PMMA samples. An absorption band at $\lambda_{max} = 355 \pm 5$ nm for the highest dose (1.5×10^{17} Ag$^+$/cm^2) sample was observed.

Absorption bands below 400 nm were earlier seen in transmission spectra of Ag:PMMA with dose of 1.0×10^{17} Ag$^+$/cm^2 (but not with dose of 1.5×10^{17}) [2]. It is assumed that the absorption band at 355 nm for the highest dose sample is due to the possible changes in size and filling factor of Ag NPs in the near-surface region of ion-implanted Ag:PMMA in agreement with the basic principles of metal nanoparticles formation by ion implantation as shown in Fig. 5.2 [1]. In order to verify this conclusion further research with other proper techniques is needed.

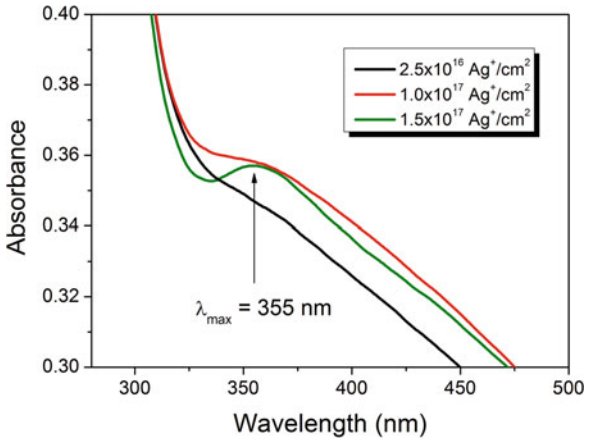

Fig. 5.1 UV-Vis absorption spectra for the irradiated Ag:PMMA samples with different doses

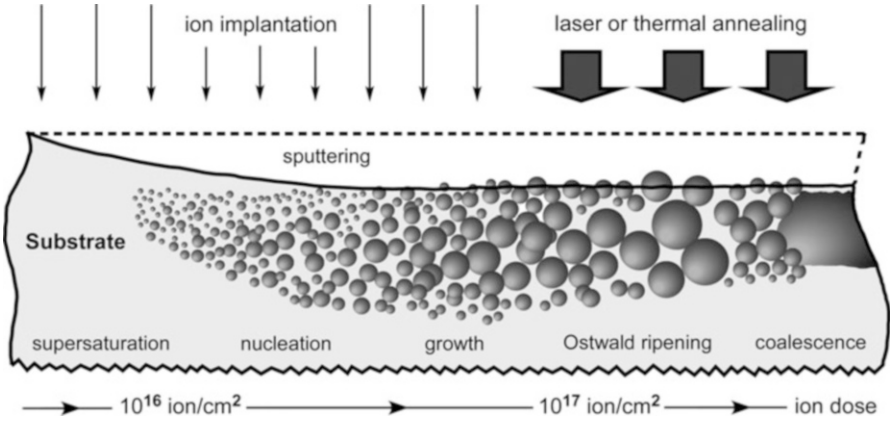

Fig. 5.2 Basic principles of nanoparticles formation by ion implantation

It must be mentioned here that the synthesis of Ag NPs by ion implantation in PMMA is quite different from that detected for SiO_2 glass [6]. So, in PMMA an unusual weak and very broad SPR band with a maximum at ~500 nm has been observed for Ag NPs, in contrast to the sharp and narrow SPR band at ~450 nm of Ag NPs in SiO_2. Some plasmonic features in Ag:PMMA have been explained [1, 6] in the framework of a carbonization of the ion-irradiated polymer and, simultaneously, with a formation of carbon-shell Ag-core nanoparticles. Moreover, it has been concluded that the size of Ag-core NPs increased as the ion dose rises. At the same time, there are some difficulties to experimentally estimate the NPs sizes directly from optical absorption for Ag:PMMA [1, 6, 7].

Figure 5.3 shows a schematic presentation of carbon-shell silver-core nanoparticles with suggested possible changes of size and filling factor of Ag NPs in the near-surface region of ion-implanted Ag:PMMA for the highest dose sample (1.5×10^{17} Ag^+/cm^2). This assumption should be further confirmed by slow positron

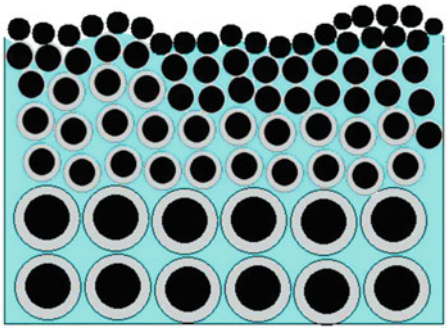

Fig. 5.3 Schematic presentation of carbon-shell silver-core nanoparticles with suggested possible changes of size and filling factor for the highest dose (1.5×10^{17} Ag^{+}/cm^{2}) Ag:PMMA

beam spectroscopy (SPBS) as unique technique allowing depth-profiles from tens of nanometers up to several micrometers. Note, that SPBS has also emerged as a key experimental tool for understanding high-dose 40 keV boron-ion-implanted polymethylmethacrylate (B:PMMA) [4, 8] with carbon nanostructures and Ag NPs loaded poly(dimethylaminoethyl methacrylate) (PDMAEMA) brushes [9, 10]. Also, the first attempt to find differences between the effects of carbonization and formation of Ag NPs in high-dose B:PMMA and Ag:PMMA nanocomposites has been done in [11] by using Doppler broadening SPBS (DB-SPBS).

5.4 Conclusion

Characterization of nanocomposites prepared by 30 keV Ag ion implantation of PMMA at three doses in order to prepare Ag NPs was performed by UV-Vis spectroscopy. For the first time an absorption band at 355 nm for the highest dose sample has been experimentally observed. Possible changes of size and filling factor of Ag NPs in the near-surface region of ion-implanted Ag:PMMA were in agreement with the basic principles of metal nanoparticles formation by ion implantation has been suggested as explanation for this absorption band to be further verified with a unique technique, for instance slow positron beam spectroscopy to probe near-surface nanometer-sized depth profiles.

Acknowledgments T.S. Kavetskyy and M.M. Kravtsiv acknowledge the Ministry of Education and Science of Ukraine (projects Nos. 0116U004737, 0117U007142 (for Young Scientists) and 0117U007143).

References

1. Stepanov AL (2004) Optical properties of metal nanoparticles synthesized in a polymer by ion implantation: a review. Tech Phys 49:143
2. Galyautdinov MF et al (2016) Formation of a periodic diffractive structure based on poly (methyl methacrylate) with ion-implanted silver nanoparticles. Tech Phys Lett 42:182
3. Stepanov AL et al (2000) Formation of metal-polymer composites by ion implantation. Phil Mag B 80:23
4. Kavetskyy T et al (2014) Structural defects and positronium formation in 40 keV B^+ -implanted polymethylmethacrylate. J Phys Chem B 118:4194
5. Stepanov AL et al (2015) Synthesis of porous silicon by ion implantation. Rev Adv Mater Sci 40:155
6. Stepanov AL (2010) Synthesis of silver nanoparticles in dielectric matrix by ion implantation: a review. Rev Adv Mater Sci 26:1
7. Boldyryeva H et al (2005) High-fluence implantation of negative metal ions into polymers for surface modification and nanoparticle formation. Surf Coat Technol 196:373
8. Kavetskyy TS, Stepanov AL (2016) In: Monteiro WA (ed) Radiation effects in materials. InTech, Rijeka, p 287
9. Panzarasa G et al (2016) Positron annihilation spectroscopy: a new frontier for understanding nanoparticle-loaded polymer brushes. Nanotechnology 27:02LT03
10. Panzarasa G et al (2017) Probing the impact of the initiator layer on grafted-from polymer brushes: a positron annihilation spectroscopy study. Macromolecules 50:5574
11. Kavetskyy T et al (2017) High-dose boron and silver ion implantation into PMMA probed by slow positrons: effects of carbonization and formation of metal nanoparticles. J Phys Conf Ser 791:012028

Chapter 6
Formation of a Periodic Structure in a Chalcogenide Film Substrate by Silver Ion Implantation

T. S. Kavetskyy, K. V. Zubrytska, A. V. Stronski, L. I. Pan'kiv, P. Petkov, V. I. Nuzhdin, V. F. Valeev, A. M. Rogov, Y. N. Osin, A. S. Morozova, and A. L. Stepanov

Abstract Recent results on the fabrication of chalcogenide photonic crystals by silver ion implantation through a nickel grid mask using $(GeSe_5)_{80}B_{20}$ chalcogenide films with a thickness of ~500 nm are reported for the first time. The periodical structures obtained are characterized by a grating period ~25 μm and a step height of ~170–200 nm that may find practical use for micro/nanoelectronics.

Keywords Ion implantation · Chalcogenide glass · Thin film · Photonic crystal

T. S. Kavetskyy (✉)
Drohobych Ivan Franko State Pedagogical University, Drohobych, Ukraine

The John Paul II Catholic University of Lublin, Lublin, Poland

K. V. Zubrytska · L. I. Pan'kiv
Drohobych Ivan Franko State Pedagogical University, Drohobych, Ukraine

A. V. Stronski
V.E. Lashkarev Institute of Semiconductor Physics, National Academy of Sciences of Ukraine, Kyiv, Ukraine

P. Petkov
Department of Physics, University of Chemical Technology and Metallurgy, Sofia, Bulgaria

V. I. Nuzhdin · V. F. Valeev
Kazan Physical-Technical Institute of RAS, Kazan, Russian Federation

A. M. Rogov · Y. N. Osin
Kazan Federal University, Kazan, Russian Federation

A. S. Morozova · A. L. Stepanov
Kazan Physical-Technical Institute of RAS, Kazan, Russian Federation

Kazan Federal University, Kazan, Russian Federation

P. Petkov et al. (eds.), *Advanced Nanotechnologies for Detection and Defence against CBRN Agents*, NATO Science for Peace and Security Series B: Physics and Biophysics, https://doi.org/10.1007/978-94-024-1298-7_6

6.1 Introduction

Chalcogenide glasses exhibit a large variety of photoinduced effects which can be used to obtain different optical elements by means of laser, electron or ion irradiation [1–3]. Doping of chalcogenide glasses by different elements significantly change their properties [1–7] with the possibility of surface relief formation using selective etching [1–3]. Modification of chalcogenide glasses by doping enables the formation of optical elements with unique properties (e.g., simultaneous formation of surface and magnetic reliefs) [5]. One frequently used modification tool for chalcogenide glasses could be ion implantation [2, 3]. Recently, ion implantation was found to be a powerful tool for the creation of a periodical diffractive structure in silica glass [8], PMMA [9] and diamond [10]. Actually, a grating was formed in these materials by implantation with copper, silver, and boron ions through a nickel grid mask with different square holes of ~20–40 μm. From a practical point of view, such diffraction gratings could be used in elements of optical communication, for the improvement of solar cells as well as in biomedical research as active substrates for the registration of biomolecules through a heterogeneous method in surface-enhanced Raman scattering (SERS) and surface plasmon resonance (SPR) of metal nanoparticles (in the case of heterogeneous method in SERS the solution of analyzing biomolecules is placed onto the surface with SERS-active centers [11]). In the present work, the ion implantation technique was applied for the formation of a periodic structure in $(GeSe_5)_{80}B_{20}$ chalcogenide films as substrate using a nickel grid mask with square holes of ~25 μm.

6.2 Experimental

Chalcogenide glass thin films with a constant ratio Ge:Se = 1:5 and 20 mol.% B were synthesized by the melt-quenching technique. Starting elements with 5 N purity were mixed and sealed in evacuated quartz ampoules, heated up to 1200 K for 12 h with heating rate of 2–3 K min^{-1}. The melted samples were quenched in a mixture of ice and water. Thin film was prepared by a vacuum evaporation of the respective bulk glass in a standard installation "Hochvacuum" B 30.2. The experimental details of the film preparation are reported elsewhere [12]. The film thickness was ~500 nm measured by an optical interference method. Implantation was carried out with Ag^+ ions with an energy of 30 keV, a dose of 8×10^{16} Ag^+/cm^2 and a current density of 2 μA/cm^2 with an ILU-3 ion accelerator at the Kazan Physical-Technical Institute of Russian Academy of Sciences (Russia). The morphology of the formed periodic structure was tested with scanning electron miscopy (SEM, Merlin, Carl Zeiss). The profile of the diffraction grating obtained was measured using atomic force microscopy (AFM, FastScan, Bruker).

6.3 Results and Discussion

Figure 6.1 shows the SEM and AFM data obtained for the fabricated sample. The period of the grating is about 25 μm, step height about 170–200 nm.

The fabrication of submicron chalcogenide glass ($As_{40}Se_{40}Te_{20}$) photonic crystal [13] and similar periodic elements [14] using resist-free nanoimprint lithography was also reported in the literature. Namely, the period of the prepared photonic crystal structure was 600 nm and the height of the rods in the imprinted structure was about 150 nm [13]. The observed difference in the period of the photonic crystal structures is due to the difference in the sizes of the stamp used in nanoimprint lithography and the square holes in the grid nickel mask used in the ion implantation technique. If one takes into account the extremely high resolution capability of chalcogenide inorganic resists [15], ion implantation is promising for fabrication of different elements with nano- or submicron sizes.

6.4 Conclusion

For the first time a chalcogenide photonic crystal was successfully fabricated by Ag ion implantation through a nickel grid mask with square holes in a $(GeSe_5)_{80}B_{20}$ chalcogenide film (thickness 500 nm). The results obtained (the period of grating is about 25 μm, the step height about 170–200 nm) are similar with the literature results for the fabrication of submicron chalcogenide photonic crystal using thermal nanoimprint lithography in $As_{40}Se_{40}Te_{20}$ glass [13] (the period of the prepared photonic crystal structure is 600 nm and the height of rods in the imprinted structure is about 150 nm). The observed difference in the period of fabricated photonic crystal structures is due to the difference in the sizes of the stamp in the case of the nanoimprint lithography and the square holes in the case of the ion implantation technique. Thus, the low-energy ion implantation technique, progressively used for the surface modification of materials and the formation of PMMA nanocomposite thin films with carbon nanostructures and metal nanoparticles [16–21], oxide materials with metal nanoparticles [22–24], porous silicon [25, 26] and porous germanium [27], periodic diffractive structure in silica glass [8], PMMA [9] and diamond [10], could be also used as alternative approach instead of nanoimprint lithography in the fabrication of photonic crystal structures with certain grating parameters in the case of chalcogenide glasses.

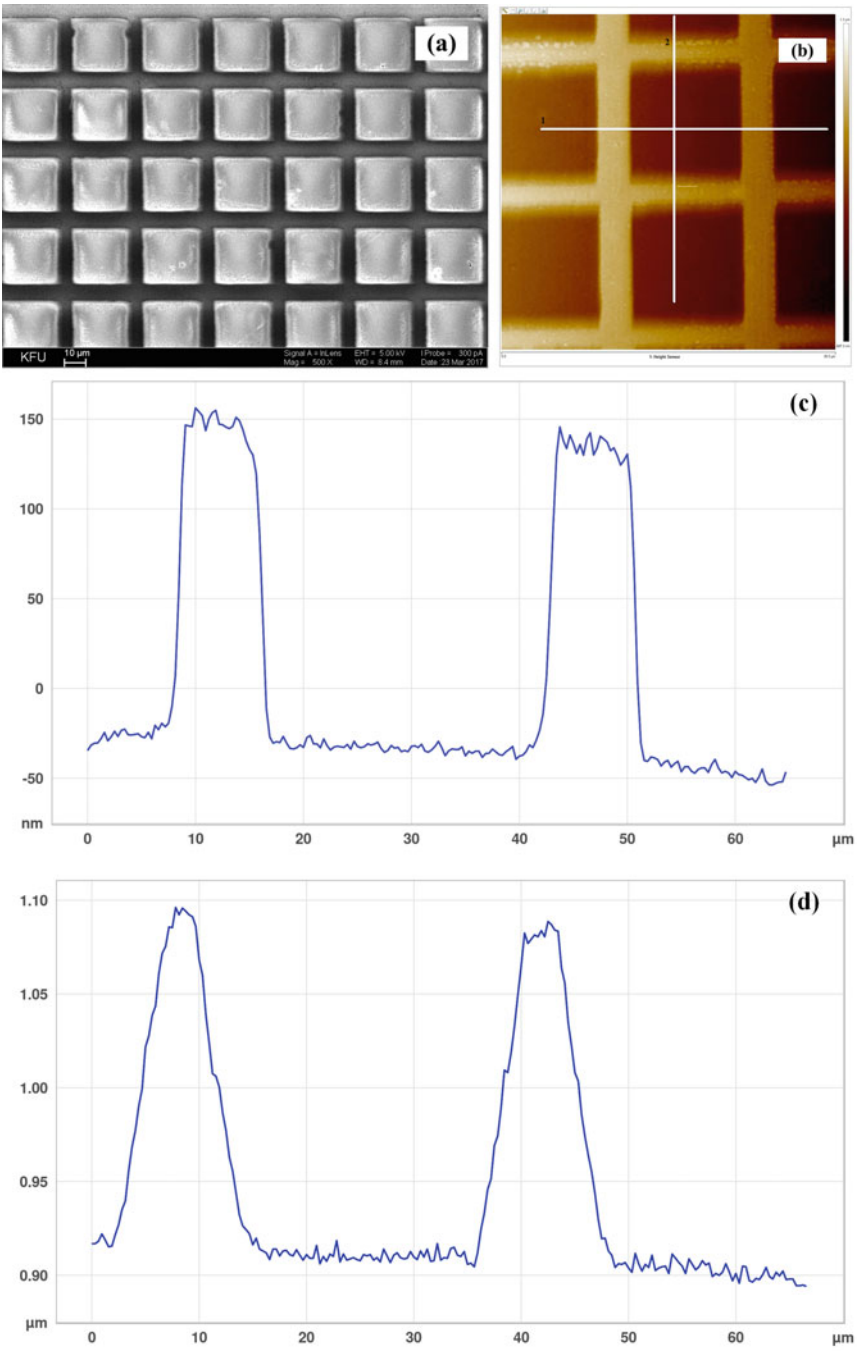

Fig. 6.1 (**a** and **b**) SEM images of the chalcogenide film implanted by 30 keV Ag ions through a nickel grid mask; (**c** and **d**) AFM cross-sections along the lines 1 and 2 shown in (**b**)

Acknowledgments T.S. Kavetskyy and K.V. Zubrytska acknowledge the Ministry of Education and Science of Ukraine (projects Nos. 0116U004737, 0117U007142 (for Young Scientists) and 0117U007143). A.L. Stepanov thanks for the partial financial support from the Russian Foundation for Basic Research (project No. 17-08-00780).

References

1. Saito K, Utsugi Y, Yoshikawa A (1988) X-ray lithography with a Ag–Se/Ge–Se inorganic resist using synchrotron radiation. J Appl Phys 63:565
2. Stronskiin AV, Harman GG, Mach P (eds) (1998) Microelectronic interconnections and assembly. Springer, Dordrecht, p 263
3. Suzuki T, Hosono H (2002) Ion-beam doping of silver in amorphous As_2S_3 thin films. J Appl Phys 92:1821
4. Stronski AV et al (2000) Raman spectra of Ag- and Cu-photo-doped $As_{40}S_{60-x}Se_x$ films. J Non-Cryst Solids 270:129
5. Stronski A et al (2017) Direct magnetic relief recording using $As_{40}S_{60}$: Mn–Se nanocomposite multilayer structures. Nanoscale Res Lett 12:286
6. Stronski A et al (2015) Effect of doping by transitional elements on properties of chalcogenide glasses. Ceram Int 41:7543
7. Paiuk AP et al (2011) Peculiarities of As–S glass structure doped with ytterbium. Proc SPIE 8306:830617
8. Kavetskyy TS et al (2013) The formation of periodic diffractive plasmonic nanostructures with implanted copper nanoparticles by local ion etching of silica glass. Tech Phys Lett 39:591
9. Galyautdinov MF et al (2016) Formation of a periodic diffractive structure based on poly(methyl methacrylate) with ion-implanted silver nanoparticles. Tech Phys Lett 42:182
10. Stepanov AL et al (2017) A diffraction grating created in diamond substrate by boron ion implantation. Tech Phys Lett 43:104
11. Mamichev DA et al (2012) Optical sensors based on surface plasmon resonance for high-sensitive biochemical analysis. Mol Med 6:3
12. Petkov P, Parvanov S, Petkova T (2006) Electron transport in amorphous $(GeSe_5)_{1-x}B_x$ films. J Optoelectron Adv Mater 8:785
13. Zeng J et al (2017) Fabrication of submicron chalcogenide glass photonic crystal by resist-free nanoimprint lithography. Appl Phys A Mater Sci Process 123:579
14. Pan WJ et al (2007) Fine embossing of chalcogenide glasses: first time submicron definition of surface embossed features. J Non-Cryst Solids 353:1302
15. Jain H, Vlcek M (2008) Glasses for lithography. J Non-Cryst Solids 354:1401
16. Kavetskyy TS et al (2014) Structural defects and positronium formation in 40 keV B^+-implanted polymethylmethacrylate. J Phys Chem B 118:4194
17. Kavetskyy T et al (2016) Carbonization in boron-ion-implanted polymethylmethacrylate as revealed from Raman spectroscopy and electrical measurements. Spectrosc Lett 49:5
18. Kavetskyy T et al (2017) High-dose boron and silver ion implantation into PMMA probed by slow positrons: effects of carbonization and formation of metal nanoparticles. J Phys Conf Ser 791:012028
19. Trzcinski M, Kavetskyy T, Telbiz G, Stepanov AL (2017) Optical characterization of nanocomposite polymer formed by ion implantation of boron. J Mater Sci Mater Electron 28:7115
20. Kavetskyy TS, Stepanov AL (2016) In: Monteiro WA (ed) Radiation effects in materials. InTech, Rijeka, p 287
21. Stepanov AL (2004) Optical properties of metal nanoparticles synthesized in a polymer by ion implantation: a review. Tech Phys 49:143

22. Stepanov AL (2010) Synthesis of silver nanoparticles in dielectric matrix by ion implantation: a review. Rev Adv Mater Sci 26:1
23. Stepanov AL (2011) Nonlinear optical properties of implanted metal nanoparticles in various transparent matrixes: a review. Rev Adv Mater Sci 27:115
24. Stepanov AL et al (2013) Catalytic and biological sensitivity of TiO_2 and SiO_2 matrices with silver nanoparticles created by ion implantation: a review. Rev Adv Mater Sci 34:107
25. Stepanov AL et al (2013) New way for synthesis of porous silicon using ion implantation. Adv Mater – Rapid Commun 7:692
26. Kavetskyy TS, Stepanov AL (2015) In: Petkov P, Tsiulyanu D, Kulisch W, Popov C (eds) Nanoscience advances in CBRN agents detection, information and energy security. Springer, Dordrecht, p 35
27. Stepanov AL et al (2017) Synthesis of porous germanium with silver nanoparticles by ion implantation. Nanotechnol Russ 12:508

Chapter 7
Optical Band Gap and Carbon Clusters in PMMA Nanocomposite Films Formed by Ion Implantation: Boron, Helium, and Xenon Ions

M. Trzciński, T. S. Kavetskyy, and A. L. Stepanov

Abstract The optical band gap and carbon clusters behavior as a function of ion dose are examined for 40 keV boron, helium, and xenon ion-implanted polymethylmethacrylate (PMMA) at the same ion doses of 3.13×10^{15}, 6.25×10^{15}, 1.25×10^{16}, and 2.5×10^{16} ions/cm^2. The values of E_g^{opt} and N^{ion} are compared and analyzed. The effect of the ion mass on the carbonization processes in PMMA nanocomposite films formed by implantation of these ions as revealed from optical absorption measurements is considered.

Keywords Optical band gap · Carbon clusters · PMMA · Ion implantation

7.1 Introduction

Ion implantation is a powerful tool for structural modification of polymers and changes of their physico-chemical properties. Investigation of depth profiles of light and heavy ions implanted into organic polymers [1] has stimulated an increasing interest to new functionalities of modified surface layers with absolutely new properties. One of the significant changes observed in the physical properties of ion-implanted polymers is an increasing absorbance in the course of the

M. Trzciński
The John Paul II Catholic University of Lublin, Lublin, Poland

T. S. Kavetskyy (✉)
Drohobych Ivan Franko State Pedagogical University, Drohobych, Ukraine

The John Paul II Catholic University of Lublin, Lublin, Poland

A. L. Stepanov
Kazan Physical-Technical Institute of RAS, Kazan, Russian Federation

Kazan Federal University, Kazan, Russian Federation

Kazan National Research Technological University, Kazan, Russian Federation

P. Petkov et al. (eds.), *Advanced Nanotechnologies for Detection and Defence against CBRN Agents*, NATO Science for Peace and Security Series B: Physics and Biophysics, https://doi.org/10.1007/978-94-024-1298-7_7

implantation, to be interpreted as the signature on the formation of carbonaceous clusters [2–4]. Recently, dose dependences of the optical band gap of boron-ion-implanted layers $E_g^{opt,B}$ and the number of carbon atoms in carbonaceous clusters N in polymethylmethacrylate nanocomposite films formed by boron ion implantation have been systematically studied [3]. Three regions of ion doses have been found: (1) 6.25×10^{14} – 3.13×10^{15}, (2) 3.75×10^{15} – 6.25×10^{15}, and (3) 1.25×10^{16} – 2.5×10^{16} B^+/cm^2, showing thresholds in the estimated $E_g^{opt,B}$ and N values as a function of ion dose; consequently, an ion-induced structural evolution towards the formation of carbon nanostructures within these thresholds has been suggested [3]. In the present work, the optical band gap and carbon clusters behavior as a function of ion dose are examined for the 40 keV boron, helium, and xenon ion-implanted PMMA at ion doses of 3.13×10^{15}–2.5×10^{16} ions/cm^2. The values of E_g^{opt} and N, respectively, are compared and analyzed. The effect of the ion mass on the carbonization processes in PMMA nanocomposite films formed by implantation of these ions as revealed from optical absorption measurements is discussed.

7.2 Experimental

As substrates for ion implantation, optically transparent 1.2-mm-thick PMMA plates were used. The B^+, He^+ and Xe^+ implantation with an energy of 40 keV, ion doses ranging from 6.25×10^{14} to 2.5×10^{16} ions/cm^2, and an ion current density of <2 μA/cm^2 was performed under a pressure of ~10^{-5} Torr at room temperature using the ILU-3 ion accelerator at the Kazan Physical-Technical Institute (KPTI, Russia). Optical absorption spectra of the pristine PMMA and ion-implanted samples were measured in the wavelength range of 200–800 nm using an Evolution 220 UV-visible spectrophotometer at room temperature.

7.3 Results and Discussion

Figure 7.1 shows UV-visible absorption spectra and the optical absorption coefficient $\alpha(h\nu)$ of implanted samples at different doses and thicknesses d of the implanted layer. The optical absorption coefficient for pristine and ion-implanted samples was calculated from the absorption spectra using the relation [5, 6]:

$$\alpha = 2.303 \times A/d, \tag{7.1}$$

where A is the absorption and d the sample thickness. The thickness d of the implanted layer was predicted by SRIM (stopping and range of ions in matter) simulations [4]. Note, that the SRIM results were found to be in good agreement

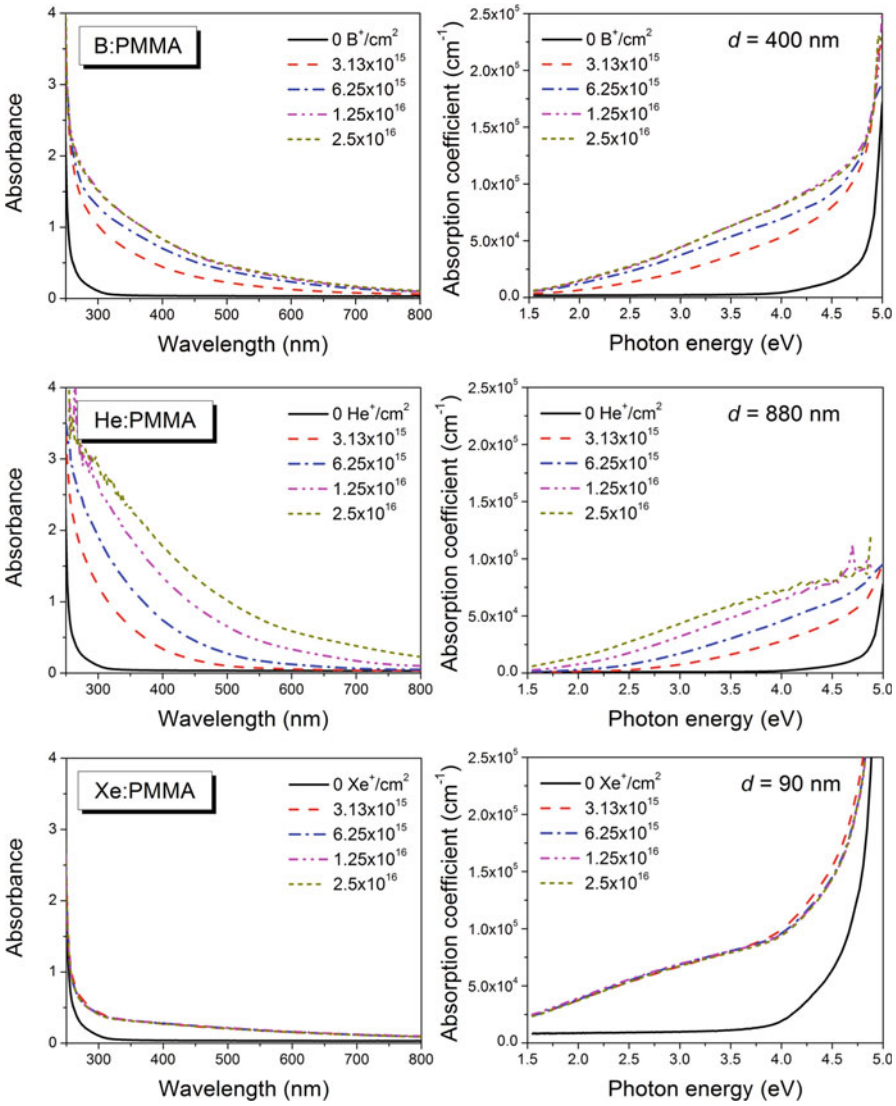

Fig. 7.1 UV-visible absorption spectra (left) and optical absorption coefficient $\alpha(h\nu)$ of implanted layers (right) for B:PMMA, He:PMMA, and Xe:PMMA samples at different ion doses and thicknesses d of the implanted layer as revealed by SRIM simulations [4]

with the experimentally obtained maximum penetration depth of B^+ ions into PMMA by slow positron beam spectroscopy [2]. The optical band gap energies E_g^{opt} for pristine PMMA and the ion-implanted layers $E_g^{opt,ion}$ were determined using Tauc plots as shown in an earlier work [3]. From the optical band gap

Table 7.1 Optical band gap energy $E_g^{opt,ion}$ and number of carbon atoms in carbonaceous clusters N^{ion} for the implanted layers at different ion doses

Dose, ions/cm^2	$E_g^{opt,B}$, eV	$E_g^{opt,He}$, eV	$E_g^{opt,Xe}$, eV	N^B	N^{He}	N^{Xe}
0	4.78	4.84	4.83	–	–	–
3.13×10^{15}	4.39	4.52	4.81	~61	~58	~50
6.25×10^{15}	4.14	3.98	4.82	~69	~74	~50
1.25×10^{16}	3.90	2.28	4.82	~77	~225	~50
2.50×10^{16}	3.90	1.66	4.82	~77	~428	~50

energy data one may calculate the number of carbon atoms in carbonaceous clusters N (e.g., $N = 60$ for buckminsterfullerene C_{60}) using the formula [7, 8]:

$$E_g^{opt} \approx 34.3 \times N^{-1/2}. \tag{7.2}$$

The estimated $E_g^{opt,ion}$ and N^{ion} data for the implanted layers of this study are collected in Table 7.1. The features of the dose dependence of the boron data have been reported in [3]. In the present work, the effect of the ion mass on the carbonization processes in PMMA nanocomposites formed by ion implantation as revealed from optical absorption measurements was studied. It can clearly be seen that the He^+ implantation into PMMA leads to dramatic changes of $E_g^{opt,He}$ and the N^{He} in comparison with the B^+ implantation, while the effect of Xe^+ implantation into PMMA is negligible. One of the reasons is the significant difference in the penetration depth for the 40 keV light He and heavy Xe ions of 880 and 90 nm, respectively, according to SRIM simulations [4]. In order to clarify the results obtained, a mechanism of ion-irradiation induced processes with low-energy light and heavy ions should be studied in more detail. Slow positron beam spectroscopy should be applied for this purpose to extract depth-selective information on defects in the implanted samples.

7.4 Conclusion

The optical band gap and carbon clusters behavior as a function of the ion dose have been examined for B:PMMA, He:PMMA, and Xe:PMMA nanocomposite films formed by ion implantation at the same ion doses and energy. It was established that He^+ implantation into PMMA leads to dramatic changes of the optical band gap and the number of carbon atoms in carbonaceous clusters N^{He} in comparison with B^+ implantation, while the effect of Xe^+ implantation is negligible.

Acknowledgments T.S. Kavetskyy acknowledges the Ministry of Education and Science of Ukraine (project No. 0116U004737). A.L. Stepanov thanks for the financial support from the Russian Foundation for Basic Research (project No. 15-48-02525).

References

1. Fink D et al (1985) Distributions of light ions and foil destruction after irradiation of organic polymers. J Appl Phys 58:668
2. Kavetskyy T et al (2014) Structural defects and positronium formation in 40 keV B^+-implanted polymethylmethacrylate. J Phys Chem B 118:4194
3. Trzcinski M, Kavetskyy T, Telbiz G, Stepanov AL (2017) Optical characterization of nanocomposite polymer formed by ion implantation of boron. J Mater Sci Mater Electron 28:7115
4. Kavetskyy TS, Stepanov AL (2016) In: Monteiro WA (ed) Radiation effects in materials. InTech, Rijeka, p 287
5. Arif S et al (2015) Influence of 400 keV carbon ion implantation on structural, optical and electrical properties of PMMA. Nucl Instr Meth Phys Res B 358:236
6. Zidan HM, El-Khodary A, El-Sayed IA, El-Bohy HI (2010) Optical parameters and absorption studies of UV-irradiated azo dye-doped PMMA films. J Appl Polym Sci 117:1416
7. Robertson J, O'Reilly EP (1987) Electronic and atomic structure of amorphous carbon. Phys Rev B 35:2946
8. Fink D et al (1995) Carbonaceous clusters in irradiated polymers as revealed by UV-Vis spectrometry. Radiat Eff Defects Solids 133:193

Part III
Structural and Optical Characterization

Chapter 8
Preparation and Characterization of SERS Substrates of Different Morphology

I. Rigó, M. Veres, L. Himics, T. Váczi, and P. Fürjes

Abstract Gold coated patterned silicon substrates of different morphology, pattern size and period were prepared by photolithography and subsequent etching. Their performance in surface enhanced Raman scattering (SERS) was tested using an organic model compound. The highest enhancement was obtained for an array of inverse pyramids, followed by inverse hemispheres and rounded-edge inverse pyramids. The SERS performance of the substrates was demonstrated with silicon-carbide nanoparticles.

Keywords Surface enhanced Raman scattering · Raman spectroscopy · SERS substrates · Photolitography · Etching

8.1 Introduction

Raman spectroscopy is a non-contact and relatively easy material characterization technique requiring no sample preparation. The Raman scattering process is inherently weak which prohibits its use for the investigation of low concentration analytes. A number of techniques are known that can increase the Raman sensitivity including the use of higher excitation energies, utilization of resonant Raman scattering or surface enhanced Raman scattering (SERS) [1]. The latter promises single molecule detection [2], and its degree of achievable sensitivity can reach attomolar (10^{-18} M) concentrations, as has been observed in many cases [3, 4]. As a spectroscopic tool SERS has the potential to combine the structural information of Raman spectroscopy with the sensitivity of fluorescence. During SERS the

I. Rigó (✉) · M. Veres · L. Himics · T. Váczi
Wigner Research Centre for Physics, Hungarian Academy of Sciences, Budapest, Hungary
e-mail: rigo.istvan@wigner.mta.hu

P. Fürjes
Institute of Technical Physics and Materials Science, Centre for Energy Research, HAS, Budapest, Hungary

P. Petkov et al. (eds.), *Advanced Nanotechnologies for Detection and Defence against CBRN Agents*, NATO Science for Peace and Security Series B: Physics and Biophysics, https://doi.org/10.1007/978-94-024-1298-7_8

scattering takes place in close vicinity of nanostructured metallic surfaces (nanoparticle or some surfaces with a nanoscopic morphology), and the interaction of the electromagnetic field of photons with the surface plasmons of the metal nanoparticles results in a gain of the excitation and/or the Raman signal, that can be several orders of magnitude [5]. The key factor for successful SERS is to find appropriate SERS-active agents (nanoparticles or substrates) that will provide the required efficiency for a given excitation wavelength.

In this work SERS active substrates of different size and morphology were prepared by a lithographic technique from silicon with subsequent gold coating and tested for their SERS enhancement performance using a highly dissolved organic solution as a test material.

8.2 Experimental

Polished silicon wafers were used as substrates for the preparation of SERS active surfaces. Arrays of inverse pyramids, spheres and rounded pyramids were formed using photolithographic techniques. The silicon surface was coated with an appropriate photoresist, in which arrays of rectangular shapes were created with 1×1 and 2×2 μ unit size and 3 μ period. The samples were then etched with isotropic and anisotropic agents as well as with their mixture, resulting in the formation of arrays of hemispheres (isotropic etching), inverse pyramids (anisotropic etching) and rounded inverse pyramids (mixed etching), respectively. Subsequently the substrates were coated with a 40 nm thick sputtered layer of gold.

The morphology of the structures was characterized using scanning electron microscopy (SEM) with a Jeol JSM-25 scanning electron microscope. SERS measurements were carried out with a Renishaw 1000 micro-Raman spectrometer attached to a Leica DM/LM microscope. A 785 nm diode laser served as excitation source, which was focused into a spot with a diameter of 1 μ. A benzophenone solution in isopropyl alcohol was used to test the SERS enhancement of the substrates. The same solution was dripped onto each array and the intact silicon substrate (serving as reference) as well. The Raman measurements were carried out after the evaporation of the solvent. For another experiment, silicon carbide nanoparticles were dried on the substrate surface from a water dispersion.

8.3 Results and Discussion

Figure 8.1 shows scanning electron microscopic images of the prepared gold coated inverse hemispheres, rounded pyramids and pyramids of different size, respectively. It can be seen that both the 1 and 2 μ unit size structures are of high uniformity. The different speed of isotropic and anisotropic etchings results in structures of somewhat different size, especially for the 1 μ samples. The slowest etching was observed

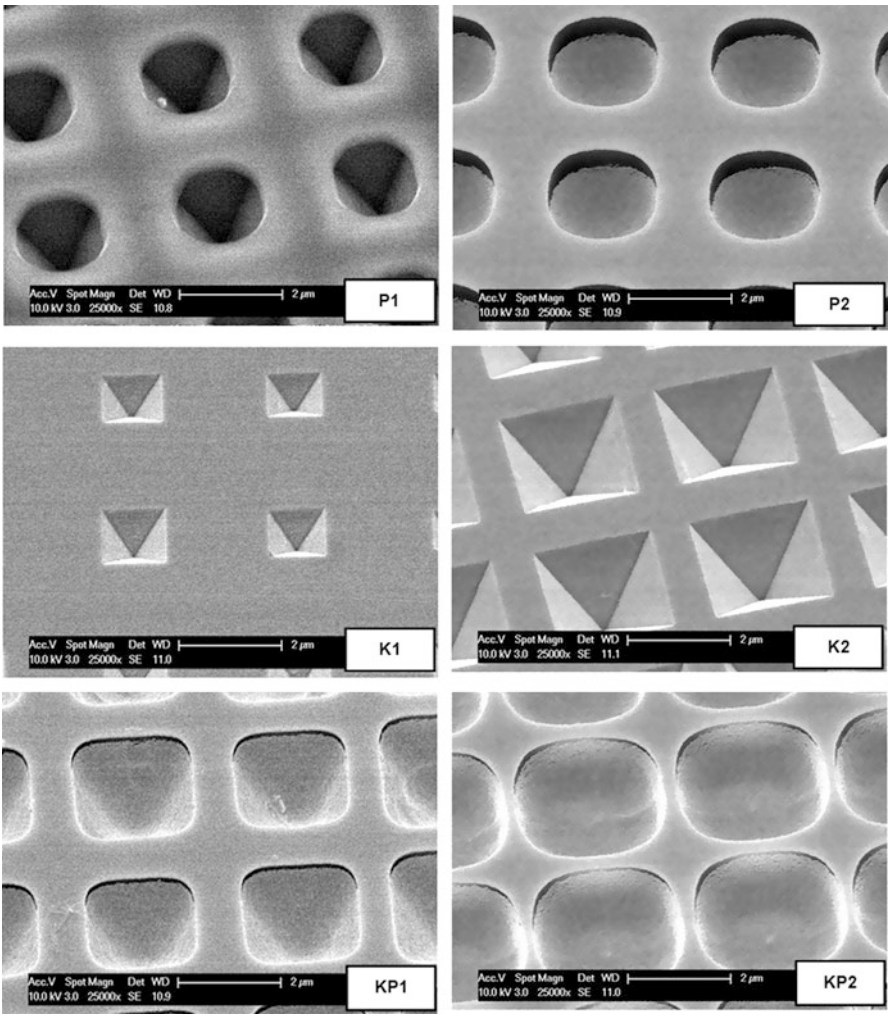

Fig. 8.1 Scanning electron microscopic images of gold coated arrays of inverse hemispheres (P1 and P2), rounded pyramids (KP1 and KP2) and pyramids (K1 and K2) with 1 and 2 μ unit size

for the 1 μ unit size inverse pyramids, while on some areas of the silicon surface even no structures were formed during the treatment process. It can be seen in Fig. 8.1 that the largest inverse shapes were obtained with the combined application of the two etchings.

The SERS spectra of the dried benzophenone solution recorded on the samples are compared on Fig. 8.2. Very weak peaks were observed in the reference spectrum and in the spectrum recorded on the KP2 substrate. More intense bands and enhancement of the intensity were seen for all other samples, indicating the effects of morphology and array unit size on the SERS performance of the gold coated

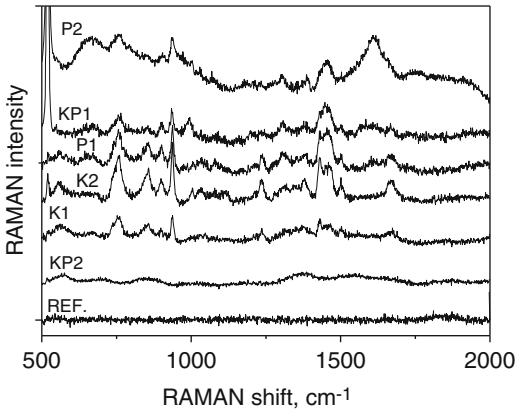

Fig. 8.2 Comparison of the SERS spectra recorded on the different substrates with a dried solution of the same concentration. The spectra are baseline corrected

Table 8.1 Relative SERS enhancement values of the SERS substrates of different morphology obtained from Raman peak intensity ratios in the SERS and reference spectra

Sample	Relative SERS enhancement
P1	1420
P2	760
KP1	740
KP2	10
K1	730
K2	2610

surfaces. Table 8.1 shows the SERS enhancements calculated from the intensity ratios of the same peak in the SERS and reference spectra. It can be seen that the values range between 10 and 2600, and are much lower than the enhancements reported in the literature. It should be noted, however, that the values in Table does not reflect the real SERS enhancement. The SERS phenomenon occurs only in the close vicinity of a metallic surface; however, the samples obtained by drying the solution constitute not a single molecular layer, but a relatively thick film of material. For this reason there is a significant non-SERS contribution to the measured spectra from the part of the samples out of the SERS enhancement region, which is present in both the SERS and the reference spectra and influences the intensity ratios and their comparison. Therefore, the SERS enhancements provided in Table 8.1 can be used only for comparative analysis of the SERS performance of the different substrates. From the six examined samples the K2 substrate has the highest relative SERS enhancement of 2610, followed by the P1 with an intensity around half of that of the K2 substrate. The K1, P2 and KP1 surfaces have similar performances, while only minimal SERS enhancement was observed forthe KP2 sample.The amplification of the SERS signal is determined by the plasmonic properties (plasmon resonance wavelength) of the metallic nanostructure and its relation to the wavelengths of Raman excitation and Raman bands. So the values describing the relative performance of the SERS substrates are true only for 785 nm excitation.

The SERS enhancement of the K2 substrate showing the highest efficiency was tested with silicon-carbide nanoparticles prepared from silicon and graphite powder

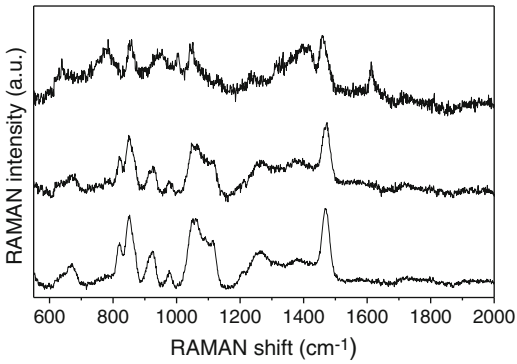

Fig. 8.3 SERS spectra recorded at different points of a silicon-carbide nanocrystal sample dried on the K2 sample surface from a water dispersion

precursors using the reactive bonding method [6]. The Raman peaks of this material were overlapped by the strong photoluminescence background during normal Raman measurements with 785 nm excitation. However, it was possible to detect Raman bands after drying the nanoparticles onto the SERS substrate (Fig. 8.3). Obviously, the interaction of the electromagnetic field of the photons with the surface plasmons of the nanostructured metal substrate can enhance the photoluminescence, as well. However, this effect is strongly distance-dependent and the photoluminescence is quenched near the metal surface [7], where SERS has the highest efficiency.

SERS spectra recorded at different points of the sample contain several relatively strong peaks. One group of bands (at 666, 820, 848, 923 and 976 cm^{-1}) can be assigned to SiC vibrations and indicate the presence of several different polytypes in the sample [8, 9]. Bands in the 1000–1650 cm^{-1} region (at 1050, 1085, 1115, 1260, 1383, 1460 and 1615 cm^{-1}) are related to different carbon-carbon vibrations, clearly showing the presence of carbon impurities in the structure. However, while the sample was prepared from a graphite precursor, only the 1615 cm^{-1} peak appearing in one spectrum resembles the Raman band of nanocrystalline graphite [10]. Being the most probable source of carbon impurities, Raman spectra show that graphite transformed into some different carbon structures during the preparation process.

8.4 Conclusions

The performance of gold coated patterned silicon surfaces of different morphology and size as substrates for surface enhanced Raman scattering was investigated. Among gold coated arrays of inverse pyramids, spheres and rounded pyramids of 1 and 2 μ unit size and 3 μ period the 2 μ sized inverse pyramids showed the highest SERS amplification with 785 nm excitation. The performance of this substrate was demonstrated on silicon carbide nanoparticles.

Acknowledgments This work was supported by National Research, Development and Innovation Fund of Hungary with the NVKP_16-1-2016-0043 grant and the VEKOP-2.3.2-16-2016-00011 grant. Miklós Veres is grateful for the support of the János Bolyai Research Scholarship of the Hungarian Academy of Sciences.

References

1. Ryder AG (2005) Surface enhanced Raman scattering for narcotic detection and applications to chemical biology. Curr Opin Chem Biol 9:489–493
2. Le Ru EC, Meyer M, Etchegoin PG (2006) Proof of single-molecule sensitivity in surface enhanced Raman scattering (SERS) by means of a two-analyte technique. J Phys Chem B 110:1944–1948
3. Etchegoin P, Maher RC, Cohen LF, Hartigan H et al (2003) New limits in ultrasensitive trace detection by surface enhanced Raman scattering (SERS). Chem Phys Lett 375:84–90
4. Futamata M, Maruyama Y, Ishikawa M (2004) Metal nanostructures with singlemolecule sensitivity in surface enhanced Raman scattering. Vib Spectrosc 35:121–129
5. Campion A, Kambhampati P (1998) Surface-enhanced Raman scattering. Chem Soc Rev 27:241–250
6. Beke D, Szekrényes Z, Balogh I, Veres M, Fazakas É, Varga LK, Kamarás K, Czigány Z, Gali A (2011) Silicon carbide quantum dots for bioimaging. Appl Phys Lett 99:213108
7. Acuna GP, Bucher M, Stein IH, Steinhauer C, Kuzyk A, Holzmeister P, Schreiber R, Moroz A, Stefani FD, Liedl T, Simmel FC, Tinnefeld P (2012) Distance dependence of single-fluorophore quenching by gold nanoparticles studied on DNA origami. ACS Nano 6:3189–3195
8. Feldman DW, Parker JH Jr Choyke WJ, Patrick L, Phonon dispersion curves by Raman scattering in SiC, polytypes 3C, 4H, 6H, 15R, and 21R. Phys Rev 173:787 (1968)
9. Wei G, Qin W, Wang G, Sun J, Lin J, Kim R, Zhang D, Zheng K (2008) The synthesis and ultraviolet photoluminescence of 6H–SiC nanowires by microwave method. J Phys D Appl Phys 41:235102
10. Ferrari AC, Robertson J (2000) Interpretation of Raman spectra of disordered and amorphous carbon. Phys Rev B 61:14095

Chapter 9
Synthesis of UV Sensitive Rare Earth Doped Materials

Irena Kostova and Dan Tonchev

Abstract In this work we report on the synthesis of photoluminescent inorganic crystalline materials by a hydrothermal process. The synthesis of rare earth doped and co-doped strontium/barium aluminates was performed in a muffle furnace in air atmosphere. The prepared powders were excited with an ultraviolet (UV) source and their emission spectra measured. The PL results show slight fluorescence and strong visible green phosphorescence under UV light. We also measured the thermal properties by differential scanning calorimetry (DSC). The structures of synthesized RE doped materials were studied by XRD analysis. The basic properties of these materials show potential for different applications. We focused on protection of security documents. For this reason, we performed additional experiments. We blended fine grinded phosphorescent powders into different polymer composites and made successfully thin films from them. The composites were prepared by polyethylene, polymethyl methacrylate and polystyrene mixed with synthesized inorganic additives.

Keywords Rare earth · Strontium aluminates · Phosphorescence · Composite materials

9.1 Introduction

Rare earth (RE) doped materials (crystalline or glassy) are widely used in various fields. Strontium aluminates are suitable host materials for RE ions such as Eu, Dy and Tb [1–3]. Strontium aluminate phosphors produce yellow-green, blue-green and

I. Kostova (✉)
Departments of Chemical Technology, Plovdiv University "Paisii Hilendarski", Plovdiv, Bulgaria
e-mail: irena_k87@abv.bg

D. Tonchev
University of Saskatchewan, Saskatoon, SK, Canada

University of Plovdiv "Paisij Hilendarski", Plovdiv, Bulgaria

P. Petkov et al. (eds.), *Advanced Nanotechnologies for Detection and Defence against CBRN Agents*, NATO Science for Peace and Security Series B: Physics and Biophysics, https://doi.org/10.1007/978-94-024-1298-7_9

blue hues for excitation wavelengths from 200 to 450 nm, with green emission at ≈520 nm, blue-green at ≈505 nm, and blue at ≈490 nm, depending on the lanthanide co-doping. The co-doping in this material is usually with Dy and Nd ions [4, 5]. Due to their luminous properties, easy preparation and chemical durability, strontium aluminates are excellent additives to different polymers. This is very important when preparing composite materials. Mishra et al. [6] reported phosphor-based polymer composites with strontium aluminates phosphors ($SrAl_2O_4$: Eu, Dy and $Sr_4Al1_4O_{25}$: Eu, Dy) in different organic matrices.

In this article, we report on an experimental study of crystalline powders co-doped with different lanthanide ions, aiming at correlating their host lattice structure and chemical composition to the luminescence features. In addition, we have prepared polymer – inorganic composite materials. For this purpose, phosphor samples were characterized by X-ray diffraction (XRD), thermal analysis, and photoluminescence (PL) spectroscopy. This investigation on the optical characterization of luminous crystalline materials doped with lanthanide ions gives information about possible applications such as light-emitting devices, luminescent pigments, ceramics and composites.

9.2 Materials and Methods

9.2.1 Synthesis of RE Doped Powders

The following raw reagents: $SrCO_3$, SrF_2, $Al_2(SO_4)_3{\cdot}18H_2O$, $CO(NH_2)_2$, Sm_2O_3, TbF_3, $Eu(SO_4)_3{\cdot}8H_2O$, SmF_3 were purchased from Alfa Aesar. The hydrothermal synthesis was performed by a solid-state reaction from solution and calcined in a muffle furnace at 500 °C. The product was cooled to room temperature and then removed from the crucible and analyzed.

The resulting crystal powders were prepared by the following chemical equations:

$$2Al(OH)_{3(s)} \rightarrow Al_2O_{3(s)} + 3H_2O_{(g)}$$
$$SrCO_{3(s)} \rightarrow SrO_{(s)} + CO_{2(g)}$$
$$xSrO + yAl_2O_3 \rightarrow Sr_xAl_{2*y}O_{3*y+x}$$

9.2.2 Characterization

DSC was performed with a Thermal Analysis TA Instrument DSC Q100 with an attached fast air cooling system (FACS) at heating rates of 2 K/min, a period of 60 s and an amplitude ±1.

Table 9.1 Concentration of RE elements in the phosphors

Phosphor	Concentration of RE elements, %		
	Sm	Tb	Eu
SAO:Sm	0.4		
SAO:Tb		0.4	
SAO:Eu			0.4
SAO:EuTb		0.2	0.4
SAO:TbSm	0.2	0.4	

The aimed stoichiometric compounds were synthesized as following: $SrAl_{12}O_{19}$:Sm (1:6), $SrAl_4O_7$:Tb (1:2), $Sr_4Al_{14}O_{25}$:Eu (4:7), $Sr_3Al_2O_6$:Sm (3:1), $SrAl_2O_4$:Eu (1:1)

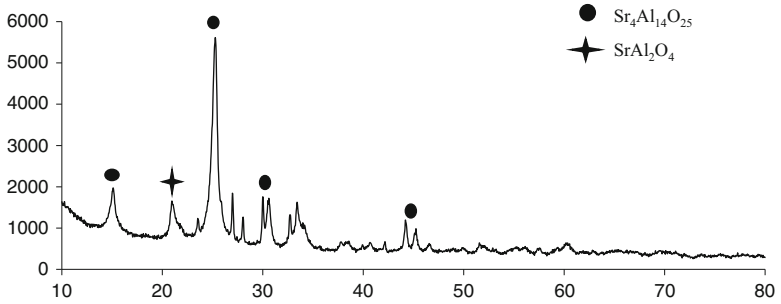

Fig. 9.1 XRD analysis of the stoichiometric sample $SrAl_{12}O_{19}$:Sm (1:6)

Photoluminescence analysis was performed by a SpectroVis Plus spectrophotometer in the range 250–1100 nm with different excitation sources in the UV-VIS range.

The X-ray diffraction measurements were performed in the Institute of General and Inorganic Chemistry, Bulgarian Academy of Science (BAS). Although the synthesis aimed at obtaining a clearly defined stoichiometric compounds, the XRD analysis indicated the presence of different phases.

9.3 Results and Discussion

In Table 9.1 the compositions of the phosphors $Sr_xAl_{2*y}O_{3*y+x}$ (SAO) doped with different RE elements are given.

9.3.1 XRD Analysis

The XRD analysis indicates the presence of different phases of polycrystalline structures as shown on the roentgenograms below (Figs. 9.1 and 9.2).

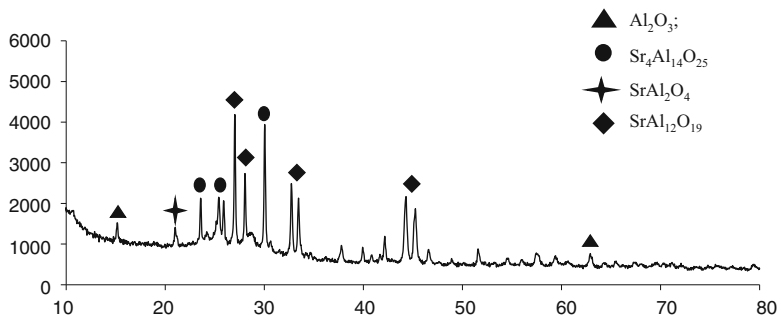

Fig. 9.2 XRD analysis of the stoichiometric sample $Sr_4Al_{14}O_{25}$:Eu (4:7)

According to the differences of the phase composition of these samples, in their XRD patterns we can observe a mixture of following crystalline phases: Al_2O_3; $Sr_4Al_{14}O_{25}$, $SrAl_2O_4$ and $SrAl_{12}O_{19}$.

9.3.2 Thermal (DSC) Analysis

The themal analysis results are shown in Fig. 9.3a–d. The thermograms are confirming the results of the XRD analysis that the structure contains two phases – an amorphous and a polycrystalline one with a low melting point T_m around 120–150 °C. This temperature is acceptable for a practical use taking into account that these materials are going to be dispersed into polymers and desposited as films. It seems that the amorphous phases of the obtained materials crystallize around 100 °C; this is more clear from the thermogram d, However the other materials also give a hint on this crystallization temperature T_c in the range from 100 to 110 °C. There is also a hint for a glass transition temperature T_g of around 55–75 °C but this is obscured by probably non-reacted sourse materials with low melting points.

9.3.3 Photoluminescence Analysis

Under irradiation with different light sources (UV, white, visible) the obtained powders exhibited visually detectable phosphorescence for a duration of 4–5 s. It is possible also to observe a weak fluorescence (not shown). The luminescent analysis was performed by different LED and laser light sources (excitation wavelengths $\lambda = 295$, 315, 325, 340, 370, 395 and 405 nm). The resulting spectra are, given in Figs. 9.4, 9.5, 9.6, and 9.7.

Looking at these spectra it is possible to observe ions peaks typical for rare-earths (RE). This means that RE elements are successfully doped into the synthesized luminescent crystals. All materials investigated by photoluminescent

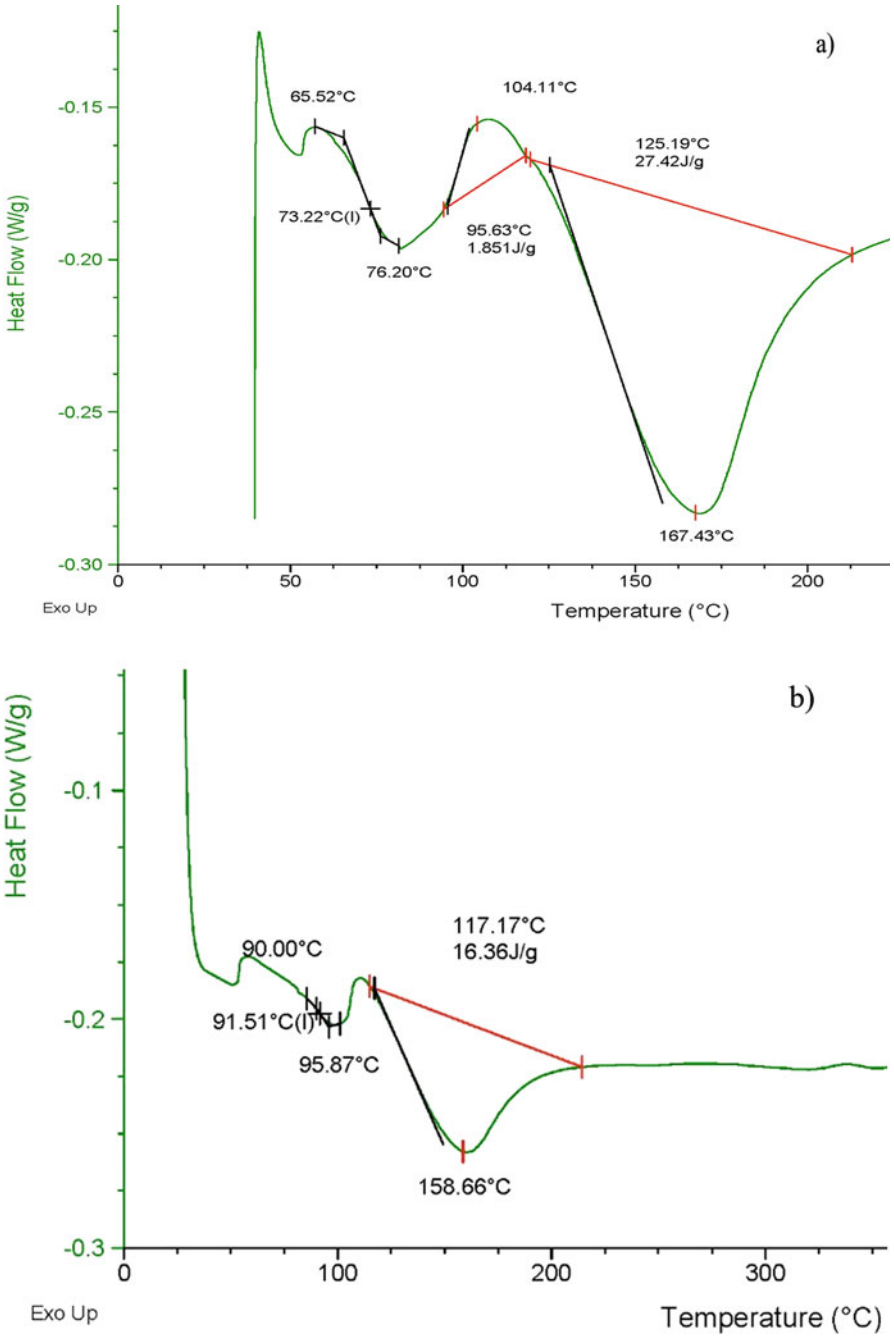

Fig. 9.3 (**a**–**d**) Thermograms of phosphours doped with different rare earth elements

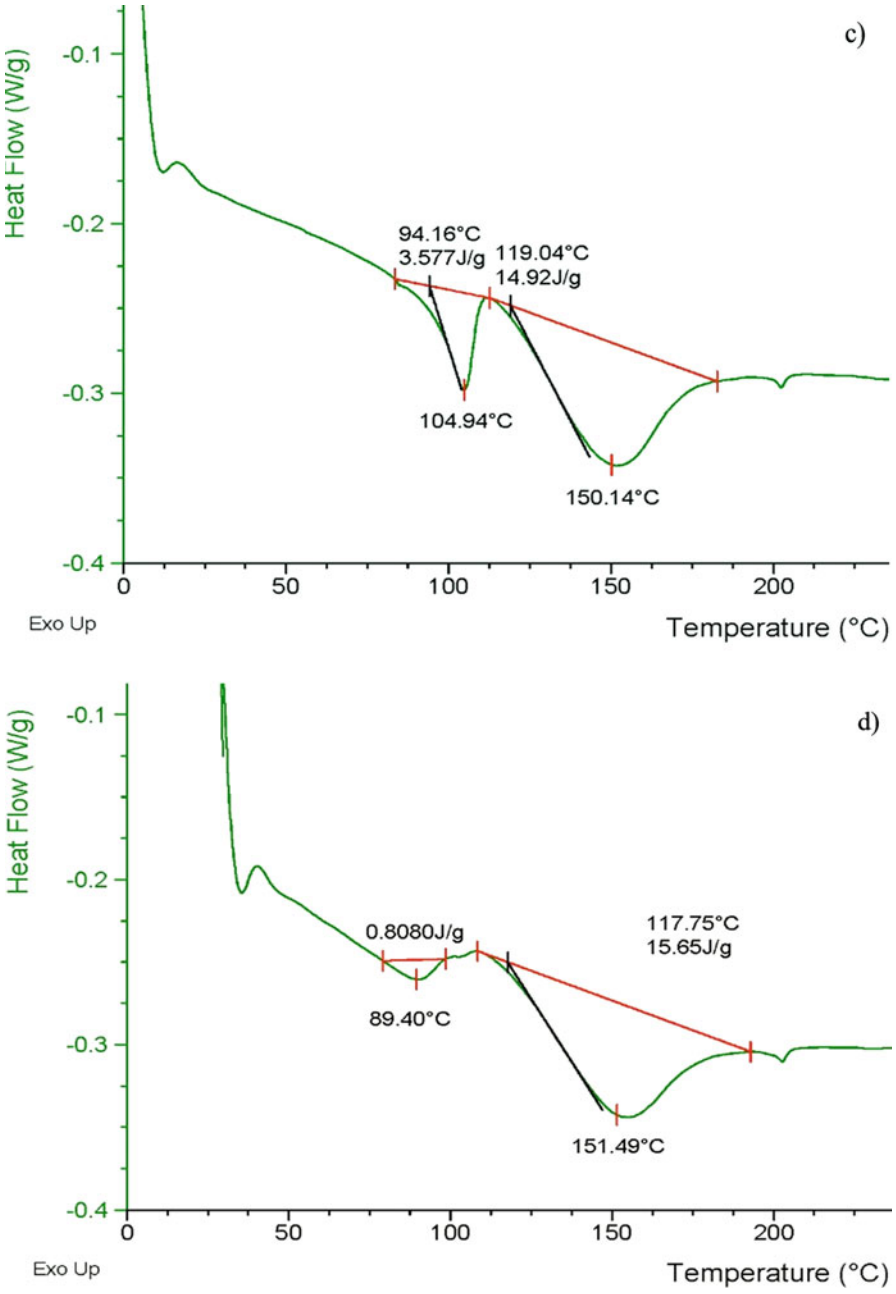

Fig. 9.3 (continued)

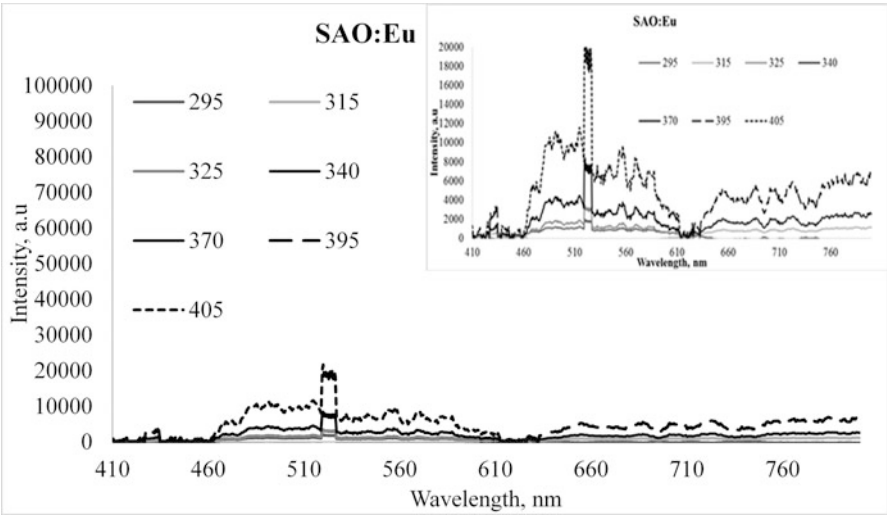

Fig. 9.4 Luminescent spectra of sample $Sr_4Al_{14}O_{25}$:Eu

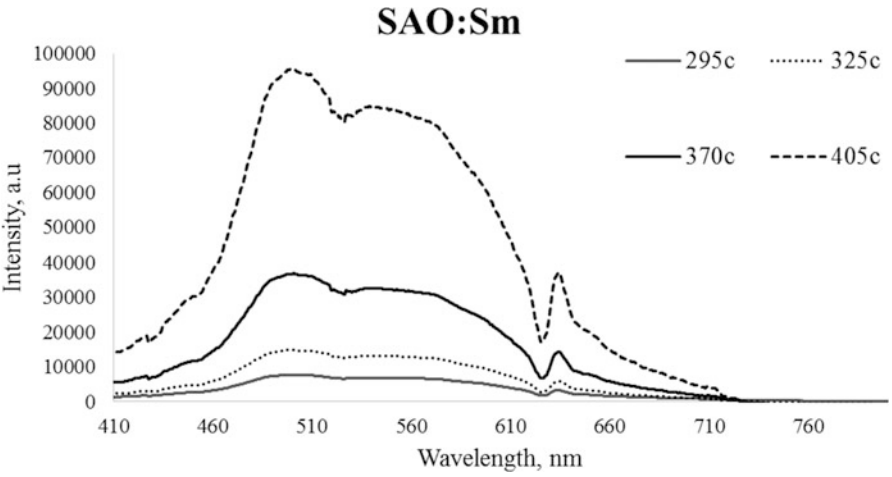

Fig. 9.5 Luminescent spectra of sample $Sr_4Al_4O_7$: Sm

(PL) spectroscopy showed signals in the wavelength range of 450–600 nm. The most intensive emission was observed when the 405 nm excitation source was used. At this wavelength the phosphorescence of the synthesized powders is very intensive. This result shows that it is possible to observe both luminescent effects (fluorescence and phosphorescence) using one excitation source.

In Fig. 9.7 that on joint doping with two materials it is possible to observe the traces of both doping RE materials. This means that rare earth ions have successfully doped into the host materials. For all examined compositions emission takes place in

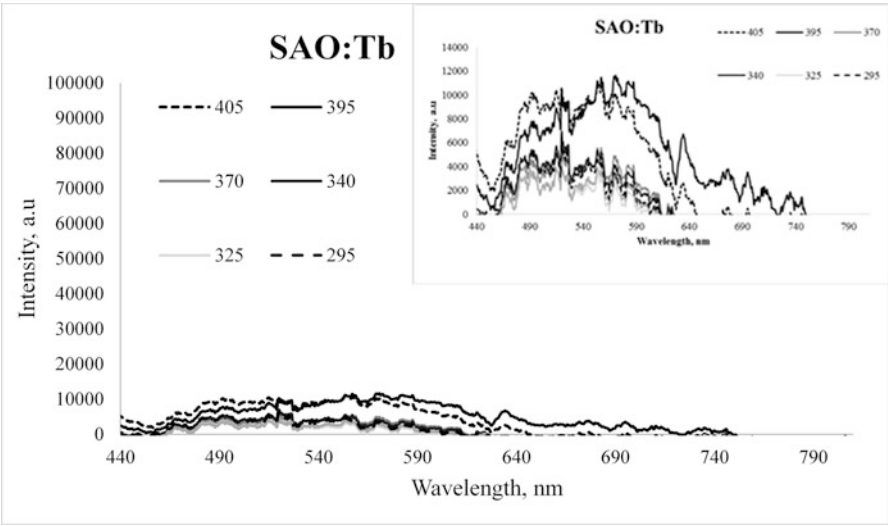

Fig. 9.6 Luminescent spectra of sample SAO: Tb

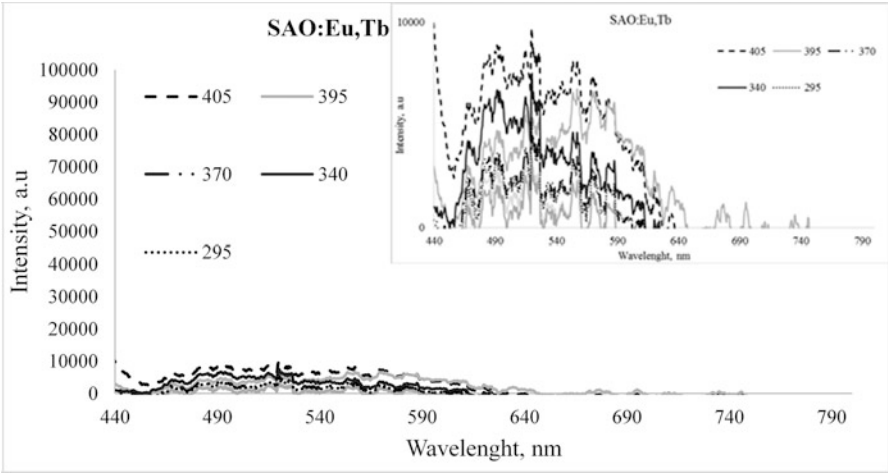

Fig. 9.7 Luminescent spectra of sample SAO: Eu, Tb

the range 450–600 nm. One can see again that the emission is most intense when the pumping source works with a wavelength of 405 nm. At this wavelength the phosphorescence of the powders is strong, which shows that using a single source it is possible to induce both effects (fluorescence and phosphorescence). In the co-doped materials bands of both dopant elements are observed.

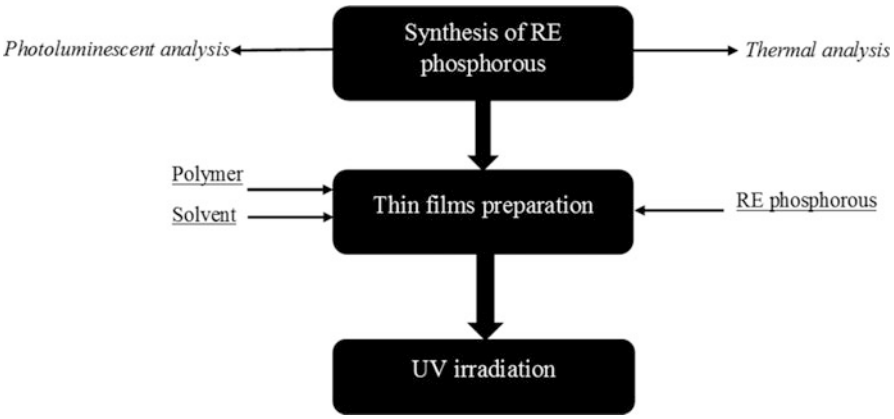

Fig. 9.8 Procedure of luminescent polymer films preparation

9.3.4 Luminescent Polymer Thin Films

Using the synthesized phosphors polymer films with defined polymer concentration were prepared. The procedure was performed according to the scheme given in Fig. 9.8.

Mixtures of polymers and luminescent powders were stirred using an ultrasonic bath. The resulting dispersions were cast on a glass or polymer (PET) substrate and left to evaporate the solvent for a day at room temperature. The whole procedure is given in Fig. 9.8. It has been found that the fillers used are evenly distributed in the polymer (when the concentration is high).

9.4 Conclusions

Stoichiometric strontium aluminates produced by hydrothermal procedure were characterized by XRD, thermal and photoluminescent methods. The roentgenograms show the presence of different phases in the powders; low values of T_g and T_c are seen in the thermograms. We explain this with the synthesis conditions and an incomplete reaction of the starting components. This actually has a positive effect on the luminescent properties of the resulting materials compared to the commercial ones. Namely, we observe a strong phosphorescence with a short time afterglow and a low fluorescence in the visible spectrum. This combination of both effects is important for their application for valuable documents protection. In addition, we have prepared polymer films these synthesized materials. We observed good dispersion of the particles in the polymer matrix and the dual (photo-and phosphorescent)

luminescent properties. Moreover, some of the resulting composites are flexible and with good adhesion to the substrates. Therefore, our studies have shown the possibility of new applications of strontium aluminates as luminophore additives for polymers and paper substrates.

References

1. Dutczak D, Jüstel T, Ronda C, Meijerink A (2015) Eu(2+) luminescence in strontium aluminates. Phys Chem Chem Phys 17(23):15236–15249
2. Kim D, Kim H, Kim C (2016) Effect of composition and impurities on the phosphorescence of green-emitting alkaline earth aluminate phosphor. PLoS One 11(1):e0145434
3. Song H, Chen D (2007) Combustion synthesis and luminescence properties of $SrAl_2O_4$:Eu^{2+}, Dy^{3+}, Tb^{3+} phosphor. Luminescence 22(6):554–558
4. Teng Y, Zhou J, Ma Z, Smedskjaer MM, Qiu J (2011) Persistent near infrared phosphorescence from rare earth ions co-doped strontium aluminate phosphors nanostructured materials, carbon nanotubes, and fullerenes. J Electrochem Soc 158(2):K17–K19
5. Sun W, Chen Y, Wu L, Jiang Y (2013) Phase composition and luminescent properties of strontium aluminate long persistence phosphor synthesized by combustion synthesis method with different Sr/Al ratios. Rare Metals 32(4):414–419
6. Mishra K, Revaprasadu N, Hillie K, Steyn W, Coetsee E, Swart H (2009) Strontium aluminate/polymer composites: morphology, luminescent properties, and durability. J Appl Polym Sci 112 (6):3347–3354

Chapter 10
Characterization of Nickel-Cobaltite Spinel Prepared by Different Methods

D. Nicheva, V. Boev, P. Petkov, G. Avdeev, and T. Petkova

Abstract $NiCo_2O_4$-spinel has been prepared by three different techniques: The Pechini method, a hydrothermal method and a precipitation reaction. The obtained samples have been examined by X-ray diffraction (XRD), differential thermal analysis (DTA) and scanning electron microscopy (SEM). The results reveal that materials prepared by the Pechini method possess two phases (Co_3O_4 and NiO), those obtained by the hydrothermal method have phases of $Ni_xCo_{3-x}O4$. Single-phase $NiCo_2O_4$ material is obtained only by the precipitation reaction. The obtained $NiCo_2O_4$ material is nanosized, exhibiting thermal stability up to 700 °C, where thermal decomposition of $NiCo_2O_4$ to Co_3O_4 and NiO takes place. In the region of thermal stability, a linear thermal expansion of the elementary cell has been observed.

Keywords $NiCo_2O_4$ · Spinels

10.1 Introduction

During the last decade oxide spinels of transition metals are subject of fundamental and applied research due to the expected encouraging properties. Different approaches are reported for the synthesis of spinel phases like thermal

D. Nicheva (✉)
Institute of Electrochemistry and Energy Systems Acad.E.Budevski, Bulgarian Academy of Sciences, Sofia, Bulgaria

University of Chemical Technology and Metallurgy, Sofia, Bulgaria
e-mail: denitza_vladimirova@abv.bg

V. Boev · T. Petkova
University of Chemical Technology and Metallurgy, Sofia, Bulgaria

P. Petkov
Department of Physics, University of Chemical Technology and Metallurgy, Sofia, Bulgaria

G. Avdeev
Institute of Physical Chemistry, Bulgarian Academy of Sciences, Sofia, Bulgaria

P. Petkov et al. (eds.), *Advanced Nanotechnologies for Detection and Defence against CBRN Agents*, NATO Science for Peace and Security Series B: Physics and Biophysics, https://doi.org/10.1007/978-94-024-1298-7_10

decomposition of oxalate precursors [1] and hydrothermal [2–4] and sol-gel methods [5]. The properties of these oxides are strongly determined by the oxidation states of the constituent cations and by the distribution of the octahedral and tetrahedral sites in the spinel structure. The synthesis method can influence both the oxidation state of the cations and the cation distribution. A study of the influence of the preparation method on the material behavior is thus of great importance. Nickel cobaltite, $NiCo_2O_4$, is one of the promising metal oxides in the family of cobaltite materials with the spinel structure AB_2O_4, where A=Ni, B=Co. Generally Ni ions occupy the octahedral sites in the $NiCo_2O_4$ structure; the Co ions are distributed over both octahedral and tetrahedral sites. The advantages of these oxides are associated with their activity, availability, low cost, thermodynamic stability, low electrical resistance and environmental friendship [6–8].

The goal of our work was to study different approaches aiming to achieve single-phase $NiCo_2O_4$. We present results on the synthesis of $NiCo_2O_4$ by three different different methods: the Pechini method, a hydrothermal method and precipitation reaction. We report the thermal behavior and particle size of the obtained materials. The crystal structure and size distribution can be controlled by adjusting the synthesis route and the molar ratio of the materials.

10.2 Experimental

10.2.1 Preparation

Pechini method: Analytical grade $Co(NO_3)_2{\cdot}6H_2O$ and $Ni(NO_3)_2{\cdot}6H_2O$ with the stoichiometric ratio of 2:1 (Co/Ni) were dissolved in ethylene glycol and citric acid under constant stirring and heated. The obtained mixture was vacuum dried for 2 h. Finally the obtained product was slowly heated in air up to 350 °C.

Hydrothermal synthesis: Nickel nitrate and cobalt nitrate were dissolved in distilled water under continuously stirring to obtain a homogenous solution. Thereafter, aqueous NaOH solution was added dropwise to the solution to reach pH = 11. The suspension was then transferred in an autoclave and heated at 180 °C for 5 h. The autoclave was naturally cooled to ambient temperature after the process. The solution was washed in 0.1N HNO_3 followed by rinsing in distilled water and ethanol. The synthesized product was dried at 100 °C for 2 h and calcinated at 500 °C for 5 h.

Precipitation reaction: Starting materials in precipitation reaction synthesis were $Co(NO_3)_2{\cdot}6H_2O$ and $Ni(NO_3)_2{\cdot}6H_2O$; they were dissolved in NH_4OH under constant stirring. The resulting precipitate was filtered and then dried for 2 h. The obtained product was slowly heated in air to 350 °C. The reactions that take place during the synthesis are:

$$2\,NH_4OH + Co(NO_3)_2 \rightarrow 2\,NH_4NO_3 + Co(OH)_2$$
$$2\,NH_4OH + Ni(NO_3)_2 \rightarrow 2\,NH_4NO_3 + Ni(OH)_2$$
$$2\,Ni(OH)_2 + 4\,Co(OH)_2 + O_2 \rightarrow 2\,NiCo_2O_4 + 6\,H_2O$$

10.2.2 Characterization

XRD analyses were performed by using a X-ray diffractometer model Philips APD-15. The data were collected at ambient temperature with a constant step of $0.02°s^{-1}$ in the range $2\theta = 20–80°$ at the wavelength $\lambda = 1.54178$ Å using a CuKα tube. The high temperature behavior of the $NiCo_2O_4$ sample were examined using a PANalytical – Empyrean diffractometer with Cu Kα radiation. The instrument is equipped with a Anton Paar HTK 16N camera. A HighScore Plus software was used to analyze the X-ray diffraction data. The sample was heated with a rate of 10°/min in the temperature range 25–900 °C. The study was conducted in a platinum crucible.

Thermal analyses of the samples were carried out with a DTA/TG Setaram Labsys Evo 1600 instrument in air atmosphere. The temperature range of investigation was between 30 and 900 °C using a heating rate of 10 K/min and flow rate of 20 ml/min. The morphology of the material was determined using scanning electron microscopy (SEM JEOL, JEM-200CX).

10.3 Results and Discussion

10.3.1 X-Ray Diffraction Analysis

In the process of identifying $NiCo_2O_4$ we two of the most widely used ICDD (PDF # 731702) and ICSD (24211) databases. The phases existing in the databases were compared to the cell parameter values of the experimentally obtained phases. Figure 10.1 presents the diffractograms of the samples obtained by the three methods. Using the Pechini method (Fig. 10.1a) a multi-phase product, i.e. a mixture of Co_3O_4 and NiO, is obtained. The amount of Co_3O_4 is 69 wt%, that of NiO of wt. 31%, determined by the Rietveld method [9]. The results show that there is no nickel incorporated into the Co_3O_4 lattice, the oxides exist individually not reacting to each other.

Hydrothermal samples consist of two phases: $Ni_xCo_{3-x}O_4$ spinel with an amount of 98 wt.% and NiO with 2 wt.% (Fig. 10.1b). The difference with the previously described synthesis is the inclusion of more nickel atoms in the spinel crystal lattice. The general chemical formula of the obtained spinel phase is $Ni_{0.93}Co_2O_4$.

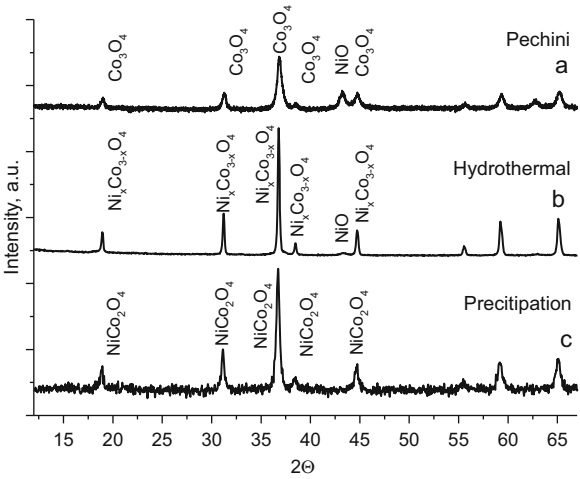

Fig. 10.1 XRD diffractograms (**a**) Pechini method, (**b**) Hydrothermal method, (**c**) Precitipation reaction

A single-phase product is achieved only by means of the precipitation reaction (Fig. 10.1c). The diffractogram does not show peaks of impurities; the $NiCo_2O_4$ obtained is well defined spinel phase with an average crystallite size between 150 and 200 nm, values obtained from the diffractogram. The profile fit of the experimental diffractogram shows that the $NiCo_2O_4$ obtained by the precipitation reaction has a slightly smaller elementary cell parameter (a = 8.101(1)) compared to that given in the databases (a = 8.1140). The chemical analysis confirms that the metal ions are in a stoichiometric ratio, for this reason the difference in the cell parameter values can only be explained by the presence of oxygen defects.

The thermal behavior of the samples was investigated simultaneously with DTA and high temperature X-ray analysis. The results from the thermal analysis of the samples obtained by the Pechini and hydrothermal methods are similar: a low weight loss at low temperatures and an endothermic peak above 860 °C due to the decomposition the material. In the TG curve of the $NiCo_2O_4$ obtained by the precipitation reaction a weight loss of 0.6% was observed in the temperature range between 40 and 150 °C due to the evaporation of adsorbed water. The next weight loss of approximately 5.6% in the 833–883 °C temperature range is accompanied by an endothermic peak at 866 °C which effects serve as an indication of the decomposition of $NiCo_2O_4$ (Fig. 10.2).

The high temperature XRD (HTXRD) structural analysis made on the sample obtained by the precipitation reaction confirms the DTA data. The $NiCo_2O_4$ compound remains stable up to 700 °C. Above this temperature changes in the diffraction picture become visible, and at temperature of 833 °C first diffractive peaks of NiO appear. As the temperature increases the NiO peaks continue to grow (Fig. 10.3). In the temperature range 25–700 °C the $NiCo_2O_4$ cell parameter shows a linear grow as shown in Fig. 10.4.

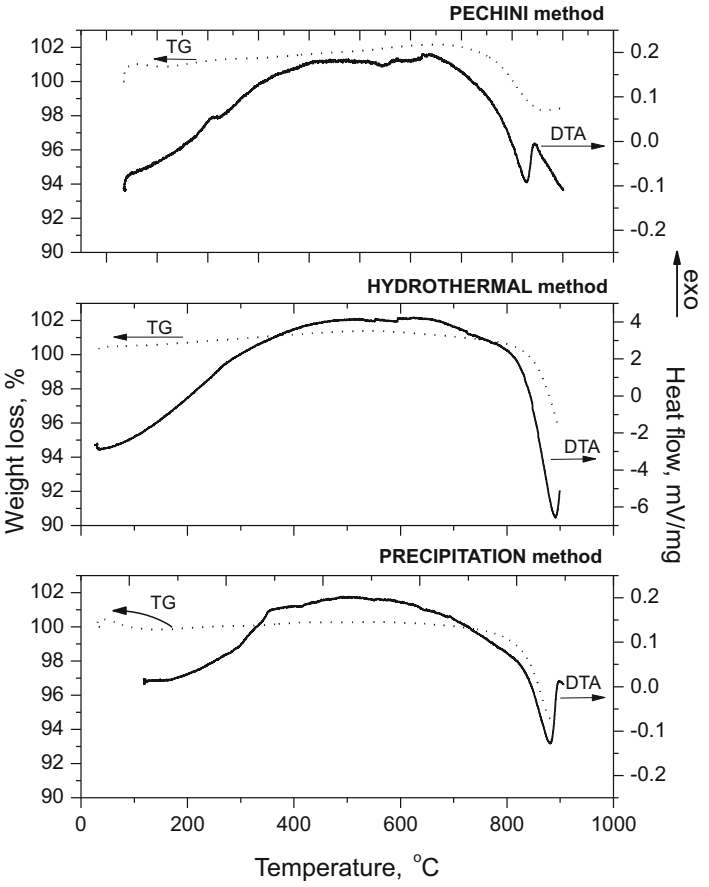

Fig. 10.2 TDA/T_g curves of materials obtained from the three methods

10.3.2 Scanning Electron Microscopy

The morphology and particles size distribution of nickel-cobalt oxides studied by SEM is shown in Fig. 10.5. The sample prepared by the Pechini method possesses a microstructure composed by spherical particles of several microns distributed among smaller nanosized particles (Fig. 10.5a).

The material prepared by the hydrothermal method is a mixture of spherical particles with size of 100 nm and others much bigger of 1–2 μ size (Fig. 10.5b). SEM images of $NiCo_2O_4$ synthesized by the precipitation method demonstrate nanosized homogeneously distributed particles equal in size and not larger than 200 nm (Fig. 10.5c).

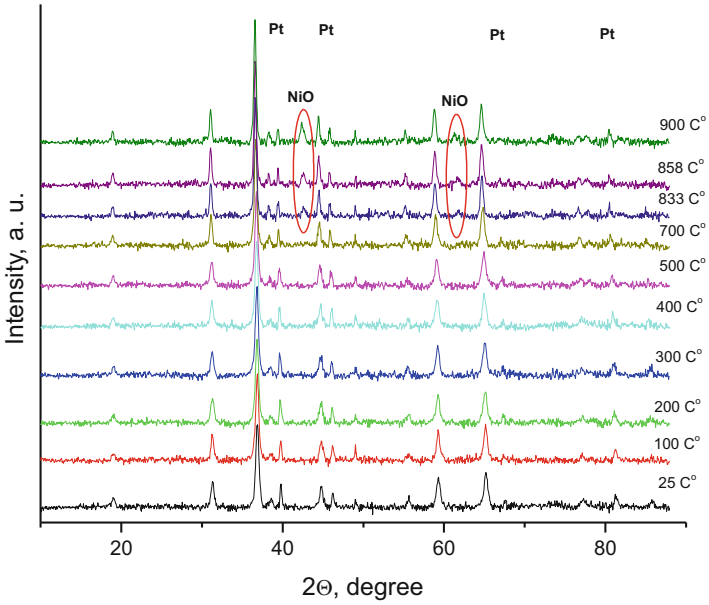

Fig. 10.3 HTXRD spectra of $NiCo_2O_4$ obtained by the precipitation reaction. Pt is platinum from the crrucible

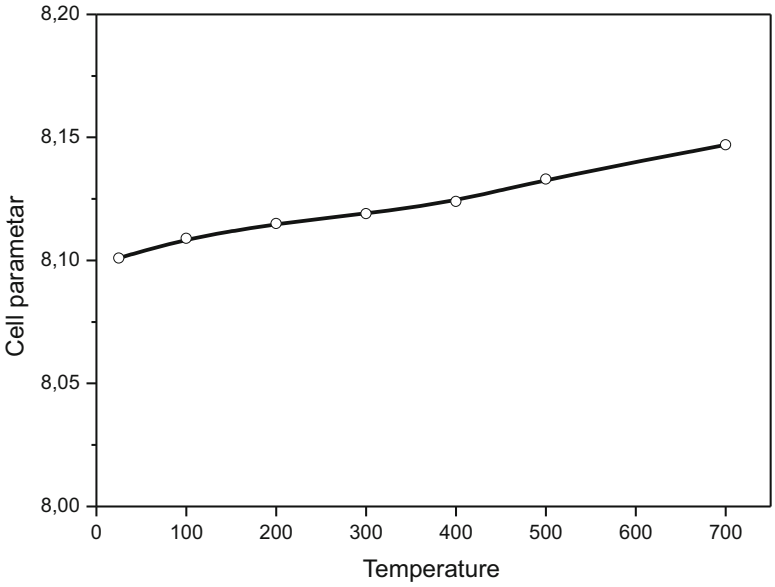

Fig. 10.4 Cell parameter of $NiCo_2O_4$ as a function of the temperature

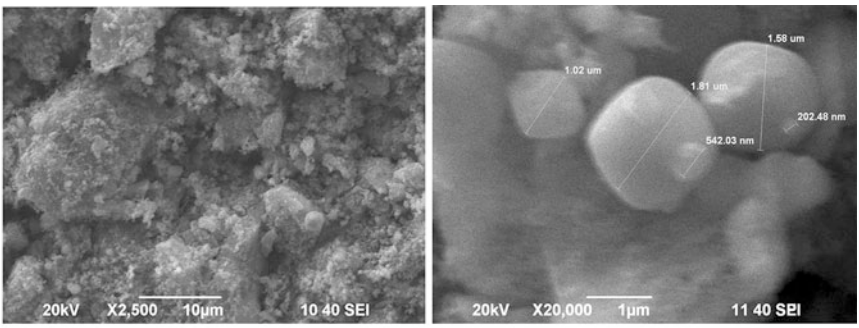

a) Pechini method

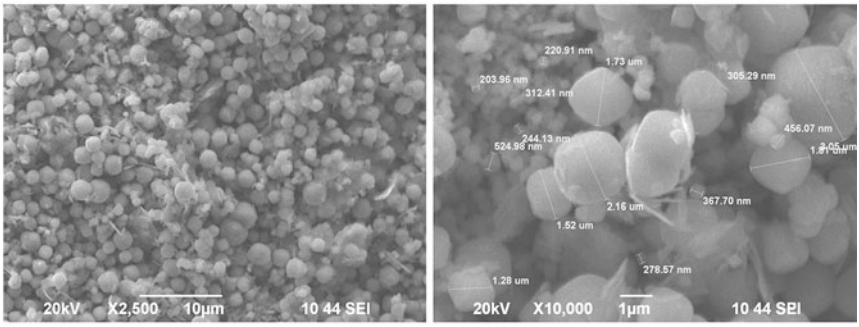

b) Hydrothermal method

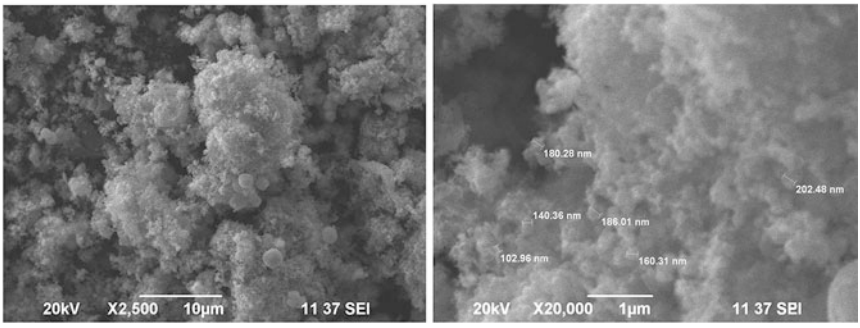

c) Precipitation reaction

Fig. 10.5 SEM images of materials prepared by different methods. (**a**) Pechini method. (**b**) Hydrothermal method. (**c**) Precipitation reaction

10.4 Conclusion

The comparison of three approaches for the synthesis of $NiCo_2O_4$ shows that the Pechini method and the hydrothermal method are not suited to obtain pure single-phase $NiCo_2O_4$. Using the precipitation reaction we achieved nanosized single-phase $NiCo_2O_4$ thermally

stable up to 700 °C. In the temperature range from room temperature up to 700 °C the cell parameter increases regularly revealing that no phase changes occur. Thermal decomposition of $NiCo_2O_4$ starts above 700 °C.

Acknowledgments PP is deeply grateful to the Bulgarian Scientific Fund for the financial support under project DUNK-01/3/2009.

References

1. Chinh VD, Trung NQ (2015) Preparation of gold-silver alloy nanoparticles supported on $NiCo_2O_4$ spinel oxides for the treatment of CO in atmosphere. J Nanosci Nanotechnol 15:4403–4408
2. Durrani SK, Asif A, Rehman U, Hussain N, Naveed S (2011) Hydrothermal synthesis and characterization of nanosized zinc cobaltite spinel ceramic. J Pak Mater Soc 5(1):5–11
3. Singh JP, Singh RN (2000) New active spinel-type $M_xCo_{3-x}O_4$ films for electro-catalysis of oxygen evolution. J New Mater Electrochem Syst 3:131–139
4. Ding R, Qi L, Jia M, Wang H (2013) Hydrothermal and soft-templating synthesis of mesoporous $NiCo_2O_4$ nanomaterials for high-performance electrochemical. Appl Electrochem 43:903–910. https://doi.org/10.1007/s10800-013-0580-z
5. Guene M, Diagne A, Fall M (2007) Preparation of nickel-cobalt spinel oxides $Ni_xCo_{3-x}O_4$. Comparison of two physical properties stemming from four different preparation methods and using carbon paste electrode. Bull Chem Soc Ethiop 21(2):255–262
6. Tjarayil NJ, Raveendran R, Varghese A, Chithra PG (2008) Optical, electrical and structural studies of nickel-cobalt oxide nanoparticles. Indian J Eng Mater Sci 15:489–496
7. Chang S, Zainal Z, Bantan K, Yusof NA, Wan Yusoff WM, Prabaharan SRS (2012) Surface morphology and crystallinity of metal oxides in nickel-cobalt binary system. Sains Malays 41(4):465–470
8. Hamdani M, Singh RN, Chartier P (2010) Co_3O_4 and Co- based spinel oxides bifunctional oxygen electrodes. Int J Electrochem Sci 5:556–577
9. Rietveld HM (1967) American crystallographic assosiation single-crystal intensity project report. Acta Crystallogr 22:151–152

Chapter 11
Structure and Thermal Behaviour of Lithium Sodium Sulphate

Z. Slavkova, O. Kostadinova, G. Avdeev, and T. Petkova

Abstract Lithium sodium sulphate (LNS) has been synthesised by two methods: mechanical ball milling and melt quenching. The obtained materials have been studied by means of X-ray diffraction, scanning electron microscopy (SEM), Infrared spectroscopy and differential scanning calorimetry. The influence of the synthesis method on the structure and behaviour of the materials will be discussed.

Keywords Lithium sodium sulphate · Nanocomposites · Mechanical ball milling · Melt quenching · Infrared absorption spectroscopy · Thermal characterisation

11.1 Introduction

From the protection of our domestic media over the environment, to the control of industrial processes, gas detection and monitoring is a necessity. Among the widely used sensors are those based on solid electrolytes [1, 2]. Reliability and performance of sensor devices are in direct correlation with the used materials and their properties and behaviour down to the molecular level. In this sense, the study of the physical and chemical behaviour of materials in the light of the structural organization is a significant point.

Lithium sodium sulphate (LNS) has been intensively studied both at room and at higher temperatures [3–5]. It is known that LNS undergoes a first order phase transition from the beta to the alpha phase at approximately 500–515 °C and that

Z. Slavkova (✉) · O. Kostadinova · T. Petkova
"Solid State Electrolytes" Section, Institute of Electrochemistry and Energy Systems – BAS, Sofia, Bulgaria
e-mail: zdravka_slavkova@iees.bas.bg

G. Avdeev
Institute of Physical Chemistry, Bulgarian Academy of Sciences, Sofia, Bulgaria

P. Petkov et al. (eds.), *Advanced Nanotechnologies for Detection and Defence against CBRN Agents*, NATO Science for Peace and Security Series B: Physics and Biophysics, https://doi.org/10.1007/978-94-024-1298-7_11

the α-phase exhibits a ionic conductivity of about 10^{-1} S/cm [5, 6]. Some electrochemical experiments with LNS as an electrolyte have been performed [7, 8].

In this work two synthesis methods – melt quenching and mechanical ball milling- are applied to obtain LNS. The goal is to define the material structure and dependence of the characteristics on the preparation method.

11.2 Experimental

Equimolar ratios of Li_2SO_4 (Sigma-Aldrich) and Na_2SO_4 (Alfa Aesar) were used for both syntheses. A mechanochemically prepared LNS sample was synthesised by means of a MicroNano Tool's PBM-2 planetary ball mill. The precursors were milled for 72 h with a planetary disk velocity of 580 rpm.

The melt-quenched sample was obtained in a Dentamatic 6000-M furnace. The initial materials were placed in a platinum crucible and heated at 800 °C for 2 h. Thereafter, the melt was rapidly quenched between two pre-cooled copper plates.

X-ray analysis of both samples was accomplished by a Panalytical multifunction X-ray diffractometer (model: Empyrean), equipped with an Anton Paar accessory for high temperatures (APHTK-16N) and a 3D PIXcel detector. FT-Infrared absorption (FTIR) spectra were measured in the middle infrared region (500–4000 cm^{-1}) with the aid of a diamond ATR-equipped Bruker Tensor 27 FT spectrometer. The spectra were collected with 64 scans at a resolution of 2 cm^{-1}, referring to air as background spectrum.

Differential scanning calorimetric investigations (DSC) were conducted by a Netzsch DSC 404 cell in argon atmosphere in Al_2O_3 crucibles and in the temperature range 50–750 °C. The heating rate was 10 °C/min.

Scanning electron microscopy/EDS measurements were performed with a Bruker EDS system coupled to a Vega3 TESCAN SEM microscope. Before measurement the samples were covered with a conductive carbon layer deposited by sputtering.

11.3 Results and Discussion

The XRD analysis reveals that at the synthesis conditions the samples consist of lithium sodium sulphate and small amounts of not completely reacted Na_2SO_4 (Fig. 11.1). No visible differences in the diffractograms are observed. The mechanically ball milled sample (MBM) is composed of 91, 6 wt. % β-LNS and 8,4 wt. % Na_2SO_4 (Fig. 11.1a), whereas the quenched sample (MQ) possesses a β-LNS content of 97 wt. % and 3 wt. % of Na_2SO_4 (Fig. 11.1b). The size of the β-LNS powder crystallites varies between 70 and 81 nm; the size of the Na_2SO_4 grain is about 160 nm. Calculations for the bulk material revealed significantly larger β-LNS crystallites (average 129 nm) and the same size for sodium sulphate. Obviously,

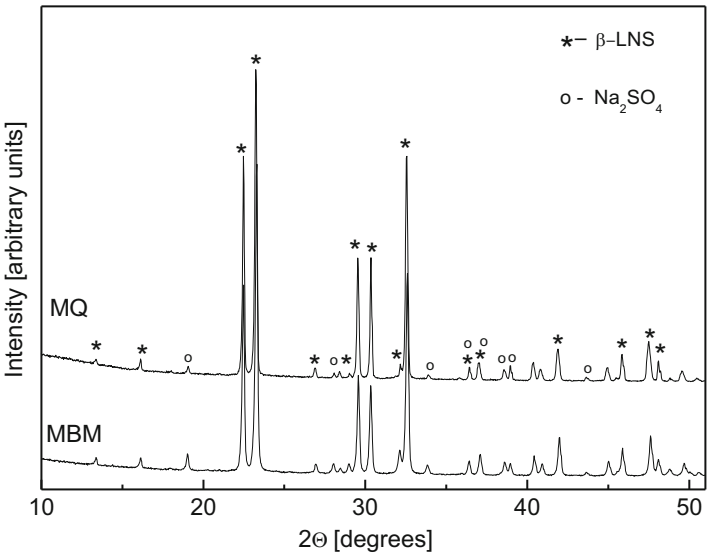

Fig. 11.1 XRD of the MBM and MQ samples

mechanical ball milling is a good approach to obtain materials with fine particles and small crystallites, but on the other hand, melt quenching allows preparation of a sample in a shorter period of time.

The $LiNaSO_4$ structure has been investigated by several authors [4, 5, 9–13]; however, there are still unclear issues regarding the structural organization and its influence on the material behaviour. Using the X-ray synchrotron technique, Freiheit et al. [10] proposed the idea that this salt is composed of SO_4 and LiO_4 tetrahedra that form a channel with strong covalent Li-O-S bond, while the Na ions are positioned inside the channels. Above the phase transition temperature from β to α phase the sulphate ions rotate and the cations move through the lattice.

Free sulphate ions belong to the T_d point group and have nine vibration modes: the non-degenerate IR-inactive ν_1 mode, the triply degenerate IR-active ν_3 and ν_4 modes, and the doubly degenerate IR-inactive ν_2 mode. In sulphate salts the sulphate anions are perturbed by crystal field effects and by covalent bonding to the cation through one or more oxygen atoms. Then, the symmetry changes from T_d to C_{3v}. As an effect of the changed coordination of the SO_4 ion, the IR-forbidden vibrations ν_1 (3A1) and ν_2 (6E) are permitted, the degenerate vibrations ν_3 (3A1+6E) and ν_4 (3A1 +6E) are split, and the fundamental frequencies are shifted. The shifts are determined by the polarising power of the cations, which in turn are determined by the cationic radius and charge [13]. Regarding the cationic vibrations, 12 phonon modes (3A1 +3A2+6E) (the so-called external modes) are expected, but and only nine of them (3A1+6E) are optically active. These external modes are located in the far-IR region [4, 11]. In most of the structural studies using the IR technique, the authors observe

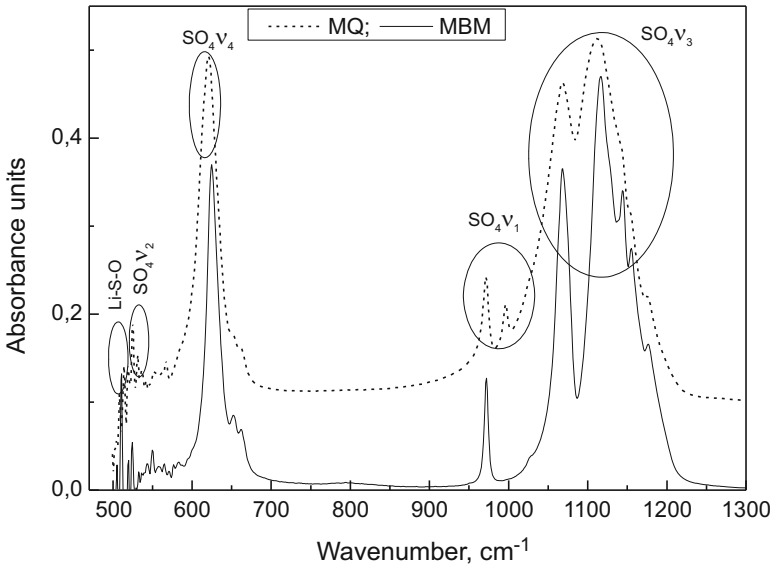

Fig. 11.2 Infrared absorption spectra of a LNS bulk sample (MQ) and a LNS powder (MBM)

only few of the predicted modes. For instance, Sahaya et al. [12] observed two of the predicted three ν_1 modes of the sulphate ion and only three of the expected six ν_2 modes. Furthermore, Lv et al. [13] found again only two ν_1 and three ν_3 modes.

In this study, the ATR FTIR method was used to probe the local environment which gives more accurate results. Thus, it is possible to observe the three predicted ν_1 vibrations for the SO_4 ion. The first two at 971 cm^{-1}, 996 cm^{-1} (in MQ) are clearly seen peaks, while the third one, positioned at 1026 cm^{-1} is seen as a shoulder (Fig. 11.2). All of them are transverse optical (TO) modes (having a field vector perpendicular to the direction of propagation of the beam). Up to now, to the best of our knowledge, only in the work of Zhang et al. [4] scientists were able to observe the third mode with the aid of a polarisation technique.

IR spectroscopy is a very sensitive vibrational technique that might give information not only on the chemical species that constitute the material and the strength of their bonds. The width of an IR peak is, in much respect, affected by the strength of the intermolecular interactions, the degree of disorder (e.g. due to inhomogenities) or strain. Thus, IR absorption can give a wide picture of the intrinsic nature of a sample. In this investigation, the two spectra bear close resemblance regarding the positions of the bands which implies similar chemical and structural organisation. Nevertheless, the melt quenched sample give a more detailed IR spectrum. This effect may be attributed to strain in the material that results from the synthesis method (Fig. 11.2).

Additionally, we observed five ν_3 vibrations: three with A_1 and two with E symmetry. The symmetric bending modes (ν_2) are expected in 470–514 cm^{-1}

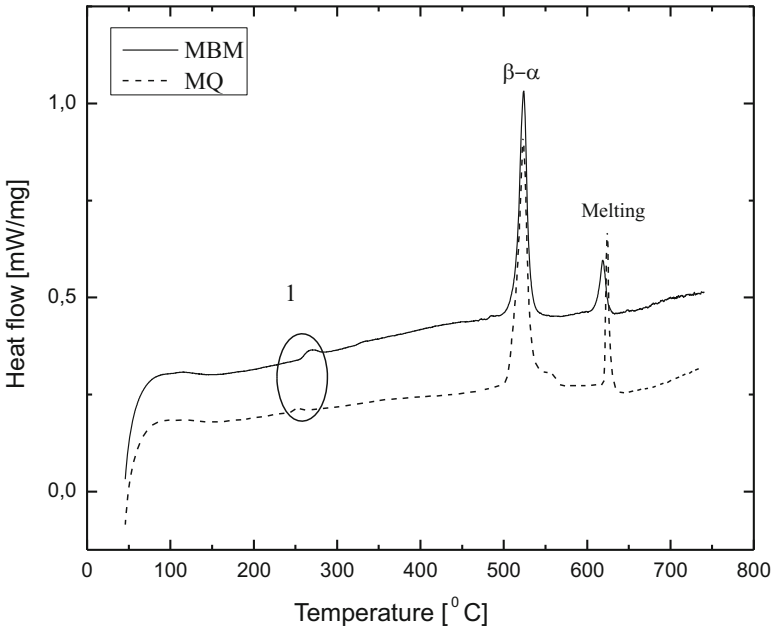

Fig. 11.3 Thermograms of bulk LNS (MQ) (dashed line) and LNS powder (MBM) (solid curves)

frequency region, so we observe only one band (the one located at 514 cm^{-1}) arising from symmetric bending vibration with E symmetry. Two of the predicted three ν_4 (A_1) modes are clearly seen at 655 cm^{-1} and 664 cm^{-1}, while third that is expected around 630 cm^{-1} is under the ν_4 E envelope with a maximum at 620 cm^{-1}. In the spectral range in between 500 and 600 cm^{-1} a number of relatively low peaks is observed. They might be attributed to cationic interactions with the SO_4 ions [10].

The DSC curves of the MQ and MBM samples show three endothermic peaks. The small peak (1) in Fig. 11.3 is associated with a phase transition of the Na_2SO_4 [14]. There is a slight difference in the values marking this transition: in the MQ sample it begins approximately at 243 °C, 11 °C lower than for the MBM sample. The variation is minor and might be attributed to the preparation method.

However, when it comes to the first order phase transition temperature of LNS (from hexagonal to a body centred cubic cell) there are no outstanding differences in the temperature values. Both samples exhibit peaks with a maximum at 523 °C.

These data are in good agreement with data reported by other authors [5, 6]. The melting point varies; the bulk material melts at 624 °C, the powder material at 618 °C. This effect might be due to the difference in the particle size. As was already discussed, the powder sample has a structure with smaller crystallites which defines the lower melting temperature of the MBM sample. SEM images of the MBM and MQ samples reveal completely different morphologies of both samples. The powder sample (Fig. 11.4) consists of very fine crystallites confirming the data from the

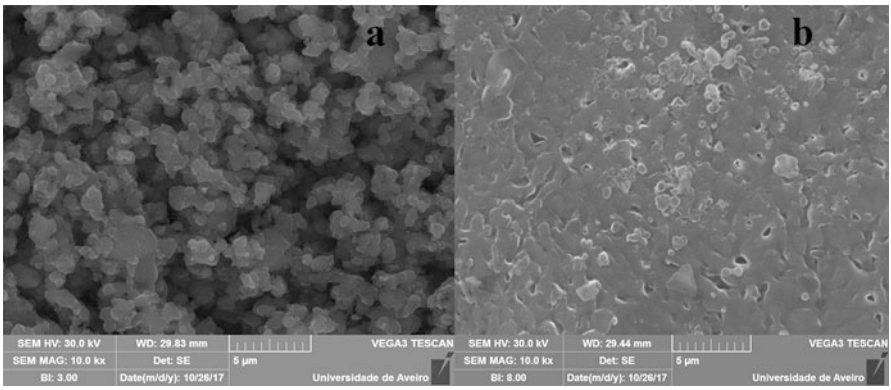

Fig. 11.4 SEM images of MBM (left) and MQ (right) samples with magnification ×10.0 k

XRD analysis. The particles are clustered in groups – a result from the synthesis method. When it comes to the bulk sample the scene is different. A variety of shapes and sizes of crystals are aligned and frozen during the quenching (Fig. 11.4b).

11.4 Conclusion

The lithium sulphate prepared by two independent methods is composed of 92–97 weight % $LiNaSO_4$ and small amounts of Na_2SO_4. The structure and the thermal behaviour of the material are matching irrespective of the preparation method. The IR study reveals that the two spectra bear close resembles regarding the positions of the bands which implies similar chemical and structural organisation. The phase transition and material melting occurs at similar temperatures. The morphology, however, is very different and depending strongly on the preparation method.

Acknowledgments The research leading to these results has received funding from the Bulgarian NSF under grant No E02/3. The authors are thankful to the Dr. M. Graca from the University of Aveiro, Department of Physics for conducting the SEM analyses.

References

1. Moseley PT (1997) Solid state gas sensors. Meas Sci Technol 8(3):223–237
2. Fergus JW (2007) Solid electrolyte based sensors for the measurement of CO and hydrocarbon gases. Sensors Actuators B 122:683–693
3. Dharmasena G, Frech R (1995) Orientational disorder in lithium sodium sulfate. J Chem Phys 102:6941
4. Zhang M, Putnis A, Salje EKH (2006) Infrared spectroscopy of superionic conductor $LiNaSO_4$: vibrational modes and thermodynamics. Solid State Ionics 177:37–43

5. Shakhovoy RA, Sarou-Kanian V, Rakhmatullin A, Véron E, Bessada C (2016) High-temperature nuclear magnetic resonance study of phase transition kinetics in $LiNaSO_4$. J Appl Phys 118:243906
6. Pimenta MA, Echegut P, Hauret G, Gervais F (1987) Lattice dynamics of $LiNaSO_4$ above room temperature studied by infrared spectroscopy. Phase Transit Multinatl J 9(2):185–203
7. Ritchie AG (1994) High temperature electrochemical discharges of lithium-copper oxide cells using solid electrolytes. Solid State Ionics 70/71:662–665
8. Feng Y, Luo J, Chuang KT (2006) Chemical stability of $LiNaSO_4$ electrolyte during operation in a H_2–O_2 fuel cell. J Electrochem Soc 153:A865
9. Morosin B, Smith DL (1967) The crystal structure of lithium sodium sulfate. Acta Cryst 22:906
10. Freiheit H-C, Kroll H, Krane H-G, Kirfel A (1999) High temperature X-ray synchrotron study on $LiNaSO_4$: anharmonic thermal vibrations and effective atomic potentials, HASYLAB annual report
11. Teeters D, Frech R (1982) Raman and infrared reflectivity spectra of $^6LiNaSO_4$ and $^7LiNaSO_4$. J Chem Phys 76(2):799
12. Sahaya Prabaharan SR, Muthusubramanian P, Saravanan R, Mohanlal SK (1992) Growth of $LiNaSO_4$ single crystals from a solution of stoichiometric pH value. Bull Mater Sci 15:355–362
13. Lv W, Tong Z, Yin Y-M, Yin J, Ma Z-F (2015, July) Novel nano-composites SDC–$LiNaSO_4$ as functional layer for ITSOFC. Nano-Micro Letters 7(3):268–275
14. Rasmussen SE, Jørgensen JE, Lundtoft B (1996) Structures and phase transitions of Na_2SO_4. J Appl Crystallogr 29(1):42–47

Chapter 12
Influence of Modification on the Structure and Physical Properties of Arsenic Trisulfide. A Short Review

Oleksandr Paiuk

Abstract This brief review summarizes some results of studies concerning the effect of modification (doping with amphoteric elements, laser and electron-beam irradiation) on the physico-structural and optical properties of chalcogenide glasses and the possibility of using doped arsenic trisulphide to create multilayer composite structures for the recording of holographic optical elements.

Keywords Chalcogenide glasses · Transition elements · Multilayer nanostructures

12.1 Introduction

Chalcogenide glasses (ChGs) are now being intensively studied as promising materials for the use as active sensor elements as well as passive constituent parts of sensor systems. ChGs are widely used due to their unique physical properties, such as the optical transparency in the infrared range, which allows them to be successfully used in various infrared optics devices [1–3], a wide glass formation area and resistance to corrosive media. The presence of a large variety of photoinduced effects [4–11] makes it possible to obtain different optical elements by means of laser, electron or ion irradiation. In addition, the glasses serve as host matrix for doping with rare-earth elements and transition or other metals [12–15], which alter the properties of the initial material as a result of structural and electronic transformations in the glass network [14, 15].

Thus, the combination of the properties mentioned above makes it possible to develop new functional nanocomposite materials, including hybrid organic-inorganic media [16] based on chalcogenide glasses and polymers for optical and optoelectronic applications. In the present review results are summarized which were

O. Paiuk (✉)
V.E. Lashkaryov Institute of Semiconductor Physics, National Academy of Sciences in Ukraine, Kyiv, Ukraine
e-mail: paiuk@ua.fm

P. Petkov et al. (eds.), *Advanced Nanotechnologies for Detection and Defence against CBRN Agents*, NATO Science for Peace and Security Series B: Physics and Biophysics, https://doi.org/10.1007/978-94-024-1298-7_12

obtained within the frame of implementation of the FP-7 SECURE R-2I project and projects N0117U000422 and No.M/95-2017 (reg. number 0117U003395) of the Ministry of Education and Science of Ukraine concerning modification of chalcogenide glasses, polymer materials, the creation of composites on their base and application of such media for the fabrication of optical elements [15, 17–25].

12.2 Chalcogenide Glasses: Characterization and Properties

Chalcogenide vitreous semiconductors are formed by a combination of one or more chalcogen elements (S, Se, Te) and other elements from the IV-th, V-th and VI-th group of the periodical table. Bulk glasses are mostly prepared in sealed vacuumed quartz ampoules by means of the melt-quenching method. X-ray analysis confirmed the amorphous nature of the investigated bulk chalcogenide glasses from the As–S system doped with Mn or Cr. Undoped and doped samples were studied by Raman spectroscopy, differential scanning calorimetry (DSC), IR spectroscopy, SQUID magnetometry, positron annihilation spectroscopy, atom force microscopy, and magnetic force microscopy.

12.2.1 Raman Spectroscopy

Raman spectra of As-S system glasses doped with manganese, chromium or ytterbium show that doping has a noticeable effect on the glass structure [14, 15, 17, 18]. Raman spectra of As_2S_3 glasses are characterized by an intense main band at 346 cm^{-1}, which is associated with symmetric stretching vibrations of As–(S)–As in $As(S)_{3/2}$ pyramids. As a result of the Mn, Cr or Yb introduction, an intensity increase of the bands at 192, 227, 236 cm^{-1} is observed, which are associated with internal vibrations of As_4S_4 structural units containing As–As homopolar bonds, and the band at 365 cm^{-1} corresponding to As-S vibrations in As_4S_4. On the contrary, band intensity at 496 cm^{-1}, which is characteristic for vibrations of S-S bonds, decreases. Thus, the study of the glass structure showed that they are microheterogeneous (nanoheterogeneous) and consist of $As(S)_{3/2}$ and other molecular structural units (As_4S_4, S_8, S_n), the relative content of which varies with the concentration level of Mn, Cr or Yb [13, 17, 18].

12.2.2 Differential Scanning Calorimetry

DSC data have shown that with the increase of the Mn content in As_2S_3 glasses the glass transition temperature and also the activation energy of the glass transition

decrease [17]. This can be connected with structural changes due to interaction of Mn with the As_2S_3 glass matrix which was considered using data of Raman and X-ray diffraction measurements [15]. It should be noted that this trend persists for glasses doped with chromium or ytterbium [15, 17, 18].

12.2.3 IR Spectroscopy

The absorption of pure As_2S_3 glass and those doped with transition metals differs. The spectral profiles of impurity absorption in the case of chromium and manganese are similar, but there are some differences in the compositional features of the main impurity absorption bands [19]. Thus, for glasses doped with chromium, an insignificant increase in the absorption band intensity of hydroxyl groups at 3601 cm^{-1} is observed, while for Mn-doped samples this band remains unchanged. Thus, the concentration changes of OH groups are not the same in both ChGs systems, and it can be assumed that the OH-impurity complexes are structurally related to sulfur atoms, the relative content of which varies with doping level and nature of the element. It should be noted that the intensity of the vibrational band at 2488 cm^{-1}, due to the presence of -S-H complexes, increases monotonically with increasing chromium admixture and is practically independent of the manganese concentration. Such features fully correspond to changes in the structural compactness of the investigated glasses, the decrease of which leads to the formation of a "free volume" in glass network and the appearance of peculiar "micro- or nanopores". -S-H complexes can be formed on the internal surfaces of these pores as a result of rapid cooling of the glass melt. On the other hand, most of the broken S-bonds arise during ChGs formation. Such bonds become inactive or saturation occurs not only due to the formation of structural chains of sulfur atoms, but also by binding them to hydrogen atoms. Moreover, during ChGs synthesis the parallel saturation process of dangling sulfur bonds by oxygen atoms (band at 1158 cm^{-1}, related to the SO_2 impurity) occurs, which can be adsorbed from the atmosphere or formed during high-temperature splitting of H_2O molecules. Formation of As-O bonds (bands at 1048 cm^{-1} and 792 cm^{-1}) and S-S bonds (980 cm^{-1}) occurs through the incorporation of SO_2 molecules into the glass network; as a consequence, the As-As bond is broken and the bond >As–O–S–O–As< is formed. The intensity of the peaks corresponding to As-O and S-S bonds increases with decreasing intensity of the SO_2 band. Note that these processes are relatively weak, because the structural chains of the glass are not fully, but only partially closed. They form bridges between neighboring atoms, fragments and blocks [19].

12.2.4 Photoluminescence Spectra

Low-temperature photoluminescence spectra for As_2S_3:Cr glasses with different Cr contents are in agreement with a model proposed by Tanaka [15, 18]. According to this model, half-gap photoluminescence arises from the recombination of electrons, trapped by anti-bonding states of wrong (and strained) bonds at around the mid-gap Fermi level, and holes in Urbach-edge states at the valence-band top. These wrong bonds are considered as the most dominant defects in covalent chalcogenide semiconductors such as As_2S_3. Rare-earth luminescence As-S glasses modified by Yb have two luminescence bands in the near IR range, located near 980 and 1060 nm. In this case, transitions from the excited state $^2F_{5/2}$ to the main state $^2F_{7/2}$ characteristic for Yb^{3+} ions are pronounced. The intensity of the photoluminescence increases with an increase of the ytterbium concentration [14]. In the case of Mn- doped As_2S_3, two luminescence peaks are observed, one at approximately 545 nm (2.28 eV) which can be connected with transitions of Mn^{2+} ions located near structural defects. The next peak at 578 nm (2.14 eV) can be associated with radiative transitions of Mn ions placed near structure defects.

12.2.5 Magnetic Properties

Chalcogenide glasses, in particular As_2S_3 glasses, are diamagnetics. Introduction of transitional (Mn, Cr) and rare earth (Yb) impurities changes the magnetic properties of the investigated chalcogenide glasses [13, 15]. In fields near 6 T, a mass magnetization dependence M=M(T) was observed, which is characteristic for paramagnetics and ferromagnetics in the paramagnetic temperature range and described by the Curie–Weiss law. A more detailed study of Mn-doped glasses showed that there is a transition from the paramagnetic to the ferromagnetic state at a temperature T~14 K. In this case, a difference between M(T) dependences for various cooling mode disappears in a field $B = 0.197$ T. It can be assumed that the influence of the external field on the orientation of the intrinsic magnetic moments of the dopant atoms on the energy value exceeds the energy of their thermal movement [13, 15].

12.3 Multilayer Nanostructures Based on Doped Arsenic Trisulfide

Using thin layers of chalcogenide glasses as high-resolution media and selective etching after exposure, high quality holographic diffraction gratings [6, 9] and other elements [4, 5, 10] were obtained. Using multilayer nanostructures based on chalcogenide glasses as recording media enables to obtain a surface relief directly during the recording process [26–28]. The development of methods of one-step surface

relief formation is considered as a promising way for the manufacturing of planar diffractive optical elements. Usually, chalcogenide layers and chalcogenide multilayer nanostructures are prepared by thermal vacuum deposition of two materials (ChGs and Se) [20–28]. The technological processes allow to deposit layers and structures onto substrate with thicknesses from 0.005 to 3.0 μm and different geometry. Using of interferometric holographic recording makes it possible to obtain grating surface reliefs based on multilayer nanostructures, for example, As_2S_3:Mn (2 wt.%) – Se and $Ge_5As_{37}S_{58}$–Se with good optical quality of the surface relief [21, 25]. Besides surface relief formation using mentioned above nanostructures, As_2S_3:Mn (2 wt.%)–Se enables to obtain simultaneously also a magnetic relief [23]. In the case of $Ge_5As_{37}S_{58}$–Se it is possible to realize direct one-step recording of diffraction gratings by e-beam exposure as well as e-beam pixel recording of other elements [24, 25].

12.4 Conclusion

- Doping with Mn, Cr or Yb causes a decrease in the glass transition temperature and leads to a change in the relative concentration of basic and non-stoichiometric structural elements characteristic for As_2S_3 and also to the change of luminescent and magnetic properties.
- IR transmission spectroscopy in the 700–4000 cm^{-1} region showed the existence of impurity absorption bands of hydroxyl, oxide and carbon-containing groups, the growth or decrease of which depends on the concentration and nature of the doping element.
- Nanomultilayered, compositionally modulated ChGs–Se multilayer structures are perspective for the recording of optical elements using light or e-beam exposure; simultaneous direct one-step recording of surface and magnetic relief formation was shown using $As_{40}S_{60}$:Mn (2 wt.%)–Se nanomultilayer structures.

References

1. Adam J-L, Calvez L, Trolès J, Nazabal V (2015) Chalcogenide glasses for infrared photonics Int J Appl Glas Sci 6:287
2. Singh V, Lin PT, Patel N, Lin H, Li L, Zou Y, Deng F, Ni C, Hu J, Giammarco J, Soliani AP, Zdyrko B, Luzinov I, Novak S, Novak J, Wachtel P, Danto S, Musgraves JD, Richardson K, Kimerling LC, Agarwal AM (2014) Mid-infrared materials and devices on a Si platform for optical sensing Sci Technol Adv Mater 15:14603
3. Starecki F, Charpentier F, Doualan J-L, Quetel L, Michel K, Chahal R, Troles J, Bureau B, Braud A, Camy P, Moizan V, Nazabal V (2015) Mid-IR optical sensor for CO detection based on fluorescence absorbance of Dy^{3+}:$Ga_5Ge_{20}Sb_{10}S_{65}$ fibers Sensors Actuators B Chem 207:518
4. Saito K, Utsugi Y, Yoshikawa A (1988) X-ray lithography with a Ag-Se/Ge-Se inorganic resist using synchrotron radiation J Appl Phys 63:565

5. Stronski AV (1998) Production of metallic patterns with the help of high resolution inorganic resists In: Harman G, Mach P (eds) Microelectron. Interconnections AssemNATO ASI Ser. 3. High Technology, vol 54, 1st edn. Springer, Dordrecht, pp 263–293
6. Vlček M, Stronski AV, Sklenař A, Wagner T, Kasap SO (2000) Structure and imaging properties of $As_{40}S_{60-x}Se_x$ glasses J Non-Cryst Solids 266–269:964
7. Stronski AV, Vlček M (2000) Imaging properties of $As_{40}S_{40}Se_{20}$ layers Opto-Electronics Rev 8:263
8. Suzuki T, Hosono H (2002) Ion-beam doping of silver in amorphous As_2S_3 thin films J Appl Phys 92:1821
9. Stronski AV, Vlček M (2002) Photosensitive properties of chalcogenide vitreous semiconductors in diffractive and holographic technologies applications J Optoelectron Adv Mater 4:699
10. Jain H, Vlcek M (2008) Glasses for lithography J Non-Cryst Solids 354:1401
11. Tanaka K, Shimakawa K (2011) Light-induced phenomena Amorphous chalcogenide semiconductors and related materials. Springer, New York, pp 141–193
12. Stronski AV, Vlček M, Stetsun AI, Sklenař A, Shepeliavyi PE (2000) Raman spectra of Ag-and Cu-photo-doped $As_{40}S_{60-x}Se_x$ films J Non-Cryst Solids 270:129
13. Gubanova A, Kryskov T, Paiuk O, Laiho R, Lahderanta E, Stronski A (2009) Some magnetic properties of chalcogenide glasses As_2S_3 and As_2Se_3 doped with Cr, Mn, and Yb Mold J Phys Sci 8:178
14. Paiuk AP, Stronski AV, Vlček M, Gubanova AA, Krys'kov TA, Oleksenko PF (2011, October 2011) Peculiarities of As-S glass structure doped with ytterbium In: Tománek P, Senderáková D, Páta P (eds) Proceedings of SPIE 8306, photonics, devices, and systems V, p 830617
15. Stronski A, Paiuk O, Gudymenko A, Klad'ko V, Oleksenko P, Vuichyk N, Vlček M, Lishchynskyy I, Lahderanta E, Lashkul A, Gubanova A, Krys'kov T, Klad'ko V, Oleksenko P, Vuichyk N, Vlček M, Lishchynskyy I, Lahderanta E, Lashkul A, Gubanova A, Krys'kov T (2015) Effect of doping by transitional elements on properties of chalcogenide glasses Ceram Int 41:7543
16. Kavetskyy T, Smutok O, Gonchar M, Demkiv O, Klepach H, Kukhazh Y, Šauša O, Petkova T, Boev V, Ilcheva V, Petkov P, Stepanov AL (2017) Laccase-containing ureasil–polymer composite as the sensing layer of an amperometric biosensor J Appl Polym Sci 134:45278
17. Paiuk O, Lishchynskyy I, Stronski A, Kryskov T, Gubanova A, Pribylova H, Vlček M (2011) Properties As_2S_3 glasses doped with manganese: calorimetrical study and Raman spectroscopy Phys Chem Solid State 12:594
18. Stronski AV, Paiuk OP, Strelchuk VV, Nasieka IM, Vlček M (2014) Photoluminescence of As_2S_3 doped by Cr and Yb Semicond Phys Quantum Electron Optoelectron 17:341
19. Paiuk AP, Stronski AV, Vuichyk NV, Gubanova AA, Krys'kov TA, Oleksenko PF (2012) Mid-IR impurity absorption in As_2S_3 chalcogenide glasses doped with transition metals Semicond Phys Quantum Electron Optoelectron 15:152
20. Achimova E, Stronski A, Abaskin V, Meshalkin A, Paiuk A, Prisacar A, Oleksenko P, Triduh G (2015) Direct surface relief formation on As_2S_3–Se nanomultilayers in dependence on polarization states of recording beams Opt Mater 47:566
21. Stronski A, Achimova E, Paiuk A, Abaskin V, Meshalkin A, Prisacar A, Triduh G, Lytvyn O (2015) Surface relief formation in $Ge_5As_{37}S_{58}$–Se nanomultilayers J Non-Cryst Solids 409:43
22. Paiuk O, Meshalkin A, Triduh G, Prisacar A, Achimova E, Stronski A, Abashkin V, Lytvyn O, Senchenko O, Gubanova A (2016) Nanomultilayer As_2S_3: Mn-Se systems: properties and use as the recording media In: Sontea V, Tiginyanu I (eds) 3rd international conference on nanotechnologies and biomedical engineering. IFMBE proceedings, vol 55. Springer, Singapore, pp 72–75
23. Stronski A, Achimova E, Paiuk O, Meshalkin A, Prisacar A, Triduh G, Oleksenko P, Lytvyn P (2017) Direct magnetic relief recording using $As_{40}S_{60}$: Mn–Se nanocomposite multilayer structures Nanoscale Res Lett 12:286

24. Stronski A, Achimova E, Paiuk O, Meshalkin A, Abashkin V, Lytvyn O, Sergeev S, Prisacar A, Triduh G (2016) Holographic and e-beam image recording in $Ge_5As_{37}S_{58}$–Se nanomultilayer structures Nanoscale Res Lett 11:39
25. Stronski A, Achimova E, Paiuk O, Meshalkin A, Abashkin V, Lytvyn O, Sergeev S, Prisacar A, Oleksenko P, Triduh G (2016) Optical and electron-beam recording of surface relief's using $Ge_5As_{37}S_{58}$–Se nanomultilayers as registering media J Nanopart Res 39:96
26. Kikineshi A (2001) Light-stimulated structural transformations and optical recording in amorphous nano-layered structures J Optoelectron Adv Mater 3:377
27. Kokenyesi S (2006) Amorphous chalcogenide nano-multilayers: research and development J Optoelectron Adv Mater 8:2093
28. Reinfelde M, Teteris J, Potanina E (2014) Surface relief grating formation in amorphous $As_{40}S_{15}Se_{45}$ and As_2S_3 films under 0.532 μm wavelength Illumination Can J Phys 92:659

Part IV
Electrical Characterization

Chapter 13
Time Domain Versus Frequency Domain in the Characterization of Materials

L. C. Costa

Abstract The development of sampling oscilloscopes provided the possibility to measure dielectric relaxation processes in materials directly in the time domain. This allows using relaxation models in time. In complex systems, the use of non-Debye models, such as Kohlrausch-Williams-Watts is common. Simultaneously, the use of frequency domain measurements is becoming very useful, due to the possibility of using highly accurate impedancemeters. To obtain a complete characterization of the dielectric response, a large range of frequencies and temperatures must be used.The different regimes of the dielectric function can be observed and the dynamics of the relaxations can be determined, using modelling with different empirical models, such as Cole-Cole, Cole-Davidson and Havriliak-Negami. In this contribution, different examples of the use of time and frequency domain measurements are presented, showing the capability of both techniques.

Keywords Time domain · Frequency domain · Impedance spectroscopy · Dielectric relaxation

13.1 Introduction

Measurements in the time domain have undergo a remarkable development in the last years, particularly in the pursuit of relaxation phenomena. The advantage inherent to this method is that the measurement of time is carried out directly, without the need to make use of the inverse Fourier transformation. The main disadvantages imposed by the fact that the measurement is made under broadband conditions, resulting in the degradation of the signal-to-noise ratio [1]. In the case of high impedance samples, the use of an electrometer in needed, which can detect currents on the order of fA. Initially, the sample is subjected to a direct voltage for

L. C. Costa (✉)
I3N and Physics Department, University of Aveiro, Aveiro, Portugal
e-mail: kady@ua.pt

P. Petkov et al. (eds.), *Advanced Nanotechnologies for Detection and Defence against CBRN Agents*, NATO Science for Peace and Security Series B: Physics and Biophysics, https://doi.org/10.1007/978-94-024-1298-7_13

sufficient time allowing to calculate the d.c. conductivity, and then it is abruptly turned off in order to study how the current decreases over time [2].

In the frequency domain, the dielectric response of a material is measured with broadband frequencies from a few mHz to hundreds of GHz [3–5]. To cover such a wide frequency range, several measurement techniques are required.

In the low frequency range, it is possible to use bridges [6], lock-in amplifiers [7] and impedance analyzers [8]. Network analyzers are used for the microwave range, based on the small perturbation theory [9].

Several advantages and limitations can be attributed to these techniques, but using broadband dielectric spectroscopy to observe the temporal evolution of materials has a relatively recent origin. In the early years, low frequency measurements were made using transient current methods [10]. An important improvement was achieved with the emergence of radio frequency electronic devices in the beginning of twentieth century, which increased the frequency range of measurement up to MHz. Finally, in the 1950s, methods including microwave frequencies measurements were developed [11].

In most cases, the electrical measurements are made in a neutral atmosphere using electrodes in the sample. The general approach is to apply an electrical stimulus and observe the response of the material. It is assumed that the properties of the electrode-material system are time-invariant, which is an important demand to the measurement method [12].

Actually,dielectric spectroscopy can deliver the complex permittivity $\varepsilon^*(\omega) = \varepsilon'(\omega) - i\varepsilon''(\omega)$ or derived quantities related to it. The dielectric modulus [13] $M = \varepsilon^{-1}$, a complex quantity with $M^*(\omega) = M'(\omega) + iM''(\omega)$ is often used for conducting materials, where the relaxation can be hidden by the conductivity. The macroscopic properties, the impedance $Z^*(\omega) = Z'(\omega) - iZ''(\omega)$ or the admittance $Y = Z^{-1}$ with $Y^*(\omega) = Y'(\omega) + iY''(\omega)$ can also define the properties of a material. The interrelations between these quantities are simple when the shape and size of the samples are known on which the measurements are made.

13.2 Time Domain

The simplest condition of a relaxation phenomenon was initially described by Debye [14], based on a physical model that consisted of dipoles immersed in a viscous medium, with the assumption that they did not interact each other. Under the action of an electric field, the dipoles were oriented, returning to the equilibrium position after turning off the field. Then, the depolarization function presents an exponential decay with time,

$$\Phi(t) = \Phi_0 \exp\left(-\frac{t}{\tau_D}\right) \tag{13.1}$$

where Φ_0 is the initial polarization and τ_D the relaxation time. The depolarization current is

$$I(t) = \frac{\partial \phi(t)}{\partial t} = I_0 \exp\left(-\frac{t}{\tau_D}\right) \tag{13.2}$$

Linearization of this expression proceeds to

$$\ln I(t) = \ln I_0 - \frac{t}{\tau_D} \tag{13.3}$$

It is known that a large class of physical systems including polymers and glasses have a comportment for the depolarization function which is not purely exponential. This behaviour can be described by a stretched exponential function, attributed to Kohlrausch in the nineteenth century [15] which was subsequently tested and used empirically by Williams and Watts [16] to study the dielectric relaxation in several materials. His analytical expression is

$$\Phi(t) = \Phi_0 \exp\left(-\left(\frac{t}{\tau_K}\right)^{\beta_K}\right) \tag{13.4}$$

where τ_k is the relaxation time and β_k is an exponent between 0 and 1.

One approach to describe this situation is to postulate a statistical distribution of relaxation times for the different atoms, molecules, aggregates or other degrees of liberty. So, assuming that these contributions are additive [17], we can write,

$$\Phi(t) = \Phi_0 \int_0^\infty g(\tau) \exp\left(-\frac{t}{\tau}\right) d\tau \tag{13.5}$$

where the distribution of relaxation times function, $g(\tau)$ must obey the normalization condition

$$\int_0^\infty g(\tau)\, d\tau = 1 \tag{13.6}$$

In this case, the depolarization current is

$$I(t) = \frac{\partial \Phi(t)}{\partial t} = I_0 \left(\frac{t}{\tau_K}\right)^{\beta_K - 1} \exp\left(-\left(\frac{t}{\tau_K}\right)^{\beta_K}\right) \tag{13.7}$$

where

$$I_0 = \frac{\Phi_0\, \beta_K}{\tau_K} \tag{13.8}$$

Another non-Debye relaxation can be expressed by the Curie-von Schweidler law [18, 19], where the depolarization current is

$$I(\mathrm{t}) \quad = A\mathrm{t}^{-s} \tag{13.9}$$

where A is a constant and $0<s<1$.

The linearization of this expression yields

$$\ln I(t) = \ln A - s \ln t \tag{13.10}$$

From a practical point of view, Eqs. (13.3) and (13.10) can be used to test if Debye or Curie-von Schweidler models are adequate to fit the experimental results. It is known that in a large number of materials these models are not acceptable, and then Kohlrausch-Williams-Watts (KWW) is the most useful representation.

13.3 Frequency Domain

To attain the frequency domain from the time domain, we can use the Fourier transformation. In the Debye model, that is, corresponding to a single relaxation time, we can obtain [1],

$$\varepsilon^*(\omega) \quad = \quad \varepsilon_\infty \quad + \quad \frac{\varepsilon_\mathrm{s} - \varepsilon_\infty}{1 + i\omega\tau_\mathrm{D}} \tag{13.11}$$

where $\varepsilon^*(\omega)=\varepsilon'(\omega)-i\varepsilon''(\omega)$, $\omega = 2\pi f$ is the angular frequency, and $\varepsilon\infty$ and εs are the dielectric constants at high and low frequencies, respectively. This equation can be solved for the real and imaginary parts:

$$\varepsilon'(\omega) \quad = \quad \varepsilon_\infty \quad + \quad \frac{\varepsilon_\mathrm{s} - \varepsilon_\infty}{1 + \omega^2{\tau_\mathrm{D}}^2} \tag{13.12}$$

$$\varepsilon''(\omega) \quad = \quad \frac{(\varepsilon_\mathrm{s} - \varepsilon_\infty)\ \omega\tau_\mathrm{D}}{1 + \omega^2{\tau_\mathrm{D}}^2} \tag{13.13}$$

Figure 13.1 shows typical curves for the real and imaginary parts of the complex permittivity for the Debye model in semi-logarithmic scale. These curves are symmetric relative to the relaxation frequency point $\omega = 1/\tau_\mathrm{D}$.

From Eqs. (13.12) and (13.13) we can obtain

$$\left(\varepsilon'(\omega) - \frac{\varepsilon_\mathrm{s} + \varepsilon_\infty}{2}\right)^2 \quad + \quad \left(\varepsilon''(\omega)\right)^2 \quad = \quad \left(\frac{\varepsilon_\mathrm{s} - \varepsilon_\infty}{2}\right)^2 \tag{13.14}$$

which is an equation of a circle. Then, in the Cole-Cole representation, that is ε'' versus ε', we have a semi-circle with radius $(\varepsilon_\mathrm{s} - \varepsilon_\infty)/2$and the center in the point $((\varepsilon_\mathrm{s} + \varepsilon_\infty))/2, 0)$. Figure 13.2 shows the data of Fig. 13.1 in this representation.

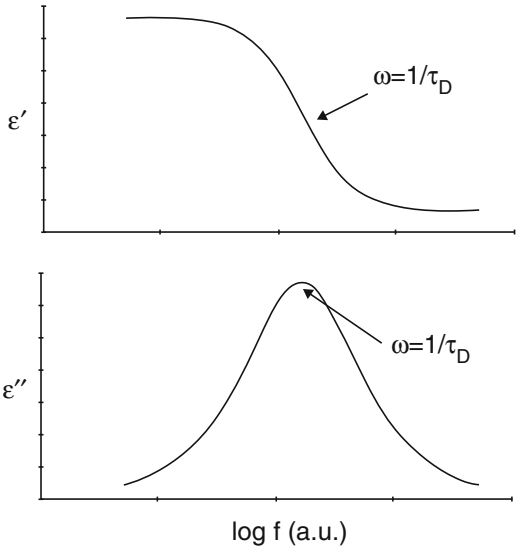

Fig. 13.1 Real and imaginary parts of the complex permittivity for the Debye model

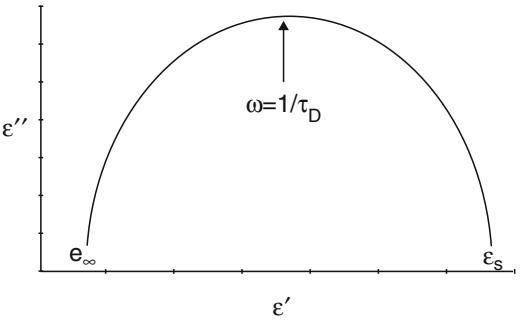

Fig. 13.2 Cole-Cole plot for the data of Fig. 13.1

For systems where non-Debye relaxation behavior is observed, Eq. (13.11) must be modified, using the concept of distribution time function, g(τ) [20]

$$\varepsilon^*(\omega) = \varepsilon_\infty + (\varepsilon_s - \varepsilon_\infty) \int_0^\infty \frac{g(\tau)}{1 + i\omega\tau} d\tau \tag{13.15}$$

the real and imaginary parts of the complex permittivity are:

$$\varepsilon'(\omega) = \varepsilon_\infty + (\varepsilon_s - \varepsilon_\infty) \int_0^\infty \frac{g(\tau)}{1 + \omega^2\tau^2} d\tau \tag{13.16}$$

$$\varepsilon''(\omega) = (\varepsilon_s - \varepsilon_\infty) \int_0^\infty \frac{\omega\tau \; g(\tau)}{1 + \omega^2\tau^2} d\tau \tag{13.17}$$

Then, for non-Debye behavior, one of the most used models is the Cole-Cole [21], described by

$$\varepsilon^*(\omega) = \varepsilon_\infty + \frac{\varepsilon_s - \varepsilon_\infty}{1 + (i\omega\tau_{cc})^{1-\alpha}} \tag{13.18}$$

where τ_{cc} is the characteristic relaxation time and α a parameter ($0<\alpha \leq 1$) that leads to a broadening of the relaxation function. In this case, the curve in the Cole-Cole plot is also symmetric, as in the Debye case, but the center of the semi-circle is not on the abscissa, but below it, as shown in Fig. 13.3. The angle of the asymptotes in the limits of high and low frequency is the same, that is $(1-\alpha)\pi/2$.

Another possibility, quite often used in complex materials, is the Cole-Davidson model [22],

$$\varepsilon^*(\omega) = \varepsilon_\infty + \frac{\varepsilon_s - \varepsilon_\infty}{(1 + i\omega\tau_{cd})^{\beta}} \tag{13.19}$$

where again the exponent β reflects the broadening of the relaxation function ($0 < \beta \leq 1$) and τ_{cd} the relaxation time. In this case, the curve in the Cole-Cole plot (ε'' versus ε') is no longer symmetric, as we can see in Fig. 13.4. In the low frequency regime, the asymptote has an angle of $\pi/2$, in the high frequency regime the angle is $\beta\pi/2$.

An even more general model function was introduced by Havriliak and Negami [23], which is a combination of Cole-Cole and Cole-Davidson functions:

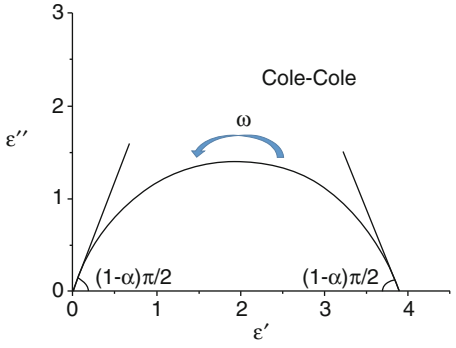

Fig. 13.3 Cole-Cole model, showing the symmetry

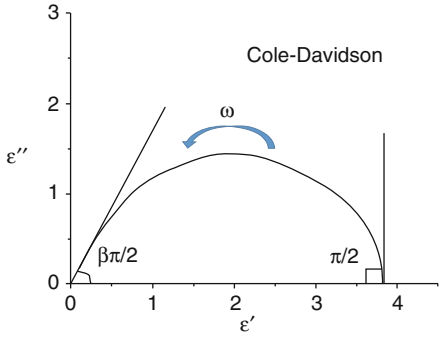

Fig. 13.4 Cole-Davidson model, showing the asymmetry

$$\varepsilon^*(\omega) = \varepsilon_\infty + \frac{\varepsilon_s - \varepsilon_\infty}{\left(1 + (i\omega\tau_{hn})^{1-\alpha}\right)^\beta} \tag{13.20}$$

The particular case of $\alpha = 0$ and $\beta = 1$ leads to the Debye relaxation.

13.4 Global Characteristics of Relaxation

One phenomenon that has been studied in detail in recent years is the emergence of more than one relaxing mechanism in the same physical system. It has been detected in microemulsions [24], viscous liquids [25], polymers [26] and glasses [27].

Conventionally, these processes are denominated as primary or α relaxation and secondary or β relaxation, each with its own characteristics. Thus, the α processes typically have high temperature-dependent relaxation times and are found at lower frequencies than that one recognized as secondary relaxations. Normally, Vogel-Fucher-Tamman (VFT) function describes the relaxation dependence on temperature accurately [28]. The secondary relaxations have a lesser variation with temperature and are described by the Arrhenius equation [29].

Figure 13.5 shows the dielectric losses ε'',as a function of frequency at constant temperature for a composite, styrene-b-isoprene-b-styrene copolymer with ferrites particles, and the best fit, where three relaxation processes are present [30]. In the low frequency region, a first α relaxation is visible (α_1), the corresponding β

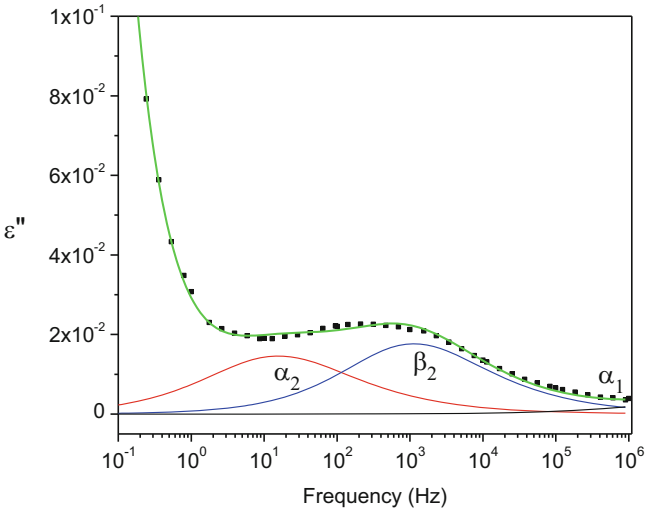

Fig. 13.5 Dielectric loss curve and best fit, showing three relaxation processes for a composite with 8% of lithium ferrite particles at constant temperature (Reprinted with permission from [30]. © 2014 AIP publishing)

relaxation appears at higher frequencies (β_1). In the high frequency region, a new α relaxation is detectable (α_2), the corresponding β relaxation is out of the frequency window of the measurement.

The relaxation map for this material is shown in Fig. 13.6, where the differences between the α and the β relaxation processes become clear, with the Vogel-Fucher-Tamman function and the Arrhenius type behaviors for the two types of relaxations observed.

13.5 Procedures to Fit the Experimental Data

To fit the experimental data points in the time domain to a Kohlrausch-Williams-Watts (KWW)function (Eq. 13.4), it is absolutely crucial to use algorithms based on well-known methods, and especially to take a special care when defining the initial values of the parameters to be determined. With three degrees of freedom as in this function, obtaining correct final values strongly depends on the initial values introduced as a starting point for the fit.

The depolarizing current, as the derivative of the polarization function, is, for KWW function

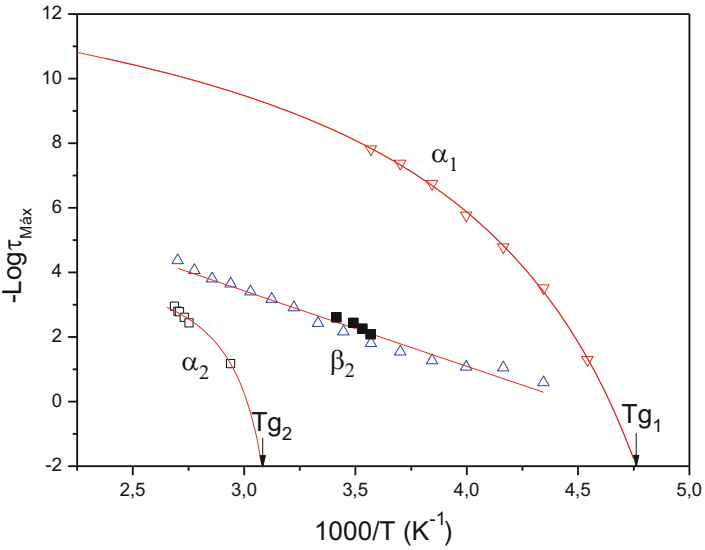

Fig. 13.6 Relaxation map for a composite with 8% of lithium ferrite particles. Tg_1 and Tg_2 are the glass transitions of the components of the copolymer, polyisoprene and polystyrene (Reprinted with permission from [30]. © 2014 AIP publishing)

$$I(t) = \frac{\partial \varphi(t)}{\partial t} = I_0 \left(\frac{t}{\tau_K}\right)^{\beta_K - 1} \exp\left(-\left(\frac{t}{\tau_K}\right)^{\beta_K}\right) \tag{13.21}$$

$$\text{with} \qquad I_0 = \frac{\Phi_0 \beta_K}{\tau_K} \tag{13.22}$$

Manipulating Eq. (13.21), we can obtain [31]

$$\frac{\partial \ln I(t)}{\partial \ln t} = (\beta_K - 1) - \beta_K \left(\frac{t}{\tau_K}\right) \tag{13.23}$$

Regarding this equation, the logarithmic derivative takes the value -1 exactly for $t=\tau_K$ independent of the values of I_0 and β_K. This value of τ_k is a good starting point as the initial value to be inserted into the numeric fitting process. In Fig. 13.7 we can observe the $\partial \ln I(t)/\partial \ln t$ versus t graph for a lead borate glass, where the point $(t, -1)$ allows to estimate the initial value of τ_K.

The next step is to calculate a first approximate value of β_K. We can look at what happens when $t>>\tau_K$, that is, in the long-time regime. Here, the following approach is valid:

$$I(t) = I_0 \exp\left(-\left(\frac{t}{\tau_K}\right)^{\beta_K}\right) \tag{13.24}$$

and we can obtain

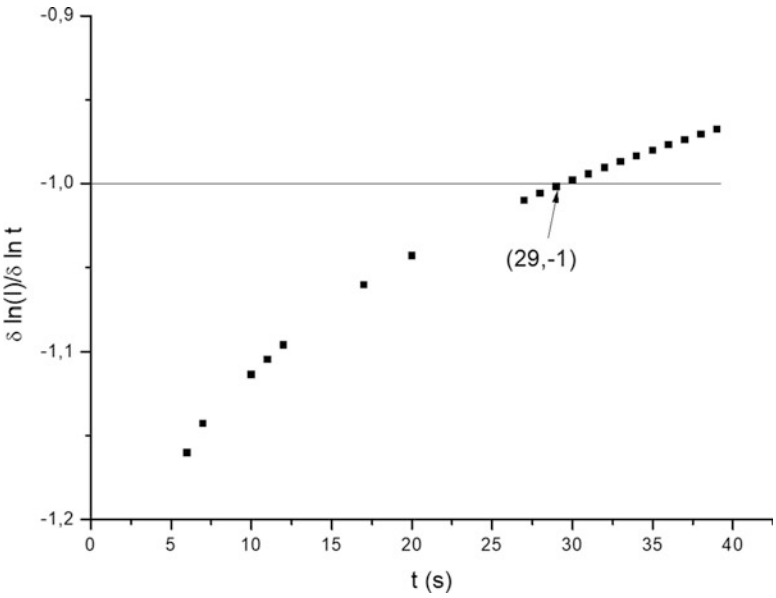

Fig. 13.7 $\partial \ln I(t)/\partial \ln t$ versus t graphic for a lead borate glass [7]

$$\ln\left(-\frac{\partial \ln I(t)}{\partial t}\right) = \ln\left(\beta_K \tau_K^{1-\beta_K}\right) - (\beta_K - 1)\ \ln t \tag{13.25}$$

From this equation, having already the value of τ_K, we can calculate β_K.With the initial values of these parameters, it is accurately possible to fit the data with the KWW function.

In frequency domain we can also obtain the relaxation parameters, using some mathematical manipulation.For the Cole-Davidson mode, which is frequently used to fit experimental data in several materials, we can use a similar strategy. First, we calculate the approximate values of those parameters from the asymptotic values of the data, and then use them as a starting point for the numerical fit [32].

For $\omega\tau_{cd} >> 1$, we can expand the Cole-Davidson Eq. (13.19) [33],

$$\frac{\varepsilon' - \varepsilon_\infty}{\varepsilon''} = \cot g\left(\beta\pi/2\right) + \left[1 + \cot g^2(\beta\ \pi/2)\right]\ \beta\ (\omega\tau_{cd})^{-1} \tag{13.26}$$

In the high limit frequency, this expression becomes

$$\frac{\varepsilon' - \varepsilon_\infty}{\varepsilon''} = \cot g(\beta\pi/2) \tag{13.27}$$

Then, the calculus of the exponent β is easy, as seen in Fig. 13.8.

The expansion in the low frequency region becomes

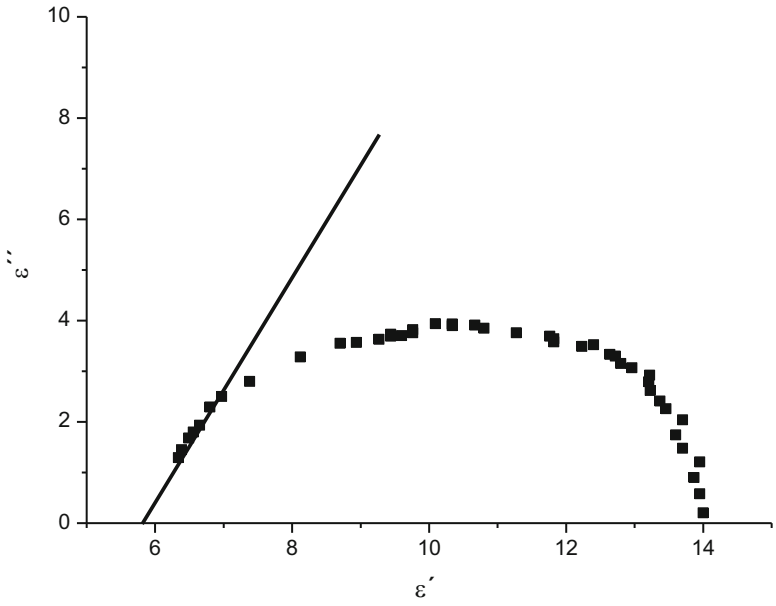

Fig. 13.8 ε'' versus ε' for a lead borate glass at aconstant temperature. The angle of the tangent to the curve with the abscissa in the high frequency region is $\beta\pi/2$

$$\varepsilon' = \varepsilon_s - 2\pi\left(\frac{1+\beta}{2}\right)\ \varepsilon''\ (\omega\tau_{cd}) + \mathrm{O}\,(\omega\tau_{cd})^4 \qquad (13.28)$$

where $O(\omega\tau_{cd})$ represents the terms higher than order three. Since in the low frequencies region these terms are negligible, the graph of ε' versus $(\varepsilon''\omega)$ is a straight line with a slope proportional to τ_{cd}, as seen in Fig. 13.9. Since we have already a value of β, it is possible to estimate a value for τ_{cd}.

13.6 Case Study

Time and frequency domain electrical measurements were madethe glass system $xGd_2O_3{\cdot}PbO{\cdot}2B_2O_3$.The depolarization current for a glass with x = 0.00 at constant temperature T = 330 K is shown in Fig. 13.10. The scales ln $I(t)$ versus t and versus ln t were used, in order to check the possibility of using Debye or Curie-von Schweidler models (Eqs. 13.3 and 13.10), as discussed previously.

It is clear that none of these models is adequate, as no straight lines are obtained in this graphic. Therefore, the Kohlrausch-Williams-Watts approach (KWW) was used to fit the data in the entire x range (0.00<x<0.20).

As can be seen, the values for the relaxation time must be high, corresponding to a low frequency relaxation.

In Fig. 13.11 the calculated relaxation parameters of the KWW function Φ_0, τ_K, β_K are shown for several concentrations of gadolinium oxide at constant temperature T = 150 K; in Fig. 13.12 we can observe the same parameters as a function of temperature for x = 0.07.

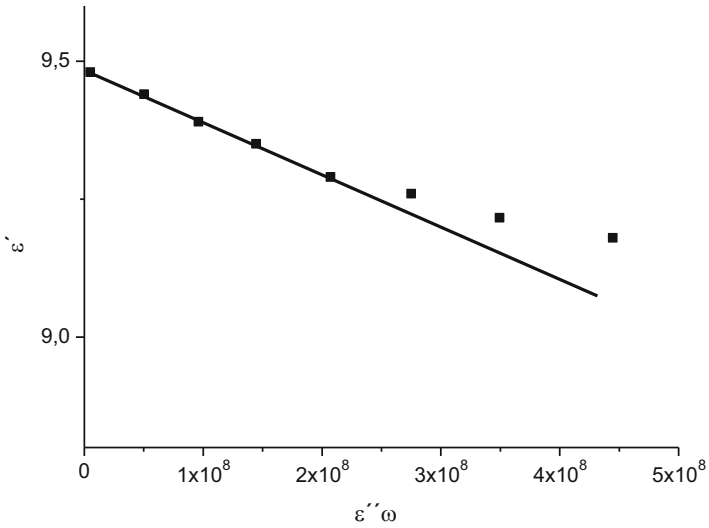

Fig. 13.9 ε' versus $(\varepsilon''\omega)$ for a lead borate glass at aconstant temperature in the low frequency region

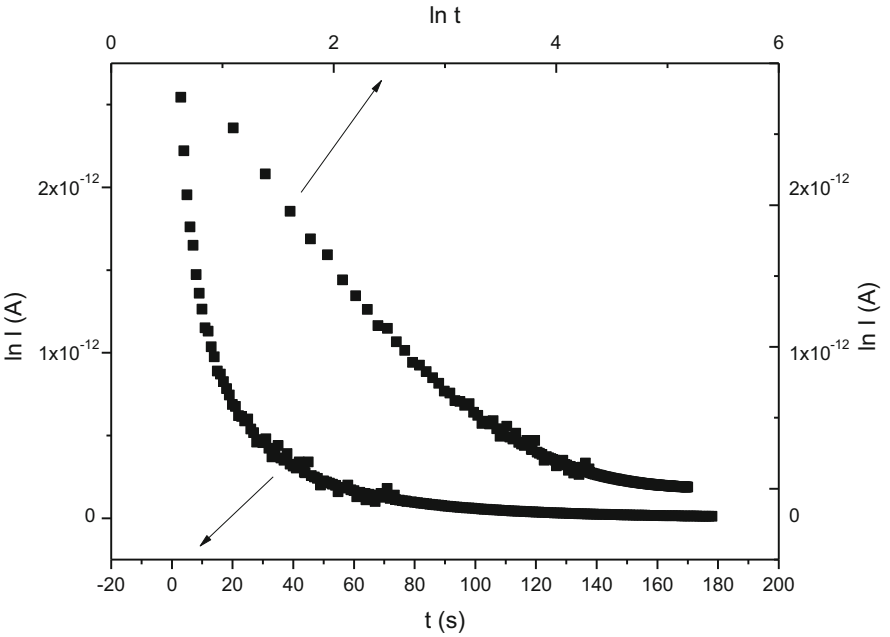

Fig. 13.10 ln $I(t)$ versus t and versus ln t, for the base glass $PbO{\cdot}2B_2O_3$, at a constant temperature

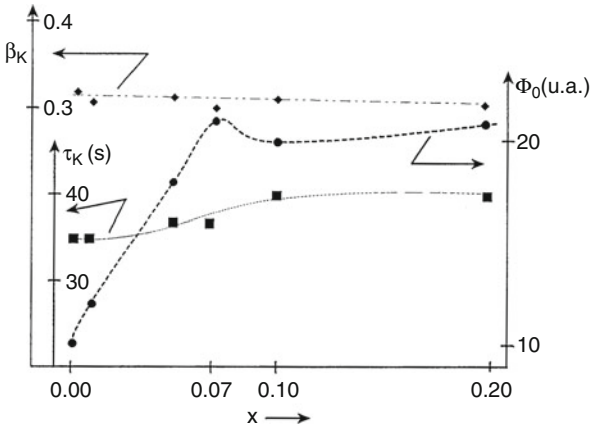

Fig. 13.11 Relaxation parameters of the KWW function, as a function of the gadolinium oxide content in the lead borate matrix at aconstant temperature T = 150 K

It can be verified that the β_K parameter is nearly independent of the concentration while increasing progressively with temperature. This parameter can be interpreted as a measure of the distribution of relaxation times [34]; in this case, it would mean that with increase of the temperature the distribution function $g(\tau)$ would become less wide. It can also be understood as a measure of coupling between the relaxing units and the system [35]; thus the coupling decreases with the temperature since β_K increases. The initial polarization increases with temperature in a quasi-linear way,

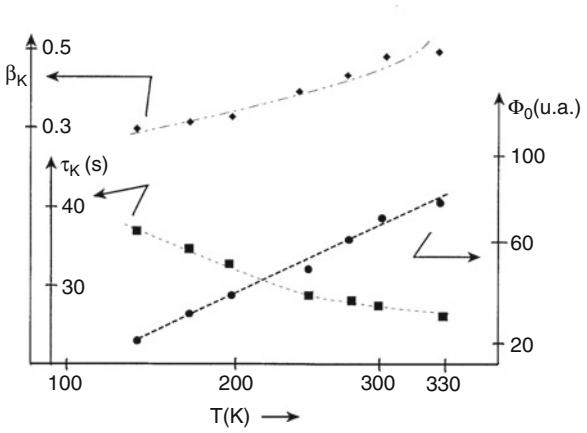

Fig. 13.12 Relaxation parameters of the KWW function as a function temperature for x = 0.07

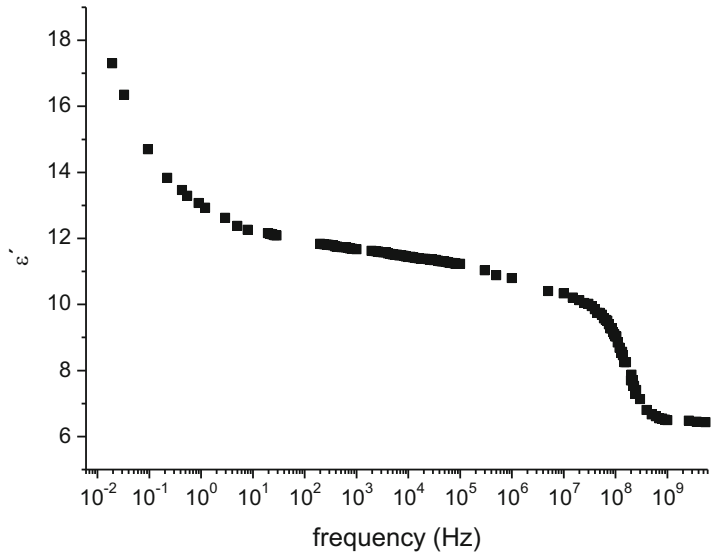

Fig. 13.13 Real part of the complex permittivity for the base glass at constant T = 300 K

till a critical concentration $x_c = 0.07$, from which on it is practically constant. The relaxation time is thermally activated, and it is observed that the activation energy does not depend on the doping concentration; therefore this low frequency relaxation process is characteristic of the lead borate glass.

The frequency domain measurements covered a large range of frequencies and temperatures. Figure 13.13 shows the real part of the complex permittivity for the base glass at constant T = 300 K.

The presence of two relaxation processes, separated by about nine decades is clear. The low frequency one corresponds to that one observed in the time domain.

Table 13.1 Relaxation parameters using the Cole-Davidson model at constant temperature T = 300 K for the high frequency process

x	τ_{cd} (ns)	β
0.00	0.90	0.89
0.01	0.92	0.88
0.03	0.94	0.87
0.05	0.96	0.86
0.07	0.96	0.85
0.10	0.97	0.85
0.20	0.99	0.84

For the analysis in the frequency domain, the Cole-Davidson model was used, as confirmed by observing Fig. 13.8, for the high frequency relaxation process. The calculated relaxation parameters are presented in Table 13.1.

We must note the increase in the relaxation time with the concentration, while the β parameter reveals a very slight decrease, but close to 1, which means that this process is close to Debye.

13.7 Conclusions

Time and frequency domain can be used to characterize electrically materials. Mathematically they are connected by the Fourier transformation.In the time domain, the Debye-like type is not very common, and then Kohlrausch-Williams-Watts or Curie-von Schweidler models can be used.In the frequency domain, Debye, Cole-Cole, Cole-Davidson or Havriliak-Negami are the used models. In our case study, relaxation processes were studied in both domains, for a lead borate glass doped with gadolinium oxide. Kohlrausch-Williams-Watts and Cole-Davidson model fits correctly the experimental data.

References

1. Jonscher AK (1983) Dielectric relaxation in solids. Chelsea Dielectrics Press, London
2. Daniel V (1967) Dielectric relaxation. Academic, London
3. Kremer F, Arndt M (1997) Broadband dielectric measurements techniques. In: Runt JP, Fitzgerald JJ (eds) Dielectric spectroscopy of polymeric materials. American Chemical Society, Washington, DC
4. McCrum NG, Read BE, Williams G (1991) Anelastic and dielectric effects in polymeric solids. Wiley, New York
5. Westphal WB, von Hippel AR (1954) Dielectric materials and applications. MIT Press/Wiley, New York
6. Armstrong D, Race WP, Thirsk HR (1968) Determination of electrode impedance over an extended frequency range by alternating current bridge methods. Electrochem Acta 13:215–239

7. Costa LC (1995) Propriedades eléctricas de vidros com alguns iões de terras raras. Ph.D. thesis, Aveiro
8. Calvert R (1948) A new technique in bridge measurements. Electron Eng 20:28–29
9. Henry F (1961) Développement de la métrologie hyperfréquences et application à l'étude de l'hydratation et la diffusion de l'eaudansles matériaux macromoléculaires. Ph.D. thesis, Paris
10. Macdonald D (2006) Reflections on the history of electrochemical impedance spectroscopy. Electrochem Acta 51:376–1388
11. Collin RE (1996) Foundations for microwave engineering. McGraw Hill, New York
12. McKubre MCH, Macdonald DD (2005) Impedance measurement techniques. In: Runt JP, Fitzgerald JJ (eds) Dielectric spectroscopy of polymeric materials. American Chemical Society, Washington, DC
13. Belatar J, Graça MPF, Costa LC, Achour ME, Brosseau C (2010) Electric modulus-based analysis of the dielectric relaxation in carbon black loaded polymer composites. J Appl Phys 107:124111
14. Debye P (1913) Ver Deut Phys Gesell. 15:777, reprinted 1954 in collected papers of P. Debye, Interscience, New York
15. Kohlrausch R (1854) Theorie des elektrischen Rückstandes in der Leidner Flasche. Ann Phys Chem 91:56–82
16. Williams G, Watts DC (1970) Non symmetrical dielectric relaxation behaviour arising from a simple empirical decay function. Trans Farad Soc 66:80–85
17. Weron K (1991) A probabilistic mechanism hidden behind the universal power law for dielectric relaxation: general relaxation equation. J Phys Condens Matter 3:9151–9162
18. Curie J (1889) Recherches sur le pouvoirinducteurspecifique et la conductibilite des corps cristallises. Ann Chim Phys 17:384–434
19. von Schweidler ER (1907) Studien über die Anomalien im Verhalten der Dielektrika. Ann Phys 329(14):711–770
20. Brown WF (1956) Dielectrics, encyclopedia of physics, vol XVII. Springer, Berlin
21. Cole KS KS, Cole RH RH (1941) Dispersion and sbsorption in dielectrics-I alternating current characteristics. J Chem Phys 9(1941):341–252
22. Davidson DW, Cole RH (1950) Dielectric relaxation in glycerol. J Chem Phys 18:1417–1419
23. Havriliak S, Negami S (1967) A complex plane representation of dielectric and mechanical relaxation processes in some polymers. Polymer 8:161–210
24. Bose TK, Delbos GG, Merabet M (1989) Dielectric properties of microemulsions by time domain spectroscopy. J Phys Chem 93:867–872
25. Johari JP, Goldstein M (1970) Vicous liquids and the glass transition. II. Secondary relaxations in glasses of rigid molecules. J Chem Phys 58(4):2372–2388
26. Soreto Teixeira S, Graça MPF, Dionisio M, Ilcíkova M, Mosnacek J, Spitalsky Z, Krupa I, Costa LC (2014) Self-standing elastomeric composites based on lithium ferrites and their dielectric behavior. J Appl Phys 116:224102
27. Costa LC, Henry F (2003) Dielectric relaxation in lead borate and lead silicate glasses: identification of distinctive regimes of behaviour. Phys Chem Glasses 44(5):353–356
28. Leon C, Ngai KL (1999) Rapidity of the change of the Kohlrausch exponent of the α relaxation of glass-forming liquids at T_B or T_β and consequences. J Phys Chem B 103:4045–4051
29. O'Connell PA, McKenna GB (1999) Arrhenius-type temperature dependence of the segmental relaxation below Tg. Chem Phys 110(22):11054–11060
30. Soreto Teixeira S, Graça MPF, Dionisio M, Ilcíkova M, Mosnacek J, Spitalsky Z, Krupa I, Costa LC (2014) Self-standing elastomeric composites based on lithium ferrites and their dielectricbehavior. J Appl Phys 116:224102
31. Mendiratta SK, Costa LC (1991) Dielectric relaxation in glasses containing different relaxing species. J Non-Cryst Solids 131–133:990–993
32. Costa LC, Mendiratta SK (1994) Dielectricbehaviour of Nd ions in the lead borate glass. J Non-Cryst Solids 172–174:1324–1327

33. Berberian JG, Cole RH (1986) Approach to glassy behavior of dielectric relaxation in 3-bromopentane from 298 to 107 K. J Chem Phys 84(12):6921–6927
34. Colmenero J (1991) α-relaxation and molecular dynamics in glass-forming polymeric systems. J Non-Cryst Solids 131–133:860–869
35. Rendell RW, Ngai KL (1984) Relaxation in complex systems. In: Wright GB (ed) Office of naval research. Arlington, VA, Springfield

Chapter 14
The Measurement of Thermally Stimulated Depolarization and Polarization Currents

M. P. F. Graça and P. R. Prezas

Abstract The measurement of thermally stimulated depolarization currents, a technique usually known by its initials (TSDC), has contributed substantially to the knowledge and understanding of charge storage and charge decay processes in several types of electret materials, i.e., materials that can have electrical polarization arising from kinetically trapped charges. The polarization of these materials may increase the magnitude of the applied electric field, until the point of dielectric breakdown. A similar, and sometimes complementary, technique consists in the measurement of thermally stimulated polarization currents (TSPC). This contribution discusses experimental and theoretical considerations regarding both techniques. Additionally, it also includes a case study regarding $LiNbO_3$ glass-ceramics, synthesized by the melt-quenching process.

Keywords TSDC · TSPC · $LiNbO_3$ · Glasses · Glass-ceramics

14.1 Introduction

The measurement of thermally stimulated depolarization and polarization currents, TSDC and TSPC, respectively, are part of a broad group of thermally stimulated experimental techniques, where a given physical property of the material is studied as a function of the temperature. In the cases of TSDC and TSPC the property in analysis, i.e., the electric current, is strictly related to dipolar polarization/depolarization and spatial charge detrapping/decay processes activated by both the temperature and the applied electric field.

The designation TSDC does not coincide with the appearance of this technique in the scientific community, which occurred in 1964 when it was introduced by Bucci and collaborators [1]. The technique was introduced under the designation ionic

M. P. F. Graça (✉) · P. R. Prezas
I3N and Physics Department, University of Aveiro, Aveiro, Portugal
e-mail: mpfg@ua.pt

P. Petkov et al. (eds.), *Advanced Nanotechnologies for Detection and Defence against CBRN Agents*, NATO Science for Peace and Security Series B: Physics and Biophysics, https://doi.org/10.1007/978-94-024-1298-7_14

thermoconductivity ITC, because it would be applied in the analysis of ion related processes such as dipolar relaxation, among others. The terminology TSDC was posteriorly adopted to include materials where both ionic and electronic charges yield a significant contribution to the magnitude of the polarization and the respective depolarization or polarization currents [2]. TSDC and TSPC have found a substantial amount of applications in the study of the electrical properties of glasses, glass-ceramics, and polymers [3, 4]. However, since the charge transport and trapping processes are not only essential for electrets, they have also found significant applications in the characterization of materials applied as thin films, such as photoconductors and electro-optic devices [5]. Additionally, features such as the very high sensitivity (capable of detecting small contributions to the polarization, due to dipole densities on the order of 10^{15} dipoles per cubic centimeter) and the resolving power contributed to the popularization of these techniques. Furthermore, the theoretical description and following mathematical formulation of the different processes contributing to the depolarization currents are already well established.

The present contribution is divided into two main sections: the first deals with the theoretical and experimental characteristics of both techniques, while the second will contain a case study regarding TSDC measurements on $LiNbO_3$ and $NaNbO_3$ containing glasses and glass-ceramics, synthesized by melt-quenching and sol-gel processes.

14.2 Background

14.2.1 TSDC: Thermally Stimulated Depolarization Currents

The experimental details and steps of the TSDC technique are directly related to the fact that when heating up a solid dielectric material which is electrically polarized through the application of an external dc electric field, the relaxation time of the sample's polarizable components will be small enough so that the polarization reaches its saturation condition in a short period.If the electric field is kept applied while the sample temperature is decreased down to a temperature low enough so that the relaxation times are very high, the polarization can be considered as "frozen". At this point, it will remain "frozen" even after the removal of the electric field, since the thermal energy is not high enough to activate the return of the charge carriers to their equilibrium positions. If the temperature of the sample is again increased, there will be a gradual release of the trapped charges, originating a depolarization current.

This process, represented schematically in Fig. 14.1, is based on the execution of the following experimental steps [6, 7]:

1. Application to the sample (with appropriate electrodes), at a polarization temperature T_p, of an electric dc field E_p during a period t_p high enough so that the polarization reaches its saturation condition.

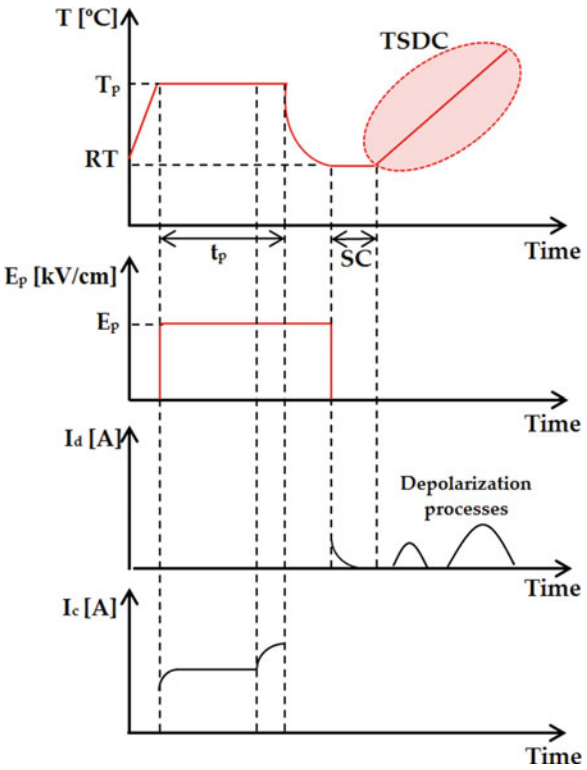

Fig. 14.1 Scheme of a typical TSDC experiment [9]

2. The sample is cooled, preferably with a high cooling rate while keeping the field E_p applied, down to a temperature T_0 where the dipolar motions can be regarded as negligible.
3. E_p is removed, and the sample is short-circuited (SC step in Fig. 14.1) for a few minutes to release weakly bonded charges.
4. The sample is connected to a very sensible electrometer (currents as low as 10^{-15} A may be detected) and warmed up with a constant heating rate β. The depolarization current is measured as function of the temperature. The origin of this current is the relaxation of the charge carriers.

Figure 14.1 also depicts the behavior of the charge current I_c and the current discharge I_d. As expected, the charge current increases during the time of E_p application, reaching a saturation condition. During the SC step, a discharge current can be detected, related tothe release of weakly bonded charges. Subsequently, the depolarization processes will be detected as currents in the I_d versus temperature plot.

As the most significant advantages of this technique, we highlight [3, 8]:

1. In materials with multiple relaxation processes, each process should originate a separated TSDC current peak.

2. It does not require an applied external electric field during the measurements, decreasing by this way the electric conduction effects.
3. Allows making quantitative measurements of: impurities concentration; molecular movements; characterization of macromolecular states; local environment characterization; chemical degradation; structural anisotropy.

As main disadvantages of this technique, the high sensibility and resolution required for the data acquisition system can be stated.

Taking into account the discussed experimental procedure, it is clear that all TSDC measurements will need some mandatory equipment. The list contains a furnace or cryostat, depending on the temperature range to analyze, a temperature controller capable of controlling a linear variation of the temperature as a function of time, with high-precision, a stable dc power supply for the electrical polarization and a sensible electrometer. Depending on the sample or type of measurement intended, a vacuum container and the possibility of controlling the atmosphere may be desirable. In conclusion, Fig. 14.2 shows a general setup for a TSDC measurement, with all the equipment that was referred to.

14.2.2 TSDC: Physical Processes and Mathematical Formulation

It is known that different processes can contribute to the measured depolarization current of a given sample. Among theseprocesses, the followingcan be highlighted:

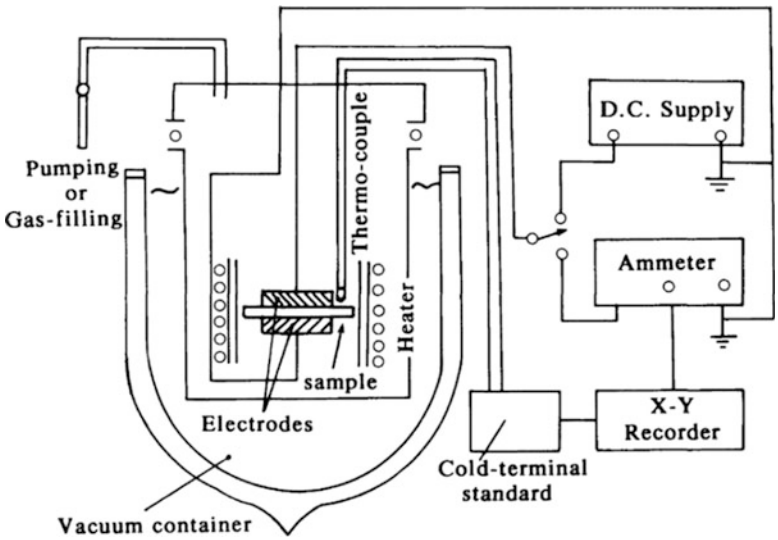

Fig. 14.2 General experimental setup for a TSDC experiment [10]

the reorientation of electric dipoles (dipolar polarization), the movement of trapped electric charges, i.e., space charge detrapping, the displacement of the electronic cloud within an atom or ion (induced electronic polarization) or the ionic displacement within a molecule (induced dipolar polarization), the formation of defect dipolar polarization, etc. [2, 10].

The analytical expressions describing the depolarization current are usually applied in materials where ionic processes dominate the response, i.e., the electronic response can be considered negligible. In such a case, two formulations are most commonly used, for dipolar reorientation and space charge detrapping processes, respectively. For a depolarization current peak originated from dipolar reorientation, and a first order process, the dependence of the current density on the temperature [J (T)] is given by Eq. 14.1 [2, 10, 11]:

$$J(T) = \frac{P_0}{\tau_0}\exp\left[-\frac{E_a}{k_B T}\right]\exp\left[-\frac{1}{\beta}\exp\left(\int_{T_0}^{T}\tau(T)d(T)\right)\right] \tag{14.1}$$

where P_0 is the equilibrium polarization (basically, the sample's polarization before starting the measurement), τ_0 is a pre-exponential factor that can be interpreted as the relaxation time when the temperature tends to infinite, E_a is the activation energy for dipole relaxation/reorientation, k_B is Boltzmann constant, β the heating rate and $\tau(T)$ the characteristic relaxation time. For dipolar reorientation, Eq. (14.1) can be modified to include an analytical expression describing the dependency of P_0 on the electric dipole density N, the individual dipole moment p, the electric field E_p, and the polarization temperature T_p, yielding the following expression [2, 10, 11]:

$$J(T) = \frac{Np^2E_p}{3k_BT_p\tau_0}\exp\left[-\frac{E_a}{k_BT}\right]\exp\left[-\frac{1}{\beta}\exp\left(\int_{T_0}^{T}\tau(T')d(T')\right)\right] \tag{14.2}$$

Equation 14.2 is usually labeled as Bucci-Fieschi theory, describing a depolarization current peak due to a dipolar reorientation process.

On the other hand, to describe a peak originating from spatial charge detrapping, the Bucci-Fieschi can be still applied to describe the depolarization of space charge, assuming that all the trapped charges have approximately the same mobility. In this case, the equilibrium polarization P_0 is given by (14.3) [12]:

$$P_0 = 2qLvNt_p\exp\left(-\frac{E_a}{k_BT}\right)\sinh\left(\frac{qLE_p}{2k_BT_p}\right) = P_{SC}\sinh\left(\frac{qLE_p}{2k_BT_p}\right) \tag{14.3}$$

where q is the ionic charge, L is the ionic jump length, v is the jump frequency, N is the density of trapped charge, t_p is the polarization time (as shown in Fig. 14.1) and E_a is the activation energy required for detrapping the charge carriers.

The mathematical treatment of Eq. (14.2) is not trivial, the main problem being the fact that the integration leads to an infinite series converging to infinite. Therefore, some approximations are needed to be considered. One of these approximations is particularly useful for the activation energy calculation: the initial rise method, introduced by Garlick and Gibson [13], is based on the fact that the integral

is negligible for temperatures lower than the peak temperature. Therefore, the equation can be simplified, and the activation energy can be evaluated through an Arrhenius dependency, as expressed in (14.4) [13] (where A is a constant):

$$J(T) = A\exp\left[-\frac{E_a}{k_B T}\right] \tag{14.4}$$

14.2.3 TSPC: Thermally Stimulated Polarization Currents

The measurement of thermally stimulated polarization currents (TSPC) is a counterpart of TSDC, and also often regarded as an inverse of TSDC. TSPC involves the measurement of the current that flows through a solid dielectric material subjected to a dc electric field as the material temperature is increased with a linear rate, from some low-temperature T_0 [6]. Therefore, in TSPC there is no necessity to polarize the material previously.

Figure 14.3 shows a scheme of a typical TSPC measurement. Initially, small and current contributions may be detected due to induced dipolar and electronic polarization. These induced polarizations are typically those that respond faster to an applied electric field, due to the small distances of displacement and also, in case of the induced electronic polarization, due to the low mass of electrons. Subsequently, as temperature linearly increases, the alignment of the dipoles or other processes will be detected as currents peaks in a current versus temperature representation [14]. The

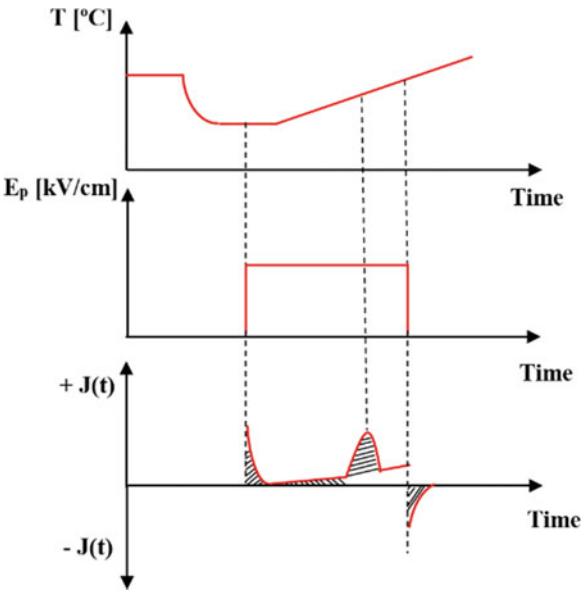

Fig. 14.3 Scheme of a typical TSPC experiment. The background current $J_B(t)$ and a dipolar contribution to the polarization current, $J_D(t)$, are also represented

reason behind the fact of TSCP being regarded as an inverse of TSDC is that while in TSDC the current peaks are caused by the depolarization processes, in TSPC they are due to thepolarization. It is also visible in Fig. 14.3 that a background current $J_B(t)$ is detected, which is also characteristic in TSDC measurements. $J_D(t)$ represents the dipolar contribution of the measured current. About the additional/complementary information that TSPC can provide, the possibility is highlighted to distinguish the physical process behind dipolar depolarization processes observed in TSDC spectra. While depolarization peaks related to dipolar reorientation will be centered at about the same temperature in both TSDC and TSPC spectra, but with opposite direction, processes related to vacancies and impurities diffusion will be detected as an exponential rise of the current in the TSPC spectrum. Figure 14.4 shows this behavior for a $BaF_2:Tb^{3+}$ single crystal [15]. While the first process at about 195 K is caused by the reorientation of F-Tb^{3+} dipoles, the second at around 340 K is assigned to the diffusion of fluoride vacancies, therefore it is detected as an exponential rise of the current. It is to be noted that the mathematical formulas for both techniques is essentially the same, i.e., the formulations discussed in the TSDC section are the same for both techniques, the only difference being that T_p has to be replaced by a variable temperature T.

The equipment required for TSPC measurements is essentially the same as described for TSDC. However, one of the reasons that explain the fact of TSDC being the most popular technique is that the signal to noise ratio in a current measurement is markedly better if the current is measured without an applied electric field.

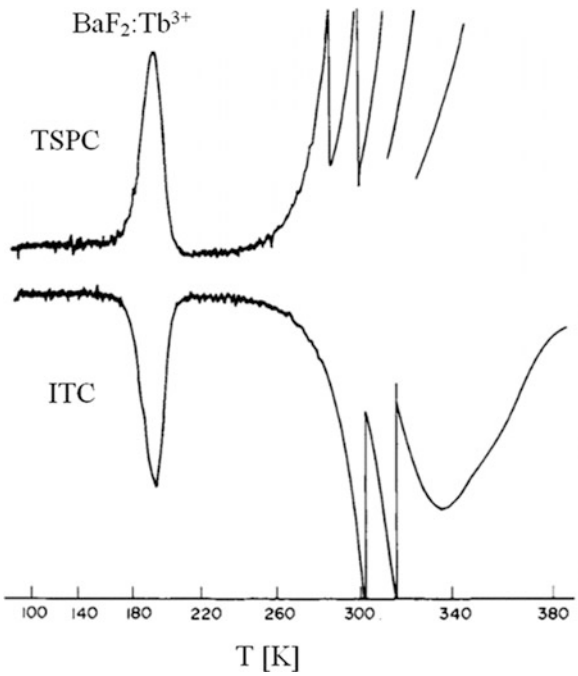

Fig. 14.4 Recorder plots of TSPC (above) and TSDC (below, designated as ITC – ionic thermo-conductivity) measurements performed with a $BaF_2:Tb^{3+}$ single crystal [15]

14.3 Case Study: Glass and Glass-Ceramics with $LiNbO_3$

Glass refers to one of the oldest known materials of mankind. It is defined, according to ASTM C-169-92, as a inorganic product obtained by rapid cooling of a melt, to conditions of rigidity, without crystallization. This definition is, however, too restrictive as it only applies to glasses prepared by the fusion method. A broader definition was proposed by A. Paul [16]: glasses possess the elastic behavior characteristic of the crystalline state and the viscous behavior of the liquid state. The most common properties of vials are transparency to visible radiation, mechanical stability, inactivity at the biological level and electrical insulation. However, due to the possibility of controlling the microstructure either by altering the initial composition or by application of heat treatments, controlling the nucleation and crystallization process [17, 18], the properties of a glass can be modified.

The initial chemical composition is a controllable factor that allows to mold some of the properties of the glass. In any glass, the units that define its structure can be divided into three categories, according to their structural function: network former,; modifier, and intermediate units. The network formers are those units which, that without addition of other components can form glass, such as SiO_2, B_2O_3, P_2O_5 and GeO_2. The network modifier do not form glass structures but are often combined with a former. Examples of modifying elements are the alkali elements (Li, Na, K, etc.) and the alkaline earth metals (Mg, Ca, etc.). The intermediate species are elements that can either have the role of the network former or the modifier (Al, Nb, etc.).

The formation of glass ceramics, for example by heat treatment of the base glass, is technologically advantageous for monocrystals and sintered ceramics. It gives the possibility to control their properties (optical, electrical, mechanical, chemical, etc.) by the volumetric fraction of the active phase dispersed in the matrix [19]. For example, to maintain optical transparency, the nucleation and crystal growth process require high control; it is achieved when the size of the crystals dispersed in the glass matrix is not high enough to cause light scattering. However, for most electrical applications it is necessary that the crystals are of sufficient size to have, for example, a ferroelectric response. This commitment is not easy to meet. Another condition which can maintain the optical transparency of a ceramic glass is a small difference between the refractive indexes of crystals and glass matrix. If this difference is insignificant, it allows, regardless of the size of the crystals, to maintain the optical transparency of the ceramic glass [20]. Thus, in recent years there has been a growing interest in the preparation, characterization and technological implementation of glass and ceramics. However, it is important to note that in general the electrical and optical properties of ceramic glasses are not as good as those of monocrystals. This is because ceramics show at least two distinct phases, a crystalline (considered the active phase) and anamorphous (support). The electrical polarization of the crystals inserted in a glassy matrix is hampered due to the low value of the dielectric constant of the glassy phase [21, 22]. On the other hand, as the growth processes of monocrystals have a high economic cost, they are now judged deprecated forceramic glasses. Some of these also have the advantage of being dense materials with no porosity [23].

Different processes can achieve crystalline growth with preferred orientation, for example: mechanical deformation; thermodynamic control; kinetic control (induced electrochemical nucleation) [18]. In glasses, the use of thermodynamic control is the most common process. However, control of crystallization with the desired crystalline phase is usually difficult as crystallization is a complex process and affected by various factors such as composition, surface conditions, and heat treatment profiles [24].

Ceramic glasses containing ferroelectric crystals are a class of materials with high technological interest as ferroelectric crystals present a structural anisotropy that results in the formation of electric dipoles and consequently a spontaneous electrical polarization [20, 25, 26]. A large part of the ferroelectric materials is in the form of crystalline ceramics. The scientific and technological development of photonicsrequires new materials that with characteristics such as optical transparency and also optical activity to be used as amplifiers in communication systems, energy, instrumentation, etc. In this way, the preparation, and the structural, electrical and optical characterization of ceramic glasses with ferroelectric properties is of great importance for possible technological applications.

Of the various ferroelectric materials, lithium niobate ($LiNbO_3$), synthesized for the first time in 1949 by Matthias and Remeika [25], has attracted more attention from many researchers because of its excellent piezoelectric, electroacoustic, pyroelectric and photorefractive properties. In the late 1960s, due to the appearance and development of optical fiber applications, several research centers, namely the Bell Laboratories [27], studied in detail the structural characteristics and properties of $LiNbO_3$ crystals, especially their electro-optical properties [28].

The fact that $LiNbO_3$ monocrystals prepared by the usual growth techniques are a challenging and expensive task, arose the scientific interest in the structural, optical and electrical study of glass-ceramics containing $LiNbO_3$ crystals, due to the possible technological applications that can be of interest.

A significant amount of research work in the field of the preparation and crystallization of glass-ceramics containing $LiNbO_3$, by melting quenching exists. In 1980, Prasad et al. [29] published a study on the preparation of ceramic glasses from the SiO_2-Li_2O-Nb_2O_5 system. The choice of SiO_2 as a network former was due to the fact that it does not contain cations that could alter the crystalline structure of $LiNbO_3$. SiO_2 satisfies this condition due to the reduced atomic radius and coordination number. Obtaining crystals without crystalline phases is achieved for a molar amount of SiO_2 between 32% and 39%, using the same molar amount of Li_2O and Nb_2O_5.

The vitreous glass-forming region of the system (SiO_2-Al_2O_3)-Li_2O-Nb_2O_5, using the melt-quenching method, was presented by Todorovic et al. [30]. They found that ifthe molar ratio $[Nb_2O_5]/[SiO_2] > 1$ and the molar amount of $[Li_2O] > 25\%$ is, transparent and homogeneous glasses can be obtained. The application of thermal treatments to the base glass allowed the crystallization of $LiNbO_3$ particles with a size of 150–350 nm, maintaining transparency. These glass-ceramics have a refractive index of 1.84–1.93 and a dielectric constant of 155–185, measured at

1 kHz and room temperature. They observed that an increase in temperature and/or thermal treatment time leads to an increase in particle size and consequent opacity of the samples.

14.4 Glass and Glass-Ceramics Preparation (Composition $60SiO_2$-$30Li_2O$-$10Nb_2O_5$ mol%)

The melt-quenching method was used to prepare transparent glasses of the ternary system SiO_2-Li_2O-Nb_2O_5. The high-purity (>99.9%) raw materials used were silicon oxide (SiO_2-BDH), lithium carbonate (Li_2CO_3-Merck) and niobium pentoxide (Nb_2O_5-Merck). The preparation of the base glass followed the procedure outlined in Fig. 14.5.The calcination step aimed to remove the CO_2 present in Li_2CO_3, thus obtaining Li_2O. The last step, the re-baking of the glass, carried out soon after the melt has been poured into the molds, has the objective of minimizing the tensions of the glass network to avoid rupture. The parameters temperature and time of calcination, temperature, melting time and temperature, and time of heat treatment (annealing) are characteristic of each system.

The base glasses were subjected to heat treatments after the annealing step to obtain ceramic glass with the crystalline phase $LiNbO_3$. Figure 14.6 represents the schematic of the thermal treatment profile used, which was carried out in a horizontal tubular furnace. The value of the threshold temperature parameter T_p is determined based on information about the glass thermal behavior.

It is important to note that prior to the heat treatment, it was necessary to polish each sample to place them with a thickness of approximately 1 mm and with the opposite surfaces as parallel as possible. Figure 14.7 shows the macroscopic appearance of the base sample and the samples heat-treated at 600 and 650 °C. It was observed that with increasing the treatment temperature the samples became in the first phase translucent and for treatments at 700 °C opaque.

Figure 14.8 shows the macroscopic appearance of the base glass in the presence of an external electric field. From the analysis of the macroscopic results, there is a

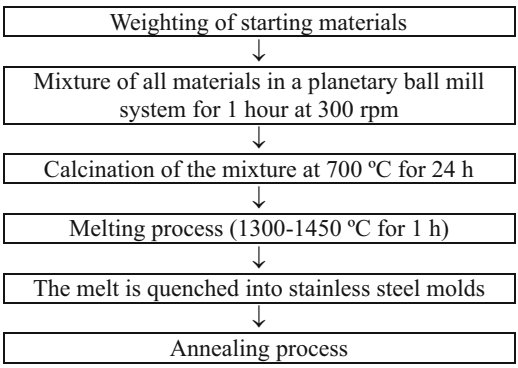

Fig. 14.5 Scheme for the preparation of base glass by the melt-quenching method

maximum electric field value that can be applied without modifying or even destroying the glass network. It is also noted that the presence of the electric field causes to the surface in contact with the negative electrode to have a different appearance from that which was with contact with the positive one, i.e., on the surface which was in contact with the positive electrode a white "film"is formed.

In Figs. 14.9, 14.10, and 14.11 TSDC spectra of the base glass and thermally at 600 and 650 °C treated samples, respectively, are shown. For a better visualization of the spectra, an enlargement of the low-temperature range is presented in each figure. All samples were polarized at 350 K for 10 min, applying an electric field of 50 kV/m.

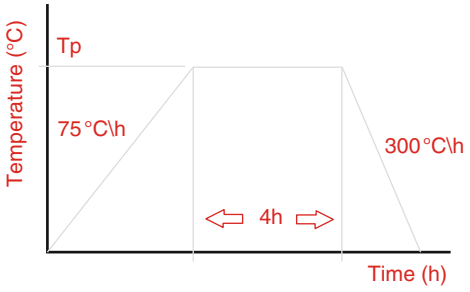

Fig. 14.6 Scheme of the heat treatment process

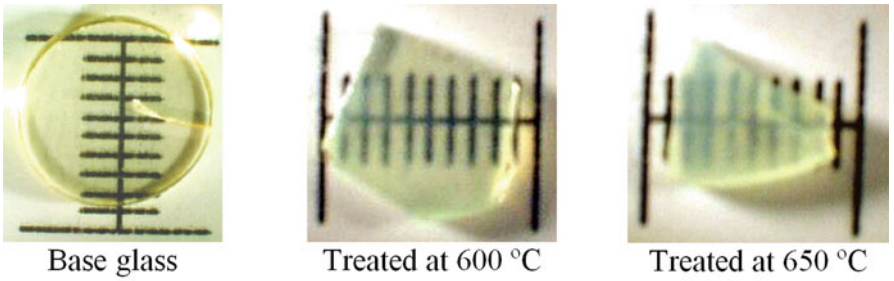

Fig. 14.7 Photographs of the base glass and thermally treated samples at 600 and 650 °C (smaller scale range = 1 mm)

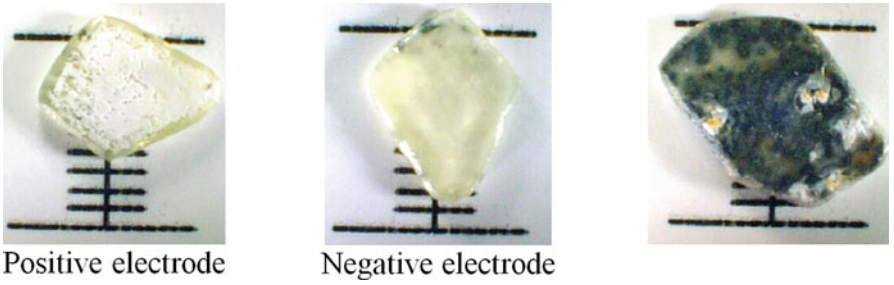

Fig. 14.8 Photographs of the base glass after thermal cycle in the presence of an external electric field (smaller scale range = 1 mm)

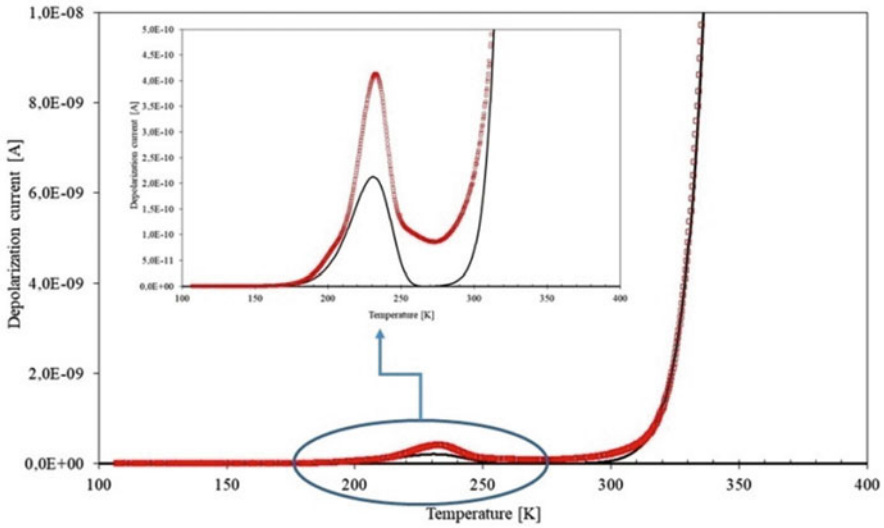

Fig. 14.9 Depolarization current as a function of the measuring temperature, for the base glass. For better visualization the inset figure shows the depolarization current at low temperatures

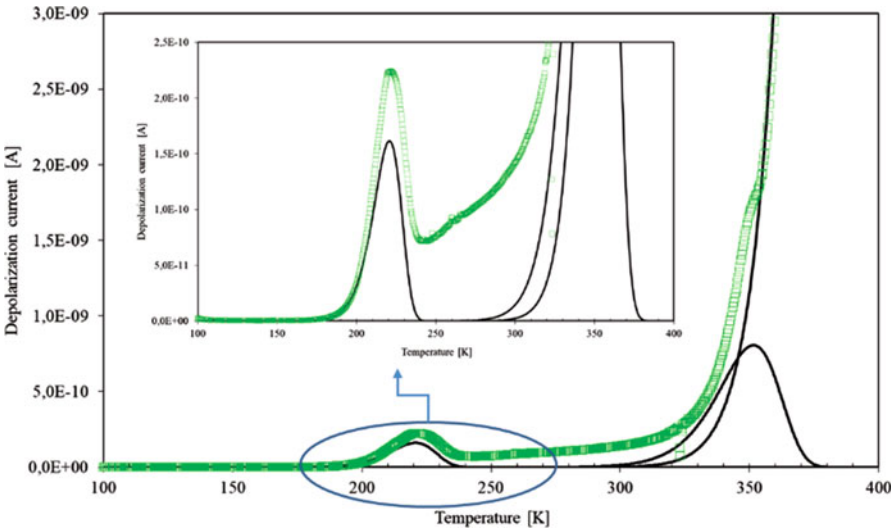

Fig. 14.10 Depolarization current as a function of the measuring temperature for the glass treated at 600 °C. For better visualization the inset figure shows the depolarization current at low temperatures

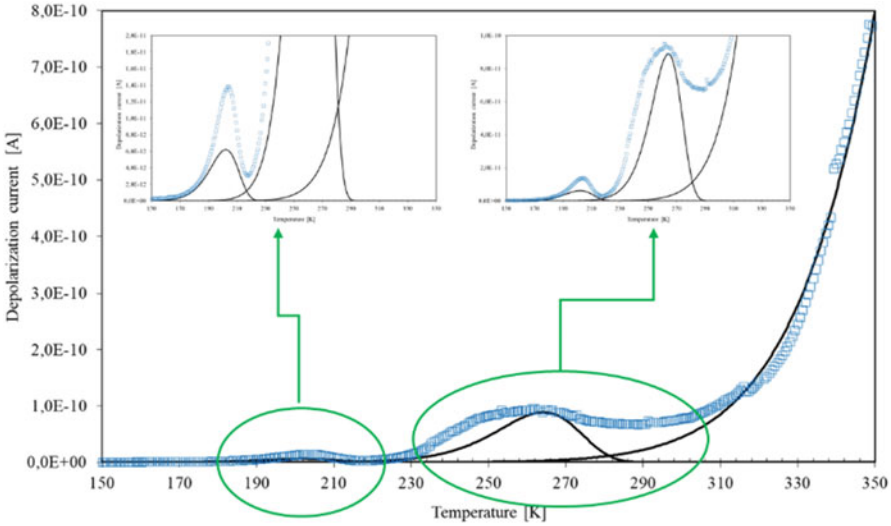

Fig. 14.11 Depolarization current as a function of the measuring temperature for the glass treated at 650 °C. For better visualization the inset figure shows the depolarization current at low T

The base glass only shows a peak of thermally active depolarization current, whereas the samples thermally treated possess two peaks, one at temperatures below ~230 K and the second at temperatures greater than 290 K. The characteristics of these peaks are listed in Tables 14.1, 14.2, and 14.3. It is observed that the temperature of the current peak in the low and high-temperature zones moves to lower temperatures with increasing heat treatment temperature. The absolute current value of both peaks also decreases from the base glass to the sample treated at 650 °C.

The activation energy E_a for each peak, calculated using the initial rise method is registered in the following tables. For the depolarization current peak at low temperatures P_1, a maximum of E_a is observed for the sample treated at 600 °C. In the high temperature zone, where the second peak P_2 is detected, there is a decrease of the correspondent E_a from the sample treated at 600 to the one at 650 °C. The relaxation time τ, associated with P_1, decreases from the base glass to the sample treated at 600 °C, but increases for the sample treated at 650 °C. For the depolarization peak P_2, the relaxation time decreases with the increase of the thermal treatment temperature.

The TSDC results of this $60SiO_2$-$30Li_2O$-$10Nb_2O_5$ %mol glass composition revealed the presence of two depolarization current peaks P_1 and P_2 in the thermally treated samples and only one depolarization peak in the base glass (P_1). The first peak P_1 is due to localized free-ion motions within the glass network. These motions give rise to a dipole orientation formed by the ion structurally inserted in the glass network (Li^+ and/or Nb^{5+}) and the non-bridge oxygen (NBO-) ion to which it is attached [31, 32]. It should be noted that in this situation the ion structurally inserted

Table 14.1 Peak temperature T_p, peak current $i_{(Tp)}$, activation energy E_a, thepre-exponential parameter $\tau_0$and the relaxation time τ, calculated for the depolarization current peak P_1, for the base glass and samples heat-treated at 600 and 650 °C

Sample	T_{P1} [K]	$i(T_{P1})$ ($\times 10^{-10}$) [A]	E_a [kJ/mol]	$\tau_{0\ (P1)}$ ($\times 10^2$) [s]	$\tau_{(P1)}$ ($\times 10^3$) [s]
Base	232.3	4.134	31.574 ± 0.198	4.159 ± 0.065	2.132
600	221.4	2.243	44.123 ± 0.265	1.262 ± 0.025	1.385
650	203.7	0.138	31.259 ± 0.151	2.626 ± 0.049	1.659

Table 14.2 Peak temperature T_p, peak current $i_{(Tp)}$, activation energy E_a,the pre-exponential parameter τ_0 and the relaxation time τ, calculated for the depolarization current peak P_2, for the samples heat-treated at 600 and 650 °C

Sample	T_{P1} [K]	$i(T_{P1})$ ($\times 10^{-10}$) [A]	E_a [kJ/mol]	$\tau_{0\ (P1)}$ ($\times 10^2$) [s]	$\tau_{(P1)}$ ($\times 10^3$) [s]
600	352.3	17.883	84.081 ± 0.959	1.044 ± 0.014	1.841
650	261.4	0.948	50.569 ± 1.843	1.646 ± 0.027	1.685

Table 14.3 Parameters of the data adjustment through the Arrhenius equation on the high-temperature measurement zone. ln(A) represents the logarithm of the pre-exponential factor, and E_a is the activation energy for the base glass and samples thermally treated at 600 and 650 °C

Sample	ln(A) [A]	E_a [kJ/mol]
Base	22,928	$115{,}775 \pm 0{,}637$
600	16,609	$108{,}232 \pm 0{,}936$
650	−3621	$80{,}431 \pm 0{,}605$

in the glass network, is not in the most favorable energetical position. According to Agarwal et al. [33], the application of an electric field results in an ion transfer towards the field thus creating electrical heterogeneity, i.e., electrical dipoles. With increasing temperature, these ions tend to return to their initial position thus creating a depolarization current that will give rise to the low-temperature peak P_1. The activation energy, associated with the origin of the electrical dipoles formed by the ions structurally inserted in the glass network, basically consists of the energy required for the movement of those ions to different positions within the structural "void" in which it is located. It can be seen that the valuesobtained for the activation energy associated with P_1 are lower than the values obtained for the dc process [34, 35] but close to those obtained for the ac conductivity [34, 35] which suggests a possible relation. Thus, the decrease in peak current P_1 with the increase in the heat treatment temperature is due to the reduction in the number of dipoles related to the decline in the number of ions structurally inserted in the glass network. The characteristic temperature of the current peak corresponds to the transition temperature from the non-equilibrium freezing state of the ions to the steady state, analogous to that occurring in the glasses with the glass transition temperature

[36]. The temperature shift of the TSDC peak P_1 with increasing heat treatment temperature can be justified based on the results of Agarwal [33] that associates it to the decrease in the number of network modifier ions.

In this type of glass containing alkaline ions a second depolarization peak can be detected, centered at higher temperatures and attributed to the dipolar depolarization coming from the movements of the electric charge transport units in limited paths, which result from the presence of micro-heterogeneities in the glass [33]. According to Hong, these movements are essentially associated with the jumps of the ions structurally inserted in the network, which is within the structural void in which they jump between different positions. Thus, the dipole formed between these ions and the non-bridging oxygen ion closest to each "free" ion, should present an activation energy higher than that associated with P_1. This motion is usually associated with a dc conductivity, giving rise to space-charge polarization. However, Agarwal et al. contend that this process must have an activation energy lower than the dc activation energy, which in this case is not verified [34, 35]. Thus, based on the values of the activation energy, the peak P2 is not assigned to space-charge depolarization but rather to the depolarization of the interfacial dipoles formed between the sample surface and the electrode. The decrease in the temperature at which peak P2 occurs with the rise of the heat treatment temperature may be related to the observed reduction in the dielectric loss factor [34, 35], which should indicate an increase in the number of dipoles. It is suggested that the presence of this current peak in the base glass sample should be detectable at temperatures above 400 K (maximum measurement limit). In addition to the P_2peak and with increasing temperature, an increase in current is observed in all samples. This current, usually referred to as background current, was adjusted by an Arrhenius expression to obtain the activation energy of this thermally activated process. It decreases with increasing heat treatment temperature indicating a greater mobility of the charge carriers in this temperature range.

Concerning the relaxation times, assuming that the value of τ calculated for each peak of depolarization current corresponds to the mean value of the relaxation times distribution, it is verified that the value of τ for P_1 (Table 14.1), displays a maximum for the base sample. We believe that this maximum may be associatedwith the fact that this sample has the highest number of ions structurally inserted in the network and, therefore, a broader distribution of relaxation times. The increase of τ related with P_1 from the sample treated at 600 to the sample treated at 650 °C, is related to the presence of $LiNbO_3$ crystals whose dipoles are difficult to depolarize resulting in a longer relaxation time. The decrease in the value of τ related toP_2, with the increase of the thermal treatment temperature, suggests that the dipoles that give rise to this depolarization are not linked to the presence of $LiNbO_3$ crystallites. Knowing that the density ratio between these crystals and the glass matrix increases and also that these crystals are difficult to depolarize, the relaxation time would otherwise greater than τ_{P1}. Thus, this relaxation time τ_{P2} should, as indicated, be associated with the depolarization produced by interfacial sample-electrode dipoles. The decrease in τ_{P2} with increasing heat treatment temperature is due to the decrease in the activation energy, which will facilitate the mobility and the return to equilibrium positions.

14.5 Conclusions

This contribution shows the principles of the thermally stimulated depolarization current method. The advantages and disadvantages are discussed; and present an example of the application of this electrical characterization technique applied to a glass and glass-ceramic samples is presented. The TSDC results of the $60SiO_2$-$30Li_2O$-$10Nb_2O_5$ glass composition, with and without heat-treatments reveal the presence of at least two thermally stimulated depolarization mechanisms. The depolarization peak current detected at lower temperatures (<250 K) is due to the depolarization of the dipoles associated with ions structurally inserted in a glass network. The second peak of depolarization, centered at temperatures >250 K, is due to the dipolar depolarization from the movements of the electric charge transport units in limited paths. The presence of depolarization current peaks at temperatures higher than the second peak should be associated with dipoles formed between the sample surface and the electrodes.

References

1. Bucci C, Fieschi R (1964) Ionic thermoconductivity. Method for the investigation of polarization in insulators. Phys Rev Lett 12(1):16–19
2. Chen R, Kirsh Y (1981) The analysis of thermally stimulated processes. Pergamon Press, New York
3. Carr SH (1982) Thermally stimulated discharge current analysis of polymers. In: Seanor DA (ed) Electrical properties of polymers. Academic, New York
4. Araujo EB, Abreu JAM, Oliveira RS, Paiva JAC, Sombra ASB (1997) Structure and electrical properties of lithium niobophosphate glasses. Can J Phys 75:747–758
5. Turnhout JV (1987) Thermally stimulated discharge of electrets. In: Sessler G (ed) Electrets. Springer, Berlin
6. Hong C, Day DE (1979) Thermally stimulated polarization and depolarization current (TSPC/TSDC) techniques for studying ion motion in glass. J Mater 14:2493–2499
7. Milankovic AM, Day DE (1993) Thermally stimulated polarization and dc conduction in iron phosphate glasses. J Non-Cryst Solids 162(3):275–286
8. Hong C, Day DE (1981) Thermally stimulated currents in sodium silicate glasses. J Am Ceram Soc 64(2):61–68
9. Prezas PR, Melo BMG, Costa LC, Valente MA, Lança MC, Ventura JMG, Pinto LFV, Graça MPF (2017) TSDC and impedance spectroscopy measurements on hydroxyapatite, β-tricalcium phosphate and hydroxyapatite/β-tricalcium phosphate biphasic bioceramics. Appl Surf Sci 424 (1):28–38
10. Xu Y (1991) Ferroelectric materials and their applications. North-Holland
11. Fillard JP, Van Turnhout J (1977) Thermally stimulated processes in solids: new prospects. J Electrost 3:1–302
12. Horiuchi N, Nakamura M, Nagai A, Katayama K, Yamashita K (2012) Proton conduction related electrical dipole and space charge polarization in hydroxyapatite. J Appl Phys 112 (7):074901
13. Garlick GFJ, Gibson AF (1948) The electron trap mechanism of luminescence in sulphide and silicate phosphors. Proc Phys Soc 60(6):574–590

14. McKeever SWS, Hughes DM (1975) Thermally stimulated currents in dielectrics. J Phys D Appl Phys 8:1520–1529
15. Kristianpoller N, Kirsh Y (1979) Thermally stimulated depolarization currents in barium floride. J Phys C Solid State Phys 12(6):1073–1079
16. Paul A (1982) Chemistry of glasses. Chapman & Hall, London
17. James PF (1995) Glass-ceramics – new compositions and uses. J Non-Cryst Solids 181:1–15
18. Keding R, Rüssel C (1997) Electrochemical nucleation for the preparation of oriented glass ceramics. J Non-Cryst Solids 219:136–141
19. Shankar MV, Varma KBR (1999) Dielectric and optical properties of surface crystallized TeO2-LiNbO3 glasses. J Non-Cryst Solids 243:192–203
20. Jain H (2004) Transparent ferroelectric glass-ceramics. Ferroelectrics 306:111–127
21. Halliyal A, Bhalla AS, Newnham RE (1983) Polar glass-ceramics – a new family of electroceramic materials -tailoring the piezoelectric and pyroelectric properties. Mater Res Bull 18:1007–1019
22. Dan A, Chakravorty D (2000) Dielectric properties of silver in a glass-ceramic containing the lithium niobate phase. J Mater Res 15(6):1324–1330
23. Prassas M. Silica glass from aerogels. http://www.solgel.com/articles/april01/aerog2.htm
24. Ding Y, Miura Y, Nakaoka S, Nanba T (1999) Oriented surface crystallization of lithium niobate on glass and second harmonic generation. J Non-Cryst Solids 259:132–138
25. Aboulleil MM, Leonberger FJ (1988) Model for ion-exchanged wave-guides in glass. J Am Ceram Soc 71:497–502
26. Vogel EM (1989) Glasses as nonlinear photonic materials. J Am Ceram Soc 72:719–724
27. Weiss GH, Bendler JT, Dishon M (1985) Analysis of dielectric loss data using the williams-watts function. J Chem Phys 83–3:1424–1427
28. Haertling GH (1999) Ferroelectric ceramics: history and technology. J Am Ceram Soc 82 (4):797–818
29. Prasad E, Sayer M, Vyas HM (1980) Li+ conductivity in lithium-niobate silica glasses. J Non-Cryst Solids 40:119–134
30. Todorovic M, Radonjic L (1997) Lithium-niobate ferroelectric material obtained by glass crystallization. Ceram Int 23:55–60
31. Agarwal AK, Day DE (1982) Thermally stimulated currents and alkali-ion motion in silicate glasses. J Am Ceram Soc 65(2):111–117
32. Hong C, Day DE (1981) Thermally stimulated currents in sodium-silicate glasses. J Am Ceram Soc 64(2):61–67
33. Agarwal AK, Day DE (1981) Polarization and conduction mechanism in mixed-alkali glasses. J Am Ceram Soc 65(5):231–237
34. Graca MPF, Ferreira da Silva MG, Valente MA (2007) Structural and electrical properties of SiO2-Li2O-Nb2O5 glass and glass-ceramics obtained by thermoelectric treatments. J Mater Sci 42:2543–2550
35. Graca MPF, Ferreira da Silva MG, Sombra ASB, Valente MA (2006) Study of the electric and dielectric properties of SiO2-Li2O-Nb2O5 solgel glass-ceramics. J Non-Cryst Solids 352:5199–5204
36. Doi A (1998) Comparison of frequency-domain and temperature-domain electrical responses of ion-conducting glass. Solid State Ionics 107:81–88

Chapter 15
Iron Concentration Effect on the Microwave Dielectric Properties of $BiNbO_4$ Ceramics

S. Devesa, M. P. Graça, and L. C. Costa

Abstract Ceramic dielectrics based on bismuth are recognized as materials with low sintering temperature and have been studied for different applications in the microelectronic area. Since 1992, when Kagata reported the microwave dielectric properties of bismuth niobate ($BiNbO_4$), various attempts have been undertaken to improve the microwave dielectric properties of this ceramic material. Besides the addition of different oxides, such as CuO, ZnO, V_2O_5, PbO, Bi_2O_3 and Fe_2O_3, several researchers tried to improve bismuth niobate properties by adding lanthanides. In this work, $(Bi_{1-x}Fe_x)NbO_4$ ($0.00 \leq \times \leq 1.00$) samples were prepared using the sol-gel method. The fine particles were pressed into cylinders and heat-treated at specific temperatures. Single phase samples of $BiNbO_4$ ($x = 0.00$) and $FeNbO_4$ ($x = 1.00$) were then used as precursors for $(Bi_{1-x}Fe_x)NbO_4$, prepared by the solid state reaction method. The microwave dielectric characterization of the samples was performed using the small perturbation method, and related to their structure. With the sol-gel method the substitution of bismuth by iron was successful, since two non-stoichiometric phases, $Bi_{1.34}Fe_{0.66}Nb_{1.34}O_{6.35}$ and $Bi_{1.721}Fe_{1.056}Nb_{1.134}O_7$, were obtained. Moreover, the inclusion of iron inhibited the formation of low and high temperature triclinic bismuth niobate. With the solid state technique, the substitution of bismuth by iron was not achieved; it was observed that the dielectric constant decreases with the increase of the $FeNbO_4$ phase and that the dielectric losses follow the opposite trend.

Keywords Bismuth niobate · Sol-gel · Solid state · Microwaves · Dielectric properties

S. Devesa (✉) · M. P. Graça · L. C. Costa
I3N and Physics Department, University of Aveiro, Aveiro, Portugal

P. Petkov et al. (eds.), *Advanced Nanotechnologies for Detection and Defence against CBRN Agents*, NATO Science for Peace and Security Series B: Physics and Biophysics, https://doi.org/10.1007/978-94-024-1298-7_15

15.1 Introduction

Microwave dielectric materials are a key factor at the present time, with a wide range of applications from terrestrial to satellite communication systems. In fact, with the widespread use of mobile phones operating in the microwave frequency regime, the research and development of dielectric materials that allow device miniaturization has been one of the biggest challenges in contemporary materials science [1–4].

In order to meet the specifications of current and future systems, enhanced dielectric materials are required. In fact, dielectric oxide ceramics have contributed to one significant change in the microwave wireless communication industry by reducing the size and cost of filters, oscillators and antenna components in applications ranging from cellular phones to global positioning systems. However, the constant need for miniaturization can be considered as an incentive for the development of more sophisticated materials to perform the same or improved functions with decreased size and weight [4–6]. The requirements that a ceramic material must fulfill to be used in microwave frequency range are a high dielectric constant ε', low dielectric losses (tg $\delta = \varepsilon''/\varepsilon'$), and a low temperature resonance frequency coefficient τ_t [7, 8].

In 1992, Kagata reported the microwave dielectric properties of bismuth niobate ($BiNbO_4$) improved with the addition of CuO and V_2O_5 [9]. After this first attempt, several researchers tried to improve the properties of bismuth niobate with the addition of other oxides, ZnO [7], PbO, Bi_2O_3 [10], and Fe_2O_3 [11]. Furthermore, the addition of lanthanides was also considered in numerous studies. $(Bi_{1-x}R_x)NbO_4$ compositions were developed and studied, where R represents different lanthanides, such as Ce, Nd, Dy, Er, La, Sm, Ta, Gd, La and Eu [12–17].

The measurement of the dielectric properties is essential for the characterization of these materials, aiming at the different potential applications. In fact, knowing the properties of a material is important to predict the system performance [4]. Several methods have been developed to study the dielectric properties of materials; according to the literature, the most accurate measurements at high frequency can be performed using the resonant cavity method [4, 18].

The relation between the structural characteristics and the dielectric properties should also be considered. Since $BiNbO_4$ exists in two polymorphs, orthorhombic (α) and triclinic (β) [19–22], the influence of the phase transitions on the dielectric properties of this material is likewise important [19].

In addition, there are other important parameters that require improvement, such as the density, since dense $BiNbO_4$ ceramics are difficult to obtain [5, 20]. The solid-state reaction has been the most common method to process bismuth niobate [21, 23–26]. The powders prepared by this method have a high crystallinity, but not always in pure and homogeneous phases, because some metastable phases are obtained under the same conditions [16]. This method may also cause other problems such as large grain growth, segregation of components and loss of stoichiometry due to the volatilization of bismuth at high temperature [25, 27]. More recently,

the application of wet-chemical techniques such as co-precipitation, alkoxide and citrate sol-gel and the flux-method lead to interesting results [27].

In particular, the sol-gel method through the citrate route is considered a simple way to obtain stable precursors and stoichiometric fine powders. This method is considered promising for achieving high homogeneity, since the formation of citrate complexes allows to mix the component cations in an atomic scale, thus they can immediately react with each other at relatively low temperatures [7, 25–27].

In this work, $(Bi_{1-x}Fe_x)NbO_4$ ($0.00 \leq \times \leq 1.00$) samples were prepared using the sol-gel method through the citrate route. The fine particles were pressed into cylinders and heat-treated at four different temperatures between 500 and 1200 °C. Single phase samples of $BiNbO_4$ (x = 0.00) and $FeNbO_4$ (x = 1.00) were then used as precursors of $(Bi_{1-x}Fe_x)NbO_4$, prepared by the solid-state reaction method.The microwave dielectric characterization of $(Bi_{1-x}Fe_x)NbO_4$ (x = 0.25, 0.50 and 0.75) samples obtained with the two methods was performed using the small perturbation theory, and related with their structure.

15.2 Experimental

15.2.1 Samples Preparation

The first process applied for the $(Bi_{1-x}Fe_x)NbO_4$ samples preparation was the sol-gel method through the citrate route. The starting materials, bismuth nitrate ($Bi(NO_3)_3{\cdot}5H_2O$), niobium chloride ($NbCl_5$) and iron nitrate ($Fe(NO_3){\cdot}9H_2O$), were reagent-grade powders, supplied by Mateck and Merk. A suspension containing stoichiometric amounts of the starting materials was previously prepared in a minor amount of hydrogen peroxide (3% V/V) and dispersed in a mixture of citric acid and ethylene glycol (supplied by Sigma-Aldrich) which performed as chelating agent and reaction medium. The obtained mixtures were stirred to promote the solubility, until clear colloidal suspensions were obtained. Finally, the prepared solutions were dried to evaporate the solvent: the solution with $x = 0.00$ was dried at 400 °C for 48 h; the solutions with $0.25 < \times < 0.75$ were dried at 300 °C for 60 h; the solution with $x = 1.0$ was dried at 300 °C for 24 h. Subsequently, the obtained powders were thermally analysed by differential thermal analysis (DTA), performed in a Lynseis Apparatus type L92/095 in the temperature range of 20–1200 °C, with a heating rate of 5 °C/min for the sample with $x = 0.00$ and 10 °C/min for the remaining samples, using Al_2O_3 as reference. Finally, the dry powders were pressed into cylinders and heat-treated according to the DTA results at temperatures between 500 and 1200 °C, using a dwell time of 4 h, with a heating rate of 5 °C/min. The flow chart for the preparation of the samples by the sol-gel method is shown in Fig. 15.1.

For comparison, samples of $(Bi_{1-x}Fe_x)NbO_4$ with $0.25 < \times < 0.75$ were also prepared by the solid -state reaction method. In this case, the precursors were the

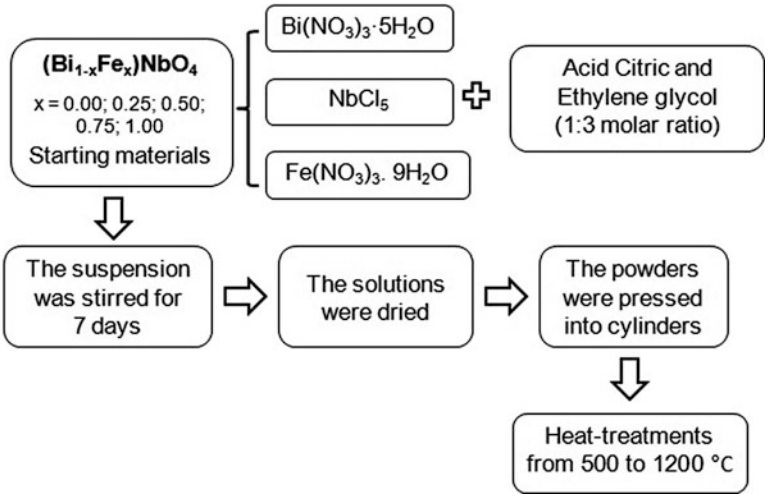

Fig. 15.1 Flow chart for the sol-gel method

pure single phases that were previously obtained with the sol-gel method. Orthorhombic bismuth niobate and iron niobate were mixed in stoichiometric quantities with a minor amount of ethanol in a planetary ball mill at 500 rpm. After being milled for 5 h, the powders were calcined at 300 °C for 5 h and heat-treated at 700 °C, using a dwell time of 4 h and a heating rate of 5 °C/min. This procedure was repeated, but with triclinic bismuth niobate, also sintered previously by the sol-gel method. The flow chart for the preparation of the samples by the solid state reaction method is shown in Fig. 15.2.

15.2.2 Material Characterization

The structural characterization was performed using X-ray diffraction (XRD). The patterns were obtained on a X'Pert MPD Philips diffractometer (CuKα radiation, $\lambda = 1.54060$ Å) at 45 kV and 40 mA with a curved graphite monochromator, an automatic divergence slit (irradiated length 20.00 mm), a progressive receiving slit (height 0.05 mm), and a flat plane sample holder in a Bragg-Brentano parafocusing optic configuration. Intensity data were collected by the step counting method (step 0.02° in 1 s), in the 2θ angle range from 10 to 60° for the samples prepared by the sol-gel method and from 10 to 80° for those obtained with the solid-state reaction.

The ceramics bulk density was measured using the Archimedes method in reference to water. The measurement of the complex permittivity was made using

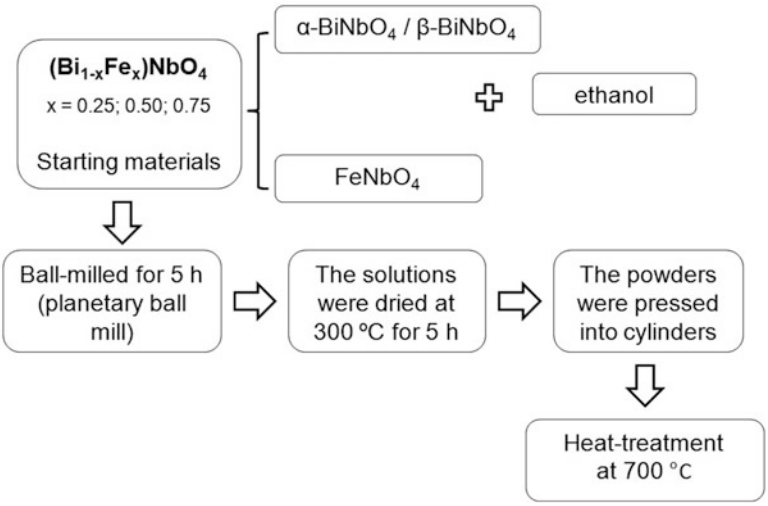

Fig. 15.2 Flow chart for the solid-state reaction method

the small perturbation theory, with a cavity operating in the TE_{105} mode at a resonant frequency of 2.7 GHz. These measurements were made using a HP 8753D coupled to the cavity resonator.

For a given cavity and a regular sample shape and well-defined dimensions, it is possible to determine the permittivity of the material. It can be calculated through the changes in the resonant frequency Δf and of the inverse of the quality factor $\Delta(1/Q)$ of the resonant cavity, when introducing a sample in the cavity, where the electric field is maximal [28, 29].The shift Δf can be related to the real part of the complex permittivity ε', whereas the change $\Delta(1/Q)$ can be related to the imaginary part ε''. Considering only the first order electric field perturbation caused by the sample [28–31], we obtain

$$\varepsilon' = K \frac{\Delta f}{f_0} \frac{V}{v} + 1 \tag{15.1}$$

$$\varepsilon'' = \frac{K}{2} \Delta\left(\frac{1}{Q}\right) \frac{V}{v} \tag{15.2}$$

where K is a constant related to the depolarization factor, which depends upon the geometric parameters, v and V are the volumes of the sample and the cavity, respectively, and f_0 is the resonance frequency of the cavity. Using a sample of known dielectric constant, in our case polytetrafluorethylene (PTFE), we can determine the constant K.

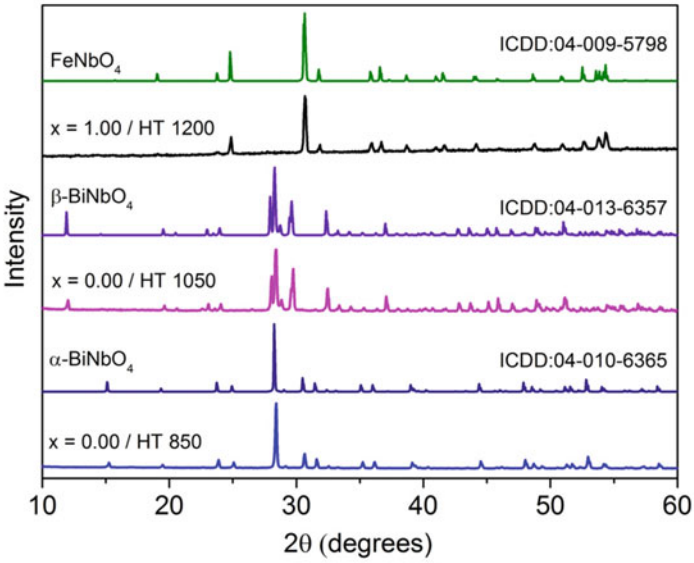

Fig. 15.3 X-ray diffraction patterns of $(Bi_{1-x}Fe_x)NbO_4$ samples for $x = 0.00$, heat-treated (HT) at 850 and 1050 °C, and x = 1.00 treated at 1200 °C

15.3 Results and Discussion

15.3.1 Structural Characterization

The details of the differential thermal analysis performed with the samples prepared by the sol-gel method were already reported in previous works [8, 27, 32]; the heat treatments were performed in agreement with these results. Figure 15.3 shows the X-ray diffraction patterns of $(Bi_{1-x}Fe_x)NbO_4$ samples for $x = 0.00$, treated at 850 and 1050 °C, and for $x = 1.00$ for the sample treated at 1200 °C, consistent with the standard ICDD codes 04-010-6365, 04-013-6357 and 04-009-5798, respectively [33–35].

For $x = 0.00$, after the treatment of the samples at 850 °C, the X-ray diffraction pattern shows the formation of pure orthorhombic $BiNbO_4$ and, with a further temperature increase, this phase is totally converted to triclinic $BiNbO_4$. These results are consistent with the literature reports, since the transition of low temperature β-$BiNbO_4$ to α-$BiNbO_4$ occurs between 600 and 750 °C, with the opposite, and supposed irreversible, transition occurring at 1020/1050 °C [36, 37]. For the samples with x = 1.00, the formation of monoclinic $FeNbO_4$, occurred even at the lowest heat-treatment temperature, nonetheless, the single phase was obtained only at 1200 °C.

The samples with $0.25 \leq \times \leq 0.75$, produced by sol-gel were also characterized using X-ray diffraction. The phases α-$BiNbO_4$ and $FeNbO_4$ were present, as

expected. However, the absence of β-$BiNbO_4$ in the samples treated at 1100 °C was unexpected, since the transition from α-$BiNbO_4$ to β-$BiNbO_4$ occurs according to previous works at 1020/1050 °C [36, 37], and was observed in the sample with x = 0.00 at 1043 °C. This means that the presence of iron inhibits the formation of high temperature β-$BiNbO_4$. Two non-stoichiometric phases, namely $Bi_{1.34}Fe_{0.66}Nb_{1.34}O_{6.35}$ and $Bi_{1.721}Fe_{1.056}Nb_{1.134}O_7$ were found, where the substitution of Bi^{3+} by Fe^{3+} ions was successful. The identification of the crystalline phases of $(Bi_{1-x}Fe_x)NbO_4$ samples obtained with the sol-gel method is presented in Table 15.1.

Figure 15.4 shows the X-ray diffraction patterns of $(Bi_{1-x}Fe_x)NbO_4$ samples prepared by the solid-state reaction method. As one can see, only the starting materials were identified, this is, the substitution of Bi^{3+} for Fe^{3+} ions was not successful. Furthermore, the possible transformation from high temperature β-$BiNbO_4$ to α-$BiNbO_4$ in bulk samples, first reported by Zhou et al. [21] in 2007, was also not observed.

The bulk density values of $(Bi_{1-x}Fe_x)NbO_4$ ceramics, prepared by the sol-gel method, for $0.25 \leq \times \leq 0.75$ were obtained in a previous work [27] and are shown in Table 15.2. For each of the x values, the bulk density increases when the treatment temperature increases for 650 °C, decreases for the treatment at 800 °C, reaching a minimum value, and increases again. Irrespective of the heat treatment, the samples with higher bulk density are the ones with $x = 0.50$.

Considering the samples obtained with the solid-state reaction method, one can see in Fig. 15.5 that the increase of $FeNbO_4$ promotes a decrease of the bulk density. This result is in agreement with the literature, since the theoretical density of $FeNbO_4$ ceramic is 5.40 g/cm^3 [38], lower than the theoretical densities of α-$BiNbO_4$ (7.345 g/cm^3) and β-$BiNbO_4$ (7.5 g/cm^3) ceramics [13, 14]. Comparing these values with the ones obtained with the sol-gel method, it is perceptible that with the solid-state reaction method it is possible a better densification at lower temperatures.

15.3.2 Dielectric Properties

Figure 15.6 presents the measured transmission of 2.7 GHz cavity, the cavity with the sample holder, and the sample holder filled with either PTFE or with the samples prepared from orthorhombic bismuth niobate using the solid-state reaction method. A shift in the resonant frequency of the cavity Δf, is observed.

Since this shift Δf can be related to the real part of the complex permittivity ε', it isto be expected that the sample with $x = 0.75$ presents the lowest ε', followed by the sample with $x = 0.50$ and finally the sample with $x = 0.25$. This prediction will be confirmed later.

Figure 15.7 shows the real (a) and the imaginary (b) parts of the complex permittivity at 2.7 GHz as function of x for the samples prepared by the solid-state reaction method. The dielectric constant decreases with the increase of the $FeNbO_4$ content. The experimental data also suggests that the decrease of the bulk density is

Table 15.1 Crystalline phases of $(Bi_{1-x}Fe_x)NbO_4$ samples obtained with the sol-gel method

HT (°C)	x = 0.00	x = 0.25	x = 0.50	x = 0.75	x = 1.00
500	Bi_2O_3	$Bi_{1.34}Fe_{0.66}Nb_{1.34}O_{6.35}$	$Bi_{1.34}Fe_{0.66}Nb_{1.34}O_{6.35}$	$Bi_{15}NbO_{25}$	$FeNbO_4$
				Fe_2O_3	Fe_2O_3
	BiOCl			$Fe_{0.33}Nb_{0.67}O_2$	
	α-$BiNbO_4$				
	β-$BiNbO_4$				
650	BiOCl	α-$BiNbO_4$	α-$BiNbO_4$	$FeNbO_4$	$FeNbO_4$
	α-$BiNbO_4$	$Bi_{1.34}Fe_{0.66}Nb_{1.34}O_{6.35}$	$Bi_{1.34}Fe_{0.66}Nb_{1.34}O_{6.35}$	Bi_2O_3	Fe_2O_3
	β-$BiNbO_4$				
800	–	α-$BiNbO_4$	$Bi_{1.721}Fe_{1.056}Nb_{1.134}O_7$	$FeNbO_4$	
		$FeNbO_4$	$FeNbO_4$	Bi_2O_3	
		Bi_2O_3			
850	α-$BiNbO_4$	–	–	–	$FeNbO_4$
					Fe_2O_3
1000	–	–	–	–	$FeNbO_4$
					Fe_2O_3
1050	β-$BiNbO_4$	–	–	–	–
1100	–	$Bi_{1.721}Fe_{1.056}Nb_{1.134}O_7$	$Bi_{1.721}Fe_{1.056}Nb_{1.134}O_7$	$FeNbO_4$	–
		$BiFeO_3$	$FeNbO_4$	$Bi_{15}NbO_{25}$	
1150	β-$BiNbO_4$	–	–	–	–
	$Bi_{3.54}Nb_{7.09}O_{22.7}$				
1200	–	–	–	–	$FeNbO_4$

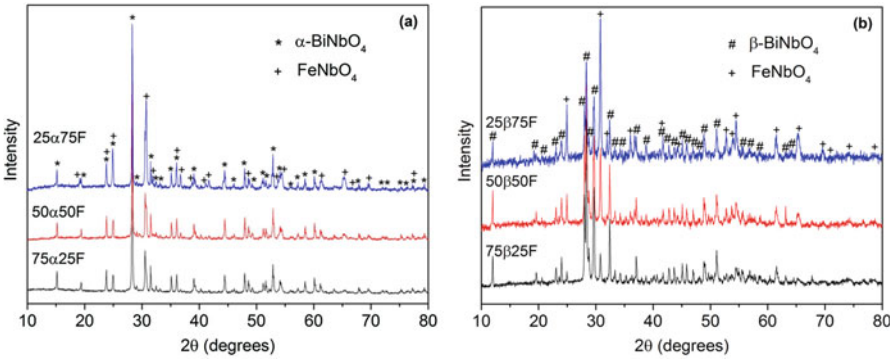

Fig. 15.4 X-ray diffraction patters of the prepared samples with (**a**) α-$BiNbO_4$ [25α75F – 25% of α-$BiNbO_4$ and 75% of $FeNbO_4$; 50α50F – 50% of α-$BiNbO_4$ and 50% of $FeNbO_4$; 75α25F – 75% of α-$BiNbO_4$ and 25% of $FeNbO_4$] and (**b**) β-$BiNbO_4$ [25β75F – 25% of β-$BiNbO_4$ and 75% of $FeNbO_4$; 50β50F – 50% of β-$BiNbO_4$ and 50% of $FeNbO_4$; 75β25F – 75% of β-$BiNbO_4$ and 25% of $FeNbO_4$] as starting material

Table 15.2 Bulk density in g/cm^3 of $(Bi_{1-x}Fe_x)NbO_4$ samples obtained with the sol-gel method

x	HT 500	HT 650	HT 800	HT 1100
0.25	3.9	4.1	2.9	5.1
0.50	4.0	4.3	3.4	5.3
0.75	2.8	3.5	2.7	5.0

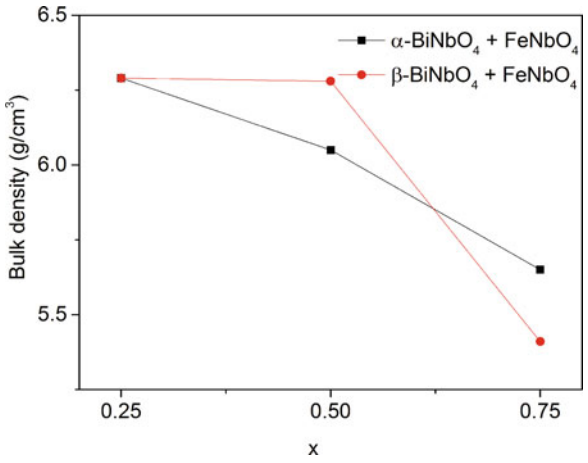

Fig. 15.5 Bulk density of $(Bi_{1-x}Fe_x)NbO_4$ samples obtained with the solid state reaction method

decisive for the decrease of the dielectric constant. Comparing the ε' values of the samples with orthorhombic and triclinic bismuth niobate, one can see that this constant is higher in the samples with α-$BiNbO_4$, except for $x = 0.75$. This possibly means that the increase of $FeNbO_4$ (and consequently, the decrease of the bulk density), overlaps the effect of the crystal structure. The dielectric constant of (Bi_{1-}

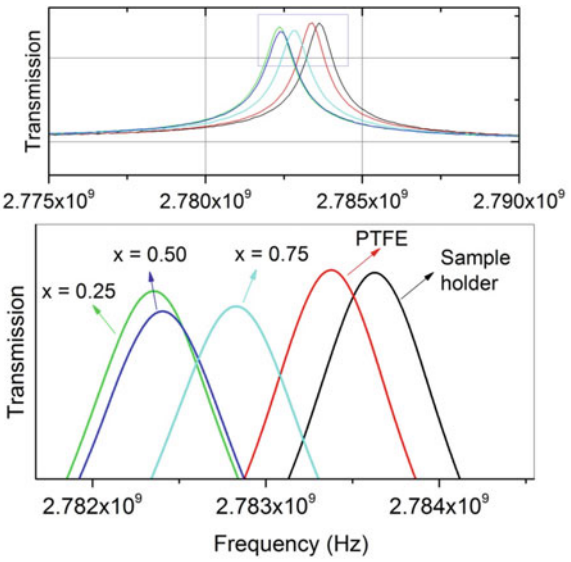

Fig. 15.6 Transmission of the unperturbed and perturbed 2.7 GHz cavity, for the samples prepared by the solid-state reaction method, using α-$BiNbO_4$ as precursor. The lower panel shows the results enlarged

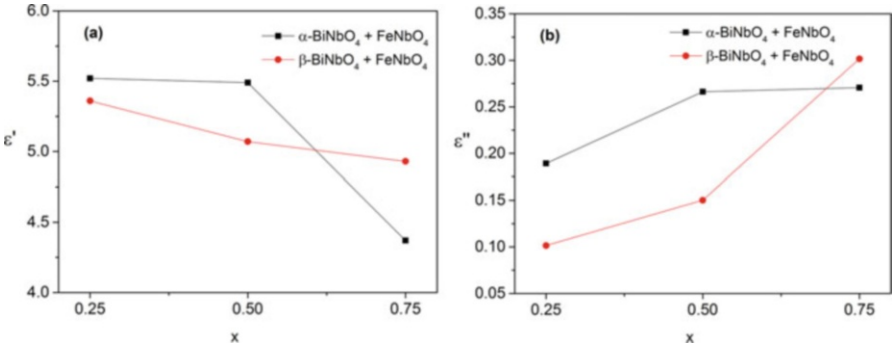

Fig. 15.7 Calculated ε' (**a**) and ε'' (**b**) of $(Bi_{1-x}Fe_x)NbO_4$ samples prepared by the solid state reaction method

$_xFe_x)NbO_4$ ceramics, prepared by the sol-gel method, for $0.25 \leq \times \leq 0.75$, were obtained in a previous work [27] and are shown in Table 15.3.

Figure 15.7b shows that the imaginary part of the complex permittivity increases with the increase of $FeNbO_4$. Confronting this data with the experimental density, we can see opposite trends, that is, the ε'' values increase with the decrease of the bulk density. Comparing the ε'' values of the samples with orthorhombic and triclinic bismuth niobate, one can also see that this constant is higher in the samples with α-$BiNbO_4$, except when $x = 0.75$. We can assume, once again, that the increase of $FeNbO_4$ (and consequently, the decrease of the bulk density), overlaps the effect of the crystal structure.

Table 15.3 Calculated ε' and ε'', for the different samples, at room temperature

	Sol-gel method								Solid state reaction method			
	HT 500		HT 650		HT 800		HT 1100		HT 700 α-BNO + FNO		HT 700 β-BNO + FNO	
x	ε'	ε''	ε'	ε''	ε'	ε''	ε'	ε''	ε'	ε''	ε'	ε''
0.25	4.24	0.08	3.74	0.06	3.65	0.07	10.7	0.22	5.52	0.19	5.36	0.10
0.50	3.81	0.09	3.81	0.09	5.59	0.15	11.2	0.35	5.49	0.27	5.07	0.15
0.75	2.83	0.08	2.37	0.03	3.57	0.15	15.9	2.59	4.37	0.27	4.93	0.30

The imaginary part of the complex permittivity of $(Bi_{1-x}Fe_x)NbO_4$ ceramics, prepared by the sol-gel method, for $0.25 \leq \times \leq 0.75$, were also presented in a previous work [27] and are shown in Table 15.3.

Comparing the two methods, one can see that the highest ε' and ε'' values were obtained with the sol-gel method, in the samples treated at 1100 °C. Nonetheless, considering treatment temperatures compatible with low temperature co-fired ceramics, the solid-state reaction method led, in general, to higher dielectric constants and higher losses.

15.4 Conclusion

In the samples prepared by the sol-gel method the substitution of Bi^{3+} by Fe^{3+} ions occurred successfully, with the formation of two non-stoichiometric phases, while in the solid-state reaction method, only the starting materials were present.

Comparing the bulk density values of the samples obtained with the two methods, it is perceptible that with the solid state reaction a better densification at lower temperatures is possible.

Considering the ε' and ε'' values of the samples with orthorhombic and triclinic bismuth niobate, obtained with the solid state reaction method, one can conclude that these parameters are higher in the samples with α-$BiNbO_4$, except when x is maximum.

Considering treatment temperatures compatible with low temperature co-fired ceramics, the solid state reaction method led, in general, to higher dielectric constants and higher losses.

References

1. Tzou W, Yang C, Chen W, Chen P (2000) Improvements in the sintering and microwave properties of $BiNbO_4$ microwave ceramics by V_2O_5 addition. J Eur Ceram Soc 20:991–996
2. Sebastian MT, Jantunen H (2008) Low loss dielectric materials for LTCC applications: a review. Int Mater Rev 53:57–90
3. Narang S, Bahel S (2010) Low loss dielectric ceramics for microwave applications: a review. J Ceram Process Res 11(3):316–321
4. Sebastian MT (2008) Dielectric materials for wireless communication. Elsevier, Amsterdam
5. Devesa S, Graça MP, Henry F, Costa L (2015) Microwave dielectric properties of $(Bi_{1-x}Fe_x)NbO_4$ ceramics prepared by the sol–gel method. Ceram Int 41(6):8186–8190
6. Zhou D, Pang L, Wang H, Yao X (2009) Phase composition and phase transformation in Bi (Sb, Nb, Ta)O_4 system. Solid State Sci 11:1894–1897
7. Wang N, Zhao M, Yin Z, Li W (2003) Low-temperature synthesis of β-$BiNbO_4$ powder by citrate sol–gel method. Mater Lett 57:4009–4013
8. Devesa S, Graça MP, Costa L (2016) Structural, morphological and dielectric properties of $BiNbO_4$ ceramics prepared by the sol-gel method. Mater Res Bull 78:128–133

9. Kagata H, Inoue T, Kato J, Kameyama I (1992) Low-fire bismuth-based dielectric ceramics for microwave use. Jpn J Appl Phys 31(9S):3152
10. Almeida J, Fernandes T, Sales A, Silva M, Júnior G, Rodrigues H, Sombra A (2011) Study of the structural and dielectric properties of Bi_2O_3 and PbO addition on $BiNbO_4$ ceramic matrix for RF applications. J Mater Sci Mater Electron 22:978–987
11. Yang Y, Ding S, Yao X (2004) Influences of Fe_2O_3 additives on the dielectric properties of $BiNbO_4$ ceramics under different sintering atmosphere. Ceram Int 30:1341–1345
12. Shihua D, Xi Y, Yu M, Puling L (2006) Microwave dielectric properties of $(Bi_{1-x}Fe_x)NbO_4$ ceramics (R= Ce, Nd, Dy, Er). J Eur Ceram Soc 26:2003–2005
13. Wang N, Zhao M, Yin Z, Li W (2004) Effects of complex substitution of La and Nd for Bi on the microwave dielectric properties of $BiNbO_4$ ceramics. Mater Res Bull 39:439–448
14. Tzou W, Yang C, Chen Y, Cheng P (2002) Microwave dielectric characteristics of $(Bi_{1-x}Sm_x)NbO_4$ ceramics. Ceram Int 28:105–110
15. Wang N, Zhao M, Yin Z (2003) Effects of Ta_2O_5 on microwave dielectric properties of $BiNbO_4$ ceramics. Mater Sci Eng B 99(1):238–242
16. Butee S, Kulkarni A, Prakash O, Aiyar R, Sudheendran K, Raju K (2010) Effect of lanthanide ion substitution on RF and microwave dielectric properties of $BiNbO_4$ ceramics. J Alloys Compd 492:351–357
17. Devesa S, Graça MP, Henry F, Costa LC (2017) Structural, morphological and microwave dielectric properties of $(Bi_{1-x}Eu_x)NbO_4$ ceramics prepared by the sol-gel method. Int J Mater Eng Innov 8(1):12–26
18. Parkash A, Vaid JK, Mansingh A (1979) Measurement of dielectric parameters at microwave frequencies by cavity-perturbation technique. IEEE Trans Microw Theory Tech 27(9):791–795
19. Kim E, Choi W, Eur J (2006) Effect of phase transition on the microwave dielectric properties of $BiNbO_4$. Ceram Soc 26:1761–1766
20. Liou Y, Tsai W, Chen H (2009) Low-temperature synthesis of $BiNbO_4$ ceramics using reaction-sintering process. Ceram Int 35:2119–2122
21. Zhou D, Wang H, Yao X, Wei X, Xiang F, Pang L (2007) Phase transformation in $BiNbO_4$ ceramics. Appl Phys Lett 90(17):2910
22. Maruyama Y, Izawa C, Watanabe T (2012) Synthesis of by the Flux method. ISRN Mater Sci
23. Sales AJ, Oliveira P, Almeida J, Costa M, Rodrigues H, Sombra A (2012) Copper concentration effect in the dielectric properties of $BiNbO_4$ for RF applications. J Alloys Compd 542:264–270
24. Filho RC, Araújo JH, Ginani MF, d'Assunção AG, Martins RA (2010) Simulation and measurement of inset-fed microstrip patch antennas on $BiNbO_4$ substrates. Microw Opt Technol Lett 52(5):1034–1036
25. Radha R, Gupta UN, Samuel V, Muthurajan H, Kumar HH, Ravi V (2008) A co-precipitation technique to prepare $BiNbO_4$ powders. Ceram Int 34(6):1565–1567
26. Almeida CG, Andrade HMC, Mascarenhas AJS, Silva LA (2010) Synthesis of nanosized β-$BiTaO_4$ by the polymeric precursor method. Mater Lett 64(9):1088–1090
27. S. Devesa, Graça MP, Costa LC (2017) Recent applications in sol-gel synthesis. InTech
28. Costa LC, Aoujgal A, Graça MPF, Hadik N, Achour ME (2010) Microwave dielectric properties of the system $Ba_{1-x}Sr_xTiO_3$. Physica B 405(17):3741–3744
29. Rubinger CPL, Costa LC (2007) Building a resonant cavity for the measurement of microwave dielectric permittivity of high loss materials. Microw Opt Technol Lett 49:1687–1690
30. Costa LC, Devesa S, Henry F (2005) Microwave dielectric properties of polybutylene terephtalate (PBT) with carbon black particles. Microw Opt Technol Lett 46:61–63
31. Silva CC, Gouveia DX, Graça MPF, Costa LC, Sombra ASB, Valente MA (2010) Study of the structural and dielectric properties of $xLiFe_5O_{8-}(100-x)\ LiNbO_3$ composites, processed using microwave energy. J Non-Cryst Solids 356:602–606
32. Devesa S, Graça MP, Henry F, Costa LC (2016) Dielectric properties of $FeNbO_4$ ceramics prepared by the sol-gel method. Solid State Sci 61:44–50
33. Lee CY, Macquart R, Zhou Q, Kennedy BJ (2003) Structural and spectroscopic studies of $BiTa_{1-x}Nb_xO$. J Solid State Chem 174(2):310–318

34. Muktha B, Darriet J, Madras G, Row T (2006) Crystal structures and photocatalysis of the triclinic polymorphs of $BiNbO_4$ and $BiTaO_4$. J Solid State Chem 179:3919–3925
35. Schmidbauer E, Schneider J (1997) Electrical resistivity, thermopower, and 57Fe Mössbauer study of $FeNb_4$. J Solid State Chem 134(2):253–264
36. Radha R, Muthurajan H, Rao NK, Pradhan S, Gupta UN, Jha RK, Mirji SA, Ravi V (2008) Low temperature synthesis and characterization of $BiNbO_4$ powders. Mater Charact 59(8):1083–1087
37. Xu C, He D, Liu C, Wang H, Zhang L, Wang P, Yin S (2013) High pressure and high temperature study the phase transitions of $BiNbO_4$. Solid State Commun 156:21–24
38. Roth RS, Waring JL (1964) Ixiolite+ other polymorphic types of $FeNbO_4$. Am Mineral 49:2242

Chapter 16
Dielectric Analysis of Phosphate-Borate Glass-Ceramics Doped with Alkali Oxides

B. M. G. Melo, M. A. Valente, and M. P. F. Graça

Abstract The synthesis of dielectric materials with high-energy density is fundamental for capacitors in power electronics and pulsed power applications. Ceramic materials have been broadly used for capacitors due to their high dielectric constant. However, they have some disadvantages such as a low breakdown strength and a high remanent polarization, which limits their application in high-voltage devices. The development of glass-ceramics with high dielectric constant and high breakdown strength can be a promising solution for applications in high-voltage and impulse power systems. In the present work, functional glasses with the molar composition $20.7P_2O_5$–$17.2Nb_2O_5$–$13.8WO_3$–$34.5A_2O$–$13.8B_2O_3$ where A=Li, Na, and K were prepared by the melt quenching technique. The base glasses were heat-treated in air at 800 °C for 4 h, which led to the formation of glass-ceramics. The present work studies the ac conductivity and dielectric properties in the 200–650 K temperature range of the glass doped with K_2O. Impedance spectroscopy was used in the frequency range 100 Hz to 1 MHz in order to characterize electrically the glass.

Keywords Glass-ceramics · Glass · Dielectric constant · Impedance spectroscopy · Ac conductivity · Electrical characterization · Dielectric relaxation

16.1 Introduction

The formation of glass-ceramics has significant advantages when compared with single crystals and ceramics because the optical, electrical, mechanical and chemical properties can be controlled/tuned by the volume fraction of the active crystalline phase dispersed in the amorphous matrix [1–3]. For this reason, there is a large interest in the preparation, characterization and technological application of glass

B. M. G. Melo (✉) · M. A. Valente · M. P. F. Graça
I3N and Physics Department, Aveiro University, Aveiro, Portugal
e-mail: bmelo@ua.pt

P. Petkov et al. (eds.), *Advanced Nanotechnologies for Detection and Defence against CBRN Agents*, NATO Science for Peace and Security Series B: Physics and Biophysics, https://doi.org/10.1007/978-94-024-1298-7_16

and glass-ceramics as substitutes for single crystal materials [1, 2]. Glass-ceramics with nanosized crystalline particles dispersed in the amorphous matrix are promising materials since the properties of the materials depend on their specific surface area. Although the electrical properties of the single crystals are usually better than those of glass-ceramic material as the amorphous phase generally has a low dielectric constant, glass-ceramics become an appealing alternative since the growth of single crystals is expensive [1–3]. Currently, ceramic dielectrics are widely used for capacitors due to their high dielectric constant. Nevertheless, their application as high-voltage devices is limited by their high remanent polarization, along with residual pores and irregular grains in their structure which restrict the increase of breakdown strength [4, 5]. However, glass-ceramics combine the advantages of glass and ceramic phases, high breakdown strength and dielectric constant [4–7].

In our recent work [3], we discussed the changes induced by a heat-treatment in air at 800 °C on the structural, electrical and dielectric properties of the glass system $20.7P_2O_5$–$17.2Nb_2O_5$–$13.8WO_3$–$34.5A_2O$–$13.8B_2O_3$ where A=Li, Na, and K. The present work studies and expands the dielectric properties of the K_2O containing sample over a broader range of temperature (200–650 K).

16.2 Experimental

Functional glasses with the desired molar composition were prepared by the melt quenching technique, using high purity (>99%) P_2O_5, Nb_2O_5, WO_3, A_2CO_3 and B_2O_3 in powder form. The experimental conditions used for the synthesis of these glasses can be found in [3]. For the formation of glass-ceramics, the as-grown glasses were heat-treated in air at 800 °C for four hours with a heating rate of 5 °C/min. The heat-treatment temperature was chosen according to differential thermal analysis [8] which revealed an exothermic phenomenon for the as-grown glasses between 530 and 600 °C. The samples discussed in this work will be termed, A-Li, A-Na, and A-K, according to the alkali oxide included on each glass, Li_2O, Na_2O, and K_2O, respectively.

X-ray diffraction (XRD) patterns were obtained at room temperature with a Philips X'Pert MPD diffractometer (CuKα radiation, $\lambda = 1.54056$ Å) operating at 45 kV and 40 mA, with a curved graphite monochromator, an automatic divergence slit, a progressive receiving slit and a flat plane sample holder in a Bragg-Brentano parafocusing configuration.The acquisition was performed using a scan step of 0.02° in 1 s, in the 2θ angle range of 10–60°. The obtained patterns are shown in Fig. 16.1.

The ac electrical conductivity (σ_{ac}) of the sample was measured in the temperature range between 200 and 380 K, using a nitrogen bath cryostat setup and an Oxford Research IT-C4 controller, and from room temperature up to 650 K in an electric furnace equipped with a Eurotherm 3508 controller. For these measurements a Network Analyzer Agilent 4294, operating between 100 Hz and 1 MHz in the C_p-R_p configuration (capacitance in parallel with resistance) was used. During the 200–400 K measurements, the sample was kept in a helium atmosphere to minimize

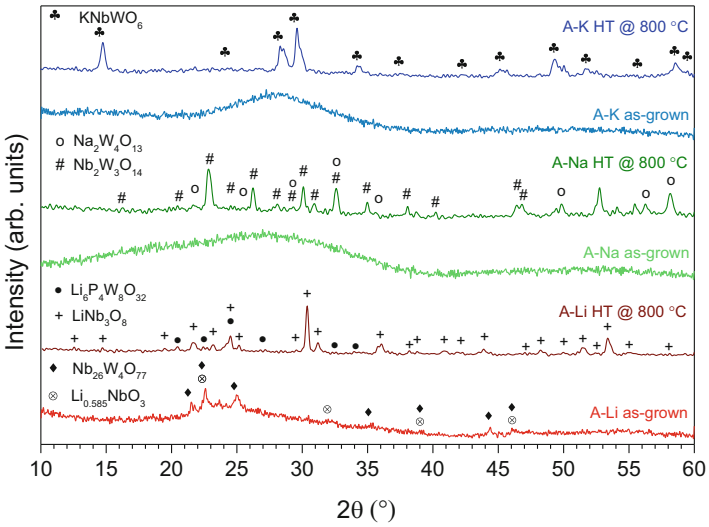

Fig. 16.1 XRD spectra of the samples (Reprinted with permission from [3]. © 2016 AIP Pulishing)

thermal gradients. Further details about the sample preparation and the mathematical formalisms used to determine ac conductivity, dielectric constant, dielectric loss, and loss tangent can be found in [3].

16.3 Results and Discussion

The XRD spectra of the as-grown glasses and heat-treated samples are shown in Fig. 16.1. Except for the Li_2O containing sample, the base glasses show XRD patterns characteristic for amorphous materials. After the heat-treatment the formation of crystalline phases was observed for all compositions. Identification and discussion of the crystalline phases obtained for A-Li and A-Na glasses heat-treated at 800 °C can be found in our recent work [3]. As mentioned before, this contribution will focus on the results for the K_2O containing glass system (A-K).

After the heat-treatment, the A-K sample shows the formation of a single $KNbWO_6$ phase with a cubic crystal system. The $KNbWO_6$ particles have a pyrochlore-type structure which possesses useful properties for applications such as a ionic conductivity (both cations and anions), electrical conductivity, and magnetic and ferroelectric properties [3, 9, 10]. Additionally, materials based of $K\Lambda WO_6$ (Λ – Nb, Sb, Ta) compounds can be used as catalysts due to their content of transition metals [9]. To evaluate these potential applications, and to provide further knowledge about the dielectric properties of glass-ceramic systems with $KNbWO_6$ crystalline particles, the impedance spectroscopy results of the A-K glass heat-treated at 800 °C (A-K glass-ceramic) will be discussed next.

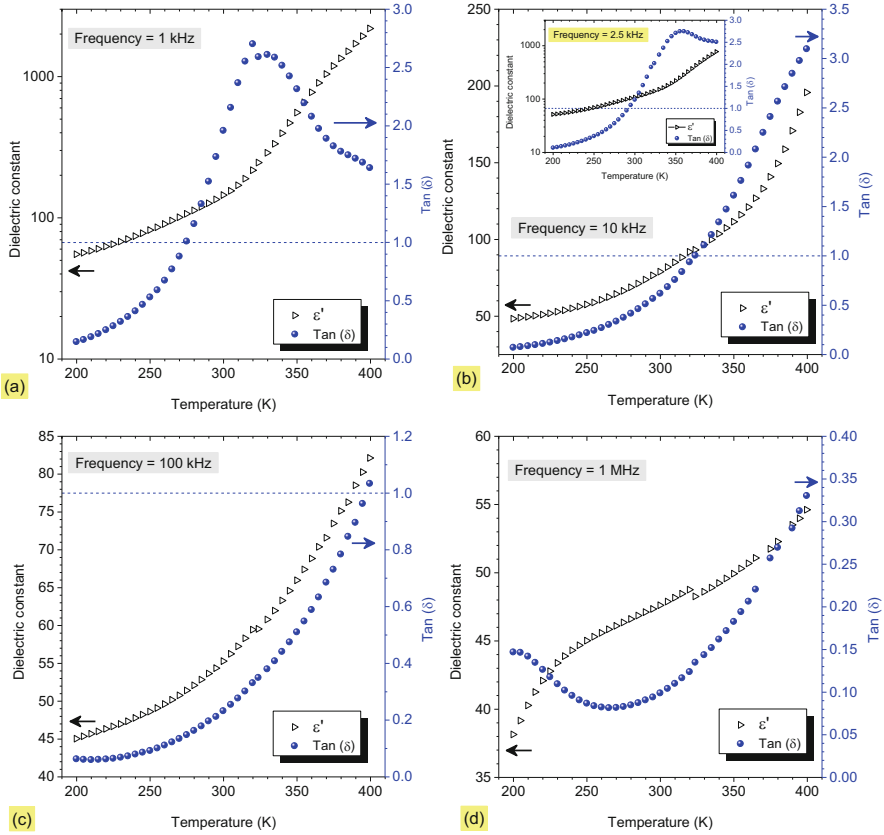

Fig. 16.2 Dielectric constant and loss tangent values of the A-K glass-ceramic as a function of temperature at (**a**) 1 kHz; (**b**) 10 kHz; (**c**) 100 and (**d**) 1 MHz. The *inset* of 2b shows the f = 2.5 kHz results

Figure 16.2. displays the temperature dependence of the dielectric constant ε′ and the loss tangent tan(δ) of the A-K glass-ceramic. This figure resumes the results obtained at different frequencies, namely, 1 kHz, 2.5 kHz, 10 kHz, 100 kHz, and 1 MHz. For all frequencies, the dielectric constant increases with temperature, as expected. Although at low frequencies (1 kHz and 2.5 kHz) the sample has high ε′ values for glass materials, but those of the loss tangent are also high. For these two frequencies, we can also see a sharp increase of ε′ above 300 K. This temperature matches the maximum observed in the loss tangent. This maximum shifts to higher frequencies with increasing temperature as seen in the inset of 2b. The dielectric constant (at 300 K and 10 kHz) is 79, which is slightly larger than the value obtained by Kar and Choudhary [10] in $KNbWO_6$ polycrystalline samples ($\varepsilon' = 44$ for the same temperature and frequency). However, the loss tangent value of the studied sample is also larger, namely 0.62, instead of 0.07 obtained in [10]. The 100 kHz (Fig. 16.2c), and 1 MHz (Fig. 16.2d) values show that ε′ decreases with frequency,

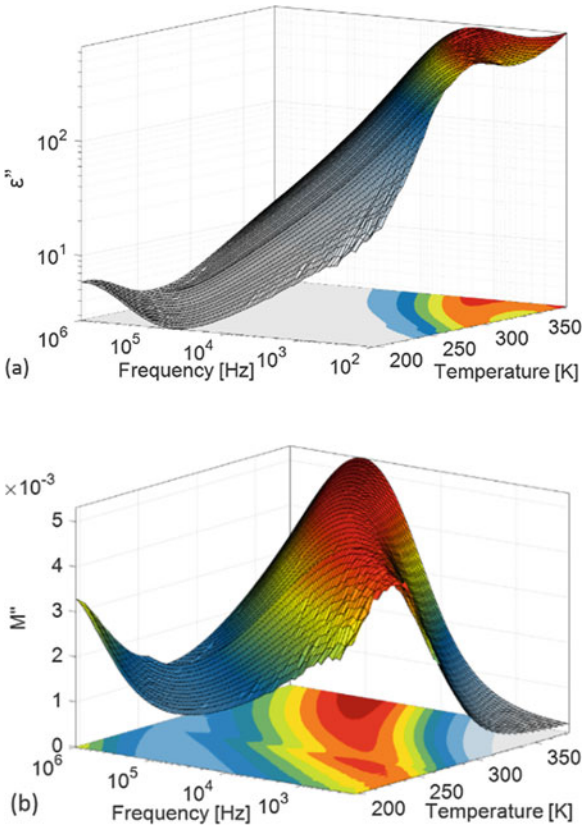

Fig. 16.3 3D graphics of the dependence of (**a**) ε″ and (**b**) M″ (**b**) on frequency and temperature

which is also the expected behavior. For these frequencies, the loss tangent also decreases and becomes below 1 in the temperature range examined.

The presence of dielectric relaxations for the A-K glass-ceramic was investigated using the dielectric loss (ε″) and dielectric modulus (M″) dependence on both temperature and frequency. The results are presented in Fig. 16.3. Sometimes the dielectric relaxation peaks are not visible in the ε″ representation. Therefore, the complex dielectric modulus (M″) formulation is often used to study the dielectric properties of glasses with a high degree of ionic conductivity since it has the advantage of minimizing high capacitance effects due to spatial charge accumulation [3, 11]. However, for this sample it is possible to observe a dielectric relaxation using both formalisms (permittivity and modulus).

The evolution of a thermally activated relaxation peak, which shifts towards higher frequencies with increasing temperature is clear for both figures. Figure 16.3a shows that in the ε″ representation the dielectric relaxation is observable only above 300 K, since below this temperature its peak is centered at a frequency smaller than 100 Hz and therefore out of the examined frequency window. However, since the relaxation peak shifts to higher frequencies with the modulus

formalism [12], we can observe the dielectric relaxation at lower temperatures in Fig. 16.3b. One can also see that both formalisms appear to show a second dielectric relaxation at lower temperatures (below 250 K), that should be visible at higher frequencies. This secondary dielectric phenomenon could be the secondary relaxation, which is faster than the primary and is supposed to originate from intermolecular motion [11]. We suggest that if we used a frequency range above 1 MHz or if we studied this sample at even lower temperatures (below 200 K), this second dielectric relaxation could be observable.

Figure 16.4a shows the Nyquist plot in the modulus formalism. The obtained plot shows a non-Debye behavior, which is typical for amorphous materials [11]. A Debye-like relaxation behavior is characterized by a single relaxation time. However, the dielectric relaxation behavior in amorphous materials rarely follows this simple picture; usually, a distribution of times is found instead [11]. The shape of the dielectric relaxation (Fig. 16.4a), namely a skewed arc, identifies this as a Cole-Davidson relaxation type. Figure 16.4b shows the frequency-dependence of the

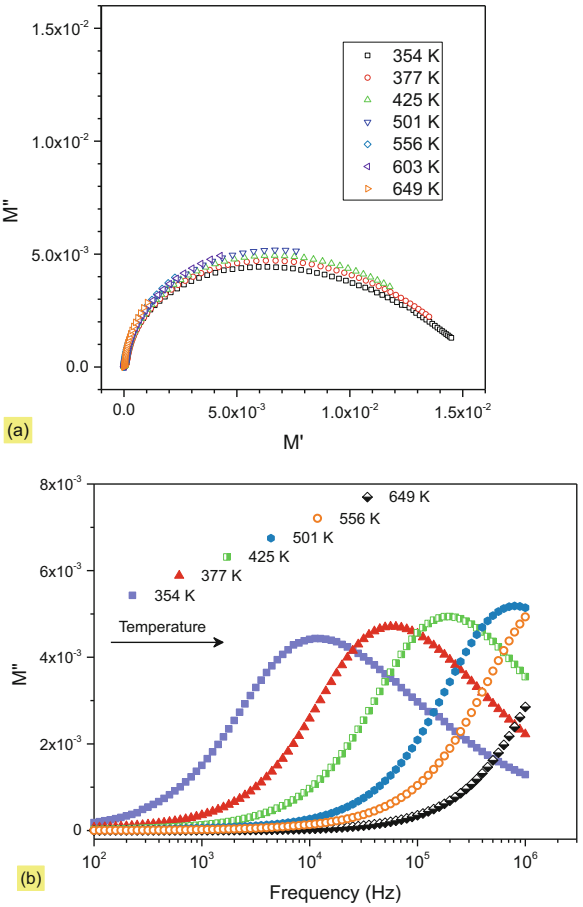

Fig. 16.4 (**a**) Nyquist (M*) plot and (**b**) frequency distribution of the imaginary part of the dielectric modulus, for the A-K glass-ceramic

imaginary part of modulus at higher temperatures (room temperature up to 650 K). Similarly to Fig. 16.3, we can see that the relaxation peak shifts towards higher frequencies with increasing temperature. However, for temperatures above 501 K, the relaxation peak shifts to frequencies above 10^6 Hz, which is outside the frequency window used.

The frequency-dependent conductivity of the A-K glass-ceramic, measured at different temperatures, can be seen in Fig. 16.5a. Two regimes can be identified within the measured frequency window: (i) a low-frequency plateau region and (ii) a high-frequency dispersion region following a power law profile. The plateau region

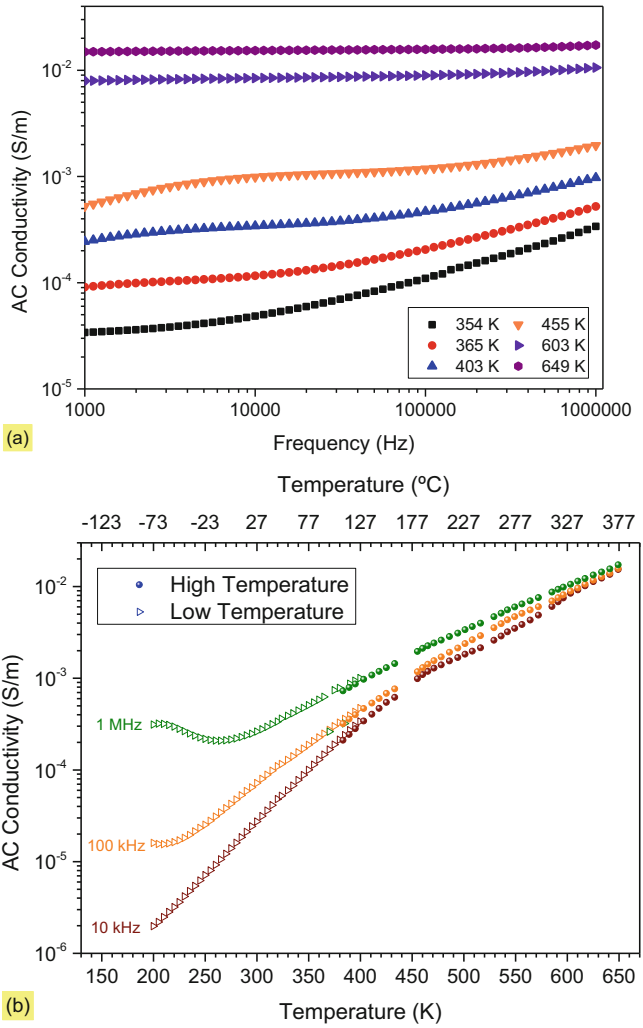

Fig. 16.5 (**a**) Frequency dependence of σ_{ac} at several temperatures and (**b**) temperature dependence of σ_{ac} for the A-K glass-ceramic

corresponds to a frequency independent conductivity and can be assigned to the dc conductivity [11]. The temperature transition point between the nearly frequency independent and the strong frequency dependence region shifts towards higher frequencies with increasing temperature. This shift can be related to the dc component, which becomes more influent than the ac contribution at higher temperatures [11]. As observed in Fig. 16.5a, at higher temperatures (650 K) the conductivity becomes practically frequency independent. At these temperatures, the conductivity of the sample is over 10^{-2} S/m. While the polycrystalline samples prepared in [10] shown a σ_{ac} value (at 300 K and 10^6 Hz) of 5.04×10^{-5} S/m, the prepared sample revealed at the same conditions, a larger conductivity value of 2.62×10^{-4} S/m.

Figure 16.5b shows the σ_{ac} values measured at 10 kHz, 100 kHz and 1 MHz in the 200–650 K temperature range. The conductivity from 200 up to 400 K (Low Temperature) was measured using the nitrogen bath cryostat setup, while from room temperature up to 650 K (High Temperature) was used the previously discussed electric furnace. The first observation we can see is that there is a good agreement in the experimental values obtained by the two apparatus. For higher frequencies, and above 350 K, the ac conductivity seems to increase logarithmically. The behavior of σ_{ac} evidenced at low temperatures (below 250 K) with increasing frequency could be related to the second dielectric relaxation previously discussed in Fig. 16.3 in this temperature range.

The $KNbWO_6$ structures are built up from corner-sharing WO_6 octahedra, creating networks of hexagonal tunnels [13, 14]. Since the univalent cations occupy large framework voids and are weakly linked to their atoms, they can easily migrate along the channels within the structure [13, 14].

The $\ln(\sigma_{ac} \times T)$ vs. 1000/T dependence can be found in Fig. 16.6a. These results were measured, once again, with the two setups described above. For the A-K glass-ceramic, we can identify three temperature regions with a thermally activated conductivity. As one can see, the activation energy E_a values are different and increase with temperature. The latter could suggest that, either three different conduction mechanisms are contributing to the total conductivity, or that the conductivity does not follow the Arrhenius model in this range of temperatures. Another possible explication could be an increased contribution from the conduction mechanism of the $KNbWO_6$ particles when the temperature increases. The $Ln(\sigma_{ac} \times T)$ vs. 1000/T results for the as-grown A-K glass show that the activation energy assigned to the dominant conduction process of the base glass, namely, the dipolar mechanism between the modifier potassium ions and the non-bridging oxygen anions in their vicinity, is smaller. This could suggest that for the A-K glass-ceramic the conduction mechanism due to the mobility of K^+ in the amorphous matrix becomes negligible for higher temperatures. Further discussion about the electrical conductivity of this sample can be found in [3, 8].

Figure 16.6b shows the activation energy values as function of frequency. As one can see, the activation energy values decrease when the frequency of the applied electric field increases. This behavior can be explained since, when the frequency is smaller, the mobile charge carriers travel a longer distance across the glass network

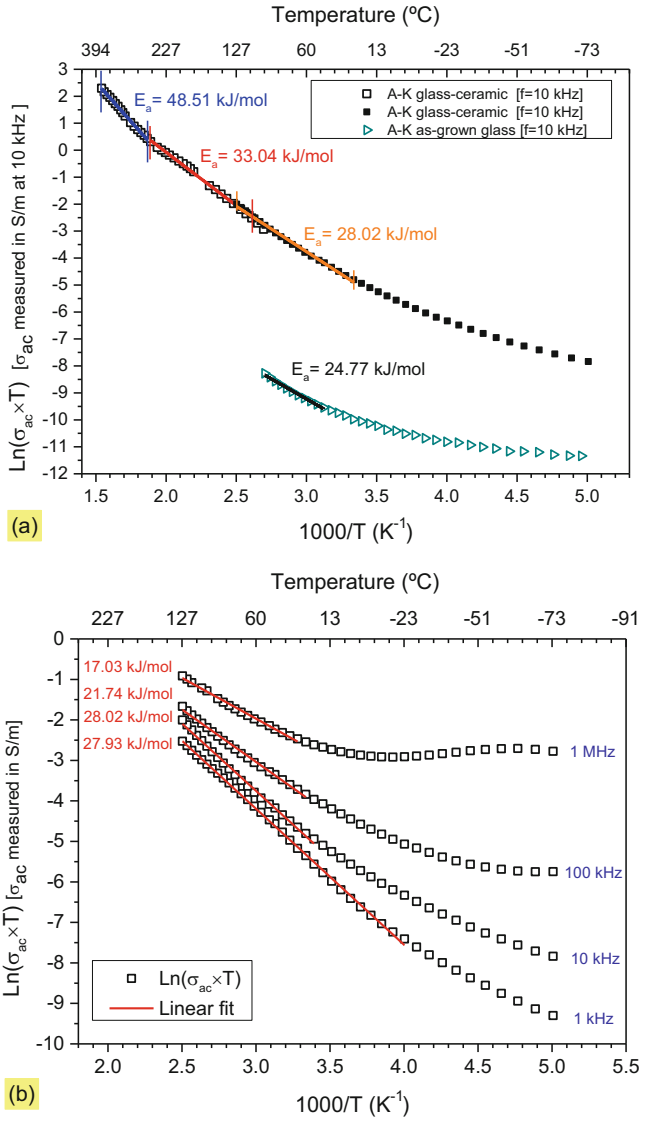

Fig. 16.6 (**a**) Linearization of σ_{ac} using the Arrhenius equation and (**b**) analysis of the activation energy values as a function of frequency

and can go through some conduction channel that requires higher energy for the migration. On the other hand, for higher frequencies, the charge carriers are excited with higher energy and oscillate over a shorter distance of the network between neighboring sites. Hence, they do not have to overcome the highest energetic barriers to contribute to the conductivity process.

16.4 Conclusions

In the present work, we discussed the ac conductivity and the dielectric properties of a glass-ceramic system prepared by a heat-treatment in air at 800 °C with the composition $20.7P_2O_5$–$17.2Nb_2O_5$–$13.8WO_3$–$34.5K_2O$–$13.8B_2O_3$. The XRD pattern of this sample indicate the formation of a single $KNbWO_6$ crystalline phase with a cubic crystal system.

The dielectric permittivity of the sample is frequency and temperature dependent. The sample was studied in the 200–650 K temperature range, using two different apparatus; we found a good agreement between the results obtained from the two experimental setups. Using both, permittivity and modulus formalisms, a thermally activated relaxation peak which shifts towards higher frequencies with the increase of the temperature, was found. The Nyquist plot using the modulus formalism revealed that this dielectric relaxation is described by a Cole-Davidson model.

In the 200–400 K temperature range, it was found that the activation energy values decrease when the frequency of the applied electric field increases. The study of the ac conductivity as a function of frequency for different temperatures showed that the dc component becomes more influent than the ac contribution for higher temperatures (above 603 K). Additionally, at higher temperatures (650 K) the ac conductivity of the sample is over 10^{-2} S/m.

References

1. Graça MPF, Valente MA (2011) Glass ceramics with para, anti or ferroelectric active phases, advances in ceramics – electric and magnetic ceramics, bioceramics, ceramics and environment. INTECH Open Access Publisher. https://doi.org/10.5772/20854
2. Graça MPF, Ferreira da Silva MG, Valente MA (2008) Structural and electrical characteristics of $LiNbO_3$ embedded in a 34% SiO_2 glass matrix. J Eur Ceram Soc 28(6):1197–1203
3. Melo BMG, Graça MPF, Prezas PR, Valente MA, Almeida AF, Freire FNA, Bih L (2016) Study of structural, electrical, and dielectric properties of phosphate-borate glasses and glass-ceramics. J Appl Phys 120(5):051701
4. Li C, Zhang Q, Tang Q, Zhou H, Tan F, Du J (2016) Dielectric and energy storage properties of BaO-SrO-Na2O-Nb2O5-SiO2 glass–ceramics with different crystallization times. J Electron Mater 45(6):3025–3029
5. Manoharan MP, Zou C, Furman E, Zhang N, Kushner DI, Zhang S, Murata T, Lanagan MT (2013) Flexible glass for high temperature energy storage capacitors. Energ Technol 1 (5–6):313–318
6. Zheng H, Pu Y, Liu X, Wan J (2016) Correlation between dielectric properties and crystallization treatment in potassium sodium niobate glass-ceramics for energy storage application. J Alloys Compd 674:272–276
7. Yadav AK, Gautam CR, Singh P (2016) Effect of donor and acceptor dopants on crystallization, microstructural and dielectric behaviors of barium strontium titanate glass ceramics. J Alloys Compd 672:52–58
8. Graça MPF, Melo BMG, Prezas PR, Valente MA, Freire FNA, Bih L (2015) Electrical and dielectric analysis of phosphate based glasses doped with alkali oxides. Mater Des 86(Supplement C):427–435

9. Knyazev AV, Mączka M, Kuznetsova NY (2010) Thermodynamic modeling, structural and spectroscopic studies of the $KNbWO_6$–$KSbWO_6$–$KTaWO_6$ system. Thermochim Acta 506 (1–2):20–27
10. Kar T, Choudhary RNP (2001) Structural dielectric and electrical conducting properties of $KB'B''O6$ (B′=Nb, Ta; B″=W, Mo) ceramics. J Phys Chem Solids 62(6):1149–1161
11. Melo BMG, Attafi Y, Ben Haj Amara A, Soreto Teixeira S, Costa LC, Valente MA, Graça MPF. Electrical and dielectric analysis of lithium chloride mixed sodium and lithium phosphate glasses. Int J Appl Glass Sci
12. Cheng PF, Song J, Li S-T, Wang H (2015) Modulus spectroscopy of grain–grain boundary binary system. Phys B Condens Matter 459(Supplement C):105–109
13. Mączka M, Ko JH, Włosewicz D, Tomaszewski PE, Kojima S, Hanuza J, Majchrowski A (2004) Heat capacity and dielectric studies of ferroelectric superionic conductor $RbNbWO_6$. Solid State Ionics 167(3–4):309–315
14. Chernaya TS, Simonov VI, Muradyan LA (1991) Structural features that cause different ionic conductivity in RbNbWO and TlNbWO. Butlletí Soc Catalanes Fís Quím Matemàtiques Tecnol 12:427–434

Chapter 17
Electrical and Magnetic Properties of Yttrium Ferrites

S. Soreto Teixeira, A. J. M. Sales, M. P. F. Graça, M. A. Valente, and L. C. Costa

Abstract The development of new materials with a high dielectric constant and low losses is one of the main targets in scientific research for applications. These properties permit to reduce the size and weight of electronic devices. A potential candidate for this goal is yttrium ferrite. Powder precursors of yttrium ferrites, $Y_3Fe_5O_{12}$ (YIG) and $YFeO_3$, were prepared by the sol-gel method through the Pechini route. The powders were heat-treated at 1000, 1300 and 1400 °C. The sample structure was characterized by X-ray diffraction (XRD), the morphology by scanning electron microscopy (SEM). For all temperatures of the heat-treatment, the YIG crystalline phase was the predominant and $YFeO_3$ the secondary phase. The highest percentage of YIG (≈90%) was obtained in the samples heat-treated at 1400 °C. By means of impedance spectroscopy measurements, the dielectric properties were studied between 100 Hz and 1 MHz, and between 200 and 400 K. The dielectric constant improves with the growth of the YIG phase, increasing grain size and decreasing porosity. The highest value of dielectric constant at 1 kHz was obtained for the sample heat-treated at 1400 °C ($\varepsilon' = 1750$; $\tan\delta = 0.18$). The values of dielectric losses are sufficiently low to use this material in electronic applications. For all samples, one non-Debye relaxation process was identified; the relaxation time versus temperature shows an Arrhenius behaviour. Magnetic measurements (M vs. T and M vs. B) were performed using a vibrating sample magnetometer (VSM). The dc magnetic susceptibility was recorded under zero field cooled (ZFC) and field cooled (FC) sequences, with a field of 0.1 T between 7 and 300 K. The results of the magnetic investigations show the presence of a blocking temperature, $T_B \approx 50$ K for the sample treated at 1000 °C and $T_B \approx 250$ K for samples treated at 1300 and 1400 °C, respectively. The saturation magnetization slightly decreases with the temperature of measurement being of ≈35 Am^2kg^{-1} at 7 K and ≈25 Am^2kg^{-1} at 300 K.

S. Soreto Teixeira (✉) · A. J. M. Sales · M. P. F. Graça · M. A. Valente · L. C. Costa
I3N and Physics Department, University of Aveiro, Aveiro, Portugal
e-mail: silvia.soreto@ua.pt

P. Petkov et al. (eds.), *Advanced Nanotechnologies for Detection and Defence against CBRN Agents*, NATO Science for Peace and Security Series B: Physics and Biophysics, https://doi.org/10.1007/978-94-024-1298-7_17

Keywords Yttrium ferrites · Impedance spectroscopy · Magnetic properties · Dielectric relaxation

17.1 Introduction

Ferrites possess interesting properties with potential industrial applications such as in electrochromic displays, waste-water cleaning, electrodes in rechargeable batteries and as strong oxidizing agents [1, 2].

The garnet $Y_3Fe_5O_{12}$ (YIG) has the general formula $3M_2O_3{\cdot}5Fe_2O_3$, where M is yttrium. The yttrium cations are of the type M^{3+} which makes electron hopping through the material very difficult and the resistivity is extremely high [3]. YIG is a ferrimagnetic material with interesting dielectric and magnetic properties, such as a controllable saturation magnetization, low dielectric losses and small linewidth in ferromagnetic resonance [4]. The magneto-electric effect of YIG is very remarkable due to the direct interaction between dielectric and magnetic properties [5]. Due to its interesting magnetic and magneto-optic properties it can be used in the telecommunication area, at very high frequencies and data storage applications [2, 3, 6]. This material can also be used in electronic devices such as insulators, circulators, transmitters, and transducers of acoustic energy [3].

Several techniques can be used to prepare the crystalline YIG phase. The conventional solid state reaction method uses yttrium and iron oxides. This method requires high temperatures of sintering; particles with micron size were obtained [7]. To prepare fine particles (submicron size) at lower temperatures, wet chemical routes can be used such as sol-gel, co-precipitation or the glycothermal synthesis [7].

On the other hand, $YFeO_3$ belongs to the $MFeO_3$ rare-earth orthoferrite perovskites, and has been studied due to its applications in solid-oxide fuel cells [6], photocatalysis, vehicle catalytic converters [8, 9], optical devices of ultrafast optical switches, magnetic fields sensors, and magneto-optical current sensors [10]. It is also a candidate for applications in the field of chemical sensors [11]. The dielectric properties, high permittivity, and low dielectric losses permits its use in wireless communication systems. $YFeO_3$ is an antiferromagnetic material with a high Néel temperature ($T_N = 640$ K) and a high resistivity [12].

The main goal of this work is to correlate the dielectric and magnetic properties with the structure and morphology of yttrium ferrites, prepared by the Pechini route at different heat treatment temperatures.

17.2 Experimental

The yttrium ferrite powders were obtained by the sol-gel method, through the Pechini route which has the advantage that no strong acids/bases or organic compounds are needed, besides being a low-temperature process. In this route, the

polymerizable complex is based on the poly-esterification reaction between citric acid (CA) and ethylene glycol (EG) [13, 14]. In detail, the metal solutions, yttrium nitrate [$Y(NO_3)_3.6H_2O$, purity>99%, Aldrich] and iron nitrate [$Fe(NO_3)_3.9H_2O$, Mateck], were used as starting materials, citric acid and ethylene glycol as chelating agents to polymerize the mixture. After the preparation of an aqueous solution of nitrates, it was mixed with CA to promote the complex formation of the metal ions; there after EG was added as a dispersant [3].

The suspension contains stoichiometric amounts of each metal, and are characterized by the use of an excess of CA (1:3 molar ratio) with a molar ratio between CA:EG of 2:3. To promote the solubility, the suspension was stirred for 30 min at room temperature. The final suspension, after the addition of EG, was mixed for 24 h. To evaporate the solvent, the solution gel was dried at 250 °C for 60 h. The obtained powder was pressed into pellets and heat-treated at 1000, 1300 and 1400 °C (HT1000, HT1300 and HT1400 respectively) for 4 h with a heating rate of 5 °C/min.

X-ray diffraction (XRD) patterns were obtained with a Philips X'Pert diffractometer (CuKα radiation, $\lambda = 1.54056$ Å) at 40 kV and 30 mA, with a curved graphite monochromator, an automatic divergence slit (irradiated length 20.00 mm), a progressive receiving slit (height 0.05 mm) and a flat plane sample holder in a Bragg-Brentano parafocusing optics configuration. Intensity data were collected by the step counting method (step 0.02° in 1 s) in the 2θ angle range of 10–60°.

Impedance spectroscopy (IS) was used to analyse the samples in pellet form, with a thickness of about 1 mm and the opposite surface sides painted with silver paste. The electrical signal was measured with an impedance analyzer Agilent 4294A. These measurements were performed in the frequency range from 10^2 to 10^6 Hz from 200 up to 400 K. In order to improve the heat transfer and to homogenize the temperature, the sample holder was maintained in a helium atmosphere during the measurements.

The magnetic properties of the samples were measured with a vibrating sample magnetometer (VSM) from Cryogenics. The magnetic properties as a function of temperature were acquired in field cooling (FC) and zero field cooling (ZFC) modes, applying a magnetic field of 0.1 T. The dc magnetic susceptibility as a function of temperature from 7 to 300 K was acquired in zero field and field cooling. The M vs. B hysteresis curves were obtained at different measurement temperatures.

17.3 Results and Discussion

The diffractograms of the samples HT1000, HT1300 and HT1400 powders are shown in Fig. 17.1. In all samples, two crystallographic systems are present: a cubic ($Y_3Fe_5O_{12}$) and an orthorhombic ($YFeO_3$) one with different weight percentages.

In order to obtain information about the composition of each crystal phase, the Rietveld refinement of the X-ray data was performed using the *DBWS Tools 2.4*

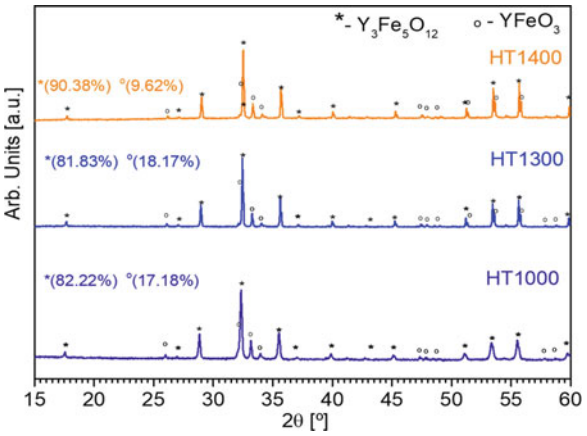

Fig. 17.1 XRD patterns of the samples HT1000, HT1300 and HT1400 powders

software. The parameter S (Goodness of Fit) has values between 1.17 and 1.37 which indicates a good fit for the refinements of all samples.

The cubic $Y_3Fe_5O_{12}$ crystalline phase has the highest weight percentage (Fig. 17.1) in all samples, with the main diffraction peaks at $2\theta \approx 28$, 32, 36, 54 and 56° [15]. The presence of a peak at about $2\theta = 33°$ indicates the presence of the orthorhombic $YFeO_3$ crystal phase [15, 16]. The sample HT1400 presents a significant increase in the weight percentage of $Y_3Fe_5O_{12}$ to 90.38% and a minimum of 9.62% for $YFeO_3$.

Figure 17.2 presents the samples surface micrographs. In all samples, grains with similar shapes but different sizes between 2 and 10 μm are perceptible. The grain size increases and the porosity decrease with the rise of the heat treatment temperature.

From impedance spectroscopy, the measured values of C_p and R_p, allow the calculation of the real (ε') and imaginary (ε'') parts of the complex permittivity [17]:

$$\varepsilon' = C_p \frac{d}{A\varepsilon_0} \tag{17.1}$$

$$\varepsilon'' = \frac{d}{\omega R_p A \varepsilon_0} \tag{17.2}$$

where d represents the sample thickness, A the area of the electrodes, ε_0 the empty space permittivity and ω the angular frequency. Figure 17.3 shows the dependence of the real and the imaginary parts of the permittivity with frequency for the sample HT1400.

In Fig. 17.3, one relaxation process and low losses for sample HT1400 are visible. As expected, the relaxation frequency increases with temperature. For high temperatures and low frequencies, the Maxwell-Wagner-Sillars (MWS) effect is present. According to the literature, this phenomenon can be attributed to the contribution of $YFeO_3$ phase reaching values of the dielectric constant higher than

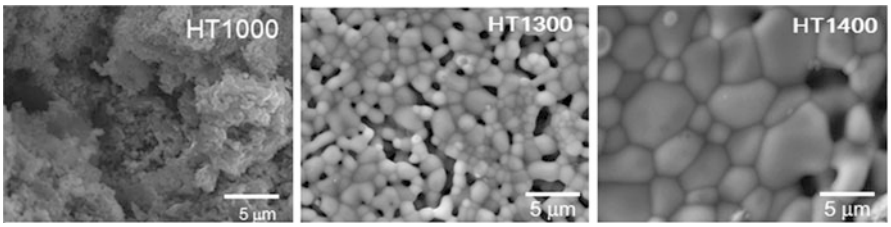

Fig. 17.2 SEM micrographs of samples HT1000, HT1300 and HT1400

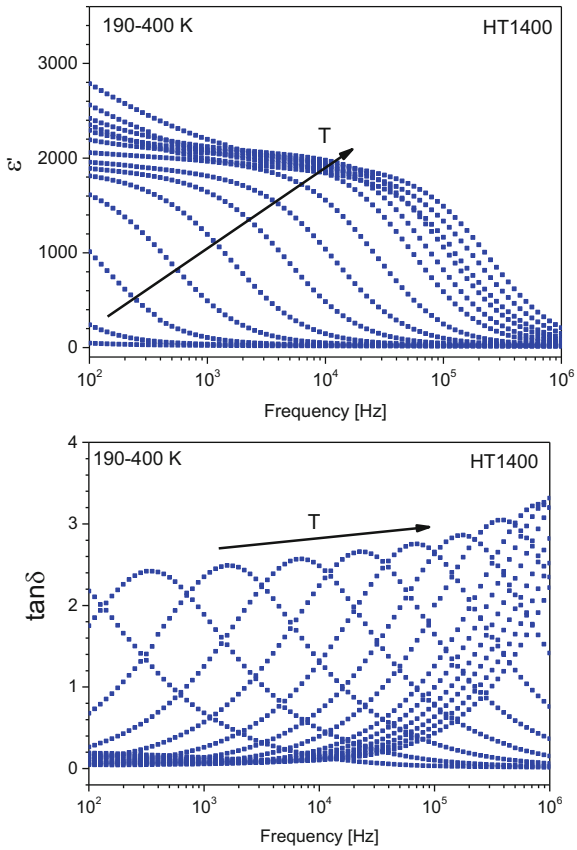

Fig. 17.3 Dielectric constant and dielectric losses vs frequency (sampleHT1400)

10^4 [18]. Nevertheless, also the pure YIG phase can reach values of ≈1000 [5]. Actually, the influence of the MWS effect is not much pronounced at frequencies higher than1 kHz and temperatures around room temperature. A comparison at different temperatures (220, 300 and 330 K) and a frequency of 1 kHz as a function of the heating treatment is shown in Fig. 17.4.

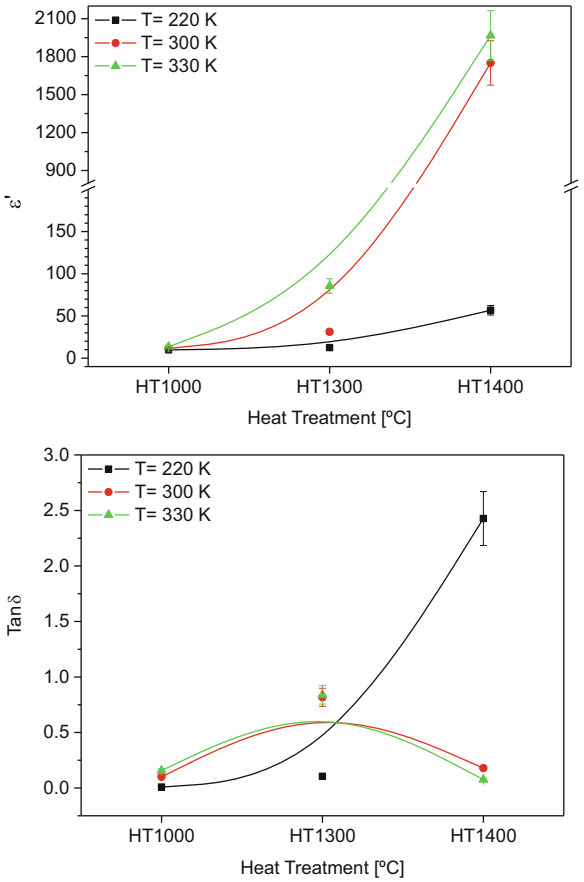

Fig. 17.4 Dielectric constant and dielectric losses at a frequency f = 1 kHz

Figure 17.4 allows to conclude that the sample which has the lowest losses and the highest values of the dielectric constant is HT1400. This fact can be due to the increases of the grain size and the decreases of porosity (Fig. 17.2) in combination with the right composition of YIG and $YFeO_3$ crystal phases (Fig. 17.1).

The magnetic measurements were done under ZFC conditions with an applied magnetic field (*B*) of 0.1 T, from 7 K up to 300 K. At 300 K, magnetization (*M*) versus *B* measurements were carried out. Then, FC measurements were performed from 300 K down to 7 K under the magnetic field of 0.1 T. Again, at 7 K, *M* versus *B* measurements were performed. The dependence of the magnetic susceptibility on the temperature is shown in Fig. 17.5.

The magnetic susceptibility varies with the heat treatment temperature being between 305 $Am^2kg^{-1}\ T^{-1}$ (HT1300; HT1400) and 325 $Am^2kg^{-1}\ T^{-1}$ (HT1000) in the FC sequences and from 300 $Am^2kg^{-1}\ T^{-1}$ (HT1300; HT1400) to 315 $Am^2kg^{-1}.T^{-1}$ (HT1000) in the ZFC sequences. A decrease of the magnetic susceptibility with

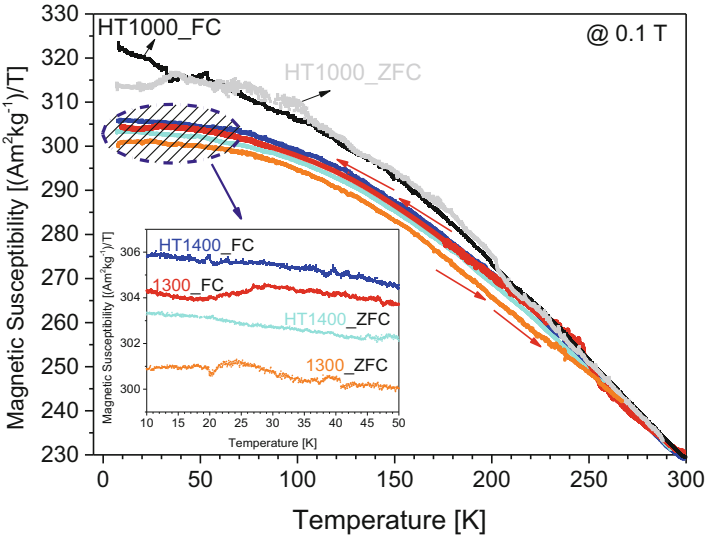

Fig. 17.5 Magnetic susceptibility versus temperature, recorded under field cooled conditions with an applied magnetic field of 0.1 T between 7 and 300 K

increasing measurement temperature is observed; this behaviour was expected as it is characteristic for ferrimagnetic materials [19, 20]. It is also visible that with increasing temperature of the heat treatment, the blocking temperature (T_B) also increases being ≈50 K for sample HT1000 but ≈250 K for samples HT1300 and HT1400. This fact may be related to the increasing of the grains size for samples treated at a higher temperature.

Figure 17.6 shows the magnetization versus the applied magnetic field, measured at 7 K and 300 K, respectively. At T = 7 K, for sample HT1000 it is visible that the saturation magnetization (M_s) is not achieved; this can be related to the presence of the $YFeO_3$ phase, which is antiferromagnetic, and the smaller size of the particles since this behaviour does not occur for sample HT1300, which has a similar amount of the $YFeO_3$ phase. For sample HT1400 a saturation magnetization of $M_s = 35$ $Am^2 kg^{-1}$ was obtained which is in agreement with literature data for the YIG phase [21]. At room temperature, all samples have similar values of the saturation magnetization, which is near to that reported in the literature for YIG phase [21] which is the majority crystal phase in all samples. In relation to the $YFeO_3$ crystal phase and according to the literature, the magnetization does not saturate in magnetic fields up to 6 T, showing a magnetization of 4 Am^2kg^{-1} at 1.5 T [22] and 3 Am^2kg^{-1} at 6 T [18]. According to our results, at room temperature, the saturation magnetization is independent of the temperature of the heat treatment. This means that the composition of YIG and $YFeO_3$ does not interfere in the magnetic hysteresis results.

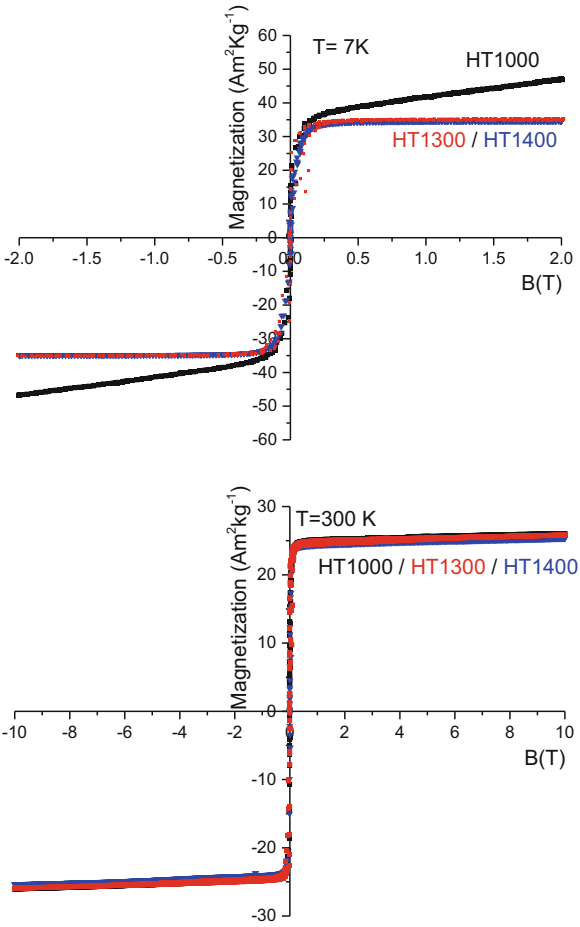

Fig. 17.6 Magnetic hysteresis curves at T = 7 K and T = 300 K

17.4 Conclusions

Yttrium ferrites can be obtained by a sol-gel method using iron and yttrium nitrates as raw materials. Cubic ferrite $Y_3Fe_5O_{12}$ (YIG) is predominant in all samples with the maximum for sample HT1400 (~90%).

One dielectric relaxation process is observed for all samples. The MW effect, due to interfacial polarization, is also present for high temperatures and low frequencies. Nevertheless, at frequencies higher than 1 kHz this contribution is not very relevant, and the dielectric constant is still huge (>1000). The right combination of the YIG and $YFeO_3$, the structural changes, the increases of the grain size and the decreases of the porosity combine giant dielectric constants with low losses. As a consequence, sample HT1400 could be a potential candidate to be used in electronic devices such as capacitors.

The magnetic susceptibility decreases with the heat treatment temperature. We obtain typical hysteresis curves; the saturation magnetization slightly decreases with the measurement temperature as expected. According to the dielectric and magnetic results, the composition of the YIG and $YFeO_3$ crystal phases, the structural changes and the increase of the grains size affect the dielectric and magnetic properties of yttrium ferrites.

References

1. Viret M, Rubi D, Colson D et al (2012) β-$NaFeO_2$, a new room-temperature multiferroic material. Mater Res Bull 47:2294–2298
2. Sugimoto M (1999) The past, present, and future of ferrites. J Am Ceram Soc 82:269–280
3. Razak J, Sufian S, Shaari K et al (2012) Synthesis, characterization and application of Y3Fe5O12 nanocatalyst for green production of NH3 using magnetic induction method (MIM). AIP Conf Proc 1482:633–638
4. Sánchez RD, Rivas J, Vaqueiro P, Caeiro D (2002) Particle size effects on magnetic properties of yttrium iron garnets prepared by a sol-gel method. J Magn Magn Mater 247:92–98
5. Wu YJ, Gao Y, Chen XM (2007) Dielectric relaxations of yttrium iron garnet ceramics over a broad temperature range. Appl Phys Lett 91:1–4
6. Minh NQ (1993) Ceramic fuel cells. J Am Ceram Soc 76:563–588
7. Rajendran M, Deka S, Joy PA, Bhattacharya AK (2006) Size-dependent magnetic properties of nanocrystalline yttrium iron garnet powders. J Magn Magn Mater 301:212–219
8. Li X, Tang C, Ai M et al (2010) Controllable synthesis of pure-phase rare-earth orthoferrites hollow spheres with a porous shell and their catalytic performance for the CO + NO reaction. Chem Mater 22:4879–4889
9. Pena MA, Fierro JLG (2001) Chemical structures and performance of perovskites oxides. Chem Rev 101:1981–2017
10. Shen H, Xu J, Jin M, Jiang G (2012) Influence of manganese on the structure and magnetic properties of YFeO3 nanocrystal. Ceram Int 38:1473–1477
11. Maiti R, Basu S, Chakravorty D (2009) Synthesis of nanocrystalline YFeO3 and its magnetic properties. J Magn Magn Mater 321:3274–3277
12. Rearick TM, Catchen GL, Adams JM (1993) Combined magnetic-dipole and electric-quadrupole hyperfine interactions in rare-earth orthoferrite ceramics. Phys Rev B 48:224–238
13. Kuz AP, Abakumov PV (2011) Raman imaging of domains and fine structure of domain walls in YFeO3 crystals. Tech Phys Lett 37:1058–1061
14. Kuzmenko AP, Abakumov PV, Dobromyslov MB (2012) Domain wall structure of weak ferromagnets according to Raman. J Magn Magn Mater 324:1262–1264
15. Ma Y, Chen XM, Lin YQ et al (2008) Relaxorlike dielectric behavior and weak ferromagnetism in YFeO3 ceramics. J Appl Phys 124111:2–5
16. Yang H, Yang Y, Lin Y, Liu M (2013) Preparation and electromagnetic properties of in-situ. Ceram Int 39:7235–7239
17. Jonscher AK (1999) Dielectric relaxation in solids. J Phys D Appl Phys 32:R57–R70
18. Wang M, Wang T, Song S et al (2017) Effect of sintering temperature on structural, dielectric, and magnetic properties of multiferroic YFeO3 ceramics fabricated by Spark Plasma Sintering. Mater (Basel) 10:267
19. Soreto S, Graça M, Valente M et al (2017) Lithium ferrite: synthesis, structural characterization and electromagnetic Properties and. In: Seehra PM (ed) Magnetic spinels – synth. Prop. Applications. InTech, pp 31–50

20. Teixeira SS, Graça MPF, Costa LC, Valente MA (2014) Study of the influence of thermal treatment on the magnetic properties of lithium ferrite prepared by wet ball-milling using nitrates as raw material. J Mater Sci Eng B 186:83–88
21. Figueiro SD, Mallmann EJJ, Góes JC et al (2010) New ferrimagnetic biocomposite film based in collagen and yttrium iron garnet. Express Polym Lett 4:790–797
22. Bolarín-miró AM, Sánchez-De Jesús F, Cortés-Escobedo CA (2014) Structure and magnetic properties of GdxY1- xFeO3 obtained by mechanosynthesis. J Alloys Compd 586:S90–S94

Part V
Materials: Graphene, Nanotubes and Nanodiamonds

Chapter 18
Nanostructured Carbon Materials: Synthesis and Applications

Alejandro Ansón-Casaos, Enrique Garcia-Bordeje, Ana M. Benito, and Wolfgang K. Maser

Abstract The family of carbon nanostructures includes a great number of forms with different properties derived from their reduced dimensionality. In particular, carbon nanotubes (CNTs) and graphene show special electronic, optical, mechanical and chemical properties that allow their potential application in new materials and devices. The real possibilities of pristine CNTs and graphene depend on their synthetic origin, which can be roughly classified into methods starting from graphite and chemical vapor deposition (CVD) processes. Applications of CNTs and graphene encompass electronics, energy devices, multifunctional composites, catalysis and sensors. Their reduced size and weight suggest potential uses in portable, wearable and mobile equipment with a high added value.

Keywords Nanotube · Graphene · Electronic properties · Energy · Composite · Sensor

18.1 Introduction

Carbon nanomaterials have been central in the development of nanoscience and nanotechnology. The discovery of carbon nanotubes (CNTs) in 1991 [1], and later of graphene [2], led to a new way of thinking in physics and materials science. Previously, the synthesis of fullerenes in the 1980s was also a revolution in chemistry and materials chemistry [3]. Nowadays, carbon allotropes constitute a family that is the paradigm of how the reduction of dimensions to the nanoscale leads to quantum confinement, and thus to new physical properties, starting from electronics and optics, but also covering thermal, mechanical and chemical properties, and even fluid dynamics.

A. Ansón-Casaos (✉) · E. Garcia-Bordeje · A. M. Benito · W. K. Maser
Instituto de Carboquímica, ICB-CSIC, Zaragoza, Spain
e-mail: alanson@icb.csic.es

P. Petkov et al. (eds.), *Advanced Nanotechnologies for Detection and Defence against CBRN Agents*, NATO Science for Peace and Security Series B: Physics and Biophysics, https://doi.org/10.1007/978-94-024-1298-7_18

Many different methods have been utilized for the synthesis of carbon nanostructures, particularly in the cases of CNTs and graphene. Fullerenes were first discovered as the products of experiments in an electric arc discharge reactor with graphite electrodes. Also CNTs, both multi-walled (MWCNTs) and single-walled (SWCNTs), were later observed by electron microscopy in an arc-discharge cathodic deposit. Chemical vapor deposition (CVD) methods have been successfully applied to the synthesis of CNTs from gaseous carbon precursors; high quality SWCNTs can be synthesized from graphite by laser ablation methods. Graphene was first prepared by exfoliation from graphite using an adhesive tape, while the current methods of production include CVD and liquid phase exfoliation of graphite, which commonly involves the interesting product known as graphene oxide (GO).

Applications of carbon nanomaterials are being investigated in many fields, some of them are already commercial, including additives for lithium ion batteries, new composites as new generation carbon fiber materials, etc. The utilization of carbon nanostructures opens up a wide field both in device miniaturization and in the improvement of the properties of bulk materials through their addition in small amounts.

In this mini-review, the most outstanding types of carbon nanostructures are first summarized and briefly described. All the nanomaterials mentioned, but especially CNTs and graphene, are currently the focus of a great number of scientific research works. The effects of dimensionality reduction are illustrated, specifically with the example of the optical spectra of SWCNTs. In the next section, the most common methods for the synthesis of CNTs and graphene are described. Knowledge on the nanostructures synthetic origin is often of paramount importance, as it limits the material properties and thus the potential applications. In the final section, the applications of CNTs and graphene are reviewed, mostly through studies developed at the Institute of Carbon Chemistry, ICB-CSIC. The applications cover the energy field, catalysis, polymer composites, inorganic composites, electronic applications, and sensors.

18.2 The Family of Carbon Nanomaterials

Diamond and graphite are the classical forms of elemental carbon in the solid state; the crystalline organization of carbon atoms is respectively purely tetrahedral sp^3 and trigonal sp^2. The natural appearance of linear acetylenic carbon or carbine, the allotrope with pure linear sp geometry, is still a topic of discussion. The discovery of fullerenes in 1985 was one of the greatest hits of physics and chemistry in the last years of the twentieth century [3]. The existence of fullerenes led to a revision of the basic concepts in carbon chemistry and general chemistry, since their characteristics of bonding and symmetry were unknown. In particular, the possibility of synthesizing closed hollow structures of only carbon atoms would have been unimaginable, as carbon bonds have to adapt to allow pentagonal rings. In fullerenes, the carbon bond geometry is between sp^2 and sp^3; the larger the number of atoms in the structure, the

nearer to sp^2. Soon after the discovery of fullerenes, their chemistry was studied, and it resulted to be extremely rich. Fullerenes can enclose metal atoms in their inner cavities, and can be also covered by one or several layers of ordered metal atoms. In addition, a great number of organic moieties can be bonded to fullerenes, resulting in new molecules.

MWCNTs were observed in 1991 during an investigation on fullerenes [1], while the existence of SWCNTs was demonstrated later in 1993 [4, 5]. CNTs are formed by cylindrical seamless graphene layers, in which carbon atoms present nearly sp^2 geometries, and are typically closed at the ends by fullerene-like caps. MWCNTs have 2–50 concentric layers, an interior diameter of 2–10 nm, an exterior diameter of 15–30 nm, and an interlayer distance of 0.34 nm, which is nearly identical to the separation between graphene layers in graphite. SWCNTs have diameters of 0.71–3 nm and easily join longitudinally to form bundles. Many different SWCNT conformations exist depending on the wall helicity. Despite having a great stability, CNT walls can be functionalized with many chemical groups, similarly to fullerenes. It can be stated that the discovery and study of CNTs has been central in the development of nanoscience and nanotechnology. Apart from fullerenes and carbon nanotubes, other related morphologies have been observed and studied, such as nanoonions and nanohorns [6, 7].

The idea of isolating a single graphene layer was realized in 2004 through mechanical exfoliation of graphite with an adhesive tape [2]. A single sp^2 carbon layer is very unstable and tends to fold, stack, or collapse. Therefore, a graphene layer can be only stabilized either on a solid substrate or in a liquid medium. Nowadays, graphene materials encompass a great variety of forms including single sheets on different solid substrates [8], multi-platelet graphene [9], graphene nanoribbons (GNRs) [10], GO and reduced graphene oxide (RGO) [11, 12]. More recently, a great interest has been focused on graphene flakes with reduced lateral dimensions, which are generically called graphene quantum dots (GQDs). Other new nanomaterials such as carbon dots and nanodiamond complete the large family of carbon nanostructures [13].

Nanostructured materials are low dimensional structures at the nanoscale. In other words, at least one of the spatial dimensions is reduced to the nanoscale. In such conditions, electrons are affected by spatial confinement and thus the electronic properties of the materials are modified. Whilst diamond and graphite are classical three dimensional (3D) structures, the thickness of a single graphene layer is <1 nm, so it is negligible against the lateral sheet dimensions (up to several μm), thus graphene can be conceptually understood as a 2D nanostructure. The configuration of carbon atoms at the edges is relevant for the graphene sheet properties, particularly when lateral dimensions are very small, for example in GNRs. In CNTs, the length/diameter aspect ratio is typically so high that they can be considered 1D. Several different carbon nanostructures behave as 0D entities or quantum dots, including fullerenes, GQDs and carbon quantum dots. Finally, classical porous materials such as activated carbons (ACs) are sometimes considered as fractal structures with a reduced dimensionality between 2D and 3D. ACs can confine ordered atoms or molecules in their small pores and can act as molecular sieves.

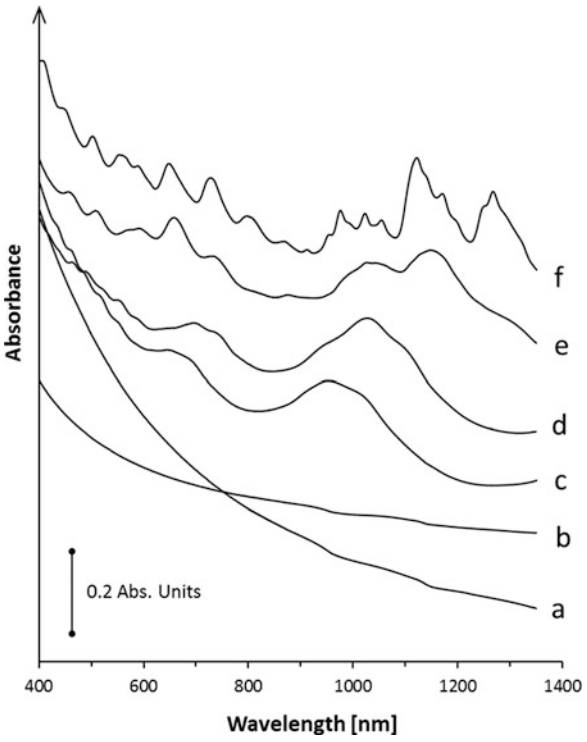

Fig. 18.1 Optical absorption spectra in the visible-near infrared region for surfactant-stabilized aqueous suspensions of different powder materials: *a* graphitic soot, *b* CVD MWCNTs, *c* laser-grown SWCNTs, *d* arc-discharge SWCNTs, *e* CoMoCAT® SWCNTs, and *f* HiPco® SWCNTs. Both CoMoCAT® and HiPco® are commercial products synthesized by CVD methods. All suspensions were diluted in their respective aqueous media until reaching 0.4 absorbance units at 850 nm

One of the effects of dimensionality reduction and electronic confinement is the special optical response of SWCNTs [14–16]. Figure 18.1 shows optical absorption spectra of four different SWCNT samples compared to a MWCNT sample and a graphitic material. All the starting powders were dispersed in a surfactant by ultrasound treatments and centrifugation. The graphitic soot (Fig. 18.1a) absorbs light in the whole visible range, decreasing towards the infrared. This absorption profile is typical of carbon materials, in accordance with their black color, and related to collective electronic excitations along the sides of sp^2 domains. Qualitatively similar spectra are measured for most of the carbon materials including MWCNTs (Fig. 18.1b), as the single nanotube optical response is hindered by their multi-layered structure. Apart from the typical spectral background of carbon materials, SWCNTs present particular absorption features, which are associated to the nanotube diameter and conformation. Electron confinement occurs in the so-called 1D van Hove singularities, and the permitted transitions between those particular electronic states give rise to the SWCNT absorption spectra. Each SWCNT type should give quite sharp spectral peaks. However, in typical SWCNT samples, which contain complex mixtures of many SWCNT types, wide bands are observed as a superposition of individual peaks (Fig. 18.1c–f). It can be observed that absorption spectra are indicative of the SWCNT synthetic origin. Also, absorption features are sensitive to SWCNT purity, functionalization and structural quality [17–19].

Other effects of electronic confinement are SWCNT fluorescence phenomena [20, 21], the electronic structure of graphene and GNRs, the fluorescence of GQDs, and so on. Also, many other special properties (optical, mechanical, chemical) are derived from the particular electronic structure of carbon nanomaterials.

18.3 Synthesis of Carbon Nanotubes and Graphene

The synthesis of CNTs can be performed by different methods, all of them based on the generation of small reactive molecular carbon units from either graphite or simple organic gases. Under certain process conditions, often in the presence of catalyst metal particles, the reactive carbon units combine to yield the cylindrical structures. Graphite evaporation can be effected in an electric arc reactor or by laser ablation methods, in which very high temperatures (>5000°) are locally achieved. On the other hand, decomposition of organic gases and the subsequent CVD process to give the nanostructures are performed in reactors at a constant temperature of around 1000 °C or lower.

The electric arc reactor method can be utilized for the synthesis of both fullerenes and CNTs under slightly different conditions. The graphite anode is evaporated when a high electrical current is passed in a sub-atmospheric pressure of certain ionizing gases. Fullerenes appear in the soot that covers the inner reactor walls after a discontinuous evaporation process without catalysts, and can be separated from the impurities by extraction in organics, particularly in toluene. MWCNTs were first observed in the inner part of the cathodic deposit. The yield of the process for the synthesis of MWCNTs in the arc reactor can be improved just by slight modifications in the operation conditions for fullerene production [22, 23]. When the graphite anode contains certain metal catalysts (Fe, Ni, Co), SWCNTs appear in the material growing around the cathode and in the soot covering the inner reactor wall [4, 5]. Higher yields of the SWCNT production were achieved with binary metal catalyst mixtures, in particular Ni/Y [24]. The temperatures between the electrodes during operation are very high (>5000°) but decrease very fast towards the reactor walls, generating strong gradients, so the growing conditions of the nanostructures are not determined [25]. Arc-discharge CNTs show a high structural quality with a low number of defects, although the as-synthesized powders contain impurities (metal catalysts, graphite particles, amorphous carbon) that often have to be removed by purification post-treatments.

In laser synthesis methods, a graphite target is exposed to a laser beam, which increases the temperature of the solid until vaporization. From the gas phase, small carbon units react and can produce nanotubes, which settle on the chamber walls as soot. The laser source, which can be both pulsed and continuous, is often a YAG or a CO_2 laser [26]. A nearly identical synthesis concept can be developed with a solar concentrator [27]. The resulting CNTs show high structural qualities, but the products contain impurities, similarly to arc-discharge CNTs.

In CVD methods, a gaseous precursor, typically CO, CH_4 or C_2H_2, acts as the carbon source, and the CNTs grow on catalyst metal particles. The method provides a large number of variable parameters, including the carbon source, carrier gas, temperature, catalyst composition and catalyst preparation [28–32]. The catalyst can be prepared from metal ion solutions and organometallic complexes, and it can be inserted in the reactor either as an aerosol or supported on silica, alumina and other materials. Since catalyst particles can be placed at defined positions on the support, it is possible to grow CNT forests, nanotubes on AFM cantilever tips and nanotubes between two electrodes. CVD methods allow the synthesis of many different CNT types and they are the preferred ones for industrial production.

CVD methods have been also successfully utilized for the synthesis of graphene. It has been demonstrated that the dimensions of the as-synthesized graphene domains (1 μm–1 cm) can be on the order of that of highly crystalline graphite [8]. Graphene is first synthesized on catalyst metal sheets, typically made of copper, nickel and other metals, then it can be transferred to other supports, usually with a certain loss in its structural quality. CVD-grown graphene is expected to reach an industrial demand, particularly in electronic applications [8].

Graphite exfoliation is the other route (top-down) for the synthesis of graphene. The micromechanical cleavage of graphite through the adhesive-tape method was utilized for the first experimental description of graphene, and it can be still useful in laboratory works. Other methodologies such as milling and chemical exfoliation in the liquid phase are the alternative for industrial applications in functional composite materials and inks. Physical milling of graphite leads to multi-platelet graphene materials that might be applied in polymer composites with improved frictional and mechanical properties [9]. Liquid phase exfoliation has been widely utilized in laboratory research, and it is usually performed through a modified Hummers methods that involve a sequence of acid oxidant treatments [12]. Liquid phase exfoliation is also possible in a surfactant or in organic solvents. A particular case of liquid phase exfoliation is the preparation of graphene nanoribbons from MWCNTs by unzipping in acid oxidant media [33, 34]. Small size GQDs can be also synthesized by chemical oxidation, and by electrochemical cleavage of graphite, a clean method that is interesting for biological applications.

18.4 Applications of Carbon Nanotubes and Graphene

Applications of carbon nanostructures can be grouped, according to the appearance of the nanostructure, into those using individual nanostructures, assemblies of nanostructures, and composite materials [35]. An special mention must be also made of processes that substantially modify the nanostructure properties, including functionalization, dispersion in a liquid, etc. [35] In the following, the most direct classification is followed, which is based on the application field. Several topics are briefly reviewed, including energy devices, catalysis, light multifunctional polymers, and sensors.

18.4.1 Energy Devices

Carbon nanomaterials have been integrated in different parts of energy devices, sometimes as the whole component, but most commonly as additives to other active materials. Since carbon nanomaterials possess high aspect ratios and good electrical and thermal conductivities, they can act as wires for electronic transport and heat dissipation channels in devices such as batteries, electrochemical double layer capacitors (EDLCs), and solar cells.

CNTs, GO and RGO were soon tested as electrodes for EDLCs, also called supercapacitors. The powder materials can be compressed in a mold and impregnated with the electrolyte, which easily enters the mesoporous network created by the randomly oriented aggregated nanostructures. CNTs typically show nearly rectangular voltammograms, which are characteristic of electrodes with a capacitive behavior. Arc discharge SWCNTs and thermally oxidized SWCNTs reach capacitance values between 30 and 140 F g^{-1}, showing that an alkaline electrolyte (KOH) provides higher energy densities, while an acid electrolyte (H_2SO_4) leads to higher power densities [36]. The specific capacitance can be improved using aligned CVD CNTs, which show a higher specific surface area, but still the values remain lower than those obtained with some microporous activated carbons (ACs). Interestingly, a high capacitance at high currents and a power density maximum is reached with certain SWCNT/AC mixtures [37]. High capacitances (231 F g^{-1}) can be also reached with graphene-based porous electrodes prepared from GO and solid organic precursors [38]. On the other hand, CNT fillers improve the thermal stability, potential window, porosity and durability of conducting polymers showing pseudo-capacitance, such as polypyrrole and polyaniline [39].

Carbon nanotubes and graphene can be integrated in new-generation solar cells as active layers [40–42], electron acceptors [43], counter electrodes [44], electron transport layers (ETLs) and hole transport layers (HTLs) [45, 46]. The utilization of CNTs and graphene as transparent conducting film (TCF) electrodes for indium tin oxide (ITO) substitution is limited by the requirements of electrical conductivity and transparency [47]. Recently, a SWCNT synthesis process by aerosol CVD has provided high quality TCFs for solar cells [48]. A polyanylyne/MWCNT (arc discharge) composite has been tested as the hole collecting electrode in photovoltaic textile applications [49].

Storage of gaseous fuels (H_2, CH_4) and CO_2 will probably have a great importance in the future energy scenario, which is expected to be based on clean renewable sources. The possibility of using carbon nanomaterials as adsorbents to improve the storage capacity of pressurized tanks was discussed for years, particularly in the case of hydrogen. Measurements of hydrogen adsorption in SWCNTs revealed low storage capacities [50, 51], even if the adsorption was catalyzed by palladium nanoparticles [52, 53]. Finally, it has been demonstrated that gas capacity (H_2, CH_4 and CO_2) can be substantially improved in a pressurized storage tank at room temperature when the tank is filled with AC monoliths, compared to simple compression [54].

Fuel cells are being widely investigated as a clean solution for powering mobile devices and vehicles. Carbon nanostructures have been successfully tested as catalyst supports for several chemical reactions that take place in different types of fuel cells. Arc discharge SWCNTs were used as supports for platinum nanoparticles, and tested for the oxygen reduction reaction, reaching efficiencies similar to typical carbon black conducting supports [55]. The Pt/SWCNT catalyst also demonstrated good activities for the oxidation of methanol and formic acid [56]. The catalyst efficiencies depend on the metal nanoparticle size and crystalline structure, which is ultimately influenced by the carbon support characteristics. Macroscopic assemblies of SWCNTs such as thick films ("buckypapers") were tested as supports of Pt/Ru nanoparticles, and the catalyst activity towards methanol oxidation was clearly dependent on the buckypaper preparation procedure [57].

18.4.2 Catalysis

Apart from the catalytic reactions that take place in fuel cells, carbon nanomaterials can be utilized in other important chemical reactions. CVD MWCNTs and GO have been tested as supports of catalytic metal particles with controlled sizes. Pd/MWCNT hybrids are active in C-C coupling and dehydrogenation reactions [58], and specially in alkene hydrogenations [59]. Au/MWCNT catalysts have proved good activities in the selective hydrogenation of nitroaromatic derivatives [60]. Also, alkene hydrogenation reactions have been selectively catalyzed by Pd/GO catalysts [61].

1D and 2D nanocarbons are excellent building blocks for 3D architectures with a developed porosity and catalytic interest. Some examples are monoliths coated with a layer of CNTs [62], monoliths coated with N-doped CNTs [63], and graphene aerogels [64]. 3D-structured nanomaterials can be applied as metal nanoparticle supports or metal-free catalysts. CNTs and N-doped CNTs have been loaded with Ru nanoparticles for the CO_2 reduction with renewable H_2 to produce CH_4 [65, 66]. Nitrogen- and boron-doped carbon nanofibers (CNFs), and nanodiamond supported on graphene aerogels have been tested as metal-free catalysts in the propane dehydrogenation to produce propene [64, 67]. NH_3 decomposition to produce H_2 can be catalyzed by metal nanoparticles on CNFs and N-doped CNFs [68]. Water cleaning applications include the ozonation of organic pollutants on CNTs and CNFs as metal-free catalysts [69], and the reduction of nitrate and bromate on CNTs or CNFs as catalyst supports [70].

18.4.3 Multifunctional Materials

Processing issues and applications of CNT and graphene polymer composites have been reviewed in previous NATO ASIs [71, 72]. The synthetic origin and

functionalization greatly influence the resulting properties of the composite material, particularly in structural polymers such as polyether ether ketone (PEEK) and epoxies [73, 74]. Polymer composites are promising light materials for mobile applications in the aeronautical and automotive industry, since a vehicle weight reduction leads to important energy savings. In SWCNT/epoxy composites, the electrical properties and toughness are maximized through the non-covalent functionalization of the SWNTs with compatibility block copolymers, while the mechanical and thermal properties are maximized through covalent functionalization with amine moieties. The improvements in the electrical conductivity of structural polymers, maintaining their mechanical performance, are typically great enough for application of the composites in electrostatic charge dissipation and electromagnetic interference shielding [75]. In addition, it has been observed that CNTs may act as radical scavengers in polymer systems, protecting the composite materials against the effects of gamma radiation. More specifically, the protective effects of arc-discharge SWCNTs, CVD MWCNTs and arc-discharge MWCNTs have been demonstrated [76–79].

18.4.4 Sensors and Biosensors

The electronic properties, together with the high specific surface area, rich surface chemistry, optical properties, thermal stability and mechanical robustness allow the application of CNTs and graphene as sensitive materials. The properties of individual nanostructures can in part be translated into micro- and macroscopic systems including thin films, fibres, inks, buckypapers and composite materials, which often constitute the active part in the sensor system. Applications of sensors based on carbon nanostructures cover many sectors.

In resistive gas sensors, the resistance of the sensitive material changes upon exposure to the gas molecules through physical adsorption. For instance, a film of Pd-functionalized SWCNTs can act as the resistive channel for the reversible detection of H_2 [80, 81], and MWCNT films have been tested for the detection of NO_2 [82]. Also, chemically functionalized SWCNT films experience sensitive changes upon exposure to explosive components [83], and biologic agent simulants [84].

Acoustic wave sensors measure the difference in wave propagation from an emitter to a detector through a tuneable guiding layer. In this type of sensors, CNTs and GO have been successfully tested as the sensitive layer for the detection of chemical warfare agents [85].

Semiconducting SWCNTs or SWCNT films can work as channels in field effect transistors (FETs), and the device response is modified through the adsorption of molecules on the SWCNT surfaces. Therefore, appropriately designed SWCNT FETs are sensitive to biological molecules such as different DNA types and anabolic steroids [86–88].

Another concept for specific biomolecule detection is based on electrochemical sensing, both by amperometric [10, 89–91], and potentiometric methods [92, 93]. In a typical device, inks, films or papers of functional carbon nanostructures are deposited on a glassy carbon electrode for improving the device sensitivity.

Finally, strain sensors have to be considered, which can be utilized for the detection of pressure and movement. The most direct way for strain sensing is the use of piezoelectric materials. Other strategies include piezoresistive SWCNT composites, in which the electrical resistance greatly changes upon bending [94, 95]. The piezoresistive effect is maximized at SWCNT loadings near the electrical percolation threshold [96].

18.5 Summary and Outlook

Nowadays, the methods for the synthesis of CNTs and graphene are well-stablished, and good quality materials can be obtained either directly after the synthesis process or applying purification treatments. Certain types of CNTs and graphene are fabricated in large amounts, allowing their use in industry. Even though improvements in the synthesis control and purification are still needed, scientific research in CNTs and graphene has mainly expanded towards the applications, covering a great number of technological fields. Some of the developed technological products have already reached the industry, and it is expected that many others will soon be ready for the market. In the meantime, other new forms of nanostructured carbons are being described, including GNRs, GQDs, nanocones and carbon dots. In all the cases, the nanostructure synthetic origin influences the properties and thus determines the applications. According to their potential, further developments in carbon nanostructures can be foreseen for the next years.

Acknowledgments The authors thank the organization of the NATO ASI taking place in Sozopol, Bulgaria from 12/09 to 20/09/2017. This work has been funded by MINECO and European Regional Development Fund (ENE 2016-79282-C5-1-R), Government of Aragon and European Social Fund (DGA-ESF-T66 “Grupo Consolidado”).

References

1. Iijima S (1991) Helical microtubules of graphitic carbon. Nature 354:56–58
2. Novoselov KS, Geim AK, Morozov SV, Jiang D, Zhang Y, Dubonos SV, Grigorieva IV, Firsov AA (2004) Electric field in atomically thin carbon films. Science 306:666–669
3. Kroto HW, Heath JR, O’Brien SC, Curl RF, Smalley RE (1985) C60: buckmisterfullerene. Nature 318:162–163
4. Iijima S, Ichihashi T (1993) Single-shell carbon nanotubes of 1-nm diameter. Nature 363:603–605
5. Bethune DS, Kiang CH, de Vries MS, Gorman G, Savoy R, Vasquez J, Beyers R (1993) Cobalt catalysed growth of carbon nanotubes with single-atomic-layer walls. Nature 363:605–607

6. Bartelmess J, Giordani S (2014) Carbon nano-onions (multi-layer fullerenes): chemistry and applications. Beilstein J Nanotechnol 5:1980–1998
7. Karousis N, Suarez-Martinez I, Ewels CP, Tagmatarchis N (2016) Structure, properties, functionalization, and applications of carbon nanohorns. Chem Rev 116:4850–4883
8. Hofmann S, Braeuninger-Weimer P, Weatherup RS (2015) CVD-enabled graphene manufacture and technology. J Phys Chem Lett 6:2714–2721
9. Chih A, Ansón-Casaos A, Puértolas JA (2017) Frictional and mechanical behaviour of graphene/UHMWPE composite coatings. Tribol Int 116:295–302
10. Martín A, Hernández-Ferrer J, Vázquez L, Martínez MT, Escarpa A (2014) Controlled chemistry of tailored graphene nanoribbons for electrochemistry: a rational approach to optimizing molecule detection. RSC Adv 4:132–139
11. Vallés C, Núñez JD, Benito AM, Maser WK (2012) Flexible conductive graphene paper obtained by direct and gente annealing of graphene oxide paper. Carbon 50:835–844
12. Taratan A, Zobelli A, Benito AM, Maser WK, Stéphan O (2016) Revisiting graphene oxide chemistry via spatially-resolved electron energy loss spectroscopy. Chem Mater 28:3741–3748
13. Nunn N, Torelli M, McGuire G, Shenderova O (2017) Nanodiamond: a high impact nanomaterial. Curr Opin Solid State Mater Sci 21:1–9
14. Kataura H, Kumazawa Y, Maniwa Y, Umezu I, Suzuki S, Ohtsuka Y, Achiba Y (1999) Optical properties of single-wall carbon nanotubes. Synth Met 103:2555–2558
15. Strano MS, Doorn SK, Haroz EH, Kittrell C, Hauge RH, Smalley RE (2003) Assignment of *(n, m)* Raman and optical features of metallic single-walled carbon nanotubes. Nano Lett 3:1091–1096
16. Weisman RB, Bachilo SM (2003) Dependence of optical transition energies on structure for single-walled carbon nanotubes in aqueous suspension: an empirical Kataura plot. Nano Lett 3:1235–1238
17. Itkis ME, Perea DE, Niyogi S, Rickard SM, Hamon MA, Hu H, Zhao B, Haddon RC (2003) Purity evaluation of as-prepared single-walled carbon nanotube soot by use of solution-phase near-IR spectroscopy. Nano Lett 3:309–314
18. Martinez MT, Callejas MA, Benito AM, Cochet M, Seeger T, Ansón A, Schreiber J, Gordon C, Marhic C, Chauvet O, Fierro JLG, Maser WK (2003) Sensitivity of single wall carbon nanotubes to oxidative processing: structural modification, intercalation and functionalization. Carbon 41:2247–2256
19. Ansón-Casaos A, González-Domínguez JM, Lafragüeta I, Carrodeguas JA, Martínez MT (2014) Optical absorption response of chemically modified single-walled carbon nanotubes upon ultracentrifugation in various dispersants. Carbon 66:105–118
20. O'Connell MJ, Bachilo SM, Huffman CB, Moore VC, Strano MS, Haroz EH, Rialon KL, Boul PJ, Noon WH, Kittrell C, Ma J, Hauge RH, Weisman RB, Smalley RE (2002) Band gap fluorescence from individual single-walled carbon nanotubes. Science 297:593–596
21. Lebedkin S, Hennrich F, Skipa T, Kappes MM (2003) Near-onfrared photoluminescence of single-walled carbon nanotubes prepared by the laser vaporization method. J Phys Chem B 107:1949–1956
22. Ebbesen TW, Ajayan PM (1992) Large-scale synthesis of carbon nanotubes. Nature 358:220–222
23. Colbert DT, Zhang J, McClure SM, Nikolaev P, Chen Z, Hafner JH, Owens DW, Kotula PG, Carter CB (1994) Growth and sintering of fullerene nanotubes. Science 266:1218–1222
24. Journet C, Maser WK, Bernier P, Loiseau A, Lamy de la Chapelle M, Lefrant S, Deniard P, Lee R, Fischer JE (1997) Large-scale production of single-walled carbon nanotubes by the electric-arc technique. Nature 388:756
25. Lange H, Saidane K, Razafinimanana M, Gleizes A (1999) Temperatures and C2 column densities in a carbon arc plasma. J Phys D Appl Phys 32:1024–1030
26. Maser WK, Muñoz E, Benito AM, Martínez MT, de la Fuente GF, Maniette Y, Anglaret E, Sauvajol JL (1998) Production of high-density single-walled nanotube material by a simple laser-ablation method. Chem Phys Lett 292:587–593

27. Laplaze D, Alvarez L, Guillard T, Badie JM, Flamant G (2002) Carbon nanotubes: dynamics of synthesis processes. Carbon 40:1621–1634
28. Pérez-Mendoza M, Vallés C, Maser WK, Martínez MT, Langlois S, Sauvajol JL, Benito AM (2005) Ni-Y/Mo catalyst for the large-scale CVD production of multi-wall carbon nanotubes. Carbon 43:3034–3037
29. Terrado E, Muñoz E, Maser WK, Benito AM, Martínez MT (2007) Important parameters for the catalytic nanoparticles formation towards the growth of carbon nanotube aligned arrays. Diam Relat Mater 16:1082–1086
30. Vallés C, Pérez-Mendoza M, Martínez MT, Maser WK, Benito AM (2007) CVD production of doublé-wall carbon nanotubes. Diam Relat Mater 16:1087–1090
31. Vallés C, Pérez-Mendoza M, Maser WK, Martínez MT, Alvarez L, Sauvajol JL, Benito AM (2009) Effects of partial and total methane flows on the yield and structural characteristics of MWCNTs produced by CVD. Carbon 47:998–1004
32. Terrado E, Tacchini I, Benito AM, Maser WK, Martínez MT (2009) Optimizing catalyst nanoparticle distribution to produce densely-packed carbon nanotube growth. Carbon 47:1989–2001
33. Hernández-Ferrer J, Laporta P, Gutiérrez F, Rubianes MD, Rivas G, Martínez MT (2014) Multi-walled carbon nanotubes/graphene nanoribbons hybrid materials with superior electrochemical performance. Electrochem Commun 39:26–29
34. Moreno-Guzman M, Martín A, Martín MC, Sierra T, Ansón-Casaos A, Martinez MT, Escarpa A (2016) Electrochemical behavior of hybrid carbon nanomaterials: the chemistry behind the electrochemistry. Electrochim Acta 214:286–294
35. Maser W, Benito AM, Muñoz E, Martínez MT (2008) Carbon nanotubes: from fundamental nanoscale objects towards functional nanocomposites and applications. NATO ASI Ser, Ser B 101–119
36. Picó F, Rojo JM, Sanjuán ML, Ansón A, Benito AM, Callejas MA, Maser WK, Martínez MT (2004) Single-walled carbon nanotubes as electrodes in supercapacitors. J Electrochem Soc 151 (6):A831–A837
37. Picó F, Pecharroman C, Ansón A, Martínez MT, Rojo JM (2004) Understanding carbon-carbon composites as electrodes of supercapacitors. J Electrochem Soc 154(6):A579–A586
38. Zhang L, Zhang F, Yang X, Lang G, Wu Y, Zhang T, Leng K, Huang Y, Mo Y, Yu A, Chen Y (2013) Porous 3D graphene-based bulk materials with exceptional high surface area and excellent conductivity for supercapacitors. Sci Rep 3:1408
39. Hernández-Ferrer J, Ansón-Casaos A, Martínez MT (2012) Electrochemical synthesis and characterization of single-walled carbon nanotubes/polypyrrole films on transparent substrates. Electrochim Acta 64:1–9
40. Kymakis E, Amaratunga GAJ (2003) Photovoltaic cells based on dye-sensitisation of single-wall carbon nanotubes in a polymer matrix. Sol Energy Mater Sol Cells 80:465–472
41. Kymakis E, Amaratunga GAJ (2002) Single-wall carbon nanotube/conjugated polymer photovoltaic devices. Appl Phys Lett 80(1):112–114
42. Kamat PV (2006) Harvesting photons with carbon nanotubes. NanoToday 1(4):20–27
43. Kongkanand A, Martínez-Domínguez R, Kamat PV (2007) Single wall carbon nanotube scaffolds for photoelectrochemical solar cells. Capture and transport of photogenerated electrons. Nano Lett 7(3):676–680
44. Li H, Cao K, Cui J, Liu S, Qiao X, Shen Y, Wang M (2016) 14.7% efficient mesoscopic perovskite solar cells using single walled carbon nanotubes/carbon composite counter electrodes. Nanoscale 8(12):6379–6385
45. Kymakis E, Strylianakis MM, Spyropoulos GD, Stratakis E, Koudoumas E, Fotakis C (2012) Sol Energy Mater Sol Cells 96:298–301
46. Stratakis E, Savva K, Konios D, Petridis C, Kymakis E (2014) Improving the efficiency of organic photovoltaics by tuning the work function of graphene oxide hole transporting layers. Nanoscale 6:6925–6931

47. Ansón-Casaos A, Mis-Fernández R, López-Alled CM, Almendro-López E, Hernández-Ferrer J, González-Domínguez JM, Martínez MT (2015) Transparent conducting films made of different carbon nanotubes, processed carbon nanotubes, and graphene nanoribbons. Chem Eng Sci 138:566–574
48. Jeon I, Chiba T, Delacou C, Guo Y, Kaskela A, Reynand O, Kauppinen EI, Maruyama S, Matsuo Y (2015) Single-walled carbon nanotube film as electrode in indium-free planar heterojunction perovskite solar cells: investigation of electron-blocking layers and dopants. Nano Lett 15:6665–6671
49. Bedeloglu A, Jimenez P, Demir A, Bozkurt Y, Maser WK, Sariciftci NS (2011) Photovoltaic textile structure using polyaniline/carbon nanotube composite materials. J Tex I 102 (10):857–862
50. Ansón A, Benham M, Jagiello J, Callejas MA, Benito AM, Maser WK, Züttel A, Sudan P, Martínez MT (2004) Hydrogen adsorption on a single-walled carbon nanotube material: a comparative study of three different adsorption techniques. Nanotechnology 15:1503–1508
51. Ansón A, Jagiello J, Parra JB, Sanjuán ML, Benito AM, Maser WK, Martínez MT (2004) Porosity, surface área, surface energy, and hydrogen adsorption in nanostructured carbons. J Phys Chem B 108:15820–15826
52. Ansón A, Lafuente E, Urriolabeitia E, Navarro R, Benito AM, Maser WK, Martínez MT (2006) Hydrogen capacity of palladium-loaded carbon materials. J Phys Chem B 110:6643–6648
53. Ansón A, Lafuente E, Urriolabeitia E, Navarro R, Benito AM, Maser WK, Martínez MT (2007) Preparation of palladium loaded carbon nanotubes and activated carbons for hydrogen sorption. J Alloys Compounds 436:294–297
54. Kunowsky M, Marco-Lozar JP, Suárez-García F, Linares-Solano A (2015) Applications for CO_2-activated carbon monoliths: I. gas storage. Int J Appl Ceram Technol 12(S3):E121–E126
55. Lafuente E, Muñoz E, Benito AM, Maser WK, Martínez MT (2006) Single-walled carbon nanotube-supported platinum nanoparticles as fuel cell electrocatalysts. J Mater Res 21 (11):2841–2846
56. Solla-Gullón J, Lafuente E, Aldaz A, Martínez MT, Feliu JM (2007) Electrochemical characterization and reactivity of Pt nanoparticles supported on single-walled carbon nanotubes. Electrochim Acta 52:5582–5590
57. Sieben JM, Ansón-Casaos A, Martínez MT, Morallón E (2013) Single-walled carbon nanotube buckypapers as electrocatalyst supports for metanol oxidation. J Power Sources 242:7–14
58. Cano M, Benito A, Maser WK, Urriolabeitia E (2001) One-step microwave synthesis of palladium-carbon nanotube hybrids with improved catalytic performance. Carbon 49:652–658
59. Cano M, Benito A, Maser WK, Urriolabeitia E (2013) High catalytic performance of palladium nanoparticles supported on multiwalled carbon nanotubes in alkene hydrogenation reactions. New J Chem 37:1968–1972
60. Cano M, Villuendas P, Benito AM, Urriolabeitia EP, Maser WK (2015) Carbon nanotube-gold nanoparticles as efficient catalyst for the selective hydrogenation of nitroaromatic derivatives to anilines. Mater Today Commun 3:104–113
61. Cano M, Benito AM, Urriolabeitia EP, Arenal R, Maser WK (2013) Reduced graphene oxide: firm support for catalytically active palladium nanoparticles and game changer in selective hydrogenation reactions. Nanoscale 5:10189–10193
62. Roldan L, Armenise S, Marco Y, Garcia-Bordeje E (2012) Control of nitrogen insertion during the growth of nitrogen-containing carbon nanofibers on cordierite monolith walls. Phys Chem Chem Phys 14:3568–3575
63. García-Bordejé E, Kvande I, Chen D, Rönning M (2006) Carbon nanofibers uniformly grown on γ-alumina washcoated cordierite monoliths. Adv Mater 18:1589–1592
64. Roldan L, Benito AM, Garcia-Bordeje E (2015) Self-assembled graphene aerogel and nanodiamond hybrids as high performance catalysts in oxidative propane dehydrogenation. J Mater Chem A 3:24379–24388

65. Roldán L, Marco Y, García-Bordejé E (2017) Origin of the excellent performance of Ru on nitrogen-doped carbon nanofibers for CO_2 hydrogenation to CH_4. ChemSusChem 10:1139–1144
66. Roldán L, Marco Y, García-Bordejé E (2015) Function of the support and metal loading on catalytic carbon dioxide reduction using ruthenium nanoparticles supported on carbon nanofibers. ChemCatChem 7:1347–1356
67. Marco Y, Roldán L, Muñoz E, García-Bordejé E (2014) Carbon nanofibers modified with heteroatoms as metal-free catalysts for the oxidative dehydrogenation of propane. ChemSusChem 7:2496–2504
68. Armenise S, Roldán L, Marco Y, Monzón A, García-Bordejé E (2012) Elucidation of catalyst support effect for NH_3 decomposition using Ru nanoparticles on nitrogen-functionalized carbon nanofiber monoliths. J Phys Chem C 116:26385–26395
69. Restivo J, Orfão JJM, Pereira MFR, Garcia-Bordejé E, Roche P, Bourdin D, Houssais B, Coste M, Derrouiche S (2013) Catalytic ozonation of organic micropollutants using carbon nanofibers supported on monoliths. Chem Eng J 230:115–123
70. Yuranova T, Kiwi-Minsker L, Franch C, Palomares AE, Armenise S, Garcia-Bordeje E (2013) Nanostructured catalysts for the continuous reduction of nitrates and bromates in water. Ind Eng Chem Res 52:13930–13937
71. Maser WK, Benito AM, Castell P, Sainz R, Martinez MT, Naffakh M, Marco C, Ellis G, Gómez MA (2009) Carbon nanotube composite materials: opportunities and processing issues. NATO ASI Ser, Ser B 181–198
72. Vallés C, Jiménez P, Muñoz E, Benito AM, Maser WK (2011) Graphene: 2D-building block for functional nanocomposites. NATO ASI Ser, Ser B 143–148
73. Diez-Pascual AM, Gonzalez-Dominguez JM, Martinez-Rubi Y, Naffakh M, Ansón A, Martínez MT, Simard B, Gómez MA. Synthesis and properties of PEEK/carbon nanotube nanocomposites. In: Polymer nanotube nanocomposites: synthesis, properties, and applications. Scrivener Publishing LLC, pp 281–313
74. Gonzalez-Dominguez JM, Diez-Pascual AM, Ansón-Casaos A, Gómez-Fatou MA, Martinez MT. Functionalization strategies for single-walled carbon nanotubes integration in epoxy matrices. In: Polymer nanotube nanocomposites: synthesis, properties, and applications: second edition. Scrivener Publishing LLC, pp 281–313
75. Ansón-Casaos A, Pascual FJ, Ruano C, Fernández-Huerta N, Fernández-Pato I, Otero JC, Puértolas JA, Martínez MT (2015) Electrical conductivity and tensile properties of block-copolymer wrapped single-walled carbon nanotube/poly(methyl methacrylate) composites. J Appl Polym Sci 132(9):41547
76. Castell P, Medel FJ, Martinez MT, Puértolas JA (2009) Influence of gamma irradiation on carbon nanotube-reinforced polypropylene. J Nanosci Nanotechnol 9:6055–6063
77. Martínez-Morlanes MJ, Castell P, Martínez-Nogués V, Martinez MT, Alonso PJ, Puértolas JA (2011) Effects of gamma-irradiation on UHMWPE/MWNT nanocomposites. Compos Sci Technol 71:282–288
78. Martínez-Morlanes MJ, Castell P, Alonso PJ, Martinez MT, Puértolas JA (2012) Multi-walled carbon nanotubes acting as free radical scavengers in gamma-irradiated ultrahigh molecular weight polyethylene composites. Carbon 50:2442–2452
79. Castell P, Martínez-Morlanes MJ, Alonso PJ, Martinez MT, Puértolas JA (2013) A novel approach to the chemical stabilization of gamma-irradiated ultrahigh molecular weight polyethylene using arc-discharge multi-walled carbon nanotubes. J Mater Sci 48:6549–6557
80. Sayago I, Terrado E, Lafuente E, Horrillo MC, Maser WK, Benito AM, Navarro R, Urriolabeitia EP, Martinez MT, Gutierrez J (2005) Hydrogen sensors based on carbon nanotubes thin films. Synth Met 148:15–19
81. Sayago I, Terrado E, Aleixandre M, Horrillo MC, Fernández MJ, Lozano J, Lafuente E, Maser WK, Benito AM, Martinez MT, Gutiérrez J, Muñoz E (2007) Novel selective sensors based on carbon nanotube films for hydrogen detection. Sensors Actuators B 122:75–80

82. Sayago I, Santos H, Horrillo MC, Aleixandre M, Fernández MJ, Terrado E, Tacchini I, Aroz R, Maser WK, Benito AM, Martinez MT, Gutiérrez J, Muñoz E (2008) Carbon nanotube networks as gas sensors for NO_2 detection. Talanta 77:758–764
83. Schnorr JM, van der Zwaag D, Walish JJ, Weizmann Y, Swager TM (2013) Sensory arrays of covalently functionalized single-walled carbon nanotubes for explosive detection. Adv Funct Mater 23:5285–5291
84. Kumar D, Jha P, Chouksey A, Rawat JSBS, Tandon RP, Chaudhury PK (2016) 4-(hexafluoro-2-hydroxy isopropyl)aniline functionalized highly sensitive flexible SWCNT sensor for detection of nerve agent simulant dimethyl methylphosphonate. Mater Chem Phys 181:487–494
85. Sayago I, Matatagui D, Fernández MJ, Fontecha JL, Jurewicz I, Garriga R, Muñoz E (2016) Graphene oxide as sensitive layer in Love-wave Surface acoustic wave sensors for the detection of chemical warfare agent simulants. Talanta 148:393–400
86. Martinez MT, Tseng Y, Ormategui N, Loinaz I, Eritja R, Bokor J (2009) Label-free DNA biosensors based on functionalized carbon nanotube field effect transistors. Nano Lett 9 (2):530–536
87. Martinez MT, Tseng Y, Salvador JP, Marco MP, Ormategui N, Loinaz I, Bokor J (2010) Electronic anabolic steroid recognition with carbon nanotube field effect transistors. ACS Nano 4(3):1473–1480
88. Martinez MT, Tseng Y, González M, Bokor J (2012) Streptavidin as CNTs and DNA linker for the specific electronic and optical detection of DNA hybridization. J Phys Chem C 116:22579–22586
89. Eguílaz M, Gutiérrez A, Gutierrez F, González-Domínguez JM, Ansón-Casaos A, Hernández-Ferrer J, Ferreyra NF, Martinez MT, Rivas G (2016) Covalent functionalization of single-walled carbon nanotubes with polytyrosine: characterization and analytical applications for the sensitive quantification of polyphenols. Anal Chim Acta 909:51–59
90. Eguílaz M, Gutierrez F, González-Domínguez JM, Martínez MT, Rivas G (2016) Single-walled carbon nanotubes covalently functionalized with polytyrosine: a new material for the development of NADH-based biosensors. Biosens Bioelectron 86:308–314
91. Guitierrez FA, Gonzalez-Dominguez JM, Ansón-Casaos A, Hernández-Ferrer J, Rubianes MD, Martinez MT, Rivas G (2017) Single-walled carbon nanotubes covalently functionalized with cysteine: a new alternative for the highly sensitive and selective Cd(II) quantification. Sensors Actuators B 249:506–514
92. Hernández R, Riu J, Bobacka J, Vallés C, Jiménez P, Benito AM, Maser WK, Rius FX (2012) Reduced graphene oxide films as solid transducers in potentiometric all-solid-state ion-selective electrodes. J Phys Chem C 116:22570–22578
93. Hernández R, Vallés C, Benito AM, Maser WK, Rius FX, Riu J (2014) Graphene-based potentiometric biosensor for the immediate detection of living bacteria. Biosens Bioelectron 54:553–557
94. Ferreira A, Rocha JG, Ansón-Casaos A, Martinez MT, Vaz F, Lanceros-Mendez S (2012) Electrochemical performance of poly(vinylidene fluoride)/carbon nanotube composites for strain sensor applications. Sens Actuat A 178:10–16
95. Gonzalez-Dominguez JM, Ansón-Casaos A, Martinez MT, Ferreira A, Vaz F, Lanceros-Méndez S (2012) Piezoresistive response of Pluronic-wrapped single-wall carbon nanotube-epoxy composites. J Intell Mater Syst Struct 23(8):909–917
96. Ferreira A, Martinez MT, Ansón-Casaos A, Gómez-Pineda LE, Vaz F, Lanceros-Mendez S (2013) Relationship between electrochemical response and percolation threshold in carbon nanotube/poly(vinylidene) composites. Carbon 61:568–576

Chapter 19
Quantum Information Technology and Sensing Based on Color Centers in Diamond

Nina Felgen, Alexander Schmidt, Boris Naydenov, Fedor Jelezko, Johann Peter Reithmaier, and Cyril Popov

Abstract Diamond is a material with a number of outstanding mechanical, optical, electrical and chemical properties. In the last decade it has additionally attracted the attention of scientists due to the promising properties of the color centers in its crystal lattice which can find applications in quantum information technology or quantum sensing on a nanometer scale. In this contribution we present the most prominent color centers in diamond, namely the nitrogen-vacancy (NV) and the silicon-vacancy (SiV) centers, and the possibilities to create them in diamond. In order to increase the collection efficiency of the photons emitted by the color centers they should be incorporated in photonic structures. We demonstrate the fabrication of nanopillars with diameters down to 50 nm in nanocrystalline diamond (NCD) films and monocrystalline diamond. In order to reduce the photon scattering from the rough NCD surfaces we developed a planarization technique which significantly reduced the surface roughness.

Keywords NV centers · SiV centers · Diamond nanopillars · Surface planarization

19.1 Introduction

Over the past years diamond gained a growing interest as a platform for quantum information technology (QIT) components and devices, like quantum memories, quantum repeaters or single photon sources, but also as component for sensing

N. Felgen · A. Schmidt · J. P. Reithmaier · C. Popov (✉)
Institute of Nanostructure Technologies and Analytics, University of Kassel, Kassel, Germany
e-mail: popov@ina.uni-kassel.de

B. Naydenov · F. Jelezko
Institute of Quantum Optics, University of Ulm, Ulm, Germany

P. Petkov et al. (eds.), *Advanced Nanotechnologies for Detection and Defence against CBRN Agents*, NATO Science for Peace and Security Series B: Physics and Biophysics, https://doi.org/10.1007/978-94-024-1298-7_19

applications. These applications are possible due to certain defects in the diamond lattice based on vacancies and impurity atoms, the so-called color centers. The advanced applications of these defects is based on their outstanding properties which include highly stable fluorescence (photo-stability), control of single coherent spins even at room temperature, sensitivity to magnetic and electric fields at the nano-scale and many others. Incorporation of these color centers into photonic structures allows for the control of light – matter interaction.

19.2 Diamond Properties and Synthesis

Diamond as a host material for color centers provides additionally a wide range of beneficial properties: it is the hardest known natural material, has the highest thermal conductivity at room temperature, possesses a high optical transparency from the deep UV to the far IR region, it is a very good electrical insulator which upon doping can obtain metallic conductivity, is biologically compatible and inert to most chemicals [1, 2]. Any colors observed in diamond arise from defects such as impurities, dislocations, vacancies and complexes, creating electronic energy levels in the bandgap [3].

Synthetic diamond can be distinguished in two groups depending on the synthesis route. The first one, high pressure high temperature (HPHT) synthesis, was developed in the 1950s imitating the conditions at which diamond is formed in the earth. The required pressure of ca. 5 GPa and temperatures of 1300–1700 °C make the method not only time consuming, but also expensive. This can be alleviated by catalysts. The catalysts used for HPHT synthesis of diamond crystals include alloys of Fe, Ni, Co, but also elements such as Ti and Al, whereas graphite serves as a carbon source [4, 5]. Almost at the same time diamond thin film deposition was realized via chemical vapor deposition (CVD) [6] where a low pressure gas is activated by plasma, hot filaments, or combustion flames. The CVD process allows control of the sample size (i.e. the coated area), crystallinity, morphology and doping [7]. By variation of the process parameters and choice of the substrates all crystalline forms of diamond can be achieved: mono-, poly-, nano- and ultrananocrystalline diamond, where many of the superior properties of the monocrystalline bulk diamond are preserved [8].

Diamond films can be grown on a variety of substrates for example Si, glass, W, Ta and many others after seeding the surface with diamond particles (pre-treatment) or after bias enhanced nucleation (BEN) [9–12], followed by diamond CVD starting from the created nucleation sites on the surface. But also diamond itself can serve as a substrate for homoepitaxy [13]. The most commonly employed carbon precursor is methane, but also other hydrocarbons, alcohols, etc. can be applied, in all cases diluted in hydrogen, nitrogen or argon. The major process parameters for diamond CVD growth are the substrate temperature, the working pressure, the total gas flow, and the gas phase composition (see for example [14–16]). They determine the crystallinity of the deposited films. In our experiments nanocrystalline diamond (NCD) films were deposited via hot filament chemical vapor deposition (HFCVD)

Table 19.1 HFCVD parameters for the growth of NCD films used in the current work

Substrate temperature T_{Sub} [°C]	850–910
Heater Voltage U_{Sub} [V]	100
Filament current I_{Fil} [A]	70 (10 A per filament)
Gas mixture CH_4/H_2 [%]	1/99
Total gas flow [sccm]	505
Deposition time T [min]	10–180
Pressure p [kPa]	2.5

from a 1% CH_4/H_2 gas mixture. A self-built setup with seven parallel tungsten filaments (0.3 mm in diameter) was employed allowing homogeneous deposition on a 3 in. wafer. The process parameters are summarized in Table 19.1.

19.3 Color Centers in Diamond

Diamond hosts hundreds of optically active point defects in its crystal lattice, the so-called color centers. Although more than 500 luminescent centers in diamond are known, only few of them have been perceived attention but some are even not fully identified by their chemical and electronic structure [17]. These defects can be a missing atom (vacancy), an impurity atom (substitutional or interstitial) or even complexes of impurities [3].

The general classification of diamond materials is based only on the presence or absence of boron and nitrogen impurities and how they are arranged in the diamond lattice, as these impurities are decisive for the appearance of natural diamond but does not make any statement on other impurities or their arrangement [18]. For example it does not consider the GR1 color center emitting at 741 nm which is only an uncharged vacancy in the diamond lattice or the 3H color center emitting at 503 nm which is thought to be an interstitial carbon atom in the diamond lattice. Especially for nitrogen impurities certain arrangements in the diamond lattice are well known such as the N3 center (415 nm) which consists of three nitrogen atoms surrounding a vacancy or the H3 center (531 nm) consisting of two nitrogen atoms separated by a vacancy [19]. The emission spectra of color centers in diamond range from the blue to the near-infrared range [20, 21]. From the large variety of luminescent centers in diamond only a few were identified (in addition to the NV and SiV centers described below) as single photon emitters: nickel-related complexes, germanium-vacancy (GeV) centers and some others which are up to now unidentified [17]. Further information about the color centers in diamond and their properties is reported in references [3, 22–24].

19.3.1 Nitrogen-Vacancy (NV) Centers

The most prominent nitrogen-related color center is the nitrogen-vacancy center (NV center). It consists of a nitrogen atom adjacent to a vacancy (Fig. 19.1, left) and occurs in an uncharged (NV^0, with zero phonon line (ZPL) at 575 nm in the photoluminescence spectrum) and a negatively charged state (NV^-, ZPL at 637 nm), see Fig. 19.1, right. The broad phonon side band in the PL spectrum ranges from 600 to 800 nm. The chemical and electronic structure of the NV center is well studied and can be described as a three level system (Fig. 19.2) [25].

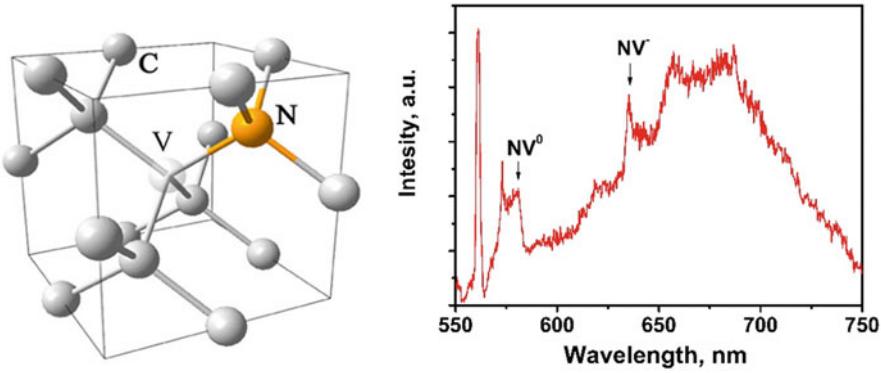

Fig. 19.1 (left) Schematic of a NV center. A nitrogen atom (N) sits adjacent to a vacancy (V) along the (111) axis; (right) room temperature photoluminescence spectrum showing the zero phonon lines of NV^0 and NV^- centers together with a broad phonon side band

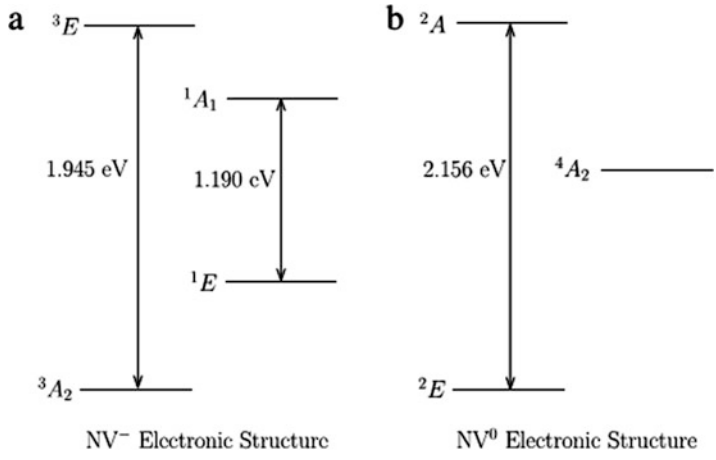

Fig. 19.2 Electronic structure of (**a**) NV^- and (**b**) NV^0 center (Reprinted with permission from [26]. © 2013, Elsevier)

The lifetime has been found to be dependent on the host material; it is around 10 ns for a single NV in bulk material and 24 ns in nanodiamonds [27, 28].

19.3.2 Silicon-Vacancy (SiV) Center

Another color center that has attracted interest in recent years is the negatively charged silicon-vacancy center (SiV center). It is a common impurity in CVD grown diamond samples due to the presence of silicon containing quartz windows and reactor walls or to the use of silicon substrates for growth [29, 30]. The center consists of a silicon atom separating two vacancies [31] as shown in Fig. 19.3.

The ZPL is centered at 737 nm and has a complicated structure due to the split ground and excited states as well as to the different silicon isotopes (Fig. 19.4) [32]. The small FWHM of 5 nm even at room temperature is a result of the weak electron-phonon coupling [33]. The linearly polarized emission spectrum shows a

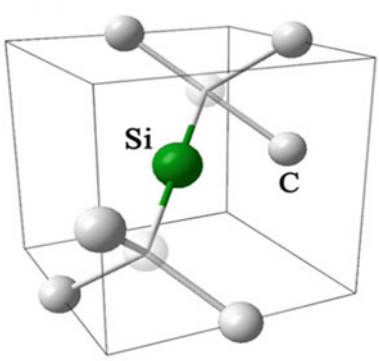

Fig. 19.3 Schematic of a SiV center, a silicon atom (Si) separating two vacancies

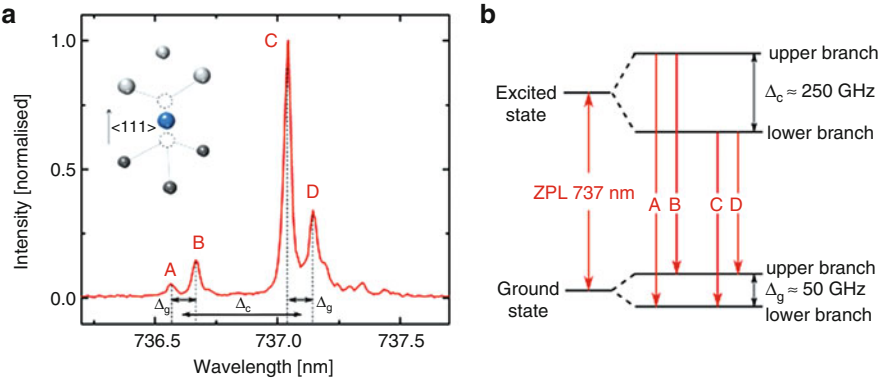

Fig. 19.4 Photoluminescence spectrum of SiV^- at 4 K (**a**) and its energy level diagram (**b**) (Reprinted with permission from [32]. © 2014, Nature Publishing Group)

sharp peak without a large phonon side band. Although the quantum efficiency (QE) is relatively low (0.05), the shorter lifetime of around 1 ns makes the SiV center an interesting candidate for single photon applications. The QE as well as the line width and ZPL center vary also with temperature and between samples grown under different conditions [34].

19.4 Creation of Color Centers

19.4.1 Implantation and Electron Irradiation

The most efficient way to create NV centers is electron irradiation of diamond type Ib (i.e. with isolated single N impurities) for the generation of vacancies and subsequent annealing at temperatures above 900 °C in vacuum. The high nitrogen content in the sample is sufficient, the high annealing temperature ensures diffusion of the vacancies towards the N atoms for the creation of ensembles of NV centers. However, this method does not allow the fabrication of single color centers; furthermore, due to other imperfections type Ib diamonds provide an imperfect environment which may deteriorate the properties of the optical centers [35]. To achieve single NV centers, different strategies employing ion implantation with subsequent annealing steps are developed such as applying a low fluence of N ion irradiation, implantation through a mask or even through a cantilever tip with a hole which serves as a small aperture [36–41]. The possibility of SRIM (Stopping and Range of Ions in Matter) simulations allows the prediction of the implantation results and vice versa the calculation of the parameters for a desired implantation profile regarding the depth, the concentration of vacancies, etc. In Fig. 19.5 the implantation conditions (ion species, energy) for the creation of shallow and deep NV centers are given as an example; the respective SRIM simulations are shown in Fig. 19.6. SiV centers can be also created with ion implantation.

19.4.2 In Situ Doping of CVD Diamond During the Growth

Due to the facts that CVD takes place at low pressures and nitrogen is an abundant component of the atmosphere it is always present in the chamber (except for ultra high vacuum conditions) and facilitates the incorporation of NV centers during growth [42, 43]. To increase the amount of nitrogen in the reactor it is possible to add nitrogen to the gas mixture [44]. Besides the unintentional self-doping from silicon substrates or glass windows, SiV centers can be created by introducing a volatile compound such as silane into the process chamber. This method gives not only the possibility for the formation of SiV centers on non-silicon containing substrates but also allows for a better control of the amount of silicon in the gas phase [45, 46].

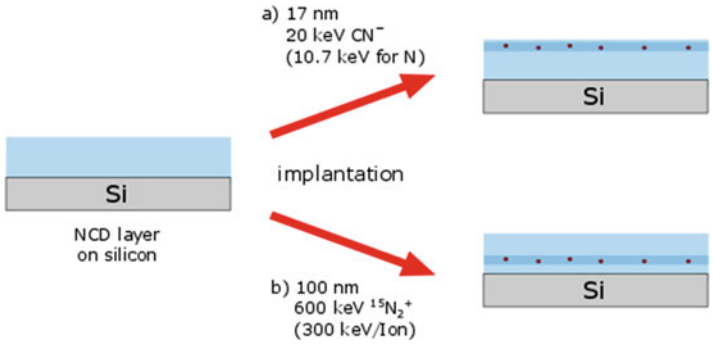

Fig. 19.5 Conditions for the creation of shallow (ca. 15 nm) and deep (100 nm) NV centers in NCD film

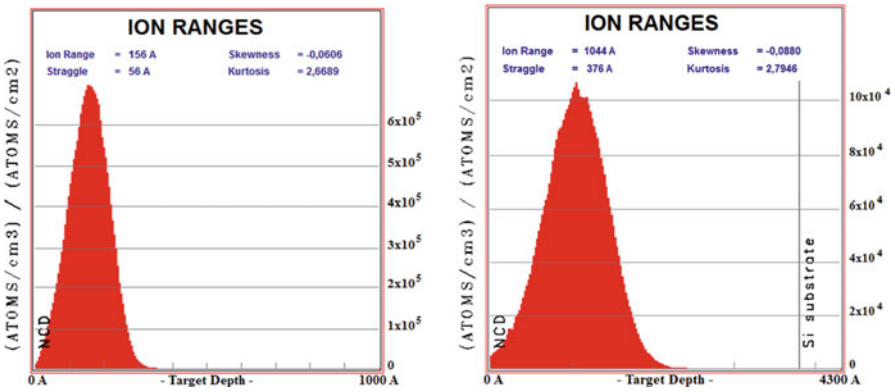

Fig. 19.6 SRIM simulations of the implantation profiles of ^{14}N (as CN^-, 20 keV) (left) and ^{15}N (as N_2^+, 600 keV) (right) for the creation of shallow and deep NV centers

19.5 Diamond Photonic Structures

The optical properties of color centers are influenced by their environment which impacts for example the emission yield. The optical transitions of the NV and SiV centers are located in the visible range making diamond with its high refractive index of $n = 2.43$ a suitable material for the realization of photonic structures. Furthermore, the collection efficiency of photons emitted by a NV center can be improved utilizing diamond nanowires instead of bulk materials as determined by finite-difference time-domain (FDTD) simulations by Hausmann et al. (Fig. 19.7). In bulk diamond the light emitted from the NV center leaks into the bulk due to total internal reflection at the air-diamond interface [47, 48].

The same authors also simulated the coupling efficiency between the NV center and the nanowire mode as a function of the diameter. With an s-polarized dipole and

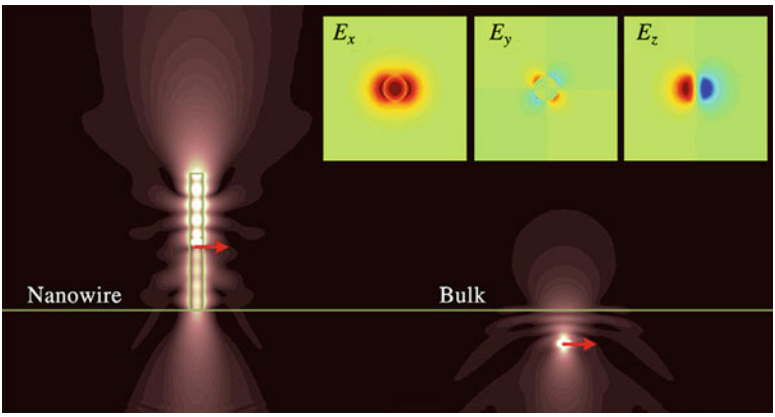

Fig. 19.7 Field profile of the radial E-field component in the case of a 2 µm long, 200 nm diameter diamond nanowire (left) and a bulk diamond (right). The dipole is polarized parallel to the interface, emitting at $\lambda = 637$ nm. The fundamental nanowire waveguide mode (HE11) (inset) is the dominant decay channel for the nanowire case (Reprinted with permission from [47]. © 2010, Elsevier)

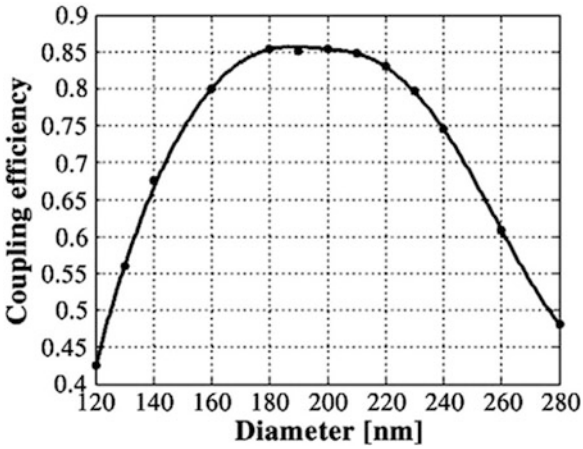

Fig. 19.8 Coupling efficiency as a function of the nanowire diameter at $\lambda = 637$ nm. The dipole is assumed to be placed at the center of the nanowire with a polarization perpendicular to the nanowire axis (s-polarized) (Reprinted with permission from [47]. © 2010, Elsevier)

a diameter between 180 and 230 nm more than 80% of the emitted photons can couple to the nanowire (Fig. 19.8) allowing a huge increase in the photon collection efficiency [47].

Besides nanopillars or nanowires there are more structures that enhance the emission yield and increase the collection efficiency of the photons emitted from the color centers in diamond. These include 1D and 2D photonic crystals [49–51] micro rings [52], and waveguides [53], solid immersion lenses (SIL) [54] or gratings [55] fabricated in poly- or nanocrystalline as well as in monocrystalline diamond. Each of these materials has its advantages and disadvantages for the preparation of photonic structures but also in view of the optical properties. For deposition of poly- and nanocrystalline diamond a broad range of substrates is available, the structuring

processes are well established but the optical properties are alleviated due to grain boundaries and the typical roughness of the films. Monocrystalline diamond exhibits excellent optical properties, but the fabrication of some of the photonic structures and the limit of substrate choices can be challenging.

19.6 Fabrication of Diamond Photonic Structures

For the fabrication of diamond nanostructures different top-down as well as bottom-up techniques are known. The top-down approaches usually start with a lithographic step which can be either photolithographic or electron beam lithographic (EBL) transfer of the desired pattern into a resist. Depending on the etching recipe and the etch time the resist can be sufficient as a mask, but often a hard mask is required which can be patterned by a lift off process or by structuring the mask material itself via dry etching. Common mask materials include gold, aluminum, chromium, but also silicon or silicon dioxide. For the structuring of diamond itself almost exclusively ion assisted plasma techniques, like reactive ion etching (RIE), are applied. They can be divided into two groups with respect to the active gas used: oxygen or oxygen-containing gas mixtures [47, 56–58] and hydrogen-containing gas mixtures [59, 60]. The latter have the disadvantage of high process temperatures in the range of the deposition temperature of diamond. Using oxygen and oxygen-containing gas mixtures, such as O_2/Ar or O_2/CH_4, the structuring can be performed at room temperature achieving high etch rates.

19.6.1 Fabrication of Diamond Nanopillar Arrays

In our group nanocrystalline diamond pillars with diameters of 1 μm, 500 nm, 200 nm, 100 nm and 50 nm, and center-to-center distance of 5 μm were fabricated using either a 200 nm gold mask with 5 nm titanium as an adhesion layer [61] or 100 nm aluminum masks. The dry etching was performed in an ICP-RIE set up with only oxygen as reactive gas under the conditions described in detail in [62]. The etch time was monitored with a laser interferometer to assure the etching of the entire NCD film to the substrate and the reduction or even complete removal of the residual diamond grass. The final structures were arrays of diamond nanopillars as shown in Fig. 19.9.

19.6.2 Fabrication of Dense Nanopillar Arrays

Once the distances between the diamond nanopillars are reduced to obtain highly dense arrays, further challenges could arise regarding the fabrication process. As

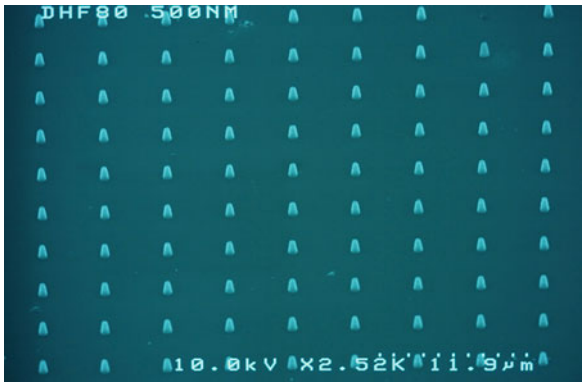

Fig. 19.9 Array of NCD nanopillars with a diameter of 500 nm

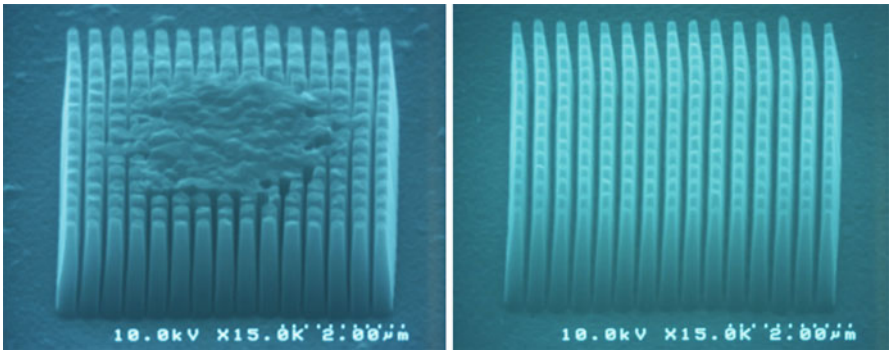

Fig. 19.10 SEM images of NCD nanopillar arrays with a diameter of 200 nm and a center-to-center distance of 400 nm: (left) with the impact of the proximity effect, (right) after suitable proximity corrections

soon as the dimensions of the structures are reduced and high package densities in electron beam lithography (EBL) are desired, the well-known "proximity effect" starts to affect severely the exposure resolution. As electrons penetrate through the resist into the substrate, electron scattering phenomena occur leading to an undesired exposure of resist areas adjacent to the scanned electron beam spot. The pattern fidelity is therefore strongly limited by the proximity effect inherent in electron–solid interactions and thus in EBL.

Especially in the case of fabrication of arrays with high densities of diamond nanopillars, the proximity effect has a crucial impact on the developed structures as it is evident in Fig. 19.10, left. The pillars are broadened and merged together leading to a pattern that strongly deviates from the desired one. This effect is more pronounced in the center of the array, due to the higher electron distribution in the center compared to the edges thus exhibiting a higher impact of the proximity effect.

The proximity effect depends on many factors like the size, shape and package density of the nanostructures as well as on the exposure conditions, but with appropriate corrective action it is possible to fabricate well developed highly dense

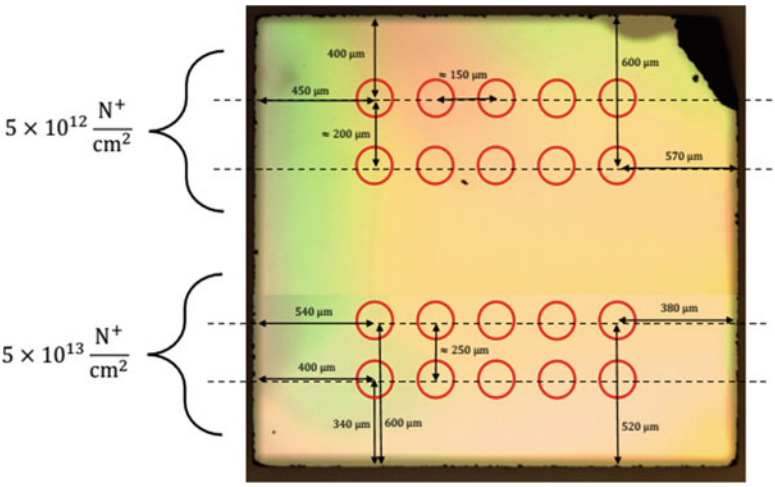

Fig. 19.11 Implantation map of a IIa diamond sample

pillar arrays (Fig. 19.10, right) [63]. Concerning the pattern design for EBL, proximity correction software was used to calculate a suitable dose distribution. Additionally, an exposure dose variation was used to find the optimal value, which leads to well developed nanopillar arrays.

19.6.3 Incorporation of NV Centers into Diamond Pillars

The approach employing N implantation and annealing followed by structuring can also be transferred to monocrystalline diamond samples. N^+ was implanted into IIa diamond with an implantation spot size of 300 µm in diameter. The implantation was performed with 5 keV and two different doses of $5{\cdot}10^{12}N^+/cm^2$ and $5{\cdot}10^{13}N^+/cm^2$ (Fig. 19.11). Prior to structuring the created NV centers were pre-characterized to ensure a successful implantation process (not shown here).

The knowledge about the implantation spots made it possible to create pillar arrays directly on implanted areas of the diamond. For this purpose a 100 nm Al mask was chosen (Fig. 19.12, left). The structuring of pillars with diameters ranging from 1 µm to 50 nm was performed with the standard etching recipe for 8.5 min assuming an etch rate of 100 nm/min (derived from a laser interferometer). The etch depth was around 850 nm (Fig. 19.12, right).

The fluorescence mapping of the structured sample exhibited the presence of NV centers only in the pillars but not in the bulk material (Fig. 19.13). Furthermore, for the 200 nm diameter pillars the strongest fluorescence signal (>100 kc/s) was detected.

Room temperature PL measurements revealed the presence of the ZPL peak of NV^- at 637 nm as well as the typical broad phonon side band (Fig. 19.14).

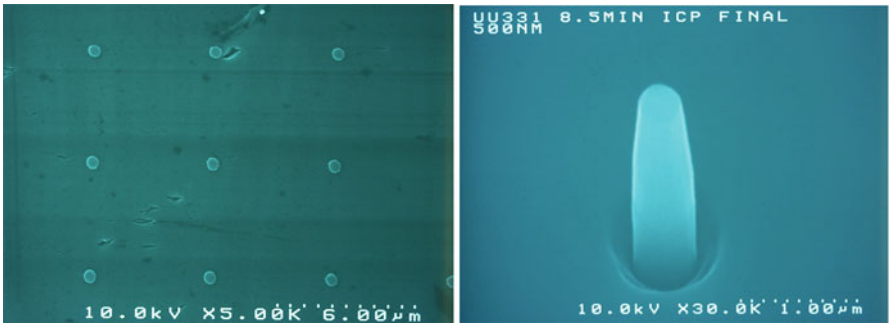

Fig. 19.12 Aluminum mask for structuring of pillars with 500 nm diameter on top of a monocrystalline diamond sample (left) and a final 500 nm diameter pillar (right)

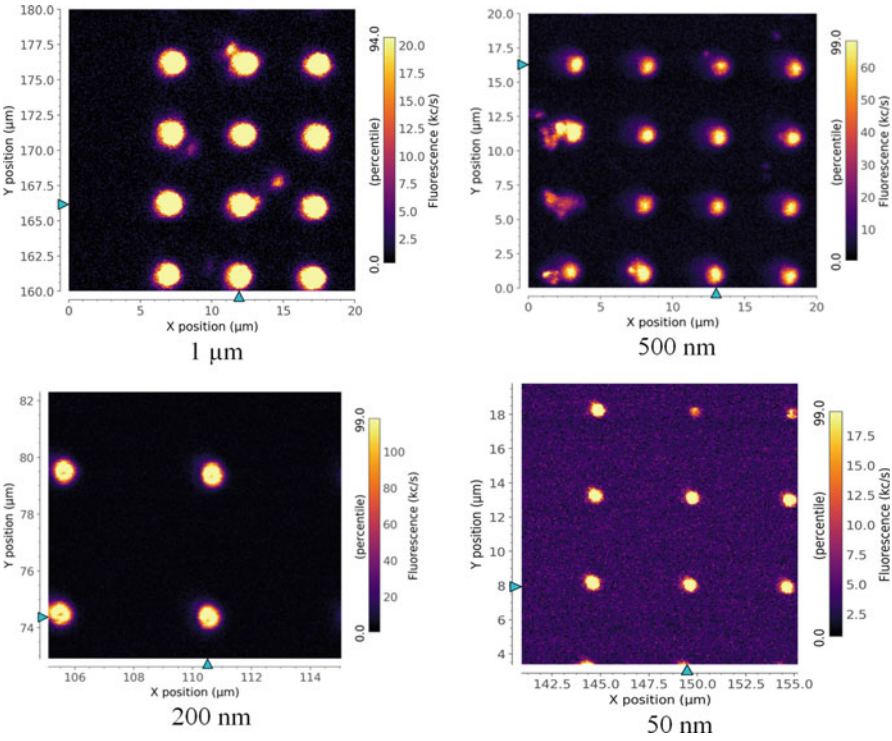

Fig. 19.13 Fluorescence mapping of the implanted IIa sample after structuring of pillars with different diameters

19.6.4 Incorporation of SiV Centers into Diamond Pillars

Incorporation of SiV centers into nanostructures was achieved by overgrowth of existing NCD pillars on a silicon substrate. The structured sample was overgrown

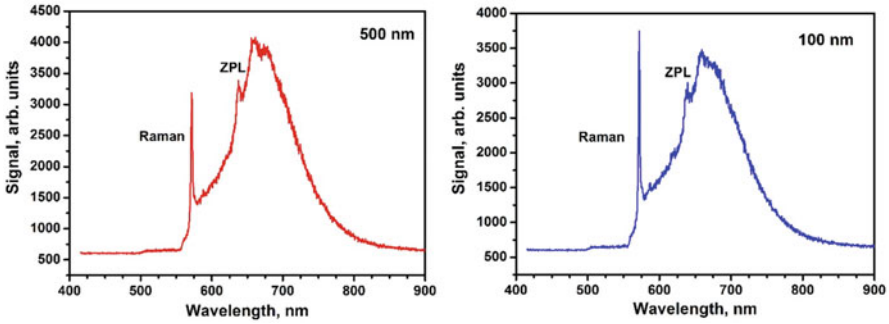

Fig. 19.14 PL spectra of 500 nm (left) and 100 nm (right) monocrystalline diamond pillars

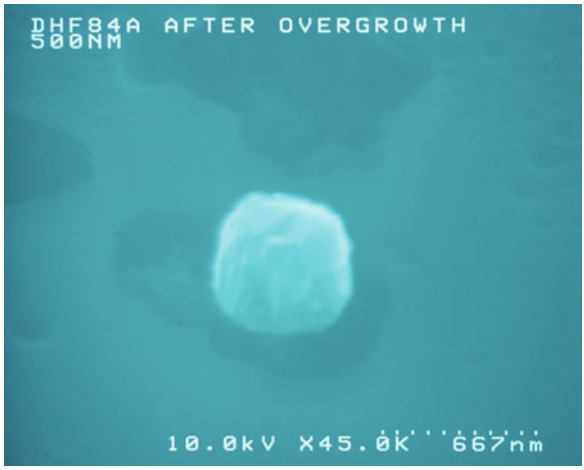

Fig. 19.15 A pillar with a diameter of 500 nm after overgrowth (Reprinted with permission from [65]. © 2016, Elsevier)

in the HFCVD chamber for 30 min using the same process parameters as for the deposition. No additional pretreatment was applied. The overgrowth took place only on the diamond pillars and not on the silicon substrate (Fig. 19.15). The bare silicon substrate was etched by the atomic hydrogen generated in the gas phase and served as silicon source for the creation of SiV centers during the growth [24, 64, 65].

The PL measurements before the overgrowth step showed no signal of SiV centers but only a broad phonon side band (Fig. 19.16a). After overgrowth the side band was strongly reduced, and a peak at 737 nm attributed to the SiV ZPL was clearly visible (Fig. 19.16b).

Comparing the SiV ZPL signal of different pillar diameters a dependency can be observed (Fig. 19.17). The strongest signal was obtained for a 200 nm pillar diameter.

The transfer of this technique for the incorporation of SiV centers into monocrystalline diamond pillars is under development.

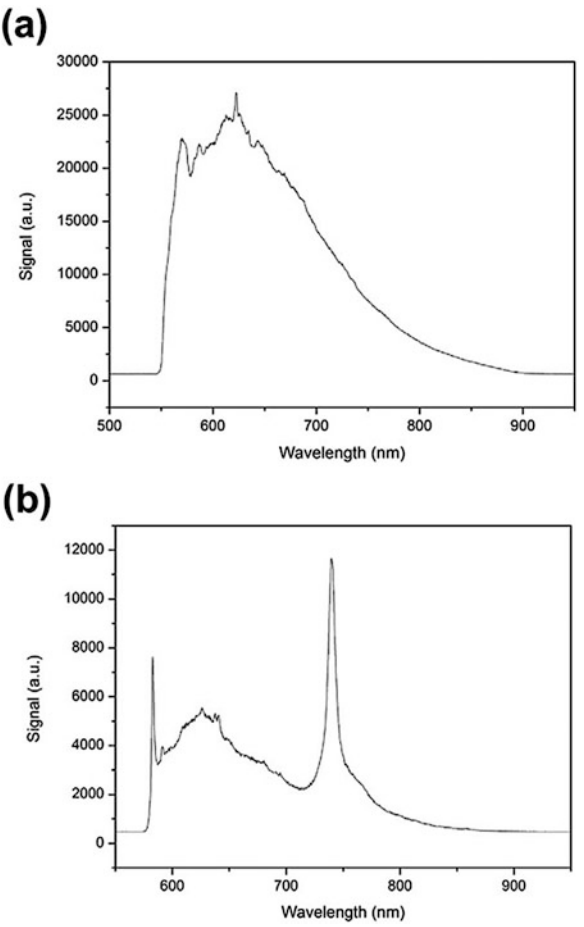

Fig. 19.16 PL spectra (**a**) before and (**b**) after the overgrowth for a 100 nm pillar (Reprinted with permission from [65]. © 2016, Elsevier)

19.7 Planarization of Nanocrystalline Diamond

Planarization of nanocrystalline diamond films is necessary for optical applications in order to reduce the scattering of light at the edges of the surface crystallites. The well-known chemical-mechanical polishing (CMP) method offers sufficient results for thick PCD and NCD films, but it is not applicable in our case due to the large amount of removed material (several μm) by the process (our NCD films have thicknesses up to 1 μm). The simple dry etching using the NCD recipe [62] resulted in less sharp crystallites which looked quite smooth, but the surface roughness was not significantly reduced. Nevertheless, efforts were made to create photonic crystals from these samples (not shown here).

To avoid the necessity of a thick diamond layer for smoothing and to overcome problems like time consumption and the risk of decoration at the grain boundaries of polycrystalline diamond samples Rabarot et al. developed a diamond layer

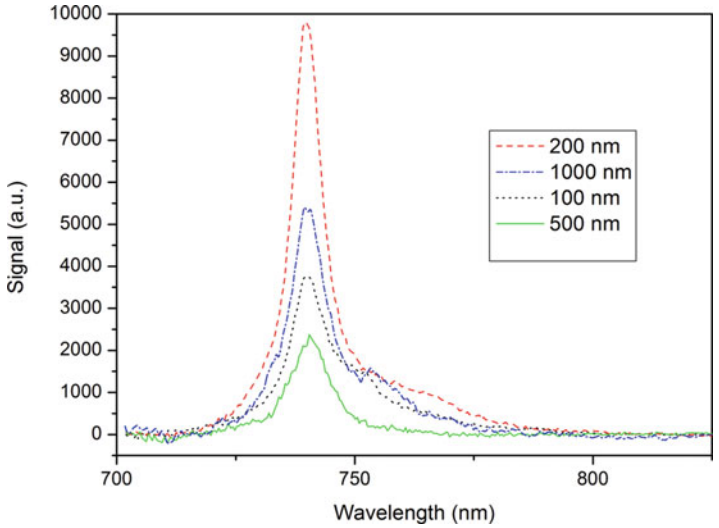

Fig. 19.17 PL signal intensity in dependence of the pillar diameter

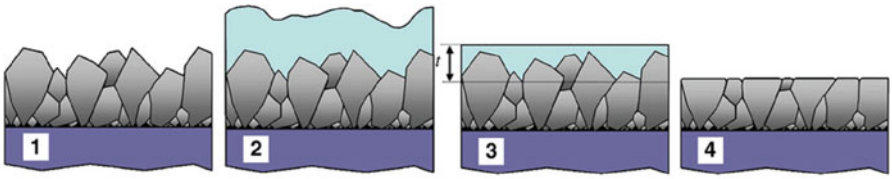

Fig. 19.18 Smoothing process of polycrystalline diamond applying deposition of SiO_2, CMP and RIE (Reprinted with permission from [66]. © 2010, Elsevier)

smoothening process called DPE (deposition, planarization, etching) including an intermediate layer of SiO_2. A thick SiO_2 layer is deposited on the diamond and smoothed by conventional CMP techniques. After that a selectively controlled reactive ion etching step (RIE) is carried out to transfer the flat surface into the diamond (Fig. 19.18) [66].

The RIE process had to be adjusted to generate an etching selectivity (S) of 1 to ensure the same etch rate of both materials, silicon dioxide and diamond. The chosen gases were oxygen (O_2) and sulphur hexafluoride (SF_6) as the first increases the etch rate of diamond, the second the etch rate of silicon dioxide (Fig. 19.19). With an etch rate of 50 nm/min Rabarot et al. achieved a surface roughness of 1.5 nm for a 200 nm thick polycrystalline diamond film [66].

To reduce the efforts for SiO_2 layer deposition and CMP another method came to the focus of interest. Checoury et al. spun hydrogen silsesquioxane (HSQ) on a NCD surface which after baking on a hot plate turned into a smooth silica-like layer on top of the diamond. The following dry etching and thus planarization process involved oxygen and argon which was adjusted to etch both, HSQ and diamond, with the

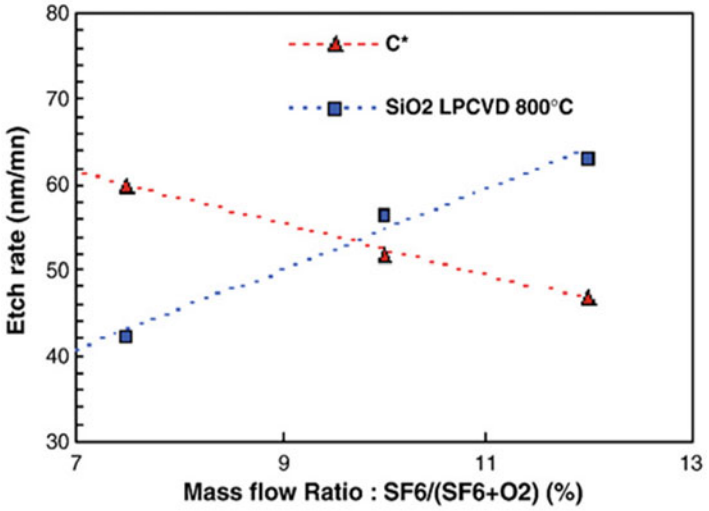

Fig. 19.19 Etch rate of RIE process using an intermediate SiO_2 layer on top of polycrystalline diamond film (Reprinted with permission from [66]. © 2010, Elsevier)

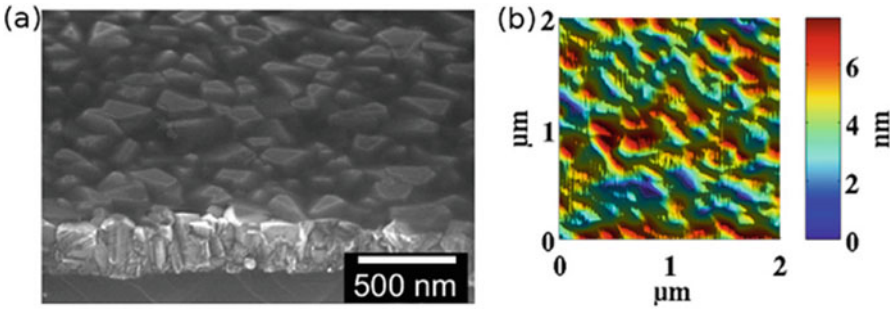

Fig. 19.20 Planarized NCD surface: (**a**) SEM micrograph, (**b**) AFM image (Reprinted with permission from [51]. © 2012, AIP Publishing LLC)

same speed. After the etching process residual silica was removed with hydrofluoric acid. The root mean square (rms) roughness dropped from around 10 nm for the as-grown layer to 1.6 nm (Fig. 19.20) [51].

Due to the relatively high price of HSQ another method was recently developed in our group. NN120-20 from durXtreme is a spin-on-dielectric or spin-on-glass (SOG) (20 wt% perhydropolysilazane (PHPS) in n-dibutylether) which should possess similar properties as HSQ. PHPS can be thermally hardened turning the liquid film into a SiO_x layer. The spin-coating parameters were chosen to obtain a smooth film covering all diamond crystallites (Fig. 19.21). After hardening of the SOG the sample was etched in a SF_6/O_2 plasma using a recipe with a gas flux comparable to the one given in literature [66] after adjusting the RF and ICP

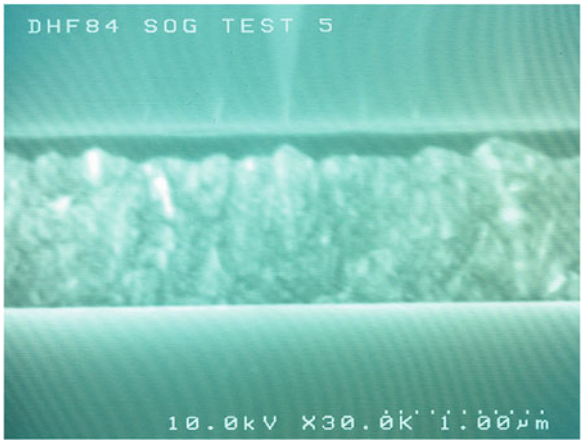

Fig. 19.21 NCD film completely covered with SOG using 6000 rpm. The charging of the film can be seen

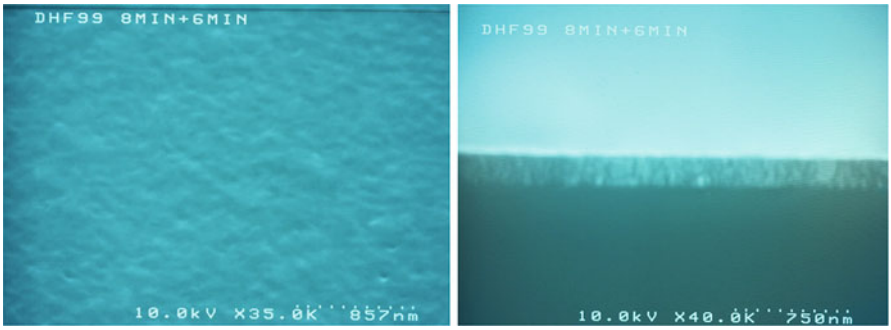

Fig. 19.22 SEM images of planarized NCD surfaces: (left) 45° view, (right) cross-section

powers. The residual SOG was removed with buffered HF; the resulting planarized NCD surfaces were flat and smooth (Fig. 19.22).

The minimum roughness which can be achieved is limited by the initial roughness of the SOG layer on top of the NCD film. Therefore, AFM images were taken before (i.e. from as-grown NCD film) and after the coating with SOG and the baking procedure. In Fig. 19.23 (right) it can be seen that there are no sharp edges or facets that bulk out the SOG layer, although one could imagine the crystallites underneath. With a peak to peak height of 16 nm and a rms roughness of around 2 nm of the SOG coating the transfer of this topography onto the NCD surface would be a huge improvement.

Different etch times were tested to prevent under- or over-etching of SOG or NCD. An etch time of 8 min decreased the rms roughness from 23 to 14 nm (Fig. 19.24 (left)). This improvement is not sufficient; therefore a second planarization step was carried out on the same sample. Starting again with spin coating and baking the SOG, the next ICP etch step needed again some adjustment regarding the etch time. Another 8 min led to the destruction of the film, because the

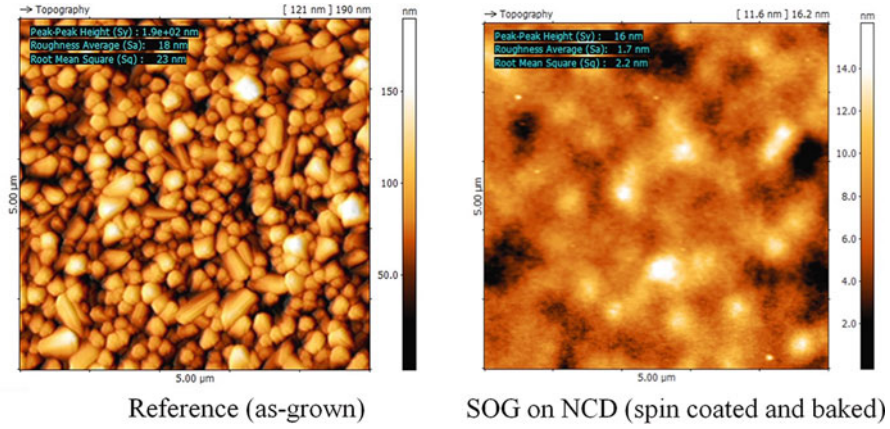

Fig. 19.23 AFM images of as-grown NCD (left) and of a NCD surface covered with a baked SOG layer (right)

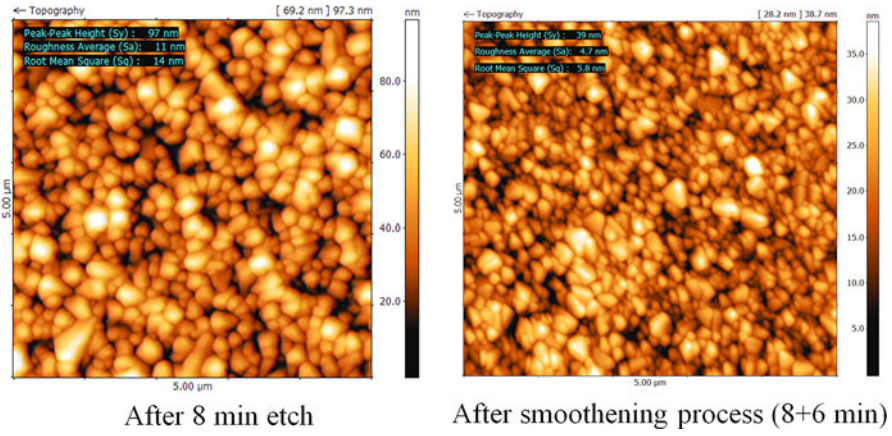

Fig. 19.24 AFM images after the first etch step of 8 min (left) and after the complete planarization process (right)

smoothening process is accompanied by a film thickness reduction due to material removal. An etch time of 6 min for the second process seems to be adequate and resulted in a rms roughness of around 6 nm (Fig. 19.24 (right)).

The evaluation of the film thickness revealed a reduction from 600 nm to around 250 nm which is in the range of thicknesses of the diamond membrane required for photonic crystals. First attempts were made to create photonic crystal slabs with this planarization procedure employing geometric parameters (hole diameters, period, slab thickness) determined by simulations. The testing of different mask materials such as Al and SiO_2 (Fig. 19.25) as well as the optimization of the process parameters are still ongoing.

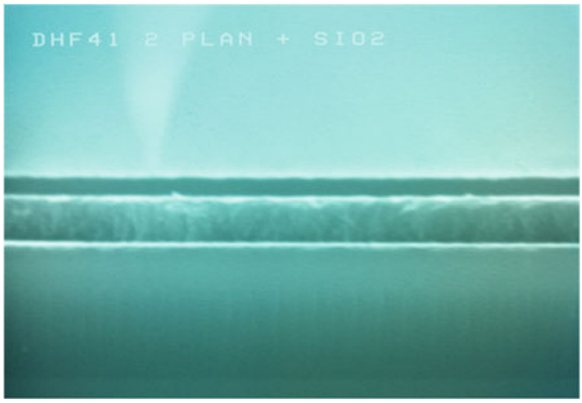

Fig. 19.25 Planarized NCD film with 150 nm SiO_2 on top (as a mask) for the fabrication of diamond photonic crystals

19.8 Summary

We presented the attractive properties of color centers in diamond, namely NV and SiV color centers and their possible applications in quantum information technology and sensing. The creation of the color centers was demonstrated using in situ doping and implantation into different diamond types, namely NCD and monocrystalline diamond. The successful fabrication of various photonic structures with a focus on nanopillar arrays was performed by EBL and dry etching. The developed planarization process will improve the optical characteristics of these structures and will be applied also to the fabrication of photonic crystals.

Acknowledgements The authors would like to acknowledge the financial support of the German Federal Ministry of Education and Research (BMBF) under the Program "Quantum Communication" (Project Q.com-H). They are grateful to Johannes Lang for the ion implantation.

References

1. Field JE (ed) (1992) The properties of natural and synthetic diamond. Academic, London
2. May PW (2000) Diamond thin films. Philos Trans R Soc A: Math Phys Eng Sci 358:473
3. Aharonovich I, Castelletto S, Simpson DA, Su C-H, Greentree AD, Prawer S (2011) Diamond-based single-photon emitters. Rep Prog Phys 74:76501
4. Bundy FP (1962) Direct conversion of graphite to diamond in static pressure apparatus Science (New York, NY) 137:1057
5. Abbaschian R, Zhu H, Clarke C (2005) High pressure–high temperature growth of diamond crystals using split sphere apparatus. Diam Relat Mater 14:1916
6. Celii FG, Butler JE (1991) Diamond chemical vapor deposition. Annu Rev Phys Chem 42:643
7. Butler JE (2003) The electrochemical society
8. Williams OA (2011) Nanocrystalline diamond. Diam Relat Mater 20:621
9. Varga M, Ižák T, Kromka A, Veselý M, Hruška K, Michalka M (2012) Open Phys 10
10. Shenderova O, Hens S, McGuire G (2010) Seeding slurries based on detonation nanodiamond in DMSO. Diam Relat Mater 19:260

11. Kulisch W, Ackermann L, Sobisch B (1996) On the mechanisms of bias enhanced nucleation of diamond. Phys Status Solidi A 154:155
12. Ali M, Ürgen M (2012) Diamond films grown without seeding treatment and bias by hot-filament CVD system. Solid State Sci 14:540
13. Nad S, Gu Y, Asmussen J (2015) Growth strategies for large and high quality single crystal diamond substrates. Diam Relat Mater 60:26
14. Gracio JJ, Fan QH, Madaleno JC (2010) Diamond growth by chemical vapour deposition. J Phys D Appl Phys 43:374017
15. Williams OA, Nesládek M (2006) Growth and properties of nanocrystalline diamond films. Phys Status Solidi A 203:3375
16. Okada K (2016) Plasma-enhanced chemical vapor deposition of nanocrystalline diamond. Sci Technol Adv Mater 8:624
17. Johnson S, Dolan PR, Smith JM (2017) Progress in quantum electronics
18. Dannefaer S (2007) Defects in diamond. Phys Status Solidi C 4:3605
19. Mainwood A (1994) Nitrogen and nitrogen-vacancy complexes and their formation in diamond. Phys Rev B 49:7934
20. Aharonovich I, Neu E (2014) Diamond nanophotonics. Adv Opt Mater 2:911
21. Zaitsev A (2001) Optical properties of diamond. A data handbook. Springer, Berlin/Heidelberg
22. Jelezko F, Wrachtrup J (2006) Single defect centres in diamond. Phys Status Solidi A 203:3207
23. Burkard G (2014) Diamond spins shining bright. Physics 7:771
24. Iakoubovskii K, Adriaenssens GJ, Dogadkin NN, Shiryaev AA (2001) Optical characterization of some irradiation-induced centers in diamond. Diam Relat Mater 10:18
25. Leifgen M, Schröder T, Gädeke F, Riemann R, Métillon V, Neu E, Hepp C, Arend C, Becher C, Lauritsen K, Benson O (2014) Evaluation of nitrogen- and silicon-vacancy defect centres as single photon sources in quantum key distribution. New J Phys 16:23021
26. Doherty MW, Manson NB, Delaney P, Jelezko F, Wrachtrup J, Hollenberg LCL (2013) The nitrogen-vacancy colour centre in diamond. Phys Rep 528:1
27. Fraczek E, Savitski VG, Dale M, Breeze BG, Diggle P, Markham M, Bennett A, Dhillon H, Newton ME, Kemp AJ (2017) Laser spectroscopy of NV and NV colour centres in synthetic diamond. Opt Mater Express 7:2571
28. Neumann P, Kolesov R, Jacques V, Beck J, Tisler J, Batalov A, Rogers L, Manson NB, Balasubramanian G, Jelezko F, Wrachtrup J (2009) Excited-state spectroscopy of single NV defects in diamond using optically detected magnetic resonance. New J Phys 11:13017
29. Barjon J, Rzepka E, Jomard F, Laroche J-M, Ballutaud D, Kociniewski T, Chevallier J (2005) Silicon incorporation in CVD diamond layers. Phys Status Solidi A 202:2177
30. Ruan J, Choyke WJ, Partlow WD (1991) Si impurity in chemical vapor deposited diamond films. Appl Phys Lett 58:295
31. Edmonds AM, Newton ME, Martineau PM, Twitchen DJ, Williams SD (2008) Electron paramagnetic resonance studies of silicon-related defects in diamond. Phys Rev B 77:1078
32. Muller T, Hepp C, Pingault B, Neu E, Gsell S, Schreck M, Sternschulte H, Steinmuller-Nethl D, Becher C, Atature M (2014) Optical signatures of silicon-vacancy spins in diamond. Nat Commun 5:3328
33. Wang C, Kurtsiefer C, Weinfurter H, Burchard B (2006) Single photon emission from SiV centres in diamond produced by ion implantation. J Phys B Atomic Mol Phys 39:37
34. Feng T, Schwartz BD (1993) Characteristics and origin of the 1.681 eV luminescence center in chemical-vapor-deposited diamond films. J Appl Phys 73:1415
35. Davies G, Hamer MF (1976) Optical Studies of the 1.945 eV vibronic band in diamond. Proc R Soc A: Math Phys Eng Sci 348:285
36. Aharonovich I, Santori C, Fairchild BA, Orwa J, Ganesan K, K-MC F, Beausoleil RG, Greentree AD, Prawer S (2009) Producing optimized ensembles of nitrogen-vacancy color centers for quantum information applications. J Appl Phys 106:124904

37. Waldermann FC, Olivero P, Nunn J, Surmacz K, Wang ZY, Jaksch D, Taylor RA, Walmsley IA, Draganski M, Reichart P, Greentree AD, Jamieson DN, Prawer S (2007) Creating diamond color centers for quantum optical applications. Diam Relat Mater 16:1887
38. Schwartz J, Aloni S, Ogletree DF, Tomut M, Bender M, Severin D, Trautmann C, Rangelow IW, Schenkel T (2014) Local formation of nitrogen-vacancy centers in diamond by swift heavy ions. J Appl Phys 116:214107
39. Spinicelli P, Dréau A, Rondin L, Silva F, Achard J, Xavier S, Bansropun S, Debuisschert T, Pezzagna S, Meijer J, Jacques V, Roch J-F (2011) Engineered arrays of nitrogen-vacancy color centers in diamond based on implantation of CN− molecules through nanoapertures. New J Phys 13:25014
40. Meijer J, Pezzagna S, Vogel T, Burchard B, Bukow HH, Rangelow IW, Sarov Y, Wiggers H, Plümel I, Jelezko F, Wrachtrup J, Schmidt-Kaler F, Schnitzler W, Singer K (2008) Towards the implanting of ions and positioning of nanoparticles with nm spatial resolution. Appl Phys A Mater Sci Process 91:567
41. Riedrich-Möller J, Pezzagna S, Meijer J, Pauly C, Mücklich F, Markham M, Edmonds AM, Becher C (2015) Nanoimplantation and purcell enhancement of single nitrogen-vacancy centers in photonic crystal cavities in diamond. Appl Phys Lett 106:221103
42. Petkov E, Rendler T, Petkov C, Schnabel F, Reithmaier JP, Wrachtrup J, Popov C, Kulisch W (2013) Investigation of NV centers in nanoand ultrananocrystalline diamond pillars. Phys Status Solidi A 210:2066
43. Rabeau JR, Stacey A, Rabeau A, Prawer S, Jelezko F, Mirza I, Wrachtrup J (2007) Single nitrogen vacancy centers in chemical vapor deposited diamond nanocrystals. Nano Lett 7:3433
44. Ohno K, Joseph Heremans F, Bassett LC, Myers BA, Toyli DM, Bleszynski Jayich AC, Palmstrøm CJ, Awschalom DD (2012) Engineering shallow spins in diamond with nitrogen delta-doping. Appl Phys Lett 101:82413
45. Bolshakov A et al (2015) Photoluminescence of SiV centers in single crystal CVD diamond in situ doped with Si from silane. Phys Status Solidi A 212:2525
46. Sedov VS, Ralchenko VG, Vlasov II, Kalinichenko YI, Khomich AA, Savin SS, Konov VI (2014) Photoluminescence of Si-vacancy color centers in diamond films grown in microwave plasma in methane-hydrogen-silane mixtures. Bull Lebedev Phys Inst 41:359
47. Hausmann BJM et al (2010) Fabrication of diamond nanowires for quantum information processing applications. Diam Relat Mater 19:621
48. Arend C, Appel P, Becker JN, Schmidt M, Fischer M, Gsell S, Schreck M, Becher C, Maletinsky P, Neu E (2016) Site selective growth of heteroepitaxial diamond nanoislands containing single SiV centers. Appl Phys Lett 108:63111
49. Wang CF, Hanson R, Awschalom DD, Hu EL, Feygelson T, Yang J, Butler JE (2007) Fabrication and characterization of two-dimensional photonic crystal microcavities in nanocrystalline diamond. Appl Phys Lett 91:201112
50. Bayn I et al (2011) Processing of photonic crystal nanocavity for quantum information in diamond. Diam Relat Mater 20:937
51. Checoury X, Néel D, Boucaud P, Gesset C, Girard H, Saada S, Bergonzo P (2012) Nanocrystalline diamond photonics platform with high quality factor photonic crystal cavities. Appl Phys Lett 101:171115
52. Faraon A, Barclay PE, Santori C, Fu K-MC, Beausoleil RG (2011) Resonant enhancement of the zero-phonon emission from a colour centre in a diamond cavity. Nature Photon 5:301
53. Hiscocks MP, Ganesan K, Gibson BC, Huntington ST, Ladouceur F, Prawer S (2008) Diamond waveguides fabricated by reactive ion etching. Opt Express 16:19512
54. Choi HW, Gu E, Liu C, Griffin C, Girkin JM, Watson IM, Dawson MD (2005) Fabrication of natural diamond microlenses by plasma etching. J Vac Sci Technol B 23:130
55. Li L, Chen EH, Zheng J, Mouradian SL, Dolde F, Schröder T, Karaveli S, Markham ML, Twitchen DJ, Englund D (2015) Efficient photon collection from a nitrogen vacancy center in a circular bullseye grating. Nano Lett 15:1493

56. Wei M, Terashima C, Lv M, Fujishima A, Gu Z-Z (2009) Chemical communications. Cambridge, UK, p 3624
57. Nebel CE, Yang N, Uetsuka H, Osawa E, Tokuda N, Williams O (2009) Diamond nano-wires, a new approach towards next generation electrochemical gene sensor platforms. Diam Relat Mater 18:910
58. Ando Y, Nishibayashi Y, Sawabe A (2004) 'Nano-rods' of single crystalline diamond. Diam Relat Mater 13:633
59. Zou YS, Chong YM, Ji AL, Yang Y, Ye Q, He B, Zhang WJ, Bello I, Lee ST (2009) The fabrication of cubic boron nitride nanocone and nanopillar arrays via reactive ion etching, Nanotechnology. Nanotechnology 20:155305
60. Zhang WJ, Wu Y, Wong WK, Meng XM, Chan CY, Bello I, Lifshitz Y, Lee ST (2003) Structuring nanodiamond cone arrays for improved field emission. Appl Phys Lett 83:3365
61. Petkov E (2014) Fabrication of diamond nanostructures and investigation of the imbedded NV centers. Dissertation, Kassel
62. Evtimova J, Kulisch W, Petkov C, Petkov E, Schnabel F, Reithmaier JP, Popov C (2013) Reactive ion etching of nanocrystalline diamond for the fabrication of one-dimensional nanopillars. Diam Relat Mater 36:58
63. Ren L, Chen B (2004) Proximity effect in electron beam lithography. In: Huang R (ed) Proceedings/7th international conference on solid-state and integrated circuits technology, 18–21 October 2004, [Beijing, China]. IEEE Press, Piscataway
64. Bergman L, McClure MT, Glass JT, Nemanich RJ (1994) The origin of the broadband luminescence and the effect of nitrogen doping on the optical properties of diamond films. J Appl Phys 76:3020
65. Felgen N, Naydenov B, Turner S, Jelezko F, Reithmaier JP, Popov C (2016) Incorporation and study of SiV centers in diamond nanopillars. Diam Relat Mater 64:64
66. Rabarot M et al (2010) Silicon-on-diamond layer integration by wafer bonding technology. Diam Relat Mater 19:796

Chapter 20
Experimental Study of Spectral Parameters of Silicon-Vacancy Centers in MWCVD Nanodiamond Films Important for Sensing Applications

L. Himics, M. Veres, S. Tóth, I. Rigó, and M. Koós

Abstract Microwave enhanced chemical vapor deposition (MWCVD) was used to prepare nanodiamond (ND) films with different process parameters containing silicon-vacancy (SiV) centers. The effect of the local environment on the spectral parameters of SiV center's zero phonon line emission, like peak position and full width at half maximum (FWHM), being important for many applications, have been studied in films having different morphological and structural properties. Relationships between the residual internal stress of the nanodiamond films and the emission parameters of the SiV centers were found and explained by shifting of the electronic levels of ground and excited states of individual SiV centers within the probed SiV ensembles due to the internal stress.

Keywords Silicon-vacancy center · Nanodiamond · Spectral parameters of ZPL · Photoluminescence

20.1 Introduction

Optically active defects or so-called color centers in nanosized diamond constitute an intensively investigated field of research nowadays. Among them the SiV center is a promising candidate for utilization in different fields like nanosensors, quantum computing and cryptography, nanoscopy, medicine or cell biology [1–3]. Most of the mentioned applications are based on the excellent light emission properties of the SiV defect. This center has a narrow zero-phonon line (ZPL) in the near infrared region around 1.68 eV (738 nm); it is a single-photon emitter and has a low electron-phonon coupling, even at room temperatures [4–6]. Many applications require well detectable (separated from the background) and indistinguishable photons, which

L. Himics (✉) · M. Veres · S. Tóth · I. Rigó · M. Koós
Wigner Research Centre for Physics, Hungarian Academy of Sciences, Budapest, Hungary
e-mail: himics.laszlo@wigner.mta.hu

P. Petkov et al. (eds.), *Advanced Nanotechnologies for Detection and Defence against CBRN Agents*, NATO Science for Peace and Security Series B: Physics and Biophysics, https://doi.org/10.1007/978-94-024-1298-7_20

means that each individual center should emit at the same frequency; for special applications a fine tuning of the emission properties is necessary. Thus a study of the effect of deposition parameters and thereby the local environment of the SiV centers on the emission properties is essential and it can offer an effective tool for tailoring the light emission characteristics of the color centers.

In this work we investigated the behavior of the 1.68 eV SiV photoluminescence (PL) emission line in different nanodiamond films prepared by changing the MWCVD deposition parameters (H_2/CH_4 ratio and substrate temperature). The properties of the ND films were characterized by micro-local residual stress obtained from Raman spectra, while spectral parameters of the SiV ZPL were determined from photoluminescence measurements. Correlations between the ZPL parameters and the local stress were found.

20.2 Experimental Details

Nanocrystalline diamond films were grown from a CH_4/H_2 gas mixture by the MWCVD technique at 1200 W microwave power and a frequency of 2.45 GHz. Silicon wafers served as substrate material; bias enhanced nucleation on the substrate surface was performed at 4% methane and 200 V bias voltage for 30 min to form diamond nuclei. The chamber pressure was kept at 40 mbar for nucleation and growth likewise. The total gas flow rate in each case was 100 sccm. The deposition of SiV containing nanocrystalline diamond film was performed at methane concentrations of 0.2%, 0.5%, 1.0%, 1.5%, 2% and 3% of the feed gas, while the substrate temperature was kept at 650, 700, 750, 800 and 850 °C. The growth process was performed for 2 h for each sample. The layer thickness was determined by in situ laser reflection interferometry; it ranges around 200 nm.

In our experiments the source of silicon impurity atom is the silicon wafer used as substrate for the ND films. The introduction of Si atoms into the methane-hydrogen plasma is accomplished by sputtering the silicon substrate with the microwave plasma. Therefore, the deposition parameters are expected to have influence on both the formation and the local environment of the SiV centers.

A Renishaw 1000B micro-Raman spectrometer attached to a Leica DM/LM microscope was used to study the light emission properties of SiV centers and the Raman scattering properties of the ND films. The ZPL parameters of the SiV centers were determined from luminescence spectra; Raman spectra were used to monitor the ND film quality and to determine micro-local residual stresses. Spectral distribution of the emitted light was analyzed in the 700–800 nm (1.77–1.41 eV) wavelength region, while Raman spectra were measured in the 1000–2000 cm^{-1} wavenumber range, with 1 cm^{-1} spectral resolution. The photoluminescence and Raman spectra were recorded from the same excited volume; for both measurements the 488 nm line of a Spectra-Physics Ar-ion laser was used as excitation source.

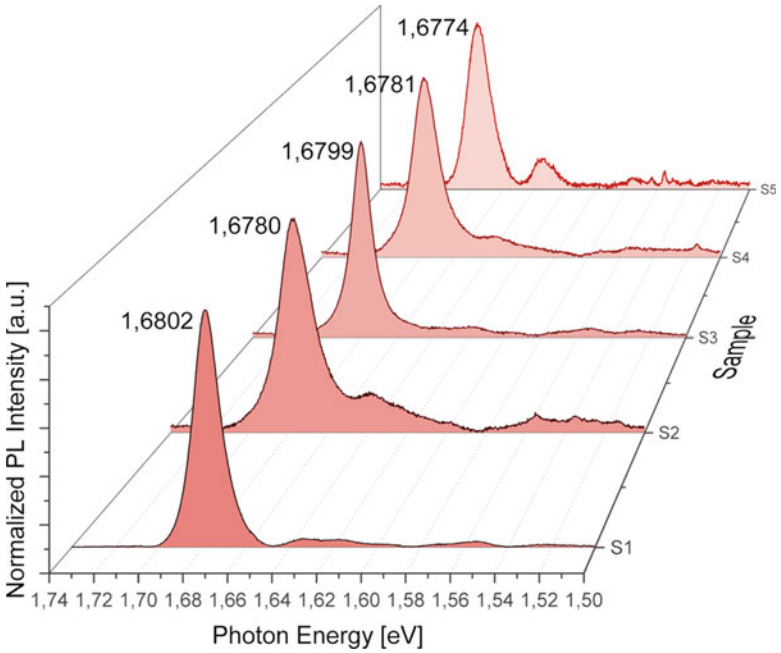

Fig. 20.1 Spectral distribution of SiV centers emission lines measured at room temperature in ND films grown at (S1) T = 700 °C and 2% CH_4, (S2) T = 750 °C and 0.2% CH_4, (S3) T = 750 °C and 3% CH_4, (S4) T = 800 °C and 1% CH_4, (S5) T = 850 °C and 0.2% CH_4

20.3 Results and Discussion

The deposition parameters of the ND films have a significant effect on the properties of the formed structures. This is especially true for the methane content of the feed gas and the substrate temperature [7, 8]. Obviously, if the deposition parameters influence the created structure, they should also affect the optically active defects located within the structure. Therefore, PL emission spectra of SiV centers have been studied in a large number of nanocrystalline diamond films deposited at different growth conditions. Some typical spectra with characteristic ZPL around 1.68 eV are shown in Fig. 20.1. These spectra were selected to demonstrate the variation of spectral shape, peak position and ZPL broadening of SiV centers in samples having distinct structural properties. The structural properties were altered by changing the deposition conditions (CH_4 content and substrate temperature). The PL spectra in Fig. 20.1 show that these parameters have a significant effect on the SiV center emission characteristics. In contrast to the line broadening, which is obviously different from sample to sample, the variation of the peak positions is not so impressive at first sight, but still detectable. A significant shift can be observed if one compares values of the peak positions determined for individual SiV containing ND films. PL scanning measurements performed on 40×40 μm^2 areas of the films

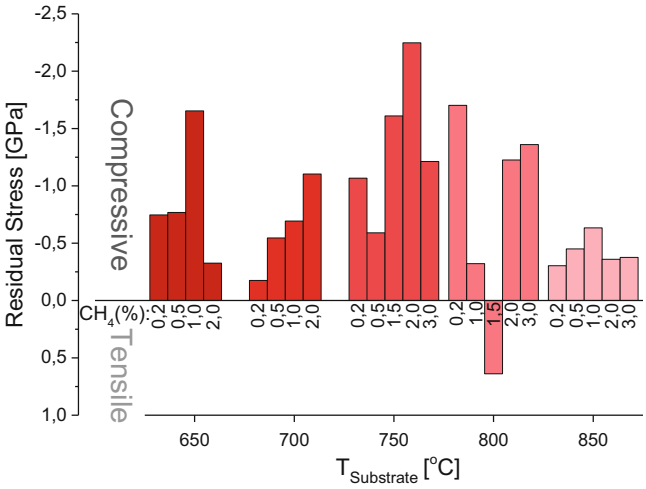

Fig. 20.2 Variation of the residual stress determined form Raman spectra in ND films containing SiV centers, grown at different substrate temperatures and CH_4 contents. The negative sign indicates a compressive, while the positive a tensile stress

showed that the peak position spread is about ~0.8 meV within one sample, which is nevertheless several times smaller than the values determined for our sample series, as will be shown later. Based on this it looks that the shift of the peak position is sample (deposition parameter) specific.

The shift and line broadening of the SiV center ZPL observed in the literature is mostly explained by stress acting in the vicinity of centers and by inhomogeneous distribution of individual SiV centers within the probed ensemble. Uniaxial stress dependence experiments performed on SiV ensembles showed that an increase of the stress magnitude causes mainly a blue shift of the ZPL [9, 10]. In contrast, recent work performed on single SiV centers states that the ZPL of individual centers is dominantly red shifted [11]. It seems to be plausible to examine the stress dependence of the SiV ZPL parameters for a large number of samples, because the results can give more insight into the behavior of the SiV ZPL parameters or even resolve contradictions reported in the literature. For this purpose we used Raman spectroscopy to determine the type and magnitude of the residual stress present within the probed sample volume from which the PL spectra of the SiV ensembles were recorded (for the details see [12]). Figure 20.2 shows the stress values measured in our samples grown at different conditions. All SiV center containing ND films exhibit compressive residual stress, except one sample, deposited at 1.5% CH_4 content and 800 °C substrate temperature, which has tensile type. The sample with highest compressive residual stress (2.25 GPa) was deposited at 750 °C substrate temperature and 2.0% methane content of the feed gas.

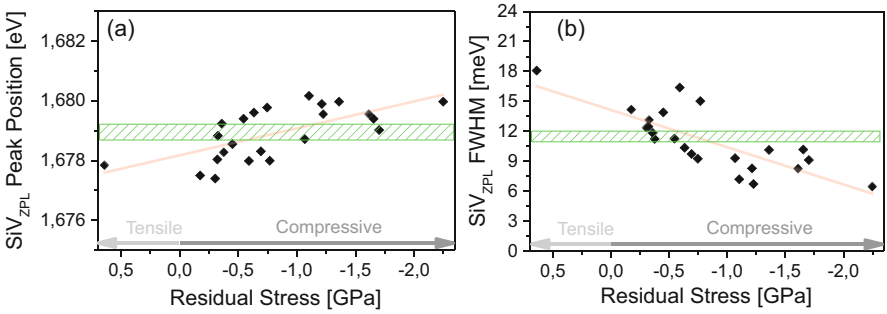

Fig. 20.3 (**a**) Peak position and (**b**) FWHM of SiV center's ZPL plotted against the estimated residual stress. Trend lines (dashed lines) are added for each plot to guide the eyes. The green rectangle shows the variation of ZPL parameters determined for one sample

Unfortunately, the Raman spectroscopy based method used to determine the type and magnitude of the stress is not able to separate and identify the different stress sources, like lattice mismatch of diamond and silicon substrate, grain boundaries and sp^2 carbon, or defect related stress sources, including optically active defects, which can be present individually or even simultaneously. However, the relatively high stress found in our samples implies that this influences the SiV centers defect structure as well, and can cause differences in the SiV ZPL characteristics.

Figure 20.3 shows the peak position and FWHM of SiV center ZPLs as a function of the estimated residual stress for all samples. Despite the variation of the values a definite tendency can be observed: increasing the residual stress from tensile to compressive type causes a blue shift of the SiV ZPL peak position. Additionally, a spectacular narrowing of the ZPL can be observed when the residual stress gradually turns from 0.75 GPa tensile to 2.25 GPa compressive type (Fig. 20.3b). The nearly threefold difference indicates a more pronounced influence of the local environment on the ZPL broadening compared to that on the peak position.

The observed phenomena can be explained by the electronic structure of the SiV center induced by stress acting on the vicinity of individual centers. It has been demonstrated that the electronic structure of the center consists of a ground (^2E_g) and an excited (^2E_u) state both having E symmetry and double orbital degeneracy [13]. The fourfold degeneracy is partially lifted by spin-orbit interactions in both the ground and the excited states [14]. The spin-orbit interaction results in four optical dipole transitions which can be well-resolved only at cryogenic temperatures. As the degree of splitting and the proportion of the four optical lines are stress and temperature sensitive, they can cause line broadening and peak position shift of the measured ZPL. High strain fields result in an increased splitting of the ground and excited electronic levels and give rise to reduced phonon occupation and suppressed relaxation [10]. This is in good accordance with our observations related to the blue shift of the peak position and the decrease of the line broadening.

20.4 Conclusions

Spectral parameters of the SiV centers were studied in a large number of ND films prepared at different deposition conditions. It was found that the deposition parameters have a significant effect on the structure of ND films containing SiV centers mainly in form of residual stress of different magnitude. Experimental results show that an increase of residual compressive stress causes a decrease of line broadening and a blue shift of the SiV ZPL. So the control of the residual stress by appropriate growth conditions allows to tailor the ZPL parameters of the SiV centers.

Acknowledgments This work was supported by the National Research, Development and Innovation Fund of Hungary with the NVKP_16-1-2016-0043 grant and the VEKOP-2.3.2-16-2016-00011 grant and by the Hungarian Science Foundation under contract number OTKA K-115805 "Complex plasmas in Action".

References

1. Aharonovich I et al (2011) Diamond-based single-photon emitters. Rep Prog Phys 74:076501
2. Fu CC et al (2007) Characterization and application of single fluorescent nanodiamonds as cellular biomarkers. Natl Acad Sci 104:727–732
3. Aharonovich I, Greentree AD, Prawer S et al (2011) Diamond photonic. Nat Photonics 5:397–405
4. Clark CD et al (1995) Silicon defects in diamond. Phys Rev B 51(23):16681–16688
5. Rogers LJ et al (2014) Electronic structure of the negatively charged silicon-vacancy center in diamond. Phys Rev B 89(23):235101
6. Zaitsev AM (2001) Optical properties of diamond. Springer, Berlin/New York
7. May PW et al (2007) Microcrystalline, nanocrystalline, and ultrananocrystalline diamond chemical vapor deposition: experiment and modeling of the factors controlling growth rate, nucleation, and crystal size. J Appl Phys 101(5):053115
8. Larson JM et al (2003) The effect of substrate temperature on the morphology of diamond films grown under acetylene-lean and acetylene-rich conditions. Diam Relat Mater 12(9):1584–1593
9. Sternschulte H et al (1995) Uniaxial stress and Zeeman splitting of the 1.681 eV optical center in a homoepitaxial CVD diamond film. Diam Relat Mater 4(10):1189–1192
10. Jahnke KD et al (2015) Electron–phonon processes of the silicon-vacancy centre in diamond. New J Phys 17(4):043011
11. Neu E et al (2011) Single photon emission from silicon-vacancy colour centres in chemical vapour deposition nano-diamonds on iridium. New J Phys 13(2):025012
12. Himics L et al (2016) Spectral properties of the zero-phonon line from ensemble of silicon–vacancy center in nanodiamond. Opt Quant Electron 48(8):394
13. Goss JP et al (1996) The twelve-line 1.682 eV luminescence center in diamond and the vacancy-silicon complex. Phys Rev Lett 77(14):3041
14. Hepp C et al (2014) Electronic structure of the silicon vacancy color center in diamond. Phys Rev Lett 112(3):036405

Chapter 21
Electrochemical Synthesis of PANI/ Graphene Nanocomposites Aimed for Sensors

Aleksandar Petrovski, Perica Paunović, Anita Grozdanov, Aleksandar T. Dimitrov, Gennaro Gentile, and Maurizio Avella

Abstract This study is concerned with the electrochemical synthesis of polyaniline (PANI) based composites reinforced by carbon nanostructures (CNSs) such as graphene. To determine the optimal conditions for electropolymerization of the aniline to PANI, an electrochemical characterization was performed by means of cyclic voltammetry, steady state polarization and galvanostatic measurements. Within the CV spectra all steps of the transformation from aniline to polyaniline were observed with corresponding potential regions. It was found that the optimal potential for electropolymerization of the PANI based nanocomposites is 0.75 V vs. saturated calomel electrode (SCE). The electropolymerization rate was observed for two ways of involving of carbon nanostructures in the polymer matrix: dispersion in the electrolyte and previous deposition at the working electrode. The produced nanocomposites were characterized by means of Scanning Electron Microscopy (SEM) and Raman Spectroscopy. Strong interaction between the quinoidal structure of PANI and carbon nanostructures were detected. Electrical properties of the nanocomposite tablets were tested using the four probe method. These measurements show the great potential of the studied materials for sensors.

Keywords Nanocomposites · PANI · Graphene · Sensors · pH

21.1 Introduction

As result of different human activities such as industry, transportation etc., the surface waters (rivers, lakes, seas, and oceans) are susceptible to pollution, which disrupts the chemical and ecological balance of the ecosystem established in them.

A. Petrovski (✉) · P. Paunović · A. Grozdanov · A. T. Dimitrov
Faculty of Technology and Metallurgy, SS Cyril and Methodius University, Rudjer Boskovic 16, Skopje 1000, Republic Macedonia

G. Gentile · M. Avella
Institute for Polymers, Composites and Biomaterials, National Research Council, Pozzuoli, Italy

P. Petkov et al. (eds.), *Advanced Nanotechnologies for Detection and Defence against CBRN Agents*, NATO Science for Peace and Security Series B: Physics and Biophysics, https://doi.org/10.1007/978-94-024-1298-7_21

Monitoring of pH changes of the surface waters is an appropriate and fast way to detect their acidification or alkalization that signalize the presence of undesirable chemicals and corresponding chemical reactions, which can move the bio-equilibrium. Application of nanocomposites based on conductive polymers and carbon nanostructures as a pH nanosensor is a very promising new approach for monitoring of pH changes, instead of the traditional methods for pH measurements (optical, electrical etc.) [1].

As result of its excellent properties (electrical, electrochemical, redox behavior, electroluminescence, environmental stability etc.), simple preparation and low cost of the precursor (aniline), PANI has been considered as one of the most promising materials among the family of the conductive polymers [2–4]. Green et al. [5], were the first who mentioned the structure of polyaniline. They proposed the octameric structure as the basic structural unit of the polymeric chain and called it leucoemeraldine (completely reduced form). The emeraldine base is the only one conductive form of polyaniline, when is converted in emeraldine salt by treating with doping acids. Due to its appropriate properties, PANI has been recognized as a suitable material for use in electronics, optical devices, energy storage devices, sensors etc. [6–8]. But there are some limitations for PANI applications, due to its poor mechanical properties and low processability.

After discovering the carbon nanostructures (CNSs) such as carbon nanotubes (CNTs) [9] and graphene [10] with extraordinary properties, one of their effective application is the reinforcing of polymers. Reinforcing of PANI with CNSs is a very appropriate approach to overcome the previous mentioned limitation for PANI applications. Because of the synergetic effect between the polymer matrix (PANI) and reinforcement (graphene), the newly formed structure posses improved properties as compared to pure PANI, but in some cases they even are better than the nanostructures [11, 12]. PANI/CNSs nanocomposites can be prepared by chemical or electrochemical polymerization [3, 13, 14]. PANI and CNSs powders can be mixed by mechanical blending, stirring or sonification.

The aim of this paper is to prepare conductive CNS/PANI nanocomposites by electrochemical polymerization, with the possibility of further sensor applications.

21.2 Experimental

Electrochemical polymerization of aniline in presence of graphene (G) was performed to obtain PANI/G nanocomposites. The electropolymerization process was performed in a standard three electrode electrochemical cell with a capacity of 250 cm^3. As working and counter electrodes, platinum tiles with a surface of 10 cm^2 were used, while a saturated calomel electrode (SCE) was used as a reference

electrode. The electrolyte contains 0.1 M aniline and 0.5 M H_2SO_4 for each experiment. The graphene (produced by molten salt electrolysis in the labs of the Faculty of Technology and Metallurgy in Skopje) were firstly modified in concentrated solution of H_2SO_4 and HNO_3 with a ratio 3:1, respectively, then purified with boiled deionized water and dried at 70 °C in air atmosphere.

Electropolymerization was conducted by dispersion of graphene in the electrolyte. Before the process starts, graphene was firstly dispersed in the electrolyte by sonification (30 min) in an ultrasonic bath. Electropolymerization was carried out at a constant potential of the working electrode of +0.75 V vs. SCE until the current reaches 110 mA. These data were determined from electrochemical measurements: cyclic voltammetry and steady-state polarization. The content of graphene was varied (1, 2 and 3 wt % wt. of the aniline).

The morphology of the nanocomposites was analyzed by means of a scanning electron microscope FEI Quanta 200 using a secondary electron detector and an acceleration voltage of 30 kV.

Using a conventional resistivity meter, pH measurements were performed in laboratory as well as field testing in marine water. Sensors were prepared by electropolymerization of PANI/G nanocomposite over commercial gold electrodes.

21.3 Results and Discussion

The curves shown in Fig. 21.1 are cyclic voltammograms of the electropolymerization of aniline in the presence of graphene. The measurements were performed at different scan rates (10, 20 50 and 100 $mV \cdot s^{-1}$).

Four oxidation peaks and the corresponding reduction peaks can be observed in the region of potential change of −0.2 to 1 V. The peak I denotes oxidation of leucoemeraldine (0) to emeraldine (1), while the peak I′ denotes the opposite transformation [15]. The redox pairs II/II′ correspond to the formation of secondary products (benzoquinone/hydroquinone) or overoxidation/degradation of PANI [15, 16], redox pair III/III′ to the transformation of p-aminophenol/benzoquinonemine [17]. The peak IV can be ascribed to oxidation of emeraldine to pernigranilline, IV′ to the opposite transformation. The working potential for electropolymerization of PANI is in this potential region between 0.65 and 0.8 V.

At the intersection of voltammograms curves with the line L (in the region of charge and discharge of electrochemical double layer), corresponding values of anodic and cathodic currents can be used to determine double layer capacity (C_{dl}) of the produced nanocomposite, using the following equation:

$$C_{\mathrm{dl}} = \frac{\mathrm{d}i_{\mathrm{cap}}}{\mathrm{d}(\partial E/\partial t)}$$

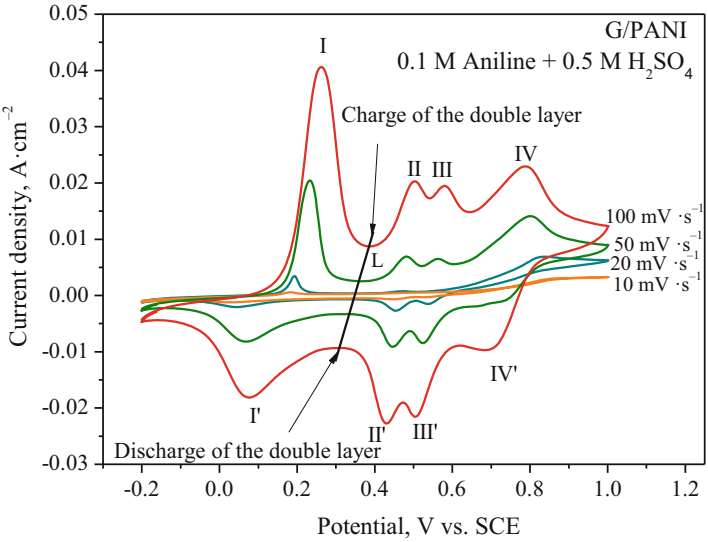

Fig. 21.1 Cyclic voltammogram of the electropolymerization of a PANI/G composite (electrolyte: 0.1 M aniline +0.5 M H_2SO_4)

The calculated value of the double layer capacity was 121 mF·cm^{-2}, which is comparable with corresponding values of some carbon nanostructures such as Vulcan XC-72 (180 mF·cm^{-2}) and MWCNTs (330 mF·cm^{-2}) [18].

For a more accurate determination of the working potential, steady-state polarization measurements were performed (Fig. 21.2). The most suitable nanocomposite with a green color which corresponds to the most conductive emeraldine salt (insert in Fig. 21.1) was obtained at 0.75 V vs. SCE [19].

The morphology of the PANI/G nanocomposite is shown in Fig. 21.3. The graphene sheets are well and uniformly wrapped with a PANI polymer matrix, which is appropriate for their strong interaction. During the deposition time of 40 min, fibrous and porous structure of PANI was formed, with fibers diameter of 75–150 nm. This is in agreement with literature data [20], which have shown that for an electropolymerization longer than 20 min, fibrous PANI was formed, instead of a granular one.

The obtained PANI/G nanocomposites were first lab tested towards their sensing activity in a simulated aqueous media in a closed pH range from pH = 7,4 to pH = 10. The resulting curves are shown in Fig. 21.4. Besides the lab testing, the obtained screen printed electrodes (SPE) were tested also in real sea water. Resistivity changes of the PANI/G nanocomposite electrodes occurred due to the different degree of protonation of the imine nitrogen atoms at the polymer chain in the presence of graphene.

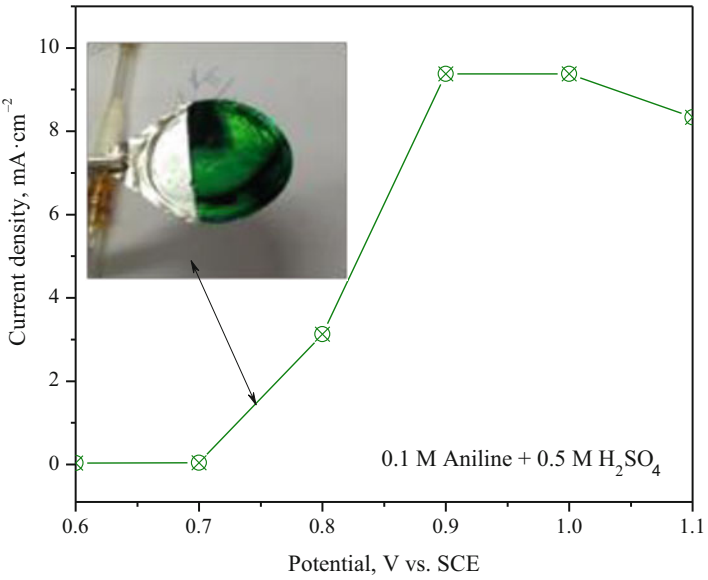

Fig. 21.2 Polarization curve of electropolymerization of PANI (electrolyte: 0.1 M aniline +0.5 M H_2SO_4)

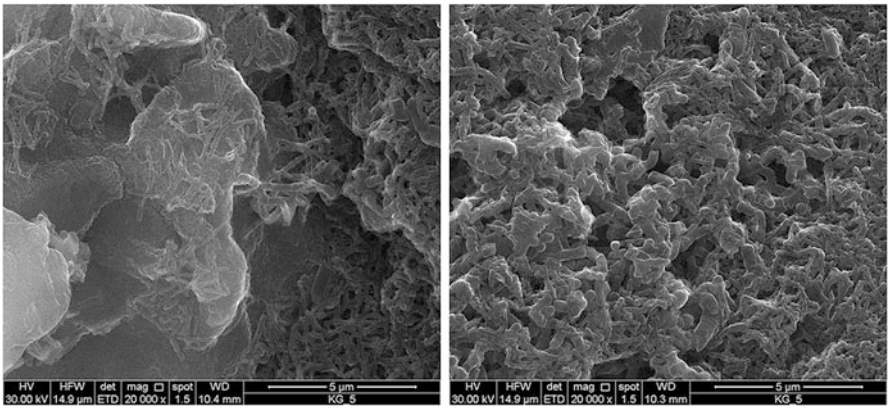

Fig. 21.3 SEM images of the PANI/G nanocomposite

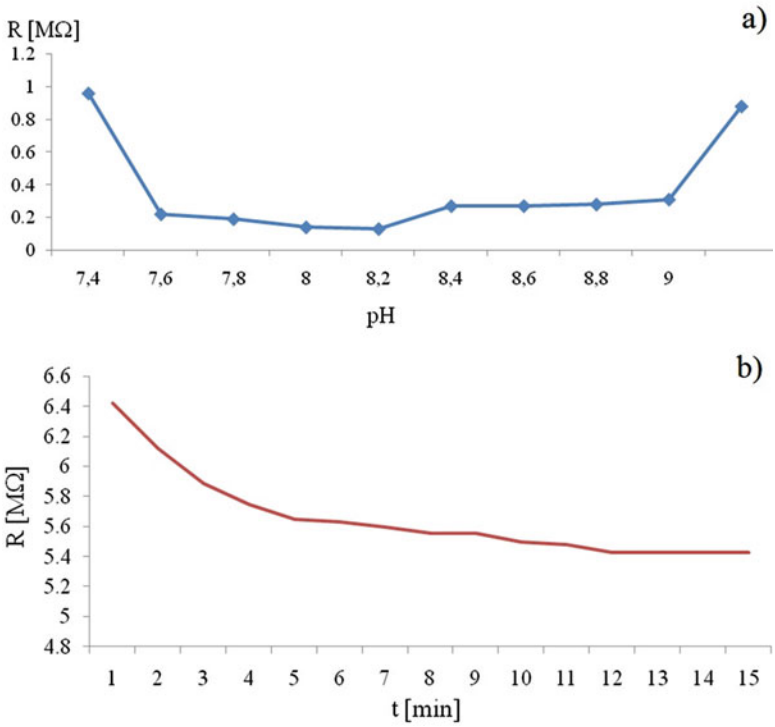

Fig. 21.4 Resistivity changes of PANI/G SPE nanosensor: (**a**) lab testing in closed pH range; (**b**) field testing curve

21.4 Conlusion

In summary, using the method of direct electropolymerization of PANI/G nanocomposites on the gold wires of SPE, pH nanosensors were produced. Characterization was done by cyclic voltammetry and SEM. pH sensitivity was tested in the lab as well as in real sea waters.

Acknowledgments This research was done within the FP7 Project "Cost-effective sensors, interoperable with international existing ocean observing systems, to meet EU policies requirements" (Project reference 614155).

References

1. Salavagione HJ, Diez-Pascual AM, Lazaro E, Vera S, Gomez-Fatou MA (2014) Chemical sensors based on polymer composites with carbon nanotubes and graphene: the role of the polymer. J Mater Chem A 2:14289

2. ZhA B, Sergeyev VG (2014) Polyaniline: synthesis, properties, and application. Polym Sci Ser C Sel Top 56:144
3. Gajendran P, Saraswathi R (2012) Polyaniline-carbon nanotube composites. Pure Appl Chem 80:2377
4. Kim WJ, Huh DS (2012) Preparation of Honeycomb-patterned Polyaniline-MWCNT/Polystyrene Composite Film and Studies on DC Conductivity. Bull Kor Chem Soc 33:2345
5. Green A, Woodhead AE (1910) Aniline-black and allied compounds. J Chem Soc 97:2388
6. MacDiarmid AG et al (1987) Polyaniline: Electrochemistry and application to rechargeable batteries. Synth Met 18:393
7. Roth S, Graupner W (1993) Conductive polymers: Evaluation of industrial applications. Synth Met 57:3623
8. Talaie A, Lee JY, Lee YK, Jang J, Romagnoli JA, Taguchi T, Maeder E (2000) Dynamic sensing using intelligent composite: an investigation to development of new pH sensors and electrochromic devices. Thin Solid Films 363:163
9. Iijima S (1991) Helical microtubules of graphitic carbon. Nature 354:56
10. Geim A, Novoselov K (2007) The rise of graphene. Nat Mater 6:183
11. Baibarac M, Romero PG (2006) Nanocomposites based on conducting polymers and carbon nanotubes: from fancy materials to functional applications. J Nanosci Nanotechnol 6:289
12. Dai L (2007) Electrochemical Sensors Based on Architectural Diversity of the π-Conjugated Structure: Recent Advancements from Conducting Polymers and Carbon Nanotubes. Aust J Chem 60:472
13. Gvozdenović MM, Jugović BZ, Stevanović JS, Trišović TLJ, Grgur BN (2011) Electrochemical polymerization of aniline (Chapter 4). In: Schab-Balcerzak E (ed) Electropolymerization. InTech, Rijeka. ISBN:978-953-307-693-5
14. Sahoo S, Karthikeyan G, Nayak GC, Das CK (2012) Modified graphene/polyaniline nanocomposites for supercapacitor application. Macromol Res 20:415
15. Mickova I, Prusi A, Grčev T, Arsov L (2006) Electrochemical polymerization of aniline in presence of TiO_2 nanoparticles. Bull Chem Technol Maced 25:45
16. Taranu BO, Fagadar-Cosma E, Popa I, Plesu N, Taranu I (2014) Adsorbed functionalized porphyrins on polyaniline modified platinum electrodes. Comparative electrochemical properties. Dig J Nanomater Biostruct 9:667
17. Gu J, Kan S, Shen Q, Kan J (2014) Effects of sulfanilic acid and anthranilic acid on electrochemical stability of Polyaniline. Int J Electrochem Sci 9:6858
18. Paunović P, Dimitrov AT, Popovski O, Slavkov D, Hadži Jordanov S (2007) Effect of carbon nanotubes support in improving the performance of mixed electrocatalysts for hydrogen evolution. Bull Chem Technol Maced 26:87
19. Petrovski A, Paunovic P, Avolio R, Errico ME, Cocca MC, Gentile G, Grozdanov A, Avella M, Barton J, Dimitrov A (2017) Synthesis and characterization of nanocomposites based on PANI and carbon nanostructures prepared by Electropolymerization. Mater Chem Phys 185:83
20. Wang H-J, Zhang P, Zhang W-G, Yao S-W (2012) Electrodeposition and characterization of polyaniline film. Chem Res Chin Univ 28:133

Chapter 22
Preparation of Metallic and Semiconducting SWCNT Inks by a Simple Chromatographic Method: A Two-Parameter Study

Ana Santidrian, Nekane Lozano, Ana M. Benito, Wolfgang K. Maser, and Alejandro Ansón-Casaos

Abstract Single-walled carbon nanotubes (SWCNTs) show either metallic or semiconducting character, and are potential candidates for the development of small electronic devices. However, commercial SWCNT materials consist of a mixture of many different SWCNT conformations and certain impurities. In this work, SWCNTs are dispersed in an aqueous medium, purified by centrifugation, and finally separated into metallic and semiconducting inks by a gel chromatography method. The separation is directly performed at ambient conditions, and the influence of the ink concentration and the chromatography column length are thoroughly evaluated. The most efficient separation, distinguishing between families of semiconducting SWCNT with different diameters, is achieved at the lowest concentration and with the longest column. These results provide a promising base for availability of SWCNTs with well-defined characteristics needed for the development of electronic devices.

Keywords Carbon nanotube · Purification · Separation · Electronic properties · Concentration · Gel chromatography

22.1 Introduction

A single-walled carbon nanotube (SWCNT) can be described as a graphene sheet that is rolled into a seamless cylinder. Since the graphene sheet can be rolled up with different angles, the possible SWCNT conformations, defined by the chiral vector *(n, m)*, are numerous. The chiral vector *(n, m)* determines their unique electronic and optical properties. Based on the electronic properties, SWCNTs can be classified into metallic and semiconducting [1]. Moreover, SWCNTs show a rich solid-state

A. Santidrian (✉) · N. Lozano · A. M. Benito · W. K. Maser · A. Ansón-Casaos
Instituto de Carboquímica ICB-CSIC, Zaragoza, Spain
e-mail: asantidrian@icb.csic.es

P. Petkov et al. (eds.), *Advanced Nanotechnologies for Detection and Defence against CBRN Agents*, NATO Science for Peace and Security Series B: Physics and Biophysics, https://doi.org/10.1007/978-94-024-1298-7_22

chemistry that is often influenced by their electronic properties [2, 3]. The characteristics of SWCNTs make them potential elements for nanoscale electronics [4–6].

The properties of SWCNTs are only observable for well-purified and individualized samples. However, SWCNT synthesis methods produce SWCNTs mixed with different amorphous and crystalline impurities such as catalyst particles, graphitic nanoparticles, and amorphous carbon. In most cases, SWCNT purification schemes involve air oxidation, acid treatments, centrifugation, filtration, etc. [7] The ultracentrifugation method has proved to be appropriate and fast for the purification of SWCNT inks. We have previously demonstrated the elimination of graphite particles, amorphous carbon and big bundles of SWCNTs by centrifugation in a surfactant [8].

Semiconducting SWCNTs find application as channels in field-effect transistors (FETs) and switches, while metallic SWCNTs could be used as conducting wires in nanoelectronic circuits. SWCNT sensor applications include resistive gas sensors [9, 10], field-effect transistor sensors for biomedical applications [11, 12] and electrochemical sensors [13, 14]. Therefore, the separation between metallic and semiconducting species is needed to improve the performance of those devices. Different approaches have been reported to achieve the separation of SWCNTs according to their electronic properties including density gradient ultracentrifugation, gel chromatography and selective polymer phase separation [15–17]. The chromatographic sorting of SWCNTs has been successfully tested as a separation method, often being a relatively complex slow process.

In this work, we study the influence of different variables in the chromatography sorting method, specifically the concentration of the starting SWCNT dispersion and the column length. In this way, aqueous SWCNT dispersions were ultracentrifugated and passed through a Sephacryl gel chromatography column. The resulting sorted SWCNT fractions were characterized by optical absorption and Raman spectroscopy in the aqueous phase. The relevance of this work is the understanding of the parameters involved in the gel chromatography separation in order to optimize the method and find the conditions for a large-scale process. In addition, we aim to keep the process in a relatively simple procedure.

22.2 Experimental

22.2.1 Materials

SWCNTs were purchased from Nanointegris Inc. Boisbriand, Quebec, Canada. The material is produced by the HiPco method and contains a residual mass of <35% from thermogravimetric analysis. The SWCNTs have diameters of 0.8–1.2 nm and lengths of 100–1000 nm, according to the provider. Sodium dodecyl sulfate (SDS) $\geq$98.5% was purchased from Sigma-Aldrich. Sephacryl gel (s-200, GE Healthcare) was used for SWCNT chromatographic sorting.

22.2.2 *Purification and Sorting*

The experimental procedure for purification and sorting consisted of three steps: dispersion, centrifugation and chromatographic separation. In a typical experiment, SWCNTs were tip-sonicated for 1 h in 10 mL of a 0.5% SDS aqueous solution. Different concentrations of the SWCNT initial dispersion were investigated: 2, 1, 0.5, 0.25 mg/mL. To avoid heating, the vial was kept in an ice bath during ultrasonication. Then, the dispersion was purified by ultracentrifugation at 200.000 × g for 1 h, removing residual catalyst particles, amorphous carbon, and big tube bundles [18]. Once the SWCNTs are individualized and purified, Sephacryl gel was used to sort metallic and semiconducting SWCNTs. Briefly, 3 mL of the SWCNT purified dispersion was allowed to pass through a plastic syringe containing the gel column at room temperature and pressure. Two different column lengths, 5 and 10 cm, were investigated, using a column diameter of 1.35 cm. Elution was done using sequentially 3 mL of 0.5%, 1%, 2% and 4% SDS, and the different fractions were collected [19].

The collected fractions were characterized by optical absorption and Raman spectroscopy. UV-Vis-NIR spectra of the dispersions were measured in 2 mL quartz cuvettes of 1 cm optical path. Raman spectra measurements were acquired using a LabRAM HR Raman spectrometer (Horiba Jobin-Yvon), and laser excitation energies of 2.33 eV and 1.58 eV.

22.3 Results and Discussion

Figure 22.1a shows a schematic diagram of a single chromatographic process consisting of only two elution stages. Specifically, 3 mL of 0.5% and 2% SDS were subsequently passed through a 5 cm column to obtain two fractions: Fr. I and Fr. II, respectively. The colors of the two fractions were different, reddish and blueish (Fig. 22.1b).

To determine the compositions of the SWCNT fractions, we measured the optical absorption spectra of the dispersions using both UV-Vis-NIR and Raman spectrophotometers. The optical absorption spectra (Fig. 22.1c) confirm the separation efficiency. While the starting SWCNTs present peaks of both semiconducting and metallic electronic transitions, the fractions Fr. I and Fr. II present predominant peaks in the region of metallic (E^{M}_{ii}) and semiconducting (E^{S}_{ii}) electronic transitions, respectively. Therefore, the Fr. I was enriched in metallic SWCNTs, and the Fr. II enriched in semiconducting SWCNTs. In the analysis of the Raman spectra we focus on one of the main SWCNT features, the so-called radial breathing modes (RBMs). The RBMs are observed between 100 and 300 cm^{-1}, where all atoms of the tube vibrate radially in phase with diameter-dependent energies [1]. Spectra in the RBM region were deconvoluted into Lorentzian line-shapes (Fig. 22.2).

The positions of the most intense RBM bands were first studied in the starting HiPco SWCNT dispersion for two laser energies (Fig. 22.2). The diameters of the

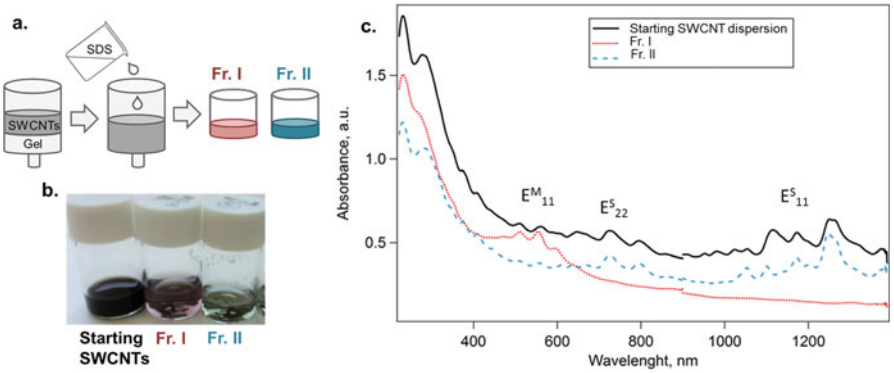

Fig. 22.1 (**a**) Schematic diagram of the SWCNT chromatographic separation with two elution stages. (**b**) Photograph of the starting SWCNT dispersion and the two collected fractions. (**c**) Optical absorption spectra of the starting SWCNT dispersion (black line) and the collected SWCNT fractions: Fr. I (red dotted line) and Fr. II (blue dashed line)

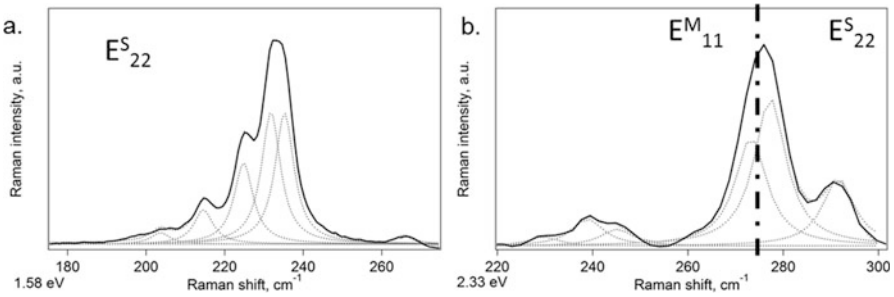

Fig. 22.2 Raman spectra in the RBM region measured on the starting SWCNT dispersion (black line) and excited by (**a**) 1.58 eV and (**b**) 2.33 eV laser energies. The RBMs are fitted with Lorentzian line-shapes. The dotted grey curves correspond to the fitted components and to the sum of them

SWCNTs in resonance were calculated from the RBM frequency values. The transition energies (denoted as E_{ii}), as well as the (n, m) index, were assigned using the Kataura plot (Table 22.1) [20, 21].

The fractions collected from the chromatography columns were also characterized by Raman spectroscopy (Fig. 22.3). The Raman spectroscopy results show that the former fraction (Fr. I) is enriched in SWCNTs in resonance *via* $E_{11}{}^M$ transitions and the latter fraction (Fr. II) mainly contains SWCNTs in resonance *via* $E_{22}{}^S$ transitions.

So far, it is evident that the SWCNT adsorption to the gel is critically influenced by the surfactant concentration; the results show that the technique effectively separates the SWCNTs between metallic and semiconducting. Now, we will study 2 process variables in the separation of SWCNTs by gel chromatography: the effect of the starting HiPco SWCNT dispersion concentration and the chromatography column length effect. Figure 22.4a shows the schematic diagram of the loading process and the

Table 22.1 Diameter distribution of the starting SWCNT dispersion calculated from the Raman RBM frequencies (ω_{RBM})

E_{laser} (eV)	ω_{RBM} (cm^{-1})	d_t (nm)	Index (n, m)	E_{ii}
1.58	204	1.2	(12, 5)	E_{22}^{S}
	215	1.15	(9, 7)	
	225	1.05	(10, 5)	
	232	1.01	(11, 3)	
	235	0.99	(12, 1)	
	267	0.92	(12, 0)	
2.33	230	1.07	(12, 1)	E_{11}^{M}
	240	1.03	(9, 6)	
	245	0.9	(10, 4)	
	274	0.85	(9, 3)	
	278	0.82	(10, 0)	E_{22}^{S}
	290	0.79	(9, 2)	

Fittings were performed with Lorentzian line-shapes. The Kataura plot was used for the assignment of the electronic transitions

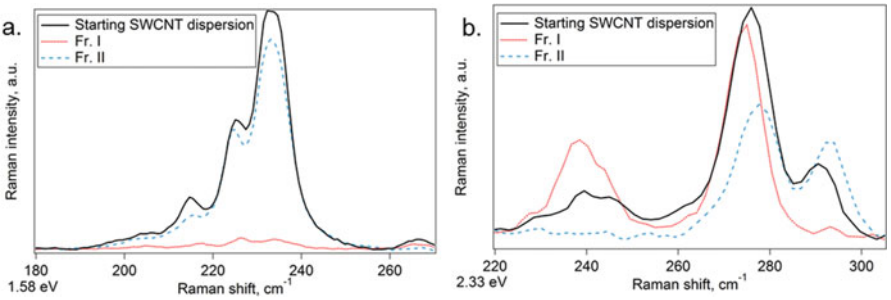

Fig. 22.3 Raman spectra in the RBM region measured on the starting SWCNT dispersion (black line), Fr. I (red dotted line) and Fr. II (blue dashed line) excited by (**a**) 1.58 eV and (**b**) 2.33 eV

fractions obtained after the separation. A volume of 3 mL of 0.5%, 1%, 2% and 4% SDS was subsequently added to obtain Fr. 1, Fr. 2, Fr. 3 and Fr. 4, respectively.

The efficiency of the gel-chromatography columns was semi-quantitatively evaluated from absorbance spectroscopy data. Each spectral band was evaluated following a practical procedure similar to that proposed by Itkis et al. [22]The procedure is based on the calculation of a normalized peak area, as it is explained in Fig. 22.5.

The value ratio A_p/A_t % was calculated by integrating the areas under the curves for the spectra as in Fig. 22.5 and applying the expression

$$ {}^{A_{p,i}}\!/_{A_{t,i}}\% = \left(\frac{{}^{A_{p,i}}\!/_{A_{t,i}}}{\sum_{i=1}^{4} {}^{A_{p,i}}\!/_{A_{t,i}}} \right) \cdot 100 \qquad (22.1) $$

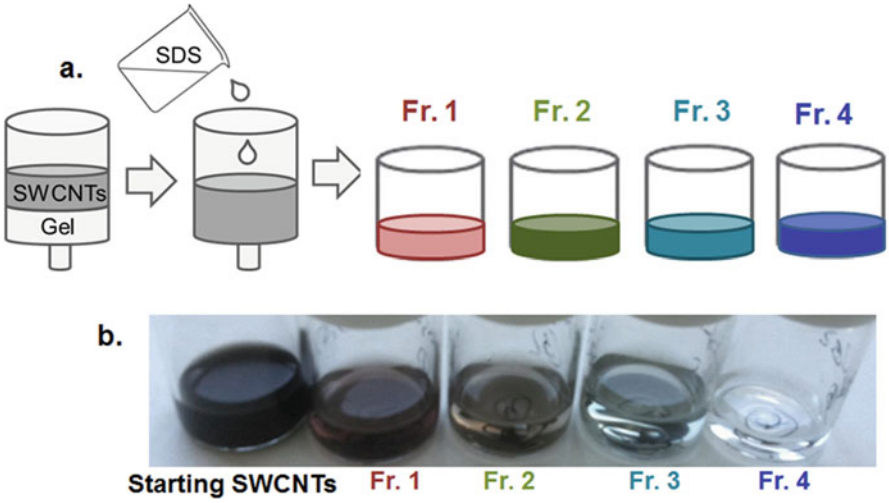

Fig. 22.4 (**a**) Schematic diagram of the SWCNT chromatographic separation with four elution stages. (**b**) Photograph of the starting SWCNT dispersion and the four collected fractions

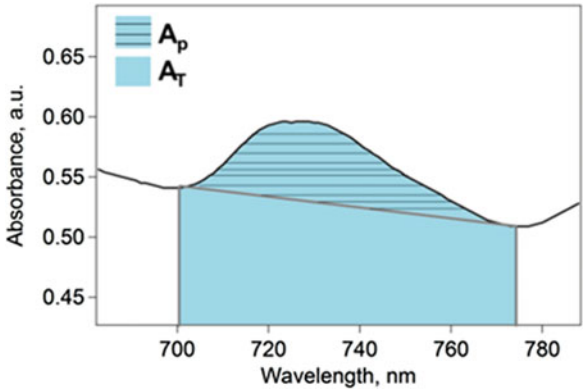

Fig. 22.5 Schematic illustration of one optical absorption band in a typical SWCNT sample. It aims to illustrate the calculation of the normalized area

where $A_{p,i}$ and $A_{t,i}$ are the areas under each band of the spectra as given in Fig. 22.5 (i denotes the band at 555 ($d_t = 0.96$ nm), 646 ($d_t = 0.90$ nm), 733 ($d_t = 0.98$ nm) and 795 nm ($d_t = 1.10$ nm)).

The top part of Fig. 22.6 shows the absorbance spectra of the collected fractions Fr. 1, Fr. 2, Fr. 3 and Fr. 4, using different starting HiPco SWCNT concentrations. The normalized coefficients A_p/A_t of the peaks at 555 ($d_t = 0.96$ nm), 646 ($d_t = 0.90$ nm), 733 ($d_t = 0.98$ nm) and 795 nm ($d_t = 1.10$ nm) are shown for all collected fractions.

In the absorbance spectra presented in Fig. 22.6, the region marked in grey is assigned to metallic SWCNTs being in resonance with the first optical transition energy E_{11}^M and represent the band at 555 nm that corresponds to a diameter distribution of 0.96 nm. The orange, purple and yellow regions represent the tubes excited via the E_{22}^S

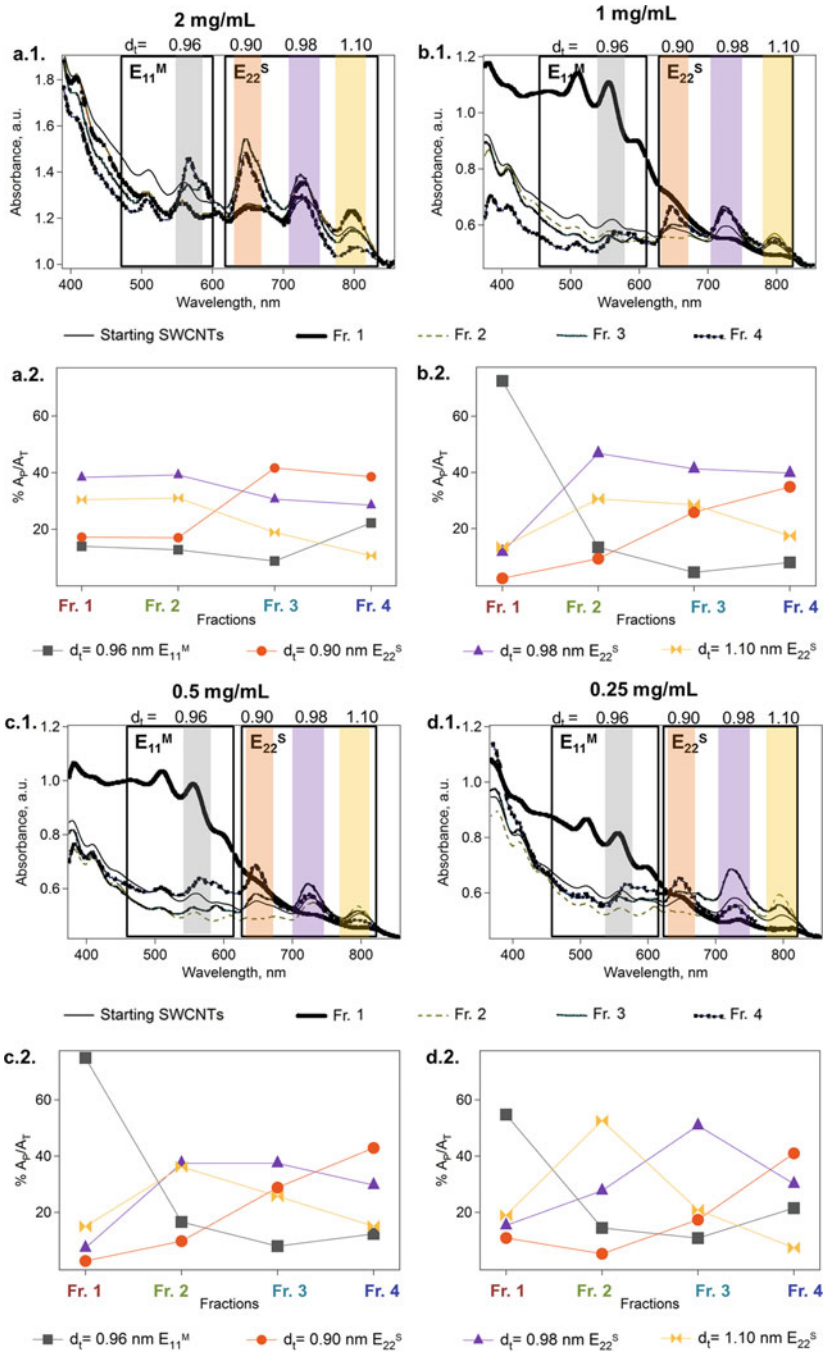

Fig. 22.6 Absorbance spectra of the starting SWCNTs and collected fractions Fr. 1, Fr. 2, Fr. 3 and Fr. 4 for different concentrations of the starting SWCNT dispersion: a. 2 mg/mL; b. 1 mg/mL; c. 0.5 mg/mL; d. 0.25 mg/mL. In Figures a.1., b.1., c.1., and d.1.,the grey, orange, purple and yellow regions correspond to SWCNTs in resonance via the $E_{11}^M$with $d_t = 0.96$ nm and via the electronic E_{22}^S transitions with $d_t = 0.90$, 0.98 and 1.10 nm, respectively

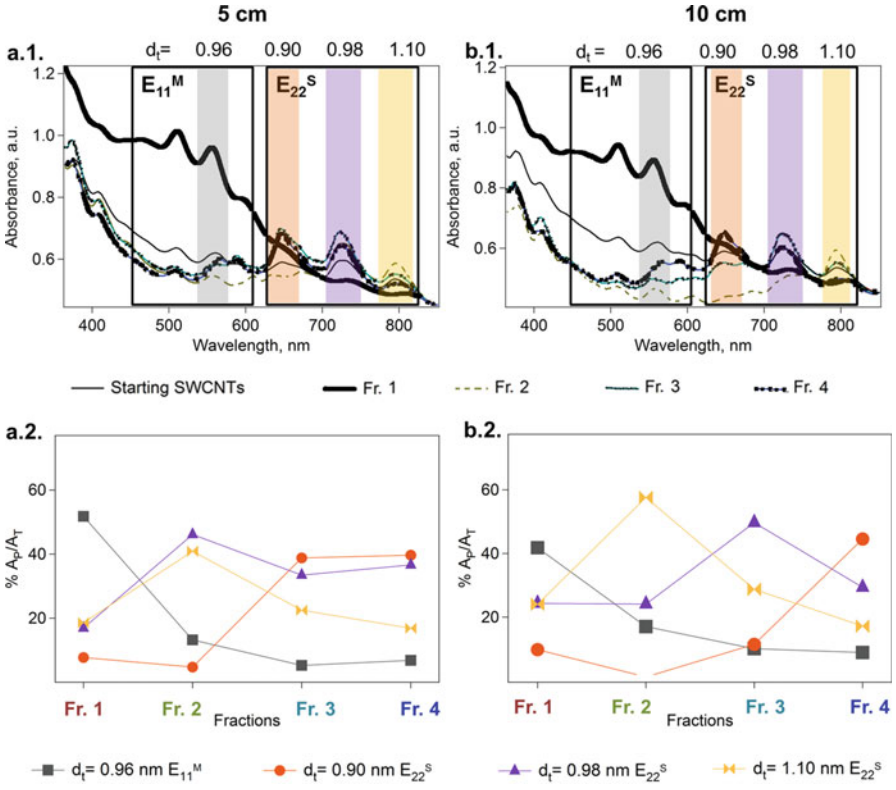

Fig. 22.7 Absorbance spectra of the starting SWCNTs (1 mg/mL) and the collected fractions: Fr. 1, Fr. 2, Fr. 3 and Fr. 4 for two different column lengths: a. 5 cm, and b. 10 cm. In Figures a.1, and b.1 the grey, orange, purple and yellow regions correspond to SWCNTs in resonance via the E_{11}^M electronic transitions with d_t = 0.96 nm and *via* E_{22}^S with d_t = 0.90, 0.98 and 1.10 nm, respectively

electronic transition, and comprise the strong bands at 646 nm (d_t = 0.90 nm), 733 nm (d_t = 0.96 nm) and at 795 nm (d_t = 1.10 nm), assigned to semiconducting nanotubes. In the bottom panels of Fig. 22.6, the A_p/A_t of the most intense bands in each region (555 nm, 646 nm, 733 nm, and at 795 nm) is represented for the fractions collected: Fraction 1 (Fr. 1), Fraction 2 (Fr. 2), Fraction 3 (Fr. 3) and Fraction 4 (Fr. 4).

In Fig. 22.6a.2, which corresponds to 2 mg/mL of the starting SWCNT concentration, the ratio A_p/A_t does not present significant changes among the different SWCNT fractions. However, in the case of 1 mg/mL (Fig. 22.6b.2) the bands corresponding to SWCNTs in resonance *via* E_{11}^M are the most intense in the first fraction (Fr. 1). On the contrary, the following fractions (Fr. 2, Fr. 3 and Fr. 4) present the most intense bands in resonance *via* E_{22}^S. Besides, in the case of 0.5 mg/mL (Fig. 22.6c.2), not only were the SWCNTs sorted by metallic and semiconducting but also those in resonance *via* E_{22}^S are sorted by diameter. The last SWCNTs to be eluted are the thinnest ones (Fr. 4). Even more, if the concentration is lower (0.25 mg/mL Fig. 22.7d.2) the separation is more

specific, and the largest diameter SWCNTs are eluted in the first place (Fr. 2). The last fractions (Fr. 3 and Fr. 4) are enriched in the thinnest SWCNTs. Decreasing the concentration of the starting SWCNT dispersions improves the SWCNT separation.

Similarly, the length of the column was evaluated using 5 and 10 cm columns (Fig. 22.7). The results shown in Fig. 22.7a.2 correspond to a column length of 5 cm. The bands corresponding to SWCNTs in resonance *via* E_{11}^{M} are the most intense in the first fraction (Fr. 1). On the contrary, the following fractions (Fr. 2, Fr. 3 and Fr. 4) present the most intense bands in resonance *via* E_{22}^{S}. In general, the separation between semiconducting and metallic was successful. In the case of the 10 cm column (Fig. 22.7b.2), not only the SWCNTs were sorted between metallic and semiconducting but also those in resonance *via* E_{22}^{S} are being sorted by diameter. The last SWCNTs to be eluted are those with the thinnest diameter (Fr. 4), and those with largest diameter are eluted in the first place (Fr. 2).

22.4 Conclusions

The results show that this simple chromatography technique effectively separates the SWCNTs into semiconducting and metallic. In addition, the concentration of the raw SWCNTs dispersion and the length of the column play important roles towards the separation of SWCNTs with specific diameters. The optimum conditions are reached with low SWCNT concentrations and long columns. This study provides new relevant data towards the up-scaling of chromatographic separation of SWCNTs. Obtaining SWCNTs with a well-controlled electronic character and specific diameters is a critical stage for the development of electronic devices and nanocircuits based on SWCNTs.

Acknowledgments This work has received funding from the European Union's Horizon 2020 research and innovation programme under the Marie Skłodowska-Curie grant agreement No 642742.

References

1. Thomsen C, Reich S (2007) Raman scattering in carbon nanotubes. Light scattering in solid IX, topic. Appl Phys 108:115–232
2. Georgakilas V, Perman JA, Tucek J, Zboril R (2015) Broad family of carbon nanoallotropes: classification, chemistry, and applications of fullerenes, carbon dots, nanotubes, graphene, nanodiamonds, and combined superstructures. Chem Rev 115:4744–4822
3. Nakashima N, Fujigaya J (2007) Fundamental and applications of soluble carbon nanotubes. Chem Lett 36:692–697
4. Saeed K (2013) Carbon nanotubes-properties and applications: a review. Carbon Lett 14:131–444
5. Trung TQ, Lee NE (2017) Materials and devices for transparent stretchable electronics. Mat J Chem C 5:2202–2222

6. Zhu ZZ (2017) An overview of carbon and graphene for biosensing applications. Nano-Micro Lett 9:1–24
7. Peng-Xiang H, Chang L, Cheng HM (2008) Purification of carbon nanotubes. Carbon 46:2003–2025
8. Ansón-Casaos A, González-Domínguez JM, Lafragüeta I, Carrodeguas JA, Martínez MT (2014) Optical absorption response of chemically modifies single-walled carbon nanotubes upon ultracentrifugation in various dispersants. Carbon 66:105–118
9. Sayago I, Terrado E, Aleixandre M, Horrillo MC, Fernández MJ, Lozano J, Lafuente E, Maser WK, Benito AM, Martínez MT, Gutiérrez J, Muñoz E (2007) Novel selective sensors based on carbon nanotube films for hydrogen detection. Sens Actuator B-Chem 122:75–80
10. Sayago I, Santos H, Horrillo MC, Aleixandre M, Fernández MJ, Terrado E, Tacchini I, Aroz R, Maser WK, Benito AM, Martínez MT, Gutiérrez J, Muñoz E (2008) Carbon nanotube networks as gas sensors for NO_2 detection. Talanta 77:758–764
11. Martinez MT, Tseng YC, Salvador JP, Marco MP, Ormategui N, Loinaz I, Bokor J (2010) Electronic anabolic steroid recognition with carbon nanotube field-effect transistors. ACS Nano 4:1473–1480
12. Martinez MT, Tseng YC, González M, Bokor J (2012) Streptavidin as CNTs and DNA linker for the specific electronic and optical detection of DNA hybridization. Phys J Chem C 116:22579–22586
13. Sieben JM, Ansón-Casaos A, Montilla F, Martínez MT, Morallón E (2014) Electrochemical behaviour of different redox probes on single wall carbon nanotube buckypaper-modified electrodes. Electrochim Acta 135:404–411
14. Gasnier A, González-Domínguez JM, Ansón-Casaos A, Hernández-Ferrer J, Pedano ML, Rubianes MD, Martínez MT (2014) Single-wall carbon nanotubes covalently functionalized with polylysine: synthesis, characterization and analytical applications for the development of electrochemical (bio) sensors. Electroanalysis 26:1676–1683
15. Arnold MS, Green AA, Hulvat JF, Stupp SI, Hersam MC (2006) Sorting carbon nanotubes by electronic structure using density differentiation. Nat Nanotechnol 1:60–65
16. Liu H, Nihide D, Tanaka T, Kataura H (2011) Large-scale single-chirality separation of single-wall carbon nanotubes by simple gel chromatography. Nat Commun 2:309
17. Khripin CY, Fagan JA, Zheng M (2013) Spontaneous partition of carbon nanotubes in polymer-modified aqueous phases. J Am Chem Soc 135:6822–6825
18. Ansón-Casaos A, González-Domínguez JM, Martínez MT (2010) Separation of single-walled carbon nanotubes from graphite by centrifugation in a surfactant or in polymer solutions. Carbon 48:2917–2934
19. Blanch AJ, Quinton JS, Shapter JG (2013) The role of sodium dodecyl sulfate concentration in the separation of carbon nanotubes using gel chromatography. Carbon 60:471–480
20. Araujo PT, Pesce PBC, Dresselhaus MS, Sato K, Saito R, Jorio A (2010) Resonance Raman spectroscopy of the radial breathing modes in carbon nanotubes. Phys E 42:1251–1261
21. Kataura H, Kumazawa Y, Maniwa Y, Umezu I, Suzuki S, Ohtsuka Y, Achiba Y (1999) Optical properties of single-walled carbon nanotubes. Synth Met 103:2555–2558
22. Itkis ME, Perea DE, Niyogi S, Richard SM, Hamon MA, Hu H, Zhao B, Haddon RC (2003) Purity evaluation of as-prepared single-walled carbon nanotube soot by use of solution-phase near-IR spectroscopy. Nano 3:309–314

Part VI
Materials: Nanowires and Fibers

Chapter 23
Loaded Nanofibers: Force Protection, Filtration, Decontamination

Ashok Vaseashta and Nimet Karagülle-Bölgen

Abstract In asymmetric and complex warfare environments, it is critical to deploy the latest technological innovations for tactical advantage over adversaries. Among others, improvements in outerwear of soldier uniform provide a significant tactical advantage. We have studied the use of loaded nanofibers, which demonstrate capabilities such as light weight, mechanical resilience, and breathability, i.e. the possibility for the evaporation of perspiration. In addition, the fibers are capable of sensing chemical/biological environment and delivering therapeutics thus providing temporary relief from injury. Furthermore, nanofibers include communication capabilities for enhanced situational awareness. This investigation outlines an ongoing research on loading electrospun nanofibers with selected materials to produce outerwear for soldiers providing tactical superiority. Fabrication and characteristics of some of such fibers are presented here along with future pathways to integrate additional capabilities.

Keywords Electrospinning · Nanofibers · Filtration · Mechanical strength · Sensors

23.1 Introduction: Justification and Methodology

In most conventional warfare, the adversaries deploy forces of a similar type and the outcome can be predicted by estimating the quantity of the opposing forces and/or by their quality. In the current asymmetric warfare scenario, this assumption does not hold because the composition or strategy of the opposition forces makes it

A. Vaseashta (✉)
Institute for Advanced Sciences Convergence, and Int'l Clean Water Institute, Herndon, VA, USA

NJCU – State University of New Jersey, NJ, USA
e-mail: prof.vaseashta@ieee.org; prof.vaseashta@nanoknowledge.info

N. Karagülle-Bölgen
Chemical Engineering Department, Mersin University Engineering Faculty, Mersin, Turkey

P. Petkov et al. (eds.), *Advanced Nanotechnologies for Detection and Defence against CBRN Agents*, NATO Science for Peace and Security Series B: Physics and Biophysics, https://doi.org/10.1007/978-94-024-1298-7_23

impossible for either side to close-in during battle. Naturally, the first line of defence is self "protection". With this as the basis, the study presented here outlines a systematic methodology to develop micro/nanofibers using electrospinning loaded with selected nanomaterials which are mixed into the solutions of high-performance polymers. The methodology involves systematic identification and selection of novel combinations of loading of nanomaterials with high-performance polymers to provide a desired set of characteristics, which include increased mechanical strength, improved sensitivity to contaminants, better filtering capabilities, improved response to electromagnetic stimuli, on-demand or time-released drug delivery, optical tunability or adaptation and conductivity, leading to system-on-fibers (SoF) and e-textiles. Additionally, high surface area of nanofibers coupled with its potential biocompatibility and biodegradable nature, offers tremendous promise for diverse applications in tissue engineering, targeted drug/vaccine delivery, non-thrombogenic materials for blood contacting applications, and sensing of chemical and biological environments.

Parallel to this work, our objective has been aimed at the use of advanced science convergence methodologies to develop automated data mining tools such as automated data analysis, mining and surveillance (ADAMS™), technology foresight and road-mapping (TechFARM™) and New and Emerging Science and Technology Trends and Surveillance (NESTTS™) to provide additional knowledge and databases. The objective of such data mining tools has been to learn technological capabilities and gaps, to provide tactical advantage, as stated earlier. Preliminary data of fibers using loaded high-performance polymers are presented here with the objective to fabricate multi-functional nano/microfibers embedded with several materials for military outerwear and gears that provide an integrated solution pathway through a revolutionary approach of using novel nanomaterials and ceramers embedded in high performance polymers, as outerwear materials for suits, masks, and embedded sensors.

23.2 Electrospinning and Nanofiber Formation

Electrospinning is a process in which polymer fibers are produced through the action of an electric field imposed on a polymer solution. The concept of electrospinning was first introduced by Formalas in his series of patents in 1934. This technique has gained scientific popularity in the last couple of decades, when several groups developed several micro and nanofibers [1–10]. A simple electrospinning apparatus consists of a high voltage power supply, a capillary to deliver the polymer and a collector electrode, as shown in Fig. 23.1. A typical laboratory electrospinning system consists of a microprocessor-controlled syringe pump with a high metering precision at a low, pulse-free pre-set rate and volume control. The internal diameter of the syringe is used by the control program to calibrate the pump and deliver a pre-determined volume and flow rate. The electric field is applied with a high voltage (typically ~30 kV) power supply by connecting the metal discharge needle and a

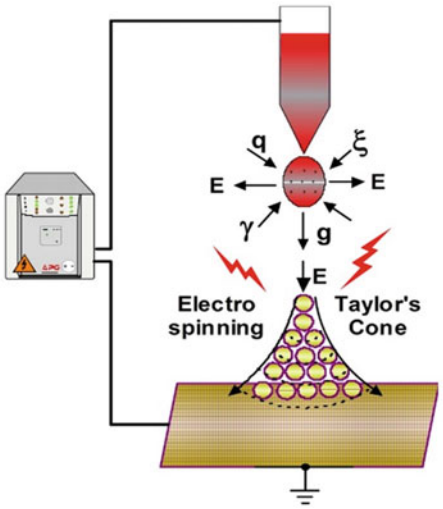

Fig. 23.1 A typical electrospinning apparatus (E field, g gravity, γ drag, ξ viscosity)

grounded stationary or rotating collector electrode. The strong electric field on a polymer fluid generates an electrostatic force on the surface against the viscous stresses of the polymeric mass, thus producing elongation jets towards the other electrode (Fig. 23.1). A Taylor cone is generated in the jet when a hydraulic effect produced by the syringe plunger to the polymer solution is modified by the strong electrostatic field. The shape of the cone, employing parameters such as viscosity; conservation of mass, charge, and momentum; electric field; surface tension; air drag; and Coulombic and gravitational forces has been modelled by several investigators [7]. Upon application of the high voltage, a polymer jet is formed and undergoes an elongation process before reaching the collector screen, the solvent evaporates, and the polymer is collected as a solidified interconnected web of nanofibers.

Several synthetic and natural polymers, polymer composites, polymers impregnated with nanoparticles, carbon nanotubes, and compounds for mechanical, electrical, and biological applications were attempted using single, double or triple jet electrospinning apparatus [11]. Table 23.1 provides a list of polymers (synthetic, natural, and biodegradable), ceramers, electro-ceramers, and bio-ceramers that were studied and reported earlier [8]. The table lists their composition, molecular weight, approximate range of loading, and intended applications. The study was later extended for several new categories of materials, including negative refractive index (NIR) materials, bioactive compounds with powerful medicinal properties, and certain oxides to study phytotoxic and genotoxic effects. Table 23.2 provides a list of materials that are currently being tested with the intended applications. Figure 23.2 shows a conceptual schematic of the possible spectrum of applications that are potentially feasible [8].

We describe below applications of loaded nanofibers in the context of force protection, filtration, and decontamination. Force protection refers to mechanical

Table 23.1 A sample list of polymers (synthetic, natural, and biodegradable) and loading materials – ceramers, electro-ceramers, and bio-ceramers [8]

Polymers and composites	Composition	Molecular weight	Loading	Applications/ comments
Synthetic	Polystyrene/dichloroethane	299,000	CNT	Field emission
	Nylon (6,12)/1,1,1,3,3,3 Hexafluoro-2-propanol	–	CNT	Flexible substrates
	Poly(etheremide)/1,1,2-Tricholoroethane	30,000	CNT	Mechanical strength – SoF
	Polyacrylonitrile (PAN)/ dimethylformamide (DMF) (also dimethyl acetamide (DMAc))	114,000 M vol.	CNT ZnO	Strength sensors (SoF)
	Polymethylmethacrylate (PMMA) in acetone, chloroform, Toluene	540,000	None	Porous fibers
	Polyvinylpyrrolidone/Ethanol/ DMF	58K-1.3M	Bi_2S_3	CT imaging
	Polyprrole in Acetonitrile (ACN), and dichloromethane (DCM)	–	TEA BF_4	Conducting polymers -SoF
	Polyeurathane/DMF polycarbonate/DMF	42,000	CNT	Protective clothing
Natural	Lecithin/dimethylformamide	–	None	Biomembranes
	Lecithin/dimethylformamide	–	Bi_2S_3	CT imaging
Biodegradable	Poly (ε-caprolactone) (PCL)	–	PLA/PGA	Wound dressing
	Poly (L-lactide/co ε-caprolactone) (PLLA/CL)	150,000	PLA/PGA collagen	Stents tissue/ scaffold
	Poly (ethylene oxide)/water	400,000	PCL	Hollow fibers
	Polyglcolide		PCL	
	Poly (ethylene oxide)/water	400,000	MoO_3, ZnO, TiO_2	Sensors
	Poly (L-lactide/co ε-caprolactone) (PLLA/CL)	150,000	Bi_2S_3 collagen	CT imaging
	Poly (L-lactide/co ε-caprolactone) (PLLA/CL)	150,000	Metal nanoparticles	Targeted drug delivery
Ceramers	Polyacrylonitrile (PAN)/ dimethylformamide (DMF)	150,000 M vol.	TiO_2	Conductive and PV polymer
	Polydiphenooxyphosphazene PDPP		SiO_2 (Y, Er)	Glass/ceramic
Electro-optic polymers	Poly(acrylic acid) -polypyrene methanol (PAA-PM)/ dimethylformamide	50,000		Optical sensors
	Poly (vinyl acetate)/Acetone		GeO_2	1D Opto-electronics
Bio-ceramers	Poly(l-lactic) acid, poly (glycolic) acid, Poly(l-lactide/ glycolide)	70K/ >150K/10-20K	Collagen mefoxin	Bone repair antibiotics

Table 23.2 List of polymers and loading materials under investigation

Polymer composition	Loading	Applications/comments
Nylon (6,12)/1,1,1,3,3,3 Hexafluoro-2-propanol	NRI NPs	Camouflage
Poly(etheremide)/1,1,2-Tricholoroethane	NRI NPs	Camouflage/mechanical Strength
Polyacrylonitrile (PAN)/ dimethylformamide (DMF) (also dimethyl acetamide (DMAc))	NRI NPs/ZnO	Camouflage/strength
Lecithin/dimethylformamide	Ag	Biomembranes
Lecithin/dimethylformamide	Bi_2S_3	CT imaging
Poly (ε-caprolactone) (PCL)	Turmeric	Wound dressing
Poly (L-lactide/co ε-caprolactone) (PLLA/CL)	Turmeric/ collagen	Tissue/scaffold
Polymers including polyamide, polyviniyl alcohol, polyurethane, poly-propylene, nylon-6, poly(viniyl chloride), polysulfone, poly(methyl methacrylate), cellulose acetate	Ag, TiO_2, Cu, ZnO, MgO, ZrO_2	Flame retardancy, UV protection, self cleaning, antistatic and antimi-crobial activities
Polyacrylonitrile (PAN)/ dimethylformamide (DMF)	MgO, TiO_2	Chem./Bio Decon

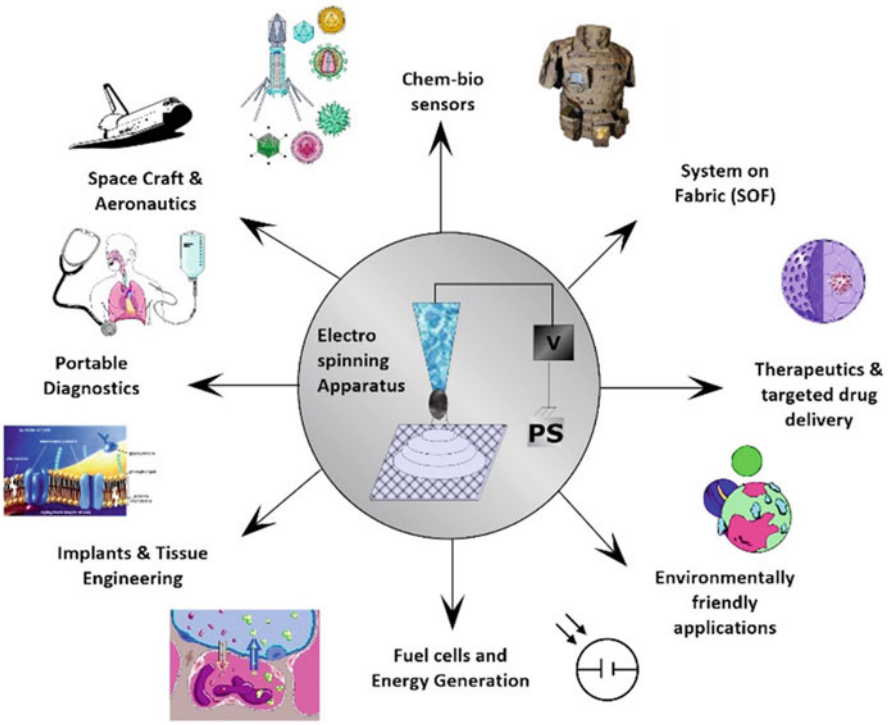

Fig. 23.2 Potential applications

properties that renders products mechanically strong, resilient, flexible, light weight, breathable, and with additional capabilities such as resistance to chemical and biological environment and the ability to camouflage. Additional built-in features include therapeutic capabilities, either built-in or through add-on layers. Filtration and decontamination capabilities include protection against ambient chemical/biological/radiological contaminants.

23.3 Characteristics and Application of Loaded Nanofibers

23.3.1 Smart Textiles: Force and Chem.-Bio Protection, and Situational Awareness

The process of electrospinning offers a unique opportunity to yield nanofibers of varying porosity with a large surface area with respect to its geometrical dimensions. Loading of various materials, such as carbon nanotubes, metal oxides, ceramers, etc. allow the formation and improvement of barrier materials for force protection. Electrospun nanofibrous materials, are light weight, breathable, comfortable and have applications in functional protective clothing for the military personnel. Several of these loaded nanofibers include: catalytic active nanofibers; chemical/biological sensors; nanofibers for reinforcement; insulating nanofibers; selective gas permeating materials; and high mechanical strength composites due to carbon nanotubes embedded in a polymeric matrix. Yet other applications that we investigated are biomimicking and optical cloaking – all of which offer promising and direct applications of loaded micro/nano fibers in outerwear for safety and security. The use of negative refractive index materials offers the outstanding possibility of optical cloaking, providing a distinct advantage in combat situations. We also investigated the use of metal-organic frameworks for visual identification in emergency situations. A selection of nano-taggants offers the possibility to trace, track, and authenticate biological threats.

Another critical feature that is relevant are embedded informational and communication technology capabilities for signal receiving and communication and sensors that respond to environmental contaminants. The ability to disperse ceramics, metal oxides, nanoparticles, and carbon nanotubes in polymer solutions and develop nanofibers ha produced new pathways for functional fibers that have electronics and interconnections woven into them. The advent of mobile and pervasive computing; wireless-networks; network appliances; flexible substrates; and e-textiles are enabling the development of systems on textile or system on fibers (SoF). Such systems demonstrate a tremendous potential towards the development of portable functional devices, such as functional fibers embedded with data communications systems, medical and health monitoring information systems, personal fitness, defence systems, mobile computing, radio frequency identification devices, global positioning systems, and interactive geographical information systems. The

technology offers feasibilities for the development of systems with physical flexibility and sizes unachievable with current and conventional manufacturing technologies. The vision of SoF represents a scenario that enables context-aware functionalities, a data communication interface, parallel detection of chemical/biological sensors, and provides for invaluable real-time information for soldiers in combat theatres to execute critical decisions in a timely manner.

The high surface area combined with biocompatibility and the biodegradable nature of certain fibers offer tremendous promise for diverse biomedical applications from tissue engineering, targeted vaccine delivery, and non-thrombogenic materials for blood contacting applications. Biodegradable polymers are highly desirable for long-term drug delivery applications since they degrade in the body to biologically inert and compatible molecules. By incorporating a drug into biodegradable polymers, dosage forms of various shapes and sizes yield built-in time-released or physiological condition based-released therapeutics. Secondary surgical procedures, common after the completion of dosing regimens are rendered moot due to such polymers.

Many biodegradable polymer chemistries have been proposed for such applications; however, the most common and successful are biodegradable polyester sutures. These polymers include poly(glycolide), poly(D,L-lactide), and their related copolymers poly(D,L-lactide-co-glycolide). Current commercial products based on these materials include Decapeptyl®, Lupron Depot®, and Sandostatin LAR®. Under suitable conditions, most synthetic and natural polymers are suited for electrospinning; thus, allowing nanofiber preparation from nanoparticles or vaccine-impregnated polymers. It was further demonstrated that antibiotic loaded biodegradable and biocompatible polymeric electrospun nanofibrous membranes can prevent post-surgery induced intra-abdominal adhesions by providing a physical barrier during the wound healing process and at the same time serve a functional barrier against strains of microorganisms, thereby reducing the local inflammatory response. The results of our previous studies including synthesis of biocompatible and biodegradable polymers, production and characterization of electrospun nanofibers from those polymers, their loading with drugs and the release of the drugs from therapeutic loaded polymeric matrices would provide a linkage for the development of new functional barriers for protection applications.

The use of biodegradable polymeric systems is an alternative and efficient route for vaccine administration, peripheral nerve regeneration, and tissue engineering, which finds interesting applications in the context of safety and security. Some relevant polymers include bio-degradable polymers which are specifically investigated for time-controlled release characteristics; copolymers with desirable hydrophilic/hydrophobic interactions; dendrimers for the immobilization of enzymes, drugs, peptides, or other biological agents; and certain blends of hydrocolloids and carbohydrate-based polymers. These biomaterials with desirable functional groups are being created for innovative drug delivery systems and as potential linings for artificial organs, as substrates for cell growth and as agents in drug targeting and immunology testing, as biomedical adhesives and bioseparation membranes, and as substances able to mimic biological systems. Some of the most promising medical

applications include treatment of primary pulmonary hypertension and pulmonary arterial hypertension by time-controlled release templates impregnated with anticoagulants and calcium channel blockers; bioscaffold that mimic the extracellular matrix topology [10], polyesters combined with phosphatidyl choline for biomimetic applications [12], intravascular stents from a blend of polyactide and trimethylene carbonate [13], dystrophin gene immobilized templates for curing aging skeletal muscles [14], cellulose based scaffolds for cartilage tissue engineering [15] and esophageal tissue engineering [16], as few examples (Fig. 23.3).

23.3.2 Filtration and Decontamination

Presently, applied protective clothing includes the use of activated charcoal impregnated with metal ions, which physically adsorb agents against chemical and biological agents. Metal oxide nanoparticles such as TiO_2 and MgO are proposed as potential catalysts for the decontamination of chemical and biological agents. The significant properties of such adsorbents are due to their high surface areas and high surface concentrations of reactive defect sites. However, there are disadvantages of modification of e-textile surfaces with nanoparticles, especially the ones which are not stabilized on the surface of the textiles. In addition to altering the physical and mechanical properties of the textile materials, associated toxic effects of nanoparticles on human systems are still under discussion. Furthermore, inhalation of those nanoparticles in high doses can result in pulmonary inflammation and allergic reactions, therefore the use of nanoparticles in powder form is difficult in protective clothing. To overcome this limitation, research effort was directed to incorporate nanoparticles with nanofibers by including of nanoparticles with polymer solution before electrospinning [17]. Nanofiber based materials suggest novel protecting clothing materials with comfortable, adsorptive and lightweight properties with active detoxyfying/decontaminating nanomaterials, primarily facilitated by their nature at nanoscale [18]. Several intended applications are listed in Table 23.3, also consistent with the priorities of defence agencies.

Electrospun chromatography is a cost-effective methodology for obtaining different surface selectivity by changing the polymer materials to electrospun filtration systems. Fabrication of polymer derived electrospun nanofibers by electrospinning as chromatographic sorbent bed for ultra-thin layer chromatography offers on-plate identification and separation of analytes from their mixture solutions. It has been reported that electrospun fiber based stationary phases in ultra-thin layer chromatography (UTLC) have an enhanced separation efficiency to provide separation of analyte mixtures in a shorter development time than those of the traditional particle-based stationary TLC phases. In addition to UTLC, incorporation of a given target molecule into a membrane to express permselectivity is also investigated for molecular recognition sites into synthetic membranes.

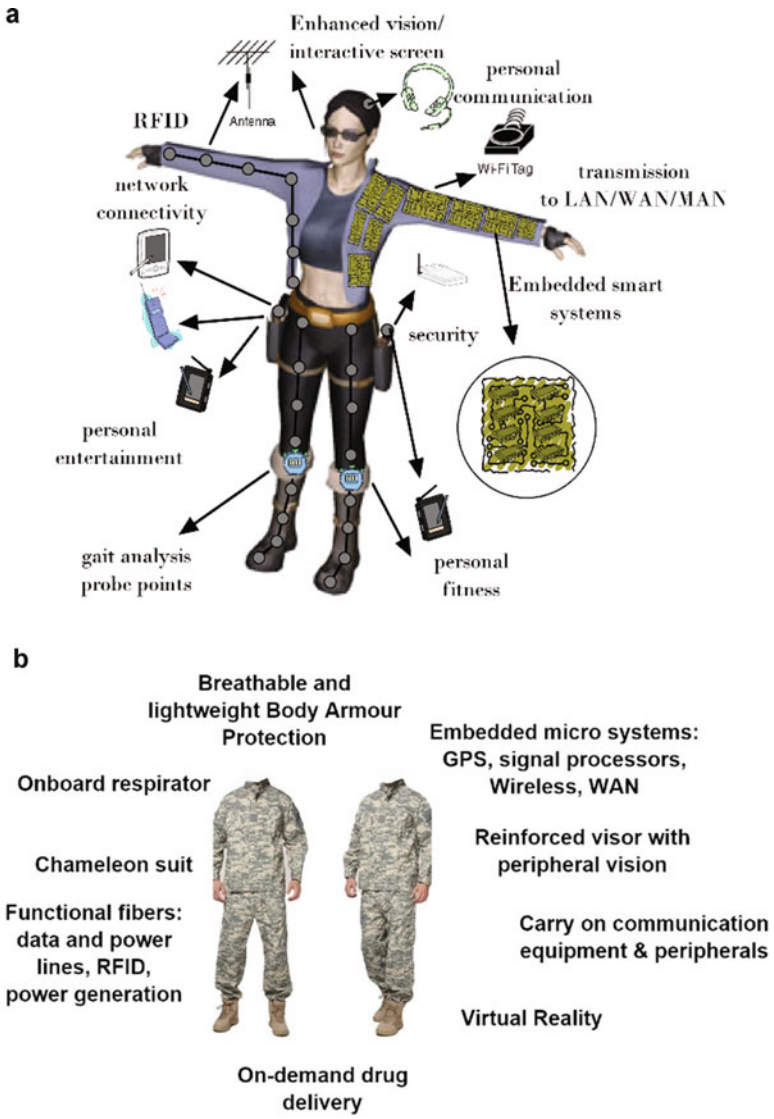

Fig. 23.3 (**a**) Use of nanofibers in information and communications technology; (**b**) Intended applications in soldier uniforms

23.4 Discussion and Path Forward

Due to the increasing interest in materials at the nanoscale and the associated interesting properties, research on electrospinning processes has increased significantly in the recent years. Using several innovative spinning techniques and

Table 23.3 Nanoscale filtration applications

Wearable kidney
Water desalination
Water purification (collagen based)
Breathable protection clothing
Wearable anti-dehydration systems
Advanced rebreathers for indefinite-length underwater presence – artificial gills
Superior gas masks
MoS_2 nanoparticles – especially for volatile organic compounds (VOC)

modified collectors [11], structures with different compositions, complex architectures [8], fiber morphologies [19], improved properties [20–22], varying degradation rates, and functional moieties have been produced. Electrospun nanostructured polymer structures of natural or synthetic origin have a multitude of possible applications in addition to defence as demonstrated here, including medicine, pharmacy, optoelectronics, sensor technology, catalysis, and filtration. Development of new and smart protective textiles for future applications include, integration of nanoparticles with multiple threat sensing capability and energy storing/harvesting devices built in the protective clothing. Smart protective textiles are still at the development phase but some of the materials are already quite close to commercial production. However, there are limitations, viz. nanofiber based protective textiles still require extensive research before large scale production. Life cycle analysis, as it relates to health and safety in all stages of the products, requires an extensive investigation and evaluation for its short and long-term health risks [23]. The selection of a polymer for use as a degradable biomaterial must match the mechanical properties and the degradation rate to specific parameters. The greatest advantage of biodegradable polymers is that they are fragmented into biologically acceptable, metabolized and removable molecules. However, biodegradable materials do produce degradation by-products that must take place with little to no adverse reactions within the biological environment. These degradation products must be tested thoroughly. Some of the factors affecting biodegradation of polymers are the presence of ionic groups, low-molecular-weight compounds, and unexpected units or chain defects. Several other contribution factors are configuration structure, molecular weight and its distribution, morphology, functionalization process, implantation site, adsorbed and absorbed compounds (water, lipids, ions, etc.), physicochemical factors (ion exchange, ionic strength, pH), and associated physical factors. Much of the development of novel materials in controlled drug delivery focuses on preparation and use of these responsive polymers with specifically designed macroscopic and microscopic structural and chemical features. These new biomaterials with desirable functional groups are being created by researchers who envision their use not only for innovative drug delivery systems but also as potential linings for artificial organs, as substrates for cell growth or chemical

reactors, as agents in drug targeting and immunology testing, as biomedical adhesives and bio-separation membranes and as substances that are able to mimic biological systems.

References

1. Huang ZM, Zhang YZ, Kotaki M, Ramakrishna S (2003) A review on polymer nanofibers by electrospinning and their applications in nanocomposites. Compos Sci Technol 63:2223–2253
2. Chua KN, Lim WS, Zhang P, Lu H, Wen J, Ramakrishna S, Leong KW, Mao HQ (2005) Stable immobilization of rat hepatocyte spheroids on galactosylated nanofiber scaffold. Biomaterials 26:2537
3. Xang W, Drew C, Lee SH, Senecal KJ, Kumar J, Samuelson LA (2002) Electrospun nanofibrous membranes for highly sensitive optical sensors. Nano Lett 2(1):1273
4. Kim JS, Renekar DH (1999) Mechanical properties of composites using ultrafine electrospun fibers. Polym Compos 20(1):124
5. Locher I, Kirstein T, Troster G (2004) Temperature profile estimation with smart textiles. In: Kiang K, Gorton J, Alert M (eds) Proceedings of 37th international symposium on microelectronics, IMAPS, p 204
6. E-Textile. Virginia Tech, Blacksburg. www.ccm.ece.vt.edu/etextiles
7. Rutledge S, Hohman MM, Shin MY, Brenner MP (2001) Electrospinning and electrically forced jets: I. Stability theory Phys. Fluids, 13 2201, and Electro-spinning and electrically forced jets: II. Apps., Phys. Fluids (2001) 13 2221
8. Vaseashta A, Stamatin I (2007) Electrospun polymers for controlled release of drugs, vaccine delivery, and system-on-fibers. J Optoelectron Adv Mater 9(6):1606–1613
9. Lu Y, Chen S (2004) Micro and nanofab. of biodegradable polymers for drug deli-very. Adv Drug Deliv Rev 56:1621
10. Kim TG, Park TG (2006) Biomimicking ECM: cell adhesive RGD peptide modified electrospun Poly(D,L-lactic-co-glycolic acid) nanofiber mesh. Tissue Eng 12(2):221
11. Vaseashta A (2007) Controlled formation of multiple Taylor cones in electrospinning process. Appl Phys Lett 90:093115
12. Hillborn J (2005) Non-thrombogenic biodegrad-able polymers for the new generation of phospholipid analogues Priv. Com
13. Medical Device Link. http://www.devicelink.com
14. Vaseashta A, Boskovic O, Webb A, Ozdemir N, Ozturk E (2006) Effect of dystrophin gene immobilized nano-structured therapeutic templates on aging skeletal muscles. In: Kassing R, Petkov P, Kulisch W, Popov C (eds). Springer, Funct. Prop of Nanostructured Mater, p 511
15. Muller FA, Muller L, Hofman I, Greil P, Wenzel MM, Staudenmaier R (2006) Cellulose-based scaffold materials for cartilage tissue engineering. Biomaterials 27(21):3955
16. Zhu Y, Chian KS, Chan-Park MB, Mhaisalkar PS, Ratner BD (2006) Protein bonding on biodegradable poly(L-lactide-co-caprolactone) membrane for esophageal tissue engineering. Biomaterials 27:68
17. Vaseashta A, Dimova-Malinovska D, Marshall JM (eds) (2005) Nanostructured & advanced materials. Springer, Dordrecht
18. Vaseashta A (2005) Nanostructured materials based next generation devices and sensors, nanostructured and advanced materials. In: Vaseashta A, Dimova-Malinovska D, Marshall JM (eds) . Springer, Dordrecht, pp 1–30
19. Sundarrajan S, Chandrasekaran AR, Ramakrishna S (2010) An update on nanomaterials-based textiles for protection and decontamination. J Am Ceram Soc 93:3955–3975
20. Thilagavthi G, Raja ASM, Kannanian T (2008) Nanotechnology and protective clothing for defence personnel. Def Sci J 58:451–459

21. Dhineshbabu NR, Karunakaran G, Suriyaprabha R, Manivasakan P, Rajendran V (2014) Electrospun MgO/Nylon 6 hybrid nanofibers for protective clothing. Nano-Micro Lett 6:46–54
22. Balasubramanian Kandasubramanian R (2013) Advancement in textile technology for defence. Def Sci J 63:331–339
23. Vaseashta A (ed) (2015) Life cycle analysis of nanoparticles – risk, assessment, and sustainability. Destech Publishers, New York 978-1-60595-023-5, (404 pages)

Chapter 24
Nanocomposites of Electrospun Polymeric Materials As Protective Textiles Against Chemical and Biological Hazards

Nimet Bölgen and Ashok Vaseashta

Abstract Chemical and biological agents effects tissues and organs which cause poisoning, disease, and deterioration. Chemical or biological weapons show significant threats to humankind. Therefore, many studies have presented approaches for protection from biological and chemical agents. There are various types of defence equipments to protect a body from those agents such as developed detectors, protective clothing materials, functional decontaminants, and others. A number of studies have reported about protective clothing against chemical and biological agents, because many of them are dermally active. New protective clothing materials (comfortable, adsorptive, light-weight) combined with active detoxifying/decontaminating nanomaterials have been produced recently. Electrospinning is one of the simplest and most versatile methods to fabricate nanofibers with high surface areas. Electrospun polymeric nanofibers were used as a protective barrier on the textile fabrics. Attempts have been made to incorporate nanoparticles, nanotubes and antimicrobials into electrospun fibers to enhance their functionality. In this contribution, a selection of studies about the use of electrospun nanofibers for protective clothing against chemical and biological agents is summarized.

Keywords Nanofibers · Electrospinning · Nanocomposites · Protective clothing · Chemical agents · Biological agents

N. Bölgen (✉)
Mersin University, Engineering Faculty, Chemical Engineering Department, Mersin, Turkey
e-mail: nimet@mersin.edu.tr

A. Vaseashta
Institute for Advanced Sciences Convergence, and Int'l Clean Water Institute, Herndon, VA, USA

NJCU - State University of New Jersey, NJ, USA

P. Petkov et al. (eds.), *Advanced Nanotechnologies for Detection and Defence against CBRN Agents*, NATO Science for Peace and Security Series B: Physics and Biophysics, https://doi.org/10.1007/978-94-024-1298-7_24

24.1 Introduction

Chemical and biological agents effects tissues and organs which cause poisoning. There are various types of defence equipments to protect a body from those agents including protective clothing. Electrospinning is one of the simplest and most versatile methods to fabricate nanofibrous textiles with a high surface area. Electrospun polymeric nanofibers were used as a protective barrier. In this contribution, studies about the use of electrospun nanofibers for protective clothing against chemical and biological agents is summarized.

24.2 Electrospinning

Electrospinning is a process in which polymer fibers are produced with diameters down to the nanometer range through the action of an electric field imposed on a polymer solution/melt. This technique became very popular in the last 10 years in the scientific area, although the fundamental idea was first described by A. Formalas in his series of patents in 1934 [1]. In a simple electrospinning system a high voltage power supply, a capillary and a collector are used (Fig. 24.1). One electrode is placed into the polymer solution present in the capillary and the other one is attached to the collector. As the high voltage is applied, the polymer jet undergoes an elongation process before reaching the collector screen, the solvent evaporates and the polymer is collected as a solidified interconnected web of nanofibers [2].

Distinct properties that make electrospun nanofibrous materials unique are their high surface area, porosity, tensile strength (stronger than steel on weight basis) and

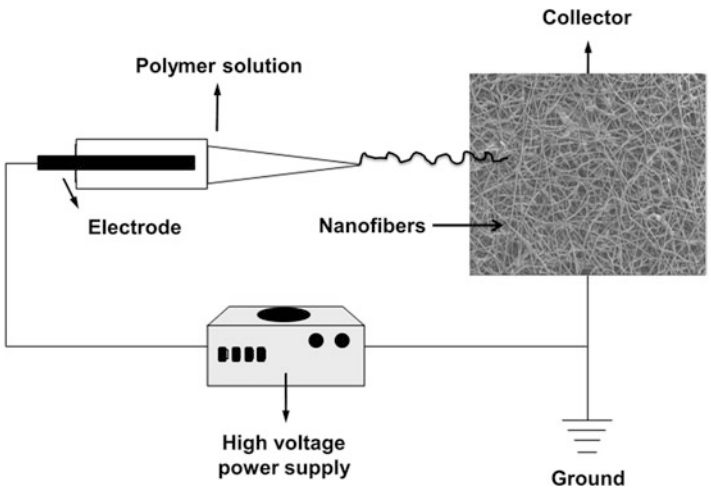

Fig. 24.1 Components of an electrospinning system

high extensibility (comparable to rubber elasticity). Indeed, the size of the fibers down to the nanometer scale make the final structures unique. Electrospinning enables to produce non-woven nanofibers which are homogeneous in size and geometry. But also it is possible to prepare oriented nanofibers. The orientation of the fibers can be accomplished using a rotating mandrel or a rotating disk collector. The applications of electrospun nanofibers include the use of pesticide containing ones or using them as a physical barrier to insects. They can also be used in the filtration of unwanted ingredients in the gases released from a factory. Space or construction technologies can apply them. Biomedicine is another area of application of the nanofibers, they can be used as tissue engineering scaffolds since they mimic very well the structure of the extracellular matrix [3]. And they can be used in protective clothing.

24.3 Protective Clothing for Chemical/Biological Hazards

Chemical and biological warfare agents target tissues and organs which cause poisoning, disease and deterioration. Chemical or biological weapons cause significant threats to humankind. For example, nerve gases can enter the body by inhalation or by skin absorption, resulting in death from acute poisoning occuring in a minute by asphyxia. Blood agents interfere with the body's ability to absorb oxygen; as a result the victim dies as the body tissues are starved of oxygen. Choking agents attack the lungs and cause them to fill with fluid.

There are different types of defence equipments to protect the body from the chemical and biological agents such as detectors, protective clothing, decontaminants and medical counter measures. A variety of studies have reported about protective clothing against chemical and biological agents, because many of the agents enter the body through the skin.

Presently applied protective clothing against chemical and biological agents include the use of activated charcoal impregnated with metal ions, which physically adsorb agents thereby creating disposal waste after its usage. Metal oxide nanoparticles such as TiO_2 and MgO are currently suggested as potential catalysts for the decontamination of chemical and biological agents. The significant properties of these "destructive adsorbents" are due to their high surface areas and high surface concentrations of reactive defect sites. However, there are disadvantages of modification of textile surfaces with those nanoparticles: nanoparticles are not stable on the surface of the textiles; they need to be stabilized by using some processes, and those processes may change the mechanical and physical properties of the textile materials such as tensile strength, softness, flexibility and appearance. In addition, the toxic effects of nanoparticles on human systems is still under discussion; inhalation of these nanoparticles in high doses can result in pulmonary inflammation and allergic reactions, therefore the use of nanoparticles in powder form is problematic in

protective clothing. To overcome this limitation, research effort was directed to incorporate nanoparticles into nanofibers by including nanoparticles into the polymer solution before electrospinning [4].

24.4 Electrospun Membrane Based Protective Clothing

Nanofiber based materials suggest novel protecting clothing materials with comfortable, adsorptive and lightweight properties conntaining active detoxyfying/decontaminating nanomaterials, due to their extraordinary physical and chemical properties at the nano level. Electrospinning is one of the simplest and cheap methods to produce nanofibrous materials [5]. There is a variety of developments related to the application of electrospun nanofibrous materials in fabricating lightweight, comfortable and functional protective clothing for military personnel. The new developed materials include catalytic active nanofibers (for chemical and biological breakdown); sensors (sensitive to absorbtion and subsequent change); nanofibers for reinforcement (antiballistic application); insulating nanofibers; selective gas permeating properties; high strength composites (carbon nanotube-polymeric nanofibers) [5].

24.5 Antibacterial Nanofibers

Studies have been made to incorporate nanoparticles into electrospun nanofibers to enhance their properties [6]. Polymers including polyamide, polyviniyl alcohol, polyurethane, polypropylene, nylon-6, poly(viniyl chloride), polysulfone, poly (methyl methacrylate), and cellulose acetate, were combined with nanoparticles such as Ag, TiO_2, Cu, ZnO, MgO, and ZrO_2. The composite materials gained functional properties like flame retardancy, UV protection, self cleaning, antistatic and antimicrobial activities.

Current developments related to the potential use of electrospun nanofibers in protective clothing include the production of antimicrobial nanofibers. Most textile materials recently used in military are open to diseases caused by microorganisms. To avoid infections and attack of microorganisms, antimicrobial properties can be gained in textile material by incorporating functional agents (metal oxides such as Ag, TiO_2, Cu, ZnO, MgO) onto fibers and fabrics. In addiditon, drug loading into textile material can be obtained by incorporating a drug during the preparation of the textile material or after the formation of it by incubating the drug with it [7].

The toxicity of elements to microorganisms is considered to be in the following sequence: Ag > Hg > Cu > Cd > Cr > Pb > Co > Au > Zn > Fe > Mn. The principle of the mechanism of the antibacterial effect of those toxic elements to microorganism includes the electrostatic interaction between negatively charged bacterial cells and

positively charged nanoparticles. As an example, the mechanism of action for Ag is to strongly bind to electron donor groups containing S, O, or N and to bring about structural and functional changes in the cell. When Ag binds to proteins in the cell wall, the wall is destroyed, and the internal cell content leaks out, resulting in the death of the bacterial cell. Consequently, this prevents the microorganism from performing its functions, like carrying out processes necessary for respiration or processing nutrients leading to the subsequent death of the bacterial cell [8].

Related to the potential use of antibacterial nanofibers, a variety of studies is present in the literature. As example from previous studies, Magnesia (MgO) nanoparticles were produced from magnesite ($MgCO_3$) using ball milling; Nylon 6 pellets were dissolved in a mixture of formic acid and acetic acid. MgO nanoparticles were added into the prepared homogenous Nylon 6 polymer solution. MgO/Nylon 6 hybrid nanofibers were coated on a cotton fabric. The values of flammability and antibacterial activity were evaluated. The burning time for MgO-Nylon fabrics were found to be higher than that of Nylon and uncoated cotton fabrics. In addition, the MgO-Nylon 6 fabric showed a higher bacterial reduction percentage when compared to the pure Nylon fabric. The MgO-Nylon6 fabric has enhanced protective surface properties through antibacterial activity [6].

The conventional electrospinning technique was not satisfactory due to the coverage of the nanoparticles by the polymeric nanofibers. To overcome this constraint, the electrospraying technique was combined with the electrospinning method. Electrospraying has been demonstrated to be one of the most promising approaches to prepare nanofibers with nanoparticles on their surfaces. The production of functionalized nanofibrous materials was carried out by electrospinning of nanofibers and electrospraying of nanoparticles. Two types of membranes were fabricated. Electrospinning of a polysulfone polymer and electrospraying of TiO_2 nanoparticles dispersed in the presence of surface modifier can be given as an example to the application of this combined technique [4].

In another work, silver loaded titania was prepared by introducing silver nanoparticles onto a titania surface. Polyurethane was dissolved in a solvent mixture of N,N-dimethylformamide and tetrahydrofuran. Polyurethane solutions were electrospun to nanofibrous structures by using an electrospinning setup with a two robot system. The equipment was basically composed of a rotating drum collector, a high voltage power supply and a syringe pump.A silver-titania spreaded polyurethane nanofibrous composite was prepared by a simultaneous electrospinning/electrospraying process. The photocatalytic degradation of a chemical agent stimulant for the nerve agent Sarin (Dimethyl methylphosphonate (DMMP)) was evaluated; the nanofibrous composite material showed photocatalytic degradation of DMMP under visible light and UV-A irradiation. The antimicrobial activity of the material was quantified against *Staphylococcus aureus*. The composite material showed a good functional antimicrobial activity against *Staphylococcus aureus*. The composite demonstrated to be able to act as a functional protection layer with the photocatalytic and antimicrobial activities against chemical and biological agents [9].

24.6 Conclusions

The development of new and smart protective textiles for future applications include the integration of nanoparticles with sensing properties, sensors and electronic devices attached into the textile structures to produce smart protective textile materials, and energy storing protective clothing. Smart protective textiles are still in the development phase and some of the materials are already quite close to commercial production. However, there are limitations: nanofiber based protective cloths are still at the development stage; extensive research is needed for the adequate production of these materials on a large scale. Furthermore, the health and safety problems related to the products which include nanoparticles require a completed investigation and evaluation in view of short and long term health risks.

References

1. Huang ZM, Zhang YZ, Kotaki M, Ramakrishna S (2003) A review on polymer nanofibers by electrospinning and their applications in nanocomposites. Compos Sci Technol 63:2223–2253
2. Pişkin E, Bölgen N, Eğri S, İşoğlu İA (2007) Electrospun matrices made of poly(α-hydroxy acids) for medical use. Nanomedicine 2:441–457
3. Pişkin E, İşoğlu İA, Bölgen N, Vargel İ, Griffiths S, Çavuşoğlu T, Korkusuz P, Güzel E, Cartmell S (2009) In vivo performance of simvastatin-loaded electrospun spiral-wound polycaprolactone scaffolds in reconstruction of cranial bone defects in the rat model. J Biomed Mater Res Part A 90:1137–1151
4. Sundarrajan S, Chandrasekaran AR, Ramakrishna S (2010) An update on nanomaterials-based textiles for protection and decontamination. J Am Ceram Soc 93:3955–3975
5. Thilagavthi G, Raja ASM, Kannanian T (2008) Nanotechnology and protective clothing for defence personnel. Def Sci J 58:451–459
6. Dhineshbabu NR, Karunakaran G, Suriyaprabha R, Manivasakan P, Rajendran V (2014) Electrospun MgO/Nylon 6 hybrid nanofibers for protective clothing. Nano-Micro Lett 6:46–54
7. Ramdayal K (2013) Balasubramanian, advancement in textile technology for defence. Def Sci J 63:331–339
8. Lala NL, Ramaseshan R, Bojun L, Sundarrajan S, Barhate RS, Ying-Jun L, Ramakrishna S (2007) Fabrication of nanofibers with antimicrobial functionality used as filters: protection against bacterial contaminants. Biotechnol Bioeng 97:1357–1365
9. Ryu SY, Park MK, Kwak SY (2013) Silver-titania/polyurethane composite nanofibre mat for chemical and biological warfare protection. Int J Nanotechnol 10:771–788

Part VII
Materials: Nanocomposites

Chapter 25
Temperature Effect on the Dielectric Response of Carbon Nanotubes Particles Filled Polyester Polymer Composites

Z. Samir, S. Boukheir, Y. El Merabet, M. P. F. Graça, M. E. Achour, and L. C. Costa

Abstract Polyester/carbon nanotubes composites were prepared, and the frequency and temperature dependence of the electrical properties were studied at concentrations below and above the percolation threshold. The analysis of the complex permittivity using the derivative formalism allows us to overcome difficulties caused by the high electrical conductivity, which can mask the dielectric relaxation processes. The dielectric permittivity was analyzed using the Havriliak-Negami model taking into account the effect of electrode polarization. This analysis enabled us to describe quantitatively the experimental data, to calculate the ohmic conductivity and the parameter characterizing the contribution of the ohmic conduction to the complex dielectric permittivity. Above the percolation threshold, using the complex permittivity the dielectric data were analyzed at several temperatures. Both below and above the percolation threshold, the activation energy decreases with an increase in the concentration of carbon nanotube in the composite, which may be due to an increase of charge carrier density leading to a decrease of the domain boundary potential of carbon nanotube aggregates in the polyester matrix.

Keywords Carbon nanotubes · Composites · Electrical conductivity · Havriliak-Negami model

Z. Samir · Y. El Merabet · M. E. Achour (✉)
LASTID Laboratory Department of Physics, Faculty of Sciences, University Ibn Tofail, Kenitra, Morocco
e-mail: achour.me@univ-ibntofail.ac.ma

S. Boukheir
LASTID Laboratory Department of Physics, Faculty of Sciences, University Ibn Tofail, Kenitra, Morocco

Laboratoire LN2E, Faculté des Sciences, Université Cadi Ayyad, Marrakech, Morocco

M. P. F. Graça · L. C. Costa
I3N and Physics Department, University of Aveiro, Aveiro, Portugal

P. Petkov et al. (eds.), *Advanced Nanotechnologies for Detection and Defence against CBRN Agents*, NATO Science for Peace and Security Series B: Physics and Biophysics, https://doi.org/10.1007/978-94-024-1298-7_25

25.1 Introduction

Carbon nanotubes (CNT) are tiny cylindrical structures, characterized by a high aspect ratio, that is, a significant length relative to their nanometric diameter, and possess exceptional transport and mechanical properties [1, 2]. CNTs can have either conducting or semiconducting properties [3, 4], which make them functional for many applications, such as polymer based nanocomposites for electromagnetic interference shielding, electrostatic discharge and electrically conductive parts of devices [5–7]. The electrical conductivity of polymer/CNT composites depends strongly on the filler network formation, providing the path of external electrical currents through the material [8–12].

Relaxation phenomena in solid dielectrics are one of the most studied topics in materials science and usually the spectra of the real and imaginary parts of the complex permittivity are extensively used to present this kind of dielectric behaviour [13]. However, this analysis may be rendered difficult because of a DC conductivity contribution that hides the dielectric relaxation processes. In order to overcome this shortcoming caused by the high electrical conductivity, a suitable alternative is introduced in this study.

In this paper, the effect of frequency and temperature on the dielectric response of CNT filled polyester matrix was studied at concentrations below and above the percolation threshold. Below the percolation threshold, we have studied the nature of the relaxation mechanisms by analyzing the frequency and temperature dependence of the real and imaginary parts of the dielectric permittivity, revealing the ohmic conductivity and the parameters characterizing that contribution, and calculating the activation energies using the Vogel-Tammann-Fulcher (VTF) equation. We have found that the calculated activation energy values decrease as the filler concentration of CNTs inside the polymer matrix increases. Above the percolation threshold, the dielectric data were also analyzed using the complex permittivity at different temperatures. The temperature dependence of the DC conductivity follows the VTF equation which allows us to estimate the activation energies of the processes in the composite materials. By adding low concentrations of CNTs the values of the activation energy decrease as a result of the impact of space charge. The addition of low concentrations creates local energy levels in the energy gap which could act as traps for charge carriers, which move by hopping between these levels. By increasing the CNT concentration, the activation energy decreases as a result of the increase of local centers.

25.2 Experimental

25.2.1 Materials

Multiwalled carbon nanotubes were purchased from Cheap-Tubes, USA, possessing average diameters about 50 nm, lengths between 10 and 20 μm and

a purity above 95 wt%. The matrix used in this work was the unsaturated polyester resin 154TB, including 31 wt% of the styrene monomer, requiring 30 min for gelation at room temperature. It was acquired from Cray Valley/Total, USA. The polyester/CNT nanocomposites were prepared by mixing 5.87 g of liquid polyester resin and 0.2% weight of cobalt octanone as reaction activator. CNTs were introduced before adding 1.0% of hardener to make each mixture cohesive. Each polyester/CNT composite was mixed at room temperature for 5 min, promoting the gelation and then it was poured into a mould. After a few hours, the samples were unmoulded, taking 24 h for having a complete polymerization.

25.2.2 DC Electrical Conductivity

For the electrical measurements, we used samples with a shape of discs, possessing a thickness of about 3 mm and diameter of 12 mm. Prior to these measurements, the sample surfaces were polished and covered with a thin layer of silver paint. DC conductivity measurements σ_{DC} were carried out using a 617 Keithley electrometer. The electrical contacts were made with silver paint. The experiment consists in measuring the electrical resistance of each sample in order to determine the DC conductivity of the different series of the composites at a constant temperature of 300 K.

25.2.3 AC Electrical Conductivity

The complex permittivity function $\varepsilon^*(\omega) = \varepsilon^{'}(\omega) + \varepsilon^{''}(\omega)$, was measured using an Agilent 4294A precision impedance analyser. The relative permittivity $\varepsilon^{'}$, and the loss factor $\varepsilon^{''}$, of the sample were calculated from the admittance $Y^*(\omega) = G(\omega) + iB(\omega) = iC_0\omega\varepsilon^*(\omega)$ of the equivalent circuit leading to $\varepsilon^{'}(\omega) = 2h \cdot B/\varepsilon_0 \cdot d^2\pi^2F$ and $\varepsilon^{''}(\omega) = 2h \cdot G/\varepsilon_0 \cdot d^2\pi^2F$, where B is the susceptance, G the conductance, F the frequency, ε_0 the vacuum dielectric constant, and h and d are the thickness and the diameter of the sample, respectively. The measurements were performed in the frequency range 100 Hz to 1 MHz under isothermal conditions, for temperatures ranging between 300 and 380 K. The imaginary part of $\varepsilon^{''}$ can be written as the sum of two terms: $\varepsilon^{''}(\omega) = \varepsilon''_{\text{cond}}(\omega) + \varepsilon''_{\text{relax}}(\omega)$, where $\varepsilon''_{\text{cond}}$ and $\varepsilon''_{\text{relax}}$ represent the contributions of an eventual conduction mechanism and relaxation phenomena in the sample, respectively.

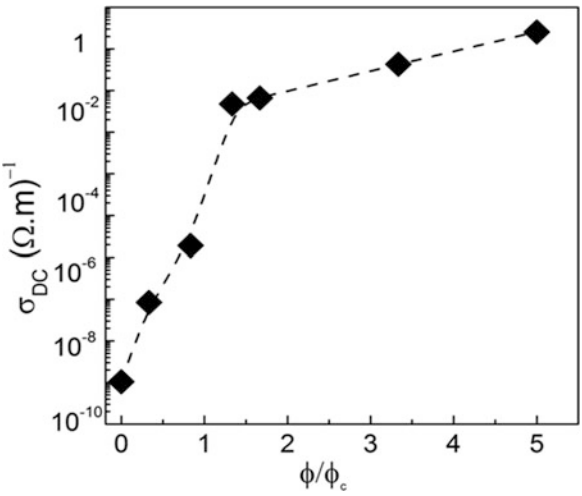

Fig. 25.1 DC conductivity as a function of ϕ/ϕ_c of the polyester/CNT composites

25.3 Results and Discussion

25.3.1 DC Conductivity

Figure 25.1 shows the DC conductivity of the composites as a function of CNT concentration, normalized by the percolation threshold ϕ_c. At low CNT loading, the composite is still an insulating material. A sharp increase in conductivity is observed at the critical concentration, indicating the formation of a percolation network. The DC conductivity above the percolation threshold can be correlated to the conductive filler volume concentration given by $\sigma \propto (\phi - \phi_c)^t$ [14], where t is the percolation exponent related to the dimensionality of the system. In our previous work [15, 16], using least squares fits, we found the percolation threshold $\phi_c \approx 0.60\%$ and the experimental exponent $t = 1.58$.

25.3.2 Dielectric Response Below the Percolation Threshold

Figure 25.2 illustrates the variation of the real ε', and the imaginary ε'', parts of the complex permittivity versus frequency, for different CNT concentrations below the percolation threshold at a constant temperature T = 300 K. It is noticed that both ε' and ε'' decrease with increasing frequency and increase with increasing CNT concentrations.

The frequency dependence of ε' and ε'' at constant temperatures for a fixed concentration of CNTs close to the percolation threshold ($\phi = 0.5\%$), is shown in Fig. 25.3a, b. The analysis of these curves reveals that ε' decreases with frequency which can be a signature of a relaxation process in the composite. In addition, we can

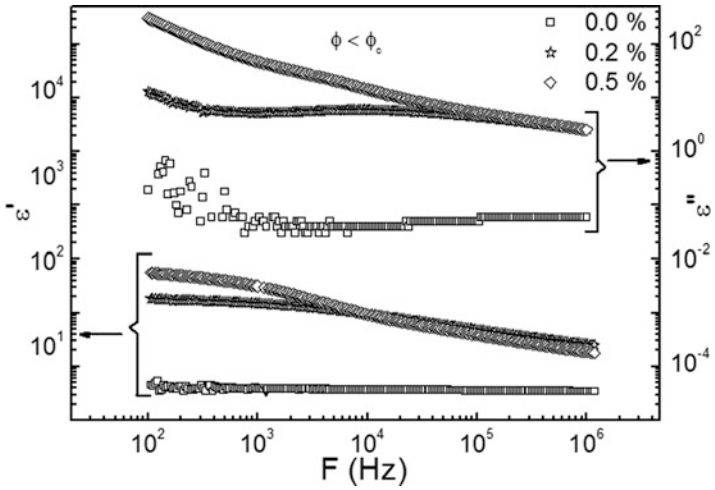

Fig. 25.2 ε' and ε'' for different concentrations of CNT below ϕ_c, at a constant temperature T = 300 K

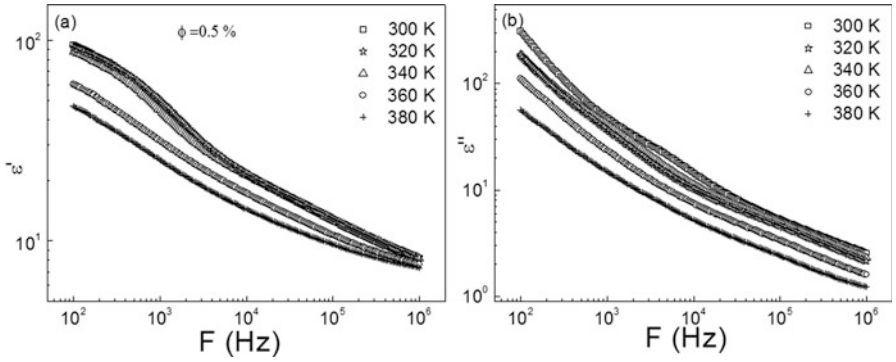

Fig. 25.3 The frequency dependence of ε' and ε'' at constant temperatures of polyester/CNT composites with 0.5% CNT inclusions

see that there is no sign of dielectric relaxation peaks in ε'' (Fig. 25.3b). These peaks are however hidden by ohmic conduction losses. In order to eliminate the ohmic conduction from the measured loss spectra and to highlight the dielectric relaxation peaks in fine, the trend towards using Kramers-Kronig relations (KK) [17, 18] seems to be the best way

$$\varepsilon''(\omega_0) = \varepsilon''_{cond}(\omega_0) + \varepsilon''_{relax}(\omega_0) = \frac{\sigma_{DC}}{\omega_0 \varepsilon_0} + \frac{2}{\pi}\int_0^{\infty} \varepsilon'(\omega)\frac{\omega_0}{\omega^2 - \omega_0^2} d\omega \qquad (25.1)$$

where σ_{DC} is the ohmic conduction, ε_0 the vacuum permittivity and ω_0 the relaxation frequency. It should be noted that both ε' and ε'' contain the information about the

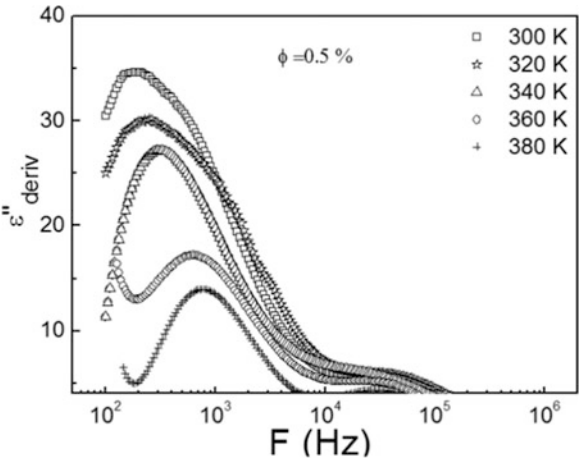

Fig. 25.4 Variation of $\varepsilon''_{\text{deriv}}$ with frequency at different temperatures of polyester/CNT composites with 0.5% CNT inclusions

relaxation process. However, ε' has made no conspicuous contribution to the frequency independent ohmic conduction. For this reason, the determination of the dielectric loss from the real part of the permittivity removes the conduction contribution. One useful technique is based on the derivation, which transforms the real part of the complex permittivity ε' into $\varepsilon''_{\text{deriv}}$, as given by Eq. (25.2) [19–23]

$$\varepsilon''(\omega) \approx \varepsilon''_{\text{deriv}}(\omega) = -\frac{\pi}{2}\frac{\partial \varepsilon'(\omega)}{\partial \ln(\omega)} \tag{25.2}$$

As seen in Fig. 25.4, $\varepsilon''_{\text{deriv}}$ possesses a sharp peak indicating the existence of a dielectric relaxation process which was previously totally masked by the DC conductivity. Indeed, when using the derivative technique, dielectric relaxation peaks are henceforth undeniably visible.

The frequency dependence of the real and imaginary parts of the dielectric permittivity reveals that the relaxation processes in these composites are rather complex. In order to determine the parameters of this processes, we analysed the results using the Havriliak–Negami model (M_{HN}), taking into consideration the ohmic conduction losses. In this model, the expression of the complex dielectric permittivity is given by Eq. (25.3) [24]:

$$\varepsilon^*(\omega) = \varepsilon_\infty + \frac{\varepsilon_s - \varepsilon_\infty}{(1 + (i\omega t)^\alpha)^\beta} + \frac{1}{i}\left(\frac{\sigma_{DC}}{\omega \varepsilon_0}\right)^N. \tag{25.3}$$

where ε_s and ε_∞ are the dielectric constants at zero and infinite frequency respectively, τ is the relaxation time, and α and β are empirical exponents. σ_{DC} is the ohmic conductivity and N a parameter characterizing the contribution of the ohmic conduction in the complex dielectric permittivity. It is worthy to notice that we are interested only in the parameters σ_{DC} and N.

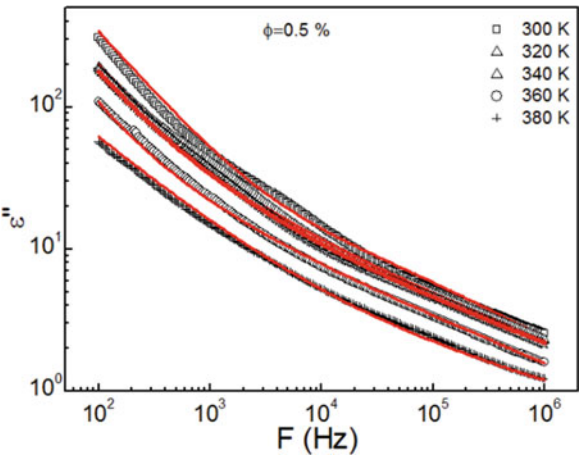

Fig. 25.5 Variation of ε'', with frequency for different temperatures below percolation threshold. Symbols are the experimental points and the solid lines are the fits for M_{HN} model

The real ε' and imaginary ε'' parts of the complex permittivity in this model are defined as follows (Eqs. (25.4) and (25.5)) [24]:

$$\varepsilon'(\omega) = \varepsilon_\infty + \frac{(\varepsilon_s - \varepsilon_\infty)(\cos(\beta \tan^{-1}(\rho)))}{\xi^{\beta/2}}. \tag{25.4}$$

$$\varepsilon''(\omega) = \varepsilon_\infty + \frac{(\varepsilon_s - \varepsilon_\infty)(\sin(\beta \tan^{-1}(\rho)))}{\xi^{\beta/2}} + \left(\frac{\sigma_0}{\varepsilon_0 \omega}\right)^N. \tag{25.5}$$

where $\varrho = \frac{(\omega\tau)^\alpha \sin(\alpha\pi/2)}{1+((\omega\tau)^\alpha \cos(\alpha\pi/2))}$ and $\xi = 1 + (\omega\tau)^{2\alpha} + 2(\omega\tau)^\alpha \cos(\alpha\pi/2)$

In order to calculate the values of σ_{DC} and N, we analyzed the experimental results of ε'' using the Havriliak-Negami model. Figure 25.5 shows that this model presents a very good adjustment for the experimental values of ε'' in the explored range of frequencies. Figure 25.6 illustrates the parameter N obtained by fitting ε'' as a function of temperature. One can clearly see that this parameter varies between 0.3 and 1.

In order to calculate the activation energy, we used the parameter σ_{DC} calculated by adjustment of ε''. Figure 25.7 shows that the conductivity increases exponentially with temperature, indicating that it is a thermally activated process, governed by the VTF law [25, 26]:

$$\sigma_{DC} \propto \exp\left(-\frac{E}{K_B(T - T_0)}\right). \tag{25.6}$$

Here E is the activation energy of σ_{DC} and K_B, T and T_0 are Boltzman's constant, absolute temperature and ordering temperature, respectively. It should be noted that E was calculated from the slopes of the straight lines of $ln\ (\sigma_{DC})$ versus $1/(T-T_0)$ (Fig. 25.7) for the volume CNT concentrations of 0.0%, 0.2% and 0.5%. The values of the activation energy for the three concentrations were calculated and are resumed in Table 25.1. As can be seen there is a decrease in the activation energy as the filler

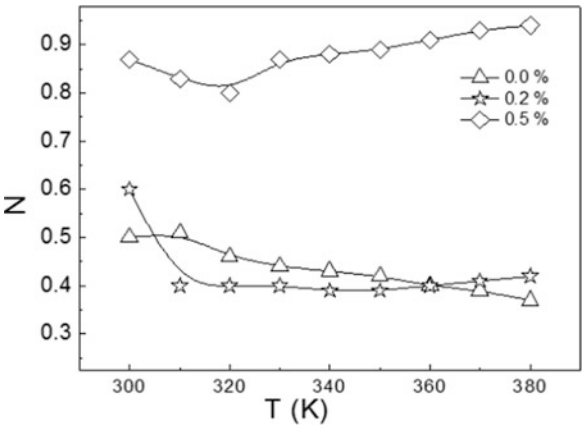

Fig. 25.6 Parameter N obtained by fitting ε'' as a function of temperature, for different volume concentrations of CNT (0.0%, 0.2% and 0.5%)

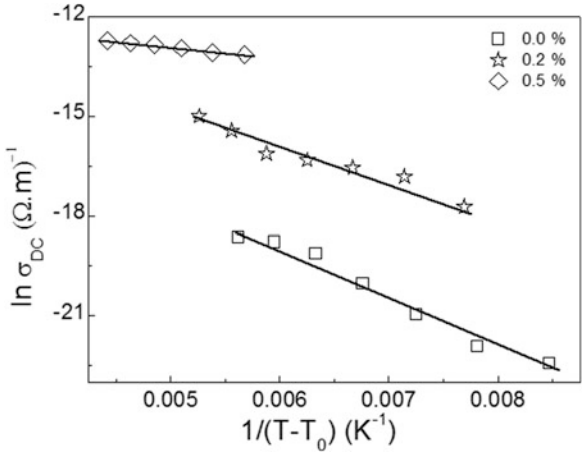

Fig. 25.7 $\ln(\sigma_{DC})$ vs. $1/(T-T_0)$ for different volume concentrations of CNT (0.0%, 0.2% and 0.5%)

Table 25.1 Summary of VTF fitting parameters E and T_0 for different volume concentrations of CNT (0.0%, 0.2% and 0.5%)

ϕ (%)	E (meV)	T_0 (K)
0.0	128.50 ± 7.22	201 ± 4
0.2	87.45 ± 5.30	190 ± 4
0.5	30.07 ± 3.62	154 ± 6

concentration of CNT increases. Similar to a study of the effect of carbon black particle on epoxy [27, 28], this behavior may be due to an increase of charge carrier density leading to a decrease of the domain boundary potential of CNT aggregates in the polyester matrix.

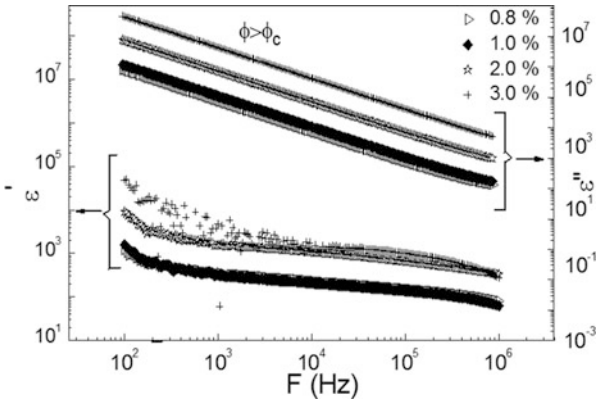

Fig. 25.8 ε' and ε'' for different concentrations of CNTs above ϕ_c, at constant temperature T = 300 K

25.3.3 Dielectric Response Above the Percolation Threshold

For $\phi > \phi_c$, the composite material is characterized by the formation of an infinite cluster of carbon nanotube particles, which allows the displacement of electrons over large distances of the sample. The interfacial polarization phenomenon on surfaces of the finite clusters can always exist but it is masked by the conduction process $\varepsilon''_{\text{relax}} \ll \varepsilon''_{\text{cond}}$ [29]. In Fig. 25.8, we depict ε'(a) and ε''(b) at a temperature of 300 K for different volume concentrations above ϕ_c of the CNT. The figure clearly demonstrates that the spectra of ε'' strongly depend on frequency and decrease with increasing frequency. These spectra are also marked by a linear behavior in the logarithmic representation in both the low and the high frequency regions. The slopes of these curves for various concentrations are practically identical (very close to 1) which is a signature of ohmic conduction losses.

The study of the AC electrical conductivity σ_{AC}, is normally carried out to better understand the frequency dependence of the electrical transport properties of the composites. Figure 25.9 shows the AC conductivity for $\phi = 1.0\% > \phi_c$ in the frequency range from 100 Hz to 1 MHz and temperatures between 300 and 380 K. We note that the value of σ_{AC}, increases with rise in frequency and becomes independent in the low frequency region; this is identified as the DC conductivity σ_{DC}. This type of behaviour is very similar to that of previous reports for carbon black composites [15, 30]. Figure 25.10 shows temperature dependence of the DC conductivity, which increases exponentially with temperature. It is noticeable that this temperature dependence also follows the VTF model (Eq. (25.6)) [25, 26].

The measured values of the activation energy E and T_0 as a function of the CNT volume fraction are given in Table 25.2, showing that there is a decrease in the activation energy as the filler concentration increases.

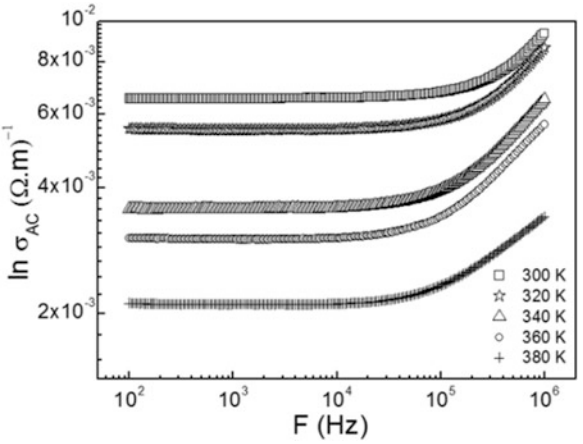

Fig. 25.9 Electrical conductivity versus frequency for a sample with a CNT concentration $\phi = 1.0\% > \phi_c$ of CNT

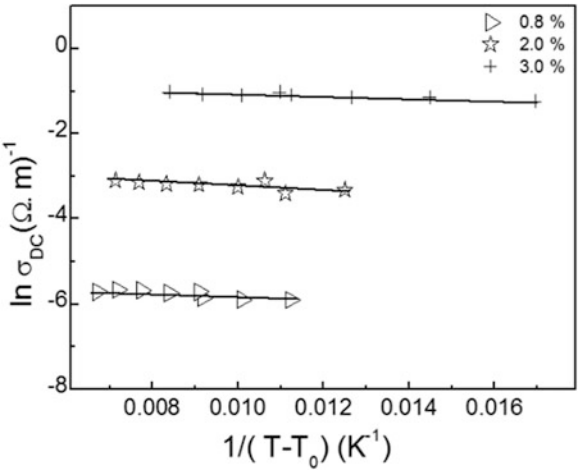

Fig. 25.10 ln (σ_{DC}) vs. $1/(T-T_0)$ for different concentrations of CNT above ϕ_c (0.8%, 2.0% and 3.0%)

Table 25.2 Summary of VTF fitting parameters E and T_0 for different volume CNT concentrations

ϕ (%)	E (meV)	T_0 (K)
0.8	5.17 ± 0.36	231 ± 2
2.0	4.26 ± 0.28	240 ± 3
3.0	1.93 ± 0.32	261 ± 4

25.4 Conclusion

In summary, the dielectric properties of polyester filled with different concentrations of CNTs have been investigated. From the obtained results, the following conclusions can be drawn. The Kramers-Kronig based derivative technique that we have applied to the real and imaginary parts of the complex dielectric seems to be more

suited when considering the objectives of our study. Indeed, when using this technique, the relaxation peaks are undeniably visible. The dielectric permittivity is found to be well fitted by the Havriliak-Negami model taking into account the effect of electrode polarization. From this model, this analysis enabled us to describe quantitatively the experimental data from which we extracted the ohmic conductivity and the parameter characterizing the contribution of the ohmic conduction in the complex dielectric permittivity. Furthermore, the temperature dependence of DC conductivity follows the VTF equation which allows us to estimate the activation energies of the processes in the composite materials. We have found that the calculated activation energy values decrease as the filler concentration of CNT contents inside the polymer matrix increases.

Acknowledgments The authors acknowledge support from CNRST-Maroc (Centre National de la Recherche Scientifique et Technique) for their financial support, and FEDER by funds through the COMPETE 2020 Program and National Funds through FCT – Portuguese Foundation for Science and Technology under the project UID/CTM/50025/2013.

References

1. Dresselhaus MS, Avouris P (2001) Carbon nanotubes. Springer, Berlin, pp 1–9
2. De Volder MFL, Tawfick SH, Baughman RH, Hart AJ (2013) Carbon nanotubes: present and future commercial applications. Science 339(6119):339–1539
3. Hamada N, Sawada S-I, Oshiyama A (1992) New one-dimensional conductors graphitic microtubules. Phys Rev Lett 68:1579–1581
4. Bandaru PR (2007) Electrical properties and applications of carbon nanotube structures. J Nanosci Nanotechnol 71:1–29
5. Amarasekera J (2005) Conductive plastics for electrical and electronic applications. Reinf Plast 49:38–41
6. Pande S, Chaudhary A, Patel D, Singh BP, Mathur RB (2014) Mechanical and electrical properties of multiwall carbon nanotube/polycarbonate composites for electrostatic discharge and electromagnetic interference shielding applications. RSC Adv 4:13839–13849
7. Park IS, Kim KJ, Nam JD, Lee JS, Yim WS (2007) Mechanical, dielectric, and magnetic properties of the silicone elastomer with multi-walled carbon nanotubes as a nanofiller. Polym Eng Sci 47(9):1396–1405
8. Fischer JE (2006) Carbon nanotubes. In: Carbon nanomaterials. Taylor and Francis Group, NewYork, pp 51–58
9. Pierson HO (1993) Handbook of carbon, graphite, diamond and fullerences. Noyes Publications, Park Ridge
10. Meyyappan M (2004) Carbon nanotubes: science and applications. CRC Press, Boca Raton
11. Boukheir S, Len A, Füzi J, Kenderesi V, Achour ME, Eber N, Costa LC, Outzourhit A, Oueriagli A (2017) Fractal structure and temperature-dependent electrical study of carbon nanotubes/epoxy polymer composites. Spect Lett 50(4):183–188
12. Boukheir S, Len A, Füzi J, Kenderesi V, Achour ME, Eber N, Costa LC, Outzourhit A, Oueriagli A (2017) Structural characterization and electrical properties of carbon nanotubes/epoxy polymer composites. J Appl Polym Sci 134(8). https://doi.org/10.1002/APP.44514
13. Kao KC (2004) Dielectric phenomena in solids. Elsevier Acad Press 525:92101–94495
14. Stauffer D, Aharony A (1992) Introduction to percolation theory. Taylor and Francis, London

15. Abazine K, Anakiou H, El Hasnaoui M, Graca MPF, Fonseca MA, Costa LC, Achour ME, Oueriagli A (2016) Electrical conductivity of multiwalled carbon nanotubes/polyester polymer nanocomposites. J Compos Mater 50(23):3283–3290
16. Samir Z, El Merabet Y, Graça MPF, Teixeira SS, Achour ME, Costa LC (2016) Impedance spectroscopy study of polyester/carbon nanotube composites. Polym Compos:1548–1569. https://doi.org/10.1002/pc.24067
17. Macdonald JR (1987) Impedance spectroscopy. Wiley, Oxford, p 197
18. Kremer F, Hartmann L (2001) Dielectric news letter
19. Steeman P, Turnhout JV (1994) Fine structure in the parameters of dielectric and viscoelastic relaxations. Macromolecules 27:5421–5427
20. Wuubbenhorst M, Turnhout JV (2002) Analysis of complex dielectric spectra. I. One-dimensional derivative techniques and three-dimensional modelling. J Non-Cryst Solids 305:40–49
21. Molak A, Paluch M, Pawlus S, Klimontko J, Ujma Z, Gruszka I (2005) Electric modulus approach to the analysis of electric relaxation in highly conducting. J Phys 38(9):1450–1460
22. Samir Z, El Merabet Y, Graça MPF, Teixeira SS, Achour ME, Costa LC (2017) Dielectric behaviour of carbon nanotubes particles-filled polyester polymer composites. J Compos Mater 51(13):1831–1837
23. Mingjuan H, Kongshuang Z (2008) Effect of volume fraction and temperature on dielectric relaxation spectroscopy of suspensions of PS/PANI composite microspheres. J Phys Chem C 112:19412–19422
24. Signorelli R, Ku DC, Kassakian JG, Schindall JE (2009) Electrochemical double-layer capacitors using carbon nanotube electrode structures. Proc IEEE 97(11):1837–1847
25. Every H, Bishop AG, Forsyth M, MacFarlane DR (2000) Ion diffusion in molten salt mixtures. Electrochim Acta 45:1279–1284
26. McFarlane DR, Sun J, Golding J, Meakin P, Forsyth M (2000) High conductivity molten salts based on the imide ion. Electrochim Acta 45:1271–1278
27. El-Tantawy F, Kamada H, Ohnabe H (2002) In situ network structure, electrical and thermal properties of conductive epoxy resin–carbon black composites for electrical heater applications. Mater Lett 56(1):112–126
28. Trihotri M, Dwivedi UK, Khan FH, Malik MM, Qureshi MS (2015) Effect of curing on activation energy and dielectric properties of carbon black–epoxy composites at different temperatures. J Nan-Cryst Solid 421:1–13
29. Achour ME (2008) In: Brosseau C (ed) Prospects filled polymers engineering: mesostructure, elasticity network, and macroscopic properties. Transworld Research Network, Kerala, pp 129–174
30. El Hasnaoui M, Graca MPF, Achour ME, Costa LC (2011) Electric modulus analysis of carbon black/copolymer composite materials. Mater Sci Appl 2:1421–1426

Chapter 26
Nanosized Ferrite Materials for Absorption of and Protection from MW Radiation

Svetoslav Kolev and Tatyana Koutzarova

Abstract Ferrite materials suitable for mm-wave circulators should exhibit ferromagnetic resonance (FMR) in the mm range with high a saturation magnetization. In addition, the magnetic and dielectric losses and the temperature dependence of the magnetocrystalline anisotropy and of the saturation magnetization should be as low as possible. Therefore, compositionally and microstructurally homogeneous materials are required. The object of the work presented was to investigate the microwave (MW) absorbing properties of nanocomposite bulk samples. As a filler we used magnetite (Fe_3O_4) with different particle sizes in a silicone rubber matrix and investigated the influence of the filler concentration and particle size in the polymer matrix on the MW nonlinearity in a large frequency range (1–20 GHz). We found that the intensity and the frequency at the reflection loss minimum depend on the particle size and particle concentration of magnetite in the samples.

Keywords Nanosized ferrites · Magnetite · Shielding · Absorption · MW radiation

26.1 Introduction

Protection from electromagnetic radiation (EMR) in the MW range has lately become a problem of pressing interest due to the world-wide spread of technologies such as cellular phones, to name but one. MW radiation shielding in medical research and in MW domestic appliances has also focused the attention of researchers. Over the last 30 years, the transmission density has doubled every 4 years, meaning that the electromagnetic pollution has gone up by around 100 times. The wavelengths used are getting shorter; we have now entered the MW era where we are dealing with minuscule dimensions. However, the shorter the waves, the more energy they produce.

S. Kolev (✉) · T. Koutzarova
Institute of Electronics, Bulgarian Academy of Sciences, Sofia, Bulgaria

P. Petkov et al. (eds.), *Advanced Nanotechnologies for Detection and Defence against CBRN Agents*, NATO Science for Peace and Security Series B: Physics and Biophysics, https://doi.org/10.1007/978-94-024-1298-7_26

The health consequences of EMR exposure vary in intensity from mild symptoms to serious diseases. Some symptoms are termed as "radio-wave sickness". EMR from transmission towers and mobile phones are suspected of initiating cancer because of interfering with the electric field inside human cells. People working or living in continuous exposure to EMR are under the greatest risk.

A solution to the above problem may be provided by the new scientific branch of nanoscience and nanotechnology, which has undergo an extraordinarily fast development in the last three decades. Tools were created that allow us to obtain materials with very small dimensions and unique physical and chemical properties. The aim of this work was to prepare and investigate materials, in particular nanosized ferrites, to be used as shields and absorbers (as films with different thickness) of electromagnetic radiation in the MW range.

26.2 Result and Discussion

The aim of our study was to clarify the contribution of a Fe_3O_4 ferrite filler (commercial and laboratory-made) to the formation of the MW and magnetic properties of composite absorbing structures.

There exists a wide variety of absorbing materials that can be used for suppressing electromagnetic radiation, depending on the requirements for a narrow or wide absorbing frequency band, or for low- or high-frequency application of the absorber. Concerning the MW range, the absorbing materials most often used are rubbers, plastics, thermoplastics etc. These are non-magnetic substances which are resistant to atmospheric influences and often contain magnetic fillers, such as ferrites, iron, or cobalt-nickel alloys. The additives alter the values of the dielectric constant and the magnetic permeability so as to achieve maximal absorption of electromagnetic radiation.

The MW absorbing structures are commonly divided into several types according to their technical parameters and the principle of functioning.

26.2.1 Functioning Principles of Absorbers

26.2.1.1 Absorbing Structures of the First Type

When an electromagnetic wave reaches a free-space/material boundary surface, a part of the incident wave is reflected back from the front surface without penetrating into the respective material (Fig. 26.1), while another part of the wave is transmitted through the material. The amplitude and phase of both the reflected and the transmitted waves change depending on the material's characteristics. In particular, the amplitude of the transmitted wave diminishes or is attenuated. This attenuation

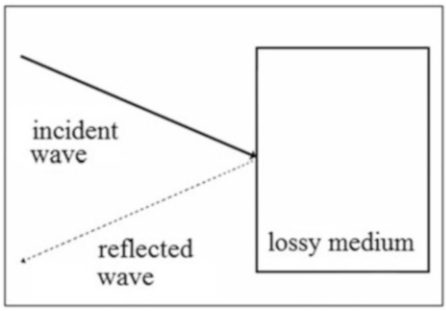

Fig. 26.1 Absorbing structures of the first type

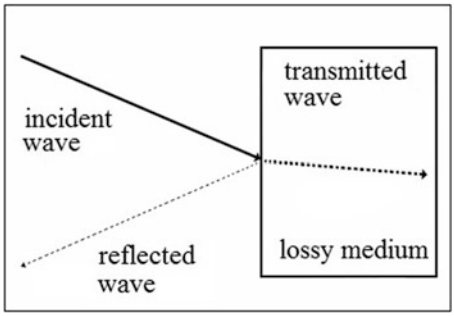

Fig. 26.2 Absorbing structures of the second type

results from dielectric or magnetic losses or both. It is a measure of the energy absorbed due to transmission only and can be calculated based on the material's properties.

The insertion losses are a measure of the total loss of energy that is due not only to attenuation but also to the reflection of part of the energy from the sample surface. The insertion losses are a function of both the material's characteristics and the thickness.

26.2.1.2 Absorbing Structures of the Second Type

When an electromagnetic wave is incident on a medium with electric characteristics different from those of free space, this medium will act as a reflector; the larger the medium's dielectric constant (i.e., the larger the difference between the impedance of free space and that of the front surface), the larger the reflection. In other words, any medium with high losses is a reflector; thus, in order to bring reflection to a minimum, the front surface impedance of the absorber should be chosen so as to be as close as possible to that of free space (Fig. 26.2).

Making use of a gradual impedance variation, namely, changing the impedance from a value close to that of free space at the front surface to a value of a high-loss medium, one can achieve a wide band absorption (Fig. 26.3).

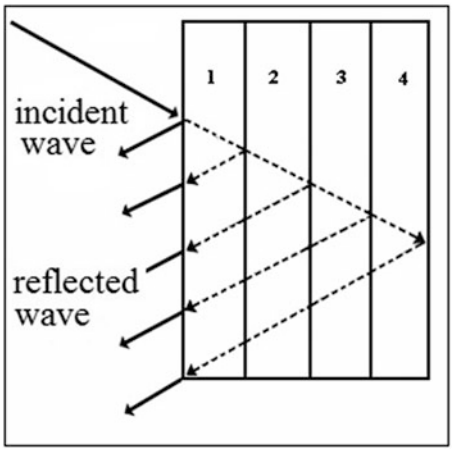

Fig. 26.3 Functioning principle of an absorber with a gradual impedance variation

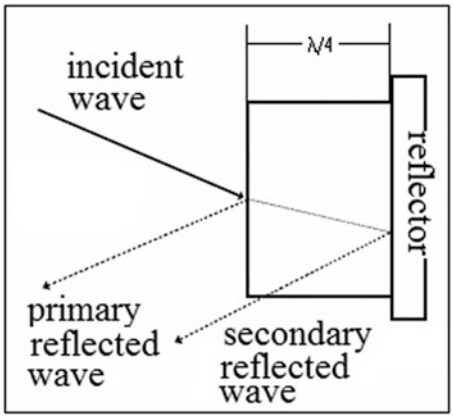

Fig. 26.4 Functioning principle of a quarter-wave absorber

26.2.1.3 Absorbing Structures of Third Type (¼ Wavelength Thickness)

The electromagnetic wave reflected from the absorber's front surface (the primary reflected wave) changes its amplitude and phase. The transmitted wave is attenuated partly in the medium and is reflected from the absorber's back surface (in the case illustrated in Fig. 26.4, from a total reflector) and leaves the front surface, thus forming a secondary reflected wave. When the phase difference of the primary and the secondary reflected waves is 180° (a quarter-wave absorber), destructive interference takes place, and the overall reflected wave amplitude is minimized.

The present interest in MW absorbing materials concerns mainly studies on ferrimagnetic composites in order to avoid radar detection in the GHz range [1–12]. These materials dissipate efficiently the electric and magnetic energy of an incident magnetic field. A widely-applied way of preparing such absorbing media is dispersing an electrically conductive powder in an insulating matrix. In the study reported here, we dealt with magnetite, which, unlike most ferrites, is a

semiconductor exhibiting a high electrical conductivity; as a consequence bulk magnetite behaves as reflector when irradiated by an electromagnetic wave. One can avoid this problem by homogeneously dispersing magnetite powder in an insulating matrix. The experiments on studying these material properties consist in irradiating them with a plane electromagnetic wave of a given frequency and detecting the transmitted and reflected signals. The latter are processed appropriately to obtain the material's dielectric constant and magnetic permeability, and to attempt to clarify the mechanisms giving rise to the magnetic losses.

Typically, the particle size of the fillers used in such experiments is 3–20 μm. In the study reported here, we compared the performance of a composite with a 30-nm Fe_3O_4 filler with that of a composite with a commercial magnetite filler with particle sizes of 300 nm and 3000 nm. With the advances in nanotechnologies allowing the preparation of nanostructured Fe_3O_4, its use as a filler has attracted growing interest due to its larger effective surface and, thus, higher potential efficiency.

To follow the characteristics of the composite structures prepared by us, we used an absorber described above as the **third type**. A TEM electromagnetic wave was directed normally to a one-layer absorber, with a perfect conductor placed behind it (short circuit) [13, 14]. This is a fast and accurate technique, allowing one to measure directly the reflection losses R_L (the ratio of the incident and the reflected power in dB).

The experimental setup employed to find the relationship between the sample's absorption properties, its thickness and the MW frequency range consisted of a scalar network analyzer (Hewlett Packard 8756 A, frequency band 1–20 GHz) and a sample mounted perpendicularly to the incident MW signal and short-circuited by a perfect conductor.

We evaluated the MW performance of magnetite powder dispersed in a polymer matrix (silicon rubber). The samples characterized contained magnetite powders with an average particle size of 30 nm (prepared by a soft-chemistry technique in the "Microwave Magnetics" laboratory IE BAS), as well as commercial products with particle sizes of 300 nm and 3000 nm (Nanostructured & Amorphous Materials Inc., USA). The ferrite powders were dispersed homogeneously in the polymer matrix. Two sets of samples were prepared for each of the three powder sizes. The first set consisted of toroidal specimens with an outer diameter of 7 mm, an inner diameter of 3 mm, different thicknesses of 1, 2, 3 and 4 mm (samples 1, 2, 3, 4) and the same filler-polymer weight ratio (Table 26.1).

The second set of samples had a thickness of 4 mm and different (increasing by the same step) degrees of filling, namely, samples A, B, C, and D – Table 26.2.

Table 26.1 Samples with different thicknesses of 1-4 mm and the same filler-polymer weight ratio

Sample	Filler-polymer weight ratio, g/cm^3	Sample thickness, mm
1	1,5:1	1
2	1,5:1	2
3	1,5:1	3
4	1,5:1	4

Table 26.2 Samples with thickness of 4 mm and different degrees of filling

Sample	Filler-polymer weight ratio, g/cm^3	Sample thickness, mm
A	1,2:1	4
B	1,5:1	4
C	1,8:1	4
D	2,1:1	4

The plots shown and commented on below were obtained under the conditions described earlier in the report, namely, a plane electromagnetic wave incident normally to a composite sample with a perfect conductor placed behind. The minima of the reflection losses curves R_L, i.e., the minimal reflected MW power, occur at certain frequencies, called matching frequencies. Generally, the plots demonstrate that the number of matching frequencies rises with the samples' thickness.

The frequency dependences of the reflection losses for nanocomposite absorbers with the same filler-polymer weight ratio and different thicknesses (1, 2, 3, 4 mm) and particles sizes of 30, 300 and 3000 nm are shown in Fig. 26.5.

Figure 26.6 illustrates the frequency dependence of the reflection losses (R_L) of nanocomposite absorbers with different filler-polymer weight ratios and equal thickness (4 mm) as well as of a polymer without filler for the three magnetite powder particle sizes (30, 300 and 3000 nm). The chosen thickness of 4 mm allowed the best conditions of measurement.

As one can see for the case of the composite absorber with a particle size of 30 nm, the sample with a thickness $d = 1$ mm exhibits one matching frequency only, with practically no reflection losses. For $d = 2$ mm, however, the losses appear at higher frequencies. For $d = 3$ mm and $d = 4$ mm, the matching frequencies shift to the lower frequencies range. The values of the matching frequencies are related to the thickness d of the samples, namely, as a sequence of odd multiples of ¼ of the wavelength, or,

$$d = n\lambda/4 \ (n = 1, 3, 5, 7, 9, \ldots\ldots),$$

where $n = 1$ corresponds to the first matching frequency at low frequency.

For the absorber with a filler particle-size of 300 nm, the second matching frequency appears first for the sample with a thickness of $d = 2$ mm, compared with the samples with the same thickness but with others fillers; in general, the reflection losses rise with the growth of the magnetite particle size.

For a proper thickness, as mentioned above, namely, when the primary and the secondary reflected waves are de-phased by 180°, the destructive interference practically extinguishes the overall reflected wave at the free-space/sample boundary.

Figure 26.7 illustrates how the value of the first matching frequency varies with the samples' thickness and the fillers' particle size.

Figure 26.8 yields information on the variation of the first matching frequency value as a function of the filling density for the different magnetite particle-sizes for samples' thickness of 4 mm. For a filler particle-size of 30 nm, the matching

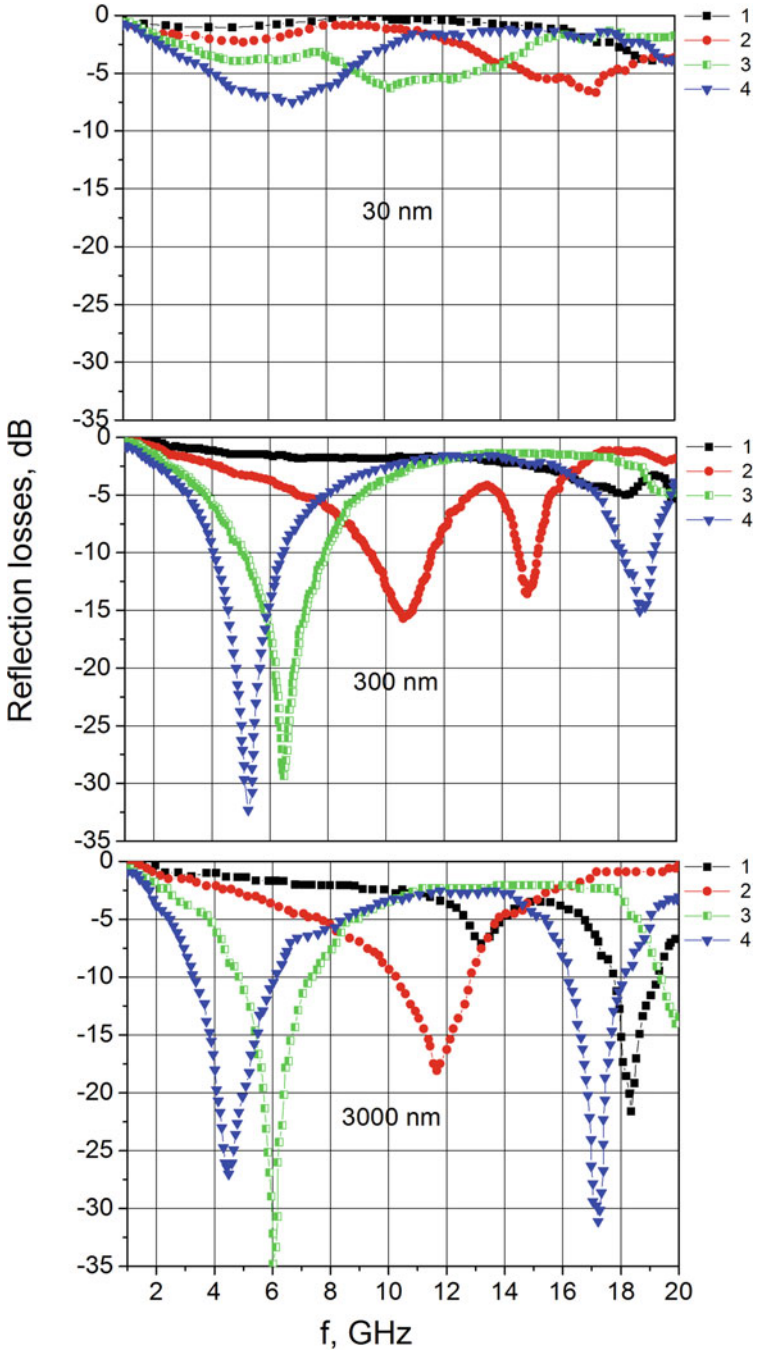

Fig. 26.5 Frequency dependence of the reflection losses R_L of nanocomposite samples of different thickness as a function of the Fe_3O_4 particle size

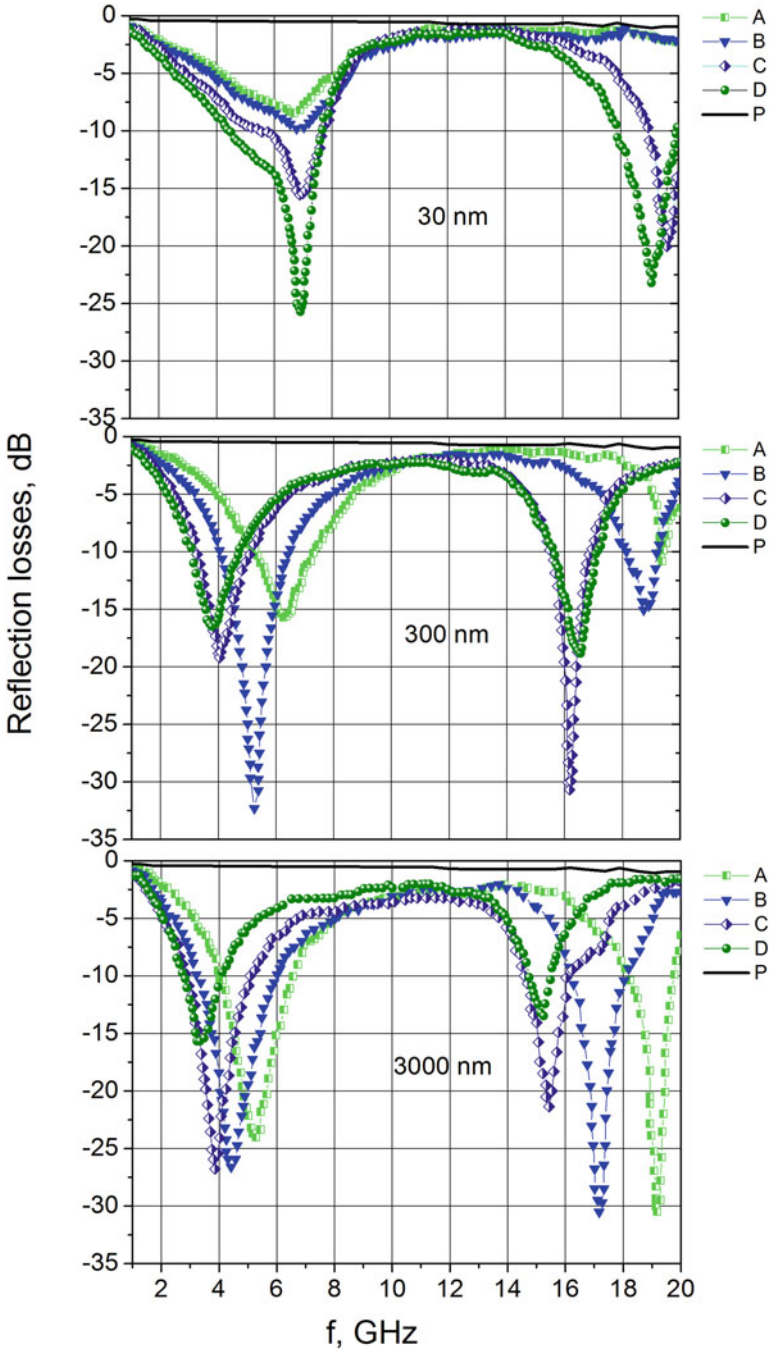

Fig. 26.6 Frequency dependence of the reflection losses R_L of nanocomposite samples with different filler-polymer weight ratios and a polymer without filler (P) as function of the Fe_3O_4 particle size

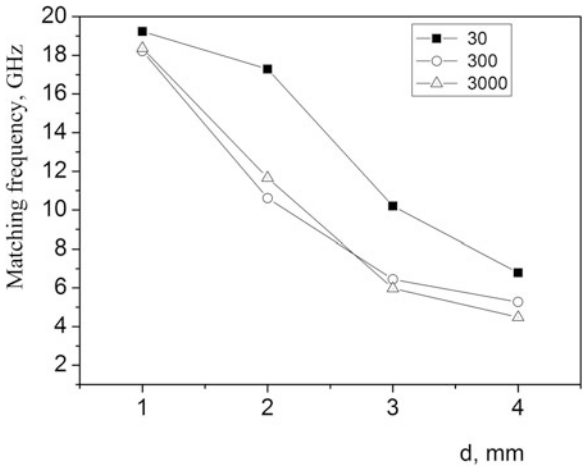

Fig. 26.7 Fe_3O_4 particle size influence on the matching frequency dependence on the sample thickness

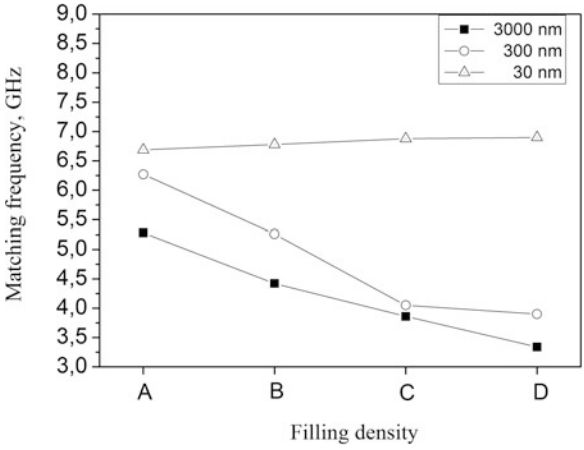

Fig. 26.8 Fe_3O_4 particle size influence on the first matching frequency dependence on the particle size

frequency value practically does not change as the filler-polymer weight ratio is raised; it varies within the 6.5–6.9 GHz interval. For the cases of 300 nm and 3000 nm particle sizse, the matching frequency value varies within much wider limits, namely, 6.3–3,7 GHz and 5,3–3,2 GHz, respectively.

Figure 26.9 provides information on the reflection losses R_L at the first matching frequency as dependent on the filling density for the different magnetite particle sizes for a sample thickness of 4 mm. The reflection losses rise as the particle size is increased. For particle sizes of 300 nm and 3000 nm, an optimal filling exists, for which the reflection losses are the highest; when the filling density is increased further, the reflected power begins to increase.

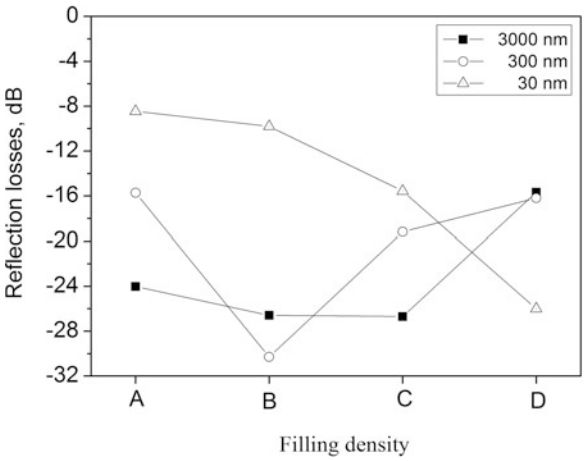

Fig. 26.9 Reflection losses R_L dependence on the filler's particle size at the first matching frequency

The results presented demonstrate that the technique used by us to determine the MW parameters of composite materials (in our case, a ferrite filler in a polymer matrix) offers a fast and efficient way of measuring the reflection losses and evaluating the material's applicability as an antireflection coating.

26.3 Conclusions

Our results prove that one can vary the matching frequencies and the reflection losses of a nanocomposite sample in a controlled way by varying the particle size of the ferrite filler while keeping the sample thickness and filler-polymer weight ratio constant; or alternatively, by varying the sample thickness and maintaining all other parameters constant. The nanocomposite structures prepared could find applications as detectors of MW electromagnetic waves or as antireflection coatings.

References

1. Dishovaski N, Petkov A, Nedkov I, Razkazov I (1994) Hexaferrite contribution to microwave absorbers characteristics. IEEE Trans Magn MAG 30:969
2. Verma AK, Saxena DC, Dube J (2003) Microwave permittivity and permeability of ferrite–polymer thick films. Magn Magn Mater 263:228
3. Wilson JL, Poddar P, Frey NA, Srikanth H, Mohamed K, Harmon J, Kotha S, Wachsmuth J (2004) Synthesis and magnetic properties of polymer nanocomposites with embedded iron nanoparticles. J Appl Phys 95:1439

4. Tagantsev AK, Sherman VO, Astafiev KF, Venkatesh J, Setter N (2003) Ferroelectric materials for microwave tunable applications. J Electroceram 11:5
5. Zhang H, Yao X, Zhang L (2002) Investigation of low-temperature formation and microwave properties of $BaFe_{12}O_{19}$ microcrystalline glass ceramic by citrate sol-gel process. Mater Res Innov 5:123
6. Verma A, Mendiratta RG, Goel TC, Dube DC (2002) Microwave studies on strontium ferrite based absorbers. J Electroceram 8:203
7. Matsumoto M, Miyata Y (2002) Polymer absorbers containing magnetic particles: effect of polymer permittivity on wave absorption in the quasimicrowave band. J Appl Phys 91:9635
8. Singh P, Babbar VK, Razdan A, Puri RK, Goel TC (2000) Complex permittivity, permeability, and X-band microwave absorption of CaCoTi ferrite composites. J Appl Phys 87:4362
9. Abbas HSM, Chatterjee R, Dixit AK, Kumar AVR, Goel TC (2007) Electromagnetic and microwave absorption properties of $(Co_{2+}–Si_{4+})(Co_{2+}–Si_{4+})$substituted barium hexaferrites and its polymer composite. J Appl Phys 101:074105
10. Mantese J, Micheli A, Fuhgan D, Geyer R, Baker-Jarvis J, Grosvenor J (1996) Applicability of effective medium theory to ferroelectric/ferrimagnetic composites with composition and frequency-dependent complex permittivities and permeabilities. J Appl Phys 79:1655
11. Tsutaoka T, Nakamura T, Hatakeyama K (1997) Magnetic field effect on the complex permeability spectra in a Ni–Zn ferrite. J Appl Phys 82:3068
12. Tsutaoka T, Ueshima M, Tokunaga T, Nakamura T, Hatakeyama K (1995) Frequency dispersion and temperature variation of complex permeability of Ni-Zn ferrite composite materials. J Appl Phys 78:3983
13. Kim SS, Jo SB, Gueon KI, Choi KK, Kim JM, Churn KS (1991) Complex permeability and permittivity and microwave absorption of ferrite-rubber composite at X-band frequencies. IEEE Trans Magn 27:5462
14. Shin JY, Oh JY (1993) The microwave absorbing phenomena of ferrite microwave absorbers. IEEE Trans Magn 29:3437

Chapter 27
Dielectric Relaxation in Biocomposites Based on Olive Pomace Grains

L. Kreit, Z. Samir, I. Bouknaitir, A. Triki, M. E. Achour, L. C. Costa, A. Kallel, A. Oueriagli, and M. Mabrouki

Abstract A polyester polymer matrix filled with olive-pomace grains was investigated using impedance spectroscopy in the frequency range 100 Hz to 1 MHz and temperatures from 300 to 360 K. Two relaxations processes were identified. One could be attributed to the α relaxation associated with the glass transition and observed in the neat matrix, while the second was attributed to the accumulation of charges at the pomace grains/polyester interfaces. The relaxation parameters were evaluated from isothermal dielectric spectra by applying the empirical Havriliak-Negami function.

Keywords Biocomposites · Dielectric relaxation · Havriliak-Negami function

27.1 Introduction

The use of natural fibers as a reinforcing agent is a development that has been gained global attention over the last few years [1–6]. Thanks to their many advantages such as renewability, recyclability, biodegradability, low specific gravity, and high

L. Kreit · Z. Samir · I. Bouknaitir · M. E. Achour (✉)
LASTID Laboratory, Sciences Faculty, Ibn Tofail University, Kenitra, Morocco
e-mail: achour.me@univ-ibntofail.ac.ma

A. Triki · A. Kallel
LaMaCoP, Faculty of Sciences of Sfax, University of Sfax, Sfax, Tunisia

L. C. Costa
I3N and Physics Department, University of Aveiro, Aveiro, Portugal

A. Oueriagli
LPSCM Laboratory, Faculty of Sciences Semlalia, Cadi Ayyad University, Marrakech, Morocco

M. Mabrouki
Laboratory LGI, Faculty of Sciences and Technics, Sultan Moulay Slimane University, Beni Mellal, Morocco

P. Petkov et al. (eds.), *Advanced Nanotechnologies for Detection and Defence against CBRN Agents*, NATO Science for Peace and Security Series B: Physics and Biophysics, https://doi.org/10.1007/978-94-024-1298-7_27

specific strength [7, 8] natural fibers have received increasing attention from both of the academic world and the industry [9, 10]. The most interesting aspect of natural fibers is the positive environmental impact [11] and their help to eliminate the increasing cost of the use of petroleum-based materials.

Relaxation phenomena are one of the most studied topics in materials sciences; the spectra of the real and imaginary complex permittivity are used extensively to evaluate this kind of dielectric behavior. The electric modulus is also proposed in this paper for the description of systems with ionic conductivity and related relaxation processes, which presents advantages in comparison to the classical approach using the real and imaginary parts of the dielectric permittivity. Furthermore, an alternative method, consisting of applying the Havriliak-Negami [12] model has been used to analyze the relaxation phenomena of the composite, exploring the interfacial region of polyester/olive pomace grains. The mechanisms inducing relaxation processes are not yet clearly understood. So, it is appropriate to investigate how the dielectric properties of such bio reinforced composites are affected by additional polarization effects caused by the presence of nanoparticles.

27.2 Experimental Details

27.2.1 Materials

We used natural olive-pomace grains of about 63 μm size, loaded in a polyester polymer matrix, forming pellets with 13 mm diameter and a thickness of about 3 mm. The matrix used in this work was unsaturated polyester resin 154TB, including 31 wt% of the styrene monomer, requiring 30 min for gelation, at room temperature, which was acquired from Cray Valley/Total, USA. The pomace/polyester nanocomposite has been prepared by mixing 5.87 g of liquid polyester resin and 0.2% weight of cobalt octanone as reaction activator. Pomace particles were introduced in different fractions before adding 1% of hardener to make each mixture cohesive. Methyl ethyl ketone peroxide (MEKP) was used to harden the mixtures and to facilitate the fabrication process. Each olive pomace grains/polyester composite was mixed at room temperature for 5 min, promoting the gelation; thereafter it was poured into a mold. After 2 h the samples were unmolded, taking 24 h for achieving a complete polymerization. In this work, different samples were prepared with concentrations in volume, Φ, between 0.0% and 15.0%.

27.2.2 Dielectric Measurements

The complex permittivity of the composite samples was measured in the frequency f range from 100 Hz to 1 MHz and in the temperature range from 300 to 360 K, using an impedance analyzer HP 4294A. Before the measurements, the samples surfaces

were polished and covered with a thin layer of silver paint. The real ε' (ω) and imaginary $\varepsilon''(\omega)$ parts of the complex permittivity were deduced from the capacitance and resistance values of the sample, respectively.

27.3 Results and Discussion

27.3.1 Polyester Matrix

Figure 27.1 shows the real and imaginary parts of the dielectric permittivity versus temperature at several frequencies. The relaxation, observed above 350 K was identified as α relaxation, which is associated with the glass–rubbery transition of the polymer [13]. The increase in permittivity was attributed to the increase of the segmental mobility of the polymer molecules with temperature near the glass transition temperature [14].

27.3.2 Composites

The dependence of the real $\varepsilon'(\omega)$ and imaginary $\varepsilon''(\omega)$ parts of the complex permittivity of the composites with 15.0% olive pomace grains loading versus frequency at different temperatures is shown in Fig. 27.2. The increase of the permittivity at low frequencies is due to the presence of impurities and water in the composite. The comparison with the net matrix shows that the reinforcement induces a new relaxation phenomenon, which can be assigned to water dipole polarization [14, 15].

The polarization of water molecules related to cellulosic olive pomace grains formed a monomolecular layer enveloping the outer surface of the fibers. Polar relaxation of water was also highlighted by Chand and Jain in sisal composites based

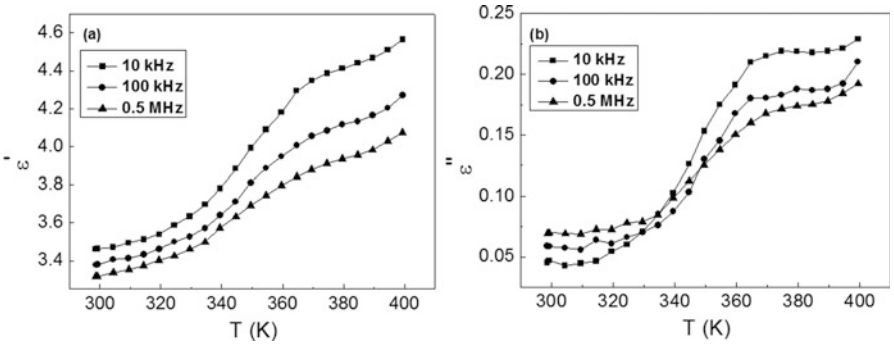

Fig. 27.1 (**a**) Real $\varepsilon'(\omega)$ and (**b**) imaginary $\varepsilon''(\omega)$ parts of the complex permittivity versus temperature for the resin matrix

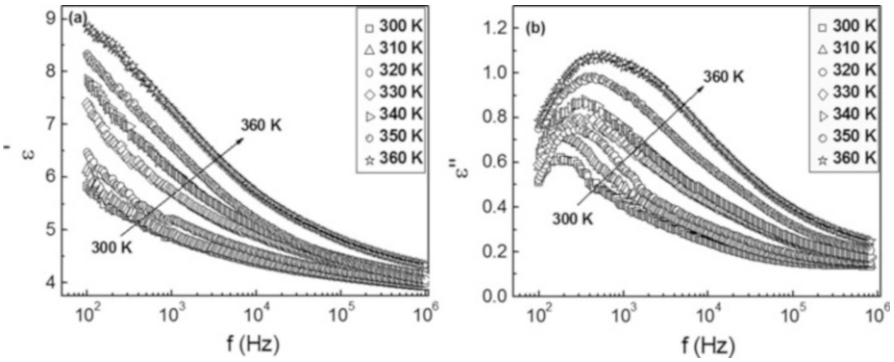

Fig. 27.2 (**a**) Real part ε′ (ω) and (**b**) imaginary part ε″ (ω) of the complex permittivity of the composite (ϕ = 15.0%) versus frequency at different temperatures

on a polyethylene or epoxy matrix and did not completely disappear after different chemical treatment of the cellulose fibers [16]. The α relaxation, which was previously seen in the polyester, was totally hidden by the water dipole polarization due to the hydrophilicity of the lignocellulosic pomace grains present in the composite.

27.3.3 Complex Modulus Analysis

Complex modulus analysis is an alternative approach to explore the electrical response of materials containing some degree of ionic conductivity [17–20]. The complex electric modulus M*(ω) = 1/ε*(ω) was calculated by using the complex dielectric permittivity with the following relations [21]:

$$M'(\omega) = \frac{\varepsilon'(\omega)}{\varepsilon'^2(\omega) + \varepsilon''^2(\omega)} \tag{27.1}$$

$$M''(\omega) = \frac{\varepsilon''(\omega)}{\varepsilon'^2(\omega) + \varepsilon''^2(\omega)} \tag{27.2}$$

Where M′(ω) and M″(ω) are the real and imaginary parts of the electric modulus. This formulation is mainly suitable to minimize the effect of the dc conductivity. It allows to diminish the large values of dielectric permittivity ε′(ω) and loss factor ε″(ω) at low frequencies, which are usually associated with the electrode material and their contacts, space charge injection phenomena and absorbed impurity conduction effects [22]. Hence, bulk relaxation properties can be interpreted.

Figure 27.3 shows the frequency dependence of the imaginary part of the complex modulus with volume fraction (ϕ = 15.0%). at different temperatures. From this figure, it can be observed that the peak moves to higher frequencies, indicating a decrease in the relaxation times. The frequency dependence has been analyzed by using the modulus

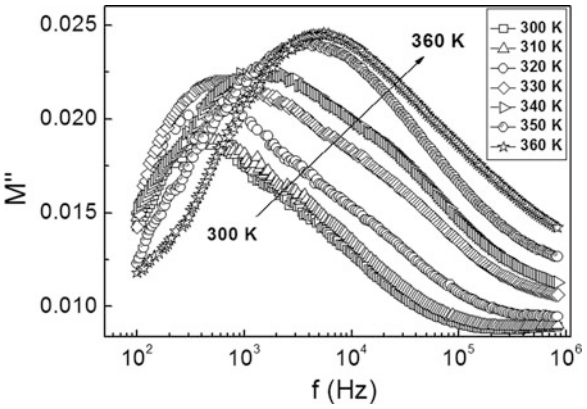

Fig. 27.3 Imaginary part of the electric modulus M″ as a function of frequency for different temperatures for 15.0% volume fraction of filler

Havriliak–Negami formalism, which is an empirical modification of the Debye relaxation model given by the following equations [17, 23]:

$$M' = M_\infty \frac{\left[M_s A^\beta + (M_\infty - M_s)\cos\beta\varphi\right]A^\beta}{M_s^2 A^{2\beta}(M_\infty - M_s)M_s\cos\beta\varphi + (M_\infty - M_s)^2} \tag{27.3}$$

$$M'' = M_\infty M_s \frac{\left[(M_\infty - M_s)\cos\beta\varphi\right]A^\beta}{M_s^2 A^{2\beta}(M_\infty - M_s)M_s\cos\beta\varphi + (M_\infty - M_s)^2} \tag{27.4}$$

$$A = \left[1 + 2(\omega\tau)^{1-\alpha}\sin\left(\frac{\omega\tau}{2}\right) + (\omega\tau)^{2(1-\alpha)}\right]^{1/2} \tag{27.5}$$

$$\varphi = \text{arctg}\left[(\omega\tau)^{1-\alpha}\cos\left(\frac{\alpha\tau}{2}\right)/\left(1 + (\omega\tau)^{1-\alpha}\sin\left(\frac{\alpha\tau}{2}\right)\right)\right] \tag{27.6}$$

where $M_s = 1/\varepsilon_s$ and $M_\infty = 1/\varepsilon_\infty$- α and β are relaxation exponents, and M_s and M_∞ the moduli at low and high frequencies, respectively.

In Fig. 27.4 the Nyquist plot of the composites for different temperatures, with olive pomace grains (ϕ = 15.0%) is shown. We should also point out that the solid curves were produced by the best fitting of the experimental points, using the Havriliak–Negami data shown below. It also noted that these plots are linked to the water dipole polarization. The parameters evaluated for the experimental data by the Havrialk-Negami-fitting method are presented in Table 27.1, for 5.0%, 10.0%, 12.0% and 15.0% volume fractions.

To further explore the dielectric relaxation in this composite, it is often useful to estimate the activation energy with the Arrhenius equation [13]:

$$f_{\max} \propto f_0 \exp\left(-\frac{E}{k_B T}\right) \tag{27.7}$$

where E, K_B and T are the activation energy, Boltzmann's constant and absolute temperature, respectively. Figure 27.5 is a plot of $\ln(f_{max})$ as a function of the inverse temperature for different olive pomace grains. It should be mentioned that the activation energy was calculated using Eq. (27.7) with the slope of the straight

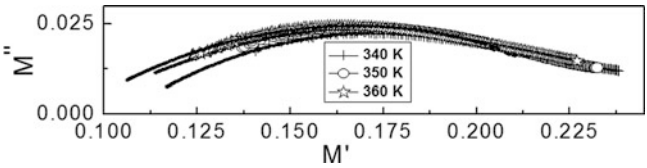

Fig. 27.4 Nyquist plot of the electric modulus M* of the composite with $\Phi = 15\%$ at 340, 350 and 360 K

Table 27.1 Parameters evaluated by fitting data according to the Havriliak–Negami equation, for 5.0%, 10.0%, 12.0% and 15.0% of filler volume

Concentration (%)	T(K)	A	β	M_s	M_∞	Δε
5	340	0.54	0.58	0.24	0.16	4.92
	350	0.48	0.42	0.24	0.14	6.94
	360	0.55	0.51	0.23	0.15	8.33
10	340	0.51	0.59	0.22	0.11	7.26
	350	0.47	0.74	0.22	0.11	8.50
	360	0.38	0.97	0.22	0.10	10.28
12	340	0.34	0.76	0.26	0.08	3.78
	350	0.38	0.82	0.25	0.09	4.54
	360	0.35	0.90	0.25	0.08	5.65
15	340	0.415	0.95	0.24	0.10	1.90
	350	0.45	0.68	0.24	0.09	2.50
	360	0.42	0.87	0.24	0.09	2.79

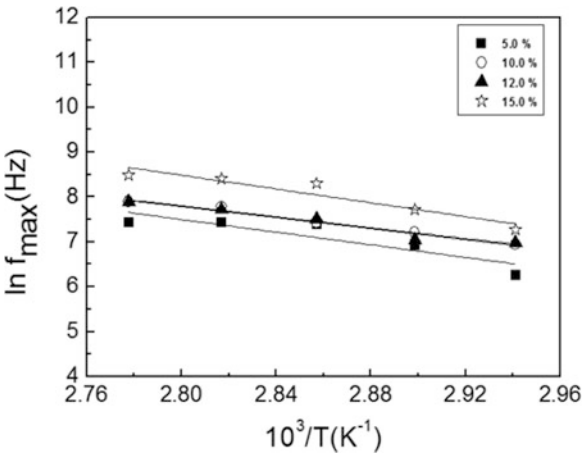

Fig. 27.5 Water dipole polarization relaxation with Arrhenius plots of the frequency of the dielectric modulus versus inverse temperature for the polyester with olive pomace grains ($\phi = 15.0\%$)

Table 27.2 Activation energies for pomace grains/polyesters composites

Concentration ϕ(%)	0.0	5.0	10.0	12.0	15.0
Activation energy (kJ/mol)	150.00	58.48	50.46	51.54	38.97

lines of Fig. 27.5 and reported in Table 27.2. The obtained values are between 38.97 and 150.00 kJ/mol. These values are in agreement with those reported for polyester reinforced with Alfa fibers [22] and palm tree fibers [14, 22, 24].

27.4 Conclusion

In the present work, composite materials based on polyester reinforced with olive pomace grains were investigated. The dielectric behavior of the neat matrix and the composite based on olive pomace grains has been studied over the temperature range from 300 to 360 K and over the frequency range from 100 Hz to 1 MHz. In addition to the α relaxation associated with the glass transition of the epoxy resin matrix, the presence of pomace grains in the composite gives rise to other relaxation associated with water polarization. The data results were analyzed using the modulus formalism, which is a very useful approach to explore the electrical response of materials containing some degree of ionic conductivity.

Acknowledgments The authors acknowledge support from CNRST-Maroc (Centre National de la Recherche Scientifique et Technique) and the FCT-CNRST bilateral cooperation, and FEDER by funds through the COMPETE 2020 Program and National Funds through FCT – Portuguese Foundation for Science and Technology under the project UID/CTM/50025/2013.

References

1. Hodzic A, Shanks R (2014) Natural fibre composites, materials, processes, and properties, 1st edn. Woodhead Publishing Series in Composites Science and Engineering, Cambridge
2. Belgacem MN, Gandini A (2005) Physical, chemical and physico-chemical modification of cellulose fibers. Compos Interfaces 12:41–75
3. Marcovich NE, Aranguren MI, Reboredo MM (2001) Polym J 42(2):815–825
4. Nunez AJ, Kenny JM, Reboredo MM (2002) Polym Eng Sci 42:733–742
5. Marcovich NE, Reboredo MM, Aranguren MI (2005) Compos Interfaces 12:3–24
6. Belgacem MN, Gandini A (2005) Surface modification of cellulose fibres. Polím Ciência e Tecnol 15:114–121
7. Mohanty AK, Misra M, Drzal LT (eds) (2005) Natural fibers, biopolymers and biocomposites. CRC Press, Taylor & Francis Group, Boca Raton
8. Joseph S, Jacob M, Thomas S (2005) Natural fibers, biopolymers and biocomposites. CRC Press, Taylor & Francis Group, Boca Raton, pp 435–472
9. Bledzki AK, Gassan J (1999) Composites reinforced with cellulose based fibers. Prog Polym Sci 24:221–274

10. Eichhorn SJ, Baillie CA, Zafeiropoulos N, Mwaikambo LY, Ansell MP, Dufresne A, Entwistle KM, Herrera-Franco PJ, Escamilla GC, Groom L, Hughes M, Hill C, Rials TG, Wild PM (2001) J Mater Sci 36:2107–2131
11. Bledzki AK, Mamun AA, Jaszkiewicz A, Erdmann K (2010) Compos Sci Technol 70 (5):854–860
12. El Hasnaoui M, Triki A, Graça MPF, Achour ME, Costa LC, Arous M (2012) J Non-Cryst Solids 358:2810–2815
13. Ben Amor I, Rekik H, Kaddami H, Raihane M, Arous M, Kallel A (2009) Studies of dielectric relaxation in natural fiber- polymer composites. J Electrost 67:717–722
14. McCrum NG, Read BE, Williams G (1967) Anelastic and dielectric effects. J Appl Polym Sci 13:617
15. Tsangaris GM, Psarras GC, Kontopoulos AJ (1991) Dielectric permittivity and loss of an aluminum- filled epoxy resin. J Non-Cryst Solids 131–133(2):1164–1168
16. Chand N, Jain D (2005) Compos Part A Appl Sci Manuf 36:594–602
17. Tsangaris GM, Psarras GC, Kouloumbi N (1998) J Mater Sci 33:2027–2037
18. Moynihan CT (1994) J Non-Cryst Solids 172–174:1395–1407
19. Moynihan CT, Boesch LP, Laberge NL (1973) Phys Chem Glasses 14:122–125
20. Hodge LM, Ingram MD, West AR (1976) J Electroanal Chem 74:125
21. Mohamed K, Moussi F, Harmon JP (2006) Polym J 47:3856–3865
22. Ghallabi Z, Rekik H, Boufi S, Arous M, Kallel A (2010) J Non-Cryst Solids 356:684–687
23. Arous M, Ben Amor I, Boufi S, Kallel A (2007) J Appl Polym Sci 106:3631–3640
24. Hammami H, Arous M, Lagche M, Kallel A (2006) Experimental study of relaxations in unidirectional piezoelectric composites. Compos Part A Appl Sci Manuf 37(1):150

Chapter 28
Green Synthesis of Silver Nanoparticles and Their Application in Thin Polymer Films

Zhana Petkova, Irena Kostova, and Ginka Antova

Abstract The focus of the present study is on synthesis procedures, morphology and application of silver nanoparticles (AgNPs). A green synthesis approach was performed with aqueous extracts from lawn grass and parsley (*Petroselinum crispum* Mill.), both of them microwave assisted. The formation of the silver nanoparticles was observed using UV-Vis spectroscopy (Boeco S26 spectrophotometer); they were characterized by transmission electron microscopy (TEM). The absorption spectra show peaks in the range 380–400 nm for all products. The TEM images depicted that the synthesis method yield nanoparticles with spherical shape and different size. This gives rise for a wide range of application of AgNPs which may be used as additives in papers and polymers due to their antimicrobial properties which depend on particle size and shape.

Keywords Green synthesis · Silver nanoparticles · Lawn grass · Parsley

28.1 Introduction

Nanotechnology has spread globally and appeared to be one of the most explored areas of research in materials sciences [1, 2]. Noble metal nanoparticles are applied in many areas such as medical industry, electronics, chemistry and can be potentially used in cosmetics and foods as well [1–3]. Many methods for the synthesis of silver nanoparticles are reported but nowadays green synthesis is prefered and commonly used, because it is considered as environmentally friendly and there is no use of toxic chemicals [2]. Different researchers have reported to use plant extracts as agent for the reduction of Ag^{+} to Ag^{0}; the obtained silver nanoparticles are smaller in size with a good dispersion [2, 4–8]. Silver nanoparticles possess an antibacterial activity and show strong inhibitory and bactericidal effects [2, 8]. For these reasons, they can be

Z. Petkova (✉) · I. Kostova · G. Antova
Department of Chemical Technology, University of Plovdiv 'Paisii Hilendarski', Plovdiv, Bulgaria

P. Petkov et al. (eds.), *Advanced Nanotechnologies for Detection and Defence against CBRN Agents*, NATO Science for Peace and Security Series B: Physics and Biophysics, https://doi.org/10.1007/978-94-024-1298-7_28

used to prevent and treat various diseases [8]. On the other hand, the antibacterial effect of silver nanoparticles is related to their well-developed surface which can be obtained by controlling the size and the shape of the particles [2].

One of the possible applications of silver nanoparticles is their addition into thin polymer films in order to become conductive, flexible and stable [9]. The application of the AgNPs could also depend on their shape. According to Kostova et al. [9] silver nanowires possess electrical conductivity and could be used in electrical devices such as touch screen displays and solar cells conductive layers. On the other hand, silver nanospheres may be used as additives in papers and polymers because of their antimicrobial properties.

The aim of the present study was to synthesize silver nanoparticles by using aqueous plant extracts from lawn grass and parsley (*Petroselinum crispum* Mill.) as well as their characterization. Furthermore, microwave-assisted synthesis was used for reducing the reaction time. The second focus of the study was to prepare thin-layer polymer films with addition of the obtained silver nanoparticles and their morphology and topography was examined.

28.2 Materials and Methods

The plants used in the study were a mixture of lawn grass and parsley (*Petroselinum crispum* Mill.). The grass material was collected from the park area of an urban district of Plovdiv (Bulgaria) and the parsley (with Bulgarian origin) was purchased on the local market. The aqueous plant extracts were prepared by taking 20 g of the plants (washed and finely cut) in 500 mL Erlenmeyer flask with 200 mL of distilled water and then boiling the mixture for 20 min. After that the extracts were filtered through Whatman No.1 filter paper (pore size 25 μm). They were stored at 4 °C and used within a week.

0.01 M aqueous solution of silver nitrate ($AgNO_3$) was prepared and used for the synthesis of silver nanoparticles. Twenty-five milliliter of the extracts was added into 25 mL of aqueous solution of 0.01 M silver nitrate for the reduction of Ag^+ ions and was heated in microwave (CEM MDS 81D) for 5 min at 100% power. Then, the silver nanoparticle solution was purified by repeated centrifugation at 5000 rpm for 10 min followed by redispersion in deionized water. The yield was estimated by atomic spectrometry of the residual Ag^+ in the filtrate.

The reduction of pure Ag^+ ions was observed by measuring the UV-Vis spectrum of the nanoparticle solution after diluting a small portion of the sample into distilled water. UV-Vis spectral analysis was done by using UV-Vis spectrophotometer Boeco S26. The average particle diameters have been estimated by a model equation on the basis of their absorption peak wavelength (nm) in their UV-Vis spectra.

The morphology and phase composition of the samples were analyzed by transmission electron microscopy (HRTEM, JEOL JEM-2100, 200 kV). Before measurement the sample suspensions were dispersed by ultrasound sonication for 3 min (42 kHz).

A polymer emulsion (trademark Styacryl V700, vinyl acetate/acrylate ester/VeoVa vinyl ester copolymer) with medium water resistance was used for the polymer film. Thin layer films were prepared as follows: 0.01 g of silver nanoparticles was thoroughly mixed up with polymer and 3 mL deionized water to a total volume of 15 mL and casted onto a plastic substrate (printing transparency sheet) using a roll hand proofer. The topography and internal characteristic of the polymer-metal nanoparticle composite films were studied by atomic force microscopy (AFM, Nanosurf Flex).

28.3 Results and Discussion

Two plant extracts were tested as reducing agent for the green synthesis of AgNPs (grass and parsley). The yield of silver nanoparticles, estimated by atomic spectrometry of the residual Ag^+ in the filtrate, was established to be over 90% for all samples.

Silver nanoparticles are known to exhibit a yellowish brown colour in aqueous solution which is due to the excitation of surface plasmon (SPR) vibrations in the silver nanoparticles [10]. The colour change of the plant extract solution is an indicator of the reduction of the silver ion to silver nanoparticles [3]. Their size and shape could be examined by UV-Vis spectral analysis (Fig. 28.1) after synthesis.

The absorbance peak of the silver nanoparticles was observed at 396 nm and 404 nm for grass and parsley extracts, respectively; the broad peaks suggest that more polydisperse particles were formed [1].

The particle size could be estimated using the following formula:

$$D[\text{nm}] = 0.715\,\lambda_{\max} - 258 \tag{28.1}$$

where D is particle diameter (nm), and λ_{max} the SPR peak position in the UV-Vis absorbance spectrum.

The estimated particle diameter of the synthesized silver nanoparticles by using grass extract was 25 nm, that from the parsley extract 31 nm. These average sizes

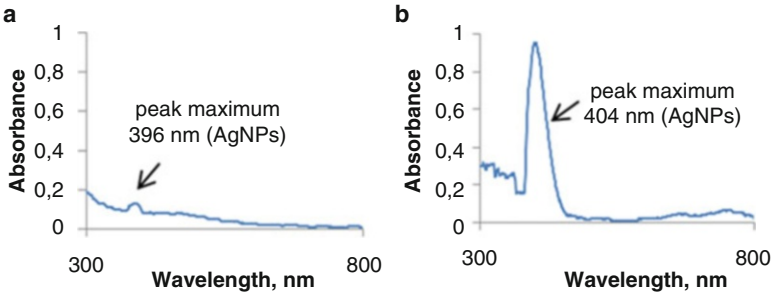

Fig. 28.1 UV-Vis absorption spectrum of silver nanoparticles. (**a**) Grass extract; (**b**) Parsley extract

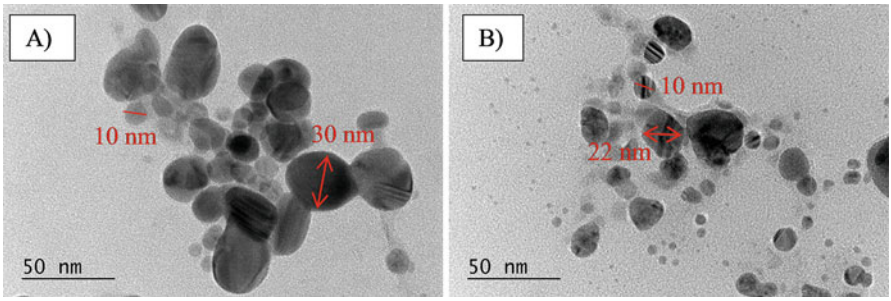

Fig. 28.2 TEM images of silver nanoparticles. (**A**) Grass extract; (**B**) Parsley extract

as well as the shape of the nanoparticles are confirmed by transmission electron microscopy (TEM) images (Fig. 28.2).

TEM analysis reveals spherical shape highly polydisperse nanoparticles with an average size about 25 nm for the grass and the parsley extract synthesis method. Selected area electron diffraction (SAED) pattern confirm the crystalline nature of the silver particles with a face-centered cubic lattice (a = 4.0772 Å). The measured interplanar distance matches well with the reference (JCPDS file no. 87-0720). TEM images of AgNPs from both used extracts depict that they are well separated. It also can be seen that the silver nanoparticles do not have a secondary capping of organic material which is present in the plants that were used. On the other hand, such of capping was noticed by Song and Kim [3] and Raut et al. [11] who used different plant extracts, such as pine, persimmon, ginkgo, magnolia, platanus and *Gliricidia sepium*, for reducing the silver ions.

The results from the present study were confirmed by Roy et al. [12] who synthesized silver nanoparticles by using parsley leaf extract and observed that they possessed spherical shapes with an average diameter of 30–32 nm.

The obtained silver nanoparticles were implemented in thin layer polymer films; their morphology and topography were examined by AFM. The thickness of the films was measured by micrometer screw gauge and was established to be 5 μm. AFM images of the thin films with added silver nanoparticles produced by grass and parsley extracts are shown in Fig. 28.3.

The AFM images show difference between the surfaces of the films. The grain size of the polymer composite filled with the larger sized AgNPs of the grass extract is larger than that of the parsley extract AgNPs polymer. The segment profile of the last has sharp points sticking up from the top, while the former display a flatter micro-profile. The images also reveal that silver nanoparticles obtained by using grass extract are evenly distributed within the thin film.

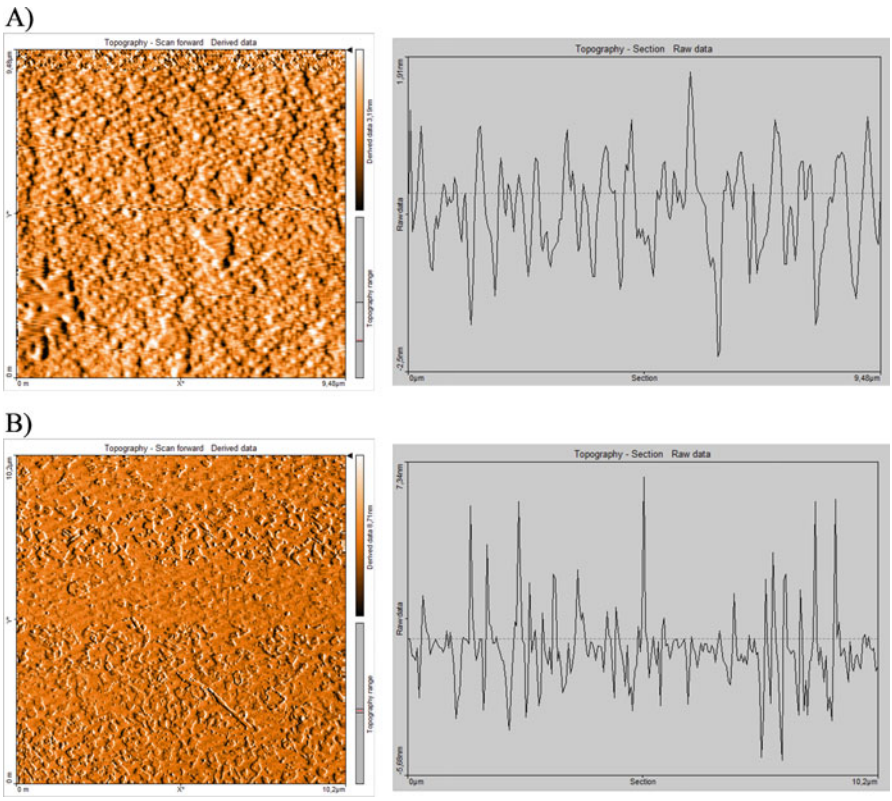

Fig. 28.3 AFM images of the thin layer films with added silver nanoparticles produced by: (**A**) grass extract; (**B**) parsley extract. The glittering spots are clusters of small silver nanoparticles

28.4 Conclusion

The plant extract synthesis of silver nanoparticles is a simple and efficient low-cost green method for the large-scale production of nanoparticles for manufacturing material with special characteristic such as antibacterial and specific optical properties. The obtained AgNPs are spherical in shape and have a face-centered cubic lattice. Their average size is 25 nm for both grass and parsley extracts.

The prepared thin polymer films with added silver nanoparticles are transparent and flexible which is a good indicator for their potential application. A variety of polymer composite thin films are suitable for thin layer coating of surfaces through their transparency or matte look, UV-protection properties, easy-laying, and plasticity.

Acknowledgments The authors are grateful to Dr. Sotir Sotirov, University of Plovdiv 'Paisii Hilendarski', Faculty of Physics for AFM analysis. The study was carried out with the support of MU17HF024.

References

1. Jain D, Kumar Daima H, Kachhwaha S, Kothari SL (2009) Dig J Nanomater Biostruct 4(3):557
2. Kaviya S, Santhanalakshmi J, Viswanathan B, Muthumary J, Srinivasan K (2011) Spectrochim Acta A Mol Biomol Spectrosc 79:594
3. Song JY, Kim BS (2009) Bioprocess Biosyst Eng 32:79
4. Badri Narayanan K, Sakthivel N (2008) Mater Lett 62:4588
5. Prathap Chandran S, Chaudhary M, Pasricha R, Ahmad A, Sastry M (2006) Biotechnol Prog 22:577
6. Dubey SP, Lahtinen M, Sarkka H, Sillanpaa M (2010) Colloids Surf B: Biointerfaces 80:26
7. Philip D, Unni C, Aswathy Aromal S, Vidhu VK (2011) Spectrochim Acta A Mol Biomol Spectrosc 78(2):899
8. Veerasamy R, Xin TZ, Gunasagaran S, Xiang TFW, Yang EFC, Jeyakumar N, Dhanaraj SA (2011) J Saudi Chem Soc 15:113
9. Kostova I, Nachkova S, Tonchev D, Kasap S (2015) In: Petkov P, Tsiulyanu D, Kulisch W, Popov C (eds) Nanoscience advances in CBRN agents detection, information and energy security, NATO science for peace and security Series A: Chemistry and Biology. Springer, Dordrecht, p 175
10. Shankar SS, Rai A, Ahmad A, Sastry M (2004) J Colloid Interface Sci 275:496
11. Raut RW, Lakkakula JR, Kolekar NS, Mendhulkar VD, Kashid SB (2009) Curr Nanosci 5 (1):117
12. Roy K, Sarkar CK, Ghosh CK (2015) Appl Nanosci 5:945

Chapter 29
Synthesis of Iron Oxide Nanoparticles Modified with Silanes and Their Heating Ability in Alternating Magnetic Fields

L. Storozhuk and N. Iukhymenko

Abstract Magnetite nanoparticles with controlled particle sizes and a hexadecyltrimethoxysilane surface coating have been synthesized as a model system to investigate the effect of surface coatings on the specific loss power (SLP) under exposure a to low-power alternating magnetic field. It is shown that with decreased surface coating thickness the SLP was improved.

Keywords Magnetite · Surface modification · Nanocomposite · Silane · Specific loss power · Low-power alternating magnetic field

29.1 Introduction

The development of magnetic nanocomposites (NPs) for medical applications is caused by the needs of medicine of a directed transport of medical preparations, which localizes activity in the desired part of a body and reduces undesirable side effects [1]; further applications are magnetic agents for the hyperthermia of tumors [2] and selective magnetic adsorbents [3].

Dispersion of superparamagnetic iron oxide nanoparticles SPIONs in water medium were investigated as MRI contrast agents [4]. Some of these materials are already used in clinical practice: Endorem (Guerbet, Belgium), Feridex (CШA), Feraheme (AMAG Pharmaceuticals, USA), Primovist and Eovist (Bayer Schering Pharma AG, Germany), some of them are in preclinical trial stage: Supravist-SHU555C (Bayer Schering Pharma AG, Germany), VSOP-C184 (Ferropharm

L. Storozhuk (✉)
Chuiko Institute of Surface Chemistry, National Academy of Sciences of Ukraine, Kyiv, Ukraine
e-mail: storozhukl@ukr.net

N. Iukhymenko
Faculty of Chemistry, Macromolecular Chemistry Department, Kiev Taras Shevchenko National University, Kyiv, Ukraine

P. Petkov et al. (eds.), *Advanced Nanotechnologies for Detection and Defence against CBRN Agents*, NATO Science for Peace and Security Series B: Physics and Biophysics, https://doi.org/10.1007/978-94-024-1298-7_29

GmbH, Germany), Ferumoxtran-AMI-227 and Ferumoxide-AMI-25 (AMAG Pharmaceuticals, USA [5–7].

One of the promising areas is the design of SPIONs based dispersions in a radiopaque Lipiodol preparation and other iod-based oil preparations. This allows for the diagnostics, delivery and retention of magnetic material in tumors with a following use of magnetic hyperthermia [8–10].

In order to ensure an effective control over the colloidal stability of magnetic nanoparticles, the nanoparticles were coated with organic compounds by attaching functional groups to the NP surface via either electrostatic interactions or covalent bonding [11, 12]. However, the overlayer can decrease the magnetic properties of NPs, which reflects in the magnetic properties and thus the heating efficiency of nanoparticles in alternating magnetic fields AMFs [13, 14].

This paper proposes a method to the modication of magnetite nanoparticles by biocompatible silanes, namely hexadecyltrimethoxysilane (HDTMS), which creates a hydrophobicity of the surface of the nanoparticles to obtain their stable dispersion in non-polar oil media such as Lipiodol for further use in magnetic hyperthermia.

29.2 Experimental

Magnetite was obtained using a co-precipitation reaction from a solution of salts of two- and trivalent iron in an alkaline medium according to the protocol described in [15].

The first step of magnetite surface modification by HDTMS consists in hydrolysis reactions of HDTMS and the following condensation of the products of the hydrolysis [16, 17]. The physicochemical mechanism of the silane modificationof the methoxy groups on the surface of iron oxide NPs is the formation of Si–O bonds and the creation of terminal functional groups available for immobilization other substances. We obtained samples with different contents of silane on the surface, the concentration of which was determined by thermal gravimetric analysis (TGA) and total organic carbon measurements (TOC) (Table 29.1). The properties of the as-prepeared magnetite and the nanocomposites based on them were investigated by a combination of physical and chemical methods.

Table 29.1 Magnetic properties of iron oxides NPs and HDTMS-modified Fe_3O_4 NPs

Sample	Concentration of org. phase (wt %)		M_s, (Am^2/kg)	H_c, (kA/m)
	TOC	TGA		
S1	44,45	43.6	35.52 ± 1	0.69 ± 0.09
S2	23,2	22.77	49.71 ± 0.32	0.933 ± 0.10
S3	14,25	12.0	55.94 ± 1.4	0.826 ± 0.15
S4	11,1	10.2	57.83 ± 1.2	1.016 ± 0.16
S5	9,8	8.25	60.8 ± 1.88	1.025 ± 0.2
Fe_3O_4	–		70.40 ± 0.68	0.975 ± 0.04

The obtained samples were characterized by a PANalytical X-Ray powder diffractometer using a cobalt target X-ray tube ($\lambda = 0.179021$ nm). The average crystallite size has been determined using Scherrer's formula: $d_{XRD} = 0{,}89 \cdot \lambda / B \cdot \cos\theta$, where d_{XRD} is the mean crystallite diameter of the particles, λ is the wavelength of the X-ray radiation, θ is the diffraction peak angle, and B is the line width at half-peak intensity.

Infrared (IR) spectra of powdered samples were recorded using a FTIR Nicolet iS5 spectrometer with a Ge-crystal, collecting 64 scans in the 400–4000 cm^{-1} range with a resolution of 2 cm^{-1}.

Magnetization curves were measured using a Vibrating Sample Magnetometer (Lake Shore 7404) at room temperature in air in a magnetic field of up to 0,795 kA/m The amplitude and the frequency of vibration were 1.5 mm and 82 Hz, respectively. The samples to be measured were in the form of powders.

The thermal response of iron oxide nanoparticles in an AMF was studied using calorimetric measurements according to the method described in [18]. The measuring system consisted of a signal generator (Agilent 33521A), a RF broadband amplifier (AR RF/Microwave Instrumentation 800A3A), an induction coil (90 mm diameter), interchangeable capacitors, and measuring units for temperature and magnetic field. The test tubes with Si-O-R coated iron oxide nanoparticles immobilized in a silicone polymer (Sylgard) and oleic acid were subjected to alternating magnetic field of 1048 kHz and 5.8 kA/m. The specific loss power (SLP) was calculated according to the equation:

$$\mathrm{SLP} = \frac{1}{m} \cdot \frac{\mathrm{d}T}{\mathrm{d}t} \cdot C,$$

where C is the heat capacity of the sample, m is the mass of the magnetic material, T is the temperature and t the time. The SLP is measured in Watts per gram of magnetic material (nanoparticles including Si-O shell) ($W \cdot g^{-1}$). The heat capacity of a sample in the form of a n-component dispersion was calculated as follows:

$$C = \sum_{i=1}^{n} x_i \cdot C = \sum\nolimits_{i=1}^{n} x_i m_i,$$

where x_i [$J \cdot g^{-1} \cdot K^{-1}$] is the specific heat capacity and m_i [g] the mass of the ith component. The following values were used in the calculations: x (silicone) = 1.3 $J \cdot g^{-1} \cdot K^{-1}$ and x (magnetite) = 0.62 $J \cdot g^{-1} \cdot K^{-1}$.

29.3 Results and Discussion

The covalent bonding between silane and magnetite was confirmed by FTIR measurements. The FTIR spectrum of a powder of the as-prepared magnetite NPs is presented in Fig. 29.1a. The representative peak at 594 cm^{-1} characterizes

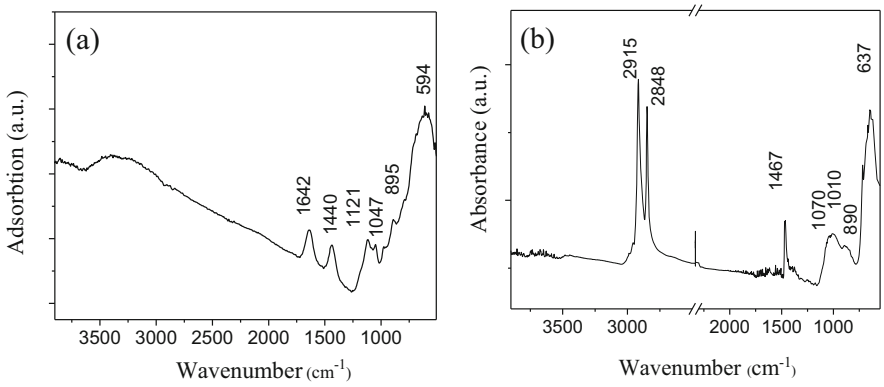

Fig. 29.1 FTIR spectra of (**a**) the as-prepared magnetite NPs and (**b**) the HDTMS-modified Fe_3O_4 NPs

oscillations of the Fe–O bonds of the iron oxides which cover the surface of the magnetite particles [10, 19]. The peaks at 895, 1047 cm^{-1} and 1121 cm^{-1} belong to deformation oscillations of the Fe–OH groups [19]. The peak at 1642 cm^{-1} is assigned to by the deformation vibrations of water molecules adsorbed on the magnetite surface.

The adsorption of the silane polymer onto the surface of the magnetite particles was confirmed by bands at 1070 and 1010 cm^{-1} assigned to the Si-O–H and Si–O–Si groups (Fig. 29.1b). The absorption band at 890 cm^{-1} reveals the presence of Si–O–H stretching and OH vibrations on the surface of magnetite. The peaks at 1467, 2848 and 2915 cm^{-1} are attributed to asymmetrical C-H bending vibrations of alkyl groups [-$(CH_2)_n$-]. The peak appearing at about 637 cm^{-1} is assigned to Fe–O–Si stretching vibration [20].

The phase and crystallinity of the as-prepared magnetite and HDTMS-modified Fe_3O_4 NPs were investigated using the XRD technique; the results are given in Fig. 29.2.

The XRD patterns in Fig. 29.2 display several characteristic peaks at $2\theta = 21.2$, 35.2, 41.43, 50.6, 63.3, 67.7 and 74.6 representing the corresponding lattice planes (111), (220), (311), (400), (422), (511) and (440), respectively, of the crystalline magnetite Fe_3O_4 phase with a cubic structure of the spinel type, which are consistent with the standard data for magnetite (JCPDS, PDF □ 9005839). Comparing the initial magnetite nanoparticles with the coated one, the XRD patterns show similar diffraction peaks.

The nano-crystalite sizes of the HDTMS-modified Fe_3O_4 NPs were estimated from XRD patterns using Scherrer's equation [21]. The calculated crystal size of the NPs is 12–15 nm for all samples.

To identify the influence of the silane overlayer on the static and dynamic magnetic properties of the magnetite NPs, were investigated. It was observed that the saturation magnetization decreases from 60.8 up to 35.5 $A \cdot m^2/kg$ in accordance with concentration of silane (Fig. 29.3). It is well known that such decrease is determined by an increase of the non-magnetic phase concentration in the material [13]. Herewith the coercivity

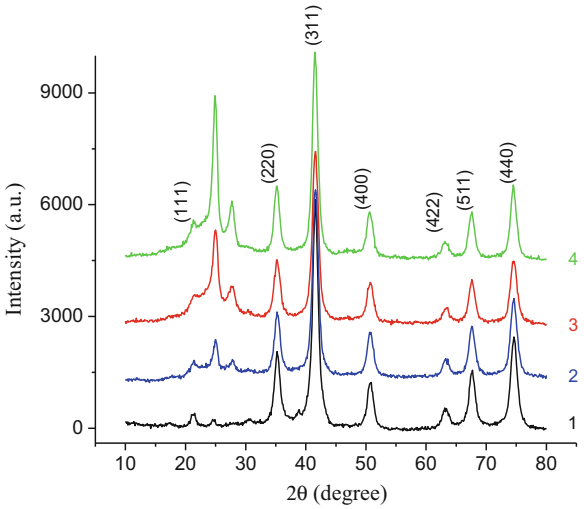

Fig. 29.2 XRD patterns of the as-prepared magnetite (1) and HDTMS-modified Fe_3O_4 NP (2–4) samples

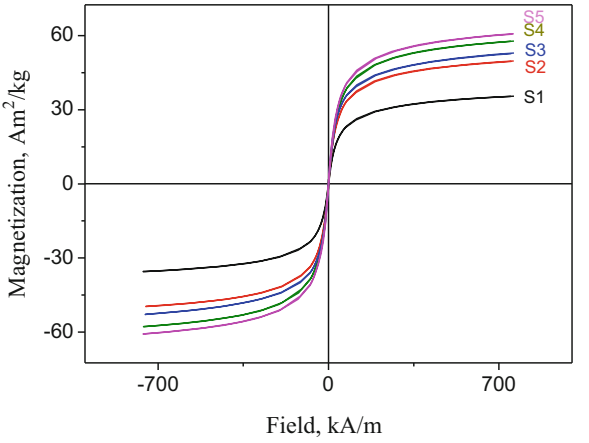

Fig. 29.3 Magnetization curves of HDTMS-modified Fe_3O_4 NPs with different overlayer thicknesses

increases from 0.69 to 1.025 kA/m it indicates the occurrence of magnetic losses of magnetostrictive nature in samples with a high content of silane.

The thermal response of NP based dispersions in silicone and oleic acid was studied in magnetic AC fields allowed for medical application. The concentration of theNPs in the dispersions was 5 wt. %, which is typical for in-vivo and clinical studies in MH [15]. The test tubes with HDTMS-modified Fe_3O_4 NPs were subjected to an alternating magnetic field of 1048 kHz and 5.8 kA/m. The results obtained are listed in Table 29.2.

Table 29.2 The heating rate and the SLP of the dispersions

	Silicone		Oleic acid		Lipiodol	
Sample	Heating rate, °C/min	SLP, W/g	Heating rate, °C/min	SLP, W/g	Heating rate, °C/min	SLP, W/g
S1	6.25 ± 0.08	2.7 ± 0,03	–	–	12.47 ± 1.04	11.53 ± 0.98
S2	9.47 ± 0.12	4,0 ± 0,08	–	–	17.8 ± 1.8	16.88 ± 1.7
S3	7.27 ± 0.09	3,1 ± 0,03	14.7 ± 1,3	14,0 ± 1.3	16.31 ± 1.92	15.3 ± 1.8
S5	3.68 ± 0.1	1,6 ± 0,07	11,1 ± 1.2	14,6 ± 1,2	18.8 ± 2.0	17.96 ± 1.9
Fe_3O_4	7.87 ± 0.25	3,4 ± 0.2	13.5 ± 1.8	14.12 ± 1.23	33.9 ± 1.95	32.08 ± 1.85

According to the obtained results, the SLP value is higher for magnetic dispersions in Lipiodol compared with oleic acid and silicone based dispersions, which can be explained by contributions of both relaxation process, Neel and Brownian. However, in the case of silicone based dispersions, the Brownian relaxation is negligible because of the immobilization of the NPs in the viscous silicone matrix. The effect of the coating on the SLP is clearly expressed for the case of dispersions in silicone. Sample S2 shows significantly higher SLP values; this can be explained by an additional contribution from hysteresis losses due to the appearance of magnetostrictive stresses in the nanoparticles.

29.4 Conclusion

Magnetite nanoparticles obtained by the coprecipitation method were modified by silanes thus formating nanoparticles with a "core-shell" structure. FTIR results showed that during the modification formation of a silane coating occurs due to the formation of Fe-O-Si- bonds.

The Si-O-R coating leads to a decrease in the absolute value of the effective saturation magnetization due to the presence of the non-magnetic phase (shell) in the sample. However, as the thickness of the coating increases, the coercivity increases due to an increase in the effective value of the magnetic anisotropy of magnetostrictive nature.

The investigation of the heating ability of dispersions based on HDTMS-modified Fe_3O_4 NPs showed that the coating does not lead to a significant decrease in the SLP value.

Acknowledgments This work was carried out in the Centre of Polymer Systems, Tomas Bata University in Zlin, Czech Republic; the authors would like to acknowledge Dr. Natalia Kazantseva for her intense help in that time.

References

1. Huang J, Li Y, Orza A, Lu Q, Guo P (2016) Magnetic nanoparticle facilitated drug delivery for cancer therapy with targeted and image-guided approaches. Adv Funct Mater 26(22):3818–3836
2. Kobayashi T (2011) Cancer hyperthermia using magnetic nanoparticles. Biotechnol J 6 (11):1342–1347
3. Adams NM, Bordelon H, Wang KK, Albert LE, Wright DW, Haselton FR (2015) Comparison of three magnetic bead surface functionalities for RNA extraction and detection. ACS Appl Mater Interfaces 7(11):6062–6069
4. Neuberger T, Schopf B, Hofmann H, Hofmann M, von Rechenberg B (2005) Superparamagnetic nanoparticles for biomedical applications: possibilities and limitations of a new drug delivery system. J Magn Magn Mater 293:483
5. Geraldes C, Laurent S (2009) Classification and basic properties of contrast agents for magnetic resonance imaging. Contrast Media Mol Imaging 4:1
6. Tran N, Webster TJ (2010) Magnetic nanoparticles: biomedical applications and challenges. J Mater Chem 20:8760–8767
7. Zhu X-M, Wang Y-XJ, Leung KC-F (2012) Enhanced cellular uptake of aminosilane-coated superparamagnetic iron oxide nanoparticles in mammalian cell lines. Int J Nanomedicine 7:953–964
8. Kong WH, Lee W, Cui ZY et al (2007) Nanoparticulate carrier containing water-insoluble iodinated oil as a multifunctional contrast agent for computed tomography imaging. Biomaterials 28:5555–5561
9. Sun H, Xu L, Fan T, Zhan H, Wang X, Zhou Y, Yang R-j (2013) Targeted hyperthermia after selective embolization with ferromagnetic nanoparticles in a VX2 rabbit liver tumor model. Int J Nanomedicine 8:3795–3804
10. Xue S, Wang Y, Wang M, Zhang L, Du X, Gu H, Zhang C (2014) Iodinated oil-loaded, fluorescent mesoporous silica-coated iron oxide nanoparticles for magnetic resonance imaging/computed tomography/fluorescence trimodal imaging. Int J Nanomedicine 9:2527–2538
11. Laurent S, Forge D, Port M, Roch A, Robic C, Elst LV, Muller RN (2008) Magnetic iron oxide nanoparticles: synthesis, stabilization, vectorization, physicochemical characterizations, and biological applications. Chem Rev 108(6):2064–2110
12. Neouze M-A, Schubert U (2008) Surface modification and functionalization of metal and metal oxide nanoparticles by organic ligands. Monatsh Chem 139:183–195
13. Cótica LF, Santos IA, Girotto EM, Ferri EV, Coelho AA (2010) Surface spin disorder effects in magnetite and poly(thiophene)-coated magnetite nanoparticles. J Appl Phys 108:064325
14. Howarter JA, Youngblood JP (2006) Optimization of Silica Silanization by 3-Aminopropyltriethoxysilane. Langmuir 22:11142
15. Smolkova I, Kazantseva N, Parmar H, Babayan V, Smolka P, Saha P (2015) Correlation between coprecipitation reaction course and magneto-structural properties of iron oxide nanoparticles. Mater Chem Phys 155:178–190
16. Yoshida W, Castro RP, Jou JD (2001) Multilayer alkoxysilane silylation of oxide Surfaces. Langmuir 17:5882–5888
17. Chiarakorn S, Areerob T, Grisdanurak N (2007) Influence of functional silanes on hydrophobicity of MCM-41 synthesized from rice husk. Sci Technol Adv Mater 8:110–115
18. Okawa K, Sekine M, Maeda M, Tada M, Abe M, Matsushita N, Nishio K, Handa H (2006) Heating ability of magnetite nanobeads with various sizes for magnetic hyperthermia at 120kHz120kHz, a noninvasive frequency. J Appl Phys 99:08H102

19. Nakamoto K (1991) IR-spectra and spectra of inorganic and coordination compounds, vol 505. Mir, Moskow
20. Szwarc-Rzepka K, Szatkowski T, Ciesielczyk F, Jesionowski T (2013) Preparation and characterization of SiO2/silane/POSS functional hybrids. Physicochem Probl Miner Process 49 (2):673–687
21. Vikesland PJ, Heathcock AM, Rebodos RL, Makus KE (2007) Particle size and aggregation effects on magnetite reactivity toward carbon tetrachloride. Environ Sci Technol 41:5277–5283

Part VIII
Materials: Glasses and Polymers

Chapter 30
Ureasil-Based Polymer Matrices As Sensitive Layers for the Construction of Amperometric Biosensors

T. S. Kavetskyy, O. Smutok, M. Gonchar, O. Šauša, Y. Kukhazh, H. Švajdlenková, T. Petkova, V. Boev, and V. Ilcheva

Abstract Ureasil and ureasil-chalcogenide glass composites of different history (fresh and aged during 1 year) were used for the immobilization of laccase and the construction of amperometric biosensors. A correlation between the microscopical free-volume of the polymer matrices as revealed by low-temperature positron annihilation lifetime spectroscopy and biosensor characteristics of the laccase-containing ureasil based biosensors is established. The observed findings could be applied for improvement of the operational parameters of the constructed biosensors, which may have potential for monitoring the level of pollution of wastewater.

Keywords Organic-inorganic hybrid · Ureasil · Enzyme · Amperometric biosensor

T. S. Kavetskyy (✉)
Drohobych Ivan Franko State Pedagogical University, Drohobych, Ukraine

The John Paul II Catholic University of Lublin, Lublin, Poland

O. Smutok · M. Gonchar
Institute of Cell Biology, National Academy of Sciences of Ukraine, Lviv, Ukraine

O. Šauša
Institute of Physics, Slovak Academy of Sciences, Bratislava, Slovak Republic

Y. Kukhazh
Drohobych Ivan Franko State Pedagogical University, Drohobych, Ukraine

H. Švajdlenková
Polymer Institute, Slovak Academy of Sciences, Bratislava, Slovak Republic

T. Petkova · V. Boev · V. Ilcheva
Institute of Electrochemistry and Energy Systems, Bulgarian Academy of Sciences, Sofia, Bulgaria

P. Petkov et al. (eds.), *Advanced Nanotechnologies for Detection and Defence against CBRN Agents*, NATO Science for Peace and Security Series B: Physics and Biophysics, https://doi.org/10.1007/978-94-024-1298-7_30

30.1 Introduction

Modern science, medicine, clinical diagnostics, biotechnologies, as well as environmental technologies all need highly selective, sensitive, rapid, and reliable methods of identifying the key ingredients or metabolites which determine the quality of products or serve as markers for diseases, the physiological state of human organism or environmental safety. Biosensors are the most novel achievement of analytical biotechnology. Development of novel nanocomposites and polymers suitable for construction of biosensor with improved operational parameters is an important field in sensor technologies. Polymer matrices based on ureasil composites [1–5] have been tested for immobilization of laccase from *Trametes versicolor* and the construction of amperometric biosensors for the first time in [6]. The biosensor characteristics such as sensitivity of the bioelectrode were determined and analyzed for ureasil, ureasil-chalcogenide glass composites, and ureasil-chalcogenide glass composites with incorporated silver nanoparticles (NPs) synthesized by high-dose 30 keV Ag^+ implantation. A very high sensitivity of the amperometric biosensor with ureasil-chalcogenide glass composite was established, and a well expressed influence on the sensor characteristics by the polymer matrix and the Ag NPs was detected [6]. It should be noted here that some other novel techniques for the fabrication of organic-inorganic hybrid nanocomposites based on chalcogenide glasses and manganese phtalocyanine has also been reported in literature [7], showing a potential for photonics applications. In other words, incorporation of inorganic chalcogenide glasses into an organic matrix is an attractive innovative approach for the fabrication of novel materials suitable for practical use in optonanoelectronics and biosensorics. In the present work, ureasil and ureasil-chalcogenide glass composites of different history (fresh and aged during 1 year) were used for the construction of laccase-containing amperometric biosensors. The relationship between the microscopical free-volume of the polymer matrices as revealed by low-temperature positron annihilation lifetime spectroscopy (PALS) [8] and the biosensor characteristics of the laccase-containing ureasil based biosensors is examined.

30.2 Experimental

The synthesis of the pure ureasil matrix (K0) and the ureasil-chalcogenide As_2S_3 composite matrix (K4) was reported elsewhere [4, 5, 9]. Polymer matrices of different history – K0-fresh and K4-fresh (2 months after preparation) and K0-aged and K4-aged (1 year after preparation) – were used for examination [8]. The low-temperature PALS experiment was carried out as described in [8]. The PAL spectra were taken using plastic scintillators coupled to photomultiplier tubes as detectors with a ^{22}Na positron source and analyzed with the free of charge LT program. The time resolution (FWHM) of spectrometer was

about 320 ps, measured with a defect free Al sample. A three component fitting procedure was applied for PALS data treatment. The long lifetime component τ_3 and its intensity I_3, ascribing to the *ortho*-positronium (*o*-Ps) pick-off annihilation in free-volume holes [10] were finally taken into account for analysis. The low-temperature measurements were performed in the range of 15–350 K using a helium cryostat (Closed Cycle Refrigerator, Janis Research Company, Inc., USA) with an accuracy of ± 1 K and a vacuum equipment (Pfeiffer Vacuum, HiCUBE, Germany) with automatically controlled vacuum in the system. The samples were measured in 'cooling-heating' cycles of with 20 K steps and an elapsed time of 3–5 h per point. Biosensitive layers of the amperometric biosensor was formed on the surface of solid state transducers as reported in [6]. The laccase enzyme was immobilized on the surface of the planar gold electrodes using the fresh and aged composites as a matrix agent. All stages for the immobilization of the laccase enzyme, the preparation of the bioelectrode using 4 mm diameter planar gold electrodes DRP-C220AT from "DropSens" (Llanera, Asturias, Spain), the estimation of the optimal working potential with cyclic voltamperometry and the conduction of an analysis with a chronoamperometric approach in respect to the corresponding substrate (2,2′-azino-bis(3-ethylbenzothiazoline-6-sulphonic acid, ABTS) were the same as previously done in [6].

30.3 Results and Discussion

Figure 30.1 shows the *o*-Ps lifetimes and their relative intensities for the investigated samples as a function of temperature in the range of 15–350 K. The temperature where the free-volume (*o*-Ps lifetime) changes its slope is assigned as glass transition temperature T_{g1}.

The determined values of the free-volume ($V_h(T_{g1}) = 4\pi R^3/3$) with radius R at the glass transition temperature T_{g1} and the thermal expansion coefficient $\alpha_{fv1} = (1/V_h(T_{g1}))$ $(\Delta V_h/\Delta T)$ [10] of the microscopical free-volume are presented in Table 30.1. In addition to the glass transition temperature T_{g1}, the lower temperature at which the slope of the $V_h(T)$ also changes in some cases, is designated as glass transition temperature T_{g2}, although the nature of the two T_g remains not understood yet.

Figure 30.2 shows calibration curves of the response on increasing concentrations of ABTS, obtained by chronoamperogramms of the bioelectrodes based on laccase immobilized by pure ureasil (K0-fresh and K0-aged) and ureasil-chalcogenide glass composites (K4-fresh and K4-aged) on the surface of the planar gold electrode. Figure 30.3 shows calibration curves of the response on increasing concentrations of ABTS for the planar gold electrodes modified by 10 μL laccase and 4 μL pure ureasil (K0) and ureasil-chalcogenide glass composites (K4) under the following conditions: 50 mM acetate buffer (pH 4.5), working potential −100 mV versus Ag/AgCl (reference electrode) under constant stirring with a magnetic mixer. Estimated from the calibration curves were the biosensor response I_{max}, the Michaelis-Menten constant K_M to ABTS as the substrate, the slope of the curve B, and the sensitivity

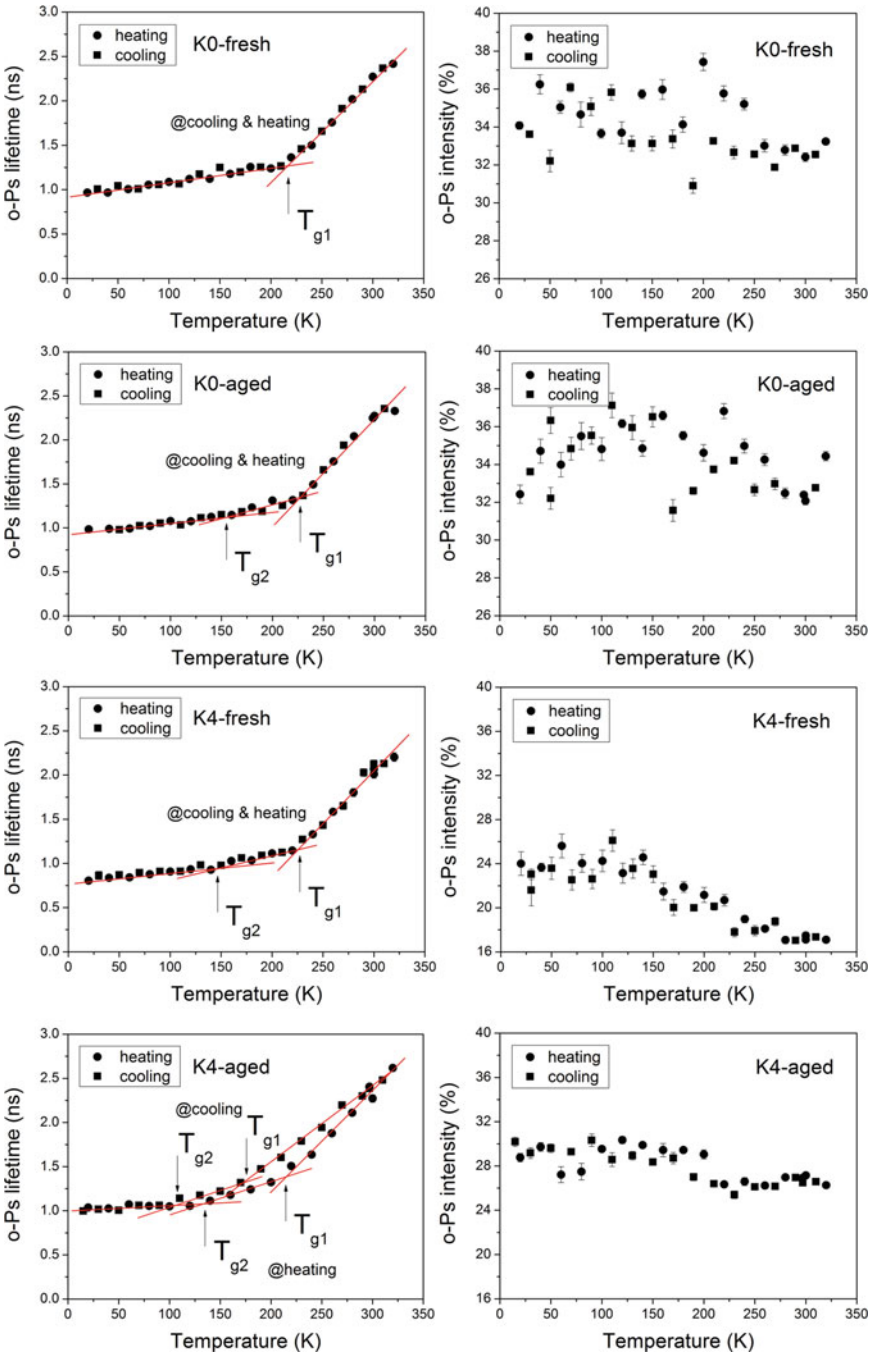

Fig. 30.1 *o*-Ps lifetime τ_3 (left) and intensity I_3 (right) as a function of temperature for the four samples of this study. The error bars are within the size of the symbol. The solid lines are drawn as a guide for the eye (See the text for details. Adapted from [8])

Table 30.1 Free-volume V_{h1} at the glass transition temperature T_{g1}, the lower temperature at which $V_h(T)$ changes its slope, designed as glass transition temperature T_{g2}, and the thermal expansion coefficient α_{fv1} of the microscopical free-volume near T_{g1} for the investigated polymer samples [8]

Sample	V_{h1} (nm^3)	T_{g1} (K)	T_{g2} (K)	$\alpha_{fv1\ (T < Tg1)}$ (10^{-4} K^{-1})	$\alpha_{fv1\ (T > Tg1)}$ (10^{-4} K^{-1})
K0-fresh (c and h)	0.123 ± 0.002	216 ± 13	–	25 ± 3	286 ± 21
K0-aged (c and h)	0.123 ± 0.003	230 ± 19	166 ± 89	53 ± 22	273 ± 99
K4-fresh (c and h)	0.104 ± 0.001	227 ± 18	126 ± 38	48 ± 10	344 ± 63
K4-aged (c)	0.134 ± 0.001	178 ± 19	88 ± 58	46 ± 17	206 ± 56
K4-aged (h)	0.123 ± 0.004	228 ± 38	130 ± 38	56 ± 22	237 ± 84

c cooling, *h* heating

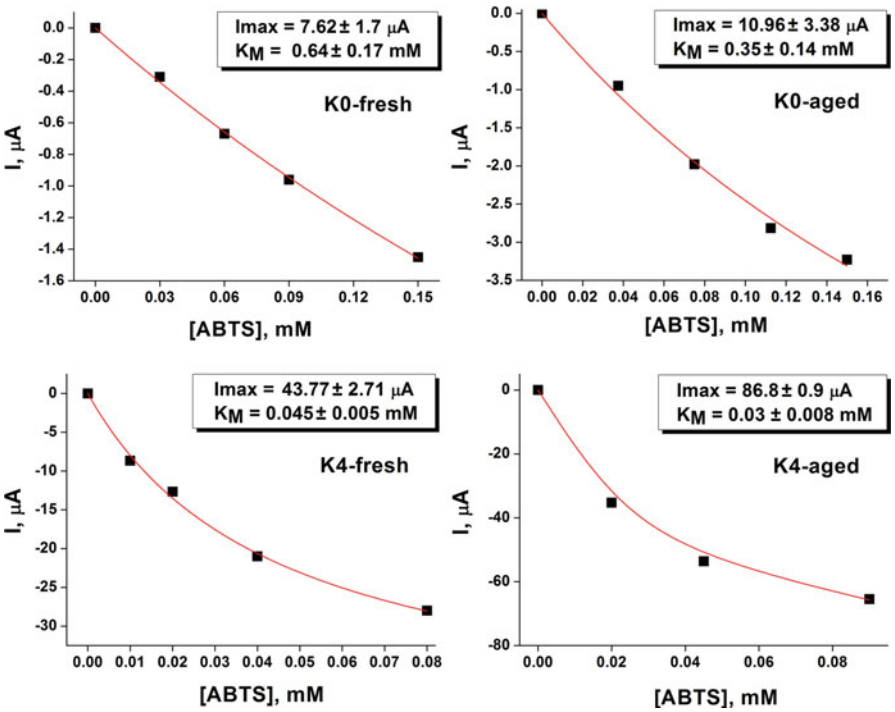

Fig. 30.2 Calibration curves of responses to increasing concentrations of ABTS for planar gold electrodes modified by laccase immobilized by pure ureasil (K0-fresh and K0-aged) and ureasil-chalcogenide glass composites (K4-fresh and K4-aged)

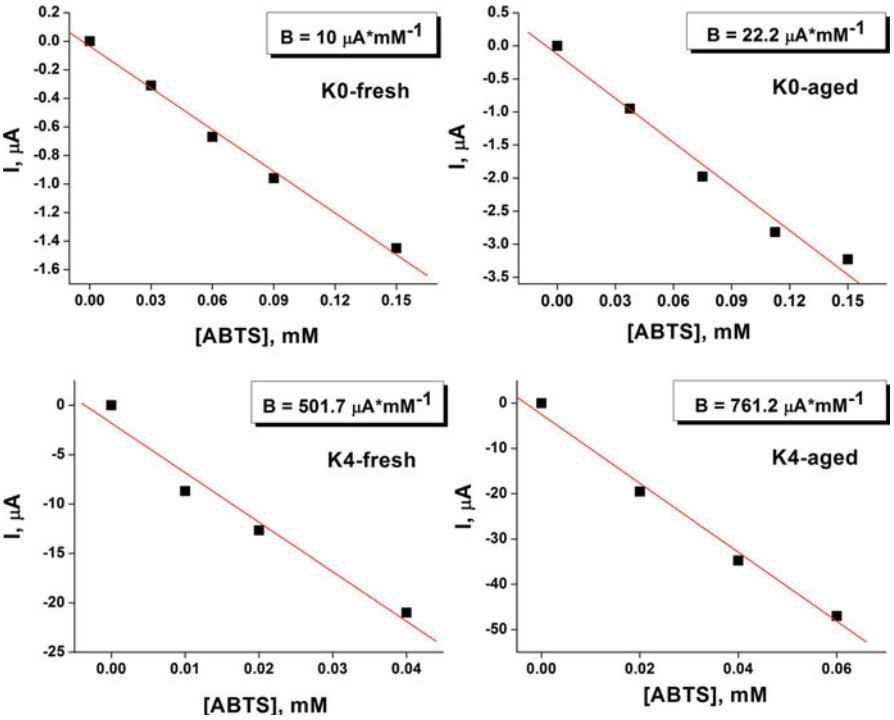

Fig. 30.3 Calibration curves of responses to increasing concentrations of ABTS for planar gold electrodes modified by 10 μL laccase and 4 μL pure ureasil (K0-fresh and K0-aged) and ureasil-chalcogenide glass composites (K4-fresh and K4-aged)

Table 30.2 Biosensor response I_{max}, Michaelis-Menten constant K_M to ABTS as the substrate, the slope of the curve B, and the sensitivity of bioelectrode constructed based on laccase immobilized by the investigated polymer samples

Sample	I_{max} (μA)	K_M (mM)	B (μA·mM^{-1})	Sensitivity (A·M^{-1}·m^{-2})
K0-fresh	7.62 ± 1.7	0.64 ± 0.17	10.0	794
K0-aged	10.96 ± 3.38	0.35 ± 0.14	22.2	1762
K4-fresh	43.77 ± 2.71	0.045 ± 0.005	501.7	39,817
K4-aged	86.8 ± 0.9	0.030 ± 0.008	761.2	60,413

of the bioelectrode, calculated as the ratio of the slope B to the area of the electrode (12.6 mm^2); these data are gathered in Table 30.2.

As seen from Table 30.2, the K_M value gradually decreases from K0-fresh to K0-aged and then to K4-fresh and K4-aged. The well-known Michaelis-Menten saturation curve for an enzyme reaction shows the relation between the substrate concentration and the reaction rate, where the constant K_M is the substrate concentration at which the reaction rate is half of the maximum rate achieved in the system at saturating substrate concentration. A lower value of K_M for the bioelectrode

indicates a high efficiency of direct electron transfer from the reduced form of the enzyme on the surface of the planar gold electrode. So, the K4-aged sample showed the best results in this regards. The biosensor sensitivity increases by a factor of 2.2 for the aged K0 sample. Likewise, the biosensor sensitivity increases 1.5 times for the aged K4. At the same time, the increase of the biosensor sensitivity is 34.3 times between the aged K4 and K0-aged samples, but 50.1 times K4-fresh and K0-fresh. Thus, K4-fresh shows the most remarkable changes in the sensitivity of the amperometric biosensor. According to the PALS results (Table 30.1), this sample K4-fresh also shows the smallest free volume. Therefore, a correlation between the microscopical free-volume of the polymer matrices and the biosensor characteristics of the laccase-containing ureasil based biosensors is established. It must be noted here, that the K4-fresh samples also showed the lowest crosslinking density and the highest swellability [8]. Thus, by controlling the network properties of polymer matrix one may control the functionality of amperometric biosensors based on a polymer matrix. The observed findings could be further applied for improvement of the operational parameters of the constructed biosensors, which may have potential for monitoring the level of pollution of wastewater.

30.4 Conclusion

Ureasil and ureasil-chalcogenide glass composites of different history (fresh and aged during 1 year) have been used for the immobilization of laccase and the construction of amperometric biosensors. A correlation between the microscopical free-volume of the polymer matrices as revealed by low-temperature positron annihilation lifetime spectroscopy and the biosensor characteristics of the laccase-containing ureasil based biosensors has been established.

Acknowledgments This work was supported by the Ministry of Education and Science of Ukraine (projects Nos. 0116U004737; to TK, OS, MG and YK, and 0117U007142 (for Young Scientists; to YK), by the Slovak Grant Agency VEGA (project No. 2/0157/17; to OŠ) and Slovak Research and Development Agency (project No. APVV-16-0369; to OŠ and HŠ) and by the National Science Fund of the Bulgarian Ministry of Education (project No. FNI-DN09/12-2016; to TK, TP, VB and VI).

References

1. Boev V, Perez-Juste J, Pastoriza-Santos I, Silva CJR, Gomes MJM, Liz-Marzan LM (2004) Flexible ureasil hybrids with tailored optical properties through doping with metal nanoparticles. Langmuir 20:10268
2. Boev VI, Silva CIR, Hungerford G, Gomes MJM (2004) Synthesis and characterization of a sol–gel derived ureasilicate hybrid organic-inorganic matrix containing CdS colloidal particles. J Sol-Gel Sci Technol 31:131

3. Boev VI, Soloviev A, Silva CJR, Gomes MJM, Barber DJ (2007) Highly transparent sol-gel derived ureasilicate monoliths exhibiting long-term optical stability. J Sol-Gel Sci Technol 41:223
4. Kavetskyy T, Lyadov N, Valeev V, Tsmots V, Petkova T, Boev V, Petkov P, Stepanov AL (2012) New organic-inorganic hybrid ureasil-based polymer and glass-polymer composites with ion-implanted silver nanoparticles. Phys Status Solidi C 9:2444
5. Kavetskyy T, Sausa O, Kristiak J, Petkova T, Petkov P, Boev V, Lyadov N, Stepanov A (2013) New organic-inorganic hybrid ureasil-based polymer materials studied by PALS and SEM techniques. Mater Sci Forum 733:171
6. Kavetskyy T, Smutok O, Gonchar M, Demkiv O, Klepach H, Kukhazh Y, Sausa O, Petkova T, Boev V, Ilcheva V, Petkov P, Stepanov AL (2017) Laccase-containing ureasil-polymer composite as the sensing layer of an amperometric biosensor. J Appl Polym Sci 134:45278
7. Grynko D, Stronski A, Telbiz G, Lytvyn O, Paiuk O, Oleksenko P (2015) Nanocomposites based on chalcogenide glass semiconductor and metal phtalocyanine. Ceram Int 41:7605
8. Kavetskyy T, Sausa O, Cechova K, Svajdlenkova H, Matko I, Petkova T, Boev V, Ilcheva V, Smutok O, Kukhazh Y, Gonchar M (2017) Network properties of ureasil-based polymer matrixes for construction of amperometric biosensors as probed by PALS and swelling experiments. Acta Phys Pol A 132:1515
9. Kavetskyy T, Kolev K, Boev V, Petkov P, Petkova T, Stepanov AL (2011) In: Riethmaier JP, Paunovic P, Kulisch W, Popov C, Petkov P (eds) Nanotechnological basis for advanced sensors. Springer, Berlin, p 103
10. Jean YC (1990) Positron annihilation spectroscopy for chemical analysis: a novel probe for microstructural analysis of polymers. Microchem J 42:72

Chapter 31
Impedance Characterization of Gas Sensitive Chalcogenide Films

Dumitru Tsiulyanu, Marina Ciobanu, and Olga Mocreac

Abstract The gas sensing performance of chalcogenide thin films, investigated by the method of impedance spectroscopy is reported and discussed in order to assess their use in future gas sensors operating at room temperature. Along with the traditional use of Te films for such applications, impedance spectra of quaternary $As_2S_3Ge_8$ – Te alloys have been investigated in both dry synthetic and humid air, as well as in their mixtures with different harmful gases. To elucidate the effect of tellurium, the quaternary compositions $As_2Te_{13}Ge_8S_3$ and $As_2Te_{130}Ge_8S_3$ with increasing concentration of Te have been investigated along with pure tellurium films. The films have been prepared by thermal vacuum evaporation onto Pyrex or sintered alumina (Al_2O_3) substrates carrying pre-deposited platinum interdigital electrodes. As shown by AFM, SEM and X–ray analysis the phase/state of the films depends on the composition, nature of the substrate and growth rate. The morphology of the films grown on sintered alumina substrates appears to consist of interconnected islands and dots, which facilitate a solid-gas interaction. It is shown that impedance spectra, being strongly influenced by the gaseous environment are also strongly influenced by material composition and phase/structural state of the film. Analyses of these spectra in the Cole – Cole interpretation allowed to evaluate the characteristic frequency, time constant, resistance and capacity of the films in both dry air and its mixture with target harmful gases. Modification of the chemical composition via addition of As, S and Ge atoms leads to structural/phase transformations, along with the appearance of new mechanisms of charge transport that influence the gas sensing performance of the chalcogenide based films.

Keywords Impedance measurements · Chalcogenide films · Gas sensors

D. Tsiulyanu (✉) · M. Ciobanu · O. Mocreac
Department of Physics, Technical University, Chisinau, Moldova

P. Petkov et al. (eds.), *Advanced Nanotechnologies for Detection and Defence against CBRN Agents*, NATO Science for Peace and Security Series B: Physics and Biophysics, https://doi.org/10.1007/978-94-024-1298-7_31

31.1 Introduction

Glassy chalcogenide based films may be used for the detection of harmful gases at room temperature. This possibility has already been pointed out in the early 2000s, when Ge-As-Te based gas sensors for atmospheric pollution control have been proposed [1, 2]. Later gas sensitive films based on $(As_2S_3)_{(100-x)}(AgI)_x$ [3], silver doped $SnSe_2$ and $Ge_2Sb_2Te_5$ [4], different compositions in the binary, ternary and quaternary systems of As-S–T(Se)-Ge [5] have been reported, as well as amorphous films based on pure Te [6–8]. In order to estimate possible applications of these materials in gas sensors, the authors have measured the variation of different physical quantities (resistivity, current, resonance, work function etc.) during gas sorption. Also, different pollutant and toxic gases (NO, NO_2, CO, NH_3, NH_4, etc.), as well as volatile organic compounds or water vapor have been used as a target gas.

Although the cross sensitivity to the gases mentioned is essentially different, the distinguishing between them becomes important. One possibility to obtain a selective detection of gases has been mentioned at the early stages of the investigation of semiconducting gas sensors [9] and consists in fast sweeping of the sensitivity of a single sensor at different frequencies. The sensitivity of a sensor to different gases at different frequencies can be quite different. That is, by monitoring the a.c. conductance at specific frequencies, the sensitivity to different gas components can be enhanced [10]. Moreover, a.c. measurements allow obtaining impedance or admittance spectra of a sensor, calculating an equivalent circuit and distinguishing between contributions from the surface, bulk or contacts to the film conductivity [11].

In the present work, we report the results of gas sensing measurements performed by means of impedance spectra in a large frequency range (5 Hz–13 MHz) at room temperature. In order to get evidence on effect of tellurium, we have investugated $As_2Te_{13}Ge_8S_3$ and $As_2Te_{130}Ge_8S_3$ as well as pure Te for comparison.

31.2 Materials and Methods

The glassy alloys were prepared by the melt-quenching method from pure (99.99%) As, S, Te and Ge in quartz ampoules evacuated to $5–10^{-5}$ Torr. The melting was performed at 900 °C. The ampoules were rotated around the longitudinal axis at a velocity of seven to eight rotations/min and were agitated for homogenization during the synthesis time (24 h) and then quenched on a copper refrigerator with running water. Two quaternary compositions $As_2Te_{13}Ge_8S_3$ and $As_2Te_{130}Ge_8S_3$ with increasing concentration of Te were synthesized as well as pure polycrystalline tellurium.

The chalcogenide based thin films have been prepared by thermal “flash” evaporation of pre-synthesized materials from tantalum boats onto either glass

(Pyrex) or ceramic Al_2O_3 substrates at a working pressure of 10^{-5} Torr. The ceramic Al_2O_3 substrates were equipped with previously deposited interdigital platinum electrodes with an electrode width of 15 μm and interelectrode distance of 45 μm. The growth velocity of the film was in the order of 30 nm/s, and the area of deposition around 5 mm^2. The thickness of the films was about 60 nm, being determined using a microinterferometer MII – 4. Structural investigations of the grown films were carried out by X–ray analyses and scanning electron microscopy (SEM). The films were encapsulated in standard TO–16 sockets, their contacts were thermally bonded to socket pins by means of copper wires.

Impedance measurements were carried out in the frequency range from 5 Hz to 13 MHz using a HP4192A impedance analyzer. For these experiments the thin film sensing devices were put into a test cell (of 10 ml volume) in which the gases were injected parallel to the film surface. Constant flow (100 ml/min) was maintained by mass flow controllers (MFC, Wigha, Germany). NO_2 vapor with a concentration of 1.5 ppm was obtained by using a calibrated permeation cylinder (Vici Metronics, USA) which was incorporated into the experimental set–up. In this work, the a.c. gas sensitivity is defined as relative variation of the impedance for a selected frequency in a mixture of the carrier gas with a target one (Z_g) and the pure carrier gas (Z_a), divided by target gas concentration C in percent/ppm:

$$\eta = \frac{|Z_a - Z_g|}{Z_a C} \cdot 100\% \tag{31.1}$$

31.3 Surface Morphology and Phase/Structure

The surface morphology of the films was made visible with a VEGA TESCAN TS 5130 MM scanning electron microscope at an acceleration voltage of 30 kV. X-ray analyses using a DRON – YM1 diffractometer with FeK $_\alpha$ radiation was applied for structural investigations of the grown films. The rotation velocity of the scintillation counter was 2 (or 4) degrees/min. Figures 31.1 and 31.2 shows SEM images of the quaternary $As_2Te_{13}Ge_8S_3$ and $As_2Te_{130}Ge_8S_3$ chalcogenides along with films of elemental Te,

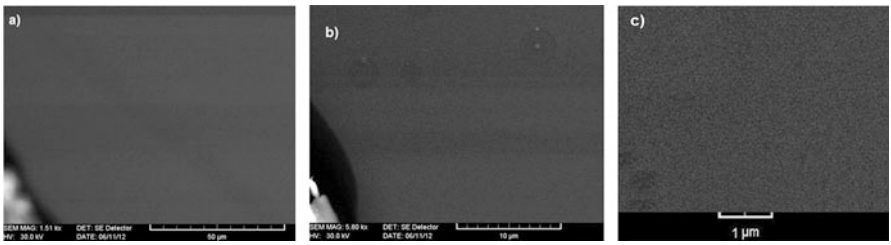

Fig. 31.1 SEM images of (**a**) $As_2Te_{130}Ge_8S_3$, (**b**) $As_2Te_{13}Ge_8S_3$ and (**c**) pure tellurium thin films grown on Pyrex glass substrates

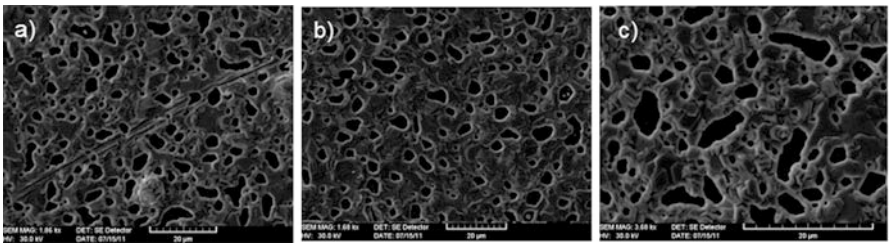

Fig. 31.2 SEM images of (**a**) $As_2Te_{130}Ge_8S_3$, (**b**) $As_2Te_{13}Ge_8S_3$ and (**c**) pure tellurium thin films grown on sintered alumina (Al_2O_3) substrates

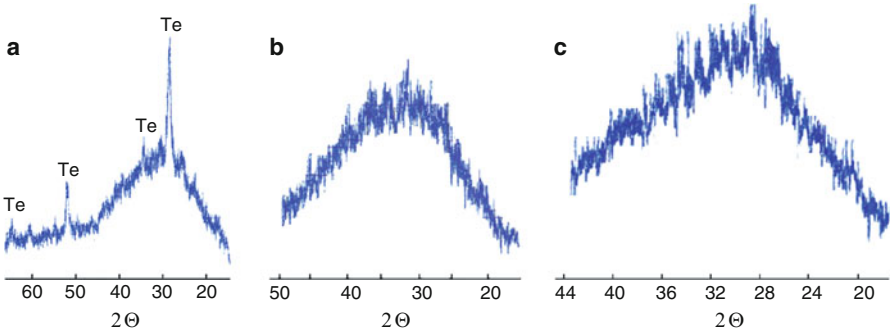

Fig. 31.3 XRD diffraction pattern of (**a**) $As_2Te_{130}Ge_8S_3$, (**b**) $As_2Te_{13}Ge_8S_3$ and (**c**) pure tellurium thin films grown on Pyrex glass substrates

grown on different substrates, using the same deposition rate (~30 nm/s). As can be seen, the films grown on glassy (Pyrex) substrates are continuous layers, but the films grown on sintered alumina consists of agglomerated islands, resulting in films with a great surface roughness. In all cases no crystallite traces are observed.

Figure 31.3 shows the XRD patterns of the films deposited on the Pyrex substrates. It can be seen that the film with the enhanced Te concentration (91 at.%) (Fig. 31.3a) contains diffraction peaks, which indicate the existence of a crystalline phase. On the other and, no peaks of crystalline Te are observed in both the $As_2Te_{13}Ge_8S_3$, and the pure tellurium films, which means that these films are in the vitreous state.

The XRD patterns of quaternary $As_2Te_{13}Ge_8S_3$, $As_2Te_{130}Ge_8S_3$ and pure Te, films deposited on alumina substrates are shown in Fig. 31.4. It is evident that the $As_2Te_{13}Ge_8S_3$ film (Fig. 31.4b) is in the amorphous state. The quaternary films with the higher Te concentration as well as pure films show very small peaks corresponding to crystalline Te phases (Fig. 31.4a, c), indicating their nearly amorphous nature. No peaks corresponding to oxides of tellurium are discernable in the XRD patterns. These results are in agreement with SEM observation.

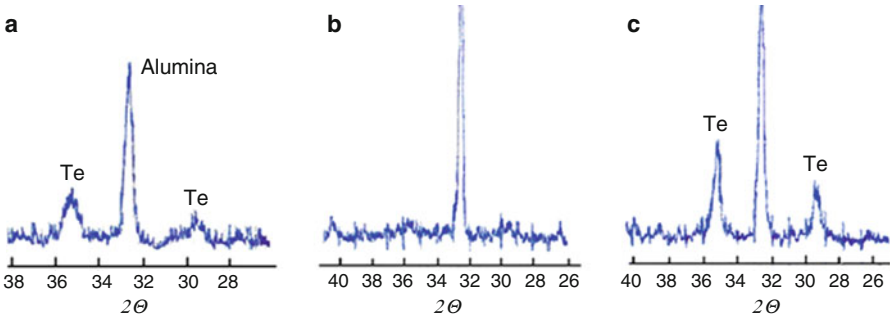

Fig. 31.4 XRD diffraction pattern of (**a**) $As_2Te_{130}Ge_8S_3$, (**b**) $As_2Te_{13}Ge_8S_3$ and (**c**) pure tellurium thin films grown on sintered alumina substrates

31.4 Impedance Characterization

31.4.1 Effect of Material Composition

It is well known that impedance measurements allow to calculate the equivalent circuit of a film system and to distinguish between contributions from the surface, bulk or contacts to the overall film conductivity [11]. For this purpose, the impedance of the thin film device is usually considered in complex form:

$$Z(\omega) = \frac{1}{Y(\omega)} = \mathrm{Re}(Z) + i\mathrm{Im}(Z) \tag{31.2}$$

$$\text{where} \quad \mathrm{Re}(Z) = \frac{R}{1 + (\omega \cdot C \cdot R)^2} \tag{31.3}$$

$$\text{and} \quad \mathrm{Im}(Z) = -\frac{\omega \cdot C \cdot R^2}{1 + (\omega \cdot C \cdot R)^2} \tag{31.4}$$

Then Im(Z) is plotted vs. Re(Z) in a Nyquist diagram.

Figure 31.5 shows the Nyquist diagrams obtained from data measured in pure dry air for thin film devices based of all chalcogenide materials studied in this work, at room temperature (22 °C). The diagrams are quite different. The diagram of the pure Te film shows a slightly depressed semi-circular arc with the center placed below the real axis owing to the presence of different circuit elements in the thin film device [11]. It seems that the complex impedance diagram of the $As_2Te_{13}Ge_8S_3$ film, calculated from the measured values of the real and imaginary parts show the semi-circular arc as well, although the diameter of the semicircle is so large that it could not be plotted completely due to the lack of data, due to device limitation. Thus, for these two compositions a simplified equivalent circuit as shown in

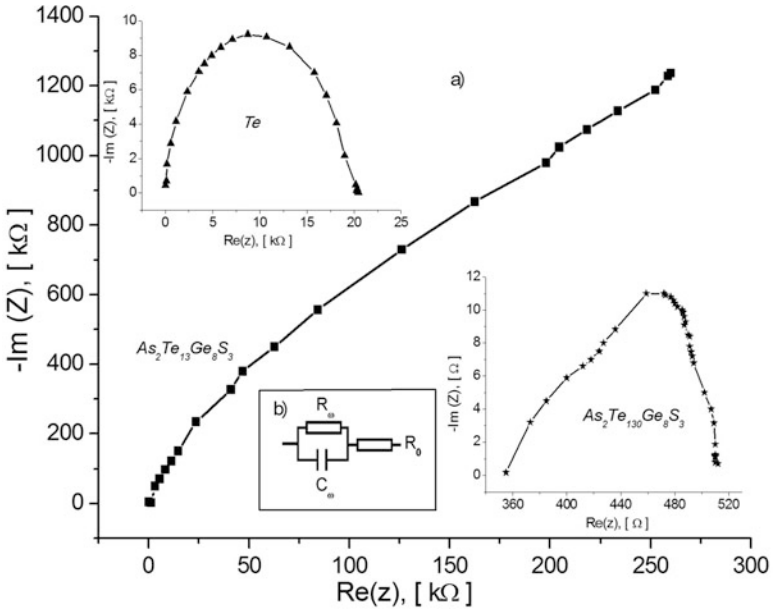

Fig. 31.5 (**a**) Nyquist diagrams of thin film devices based on $As_2S_3Ge_8$ – Te alloys in dry air at 22 °C and (**b**) suggested equivalent circuit

Fig. 31.5b can interpret the Nyquist plot. The frequency independent serial resistance R_0 is due to the sum of the Ohmic resistances of the electrical connections, but the resistance R_ω and the capacity C_ω are due to other contributions, among them contact resistance and capacity seem to be the most important. The circles on these diagrams are depressed due to the dependence of both R_ω and C_ω on frequency. The complex impedance diagram of the $As_2Te_{130}Ge_8S_3$ film does not resemble a semicircular arc. This means, the equivalent circuit is much more complicated than a simple RC parallel one.

From simple analysis of the equivalent circuit the values of R_ω and C_ω of the film can be evaluated as:

$$R_\omega = \frac{\mathrm{Im}^2(Z) + \mathrm{Re}^2(Z)}{\mathrm{Re}(Z)} \tag{31.5}$$

$$C_\omega = \frac{\mathrm{Im}(Z)}{\omega\left[\mathrm{Im}^2(Z) + \mathrm{Re}^2(Z)\right]} \tag{31.6}$$

Equations (31.5) and (31.6) allows an estimation of the resistance and capacitance of the film at any frequency entire the spectrum, including the characteristic frequency f_m, at which the imaginary part Im(Z) reaches its maximal value.

Calculated from Eqs. (31.5) and (31.6), resistance R_ω and capacity C_ω of the films at the characteristic frequency R_m and C_m, as well as the film impedance Z_m and the time constant calculated as [12]:

Table 31.1 Impedance and R-C values at the characteristic frequency

Composition	Te		$As_2Te_{13}Ge_8S$		$As_2Te_{130}Ge_8S$	
Environment	Dry air	1.5 ppm NO_2	Dry air	1.5 ppm NO_2	Dry air	1.5 ppm NO_2
f_m, [kHz]	450	950	–	140	1000	800
Z_m, [kΩ]	13.3	6.6	–	120	0.48	0.42
$\tau_m \times 10^{-7}$ s	3.5	1.7	–	11.4	1.6	2.0
R_m, [kΩ]	18.5	9.3	–	167	0.49	0.43
C_m, [pF]	18.3	17.8	–	6.8	8.7	8.1

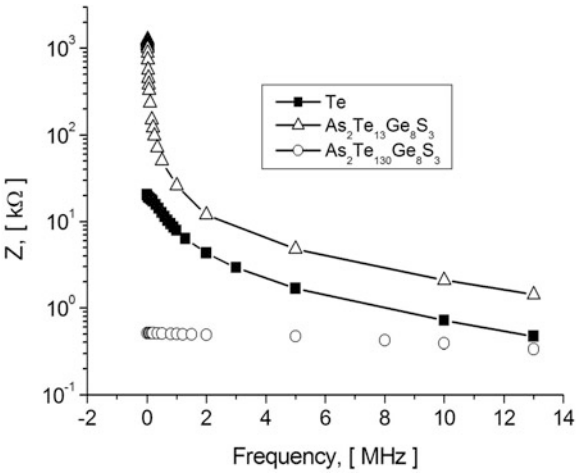

Fig. 31.6 Impedance of chalcogenides semiconductors $As_2S_3Ge_8$ – Te vs frequency of the applied voltage at room temperature (22 °C)

$$\tau_m = \omega_m^{-1} = \frac{1}{2\pi f_m} = R_m C_m \tag{31.7}$$

are listed in Table 31.1. Note that the respective values for the high resistive $As_2Te_{13}Ge_8S_3$ film could not be calculated due to the reason mentioned above. On the other hand, we have assessed the characteristic frequency f_m of the low resistivity films with the composition $As_2Te_{130}Ge_8S_3$ as the frequency, at which the imaginary part of the impedance reaches the maximal value, in spite of the not semicircular form of its Nyquist diagram. Further, we have applied the value of f_m to calculate Z_m, R_m and C_m of the films as well, which also are listed in Table 31.1. It is noticeable that in spite of the low concentration of other elements introduced in this alloy (2.1 at.% S; 1.4 at% As and 5.6 at % Ge), both the impedance and the electrical resistance decrease dramatically in comparison with the pure Te film by two and three orders of magnitude, respectively.

As far as the regular impedance spectra are concerned, they also strongly depend on the material composition. Figure 31.6 illustrates the frequency dependent impedance of the chalcogenides examined in this work. It can be seen that the impedance of pure Te and $As_2T_{13}Ge_8S_3$ films strongly decrease with increasing frequency. On the other hand, the variation of the impedance

with increasing frequency in $As_2T_{130}Ge_8S_3$ films is neglegible. This behavior can be due to different mechanisms of charge transport in these materials as will be considered below.

31.4.2 *Effect of NO_2 Adsorption*

Figure 31.7a–c shows the complex impedance diagrams in the Cole-Cole presentation (Nyquist diagram) of thin film devices discussed in this study measured both in dry air and upon exposure to NO_2 at room temperature (22 °C). The addition of nitrogen dioxide to dry air does not change the general shape of the impedance spectra of pure tellurium (a) and $As_2T_{130}Ge_8S_3$ (b) films; that is, the NO_2 influences

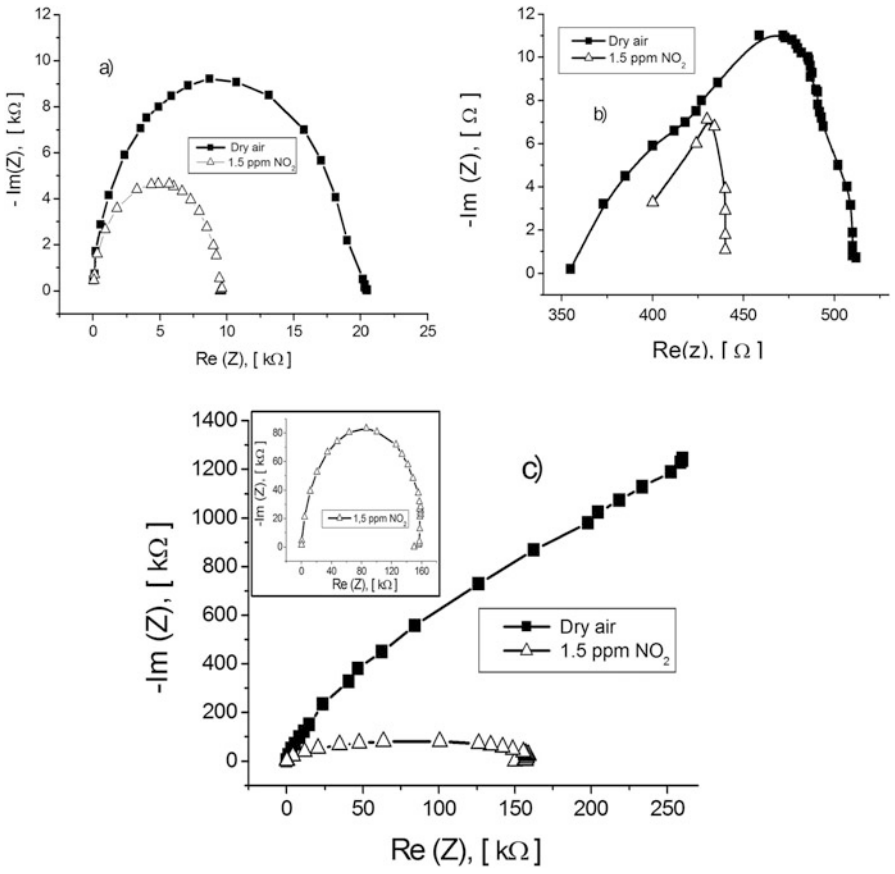

Fig. 31.7 Nyquist diagrams of (**a**) Te, (**b**) the quaternary $As_2Te_{130}Ge_8S_3$ and (**c**) $As_2Te_{13}Ge_8S_3$ films in both dry air and a mixture with NO_2, at room temperature (22 °C). The picture inserted in (**c**) shows separately the diagram obtained under the application of NO_2 only

all elements of the equivalent circuit. The values of the characteristic frequency, the impedance and the time constant τ_m of the films at this frequency for a concentration of NO_2 of 1,5 ppm, at room temperature are summarized in Table 31.1.

From this table it is seen that if the environment is changed from dry air to this mixture the resistance R_m is strongly influenced while the capacitance C_m does not vary essentially.

The complex impedance diagram of devices based on the highly resistive $As_2Te_{13}Ge_8S_3$ film (Fig. 31.7c) show in the presence of NO_2 vapor the typical semicircular arcs. The resistance R_ω and capacity C_ω of the film at characteristic frequency, i.e. R_m and C_m as well as the film impedance in this environment, calculated from Eqs. (31.5) and (31.6), are listed in Table 31.1. It can be seen that under application of 1,5 ppm NO_2, the impedance and electrical resistance of the $As_2Te_{13}Ge_8S_3$ film are about 20 times higher than the respective values of pure tellurium films, but the capacity is twice smaller.

The change of frequency dependent impedance of the chalcogenides in question upon exposure to a low concentration of NO_2, make their abilities to be used in sensor development evident. In a first approximation, the data given in Table 31.1 allow assessing the effect of nitrogen dioxide on the device impedance and its sensitivity. However, this assessing is valid only at the characteristic frequency, which in turn becomes essentially influenced by gas adsorption. More complete information concerning the gas sensing properties of the films can be obtained by investigating their full impedance spectra, both in dry air and its mixture with a target gas. Furthermore, using relation (31.1) the spectra of gas sensitivity can be evvaluated, and the frequency, at which the maximum sensitivity occurs, can be determined. Figure 31.8 shows the frequency dependent sensitivity of the films in question towards NO_2, at room temperature.

It is observed that the frequency most strongly influences the gas sensitivity of the Te and $As_2Te_{13}Ge_8S_3$ films, while that of $As_2Te_{130}Ge_8S_3$ remains nearly

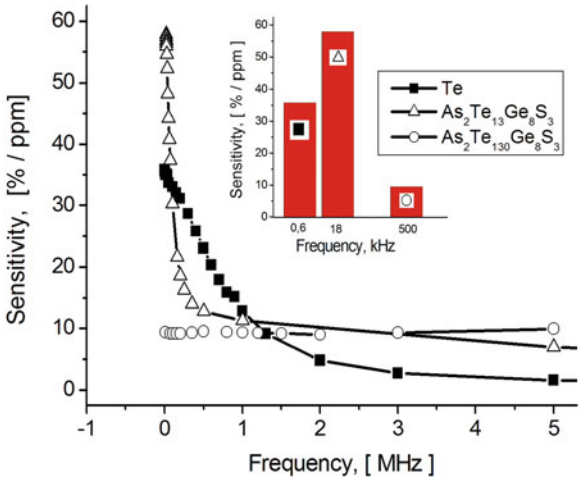

Fig. 31.8 Sensitivity spectra of chalcogenide $As_2S_3Ge_8$-Te thin films to 1,5 ppm NO_2 in dry air at room temperature. The inset show a comparison of the maximum sensitivities at the respective frequencies for the materials in question

independent of the applied frequency. The essential difference in the velocity of the decrease of the sensitivity for $As_2Te_{13}Ge_8S_3$ and pure tellurium film is also noticeable. The sensitivity of the $As_2Te_{13}Ge_8S_3$ film decreases sharply with increasing frequency but tends to saturate already at approximately 500 kHz. On contrary, the sensitivity of Te film diminishes quite slowly and tends to saturation only at approximately 3 MHz. The inset in Fig. 31.8 reports for each composition the maximal value of the sensitivity, while the abscissa indicates the frequency at which this maximum sensitivity occurs.

31.4.3 Cross Sensitivity to Other Gases

Thus, the chalcogenide films in question show remarkable sensing properties to NO_2 and are suitable for the development of sensors operating at room temperature. In this context the interfering effect of the other accompanying gases in the environment becomes important, as well as the cross sensitivity to water vapor.

Figure 31.9 reports the complex impedance spectra of the tellurium film upon exposure to different test gases: NO_2, H_2, and H_2S. It is seen that addition of these gases to dry air does not change the general shape of the curve, i.e. they influences all elements of the equivalent circuit.

From these diagrams both the characteristic frequency and the impedance of the film at this frequency have been determined. The values (Table 31.2) shows that the addition of NO_2 to dry air leads to a decrease of the impedance, while the addition of H_2 or H_2S results in its increase.

In this context it becomes interesting to analyze the frequency dependences of the sensitivity to different target gases through the impedance change. Figure 31.10 shows the sensitivity spectra of pure tellurium films toward nitrogen dioxide, hydrogen sulfide and molecular hydrogen at room temperature. Although the

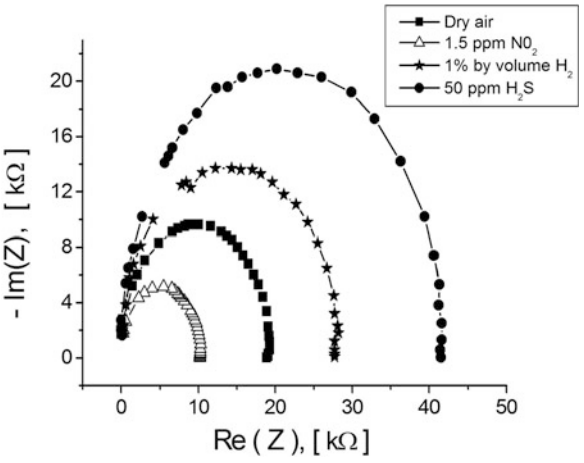

Fig. 31.9 Nyquist diagrams of the tellurium thin film in different environmental conditions at room temperature

Table 31.2 Impedance of tellurium based films at characteristic frequency in different environments

Environment	f_m [kHz]]	Z [kΩ]
Dry air	900	13,3
1,5 ppm NO_2	1500	7,5
H_2 1% by volume	600	19,8
50 ppm H_2S	400	29

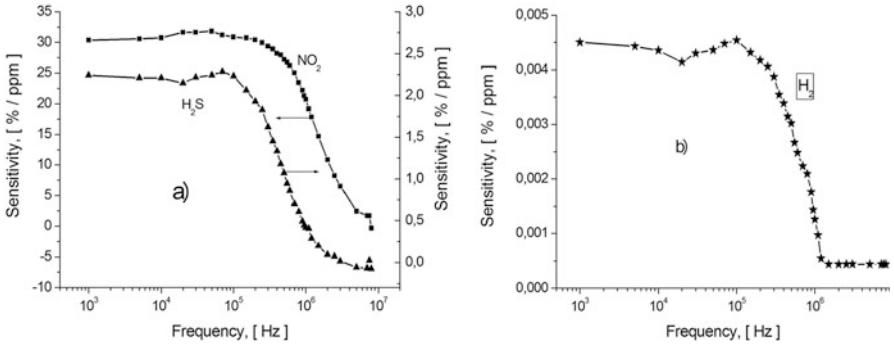

Fig. 31.10 Sensitivity of tellurium thin films toward different gases vs. frequency

sensitivity towards these gases differs very much, there is always a frequency dependent edge of sensitivity, which also depends of the nature of the adsorbed species.

At this edge, the sensitivity increases with decreasing frequency, reaching saturation at low frequencies (dependent of gas species). A comparison of the saturation sensitivity towards the gases in question shows that the sensitivity to NO_2 is more than ten times higher than that towards H_2S and by four orders of magnitude higher than that towards molecular hydrogen.

The interfering effect of humidity on NO_2 detection has been investigated using the quaternary $As_2Te_{13}Ge_8S_3$ based films. Figure 31.11 shows the influence of humidity on the impedance spectra of the $As_2Te_{13}Ge_8S_3$ film during NO_2 detection at 22 °C. It can be observed that at room temperature, the interfering effect of water molecules is not so essential. The frequency dependent effect of water vapor consists in increasing the impedance by (30–200 kΩ) at 58% RH. This impedance increase diminishes the sensor sensitivity to NO_2 by approximately 15%/ppm, independent of the applied frequency.

31.5 Discussion

The chalcogenide materials considered in this work belong to the disordered so-called lone-pair semiconductors. The states of lone-pair (unshared) p – electrons of the chalcogen atoms in these materials form a band which overlaps with the

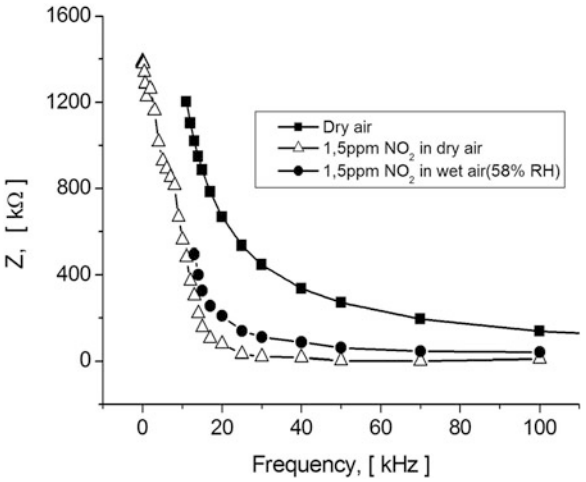

Fig. 31.11 Effect of humidity on the impedance spectra of a $As_2Te_{13}Ge_8S_3$ film during detection of nitrogen dioxide at room temperature

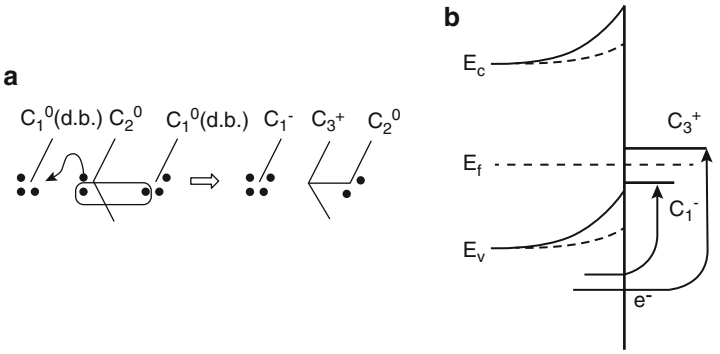

Fig. 31.12 (**a**) Model of the dangling bond lone-pair electrons interactions and (**b**) the band-bending at the surface

valence band, forming its upper part. The interaction between lone-pair electrons of chalcogen atoms as well as their interaction with "dangling" bonds create the specific charge defects C_3^+ and C_1^- (Fig. 31.12a) which operate as localized states in the forbidden gap, pinning the Fermi level close to the valence band, i.e. determining the p-type conductivity [13]. The interaction of lone-pair electrons with "dangling" bonds will be maximal at the film surface, as at the surface the maximum concentration of dangling bonds occurs. This interaction means capturing of electrons from the valence band, which results in the formation of a hole enriched (accumulation) region adjacent to the surface, so that the bands bend up as shown in Fig. 31.12b. In this context, the surface phenomena caused by gas adsorption can be considered as an external control of the band-bending at the surface, owing to a variation of the hole density in the accumulation region in the presence of gaseous media.

For instance, the sensing properties of the materials in question toward nitrogen dioxide originate from the odd electrons (single unpaired electrons) of the NO_2 molecules [14]. Being adsorbed on the surface of the chalcogenide semiconductor, the NO_2 molecule acts as a dangling bond, that can accept a lone-pair electron to form an electron pair, that is chemisorption occurs. Capture of a lone-pair electron means the transition of an electron from the upper part of the valence band to a NO_2 acceptor level, accompanied by releasing an additional hole. Thus, the adsorption of nitrogen dioxide leads to an increase of the concentration of majority carriers adjacent to the surface layer, which results in both further bands – bending and increasing the electrical conductivity of the film. The high sensitivity, as well as the large frequency range of response to NO_2 support this mechanism of "strong" chemisorption, owing to interaction between the odd electrons of the NO_2 molecules and lone-pair electrons of chalcogen atoms of the films.

Elemental hydrogen occurs only as biatomic gas molecules at normal conditions. These molecules do not comprise unpaired (dangling) electrons, i.e. a strong chemisorption of hydrogen on the surface or within the chalcogenide film cannot be expected. Perhaps, the very low sensitivity (Fig. 31.10b) to H_2 is due to the reducing effect of oxygen already absorbed on the surface of the film from the carrier (dry air) gas. In our previous paper [15] it was shown that the "weak" chemisorption of symmetric O_2 molecules from the carrier gas is accompanied by localization of lone-pair electrons near the surface, which leads to a decrease the film resistance. Besides, the high concentration of oxygen in carrier gas promotes the formation of a catalytic gate [16], which can be removed by other gases. Thus, assuming that the molecular hydrogen removes already adsorbed oxygen, the decrease of the surface conductivity of the film can be expected.

Hydrogen sulfide leads to an increase of the impedance of the film (Fig. 31.9). The sensitivity of the tellurium films to H_2S is by three orders of magnitude higher than that to H_2 but remains almost ten times smaller than the sensitivity to NO_2 (Fig. 31.10). Besides, the edge of sensitivity to H_2S is shifted to 1 MHz, being the same as that of the sensitivity to hydrogen. These peculiarities indicate that interaction of H_2S with chalcogenide films can be attributed neither to "strong" chemisorption of H_2S molecules nor to a reduction of existing "weak" chemisorbed oxygen from the carrier gas. Taking into consideration that the electron configurations of water and hydrogen sulfide molecules are similar, the interaction of chalcogenude films with H_2S is likely to take place similar to the mechanism proposed in [17] the interaction of water vapor with these films. This mechanism assumes orientational polarization of polar gas molecules physically adsorbed on the film surface, followed by the formation of weak bonds of electrostatic origin, which can localize the free holes at the surface and therefore diminishes the electrical conductivity.

Another factor that can affect the gas sensing is structural and compositional disorder. Disorder creates a random potential, which results in the formation of both tails of extended bands and a finite value of localized states close to the Fermi level $N(E_f)$ [18] This means that the a.c. conductivity can be realized by three mechanisms:

band-to-band conduction with an activation energy E_g (forbidden gap of the considered material), hopping between localized states in the extended band tails or tunneling (variable range hopping) between localized states situated close to the Fermi level. The contribution of each mechanism depends on material composition, frequency range and temperature regime. As all experiments were performed at room temperature, only the effect of frequency on impedance can somewhat elucidate the predominant mechanism of current flow. The negligible variation of impedance with frequency increase in $As_2Te_{130}Ge_8S_3$ (Fig. 31.6) indicates that conductivity via extended states, i.e. band-to-band mechanism is the main effect. On the other hand, the strong decrease of the impedance in the pure Te and $As_2Te_{13}Ge_8S_3$ films with frequency increase shows that the hopping mechanism of conductivity through localized states is dominant. In order to distinguish between hopping via localized states of the extended bands tails and variable range hopping over localized states near Fermi level, an additional investigation of the effect of temperature on the a.c. conductivity is required, which constitutes a subject of a future study.

As far as the effect of the material composition is concerned, we assume that the basic interaction mechanism discussed early for pure Te layers [19] also occurs in the Te based alloys studied in this work, but addition of As, S and Ge atoms can result in structural/phase transformations, the appearance of new mechanisms of current flow and obviously, in a modification of the gas sensing peculiarities. Indeed, as shown by the X ray diffraction measurements, addition of only 5.6 at% Ge, 2.1 at % S and 1.4 at% As (alloy $As_2Te_{130}Ge_8S_3$) diminishes the fraction of crystalline tellurium, but leads to a dramatic decrease of the impedance by two orders of magnitude, followed by a fourfold decrease of the gas sensitivity. In contrast, addition of higher concentrations of these elements (30.8 at% Ge, 11.6 at% S and 7.6 at% As, alloy $As_2Te_{13}Ge_8S_3$) transforms the film into an amorphous state with a dramatic increase of the impedance by at least two orders of magnitude, followed by an more than twofold increase of gas sensitivity. As has been mentioned above, these results shows how the composition and phase/structural state of the film control not only the mechanism of current flow but also their gas sensing properties and finally, their abilities to be used in the development of gas sensing devices operating at room temperature.

31.6 Conclusions

Glassy chalcogenides can be used for the development of effective impedance operating gas sensitive devices. The sensors can operate at room temperature with a good sensitivity in the ppm and sub-ppm concentration range.

The phase/structural state of the $As_2Ge_8S_3$-Te, film grown onto both glassy and sintered alumina substrates via high speed thermal deposition in vacuum, is predominantly amorphous. Material composition and the phase/structural state of the chalcogenide films, as well as the gaseous environment strongly influence the

impedance spectra of the films and their sensitivity to target toxic or pollutant gases. Addition of NO_2 decreases the impedance, whereas addition of H_2 or H_2S increases it in a large range of frequencies due to the different mechanisms of interaction between these gases with the films in question. The NO_2 sensing mechanism involves "strong" chemisorption, which results in an increase of band bending and surface electrical conductivity. The impedance sensitivity, being maximal for amorphous $As_2Te_{13}Ge_8S_3$ is assumed to be controlled also by the competition of several transport mechanisms.

Acknowledgements This work was financially supported by the Technical University of Moldova through the Institutional Grant 15.817.02.29A. The authors express gratitude to Dr. M. Enache from NCMST of TUM for SEM analysis and Dr. G. F. Volodina from IAP ASM for XRD analysis.

References

1. Marian S, Tsiulyanu D, Liess H-D (2001) High sensitive tellurium based NO_2 gas sensor. Sens Actuators B Chem 78:191
2. Marian SI, Tsiulyanu DI, Marian TI, Liess H-D (2001) Chalcogenide – based chemical sensors for atmospheric pollution control. J Pure Appl Chem 73:2001
3. Koleva K, Popov C, Petkova T, Petkov P, Mihailescu IN, Reithmaier J-P (2009) Complex $(As_2S_3)_{(100-x)}(AgI)_x$ chalcogenide glasses for gas sensors. Sens Actuators B Chem 143:395
4. Popescu M, Velea A, Sava F, Lorinczi A, Tomescu A, Simion C, Matei E, Soco G, Mihailescu IN, Andonie A, Stamatin I (2010) Structure and properties of silver doped $SnSe_2$ and $Ge_2Sb_2Te_5$ thin films prepared by pulsed laser deposition. Phys Status Solidi A 207:516
5. Wüsten J, Potje-Kamloth K (2010) Chalcogenides for thin film NO sensors. Sens Actuators B Chem 145:216
6. Tsiulyanu D, Mocreac O (2013) Concentration induced damping of gas sensitivity in ultrathin tellurium films. Sens Actuators B Chem 177:1128
7. Tsiulyanu D, Mocreac O, Ciobanu M, Enachi M, Volodina G (2014) Peculiarities of ultrathin amorphous and nanostructured Te thin films by gas sensing. J Nanoelectron Optoelectron 9:282
8. Petkov P, Tsiulyanu D, Kulisch W, Popov C (2015) Nanoscience advances in CBRN agents detection, information and energy security. Springer, Dordrecht, p 535
9. Sberveglieri G (1995) Recent developments in semiconducting thin films gas sensors. Sens Actuators B Chem 23:103
10. Weimer U, Gopel W (1995) AC measurements of thin oxide sensors to improve selectivities and sensitivities. Sens Actuators B Chem 26–27:13
11. Macdonald JR (1987) Impedance spectroscopy. Wiley, New York, p 341
12. Tsiulyanu D, Ciobanu M (2016) Room temperature a.c. operating gas sensors based on quaternary chalcogenides. Sens Actuators B Chem 223:95
13. Kastner M, Fritzsche H (1978) Defect chemistry of lone – pair semiconductors. Philos Mag B 37:199
14. Greyson J (1990) Carbon, nitrogen and sulfur pollutants and their determination in air and water. Marcel Dekker Inc, New York
15. Tsiulyanu D, Stratan I, Tsiulyanu A, Liess HD, Eisele I (2007) Investigation of the oxygen, nitrogen and water vapour cross – sensitivity to NO_2 of tellurium based thin films. Sens Actuators B Chem 121:406
16. Lundstrom I (1996) Approaches and mechanisms to solid state based sensing. Sens Actuators B Chem 35–36:11

17. Tsiulyanu D, Ciobanu M, Liess H-D (2016) Work function and a.c. operating gas sensors based on quaternary chalcogenides. Phys Status Solidi B 253:1046
18. Mott NF, Davis EA (1979) Electron processes in non –crystalline materials. Clarendon Press, Oxford
19. Tsiulyanu D, Moraru A (2015) Nanocrystalline tellurium films: fabrication and gas sensing properties. In: Petkov P et al (eds) Nanoscience advances in CBRN agents detection, information and energy security. Springer, pp 389–408

Chapter 32
Swelling Behavior of Organic-Inorganic Ureasil-Based Polymers

T. S. Kavetskyy, H. Švajdlenková, Y. Kukhazh, O. Šauša, K. Čechová, I. Mat'ko, N. Hoivanovych, O. Dytso, T. Petkova, V. Boev, and V. Ilcheva

Abstract The swelling behavior of pure ureasil and ureasil-chalcogenide glass composites of different history (fresh, aged and thermally heated) was examined using ethyl alcohol. Swelling experiments showed the structure of the network of samples aged for 1 year after preparation has a lower swelling ability compared with pure ureasil as well with the composite, but the effect is more expressed for the pure polymer. In the cases of a thermally heated pure ureasil sample and a more than 5 years after preparation aged sample of the composite, the structure network has practically the same swelling ability as the fresh pure ureasil and the composite samples. It is suggested that one of the factors influencing the swelling is the change of the basic ureasil network due to aging and/or thermal heating.

Keywords Swelling · Organic-inorganic hybrid · Polymer · Composite · Ureasil

T. S. Kavetskyy (✉)
Drohobych Ivan Franko State Pedagogical University, Drohobych, Ukraine

The John Paul II Catholic University of Lublin, Lublin, Poland

H. Švajdlenková
Polymer Institute, Slovak Academy of Sciences, Bratislava, Slovak Republic

Y. Kukhazh · N. Hoivanovych · O. Dytso
Drohobych Ivan Franko State Pedagogical University, Drohobych, Ukraine

O. Šauša · K. Čechová · I. Mat'ko
Institute of Physics, Slovak Academy of Sciences, Bratislava, Slovak Republic

T. Petkova · V. Boev · V. Ilcheva
Institute of Electrochemistry and Energy Systems, Bulgarian Academy of Sciences, Sofia, Bulgaria

P. Petkov et al. (eds.), *Advanced Nanotechnologies for Detection and Defence against CBRN Agents*, NATO Science for Peace and Security Series B: Physics and Biophysics, https://doi.org/10.1007/978-94-024-1298-7_32

32.1 Introduction

Nanocomposite materials containing glass [1], glass-ceramics [2], metal alloys [3] and polymers [4] are of increasing interest due to a variety practical application. Urea-silicates or ureasils are well-known representatives of organic-inorganic hybrid polymer nanocomposite materials successfully examined as dispersion media for luminescent Eu^{3+} salts, ion conducting Li^{+} salts, organic dyes, semiconductors and metal nanoparticles [5, 6]). For the first time, ureasil-based composites were also tested for the immobilization of commercial laccase from *Trametes versicolor* (a common polypore mushroom) and the construction of amperometric biosensors [7]. It has been found that the biosensor based on the ureasil-chalcogenide glass composite was characterized by very high sensitivity, 38.3 times higher in compare with pure ureasil. On the other hand, application of the ureasil-chalcogenide glass composite with incorporated silver nanoparticles synthesized by high-dose 30 keV Ag^{+} ion implantation results in decreasing the biosensor sensitivity up to 2390 times. In the present work, the swelling behavior of pure ureasil and ureasil-chalcogenide glass composites of different history (fresh, aged and thermally treated) was examined using ethyl alcohol (EtOH). Numerical parameters such as the bulk density of the polymeric sample ρ_p and the molecular weight between two crosslink points M_c are considered.

32.2 Experimental

The pure ureasil matrix was synthesized as follows [8–10]: O,O′-bis (2-aminopropyl)-polypropylene glycol-block-polyethylene glycol-block-polypropylene glycol-500 (Jeffamine ED-600) was dried under vacuum for 30 min; 3-isocyanatepropyltriethoxysilane (ICPTES), tetraethoxysilane (TEOS, 98%) and n-butyl amine were used as received; Jeffamine and ICPTES were mixed in a stoichiometric ratio of 1:2 in order to obtain a liquid ureasilicate monomer; thereafter, TEOS (1.12 mmol) and n-butylamine were added to the mixture, which was kept under stirring for more than 20 min. The mixture was then transferred into a plastic Petri dish and jellified under appropriate conditions; the obtained gels were heated in a vacuum furnace at 333 K at ambient conditions; and a non-rigid, homogeneous and highly transparent xerogel in form of a disk with a diameter of 40 mm and a thickness of 0.25 mm was obtained within 1 day. At the same time, the ureasil-chalcogenide As_2S_3 glass composite matrix was synthesized as follows [8–10]: the As_2S_3 ingots were synthesized by melt quenching method from As (5 N) and S (5 N) in sealed quartz ampoules at 923 K; the melt was quenched to room temperature, and the obtained glassy samples were finely grounded in powder form and dissolved in an organic solvent (3 ml n-butylamine) to the 0.4 M concentration; and the As_2S_3/ureasil composite was obtained by mixing the ureasilicate monomer with the solution of chalcogenide clusters. The stiff gel was obtained as described above.

The investigated samples were swollen in anhydrous ethyl alcohol (EtOH) during 8 days at room temperature (301 K). At first, the initial weight of the samples (m_0) was determined, then that of the samples after 24 h for 8 days; the maximum weight observed is called m_{swollen}. An equilibrium was achieved after 6–7 days. On the 8th day the weight did not change, i.e. the maximum saturated weight (m_{swollen}) was achieved. After that the room temperature samples were dried at 333 K in argon atmosphere by using the thermo gravimetric analysis (TGA) method where the weight of dry sample (m_{dry}) was obtained as the minimum saturated mass. The percent equilibrium mass swelling (S) was determined as:

$$S = \left[\left(m_{\text{swollen}} - m_{\text{dry}}\right)/m_{\text{dry}}\right] \times 100 \tag{32.1}$$

The molecular weight between two crosslink points M_c was calculated based on the Flory-Rehner equation [11, 12] as

$$\nu = 1/M_c = -\left[\left(V_r + \chi V_r^{\,2} + \ln\left(1 - V_r\right)\right)/\left(\rho_p V_0\left(V_r^{\,1/3} - V_r/2\right)\right)\right] \tag{32.2}$$

where ν is the crosslinking density, ρ_p is the bulk density of the polymeric sample, and V_r is the volume fraction of the polymer in the swollen state given by

$$V_r = 1/(1+Q) \tag{32.3}$$

$$Q = \left[\left(m_{\text{swollen}} - m_0\right)\rho_p\right]/\left(m_0\rho_{\text{liquid}}\right) \tag{32.4}$$

where ρ_{liquid} is the density of the liquid and V_0 is the molar volume of the liquid (for EtOH, V_0 is 57.62 cm^3/mol); the parameter χ is the Flory-Huggins interaction parameter between the polymer and the liquid (the values of χ for polymer-solvent interactions were calculated via the cohesive energy of the atomic groups). The density of the investigated polymeric samples was determined using the gravimetric method (Archimedean principle). The samples were immersed into EtOH at room temperature. The bulk density of individual samples was calculated by

$$\rho = \rho_{\text{EtOH}}\left[m_0/\left(m_0 - m_1 + m_{\text{wire}}\right)\right] \tag{32.5}$$

where ρ_{EtOH} is the density of EtOH at 301 K, m_{wire} is the weight of the wire on which the sample is hanged in EtOH, and the values of m_0 and m_1 are the sample weights in air and after immersion into EtOH.

32.3 Results and Discussion

Figure 32.1 shows the images of investigated samples used for this research. It can clearly be seen that the physical aging of sample leads to decreasing of its optical transparency, while heating of the sample up to 420 K does not change visibly its optical properties.

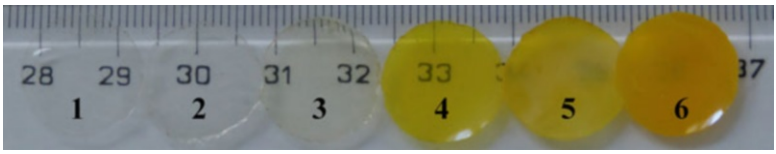

Fig. 32.1 Photos of the investigated polymer samples used for the research: *1* K0-fresh: pure ureasil polymer, fresh (2 months after preparation); *2* K0-heated: pure ureasil polymer, fresh and thermally heated up to 420 K; *3* K0-aged: pure ureasil polymer, aged during 1 year after preparation; *4* K4-fresh: ureasil-glass composite, fresh (2 months after preparation); *5* K4-aged: ureasil-glass composite, aged during 1 year after preparation; *6* K4-very aged: ureasil-glass composite, aged more than 5 years after preparation

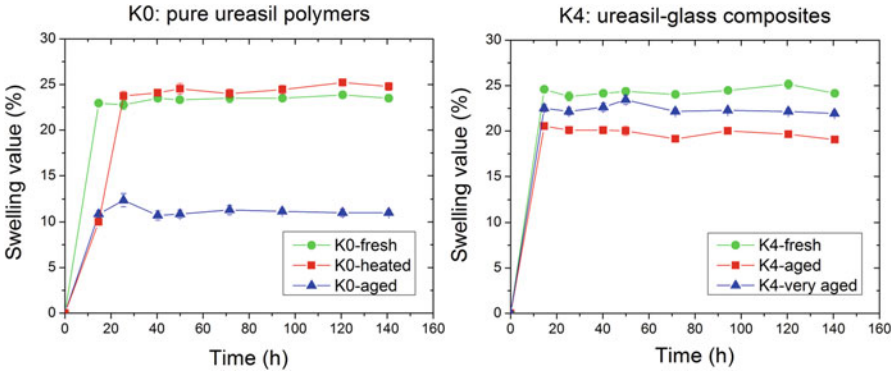

Fig. 32.2 The swelling values as a function of time for the pure ureasil polymers (K0: fresh, heated, and aged) and the ureasil-glass composites (K4: fresh, aged, and very aged) in EtOH at room temperature. The samples are labeled as shown in Fig. 32.1

Figure 32.2 shows the results of the swelling experiments for the investigated samples in EtOH. The numerical parameters such as the bulk density of the polymeric sample ρ_p and the molecular weight between two crosslink points M_c are presented in Table 32.1.

Higher M_c values mean a lower crosslinking density and higher swellability. Thus, swelling experiments using EtOH showed that the structure of the network of samples aged for 1 year after preparation (K0-aged) has a lower swelling ability compared with pure ureasil (K0-fresh) as well with the composite (K4-fresh), but the effect is more expressed for the pure polymer. In the cases of a thermally heated pure ureasil sample (K0-heated) and a more than 5 years after preparation aged sample of the composite (K4-very aged), the structure network has practically the same swelling ability as the fresh pure ureasil and the composite samples (K0-fresh and K4-fresh, respectively). It is suggested that one of the factors influencing the swelling is the change of the basic ureasil network due to aging and/or thermal heating. Further experiments with the construction of biosensors based on ureasil polymer matrixes [7] using the investigated polymers would be useful to examine

Table 32.1 Density of the polymeric sample ρ_p, molecular weight between two crosslink points M_c and comparative analysis of crosslinking density or swellability for the investigated polymers in the group of K0 and K4

Sample	ρ_p (g/cm^3)	M_c	Comparative analysis in the group
K0: pure ureasil polymers			
K0-fresh	1.1778 ± 0.0021	92.47	Lower swellability
K0-heated	1.2080 ± 0.0163	106.37	The highest swellability
K0-aged	1.1814 ± 0.0012	44.0	The lowest swellability
K4: ureasil-glass composites			
K4-fresh	1.2015 ± 0.007	99.22	The highest swellability
K4-aged	1.2170 ± 0.003	76.52	The lowest swellability
K4-very aged	1.1986 ± 0.010	89.50	Lower swellability

The samples are labeled as shown in Fig. 32.1

the relationship between the network properties and the bio-functionality of amperometric biosensors.

32.4 Conclusion

Swelling behavior of the pure ureasil and ureasil-chalcogenide glass composite samples of different history has been examined using EtOH. It is suggested that one of the factors influencing swelling is the change of the basic ureasil network due to aging and/or thermal heating.

Acknowledgments This work was financially supported by the Ministry of Education and Science of Ukraine (projects Nos. 0116U004737, 0117U007142 (for Young Scientists) and 0117U007143; to TK and YK), by the Slovak Grant Agency VEGA (project No. 2/0157/17; to OS and project No. 2/0127/17; to IM), by the Slovak Research and Development Agency (project No. APVV-16-0369; to HS, OS, KC and IM) and by the National Science Fund of the Bulgarian Ministry of Education (project No. FNI-DN09/12-2016; to TK, TP, VB and VI).

References

1. Stronski A et al (2016) Holographic and e-beam image recording in $Ge_5As_{37}S_{58}$-Se nanomultilayer structures. Nanoscale Res Lett 11:39
2. Duriagina Z et al (2017) Comparative estimation of the structure and electrical properties of functional layers based on PbO-ZnO-B_2O_3 glass-ceramic sealant. Powder Metall Met Ceram 55:580
3. Cherepova TS, Dmytrieva HP, Dukhota OI, Kindrachuk MV (2016) Properties of nickel powder alloys hardened with titanium carbide. Mater Sci 52:173
4. Rajesh AT, Kumar D (2009) Recent progress in the development of nano-structured conducting polymers/nanocomposites for sensor applications. Sensors Actuators B 136:275

5. Boev VI et al (2004) Flexible ureasil hybrids with tailored optical properties through doping with metal nanoparticles. Langmuir 20:10268
6. Sa Ferreira RA et al (2001) Energy-transfer mechanisms and emission quantum yields in Eu^{3+}-based siloxane-poly(oxyethylene) nanohybrids. Chem Mater 13:2991
7. Kavetskyy T et al (2017) Laccase-containing ureasil-polymer composite as the sensing layer of an amperometric biosensor. J Appl Polym Sci 134:45278
8. Kavetskyy T et al (2011) In: Riethmaier JP, Paunovic P, Kulisch W, Popov C, Petkov P (eds) Nanotechnological basis for advanced sensors. Springer, Berlin, p 103
9. Kavetskyy T et al (2012) New organic-inorganic hybrid ureasil-based polymer and glass-polymer composites with ion-implanted silver nanoparticles. Phys Status Solidi C 9:2444
10. Kavetskyy T et al (2013) New organic-inorganic hybrid ureasil-based polymer materials studied by PALS and SEM techniques. Mater Sci Forum 733:171
11. Flory PJ, Jr RJ (1944) Effect of deformation on the swelling capacity of rubber. J Chem Phys 12:412
12. Flory PJ (1950) Statistical mechanics of swelling of network structures. J Chem Phys 18:108

Chapter 33
Synthesis and Characterization of Organically Modified Silicates Obtained by Co-condensation of Two Organic – Inorganic Ureasilicate Monomers

V. Ilcheva, V. Boev, D. Tatchev, G. Avdeev, G. Zamfirova, V. Gaydarov, V. Lilova, and T. Petkova

Abstract Transparent organic-inorganic ureasilicate materials (ureasils) were synthesized by hydrolysis and co-condensation of two organic – inorganic precursors, obtained by reactions between 3-isocyanatepropyltriethoxysilane (ICPTES) and double terminated polyetheramine (Jeffamine), and between ICPTES and 3-aminopropyl triethoxysilane (APTES), respectively. The prepared samples were characterized by optical UV – VIS spectroscopy, small-angle X-ray scattering (SAXS), FTIR spectroscopy and the depth sensing indentation method (DSI). It is shown that the molar ratio between the initial components influences on the mechanical and optical properties of the materials in the investigated range.

Keywords Ureasilicate materials · Sol-gel · Organic-inorganic hybrids · Microhardness

V. Ilcheva (✉) · V. Boev · T. Petkova
Institute of Electrochemistry and Energy Systems "Academician Evgeni Budevski", Bulgarian Academy of Sciences, Acad. G. Bonchev str., bl. 10, 1113 Sofia, Bulgaria
e-mail: vania.ilcheva@iees.bas.bg

D. Tatchev · G. Avdeev
Institute of Physical Chemistry, Bulgarian Academy of Sciences, Acad. G. Bonchev str., bl.11, 1113 Sofia, Bulgaria

G. Zamfirova · V. Gaydarov
Transport University "T. Kableshkov", Geo Milev str., 158, 1574 Sofia, Bulgaria

V. Lilova
University of Chemical Technology and Metallurgy, 8 Kliment Ohridski Blvd., 1756 Sofia, Bulgaria

P. Petkov et al. (eds.), *Advanced Nanotechnologies for Detection and Defence against CBRN Agents*, NATO Science for Peace and Security Series B: Physics and Biophysics, https://doi.org/10.1007/978-94-024-1298-7_33

33.1 Introduction

Research in sol-gel derived organic/silica hybrids and investigation of the structure-property-performance relations is a rapidly growing area. The most attractive feature of organic-inorganic hybrids is the possibility to combine the initial components in a way, which can provide fine tuning of the properties of the final material (mechanical, optical, etc.) as well as unique design opportunities [1–7]. Subject of intense study are the so-called ureasilicates, characterized by high optical transparency in the visible region, a good flexibility and a long term stability of the optical and mechanical properties.

Basically, the synthesis of a organic-inorganic ureasilicate matrix consists of the reaction between double functionalized polyetheramines (Jeffamines) with 3-(isocyanatepropyl) triethoxysilane acting as a crosslinker agent [8, 9]. The structure of these materials can be represented as reticulated siliceous backbone covalently bonded to polyether-based segments by urea (-NHCONH-) linkages. The hybrid structure consists of hard siliceous nanodomains connected with soft polyoxy (ethylene)/polyoxy (propylene) (POE/POP) chains. The hard, rigid segments segregate into a glassy domain, and the polyoxyalkylene soft segments form an amorphous or rubbery matrix in which the hard segments are dispersed [10]. Addition of different fillers derived from an in situ hydrolysis and condensation reaction of different silica alkoxides (TEOS, TMOS, APTES, MTEOS) can reinforce the relative weakness and influence the surface properties of the materials. It was proven that organic-inorganic sol-gel derived hybrids can be used as an interface material, which improves the contact between human skin and electrodes and makes them less prone to fluctuations due to skin to electrode interfacial impedance [11]. Also, in our previous work, the possibility for using ureasil-chalcogenide glass composites as a support for the immpobilization of laccase on the transducer surface of a biosensor was reported [12]. It was found that the biosensor demonstrates a high sensitivity for monitoring the level of pollution of xenoestrogen containing wastewater. The sensitivity of the sensor could also depend on the composition of the ureasilicate matrix used as host medium for embedding different types of guest materials.

The present work is focused on the preparation of ureasilicate materials with addition of the silica alkoxide APTES. The influence of the molar ratio between the components on the optical and mechanical properties is studied. By variation of the composition we expect to acquire new scientific facts about the correlation between composition, structure and properties in order to obtain modified materials with desired parameters for biosensors or optical application.

33.2 Experimental Details

O,O′-bis(2-aminopropyl)-polypropylene glycol-block-polyethylene glycol-block-polypropylene glycol-500 (Jeffamine ED-600, Sigma – Aldrich), 3-(isocyanate propyl)triethoxysilane (ICPTES, Sigma – Aldrich), 3-(aminopropyl)triethoxysilane

Table 33.1 Molar ratios between the reagents used for the preparation of ureasilicate samples

Sample	Molar ratio ICPTES/Jeffamine	Molar ratio APTES/Jeffamine
A1t	2	1
A2t	2.5	1
A3t	3	1
A4t	3.5	1
A5t	4	1

(APTES, Sigma – Aldrich), ethanol (96%, Alfa Aesar), and ammonia solution (25%, Alfa Aesar) were used as received. Distilled water was used for the preparation of diluted aqueous ammonia solutions.

Sol – gel derived ureasilictate monoliths were obtained as follows: ICPTES and APTES were mixed in an appropriate molar ratio under stirring at 200 rpm for 10 min, so that rapid formation of the first ureasilicate precursor took place (the molar ratios are summarized in Table 33.1). Thereafter, Jeffamine was added to the reaction mixture, and stirring was continued for another 20 min. During this period of time, the reaction between an excess supply of ICPTES and Jeffamine occurred, resulting in formation of the second precursor. Ethanol (EtOH) was used as a homogenizing agent and added after that. Subsequent addition of 4.1 M aqueous ammonia solution led to a catalyzed hydrolysis/condensation reaction under basic conditions, resulting in the formation of siloxane groups. After 10 min of stirring, the final mixture was poured into polystyrene cells sealed with Parafilm, which was pin-holed after gelling. The gelling time varied from 24 to 48 h depending of composition. Drying of the sample was carried out at room temperature within 2 weeks. It led to a sample shrinkage of about 30%. During the final step the cell with the obtained gel was kept in an oven for 24 h at 40 °C. As a result, monoliths with polygonal shape with a base of 7×7 mm^2 were obtained. Also samples with the same composition were prepared with a round shape with a diameter ca. 30 mm and a thickness about 0.5 mm for SAXS measurements.

UV-visible transmission spectra of the samples were measured in the wavelength range from 350 to 500 nm at room temperature using a double-beam computer-controlled JASCO spectrophotometer with an accuracy of ± 0.5 nm. Small-angle X-ray scattering (SAXS) studies were performed with a Panalytical Empyran XRD device equipped with SAXS accessory with a slit collimation system. Infrared (IR) spectra were recorded on a Bruker Tensor 27 FT spectrometer by accumulating 64 scans with 2 cm^{-1} resolution. The spectra were measured in the solid state by directly applying the sample on a diamond ATR crystal and referencing to an air background. Depth-sensing indentation method (DSI) was applied for the measurements of the mechanical characteristics of the samples. The measurements were performed on a Dynamic Ultra Micro Hardness Tester DUH-211S from Shimadzu (Japan) according to ISO 14577-1. The Martens hardness (HMV) was determined after reaching the specified maximum test force F_{max}, by dividing by the surface area A_s of the indenter penetrating beyond the zero-point of the contact. The tests were made in the "load – hold – unload" mode with a holding time at load of 30 s, a

loading speed of 0.2439 mN/s and a preset controlled indentation depth of 10 μm. All measurements were performed at room temperature using a Vickers pyramidal intender. Average microhardness values based on at least ten indentations on every sample were determined. The calculated percent error is in the frame of 3%, which indicates relatively good sample homogeneity.

33.3 Results and Discussion

The visual aspect of the round sample is shown in Fig. 33.1. It demonstrates a high transparency in the visible range and high flexibility of the prepared material.

Sample A1t (ICPTES/Jeffamine = 1/2, APTES/Jeffamine = 1/1) was obtained in a solid form but exibited some inhomogeneity expressed in the appearance of viscous liquid droplets on its surface. For this reason, the properties of this sample are not described in the present study.

The optical transmission spectra are shown in Fig. 33.2. The transmission curves of the samples with higher ICPTES/Jeffamine ratio (A3t, A4t) exhibit transmittances about 56% at 400 nm. When the ICPTES/Jeffamine ratio is lower (A2t, A3t), the transmission curves slightly shift to longer wavelengths, reaching transmittances about 53% at 400 nm. This change in transmittance could be explained by a native pale yellow coloration, inherent to polyetheramines and associated with the process of degradation of oxyethylene/oxypropylene chains, accelerated by the oxidation of the amino groups. This observation proves the excitation of some unreacted amino groups in the material, prepared at lower ICPTES/Jeffamine ratios.

Figure 33.3 shows the SAXS curves as measured for four ratios of ICPTES to Jeffamine. The data for ICPTES/Jeff = 2.5 ÷ 4.0 were fitted with slit-smeared Gaussian peak. The correlation distance between the silica nanoparticles was derived from the fitting parameters, according to the procedure described in [13].

Figure 33.4 shows the correlation distance in the polymer matrix as a function of ICPTES/Jeffamine molar ratio at constant molar ratio of APTES/Jeffamine ratio. Distances are calculated from the peak positions, so they are reliable. There is obvious decreasing trend, which means that the scattering entities are getting closer.

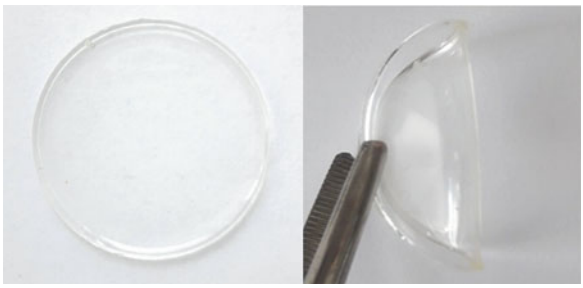

Fig. 33.1 Photograph of sample A2t with a diameter ca. 30 mm and a thickness about 0.5 mm

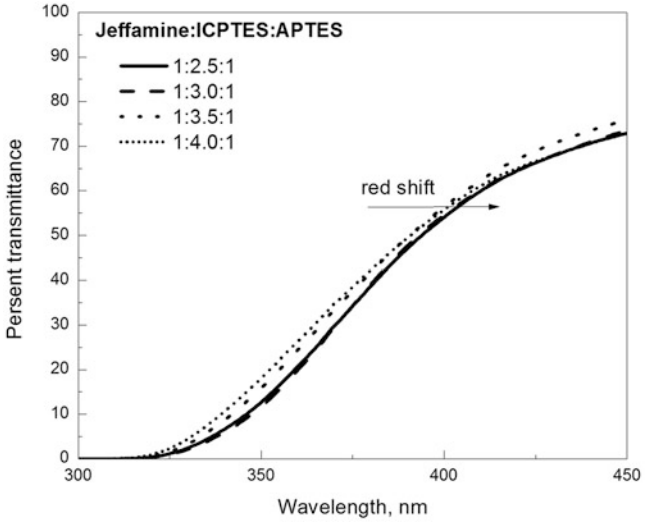

Fig. 33.2 UV-VIS transmission spectra of the samples with optical path length of about 7 mm

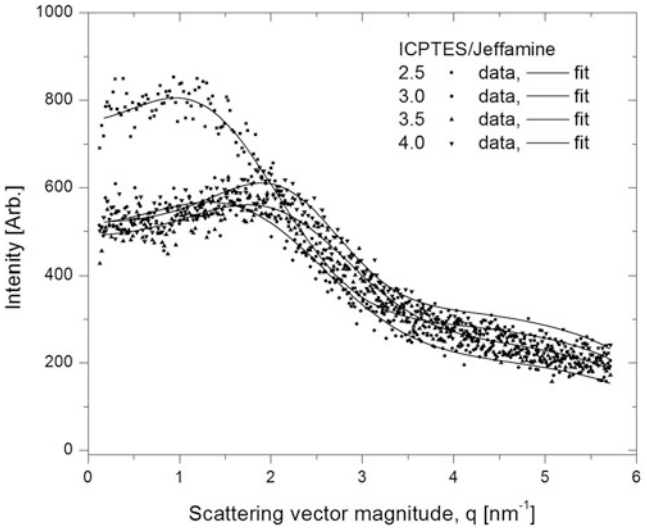

Fig. 33.3 SAXS curves with a constant Jeff/APTES ratio of 1:1 and different ICPTES content

This result suggests the formation of a greater number of the siliceous nanoclusters with the increase of the ICPTES concentration.

Samples with different ICPTES to Jeffamine molar ratios and an APTES to Jeffamine ratio equal to 1 were investigated by FTIR spectroscopy. The vibrational spectra are presented in Fig. 33.5. The region between 1700 and 1500 cm^{-1} is attributed to the urea (-NHCONH-) linkages, where the peak around 1656 cm^{-1} is

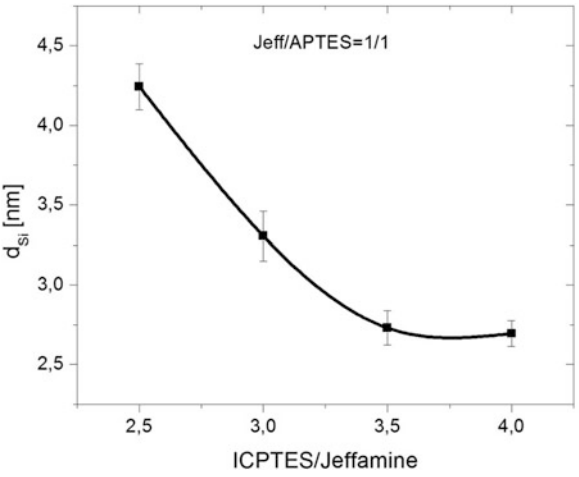

Fig. 33.4 Correlation distances related to the microphase separation between the hard segments (clusters of siloxane, chemically bonded by urea bridges) to the soft segments (polymer chains)

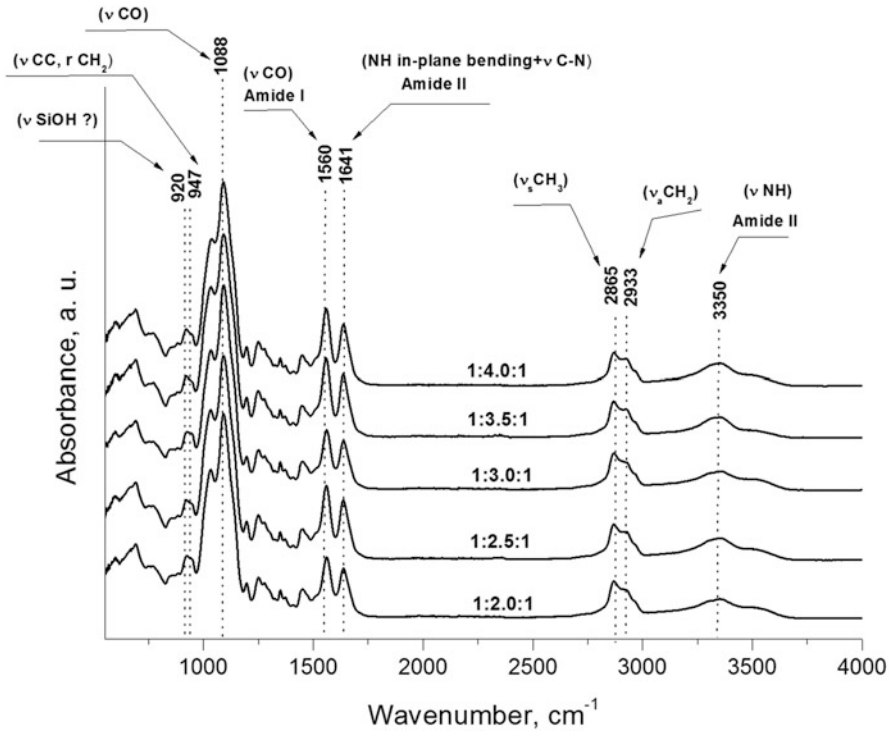

Fig. 33.5 IR spectra of polymers with a constant APTES/Jeffamine ratio and different ICPTES amounts

assigned to the C=O stretching band (amide I region); the peak at 1565 cm^{-1} belongs to a combination of N-H in-plane bending and C-N stretching vibrations (amide II region). In the higher frequency range the spectra demonstrate vibrational modes attributed to ν_a (CH_2) and ν_s (CH_3) [9]. The increase in the intensity of the bands, associated with the amide I and amide II regions proves the higher concentration of urea bonds with increase of the ICPTES/Jeffamine ratio. The existence of Si-OH groups is supposed, due to vibrations in the low frequency region at 920 cm^{-1}. The presence of a Si-OH band is difficult to confirm because it could be masked by vibrations attributed to the molten state of oligopoly (oxyethylene) implying a high level of disorder in the structure. C-C stretching vibrations and CH_2 rocking modes, which are characteristic for the IR spectra of Jeffamine, are identified at 947 cm^{-1} [9]. Si-O-Si stretching vibrations in the polyoxyethylene/poly-oxypropylene containing hybrid materials are also obscured by the strong band arising from C-O stretching vibration of polyether groups.

Figure 33.6 demonstrates the changes of the Martens hardness with the increase of the ICPTES/Jeffamine ratio. A drastical decrease is evident.To explain this change in mechanical behavior it is necessary to look for the reason at the structural level. The obtained results from the SAXS measurements indicate that with an increase of the ICPTES/Jeffamine ratio the distance between the hard segments (clusters of siloxane) decreases or, in other words, their concentration increases. It is logical to expect that hardness will grow with the increase of the concentration of the harder phase but actually a rapidly decrease is observed. Evidently this is a case where the additive law can not be applied. According this law the hardness of systems can be determined as the sum of the hardnesses of the components of the system taking in account their relative fraction. According to the theory reported in [14], the additive law is not valid when there is a large difference in the hardness of the phases, because the harder particles only sink in the softer matrix under the penetrating indenter and do not contribute to the system's hardness. Thus the

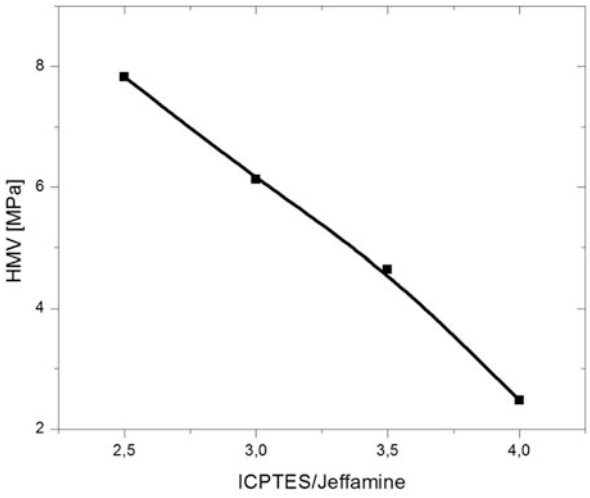

Fig. 33.6 Martens hardness as function of the ICPTES/Jeffamine ratio at APTES/Jeffamine = 1

hardness measured depends only on the resistance of the structure of the softer phase. In the case of the present system and according to the model presented by Dahmouche et al. [15] the clusters formed are the harder phase. The softer phase is represented by the molecular binding segments between the siloxane clusters, consisting of easily movable polyethylene oxide and polypropylene oxide blocks. During the penetration, the flexible blocks are subjected to conformation changes, which signify elastic deformation on the micro-level scale. The greater the distant between the cluster groups are, the more stretched the molecular binding segments will be, and therefore they will have a stronger resistance against penetration. This means a higher value of HMV.

The closer the clusters are, the more corrugated are the binding segments, which allows them to transit easily to more stretched conformation shapes during the penetration. This means a lower value of HMV. The indentation curves show that about 90–95% of the deformation is reversible, which confirms the above discussed idea that at the supramolecular level mainly conformational transformations take place.

33.4 Conclusions

Urea silicate materials with different ICPTES/Jeffamine and constant APTES/Jeffamine ratios were synthesized and characterized optically and mechanically. The transparency of the samples is affected by the composition and slightly increases at higher ICPTES/Jeffamine ratios. It has been found that the mechanical properties are easily controllable by variation of the silicon ethoxide concentration. All investigated samples demonstrate a high level of elasticity. It has been established that at higher ICPTES/Jeffamine ratios the material becomes softer. We assume this is because of the decrease in the distance between the silica cluster groups. The high flexibility of the hybrid materials could be very useful in practical applications such as coating on non-planar substrates, host medium for embedding optically active functionalities and enzymes and for biocompatible thin film manufacturing.

Acknowledgments The authors are grateful for the financial support of this work by the Bulgarian Ministry of Education and Science (NSF DN09/12).

References

1. Kickelbick G (2007) Hybrid materials. Synthesis, characterization and applications. Wiley-VCH Verlag GmbH & Co. KGaA, Weinheim
2. Barbosa PC, Silva MM, Smith MJ, Gonçalves A, Fortunato E, Nunes SC, de Zea Bermudez V (2009) Di-ureasil xerogels containing lithium bis(trifluoromethanesulfonyl)imide for application in solid-state electrochromic devices. Electrochim Acta 54:1002

3. Moura LA, de Oliveira LK, Ciuffi KJ, Molina EF (2015) Influence of the hydrophilic/hydrophobic nature of polyetheramines on the interaction between amine–alcohol–silicate hybrids and anionic dyes for effective water cleaning. J Chem A 3:16020
4. Truffault L, Rodrigues DF, Salgado HRN, Santilli CV, Pulcinelli SH (2016) Loaded Ce-Ag organic-inorganic hybrids and their antibacterial activity. Colloids Surf B Biointerfaces 147:151
5. Cardoso MA, Fernandes M, Rodrigues LC, Leones R, Silva MM, de Zea Bermudez V (2014) Quasi-anhydrous proton conducting di-ureasil hybrid electrolytes incorporating a protic ionic liquid. Electrochim Acta 147:288
6. Ferreira RAS, Brites CDS, Vicente CMS, Lima PP, Bastos ARN, Marques PG, Hiltunen M, Carlos LD, André PS (2013) Photonic-on-a-chip: a thermal actuated Mach-Zehnder interferometer and a molecular thermometer based on a single di-ureasil organic-inorganic hybrid. Laser Photonics Rev 7:1027
7. Guglielmi M, Kickelbick G, Martucci A (2014) Sol-Gel nanocomposites. Springer, New York
8. Armand M, Poinsignon C, Sanches JV, Bermudez VZ (1994) U. S. Patent 5283310
9. Bermudez VZ, Carlos LD, Alcácer L (1999) Sol−gel derived urea cross-linked organically modified silicates. 1. Room temperature mid-infrared spectra. Chem Mater 11:569
10. Dahmouche K, Carlos LD, Bermudez VZ, Ferreira RAS, Santilli CV, Craievich AF (2001) Structural modelling of Eu3+-based siloxane–poly(oxyethylene) nanohybrids. J Mater Chem 11:3249
11. Trigueiros JP, Ferreira Martins LA, Ribeiro DM (2011) Patent WO2011070403A1
12. Kavetskyy T, Smutok O, Gonchar M, Demkiv O, Klepach H, Kukhazh Y, Šauša O, Petkova T, Boev V, Ilcheva V, Petkov P, Stepanov AL (2017) Laccase-containing ureasil–polymer composite as the sensing layer of an amperometric biosensor. J Appl Polym Sci 134:45278
13. Oliveira DC, Macedo AG, Silva NJO, Molina C, Ferreira RAS, André PC, Dahmouche K, De Zea Bermudez V, Messaddeq Y, Ribeiro SJL, Carlos LD (2008) Photopatternable di-ureasil−zirconium oxocluster organic−inorganic hybrids as cost effective integrated optical substrates. Chem Mater 20:3696
14. Zamfirova G (2012) Applicability of additive law in microhardness measurement on polymer materials. Chem List 106(Suppl. 3):564
15. Dahmouche K, Santilli CV, Pulcinelli SH (1999) Small-angle x-ray scattering study of sol−gel-derived siloxane−PEG and siloxane−PPG hybrid materials. J Phys Chem B 103:493

Chapter 34
Sr-Substituted Barium Titanate Glass Ceramics from Oxide Glasses As Potential Material for Sensor Preparation

Ruzha Harizanova, Liliya Vladislavova, Christian Bocker, Georgi Avdeev, and Christian Rüssel

Abstract The present work reports on the synthesis of glasses in the system Na_2O/Al_2O_3/BaO/SrO/TiO_2/B_2O_3/SiO_2/Fe_2O_3 from which, after appropriate thermal treatment, barium titanate and strontium-substituted barium titanate glass-ceramics are crystallized. The characteristic temperatures of the glasses are determined by differential scanning calorimetry DSC and show that higher alumina concentrations result in the stabilization of the glass network while an increasing Sr-concentration at constant alumina concentrations leads to a decrease of the glass transition temperature. The phase composition of the prepared materials was analysed by X-ray diffraction and shows precipitations of cubic barium titanate, $BaTiO_3$ and strontium-substituted barium titanate, $Ba_{1-x}Sr_xTiO_3$. For isothermal treatments and longer annealing times, an additional crystalline phase occurs, i.e. fresnoite ($Ba_2TiSi_2O_8$). The microstructure investigations of the glass ceramics by scanning electron microscopy witness the occurrence of globular bright crystals enriched in the heavier elements, here Ba, Sr and Ti.

Keywords Barium-strontium titanate · Glass-ceramics · Phase separation · Crystallization · Sensors

R. Harizanova (✉)
Department of Physics, University of Chemical Technology and Metallurgy, Sofia, Bulgaria
e-mail: rharizanova@uctm.edu

L. Vladislavova
Department of Physics, University of Chemical Technology and Metallurgy, Sofia, Bulgaria

Otto Schott Institute, University of Jena, Jena, Germany

C. Bocker
Otto Schott Institute, University of Jena, Jena, Germany

j-fiber GmbH, Jena, Germany

G. Avdeev
Institute of Physical Chemistry, Bulgarian Academy of Sciences, Sofia, Bulgaria

C. Rüssel
Otto Schott Institute, University of Jena, Jena, Germany

P. Petkov et al. (eds.), *Advanced Nanotechnologies for Detection and Defence against CBRN Agents*, NATO Science for Peace and Security Series B: Physics and Biophysics, https://doi.org/10.1007/978-94-024-1298-7_34

34.1 Introduction

The synthesis and investigation of the properties of barium titanate containing oxide glass-ceramics with additions of 3d-transition metals is motivated by their potential for application as part of resistive sensors, multilayered capacitors and optoelectronic devices [1–7]. Barium titanate is a promising dielectric material as a substitute of lead-containing dielectrics [7]. It was discovered in the 1950s of the last century and is known to possess several allotropic modifications – orthorhombic, rhombohedral, tetragonal, and cubic – as well as a very high melting temperature of about 1600 °C [8]. The modification of $BaTiO_3$ which is stable at room temperature depends on the preparation method and the size of the precipitated $BaTiO_3$ crystals [3]. Also, the substitution of Ba^{2+} against different ions, i.e. Sr, Ca or Mg, and that of Ti^{4+} by nominally Zr^{4+} ions is reported [9–12]. Pure $SrTiO_3$ has also a high dielectric constant and a high refractive index, and possesses good insulating properties and chemical stability. It has two allotropic modifications, cubic and tetragonal, as the transition to cubic manifests above 105 K. It has different applications such as phase shifters, filters, tunable oscillators, tunable microwave electronics, etc. At 1 K it may exhibit superconductivity when doped. The melting temperature of strontium titanium oxide is 2100 °C [13]. This prevents it from a wide use and also makes the production of devices expensive. However, by using the classical technology of melting, a glass with high concentration of oxides of the alkaline earth and 3d-transition metals and less than 30% of glass forming oxide, can be obtained which melts at the significantly lower temperature of 1250 °C [5, 14, 15]. Using appropriate heat treatment schedules further enables to prepare crystals of $BaTiO_3$ and mixed crystals of the type $Ba_{1-x}Sr_xTiO_3$ from this glass. Depending on the degree of substitution, such solid solutions could find applications as electroceramics for piezoelectric transducers, pyroelectric detectors and as part of some electro-optical devices [9, 10].

Barium titanate-based materials are often prepared by using sintering of carbonate powders as raw materials, by sol-gel method [7] and subsequently, the electrical properties of the resulting materials were studied. Another approach to obtain glass ceramic materials containing $BaTiO_3$ is to crystallize it from oxide glasses [14–16]. The crystallization of dielectric phases from oxide glasses allows the controlled precipitation of the desired crystalline phase with tailorable size, a narrow-size-distribution and a large volume fraction as already observed also in our work for compositions similar to those reported here [15].

The synthesis of glasses and glass-ceramics derived hereof with advantageous dielectric properties is studied for the following series of compositions $20.1Na_2O/3Al_2O_3/(23.1\text{-}y)BaO/ySrO/23TiO_2/7.6B_2O_3/17.4SiO_2/5.8Fe_2O_3$ with $y = 0.5, 1, 2$ and 3 mol %. The resulting phase compositions and microstructures are investigated.

34.2 Experimental

34.2.1 Preparation of the Glasses

Reagent grade raw materials: Na_2CO_3, SiO_2, Fe_2O_3, $BaCO_3$, $B(OH)_3$, $Al(OH)_3$ and TiO_2 were used for the preparation of the glasses. The batches (60 g) were homogenized and melted in Pt-crucibles using a silicon carbide furnace and a melting temperature of 1250 °C for 1 h in air. Some of the melts were quenched on a Cu-block and after quenching transferred into a pre-heated graphite mould. The glasses cast into the graphite mould were transferred to a muffle furnace and kept at 450 °C for 10 min. Then, the furnace was switched off and the samples were allowed to cool to room temperature with a velocity of approximately 2 K/min. All glassy samples were heat treated at temperatures above T_g for different times.

34.2.2 Characterization Methods

The phase compositions were analyzed by X-ray diffraction (XRD) on powdered samples, using $Cu_{K\alpha}$-radiation with the 2θ-values in the range from 10 to 60° (Rigaku MiniFlex and Siemens D 5000). The densities of the obtained glasses were determined by a helium pycnometer (Micromeritics, AccuPyc 1330 V3.00). The glass transition temperatures were determined by differential scanning calorimetry DSC (DSC 822 Mettler Toledo) using a heating rate 10 K/min, powdered samples with fractions between 100 and 250 μm and Al_2O_3 as reference material. The microstructure was investigated by scanning electron microscopy (SEM) using backscattered electron (BSE) and secondary electron (SE) detectors (JEOL 6510LV and JSM-7001F). The samples for SEM imaging were cross-fractured, immobilized in epoxy resin and polished to optical quality. Then they are covered with a thin carbon layer to avoid charging of the surface during interaction with the electron beam.

34.3 Results and Discussion

Previous work had been carried out in the system (23.1-z)Na_2O/zAl_2O_3/23.1BaO/23TiO_2/7.6B_2O_3/17.4SiO_2/5.8Fe_2O_3 for z = 0, 3, 7 and 11 mol% [14], where the ratio of Na_2O to Al_2O_3 was varied in order to trace its influence on the glass formation ability in the system mentioned. This revealed best glass forming abilities for the compositions with 3 and 7 mol% Al_2O_3. However, additionally to the glass-forming ability in the system studied, also the possibility to precipitate, during appropriate thermal treatment, barium titanate as sole crystalline phase with a large volume fraction and crystallite size, leading to a high dielectric constant of the

Table 34.1 Glass transition (T_g) and crystallization temperature (T_c) of the parent glass and the Sr-substituted glasses

□	SrO [mol%]	T_g [°C]	T_c [°C]
1	0 – parent glass	450	550
2	0.5	433	567
3	1	439	574
4	2	435	574
5	3	435	570, 580

prepared glass-ceramics, is important for potential applications. The investigation of the phase composition and the microstructure of the glass-ceramics with 3 and 7 mol % alumina showed that the compositions with 7 mol% have a very fine interpenetrating crystalline structure corresponding to barium titanate. However, in this composition also nepheline ($NaAlSiO_4$) occurs as a secondary crystalline phase [15] which is not desired. Further thermal treatment of the as chosen composition with 3 mol% alumina by applying different time-temperature schedules resulted in the formation of barium titanate as the only crystalline phase for a broad temperature and time interval range. Only after increasing the annealing temperature above 600 °C and the annealing time above 3 h, the occurrence of an additional crystalline phase (fresnoite, $Ba_2TiSi_2O_8$) was observed [14]. The micro-computed tomography investigation of the glass-ceramic samples showed that the barium titanate phase is crystallized in a large volume fraction of 58 ± 1% [15] which is important for potential practical applications. Also, by SEM imaging and according to the preliminary information gathered about the studied system [17], the system of choice is prone to phase separation which results in the formation of droplet-like structures enriched in Ba and Ti where later $BaTiO_3$ is precipitated [14, 15]. Thus, the composition with 3 mol% Al_2O_3 was chosen and further modified by substituting BaO with SrO, in order to see which influence this substitution will have on the phase composition, microstructure and eventually practical applications. The series of compositions $20.1Na_2O/3Al_2O_3/(23.1\text{-}y)BaO/ySrO/23TiO_2/7.6B_2O_3/17.4SiO_2/5.8Fe_2O_3$ with y = 0.5; 1; 2 and 3 mol % is melted as described above. The quenching of the melts for all SrO concentrations results in amorphous products, only for the sample with 3 mol% SrO a slight crystallization on the surface is observed. To achieve higher mechanical stability and to release the mechanical stresses in the glasses they were transferred to a graphite mould and annealed around the glass-transition temperature. The T_g and T_c values determined by DSC are given in Table 34.1 and show that the Sr-substituted glass compositions have lower T_g values than the parent glass without strontium oxide. Actually, a slight increase of T_g of the Sr-containing glasses occurs up to 1 mol% SrO, then T_g decreases and remains constant up to 3 mol % SrO. The crystallization temperatures as peak maximum positions are also very similar though higher than that of the parent glass. For the composition with 3 mol% SrO, a second crystallization peak can clearly be resolved at about 580 °C.

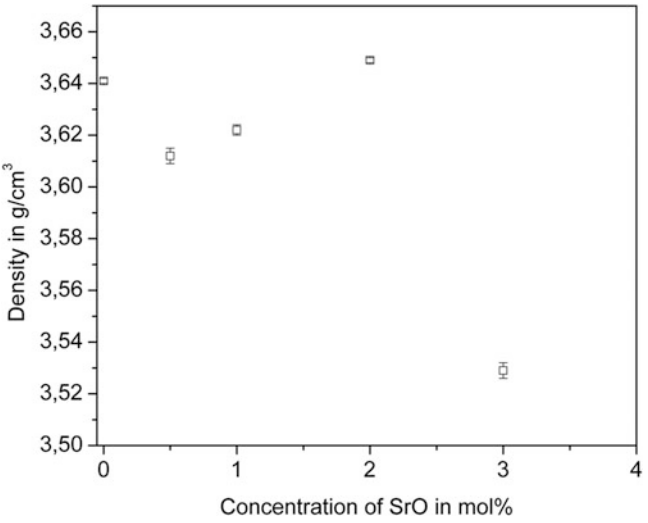

Fig. 34.1 Densities of the Sr-substituted glasses as function of the SrO concentration

The densities of the obtained glasses were determined pycnometrically; as seen in Fig. 34.1, they do not significantly vary compared to the density of the parent glass with 0 mol% SrO up to 2 mol% SrO. However, for 3 mol% SrO, a decrease of the density of the respective Sr-substituted glass is observed. This could be attributed to the fact that the strontium concentration is initially too small to lead to some significant structural changes in the glass, but for 3 mol% already the presence of Sr would lead to structural changes in the glass network due to the smaller ionic radius of Sr^{2+} (0.118 nm) compared to that of Ba^{2+} (0.135 nm).

The stabilized glasses obtained were subjected to thermal treatments at different temperatures near the crystallization peak maximum (from the DSC-thermograms) for different time intervals. The result, as shown for different Sr-concentrations in Figs. 34.2, 34.3, 34.4, and 34.5 is the crystallization of a solid solution of the type $Ba_{1-x}Sr_xTiO_3$ with the peaks slightly shifting with increasing concentration of SrO to higher 2θ values. Actually, the X-ray diffraction patterns show that for the glass-ceramics with 0.5 mol% SrO, the composition of the mixed crystals formed is $Ba_{0.592}Sr_{0.408}TiO_3$ (JCPDS 96-152-2091), while for higher concentrations of strontium, the formed solid solutions possess the composition $Ba_{0.5}Sr_{0.5}TiO_3$ (JCPDS 96-151-2124). Longer annealing times result in a slight shift of the crystallization peak maxima to Ba-richer solid solutions for the 3 mol% SrO glass-ceramics, as can be seen in Fig. 34.5. Also, longer annealing times as well higher annealing temperatures lead to the precipitation of a second phase – fresnoite, $Ba_2TiSi_2O_8$ (JCPDS 96-100-7235) – which might lead to a Ba deficiency in the growing barium-strontium titanate crystals. The increase of annealing time or temperature also results

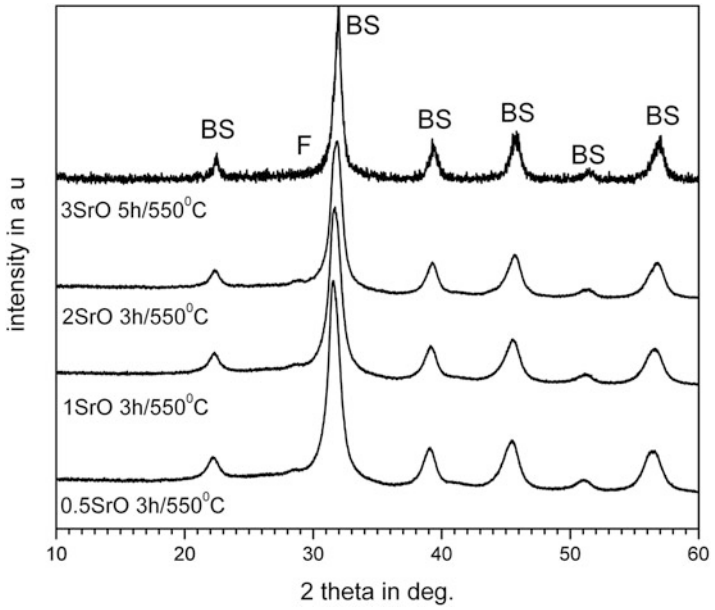

Fig. 34.2 XRD patterns of samples with 0.5, 1, 2 and 3 mol% SrO annealed at 550 °C for different times: crystallization of $Ba_{1-x}Sr_xTiO_3$

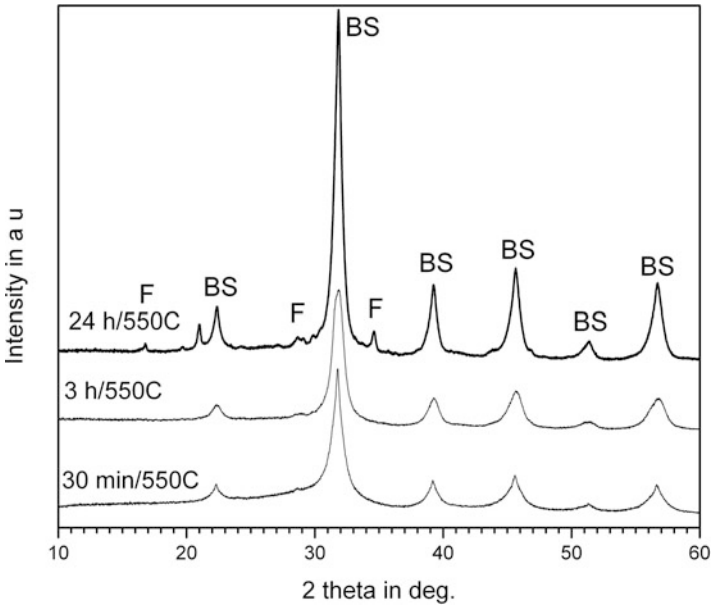

Fig. 34.3 XRD pattern of a sample with 2 mol% SrO annealed at 550 °C for different time intervals – crystallization of $Ba_{0.5}Sr_{0.5}TiO_3$ (BS) and fresnoite $Ba_2TiSi_2O_8$ (F)

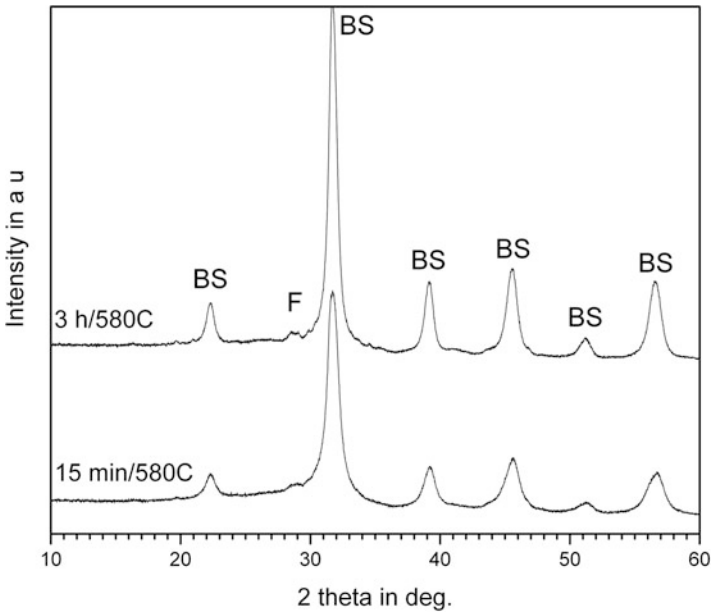

Fig. 34.4 XRD pattern of a sample with 2 mol% SrO annealed at 580 °C for different times – crystallization of $Ba_{0.5}Sr_{0.5}TiO_3$ and fresnoite even for shorter annealing times

in crystal growth, and the volume fraction of the formed crystals increases as witnessed by the narrower and more intense peaks of the X-ray diffraction patterns. Some authors working with similar systems report the precipitation of Fe_3O_4 and $BaTiO_3$ in the glass and the occurrence of core-shell structures [5]. We do not have evidence from our analyses in the present set of compositions that Fe is incorporated in the crystalline phases as detected by X-ray diffraction. The results from the qualitative X-ray analyses are confirmed by microstructural characterization by means of scanning electron microscopy. In Fig. 34.6, the typical microstructure for all annealed samples is shown, droplet-like bright crystals which are formed in the phase separated glass after applying the respective annealing programs. It is assumed [14, 15, 17] that in the glass, two phases are formed, one enriched in Ba, Ti and Sr where later the $Ba_{1-x}Sr_xTiO_3$ solid solution or/and pure $BaTiO_3$ will crystallize, and a second phase, which contains all other constituents of the glass composition. After annealing above T_g, in the droplet-like regions, $BaTiO_3$ [14, 15] or in the present case, $Ba_{1-x}Sr_xTiO_3$ crystallizes. The isothermal annealing for longer times will lead to aggregation of the liquid droplets into larger formations, as shown in Figs. 34.7, 34.8, and 34.9. The volume fraction of the crystalline phase, as seen from the SEM micrographs will also increase for longer annealing times. However, due to very close average atomic numbers and thus similar contrasts, the standard SEM analysis could not really differentiate between the formed barium-strontium titanate and the second precipitated phase fresnoite.

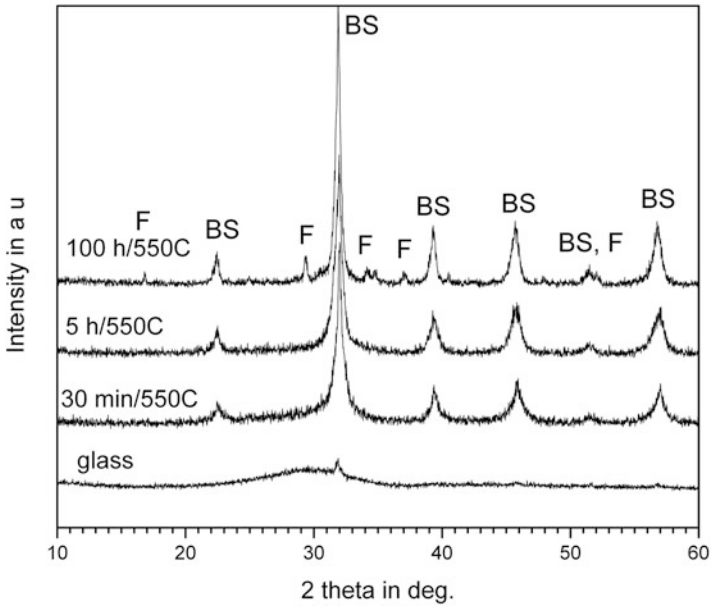

Fig. 34.5 XRD pattern of a sample with 3 mol% SrO annealed at 550 °C for different time intervals – crystallization of $Ba_{1-x}Sr_xTiO_3$ and fresnoite and shift of the peaks to smaller 2θ values with increasing annealing time

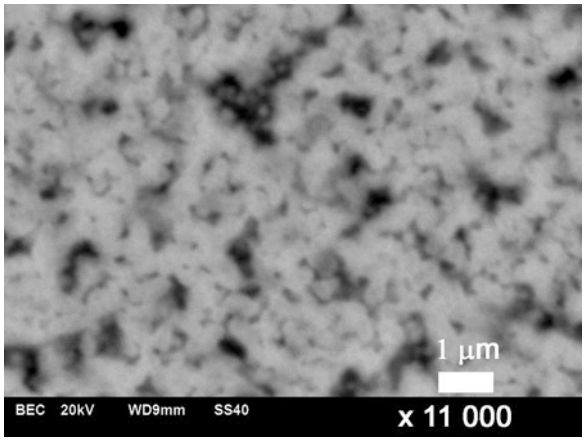

Fig. 34.6 Uniform crystallization of a sample with 0.5 mol % SrO annealed for 3 h at 550 °C

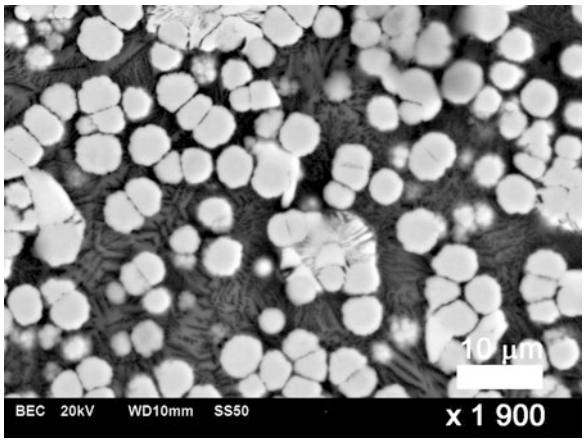

Fig. 34.7 Sample with 0.5 mol% SrO (24 h/ 550 °C): crystal growth for longer annealing times

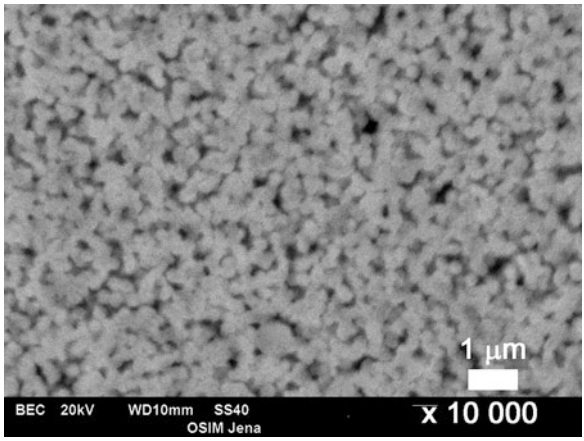

Fig. 34.8 Sample with 3 mol% SrO annealed for 30 min at 550 °C: growth of droplet-like structures

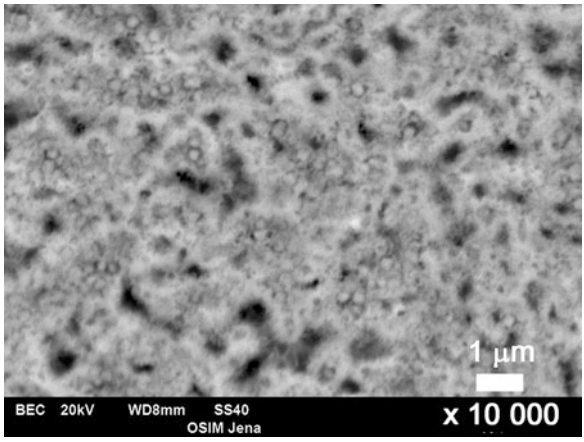

Fig. 34.9 Sample with 3 mol% SrO annealed for 100 h at 550 °C: further growth of the formed particles

34.4 Conclusions

Glasses in the system $Na_2O/BaO/SrO/TiO_2/B_2O_3/SiO_2/Al_2O_3/Fe_2O_3$ with up to 3 mol % SrO substitution of BaO were synthesized. The glass transition temperature and the density of the respective glasses decrease with increasing strontium concentration. Annealing of the glasses always results in the crystallization of a solid solution of the type $Ba_{1-x}Sr_xTiO_3$ as the first phase. Higher concentrations of SrO in the glass lead to a shift of the solid solution compositions to the Sr-richer ones. For longer crystallization times also as second crystalline phase fresnoite crystallizes. In all annealed glasses, the microstructure initially consists of droplet-like structures which with increasing annealing time grow together. The addition of Fe to the composition stabilizes the glasses mechanically and chemically but does not lead to the precipitation of Fe-containing crystalline phases.

Acknowledgments This work is financially supported by contract NIS 11 663, Scientific sector of UCTM, Bulgaria and contract DN08/13, Bulgarian National Scientific Fund.

References

1. Zhang F, Shi Y, Zhao Z, Ma B, Wei L, Lu L (2014) Amino-functionalized Fe_3O_4/SiO_2 magnetic submicron composites and In3+ ion adsorption properties. J Mater Sci 49:3478–3483
2. Libor Z et al (2011) Rheological properties of magnetic and electro-active nanoparticles in non-polar liquids. J Mater Sci 46:5385–5393
3. Capsal JF et al (2010) Nanotexture influence of BaTiO3 particles on piezoelectric behaviour of PA 11/$BaTiO_3$ nanocomposites. J Non-Cryst Solids 356:629–634
4. Joshi U, Yoon S, Baik S, Lee JS (2006) Surfactant-free hydrothermal synthesis of highly tetragonal barium titanate nanowires: a structural investigation. J Phys Chem B 110:12249
5. Maiti RP, Basu S, Bhattacharya S (2009) Multiferroic behavior in silicate glass nanocomposite having a core–shell microstructure. J Non-Cryst Solids 355:2254–2259
6. Du G (2010) P et al, Effects of niobium donor doping on the phase structures and magnetic properties of Fe doped $BaTiO_3$ ceramics. J Alloys Compd 492:L79–L81
7. Vijatović MM, Bobić JD, Stojanović BD (2008) History and challenges of barium titanate: part II. Sci Sinter 40:235–244
8. Smith MB, Page K, Siegrist T, Redmond PL, Walter EC, Seshadri R, Brus LE, Steigerwald ML (2008) Crystal structure and the paraelectric-to-ferroelectric phase transition of nanoscale $BaTiO_3$. J Am Chem Soc 130:6955–6963
9. Ridha NJ, Mahmood W, Yunus M, Halim SA, Talib ZA (2009) Effect of Sr substitution on structure and thermal diffusivity of $Ba_{1-x}Sr_xTiO_3$ ceramic. Am J Eng Appl Sci 2(4):661–664
10. Lemans VV, Smirnova EP, Syrnikov PP, Tarakanov EA (1996) Phase transitions and glasslike behavior in $Sr_{1-x}Ba_xTiO_3$. Phys Rev 54(5):3151–3157. 0163-1829/96/54
11. Dobal PS, Dixit A, Katiyar RS, Yu Z, Guo R, Bhalla AS (2001) Micro-Raman scattering and dielectric investigations of phase transition behavior in the BaTiO3 –BaZrO3 system. J Appl Phys 89:8085–8091
12. Yoon MS, Ur SC (2008) Effects of A-site Ca and B-site Zr substitution on dielectric properties and microstructure in tin-doped $BaTiO_3$ –$CaTiO_3$ composites. Ceram Int 34:1941–1948
13. Yamada H, Miller GR (1973) Point defects in reduced strontium titanate. J Solid State Chem 6:169–177

14. Harizanova R, Mazhdrakova A, Vladislavova L, Avdeev G, Bocker C, Gugov I, Rüssel C (2015) Crystallization behaviour of the systems $Na_2O/BaO/TiO_2/SiO_2/B_2O_3/Al_2O_3$ and $Na_2O/BaO/TiO_2/SiO_2/B_2O_3/Fe_2O_3/Al_2O_3$. J Chem Technol Metall 50:375
15. Harizanova R, Tatchev D, Avdeev G, Bocker C, Karashanova D, Mihailova I, Gugov I, Rüssel C (2017) Investigation on the crystallization behaviour of sodium-aluminoborosilicate glasses with high concentrations of Ba and Ti. Bulg Chem Commun 49:119–125
16. Buscaglia V, Buscaglia MT, Viviani M, Mitoseriu L, Nanni P, Trefiletti V, Piaggio P, Gregora I, Ostapchuk T, Pokorny J, Petzelt J (2006) Grain size and grain boundary-related effects on the properties of nanocrystalline barium titanate ceramics. J Eur Ceram Soc 26:2889–2898
17. Vogel W (1985) Glass chemistry, 2nd edn. Springer, Berlin

Chapter 35
$BaO/SrO/ZnO/SiO_2$ Glass System: Influence of Different Nucleation Agents: Bulk Versus Surface Crystallisation

Liliya Vladislavova, Christian Thieme, Tilman Zscheckel, Christian Patzig, Thomas Höche, and Christian Rüssel

Abstract In the present study, detailed investigations on the crystallisation behaviour for the recently discovered $Ba_{1-x}Sr_xZn_2Si_2O_7$ phase were performed. This solid solution may possess zero to negative thermal expansion. In contrast to many other phases with negative thermal expansion, this phase can be crystallised from glasses and hence should be suitable for the preparation of cooking panels, telescope mirrors, and other mass production materials, where the thermal expansion properties have to be tailored exactly. Due to the high anisotropy of the phase, inducing volume crystallisation and reducing the crystal size is of main interest. The influence of ZrO_2 and Pt as nucleating agents in the glass system $BaO/SrO/ZnO/SiO_2$ was studied by calculating the Avrami parameter (n). The microstructure was investigated with scanning electron microscopy.

Keywords Nucleation · Glass-ceramics · Platinum-ZrO_2 · Activation energy · Avrami parameter

35.1 Introduction

The $Ba_{1-x}Sr_xZn_2Si_2O_7$ phase is a new and challenging solid solution which has a similar structure as the high-temperature (HT) modification of $BaZn_2Si_2O_7$. The new solid solution possesses negative or close to zero thermal coefficients which make it suitable for fabrication of materials such as cooking panels, telescope mirrors and

L. Vladislavova (✉) · T. Zscheckel · C. Rüssel
Otto Schott Institute, Chair of Glass Chemistry I, Jena University, Jena, Germany
e-mail: liliya.vladislavova@uni-jena.de

C. Thieme
Otto Schott Institute, Chair of Glass Chemistry I, Jena University, Jena, Germany

Fraunhofer Institute for Microstructure of Materials and Systems IMWS, Halle, Germany

C. Patzig · T. Höche
Fraunhofer Institute for Microstructure of Materials and Systems IMWS, Halle, Germany

P. Petkov et al. (eds.), *Advanced Nanotechnologies for Detection and Defence against CBRN Agents*, NATO Science for Peace and Security Series B: Physics and Biophysics, https://doi.org/10.1007/978-94-024-1298-7_35

others [1, 2]. Using single-crystal X-ray diffraction (XRD), the thermal expansion was determined as a function of temperature and crystallographic directions, combined with a Rietveld refinement [3]. The thermal expansion varies significantly in the different crystallographic directions which causes a high anisotropy in the system and may lead to crack formation in the obtained materials. Reducing the crystal size and provoking volume crystallisation is one of the most commonly applied methods to overcome crack formation [1]. Both ZrO_2 and Pt are well-known nucleation agents used in the past e.g. for the $Li_2O{\cdot}2SiO_2$ system [1, 4]. This paper describes the effect of Pt and ZrO_2 as nucleating agents in glasses from the system BaO/SrO/ZnO/SiO_2/ZrO_2.

35.2 Experimental

35.2.1 Preparation of the Glasses

The glass batch was prepared from the following chemically pure raw materials: $BaCO_3$, $SrCO_3$, ZnO, SiO_2, ZrO_2, and $PtCl_4$. For the platinum containing glass, 0.01 mol% $PtCl_4$ was dissolved in acetone and then given to the glass batch, thoroughly mixed for 2 h and subsequently dried. The batch (for 400 g glass) was melted at 1300–1350 °C for 1 h in a platinum crucible using an induction furnace. Then, the temperature was increased to 1450 °C for 2 h. During this time, the melt was stirred with 60 min^{-1}. Then, the stirrer was removed and the glass was soaked for 10–15 min. The glass was cast in a preheated steel mould and transferred to a muffle furnace preheated to 700 °C. The furnace was switched off allowing the sample to cool to room temperature. The base chemical compositions of the glasses is 8BaO/8SrO/34ZnO/44SiO_2/6ZrO_2.

35.2.2 Characterization Methods

Differential Scanning Calorimetry (DSC) was carried out using a Linseis DSC Pt 1600. Characteristic temperatures such as the glass transition temperature (T_g), the onset of the crystallisation peak (T_{on}), the offset of the crystallisation peak (T_{off}) and the crystallisation maximum (T_p) were determined. Bulk samples were used in order to minimise the effect of surface crystallisation; samples with a mass of 0.15 g were remelted in a DSC platinum crucible at 1450 °C and then quenched in air. The measurements were performed up to a temperature of 1200 °C, using heating rates of 2, 5, 10, 15 and 20 K/min.

Scanning Electron Microscopy was carried out using an (SEM) JEOL 7001 F. The samples were mounted using Ag paste; a carbon coating was applied at about 10^{-5} Pa in order to avoid surface charging.

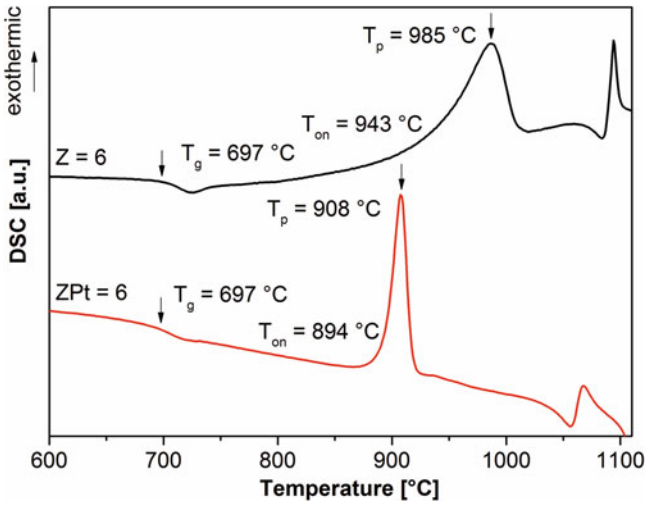

Fig. 35.1 DSC profiles: glasses with 6 mol% ZrO_2 with and without platinum, using a heating rate of 10 K/min

35.3 Results and Discussion

The produced glasses appear to be without bubbles, crystals, and striae. The sample which contained only ZrO_2 is transparent. However, adding platinum to the system led to the formation of small platinum particles with a mean size of 1 μm in the non–thermally treated glass which causes a greyish colouration [5].

Figure 35.1 shows the DSC profiles of the glasses prepared with (Z6Pt) and without (Z6) addition of platinum recorded with a heating rate of 10 K/min. The platinum addition does not affect T_g which for both systems is equal to 697 °C. The onset and peak temperatures of the Pt-containing and the Pt-free glass vary significantly. The Pt-containing glass has an onset at 894 and a peak temperature at 908 °C, whereas the Pt-free glass shows these characteristics at 943 and 985 °C, respectively. Also, a significant change in the shape of the crystallisation peaks can also be seen. The platinum-containing glass has a sharp and narrow peak whose intensity is much higher compared to that of the ZrO_2 containing glass, where the intensity is significantly lower and the peak is broader. As already reported in the literature, this is a significant indication for a change in the crystallisation mechanism [5–7].

Figure 35.2 presents Ozawa plots for the determination of the Avrami parameter for the studied glasses. The plots are obtained according to Eq. (35.1) where (ln(-ln (1-x))) is plotted versus ln (β) and the parameter value is determined from the slope using a linear regression [8, 9]. To obtain statistically significant data, the measurements were performed using five different heating rates.

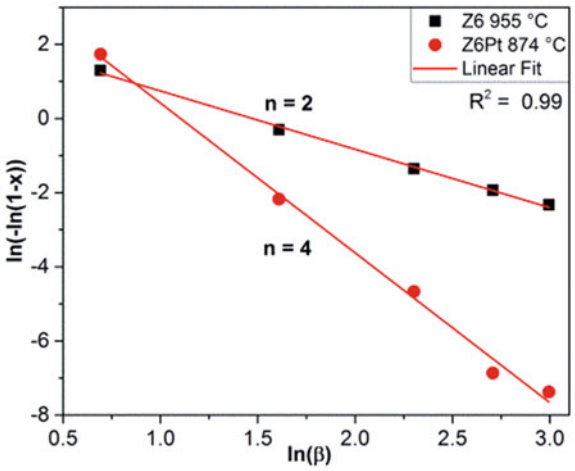

Fig. 35.2 Ozawa plot of (ln-(ln(1-x))) versus ln (β) used to calculate the Avrami parameter for Z6: 955 °C and Z6Pt: 874 °C

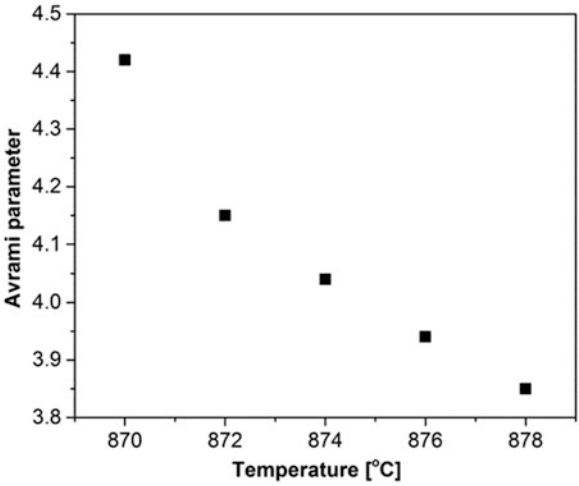

Fig. 35.3 Avrami parameter versus temperature for Z6Pt

$$-n = \left|\frac{\mathrm{d}[\ln(-\ln(1-x))]}{\mathrm{d}(\ln\beta)}\right|_{\mathrm{T}} \tag{35.1}$$

In this equation, n is the Avrami parameter and $x = A_t/A$ where A is the total area under the exothermic peak, A_t is the area under the exothermic peak up to a chosen temperature, and β is the heating rate.

The calculated Avrami parameter for the glass with 6 mol% ZrO_2(Z6) for 955 °C is approximately equal to 2 which is an indication of a mix between surface and volume crystallisation [8]. The glass composition with platinum (Z6Pt) has an Avrami parameter equal to 4 at 874 °C. This is an indication of 3D bulk crystallisation [8, 9]. As can be seen from Fig. 35.3, the Avrami parameter versus the temperature can vary slightly depending on the chosen temperature. In order to

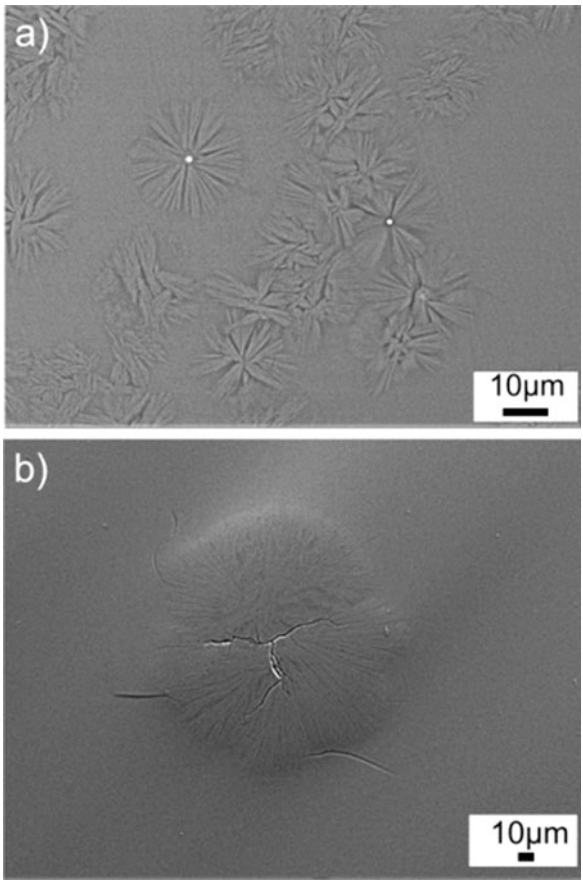

Fig. 35.4 SEM-micrographs of different samples: (**a**) Z6Pt thermally treated in the first step at 720 °C for 48 h and then at 780 °C for 5 h; (**b**) Z6 thermally treated in a first step at 720 °C for 48 h and then at 840 °C for 1 h

obtain more accurate Avrami parameters, the following should be taken into account: The heating rates should be chosen in a way that the area under the peak is the range from $0.2 \leq \times \leq 0.8$. As seen from Fig. 35.3, the Avrami parameter for the platinum containing glass varied between 4.42 and 3.85 which is close to 4. Despite the fact that the Ozawa method is quite accurate in the prediction for the crystallisation mechanism regarding the $Ba_{1-x}Sr_xZn_2Si_2O_7$ phase, additional microstructural studies are necessary for a complete overview of the crystallisation processes.

Figure 35.4 shows SEM micrographs of the studied glass ceramics. Figure 35.4a presents the platinum containing sample nucleated at 720 °C for 48 h and then thermally treated at 780 °C for 5 h. A significant amount of volume crystals is observed in the micrographs. From statistical analyses made on the samples, the mean particle size of the volume crystals was determined to be around 11 μm. The bright spheres in the middle of the crystals are platinum particles with a mean size of 1 μm which are formed during cooling of the glass [5]. All volume crystals should have a platinum particle in their centres which, however, in many cases are not

visible in the SEM micrographs, due to the different cut planes and the limited information depth of SEM. This is a good example of a heterogeneous nucleation where the metal particles act as a precursor of the crystal phase. Figure 35.4b shows the ZrO_2 containing sample nucleated at 720 °C for 48 h and then thermally treated at 840 °C for 1 h. In this case, the mean size of the volume crystals is 180 µm and the number of the crystals is significantly reduced. Also, crack formation is visible from the centre of the crystal which in combination with the surface crystallisation leads to a brittle material [7]. From this observation it can be concluded that ZrO_2 alone is not a sufficient nucleation agent.

35.4 Conclusions

Using DSC and applying the Ozawa method in order to determine the Avrami parameters proved to be suitable to predict the crystallisation behaviour and also the microstructure. The addition of 6 mol% ZrO_2 induces predominantly surface and besides, a small amount of volume crystallisation. The mean crystallite size is 180 µm which is too large for overcoming the crack formation in the samples. Adding small quantities of Pt significantly increases the volume crystallisation and reduces the mean crystallite size to 11 µm. Nevertheless, some cracks still occur inside the samples, but they are localised and do not lead to a destruction of the material.

References

1. McMillan PW (1979) Glass-ceramics, 2nd edn. Academic, London
2. Bach H, Krause D (2005) Low thermal expansion glass ceramics, 2nd edn. Springer, New York
3. Thieme C, Görls H, Rüssel C (2015) $Ba_{1-x}Sr_xZn_2Si_2O_7$-A new family of materials with negative and very high thermal expansion. Sci Rep 5:18040
4. Rindone G (1962) Further studies of the crystallization of a lithium silicate glass. J Amer Ceram Soc 45:7–12
5. Vladislavova L, Thieme C, Zscheckel T, Patzig C, Höche T, Rüssel C (2017) Heterogeneous nucleation of $Ba_{1-x}Sr_xZn_2Si_2O_7$ from a BaO/SrO/ZnO/SiO_2 glass using platinum as nucleation agent. J Eur Ceram Soc 37:4801–4808
6. Massera J, Fagerlund S, Hupa L, Hupa M (2012) Crystallization mechanism of the bioactive glasses, 45S5 and S53P4. J Am Ceram Soc 95:607–613
7. Vladislavova L, Thieme C, Rüssel C (2017) The effect of ZrO_2 on the crystallization of a glass in the system BaO/SrO/ZnO/SiO_2: surface versus bulk crystallization. J Mater Sci 52:4052–4060
8. Guedes M, Ferro AC, Ferreira JMF (2001) Nucleation and crystal growth in commercial LAS compositions. J Eur Ceram Soc 21:1187–1194
9. Donald IW (2004) Crystallization kinetics of a lithium zinc silicate glass studied by DTA and DSC. J Non-Cryst Solids 345:120–126

Chapter 36
Bismuth-Titanate $Bi_2Ti_2O_7$ Crystallization in the $Bi_2O_3/TiO_2/SiO_2/Nd_2O_3$ System

Stanislav Slavov and Zheng Jiao

Abstract Electronic devices for high frequency applications become more and more useful in recent years. The general aim of this study is to demonstrate a way to synthesize compositions from the system $Bi_2O_3/TiO_2/SiO_2/Nd_2O_3$ in which only one crystalline phase is present: bismuth-titanate pyrochlore ($Bi_2Ti_2O_7$). Synthesis was performed in two successive steps: a starting oxide homogenization in 15 min and melting at temperatures of 1100 °C and 1450 °C, respectively. The free cooling was carried out to room temperature with about 100 K/min. The phase composition of selected samples was determined by X-ray diffraction (XRD) analysis. The microstructure was observed by scanning electron microscopy (SEM). Infrared spectroscopy (FTIR) was applied in order to identify the structure and microcrystals distribution in the matrix. Thorough control of the initial amounts of the starting composition leads to obtain monophase polycrystalline glass-ceramics and ceramics containing the phase $Bi_2Ti_2O_7$.

Keywords Pyrochlore oxides · Bismuth-titanates · Glass-crystalline materials

36.1 Introduction

Ferroelectric materials are the subject of a vast number of studies published in recent years. The Aurivillius phase is the most popular of bismuth titanate [1–3], but it is well-known that pyrochlore titanate with the chemical formula $A_2Ti_2O_7$ (A=La, Nd, Ca) are very promising for high frequency (microwave) applications [4–6]. In one excellent work Hector and Wigin [7] discuss the synthesis of a stoichiometric cubic structure of pyrochlore by low-temperature methods such as

S. Slavov (✉)
Department of Physics, University of Chemical Technology and Metallurgy, Sofia, Bulgaria

Z. Jiao
School of Environmental and Chemical Engineering, Shanghai University, Shanghai, People's Republic of China

P. Petkov et al. (eds.), *Advanced Nanotechnologies for Detection and Defence against CBRN Agents*, NATO Science for Peace and Security Series B: Physics and Biophysics, https://doi.org/10.1007/978-94-024-1298-7_36

sol-gel or CVD with the idea of obtaining low cost electro-ceramics. Based on the above-mentioned scientific results, the present work is motivated by the practical necessity of: (1) synthesis of a monophase perovskite material (pyrochlore $Bi_2Ti_2O_7$); (2) use of a method which avoids high cost of precursors (as sol-gel) or costly equipment (as CVD), and (3) the production of material (ceramics and glass-ceramics) with an oriented microstructure. The most popular synthesis methods for ceramics are sol-gel, CVD, solid-state reaction, co-preparation, molten salt synthesis, and mechanochemical synthesis. In the present work we use melting, free cooling to room temperature and a combination of different precursors in order to control precisely the phase formation. Additionally, adding a glass phase between crystalline materials is due tothe production of new materials with fine-granded, pore-free and nano-structured materials [8]. Typically, in some high frequency applications, bulk materials are used, so their dielectric properties are strongly influenced by phase composition, grain size, the glass phase content, and grain boundary effects [9]. This work shows one possibility to control the phase formation and texturing ability in ceramic and glass ceramic materials from the system Bi_2O_3-TiO_2-SiO_2-Nd_2O_3. Their synthesis from well-known readily available and inexpensive starting materials, and the used equipment is available in any electro-ceramics laboratory.

36.2 Experimental

For bulk materials synthesis in the system Bi_2O_3-TiO_2-SiO_2-Nd_2O_3 two successive procedures were used: starting oxide homogenization in 15 min and melting at temperatures of 1450 °C and 1100 °C, in dependence of the batch composition. Melting was done in a SiC tube furnace KTM-GSL1700X using alumina crucibles; the melts were freely cooled to room temperature in graphite crucibles (Table 36.1) with a rate around 100 K/min.

By the X-ray diffraction the phase composition was determined using a XRD Ridacu D/MAX2500V, using CuKa radiation (a = 1.5406 Å); by scanning electron microscopy the microstructure was observed using a SEM Hitachi SU1510. The infrared spectra of selected samples was examined with a FTIR Thermo Nikolet – Avatar 370 FT-IR.

Table 36.1 Starting, phase composition and melting conditions of selected samples in the system Bi_2O_3-TiO_2-SiO_2-Nd_2O_3. The composition is given in mol%

No	Name	Bi_2O_3	TiO_2	SiO_2	Nd_2O_3	t_m [°C]	t [min]	Phases according to XRD
1	A	19	66	8	7	1450	20	$Bi_2Ti_2O_7$
2	B	23	66	4	7	1450	20	$Bi_2Ti_2O_7$
3	C	45	0	50	5	1100	15	Glass + $Bi_2Ti_2O_7$

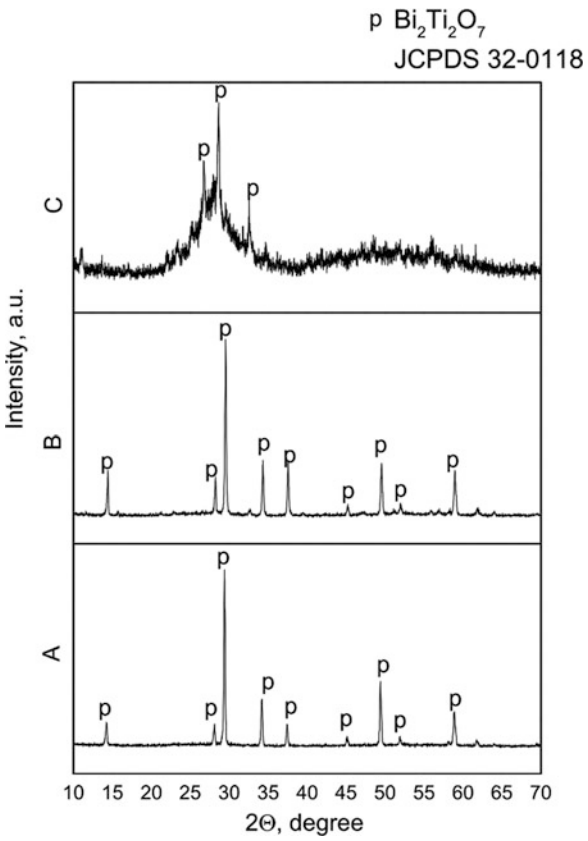

Fig. 36.1 XRD patterns of samples **a**, **b** and **c**

36.3 Result and Discussion

According to the X-ray patterns the samples haves the same mono-phase composition, i.e. $Bi_2Ti_2O_7$ (Fig. 36.1). There are no different phases, but in sample C an amorphous halo is hinting at a possible amorphous structure. The SEM image in Fig. 36.2c shows that an amorphous glass structure is observed with addition of a small amount of crystals, in contrast to the other two examined samples A and B having a dense crystalline microstructure (Fig. 36.2a, b). In these samples well-defined boundaries between crystalline structures are formed. For sample B the cubic pyrochlore microstructure (according the XRD data) is ordered on a separated layer, while the structure in sample A is randomlike.

More details of the structure can be discovered by infrared spectra (FTIR from 400 to 1400 cm^{-1}). The spectra of selected samples (Fig. 36.3) include the vibrational frequencies of the phases detected by X-ray and also of the units of the amorphous network between them.

In a number of studies Kojima et al. [9–13] defscribed a series of bismuth layered compounds with bands about 820 cm^{-1}, 537 cm^{-1} at 615 cm^{-1} which we observed

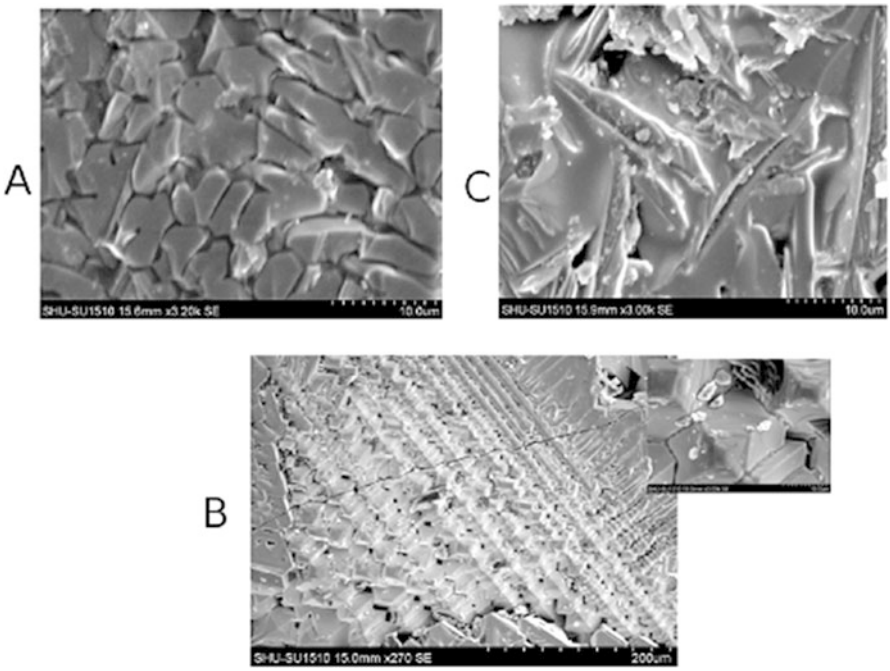

Fig. 36.2 SEM observations of samples: **a**, **b** and **c**

in all the three studied samples (Fig. 36.3). In parallel the band around 830 cm^{-1} can be associated with the symmetric vibrations, that around 600 cm^{-1} to asymmetric and deformation vibrations of the Ti-O linkages in TiO_6 octahedrona [14], typical for the same type of compounds. In sample A the bands near 832 and 1112 can, according to Roy [15] be assigned to an appearing of antisymmetric stretching vibrations of the Si-O-Si networks and also of deformed SiO_4 polyhedral units (broken Si-O-Si – linkages with a band around 906 cm^{-1}); in contrast the vibration of Si-O-Al can be found for sample B. The reduction of the Si-O-Si bands in sample B compared to sample A may be due, on the one hand, to the reduction of the SiO_2 content in the starting composition and, on the other hand, to the reaction of the Si-O groups with Al of the crucible. For all three compositions, the band at 480 cm^{-1} is associated to TiO_6 and BiO_6; both are typical of the cubic pyrochlore blocks. Increasing the amount of SiO_2 to 50 mol% in the starting composition without any quantity of TiO_2 in sample C initiates the formation of a multi-component amorphous matrix containing BiO_6 (480 cm^{-1}), Bi-O-Bi linkages (463 cm^{-1}, 448 cm^{-1}) as well as depolymerized SiO_4 groups (811 cm^{-1}, 892 cm^{-1}) which is confirmed in the works of Todea and Simon [16]. In our previous work [17] we have prepared glass with elements of crystalline phases with a controlled TiO_2 content by supercooled melts. In the glass-ceramic sample C (with the participation of a crystaline pyrochlore $Bi_2Ti_2O_7$ phase) the nontraditional glass formers with absence or minimal content of expected Si-O-Si-linkages (1034 cm^{-1}, 1098 cm^{-1}) forms solid

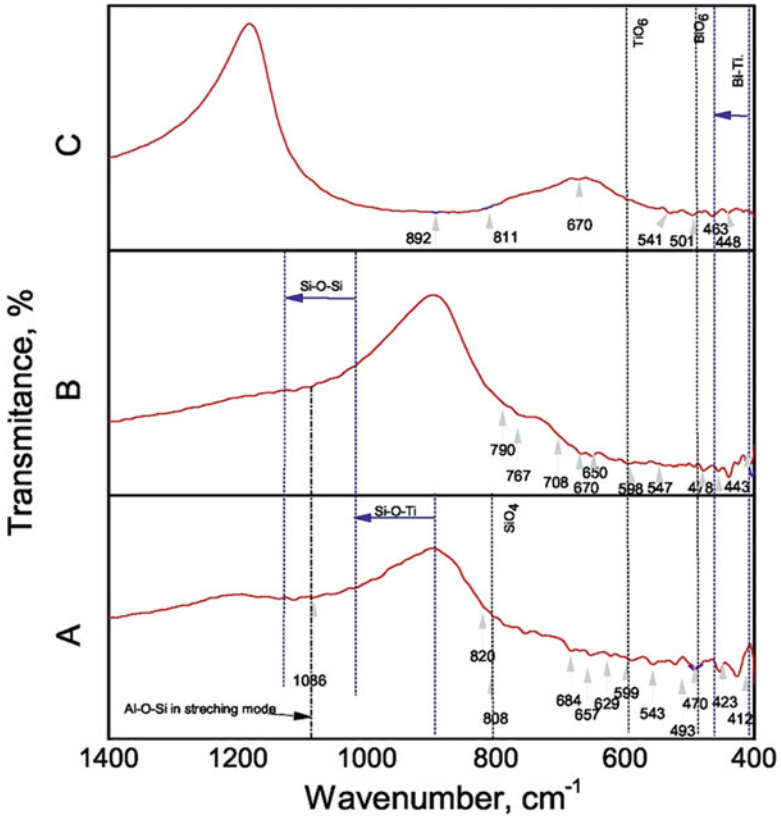

Fig. 36.3 IR spectra of samples **a**, **b** and **c**

solutions (as is described in a few works [18, 19]) of polyhedral BiO_6 and tetragonal polymerized SiO_4 groups. The samples thus described are a good start for future dielectric studies and future applications due to the combination of the mono-crystalline phase – the bismuth-titanate pyrochlore with different compositions – and a quantity amorphous phases.

36.4 Conclusions

As a result from this work, the following conclusions can be drawn:

1. We were managed to synthesized pure $Bi_2Ti_2O_7$ phases in the investigated system Bi_2O_3-TiO_2-SiO_2-Nd_2O_3 using free cooling from the melt;
2. Bonding of cubic pyrochlore blocks structures in line-stacked layers of the phase $Bi_2Ti_2O_7$ was obtained;

3. A glass-crystalline sample was obtained with the participation of a $Bi_2Ti_2O_7$ phase and non-traditional glass former such as Bi_2O_3 and polymerized SiO_4 octahedrals.

Acknowledgments This work was financially supported by Swap and Transfer, Erasmus Mundus Action 2 Mobility Lot 12, Grant ID number SAT-2542.

References

1. Pineda-Flores JL, Chavira E, Reyes-Gasga J, Gonzalezc AM, A. (2003) Huanosta-Tera, synthesis and dielectric characteristics of the layered structure $Bi_{4-x}R_xTi_3O_{12}$ (R_x=Pr, Nd, Gd, Dy). J Eu Ceram Soc 23:839–850
2. Buhay H, Sinharoy S, Kasner WH, Francombe MH, Lampe DR, Stepke E (1991) Pulsed laser deposition and ferroelectric characterization of bismuth titanate films. Appl Phys Lett 58:1470
3. Huanosta A, Alvarez-Fregoso O, Amano Mexico E, Tabares Munoz C, Mendoza-Alvarez ME, Mendoza-Alvarez JGME (1991) AC impedance analysis of crystalline layered and polycrystalline bisnuth titanate. J Appl Phys 69:404
4. Yamamoto JK, Bhalla AS (1991) Microwave dielectric properties of layered perovskite $A_2B_2O_7$ single-crystal fibers. J Matt Lett 10(11, 12):497–500
5. Lee CK, Kim WS, Park H-H (2004) Structural and electrical properties of $Nd_2Ti_2O_7/Y_2O_3$/Si structures through interface treatment. Thin Solid Films 155–159. https://doi.org/10.1016/j.tsf.2004.06.020
6. Bian JJ, Song GX, Yan K (2008) Structure and microwave dielectric properties of $Nd_{(2-x)/3}Li_xTiO_3$. Ceram Int 34:893–896. https://doi.org/10.1016/j.ceramint.2007.09.054
7. Hector AL, Wiggin SB (2004) Synthesis and structural study of stoichiometric $Bi_2Ti_2O_7$ pyrochlore. J Solid State Chem 177:139–145. https://doi.org/10.1016/S0022-4596(03)00378-5
8. Murugan GS, Subbanna GN, Varma KBR (1999) Nanocrystallization of ferroelectrics bismuth unstated in lithium borate glass matrix. Mater Sci Lett 18:1687–1690
9. Kojima S, Hushur A, Jiang F, Hamazaki S, Takashige M, Jiang M, Shimada S (2001) Crystallization of amorphous bismuth titanate. J Non-Cryst Sol 293–295:250
10. Kojima S, Shimada S (1996) Soft mode spectroscopy of bismuth titanate single crystals. Physica B 219–220:617
11. Kojima S, Tsumura N, Takeda M, Nishiava S (2003) Far-infrared phonon-polariton dispersion probed by terahertz time-domain spectroscopy. Phys Rev B 67:035–102
12. Kojima S, Imaizumi R, Hamazaki S, Takashige M (1995) Raman study of ferroelectric bismuth layer-oxides ABi4Ti4O15. J Mol Struct 37:348
13. Kojima S, Imaizumi R, Hamazaki S, Takashige M (1994) Raman scattering study of bismuth layer-structure ferroelectric. Jpn J Appl Phys 33:5559
14. Du Y, Zhang M, Chen Q, Yin Z (2003) Investigation of size-driven phase transition in bismuth titanate nanocrystals by Raman spectroscopy. Appl Phys A Mater Sci Process 76:1099
15. Roy J, Bandyopadhyay N, Das S, Maitra S (2011) Studies on the formation of mullite from diphasic Al_2O_3-SiO_2 gel by fourier transform infrared spectroscopy. Iran J Chem Chem Eng 30:1
16. Todea M, Simon S (2007) Vibrational spectroscopic study on iron doped silica-bismuthate glasses and glass ceramics. J Optoelectron Adv Mater 9(3):621
17. Slavov S, Dimitriev Y (2016) Glass formation in the system Bi_2O_3-TiO_2-SiO_2. J Chem Technol Metall 51(5):536–546
18. Stanek CR, Minekviki Z, Grimes RW (2002) Nonstoihiometry in $A_2B_2O_7$ pyrochlores. J Am Ceram Soc 85(11):792–798
19. Minekvini Z, Grimes RW (2008) Disorder in pyrochlore oxides. J Am Ceram Soc 83 (8):1873–1878

Part IX
Applications: Sensors and Detectors

Chapter 37
Application of Sm Oxide Doped Oxyfluoride Glasses for the Development of Extrinsic Fibre Optical X-Ray Sensors

T. Eftimov, D. Tonchev, I. Kostova, G. Patronov, and T. Pashova

Abstract The fabrication and optical properties of Sm oxide doped oxyfluoride glasses and their spectral response to X-ray radiation are presented. We report on the observation of a spectrally dependent, radiation induced attenuation of the radio and photo luminescence spectra which follow a power law with different fitting parameters. The spectral maxima in the visible attenuate differently during irradiation which permits the development of extrinsic sensors in which scintillation responses and fluorescence from laser excitation are observed separately using time multiplexing. Due to substantially different time scaling parameters lower doses can be measured using fluorescence while larger doses can be measured using the spectrally differentiated scintillation responses.

Keywords Sm oxide · Oxyfluoride glasses · Optical fibre · X-ray sensors

37.1 Introduction

Optical fiber radiation sensing technology has developed significantly in the last two decades, and a variety of sensing principles and fibre-based radiation sensors have been proposed [1, 2]. The application areas are absorbed dose measurement in radiotherapy, spatial dose distribution in linear accelerators, radiation dosimetry in computed tomography, remote monitoring of radioactive contamination and radioactive waste, radiation protection and monitoring of nuclear installations,

T. Eftimov (✉)
Université du Québec en Outaouais, 101 St. Jean Bosco St., Gatineau, QC J8X 3X7, Canada
e-mail: tinko.eftimov@uqo.ca

D. Tonchev
University of Saskatchewan, Saskatoon, SK, Canada

University of Plovdiv "Paisij Hilendarski", Plovdiv, Bulgaria

I. Kostova · G. Patronov · T. Pashova
University of Plovdiv "Paisij Hilendarski", Plovdiv, Bulgaria

P. Petkov et al. (eds.), *Advanced Nanotechnologies for Detection and Defence against CBRN Agents*, NATO Science for Peace and Security Series B: Physics and Biophysics, https://doi.org/10.1007/978-94-024-1298-7_37

neutron or mixed gamma-ray neutron dosimetry, sterilization of medical instrumentation, measurement of gamma radiation in food industry, etc. [1, 2].

The advantages of using of both silica and plastic optical fibers in sensing technology has been widely recognized; optical fibers in radiation sensing have been used both as sensing elements and/or light-guiding medium to a radiation sensing element. In the former case we have intrinsic, in the latter extrinsic fiber optic sensors (see Table 37.1). In both of them sensing is based on radiation induced effects in materials based on the interaction of highly energetic radiation and matter, either fibers or other materials. Highly energetic radiation includes: (i) uncharged particles such as UV photons, gamma- and X-rays; (ii) charged particles (electrons, positrons, ions) and (iii) constituents of the nucleus (neutrons, protons).

Intrinsic fiber optic sensors are based on changes in the transmission (losses) or on light emission from fibers [3–9]. The effects are: (i) radiation induced attenuation (RIA) which depends on the fiber dopants, glass type, thermal stresses, fabrication technology, type of radiation and irradiation conditions, etc.; (ii) Cerenkov radiation in the UV caused by charged particles travelling at a velocity greater than the phase velocity in the medium; (iii) radiation induced luminescence (RIL) in the visible superimposed on the Cerenkov radiation [1]; and (iv) refractive index changes under ionizing radiation [1], which also affects the fiber Bragg grating (FBG) spectrum [5]. Specially doped fibers can be made to exhibit increased transmission spectrally dependent losses (color changes) [5], or to scintillate by embedding a Gd_2O_2S:Tb phosphor in PMMA (polymethyl methacrylate) plastic fibres [8]. The advantages of intrinsic sensors are that they can measure radiation at single or multiple points and also for an arbitrary spatial distribution by making use of optical time domain reflectometers (OTDR) [4].

Extrinsic fibre optic sensors are based on the use of an external transducer converting high energy alpha, beta and gamma radiation into optical radiation [1, 10–16]. Although optical fibers are used only as lead-in and lead-out components, depending on the application field, the length of the lead fibers and the particular installation, and radiation effect characteristics of optical fibers can influence the performance of extrinsic sensors.

Extrinsic sensors are based on the use of scintillation, thermoluminescence or optically stimulated luminescence in specific materials. Scintillation is a process in

Table 37.1 Comparative table between intrinsic and extrinsic fiber optic sensors

Fiber optic sensors	
Intrinsic sensors	Extrinsic sensors
Radiation induced absorption (RIA):	Scintillation:
Point sensors	Organic
Distributed sensing (OTDR)	Inorganic
Radiation induced luminescence (RIL)	Thermolunimescence (TL)
Cerenkov radiation	Optically stimulated luminescence (OSL)
Refractive index changes	
Fiber Bragg gratings	

which high energy radiation is converted into an optical radiation in the UV-visible spectral range by a material called a scintillator. Optically stimulated luminescence (OSL) is observed when a material pre-exposed to ionizing radiation and then further subjected to an appropriate optical stimulation, emits a light signal proportional to the absorbed dose at a wavelength characteristic of the OSL material. OSL is analogous to thermo-luminescence (TL) process in which the stimulation is carried out thermally rather than optically. The principles of operation of both types of sensors are compared in Table 37.1.

In this paper we consider the application of Sm oxide doped oxyfluoride glasses for the development of extrinsic fibre optical X-ray radiation sensors.

37.2 Extrinsic Fiber Optic Radiation Sensors

37.2.1 Overview and Classification

As outlined above extrinsic fiber optic sensors are offering specific advantages compared to intrinsic sensors, and a large variety of them has been proposed depending on the type of application, sensing principle, material, construction etc.

One classification can be by the type of scintillating material which can be organic as BSF-60 [1] or inorganic like La_2O_2S:Eu, La_2O_2S:Tb, $Y_3Al_5O_{12}$:Ce, Gd_2O_2S:Eu, Gd_2O_2S:Pr, CaWO4, ZnS:Ag, Tb used in combination with phosphorus [8, 10, 11, 14].

Extrinsic FO sensors can also be grouped according to the type of radiation measured as single radiation and combined sensors. The former are basically intended to detect a particular type of high energy radiation. For example electron detection based on absorption and fluorescence has been studied [3], or a gamma sensor using higher efficiency BGO (Bismuth Germanate – $Bi_4Ge_3O_{12}$) with a plastic optical fiber [1], X-ray detection [8–12], and also UV radiation [16]. Combined radiation sensors, on the other hand, allow for the separate measurement of different types of radiation. Gamma-ray was detected with a BCF-20 Saint Gobin scintillating material, and thermal neutrons were separately detected using ^{6}Li converters [1]. Also a combined extrinsic fiber optic sensor for the measurement of gamma and UV radiation has been proposed [15].

The extrinsic sensors can be configured as a single sensor and as multichannel devices [13] with up to 80 accessible scintillations, or multiple sensors (coherent bundles); or scintillating fiber optic gamma endoscopes [15].

A grouping by the principle of operation can subdivide them in those which mostly employ a single type of phenomenon, and those using a combination of sensing principles so as to improve performance. Thus radioluminescence in a scintillating fiber providing a fast signal for timing and radiation induced absorption in a Ge-doped silica fiber have been used [4] to develop an X-ray burst detector for space applications [9].

We describe here the performance of Sm oxide doped oxyfluoride glasses when irradiated by X-rays and the possibilities they offer to develop combined compact extrinsic fiber radiation sensors using spectrally selective X-ray induced attenuation of radioluminescence and fluorescence.

37.2.2 *Synthesis and Properties of Sm Oxide Doped Oxyfluoride Glasses*

The base system $ZnO\text{-}ZnF_2\text{-}P_2O_5\text{-}B_2O_5$ was investigated by varying the composition, doping with different amounts of samarium (Sm) and other rare earth (RE) elements with examination of the obtained materials using a combination of techniques such as:

- X-ray powder diffraction
- Thermal analysis (DSC and TMDSC)
- UV fluorescence
- X-ray fluorescence.

For the realization of this study $ZnO - ZnF_2 - P_2O_5 - B_2O_3$ compositions were synthesized. In the first stage, the approach is the introduction of equal amounts of zinc oxide and zinc fluoride by keeping their total molar content constant, and variation of the content of samarium oxide (Sm_2O_3) and samarium fluoride (SmF_3) with a progressive increase of their contents in the zinc – boro – phosphate system (samples 1–7 of Table 37.2). In the second stage, after determining the appropriate amount of Sm system only the influence of zinc fluoride is monitored (samples 8–11 in Table 37.2). Thus nine samples with the compositions given in Table 37.2 were synthesized. In addition, two more samples are given for comparison. For the synthesis of the first only ZnF_2 was used, for the synthesis of the second only ZnO.

Table 37.2 List of the samarium doped zinc phosphate samples [17]

№	ZnO	ZnF_2	B_2O_3	P_2O_5	Sm_2O_3	SmF_3	T_g, °C
1	–	71.81	18.00	9.69	–	0.500	–
2	71.81	–	18.00	9.69	–	0.500	537
3	36.03	36.03	18.00	9.69	0.125	0.125	505
4	35.90	35.90	18.00	9.69	0.250	0.250	500
5	35.60	35.60	18.00	9.69	0.175	0.175	531
6	36.08	36.08	18.00	9.69	0.075	0.075	499
7	36.13	36.13	18.00	9.69	0.025	0.025	528
8	64.85	7.21	18.00	9.69	0.125	0.125	533
9	57.65	14.41	18.00	9.69	0.125	0.125	531
10	50.44	21.62	18.00	9.69	0.125	0.125	518
11	43.24	28.82	18.00	9.69	0.125	0.125	504

All concentrations are given in mol%

According to lines 3–7 Table 37.2, the first composites examine the content of samarium compounds. The resulting compositions provide information on the optimum content of rare earth elements in terms of transparency. It has been found that composition 3 containing 0.125 mol% of both dopant components is a transparent and homogeneous glass as evidenced in Fig. 37.6. For this reason, the second compositional series (8–11) is based on this Sm_2O_3/SmF_2 (Fig. 37.1) content. The glass transition temperatures of the first set of samples (3–7) shown in the table were determined by thermal analysis; as can be seen, they are in the range 485–514 °C without a linear correlation to the content of rare earth ions.

37.2.3 Optical Properties

The set-up consists of a light source, a sample and a detection system. The light source is a combination of a Deuterium and a Halogen lamp, providing a spectrum in the 200–2500 nm range for transmission and absorption measurements, and semiconductor light emitting diodes (LEDs), emitting at 370 nm, 395 nm, 420 nm and 450 nm to pump directly the sample under study for fluorescence measurements.

The basic element of the experimental set-up is the correctly positioned sample of the Sm^{3+}: $ZnO\text{-}ZnF_2\text{-}P_2O_5\text{-}B_2O_3$ glass. The sample is placed in a special holder with its parallel polished planes in the direction of the transmission and the side polished plane at 90° to pick up fluorescence. The holding jig allows manipulation and orientation of the sample for the different regimes of measurements.

The photoluminescence spectra were measured by optical CCD Avantes spectrometer Avaspec 2048.

Representative emission and absorption spectra of the synthesized sample are illustrated in Figs. 37.2 and 37.3. All Sm-doped samples display photoluminescence, in contrast to undoped samples (not shown). Typical photoluminescence of Sm^{3+} ions is observed with three emission bands corresponding to the following transitions:

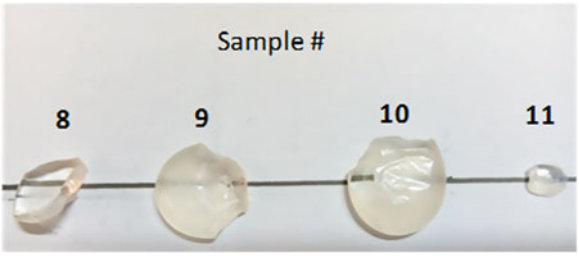

Fig. 37.1 The high content of Sm_2O_3 changes the appearance of the samples due to occurring structural rearrangements

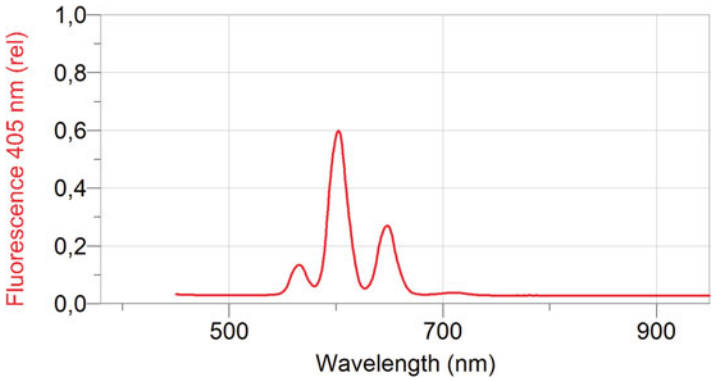

Fig. 37.2 Representative emission spectrum for sample 8

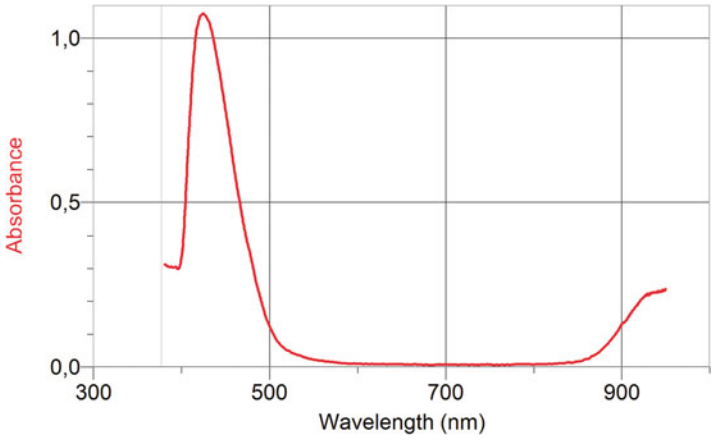

Fig. 37.3 Absorption spectrum for sample 8

564 nm – $^4G_{5/2} \rightarrow {}^6H_{5/2}$
600 nm – $^4G_{5/2} \rightarrow {}^6H_{7/2}$
645 nm – $^4G_{5/2} \rightarrow {}^6H_{9/2}$

The band at 600 nm corresponding to orange emission is the most intense.

The amorphous nature of composition 3 is indicated by X-ray diffraction analysis performed (Fig. 37.4). In the pattern of this sample the presence of an amorphous state with low intensity peaks is observed. These peaks are also clearly visible in the X-ray diffraction pattern of the sample with composition 4 which has a crystalline structure (Fig. 37.5).

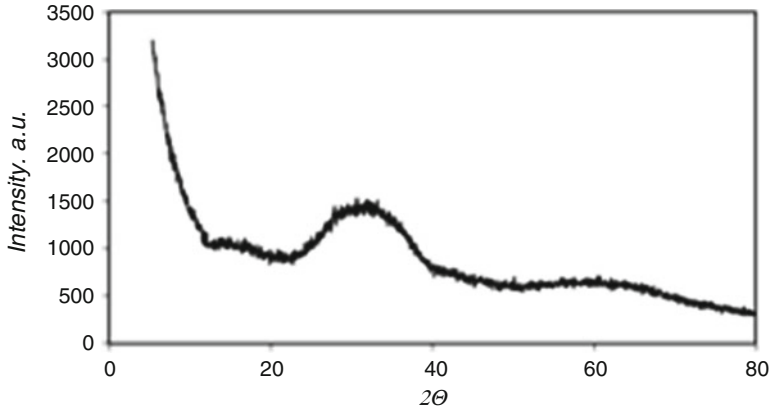

Fig. 37.4 X-ray diffraction pattern of sample 3

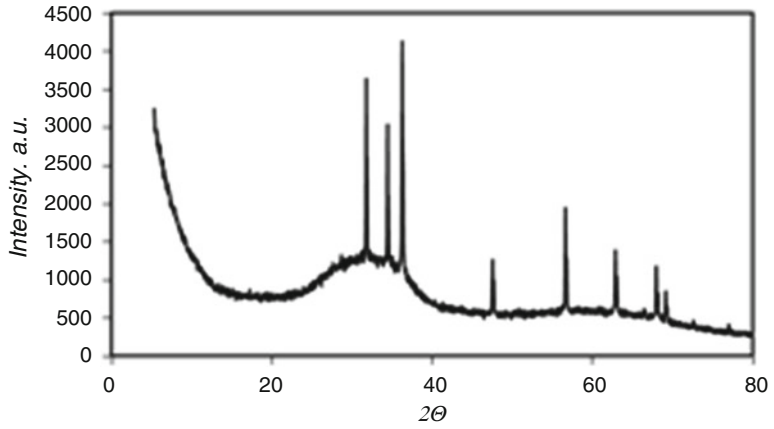

Fig. 37.5 X-ray diffraction pattern of sample 4

37.3 Application of Sm Oxyfluoride Glasses for the Development of Extrinsic X-Ray Fibre Sensors

37.3.1 Spectrally Dependent X-Ray Induced Attenuation in Sm Oxide Doped Oxyfluoride Glasses

For the purpose of developing X-ray sensors, the behaviour of Sm ions on the emission spectra during and after X-ray irradiation has been studied. Sample 3 was irradiated at the Canadian Synchrotron (CLS Canadian Light Source) for different time intervals (15 μs, 30 μs, 120 μs, 300 μs and 600 μs) with a dose rate of 110 Gy/min. Overall attenuation and spectral changes were observed. X-radiation causes a darkening of the sample caused by increased absorption as is evidenced in Fig. 37.6.

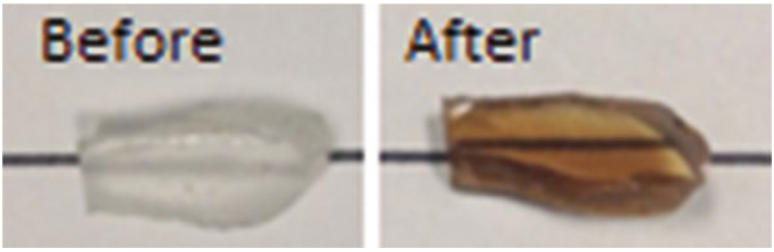

Fig. 37.6 A Darkening of Sm doped oxyfluoride glasses (sample 3) under X-ray exposure

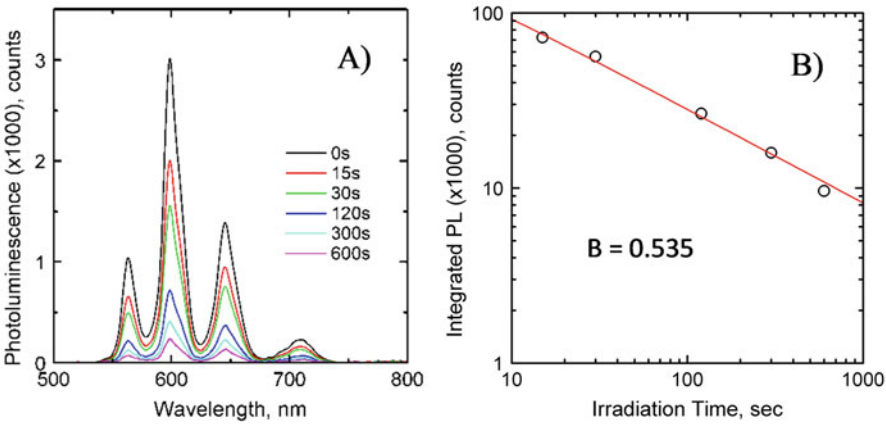

Fig. 37.7 Fluorescence spectra (**a**) and integrated signals (**b**) of sample 3 for different irradiation durations

Photoluminescent spectra of the sample after exposure for different time durations is shown in Fig. 37.7a. A blue laser with a wavelength of 460 nm was used as an excitation source. From this figure a reduction of the intensity of the photoluminescence under continuous irradiation with X-ray radiation is seen. Figure 37.7b shows a double logarithmic plot of the total integrated photoluminescence signal reduction with irradiation time. Based on these results the so-called constant attenuation B was calculated, which provides information on the stability of the test substance against X-ray radiation. The value of B for the sample with the composition 3 is $B = 0.535$, indicating that the sample is relatively resistant to radiation.

The X-ray luminescence spectra of sample 3 during irradiation with X-rays are presented in Fig. 37.8a. Figure 37.8b shows the integrated X-ray luminescence signal vs. irradiation duration. The dose at which the sample was irradiated is 1.3 Gy/s. The curve shows good stability of the sample under irradiation ($B = 0.171$).

In Fig. 37.8a there is a splitting of the peak at about 700 nm, unlike in Fig. 37.7a, where it is slanting. This effect is an indication of the formation of samarium ions of the second valence during irradiation, which are not present any more after removal of the X-ray source.

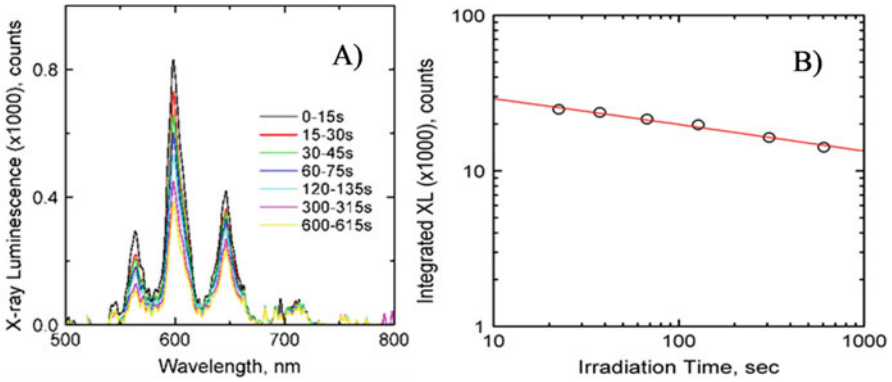

Fig. 37.8 Luminescence spectra (**a**) and integrated signals (**b**) of sample 3 for different irradiation durations

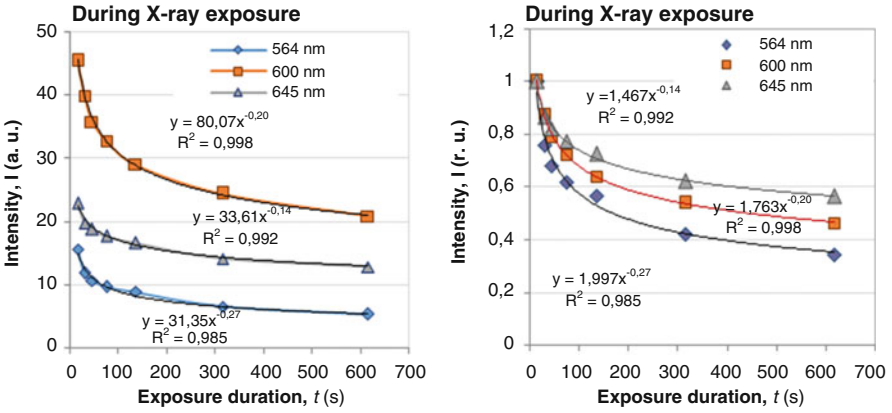

Fig. 37.9 Plots (experimental data in points) and power law fits (lines) for X-ray irradiation. (**a**) Intensity attenuation curve; (**b**) normalized to unity attenuation curves

Figures 37.7b and 37.8b definitely suggest a power law decrease of the spectrally integrated overall intensity for both photoluminescence (fluorescence) and X-ray induced luminescence (scintillation) with different characteristic parameters. Nevertheless, a closer inspection of the spectral fluorescence changes in Fig. 37.7 and of the X-ray induced scintillation in Fig. 37.8 provides reasons for an application of these glasses for the development of extrinsic optical fiber X-ray sensors.

A plot of the intensity decrease with time for the scintillation is shown in Fig. 37.9a. It clearly reveals a spectrally dependent attenuation of for each of the fluorescence peaks at 564 nm, 600 nm and 645 nm during X-ray exposure. To compare the different rates of attenuation increase a normalized plot is shown in Fig. 37.9b. The decrease of scintillation proves to follow a power law dependence.

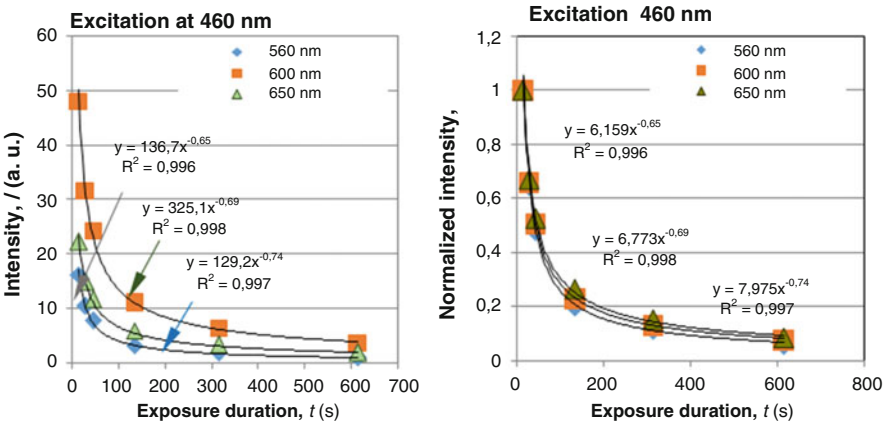

Fig. 37.10 Plots (experimental data in points) and power law fits (lines) for the decrease of the fluorescence intensity of each peak for blue light irradiation at 460 nm: (**a**) intensity attenuation curves; (**b**) normalized to unity attenuation curves

Analogously, the spectral attenuation for each peak shown Fig. 37.10b for a 460 nm laser exposure is also wavelength dependent but develops faster in time, and the differences are far less pronounced.

37.3.2 Possibility of Developing Extrinsic Fiber Optic X-Ray Sensors

The intensity and the normalized intensity curves are found to be best fitted by a power law in the form

$$I = I_0 \cdot t^{-\alpha} \tag{37.1}$$

where I_0 is the initial intensity.

This equation can be rewritten in a normalized form as:

$$I = \left(\frac{t}{\tau}\right)^{-\alpha} \tag{37.2}$$

where the time scaling parameter τ is related to the initial intensity I_0 and the power α as:

$$\tau = I_0^{1/\alpha} \tag{37.3}$$

The values of the fitting parameters parameter I_0 and α and the time scaling parameter τ are given in Table 37.3.

Table 37.3 Values of the parameters α, I_0 and the time scaling parameterτ in the case of X-ray irradiation

λ (nm)	α	I_0	τ
645	0.1488	1.4679	13.1908 s
600	0.2079	1.7637	15.3216 s
564	0.271	1.997	12.8353 s

Table 37.4 Values of the parameters α, I_0 and the time scaling parameterτ in the case of 460 nm irradiation.

λ (nm)	α	I_0	τ
650	0.6522	6.1592	16.2388 s
600	0.6899	6.7734	16.0045 s
560	0.7461	7.9753	16.1664 s

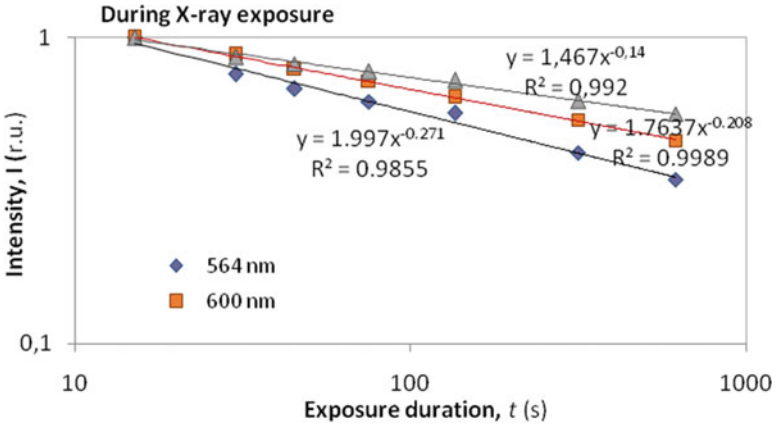

Fig. 37.11 Double logarithmic plot of the power law plots in Fig. 37.9

Using the values for τ and α we used (37.2) and (37.3) for each spectral component and plot the theoretical fit and compare with the experimental data shown in Fig. 37.9 and in Fig. 37.10. The power and time scaling fitting parameters for the from Fig. 37.8 and Fig. 37.10 are provided in Table 37.3 and Table 37.4 respectively.

The normalized curves in Figs. 37.9 and 37.10 show that the loss of transparency is wavelength dependent, both the power α and the time-scaling parameters τ are wavelength dependent and hence $\alpha(\lambda)$ and $\tau(\lambda)$. A log-log plot for scintillation decrease is shown in Fig. 37.11. These plots are the spectral components of the integrated signal drop shown in Fig. 37.9b.

We first note that as a whole the scintillation intensity, measured over a 15 s time period, is considerably weaker than that of fluorescence. Second, we note that the fluorescence intensity drops much faster compared to scintillation intensity. The time scaling parameters for the three spectral components of fluorescence are all around 16 s vs. 12.83–15. 32 s for scintillation.

Third we note that the spectral differences in the attenuation behaviour for scintillation vary much more compared to fluorescence. Thus, the power parameter α for fluorescence reduction during X-ray exposure varies by a factor of almost 2 for 564 nm and 645 nm.

This temporal behaviour means that the observation of the spectrally differential reduction in fluorescence can be used to measure X-radiation over a large range of time intervals.

For example, it takes about 40 s for the fluorescent signal to drop to the 0.6 level from the initial intensity while for scintillation it takes about 85 s at 564 nm, about 180 s at 600 nm and about 400 s at 645 nm. This practically means that if both the scintillation and the fluorescence spectra are monitored, the faster responses of fluorescence can be used to track X-ray doses over shorter intervals of time while the two to ten times slower responses of scintillation decrease can be used to measure larger doses accumulated over longer periods of time with the same accuracy. For such longer durations, further changes of intensity drop of fluorescence will be too weak for measurements with the same accuracy.

A suitably shaped Sm doped glass sample can be attached to the extremity of a large core glass or plastic optical fiber which is both a lead-in fiber for laser induced fluorescence and a lead-out fiber for both spectral scintillation and fluorescence measurements. The sensor tracks spectral scintillation changes and the laser (or LED) is switched on over shorter intervals of time to track faster occurring changes. Scintillation and fluorescence measurements are thus time multiplexed in a combined fiber optic extrinsic sensor.

37.4 Conclusions

We have analyzed the structural and optical properties of Sm doped oxifluoride glasses and studied their fluorescence and X-ray luminescence spectra. It has been found the fluorescence intensity decreases faster in time with irradiation while scintillation decreases with a slower rate. It has also been found that X-ray induced scintillation reduces at different rates for the different spectral maxima. Both fluorescence and scintillation attenuation follow a power law time dependence which is strongly wavelength dependent. These observations allow the development of extrinsic optical fiber sensors in which both scintillation and fluorescence spectra are analyzed, and the signals are time multiplexed. Fast fluorescence attenuation allows for smaller doses to be measured while the slower spectrally dependent scintillation attenuations allow for larger doses to be measured with the same accuracy.

Acknowledgments Acknowledgments The authors are grateful to Professor Safa Kasap, DSc, George Belev, PhD and Go Okada, PhD from University of Saskatchewan and CLS, Saskatoon, Canada.

References

1. Sporea D, Sporea A, O'Keeffe, McCarthy D, Lewis E (2012) Chapter 23: Optical fibers and optical fiber sensors used in radiation monitoring. In: Moh Yasin D (ed) Selected topics on optical fiber technology. INTECH, pp 607–652
2. Woulfe P, Sullivan FJ, O'Keeffe S (2016) Optical fibre sensors: their role in in vivo dosimetry for prostate cancer radiotherapy. Cancer Nano 7:7
3. Kir'yanov A (2016) Chaper I: Radiation effects in materials, 'Effects of electron irradiation upon absorptive and fluorescent properties of some doped optical fibers'. In: Monteiro WA (ed) Radiation effects in materials, pp 3–36
4. Henschel H, Körfer M, Wittenburg K, Wulf F (2000) Fiber optic radiation sensing systems for TESLA. TESLA Report No. 2000-26, pp 1–11
5. Avino S, D'Avino V, Giorgini A, Pacelli R, Liuzzi R, Cella L, Natale PD, Gagliardi G (2015) Ionizing radiation detectors based on Ge-doped optical fibers inserted in resonant cavities. Sensors 15:4242
6. O'Keeffe S, Lewis E (2009) Polymer optical fibre for in situ monitoring of gamma radiation processes. Int J Smart Sens Intell Syst 2:490
7. Tomashuk A, Grekov M, Vasiliev S, Svetukhin V (2014) Fiber-optic dosimeter based on radiation induced attenuation in P-doped fiber: suppression of post-irradiation fading by using two working wavelengths in visible range. Opt Express 22:16778
8. Sporea D, Mihai L, Vâță I, McCarthy D, O'Keeffe S, Lewis E (2014) Characterization of scintillating x-ray optical fiber sensors. Sensors 14:3445
9. Moss C, Casperson D, Echave M, Edwards B, Miller J, Saylor W, Sweet M, Valencia J (1994) A space fiber-optic x-ray burst detector. IEEE Trans Nucl Sci 41:1328
10. O'Keeffe S, Zhao W, Sun W, Zhang D, Qin Z, Chen Z, Ma Y, Lewis E (2016) An optical fibre-based sensor for real-time monitoring of clinical linear accelerator radiotherapy delivery. IEEE J Sel Top Quantum Electron 22:5600108
11. Lee BS, Hwang YM, Cho HS, Kim S, Cho S (2004) Fabrication of fiber-optic radiation sensor tips with inorganic scintillator for remote sensing of X or γ – ray. In: Nuclear science symposium conference record, Rome 865
12. McCarthy D, O'Keeffe S, Lewis E, Sporea D, Sporea A, Tiseanu I, Woulfe P, Cronin J (2014) Radiation dosimeter using an extrinsic fiber optic sensor. IEEE Sensors J 14:673
13. Becks K, Drees J, Goldmann K, Gregor I, Heintz M (2000) A multichannel dosimeter based on scintillating fibers for medical applications. Nucl Inst Methods Phys Res A 454:147
14. Darafsheh A, Zhang R, Kanick S, Pogue B, Finlay J (2015) Spectroscopic separation of Cerenkov radiation in high-resolution radiation fiber dosimeters. J Biomed Opt 20(9):095001
15. Kim M, Yoo W, Lee B (2017) Development of a fiber-optic gamma endoscope to measure both optical and gamma images in a confined space. Opt Express 25:20087
16. Jože A, Bajić J, Stupar D, Slankamenac M, Jelić M, Živanov M (2012) Simple and low-cost fiber-optic sensors for detection of UV radiation. Telfor J 4:133
17. Tonchev D, Kostova I, Okada G, Pashova T, Belev G, Patronov G, Eftimov T, Wysokinski T, Chapman D, Kasap SO (2015) Samarium doped borophosphate glasses and glass-ceramics for X-Ray radiation sensing. In: Petkov P et al (eds) Nanoscience advances in CBRN agents detection, information and energy security, NATO science for peace and security series a: Chemistry and biology. Springer, Dordrecht, p 347

Chapter 38
MWCNT/PANI Screen Printed Electrodes for Gas Sensors

Gorazd Chepishevski, Aleksandar Petrovski, Anita Grozdanov, Perica Paunović, Aleksandar T. Dimitrov, Gennaro Gentile, and Maurizio Avella

Abstract During the last 10 years, CNT based nanocomposites belong to a group of new materials that have intensively been tested for gas sensing, and great efforts have been spent for the development of gas sensors. The construction of SO_x sensors is an important task because SO_x containing oxides are dangerous having a negative influence on the environment and humans. Most of the literature data are related to MWCNTs based sensors for gases such as water vapors, NH_3, CO_2 and CO. In the present work, a promising application of screen printed electrodes with MWCNT/PANI nanocomposites prepared by a direct electro-polymerization method as a gas sensor was tested. Resistivity variations were found for different acid concentration. Surface changes of the SPE sensors before and after acid exposure, were followed by SEM. Polymer/CNTs interactions and their changes due to the acid vapors were studied by FTIR-ATR spectroscopy. The obtained results confirmed polymer/CNT – SO_4^{2-} interactions and their characteristic band-shifting. SEM photos show the formation of typical oxid nanorods.

Keywords Nanocomposites · PANI · Multiwalled carbon nanotubes · Gas sensor

38.1 Introduction

In the last decade, gas sensors were in the focus of the researchers due to their extensive applications in industry and environmental monitoring. Gas-sensing materials mainly include semiconducting metal oxides, vapor sensitive polymers, porous silicon, etc. Based on the gas-sensing principle of adsorption/desorption of target gas

G. Chepishevski · A. Petrovski · A. Grozdanov · P. Paunović (✉) · A. T. Dimitrov
Faculty of Technology and Metallurgy, University "Ss Cyril and Methodius", Skopje, Macedonia
e-mail: pericap@tmf.ukim.edu.mk

G. Gentile · M. Avella
Institute for Polymers, Composites and Biomaterials, IPCB-CNR, Naples, Italy

P. Petkov et al. (eds.), *Advanced Nanotechnologies for Detection and Defence against CBRN Agents*, NATO Science for Peace and Security Series B: Physics and Biophysics, https://doi.org/10.1007/978-94-024-1298-7_38

molecules on the sensor surface, significant enhancement in sensitivity could be achieved by increasing the interfacial contact among the sensor surface and the target gases. Due to their excellent electron transport properties, multi wall carbon nanotubes (MWCNT) have proven their ability to be used as sensing material in conductometric gas sensors [1, 2].

Polyaniline (PANI) belongs to the group of the most important organic conducting polymers today due to several facts such as its facile synthesis and processing, environmental stability and low cost. Because of these advantages, PANI was selected for this study as a polymer matrix for nanocomposite sensors with MWCNTs. State-of-the-art literature has shown that PANI was widely applied as new sensitive layer for various gas sensors in chemiresistors and optical sensors since it exhibit significant electrical reesponses [3]. The tested gases include NH_3 [3], NO_x [4], H_2S [5], SO_2 [4], CO_2 [5], chloroform [6] and humidity [7]. It was also found that compared to other inorganic sensor materials (specially SnO_2), PANI films as gas sensitive material possess the advantage of high sensitivity to analytes at room temperature. He et al. [8] prepared polyaniline-coated MWCNTs via in situ polymerization for the detection of ammonia. They demonstrated a fast response and a good reproducibility at room temperature. A linear response was obtained for ammonia concentrations in the range from 0.2 to 15 ppm [8]. Zhang et al. [9] performed an electrochemical functionalization of CNTs with polyaniline. On-line detection of NH_3 was obtained by the PANI-CNT network based sensors. Its sensitivity $\Delta R/R$ was up to 2.44% per ppm NH_3, which was 60 times more than for pristine CNTs. The recovery time was in hours, the response time in minutes, while its sensitivity was high when the temperature was low. Lim et al. [10] investigated electrical and gas sensing properties of single-walled carbon nanotube networks functionalized with polyaniline (PANI–SWNTs) in order to understand the gas sensing mechanisms and to optimize the sensing performance. The temperature-dependent electrical resistance and field-effect transistor (FET) transfer characteristics indicated that the electrical properties of PANI–SWNTs were dominated by the PANI coating. The transfer characteristics of FETs exposed to different NH_3 concentrations indicated that the dominant sensing mechanism was the deprotonation of PANI by NH_3. Sensing experiments with different gas analytes revealed that PANI–SWNTs responded positively to NH_3, and negatively to NO_2 and H_2S with sensitivities of 5.8% per ppm_v of NH_3, 1.9% per ppm_v of NO_2, and 3.6% per ppm_v of H_2S.

The aim of this work is to produce and test a gas sensor based on MWCNT/PANI nanocomposite SPE electrodes using resistivity changes.

38.2 Experimental

Nanosensors based on screen printed electrodes (SPE) were prepared by direct electro-polymerization of polyaniline and MWCNT on the gold wires of the electrodes. Electro-polymerization was performed in an electrochemical cell using an electrolyte of 0,1 M aniline and 0,5 M H_2SO_4. A SPE was used as a working electrode, a saturated calomel electrode (SCE) as a reference one. MWCNT (3% wt) were dispersed into the electrolyte by ultra-sonication for 30 min.

Characterization of the SPE nanosensors, before and after the acid vaporization, was done by SEM and FTIR-ATR spectroscopy. FTIR-ATR spectra were collected by a Perkin Elmer-Spectrum 100 machine at 64 scans. The surface morphology of the electrodes was analyzed by FEI Quanta 200 scanning electron microscope, using a secondary electron detector and an acceleration voltage of 30 kV. The gas sensitivity was tested using resistivity measurements of the electrodes vaporized with different concentrations of H_2SO_4 (50%, 25%, 12.5%, 6% and 3%).

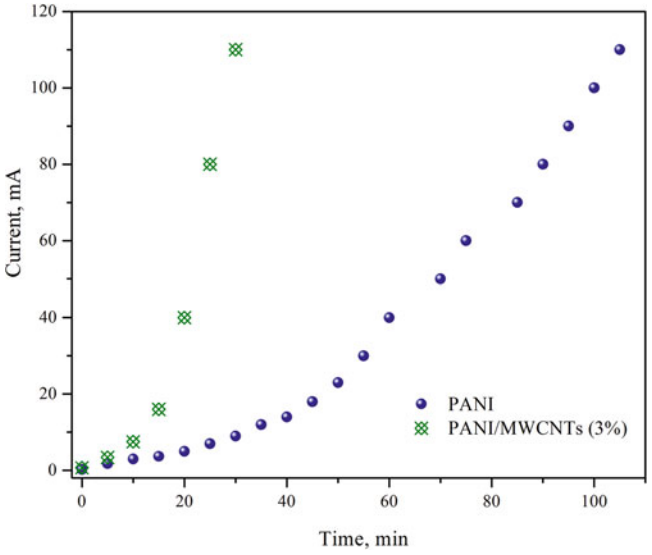

Fig. 38.1 Change of current density during electro-polymerization of PANI and PANI/MWCNT nanocomposites

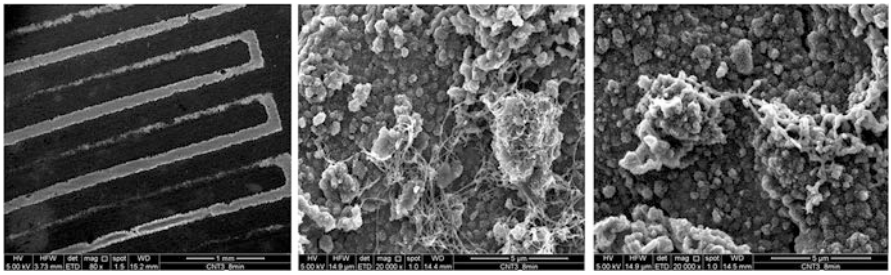

Fig. 38.2 SEM images of the studied 3%wt MWCNT/PANI sample: (**a**) ×80, (**b** and **c**) ×20,000

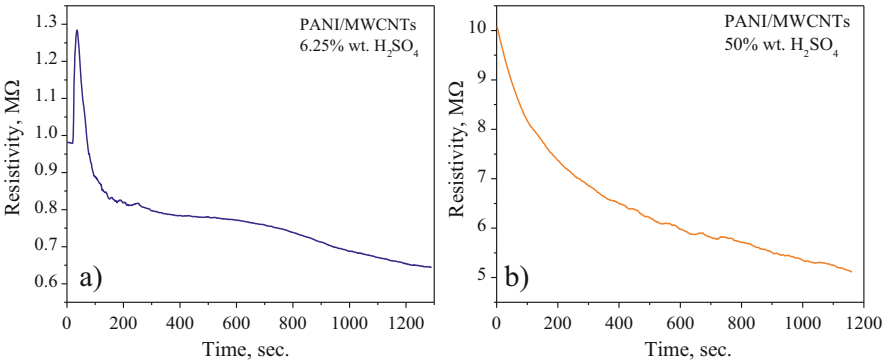

Fig. 38.3 Resistivity changes of the tested SPE sensors: MWCNT/PANI SPE exposed to (**a**) 6% H_2SO_4; (**b**) 50% H_2SO_4

38.3 Results and Discussion

Electrochemical synthesis of MWCNT/PANI nanocomposites was performed directly on the gold wires of the screen printed electrodes at a working potential of 0.75 V. The presence of the carbon nanotubes in PANI increased the electropolymerization rate versus pure PANI, as shown in Fig. 38.1. The characteristic morphology of the obtained nanocomposites is shown in Fig. 38.2.

The gas sensitivity of the obtained MWCNT/PANI nanocomposite SPE electrodes were tested by exposure the SPEs to vapors originated from different concentration of H_2SO_4 using resistivity measurements. Characteristic responses of the performed measurements are shown in Fig. 38.3. Generally, the tested electrodes

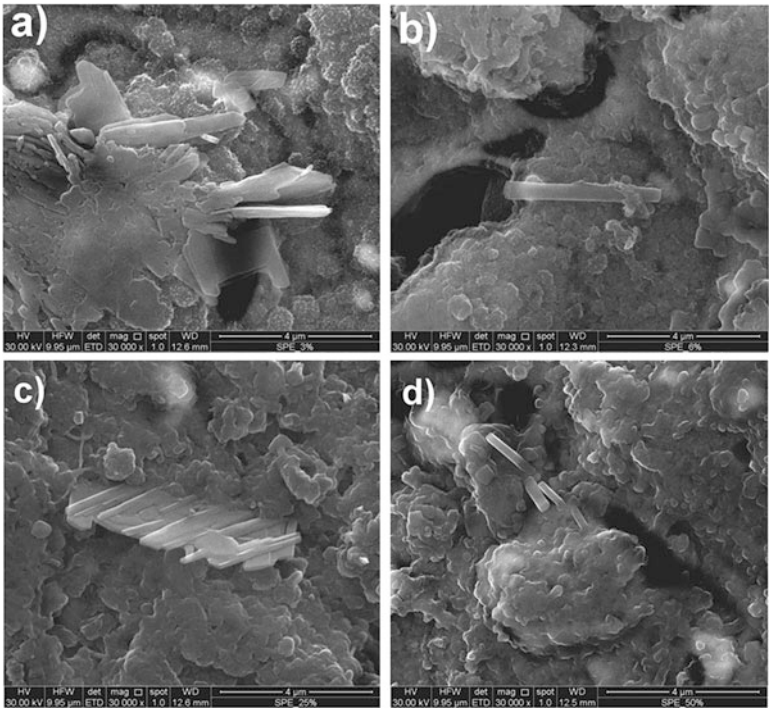

Fig. 38.4 SEM images of the acid treated SPE samples: (**a**) 3% H_2SO_4 (×30,000); (**b**) 6% H_2SO_4 (×30,000); (**c**) 25% H_2SO_4 (×20,000); (**d**) 50% H_2SO_4 (×30,000)

demonstrated a non-linear response. For all tested acid concentrations, it was found that in the first 100 s the resistivity decreased, i.e. the conductivity increased which is in agreement with literature data for PANI-based gas sensors [11]. This trend continued for the response to 6 and 50% H_2SO_4, while for 12,5% and 25% H_2SO_4 it was found that after the first 100 s the resistivity increased and conductivity decreased.

Due to the acid treatment of the SPE electrodes, morphological changes occurred on the nanocomposite surface. Some of the characteristic microphotographs are shown in Fig. 38.4. Due to the acid treatement, typical nanorods of salt structures were found in all tested samples. Actually these salt nanorods are responsible for the increased conductivity. Due to the acid vaporization, also smaller voids and fractures were found in all treated SPE nanosensors (Fig. 38.5).

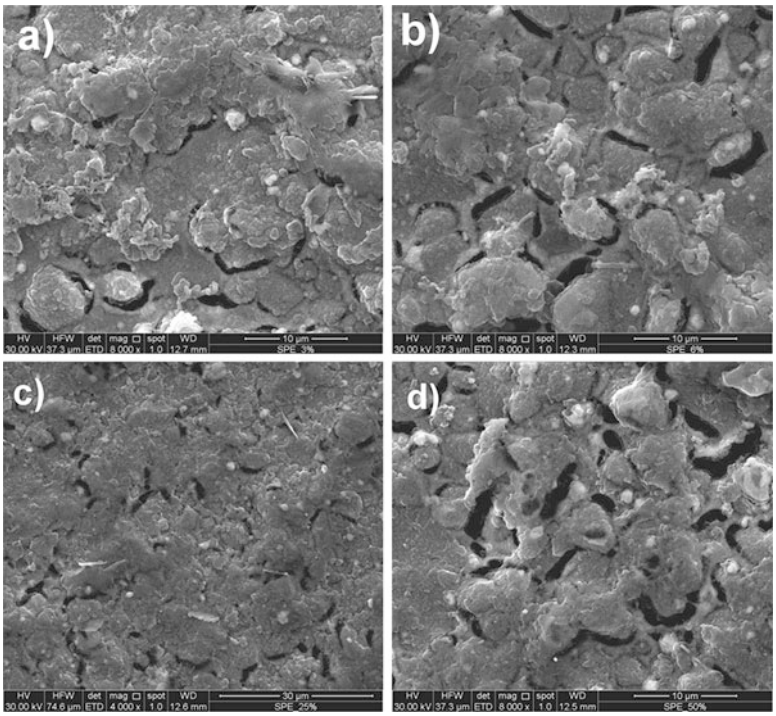

Fig. 38.5 SEM images of the acid treated SPE samples: (**a**) 3% H_2SO_4 (×8000); (**b**) 6% H_2SO_4 (×8000); (**c**) 25% H_2SO_4 (×4000); (**d**) 50% H_2SO_4 (×8000)

Structural changes of the acid-treated electrodes were studied by FTIR-ATR spectroscopy. The obtained spectra are shown in Fig. 38.6. The main peaks at 1568 and 1480 cm^{-1} were assigned to the stretching vibrations of quinone and benzene rings, respectively. The peaks at 1292 and 1236 cm^{-1} correspond to C-N stretching vibration. The peaks at 1131 and 800 cm^{-1} were attributed to in-plane out-of-plane bending of C-H, respectively. These suggest that PANI was polymerized in the conductive emeraldine salt form during the polymerization. Due to the acid vaporization, by increasing the acid concentration the intensity of the peaks at 1137 cm^{-1}, 1296–1300 cm^{-1}, 1580 cm^{-1} decreased, while that of the peaks at 1460 cm^{-1} and 1750 cm^{-1} increased, and some peak shifting of the characteristic bands occurred.

38.4 Conclusions

This work presents a method for the production of gas sensor based on MWCNT/PANI SPE electrodes using resistivity changes.

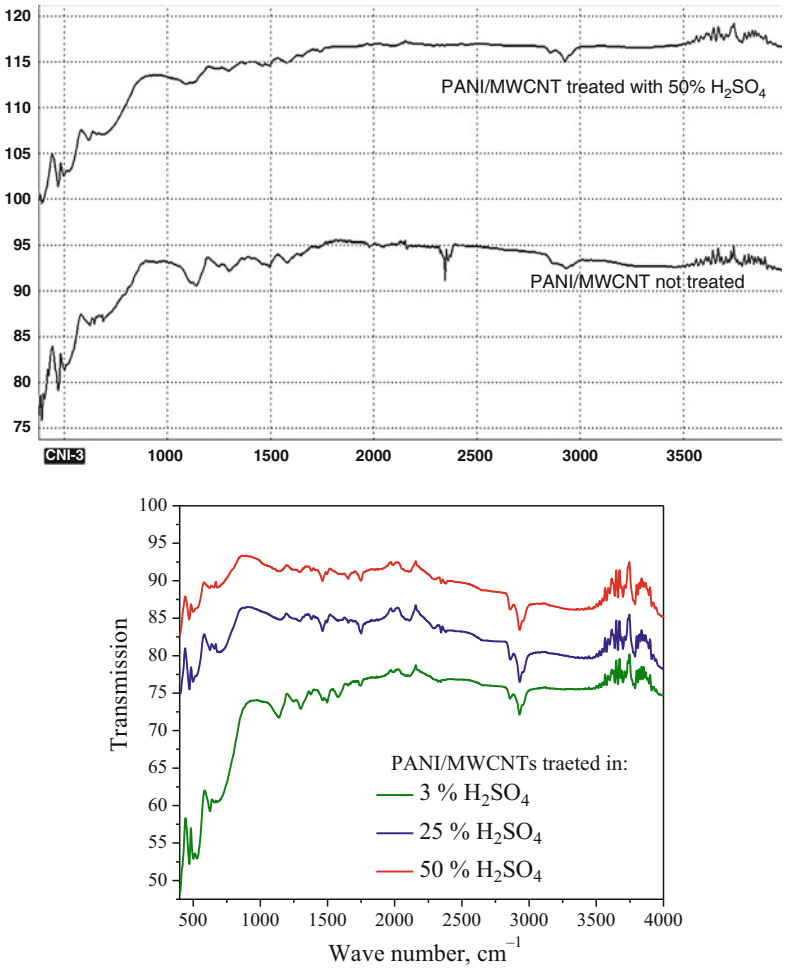

Fig. 38.6 FTIR-ATR spectra of SPE nanocomposite before and after acid exposure

- SEM images have shown that in the vaporized samples nanorod structures of the salts were found. Because of the aggressive acid vaporization, also smaller voids and fractures were found in all treated SPE-nanosensors
- Using the FTIR-ATR spectroscopy, it was shown that PANI was polymerized in conductive emeraldine form. Because of the acid treatment some structural changes were found which induced peak shifting of the characteristic bands.

Acknowledgments This research was done within FP7 Project "Cost-effective sensors, interoperable with international existing ocean observing systems, to meet EU policies requirements" (Project reference 614155).

References

1. Tang R, Shi Y, Hou Z, Wei L (2017) Carbon nanotube-based chemiresistive sensors. Sensors 17:882
2. Kukla AL, Shirshov Y, Piletsky SA (1995) Ammonia sensors based on sensitive polyaniline films. Sens Actuator B Chem B37:135
3. Agbor NE, Petty MC, Monkman AP (1995) Polyaniline thin films for gas sensing. Sens Actuator B Chem B28:173
4. Do JS, Chang WB (2001) Amperometric nitrogen dioxide gas sensor: preparation of PAn/Au/SPE and sensing behavior. Sens Actuator B Chem B72:101
5. Takeda S (1999) A new type of CO2 sensor built up with plasma polymerized polyaniline thin film. Thin Solid Films 343–344:313
6. Sharma S, Nirkhe C, Pethkar S, Athawale AA (2002) Chloroform vapour sensor based on copper/polyaniline nanocomposite. Sens Actuator B Chem B85:131
7. Barker PS, Bartolomeo CD, Monkman AP, Petty MC (1995) Gas sensing using a charge-flow transistor. Sens Actuator B Chem B25:451
8. He L, Jia Y, Meng F, Li M, Liu J (2009) Gas sensors for ammonia detection based on polyaniline-coated multi-wall carbon nanotubes. Mater Sci Eng B 163:76
9. Zhang T, Nix MB, Yoo B-Y, Deshusses MA, Myung NV (2006) Electrochemically functionalized single-walled carbon nanotube gas sensor. Electroanalysis 18:1153
10. Lim JH, Phiboolsirichit N, Mubeen S, Deshusses MA, Mulchandani A, Myung NV (2010) Electrical and gas sensing properties of polyaniline functionalized single-walled carbon nanotubes. Nanotechnology 21:7
11. Pasti IA, Lezaic AJ, Ciric-Marjanovic G, Mirsky VM (2016) Resistive gas sensors based on the composites of nanostructured carbonized polyaniline and Nafion. J Solid Sate Electrochem 20:3061

Chapter 39
Synthesis of RGO/SiO_2 and Ag/RGO/SiO_2 Nanocomposites and Study of Their Sensitivity Towards Humidity

A. S. A. Shalaby, Sh. Safwat-Mansour, Ahmed S. Afify, M. Hassan, and A. Staneva

Abstract In recent years, many interesting researches published on the study of new nanocomposite materials involves active components such as reduced graphene oxide (RGO), silver nanoparticles (Ag-NPs), and silica, which indicated very interesting properties and applications. The present work demonstrates the preparation of nanocomposite powders with the participation of Ag-NPs, RGO and tetraethylorthosilicate (TEOS) using the sol-gel technique. The phase formations are verified by X-ray diffraction analysis. The thermal behavior was studied using differential thermal analysis (DTA/TG) in air. The sensitivity against humidity was tested in a laboratory apparatus made of a thermostatic chamber operating at 25 °C, in which the RH could be varied between 0% and 96%.

Keywords Reduced graphene oxide · Silver nanoparticles · Sol-Gel technique · Humidity sensor

39.1 Introduction

In recent years, nanocomposites as new applicable materials have captured and held the attention and imagination of scientists and engineers in order to satisfy the requirements of society. There are significant efforts to prepare new nanocomposites

A. S. A. Shalaby (✉)
Science and Technology Center of Excellence (STCE), Cairo, Egypt
e-mail: ashalaby@outlook.com

S. Safwat-Mansour · A. Staneva
University of Chemical Technology and Metallurgy, Sofia, Bulgaria

A. S. Afify
Department of Applied Science and Technology (DISAT), Politecnico di Torino, Torino, Italy

M. Hassan
Department of Applied Science and Technology (DISAT), Politecnico di Torino, Torino, Italy

Department of Natural Science, Obour Institute of Engineering and Technology, Cairo, Egypt

P. Petkov et al. (eds.), *Advanced Nanotechnologies for Detection and Defence against CBRN Agents*, NATO Science for Peace and Security Series B: Physics and Biophysics, https://doi.org/10.1007/978-94-024-1298-7_39

based on graphene which are considered as very promising material with large surface area and specific electrical, optical and mechanical properties [1–3]. A graphene/silica nanocomposite shows an interesting property due to the local atomic configuration, and the binding sites between them. Silica acts as a carrier and considered an excellent supporting material because of their large surface area, flexible pore size and thermal stability. In addition, silica matrix improved the degree of dispersion which reduces the agglomeration of nanoparticles [4]. The nanocomposites containing reduced graphene oxide, silver nanoparticles and silica exhibit unique physical, chemical, and biological properties [5]. Ag/RGO/SiO_2 nanocomposites have an exceptional catalytic activity toward the reduction of 4-nitrophenol [6], are used as anode material in lithium-ion batteries [7], and show a surface-enhanced Raman scattering (SERS) performance for the detecting traces of organic colorants compared with graphene/Ag nanocomposites [8].

The present work demonstrates the preparation of nanocomposites with participation of Ag, RGO and SiO_2 nanostructures by the sol-gel technique in order to study their structure formation, phase transformations, thermal stability, and their sensitivity against humidity.

39.2 Experimental Procedure

39.2.1 Synthesis of Reduced Graphene Oxide (RGO)

RGO has been prepared by chemical exfoliation of purified natural graphite (Graphite flaks, 99.9%, Alfa Aesar) as described in our study [9]. Briefly, the preparation in three steps can be summarizes as follow:

1. Graphite was oxidized by strong acid to obtain graphite oxide.
2. Graphite oxide solution was ultrasonicated for 2 h to prepare dispersion solution of graphene oxide;
3. This dispersion solution was reduced using the strong reducing agent sodium borohydride ($NaBH_4$, 98%, Alfa Aesar) to obtain reduced graphene oxide.

39.2.2 Synthesis of Silver Nanoparticles (Ag-NPs)

Silver nanoparticles were synthesized by a chemical reduction method [10, 11] by adding an excess of the reducing agent sodium borohydride to silver nitrate ($AgNO_3$, Fluka AG) following the chemical equation:

$$AgNO_3 + NaBH_4 \rightarrow Ag + 1/2\ H_2 + 1/2\ B_2H_6 + NaNO_3$$

A specific volume of $AgNO_3$ (1 mM) solution was added to a cooled volume of $NaBH_4$ (2 mM) solution in the ratio 1:3 dropwise. The color of the solution

converted from yellow at the beginning of addition to yellowish brown due to increase of silver content. Finally, few drops of NaCl (1.5 M) were added in order to precipitate the colloid. The solution was settled for 2 h before the filtration. The filtrated nanopowder was washed with destilled water many times, then dried at 80 °C for 2 h.

39.2.3 Synthesis of RGO/SiO_2 Nanocomposite

RGO/SiO_2 nanocomposites (20 RGO:80 SiO_2 (wt %)) were prepared using the sol-gel technique due to the surface hydroxyl groups of the RGO sheets acting as nucleation sites for the hydrolysis step, which facilitates chemical bonding with the surrounding materials. The method of preparation of this type of nanocomposite followed our previous study [12] Briefly, we can summarize the steps of preparation as follows: A dispersed mixture of as prepared RGO (20 wt %) in deionized water was prepared as above and then added to the TEOS (Si $(OC_2H_5)_4$, >99%, Aldrich) solution which was prepared by ethanol under stirring for 1 h at 100 °C. Thus, the gel was obtained.

39.2.4 Synthesis of Ag/RGO/SiO_2 Nanocomposite

Following the scheme in Fig. 39.1 we successfully obtained a nanocomposite powder with the nominal composition 10 Ag*20 RGO*70 SiO_2 (wt%).

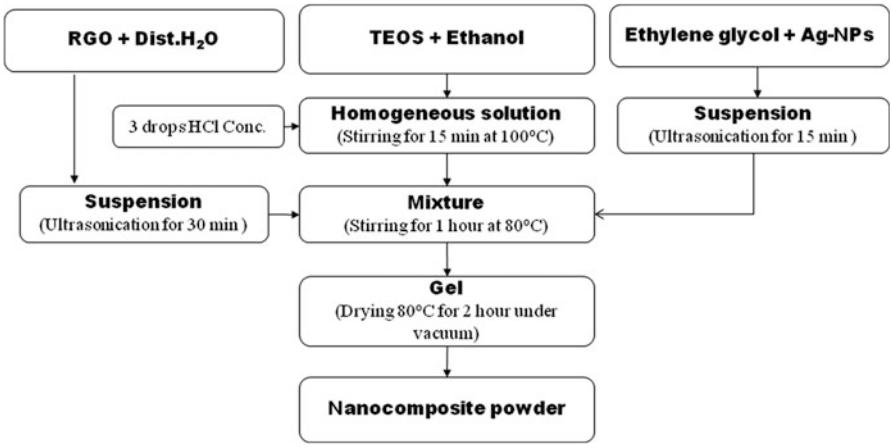

Fig. 39.1 Scheme of preparation of Ag/RGO/SiO_2 nanocomposites using sol-gel technique

39.2.5 Sensing Film Preparation and Sensing Mechanism

The sensing films were prepared as expressed previously in [13]. An apparatus made of a thermostat chamber, operating at RT, was used to perform the humidity sensing measurements in which the relative humidity could be varied between 0% and 96% [14]. An external alternating voltage (V = 3.6 V at 1 kHz) was applied on each tested sensor, acting as a variable resistance in the above-mentioned electrical circuit. A 2000 series Keithley digital multi-meter was used to measure the voltage V_{DC} at the output of the circuit [14]. Determination of the sensor resistance was realized by a calibration curve drawn substituting the sensors, in the circuit by known resistances. The sensor response SR, expressed in %, was defined as the relative variation of the starting resistance, compared with the resistance measured under gas exposure (Eq. 39.1):

$$SR(\%) = 100\frac{|R_0 - Rg|}{R_0}. \tag{39.1}$$

where R_0 and R_g are the starting resistance (in the absence of the test gas) and the measured resistance of the sensors under exposure, respectively.

39.3 Results

The X-ray diffraction patterns of samples with the nominal compositions 20 RGO*80 SiO_2 and 10 Ag*20 RGO*70 SiO_2 (wt %) heated up to 100 °C are shown in Fig. 39.2. The diffraction curve of sample RGO/SiO_2 show the amorphous nature of the composite which is related to the amorphous or glassy nanoscale silica, which is the major component of the composite while, the RGO appeared as very small peaks at positions $2\theta = 26.3°$ and $2\theta = 42.9°$ which are hardly detectable.

In the diffraction curve of sample Ag/RGO/SiO_2 different phases appeared such as amorphous silica, RGO with a very small peak at $2\theta = 26.3°$, Ag-NPs (Ref. code: 00-004-0783) and AgCl (Ref. code: 00-031-1238). Silver chloride (AgCl) appeared due to the preparation method which used a few drops of concentrated HCl acid to accelerate the gelation reaction in the sol-gel technique. Some metallic Ag-NPs reacted with the acid and formed AgCl nanocrystal. The average of the crystal size calculated from the broadening of the diffraction line using Sherrer's equation for Ag-NPs inside the composite was about 33 nm while for the AgCl nanocrystal it was about 41 nm.

The phase transformation of the sample with the nominal composition 10 Ag*20 RGO*70 SiO_2 (wt%) was studied after heating at 100 °C, 350 °C, and 600 °C. The diffraction curve of the sample heated up to 100 °C shows that the nanocomposite

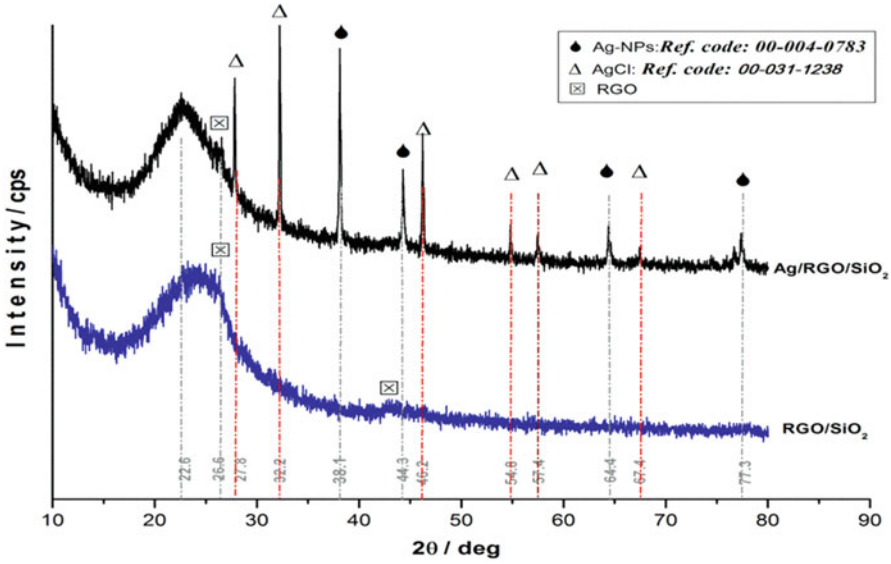

Fig. 39.2 XRD patterns of samples with nominal compositions 20 RGO*80 SiO_2 (wt %) and 10 Ag*20 RGO*70 SiO_2 (wt%) heated up to 100 °C

contains an amorphous hump at $2\theta = 22.6°$ which is connected to the existence of amorphous silicate; there are different crystal phases such as RGO nanoparticles, Ag-NPs and AgCl nanocrystals. The average crystal size calculated from Sherrer's equation is 70 nm as shown in Fig. 39.3.

At higher temperatures (350 °C) the amorphous hump decreased in intensity with increasing heating temperature; the peak at $2\theta = 26.2°$ which is connected to the existence of RGO became clearer than before. At a temperature of 600 °C, the diffraction curve showed that the peak at $2\theta = 26.2°$ connected to the existence of RGO almost disappeared. It is well known that all carbon phases start to burn in air above 400 °C. Furthermore, there are no significant effects of increasing the temperature up to 600 °C on the Ag-NPs and AgCl phases as shown in Fig. 39.3.

According to the DTA/TG curves shown in Fig. 39.4 both samples showed significant weight loss above 100 °C. This is attributed to the elimination of water as well as removal of the weak oxygen-containing functional groups (CO, CO_2 and H_2O vapors).

As one can see for the sample RGO/SiO_2, a strong exothermic effect appeared at 565 °C due to strong combustion of carbon. The total mass loss after heating up to 800 °C was about 41% of the mass of the obtained nanocomposite as shown in Fig. 39.4. In the sample Ag/RGO/SiO_2, the endothermic effect appears at 150 °C; it may be related to the thermal dehydration; there are many exothermic effects apparent at 340 °C, 440 °C and 580 °C possibly due to the gradual combustion of carbon of the organic precursors and carbon of RGO. The mass lost gradually

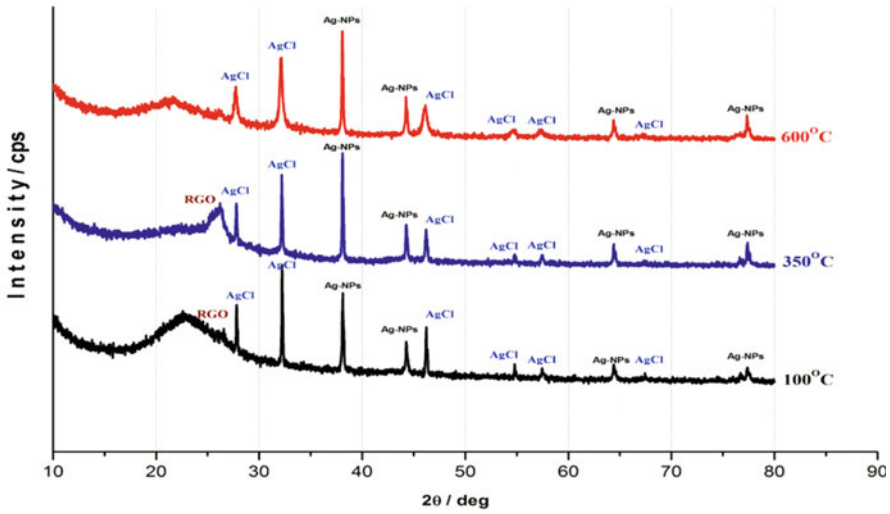

Fig. 39.3 XRD patterns of samples with the nominal composition 10 Ag*20 RGO*70 SiO_2 (wt%) heated up to 100 °C, 350 °C and 600 °C

increases during the heating up to 800 °C. It was about 58% from the mass of the obtained nanocomposite as shown in Fig. 39.4.

39.4 Sensitivity Towards Humidity

Figure 39.5 illustrates the sensor response towards RH. Samples RGO/SiO_2 and Ag/RGO/SiO_2 showed a significant response towards RH at room temperature, starting from 33% RH.

39.5 Conclusions

We successfully prepared novel nanocomposite materials containing Ag-NPs, RGO and SiO_2 using the sol-gel technique. The structure formation and phase transformations were confirmed by XRD analysis. According to DTA/TG analysis the thermal stability of RGO/SiO_2 composite was better than that of Ag/RGO/SiO_2 nanocomposites. The as prepared nanocomposites have significant sensitivity response towards humidity but the RGO/SiO_2 composite was better. This could open a channel to use the Ag/RGO/SiO_2 samples as NO_x or CO_x sensors.

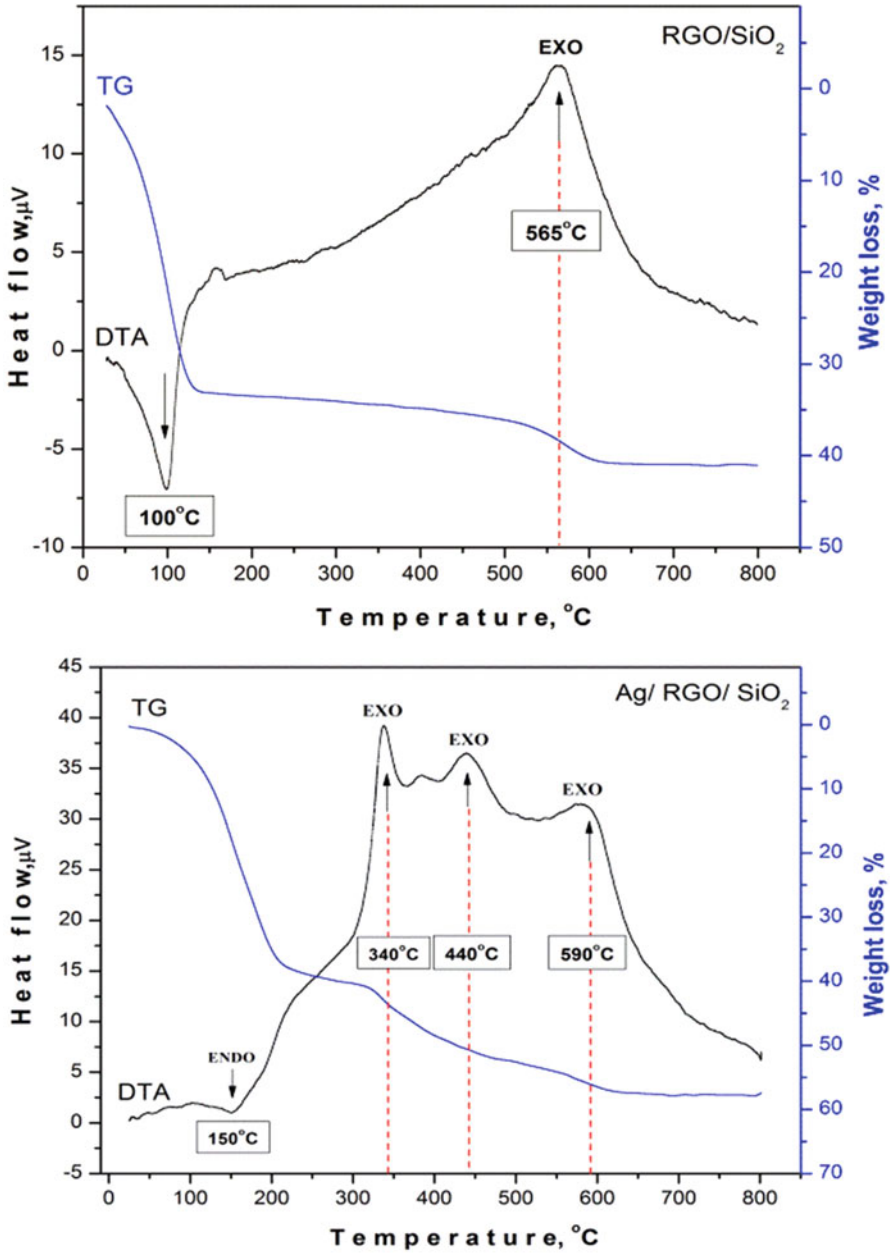

Fig. 39.4 DTA/TG patterns of the samples RGO/SiO_2 and Ag/RGO/SiO_2

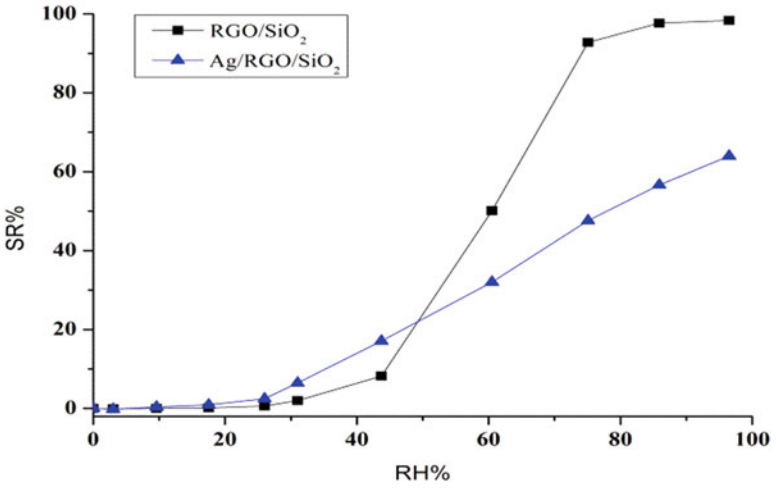

Fig. 39.5 Sensor response toward relative humidity changes

References

1. Machado BF, Serp P (2012) Graphene-based materials for catalysis. Catal Sci Technol 2(1):54
2. Dreyer DR, Park S, Bielawski CW, Ruoff RS (2010) The chemistry of graphene oxide. Chem Soc Rev 39(1):228
3. Mwakikunga BW, Hillie KT (2011) In: Gong J (ed) Chapter 5: Graphene synthesis, catalysis with transition metals and their interactions by laser photolysis. Graphene – synthesis, characterization, properties and applications. InTech, p 59
4. Pham DP, Huynh KK, Tran CV, Vu VQ, Tran TTV (2014) Preparation and structural characterization of Sol-gel-derived silver silica nano composite powders. Int J Mater Sci Appl 3 (5):147
5. Tran QH, Nguyen VQ, Le A-T (2013) Silver nanoparticles: synthesis, properties, toxicology, applications and perspectives. Adv Nat Sci Nanosci Nanotechnol 4:033001
6. Xiao W, Zhang Y, Liu B (2015) Raspberrylike SiO_2@reduced graphene oxide@AgNP composite microspheres with high aqueous dispersity and excellent catalytic activity. ACS Appl Mater Interfaces 7(11):6041
7. Du FH, Wang KX, Fu W, Gao PF, Wang J F, Chen JS (2013) A graphene-wrapped silver–porous silicon composite with enhanced electrochemical performance for lithiumion batteries. J Mater Chem A 1:13648
8. Huang Q, Wei W, Yan Q, Wu C, Zhu X (2015) A facile and green method for synthesis of rGO@SiO_2@FeOOH@Ag nanocomposite as efficient surface enhanced Raman scattering (SERS) platforms. Mater Lett 152:203
9. Shalaby A, Yaneva V, Staneva A, Aleksandrov L, Iordanova R, Dimitriev Y (2014) Thermal stability of RGO and RGO/SiO_2 nanocomposite prepared by sol-gel technique. Nanosci Nanotechnol, (Sofia, Bulg) 14:120
10. Mavani K, Shah M (2013) Synthesis of silver nanoparticles by using sodium borohydride as a reducing agent. IJERT 2(3):1
11. Mozghan B (2008) Synthesis of noble metal nanoparticles. Dissertation, Drexel University, USA

12. Shalaby ASA, Staneva AD, Aleksandrov LI, Iordanova RS, Dimitriev YB (2016) Preparation, characterization and thermal stability of reduced graphene oxide/ silicate nanocomposite. Bulg Chem Commun 48(1):38
13. Afify AS, Hassan M, Piumetti M, Peter I, Bonelli B, Tulliani J-M (2015) Elaboration and characterization of modified sepiolites and their humidity sensing features for environmental monitoring. Appl Clay Sci 115:165
14. Tulliani J-M, Bonville P (2005) Influence of the dopants on the electrical resistance of hematite-based humidity sensors. Ceram Int 31:507

Chapter 40
Preparation of Nanoporous Hybrid Materials with Bridged Tetra Sulfide Functional Groups and Determination of Their Sensing Characteristics Towards Relative Humidity

M. Abdallah, N. Velikova, Y. Ivanova, Ahmed S. Afify, M. Ataalla, and M. Hassan

Abstract Nano porous hybrid materials were synthesized by co-condensation of organically bridged tetra sulfide bis [3-(triethoxysilyl) propyl] tetra sulfide (BTPTS) and tetra ethoxylsilane (TEOS) in the presence of the non-ionic surfactant triblock copolymer poly(ethylene glycol)-block-poly (propylene glycol)-block-poly (ethylene glycol) ($EO_{20}PO_{70}EO_{20}$) in acidic media as revealed by the measurement of nitrogen adsorption. The structure and chemical state of the materials were characterized by chemical analysis, Fourier–transform infrared spectroscopy (FTIR), ^{29}Si MAS NMR, and thermo-gravimetric analysis (DTA/TG), revealing the integrity of organic groups inside the framework. The synthesized powders were prepared as sensors using the screen-printing technique and then evaluated on view of their sensing characteristics in the

M. Abdallah (✉)
Research and Development Department, MEPACO-MEDIFOOD, Cairo, Egypt

Department of Silicate Technology, University of Chemical Technology and Metallurgy, Sofia, Bulgaria

N. Velikova · Y. Ivanova
Department of Silicate Technology, University of Chemical Technology and Metallurgy, Sofia, Bulgaria

A. S. Afify
Department of Applied Science and Technology (DISAT), Politecnico di Torino, Torino, Italy

M. Ataalla
Faculty of Engineering and technology, Badr University in Cairo (BUC), Badr City, Egypt

M. Hassan
Department of Applied Science and Technology (DISAT), Politecnico di Torino, Torino, Italy

Department of Natural Science, Obour Institute of Engineering and Technology, Cairo, Egypt

P. Petkov et al. (eds.), *Advanced Nanotechnologies for Detection and Defence against CBRN Agents*, NATO Science for Peace and Security Series B: Physics and Biophysics, https://doi.org/10.1007/978-94-024-1298-7_40

range from 0.0% to 96% relative humidity (RH) at room temperature. Sensors with a higher content of BTPTS show a better response towards RH.

Keywords Hybrid materials · Nanoporous materials · Porosity · Relative humidity · Screen-printing · Sensors

40.1 Introduction

Since the first synthesis of mesoporous silica [1, 2] there has been a tremendous amount of effort dedicated to the development of organic–inorganic mesoporous hybrid materials particularly with regard to some potential applications such as adsorption, biotechnology, host–guest chemistry, chromatography, catalysis, sensor technology, and gas storage [3–7]. The organic groups can be placed selectively on internal and/or external pore surfaces or even within the pore walls. The organic modification in principle permits a fine tuning of materials properties, including surface properties such as hydrophilicity/hydrophobicity or potential interactions with guest molecules. In addition, the surface reactivity can be altered and protected by organic groups with respect to chemical attacks; bulk properties, e.g. mechanical or optical properties can also be changed. This flexibility in choosing organic, inorganic or even hybrid building blocks allows one to control the materials properties [8]. According to IUPAC the pores of solids are classified according to their size, pore sizes in the range of 2 nm and below are called micropores, those in the range of 2–50 nm are denoted as mesoporous, and those above 50 nm are called macropores. The distribution of size, shape and volume of the void spaces in porous materials is directly related to their ability to perform the desired function in a particular application. The need to create uniformity of the pore size, shape and volume has steadily increased over recent years as it could be optimized for the desired application [9]. Recently, we reported the synthesis of tetra sulfide-functionalized materials by co-condensation of bis[3-(triethoxysilyl)propyl]tetra sulfide (BTPTS) and tetraethoxylsilane (TEOS) [10]. There is a great demand for humidity sensors which can be used for several applications in different fields under certain conditions [11–14]. Many materials have beeb developed as humidity sensors such as ceramics, electrolytes, and organic polymeric materials [11]. The aim of this research was to study the influence of high concentrations of BTPTS on the structure and morphology characteristic of the final hybrid materials and to determine their sensing properties towards relative humidity.

40.2 Experimental

40.2.1 Materials Synthesis

The tri-block copolymer Pluronic (P123), 1,4-bis (triethoxysilyl) propane tetra sulfide (BTPTS), $(CH_3CH_2O)_3Si(CH_2)_3S–\ S–S–S(CH_2)_3Si(OCH_2CH_3)_3)$, xylene, hydrochloric acid (HCL) and tetraethyl ortho silicate (TEOS) (all Sigma Aldrich) were used without further purification. All other chemicals were analytical grade. The precursor solutions were prepared by the following procedures: A total of 1.2 g of P123 and 3.5 g of potassium chloride were dissolved in 10 g of distilled water and 52 ml of 2M HCL, then magnetically stirred at room temperature until complete dissolution to obtain a homogenous solution. Thereafter, 2.64 ml of xylene were added into the surfactant solution accompanied by stirring for 1 h, followed by the addition of 2.64 ml of TEOS and continue stirring for 1 h. Then, different amounts of the organosilane precursor (BTPTS) were added as seen in Table 40.1 with continuous stirring at 40 ± 0.1 °C for 1 h. Finally, the resultant slurry was dried at 100 °C for 24 h, the surfactant was extracted by soaking 1.0 g of the solid in 150 ml ethanol, containing 1.7 ml of concentrated HCl at 50 °C for 24 h.

40.2.2 Materials Characterizations

Thermo gravimetric analysis (TGA) was performed with a PT1600 TG-DTA/DSC (STA Simultaneous Thermal Analysis, LINSEIS Messgeräte GmbH, Germany). The working conditions were a heating rate of 10 °C min^{-1} under a flow of air. Fourier transform infrared spectroscopy (FTIR) of KBr powder-pressed pellets was recorded with a Varian 660-IR spectrometer. The sulfur content of the extracted samples was analyzed quantitatively by elemental analysis (Elemental analyzer SPA Euro Vector EA 3000). ^{13}C cross-polarization magic angle spinning (CP MAS, 100.61 MHz) and ^{29}Si MAS solid-state NMR experiments (79.49 MHz) were recorded on a 9. 4T BrukerAvance 400 spectrometer. The experimental parameters for ^{13}C CP MAS NMR experiments were 9 kHz spin rate, 5 s pulse delay, for ^{29}Si MAS NMR experiments 5 kHz spin rate and 60 s pulse delay. Nitrogen adsorption/desorption analysis was carried out with an ASAP 2020 system in the static measurement mode;

Table 40.1 Sample compositions

Sample ID	BTPTS mol %	TEOS mol %	P123 [g]	Water [ml]	KCl [g]	2M HCl [ml]	Xylene [ml]
S3	50	50	1.2	10	3.5	52	2.6
S4	57	43					
S5	62	38					

then pore size distributions were determined based on Barrett-Joyner-Halenda (BJH) desorption curves.

40.2.3 Preparation and Testing of Humidity Sensor

Sensors were prepared and tested starting from the preparation of the interdigitated platinum electrodes where a platinum conducting paste (ESL 5545, from Electro-Science, King of Prussia, PA, USA) was deposited manually by the screen-printing technique onto planar α-alumina substrates (ADS-96 R, 96% alumina, Coors Tek, USA, 0.85 × 5 cm) by using a rubber squeegee through a 270 mesh steel screen; after drying overnight, these devices were heated at 980 °C for 20 min with a 2 °C/min heating/cooling ramp according to the ink's manufacturer recommendations in order to optimize the electrical conductivity of the electrodes. Then a screen-printable ink was prepared by dispersing the synthesized powders in a suitable amount of the organic solvent ethylene glycol mono butyl ether (Emflow 227, Emca-Remex products, England) to reach an appropriate rheological behavior, adherence to the substrate, and to achieve correct thermal shrinkage properties during the process of screen-printing to obtain a good film. The third step was the preparation of the sensing film manually by depositing the screen-printable ink onto the interdigitated platinum electrodes by screen-printing technique using a rubber squeegee through the abovementioned steel mesh screen; once these films were dried, the sensors were heated at 500 °C for 1 h with a 2 °C/min heating/cooling ramp. The formed films had thicknesses of about 30–40 μm and areas of about 1 cm^2; scotch tests on the dried films revealed a good adhesion on the substrates. Finally, the sensors were electrically characterized using a laboratory apparatus made of a thermos stated chamber working at 25 °C in which the RH could be varied from 0% to 96%. The experimental details have been reported previously [15]. RH values were measured by means of a commercial humidity and temperature probe (Delta Ohm DO9406, Italy). Each tested sensor was alimented by an external alternating voltage (V = 3.6 V at a frequency of 1 kHz); it constituted a variable resistance of this electrical circuit. A 2000 Keithley digital multimeter was used to measure the voltage VDC at the output of the circuit. The sensor resistance was determined by substituting it in the circuit by known resistances and then plotting a calibrating curve R = f(VDC). The sensor response SR, expressed in %, was defined as the relative variation of the starting resistance, compared with the resistance measured under gas exposure as in Eq. (40.1):

$$SR(\%) = 100\frac{|R_0 - Rg|}{R_0} \tag{40.1}$$

where R_0 and R_g are the starting resistance (in the absence of the test gas) and the gas exposed measured resistance of the sensors, respectively.

40.3 Result and Discussion

FTIR spectra of the samples with different BTPTS contents are shown in Fig. 40.1. The bands around 1070, 800, and 450 cm^{-1} are assigned to the Si–O–Si stretching and bending vibrations of a condensed silica network [16–18]. The intensity of the peak around 1240 cm^{-1} attributed to Si-C bonds [19] increased with increasing BTPTS amount due to high degree of condensed precursors and a higher cross-linking of the silica framework. The broad band close to 3450 cm^{-1} can be assigned to OH stretching modes of silanol groups. The bands for -CH_2 and -CH_3 groups appeared around 2978–2930; moreover, the Si-CH_2 vibration was observed around 1411 cm^{-1} The intensity of these bands increased with increasing BTPTPS amount confirming the successful incorporation of organofunctional group into the silica framework [20]. The presence of –S–S– and –S–C– bonds is reflected by vibration bands around 690 and 565 cm^{-1} [20–23]. The intensity of these bands increases with increasing BTPTS amount thus confirming the successful incorporation of organo-functional group after copolymer extraction [24]. This result was confirmed by elemental analysis (Tables 40.2 and 40.3) as the sulfur content increases from 18% to 30% for samples S3 and S5, respectively.

Figure 40.2 shows ^{29}Si MAS NMR spectra of the synthesized hybrid materials. They clearly show both Q and T sites, as expected. The prominent signals at −110 ppm, −101 ppm and −92 ppm, labeled Q^4 [Si $(OSi)_4$], Q^3 [(OH) Si $(OSi)_3$] and Q^2 [$(HO)_2$ Si $(OSi)_2$], respectively, imply a high degree of condensation and cross linking between the precursors. Obviously, the Q^2 peak disappeared in the samples (S3–S5), but T^3, Q^3, and Q^4 peaks were present in the spectra from the mesoporous materials, suggesting that the

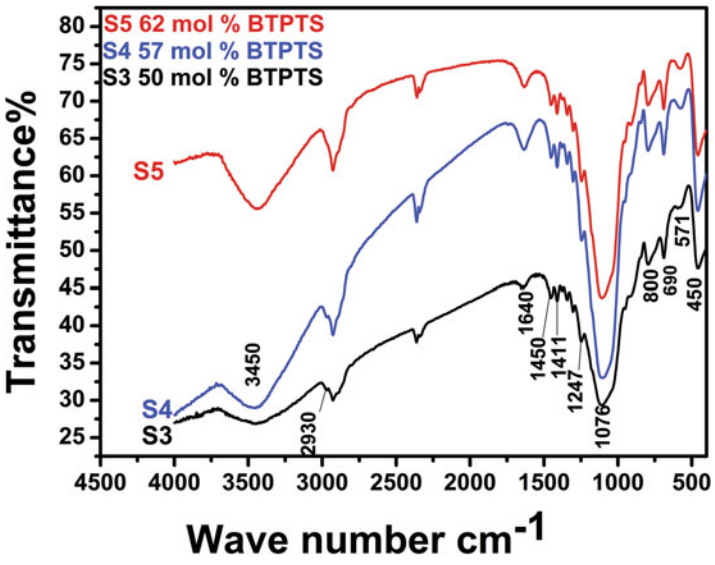

Fig. 40.1 Infrared spectrum of synthesized S3, S4, and S5

Table 40.2 Wave numbers of the vibration of functional group

Vibration of functional group	Wave number cm^{-1}	Vibration of functional group	Wave number cm^{-1}
ν_s Si-O-Si	800	-OH	1640
S-S	690	Si-C	1240
S-C	570	ν_{as} Si-O-Si	1070
ν_d Si-O-Si	450	Si-OH	950

Table 40.3 Elemental analysis of samples S3, S4, and S5

Sample ID	Weight (mg)	C%	H%	S wt. %	Theoretical S%
S3	1.1310	19.7	4.1	18.6	23.69389
S4	2.2650	15.3	3.2	27.6	27.22887
S5	1.8440	20.3	4.2	30.1	29.80844

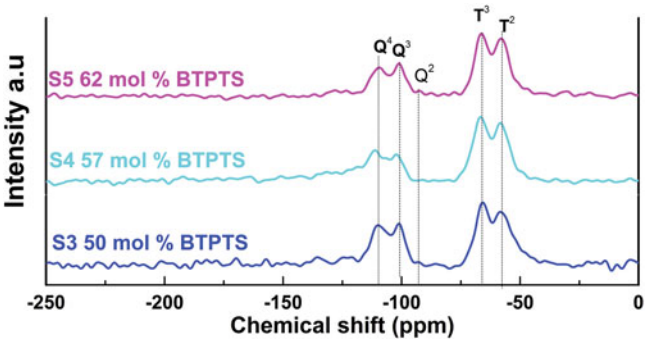

Fig. 40.2 ^{29}Si MAS NMR Spectra of synthesized samples S3, S4 and S5

condensation degree of the mesoporous framework was significantly increased with increasing BTPTS amount [25]. These results confirm the results from the FTIR analysis showing the presence of peaks around 950 and 1240 cm^{-1}. The Q^n peaks are characteristic for the TEOS precursor. The intensity of the Q^n peaks decrease since the ratio TEOS/BTPTS in the synthesis mixture decreases. The signals stemming from silicon bridged by organic group can be found in the range from −50 to −66 ppm. The strong resonances at −57.0 and −66.0 ppm could be assigned to C-Si(OH)$(OSi)_2$ (T^2) and C-Si $(OSi)_3$ (T^3) sites, respectively, suggesting the organic moiety is stable at the current synthesis conditions allowing successful incorporation of BTPTS into the silica framework [17, 21, 26, 27].

It can be seen in Fig. 40.3 that the ^{13}C CP MAS NMR spectra of the synthesized hybrid materials exhibit three signals corresponding to carbons in different environments at 12.6, 23.8 and at 42.5 ppm which correspond to carbon atom of bridging organic group in the direction from a Si atom to a S atom [28]. The two weak signals

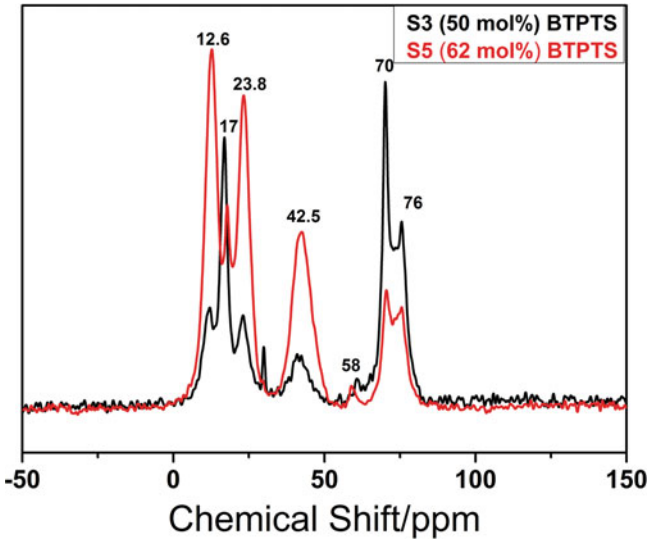

Fig. 40.3 ^{13}C CP MAS NMR spectra of synthesized samples S3 and S5

at 17 and 58.6 ppm are assigned to the carbons in the surface ethoxy groups ($Si\text{-}OCH_2CH_3$), which were formed during the surfactant extraction by acidified ethanol. Additionally, these signals could originate from physisorbed/chemisorbed ethanol as well, especially if the samples were not well dried [29]. The peaks centered at 70 and 76 ppm are due to the remnant surfactant Pluronic P123 [30]. ^{13}C CP MAS NMR and ^{29}Si MAS NMR show that the synthesized gel materials are hybrids; they can be classified as class II hybrid materials.

Thermogravimetric analysis is commonly employed to determine the characteristics of materials such as moisture content, reaction temperatures, stability of organic groups, etc. TGA and DTA curves of samples S3, S4 and S5 are presented in Fig. 40.4. The 5 wt% loss at temperatures below 100 °C is mainly due to the removal of physically adsorbed water from the materials. Decomposition of bridging organic group and residual P123 occurs between 300 and 600 °C [31], samples S3, S4 and S5 show weight losses of 45, 47 and 49 wt% respectively. The weight loss increases as a result of increasing amounts of tetra sulfide functionalized precursor which confirm the incorporation of tetra sulfide organic functional group into the silica framework at high BTPTS content. The weight losses observed above 600 °C may be attributed to the combustion of residual organic material and/or to desorption of water resulting from silanol condensation [29]. The result implies that the tetra sulfide-bridged groups can be stable up to 300 °C in air [32, 33].

The N_2 adsorption/desorption isotherms of the materials are presented in Fig. 40.5. According to the IUPAC classification [34] the materials are classified as type IV isotherms which are typical for mesoporous materials (average pore size is in the range between 2 and 50 nm). Sample S3 and S4 show a hysteresis loop type H2 according to the IUPAC classification which is typical for ink bottle like pores

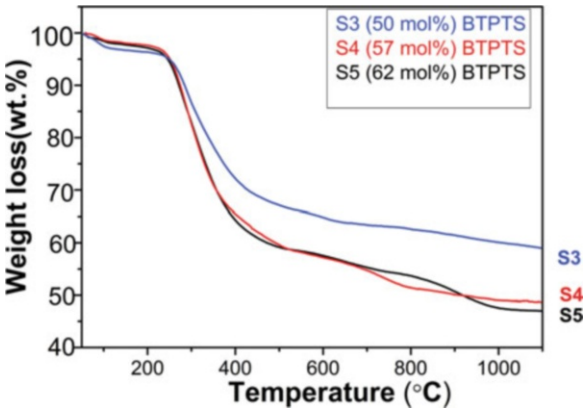

Fig. 40.4 DTG profiles of samples S3, S4 and S5

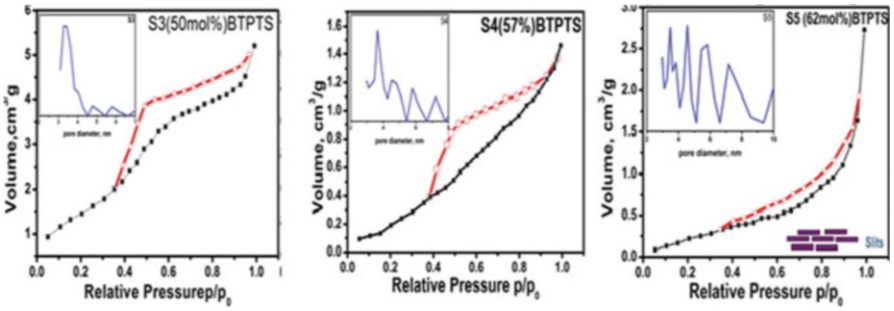

Fig. 40.5 Nitrogen adsorption/desorption isotherms and BJH pore-size distribution profiles of samples S3, S4 and S5

[34]. The H2 hysteresis loop has a smoother adsorption and a sharp desorption step. This is typical for materials with non-uniform pore shapes and/or sizes. The hysteresis loop type of sample S5 is H3 characteristic for slit like pores [35]. These results show that increasing the BTPTS amount lead to changes in the pore shapes.

For the sensitivity towards RH of the samples at room temperature, Fig. 40.6 illustrates the sensors' response of the samples. Sample S4 shows a significant response starting from 60% RH, while other samples show a lower sensitivity. It is well known that controlling of pore size plays a significant role to obtain better response towards RH in particular in the range of 20–500 nm [36]. Thus, the investigated samples are mesoporous materials which have pore sizes of 2–50 nm. Thus they are favorable to capillary condensation and can be implemented as a sensing material.

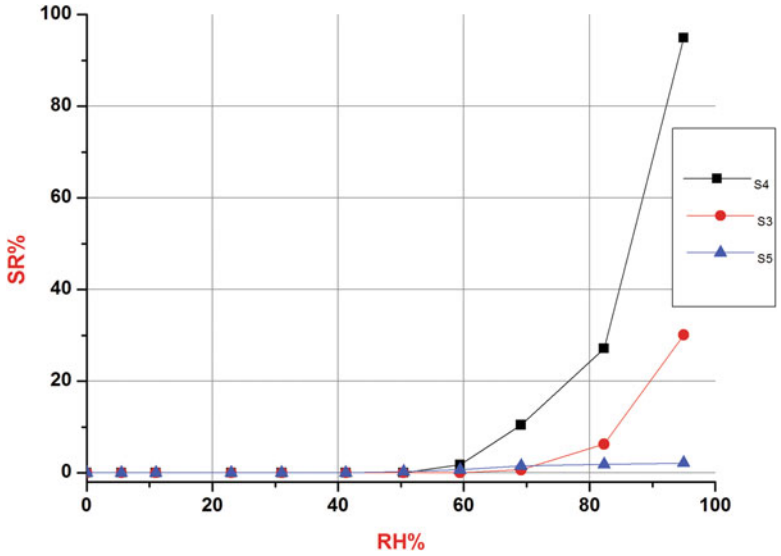

Fig. 40.6 Sensor response towards relative humidity

40.4 Conclusion

On the bases of the experiments which have been presented in the previous sections we can summarize that:

- The synthesized materials are Class II hybrid tetra sulfide-functionalized hybrid materials.
- Increasing intensity of bands corresponding to Si-C, S-C and S-S bonds in FT-IR spectra were observed and also increasing intensity of T the peaks in ^{29}Si MAS NMR. According to DTA/TG analysis the materials are stable up to 300 °C taking into account exo-effect; according to elemental analysis there is no significant difference of the sulfur content between the theoretical and experimental.
- Successful co-condensation reactions between BTPTS and TEOS at high BTPTS amount are achieved in the concentration range from 50 to 62 mol%.
- It was determined that BTPTS amount up to 57 mol% lead to formation of ink-bottle like pores. Above this concentration (62 mol% BTPTS) the pores in the materials are of slit-like shape. In the whole concentration range the synthesized hybrid materials are mesoporous.
- Pore size distribution curves form a sharp peak at BTPTS concentration up to 50 mol% which shows that the pores in the materials possess the same size. Above 50 mol% BTPTS concentration the curves form multiple peaks corresponding to different pore sizes.
- Additives have no influence on the structure of organic bridging groups in the final materials but they have influence on the condensation degree and pore shape.

- The sensing properties of the tested samples towards relative humidity show that a increasing BTPTS concentration leads to mesoporous materials which have better response towards RH at room temperature starting from 60% RH, compared to the other samples.

Acknowledgments The authors gratefully acknowledge Professor Jean Marc Tulliani from department of applied science and technology (DISAT), Politecnico di Torino, Turin, Italy, for working in his laboratory facilities for gas sensors testing and useful discussions.

References

1. Kresge C, Leonowicz M, Roth W, Vartuli J, Beck J (1992) Nature 359:710
2. Yanagisawa T, Shimizu T, Kuroda K, Kato C (1990) Bull Chem Soc Jpn 63:988
3. Stein A (2003) Adv Mater 15:763
4. Kickelbick G (2004) Angew Chem Int Ed 43:3102
5. Hatton B, Landskron K, Hhitnall W, Perovic D, Ozin G (2005) Acc Chem Res 38:305
6. Huncks W, Ozin G (2005) J Mater Chem 15:3716
7. Sayari A, Hamoudi S (2001) Chem Mater 13:3151
8. Schüth F, Sing KSW, Weitkamp J (2002) Handbook of porous solids. Wiley-VCH, Weinheim
9. Davis ME (2002) Nature 417:813
10. Abdallah M, Velikova N, Ivanova Y, Dimitriev Y (2013) J Chem Technol Metall 48:571
11. Patissier B (1999) Sens Actuator Chem B 59:23
12. Laville C, Deletage JY, Pellet C (2001) Sens Actuator Chem B 76:304
13. Kanan SM, El-Kadri OM, Abu-Yousef IA, Kanan MC (2009) Sensors 9:8158
14. Seiyama T, Yamazoe N, Arai H (1983) Sensors Actuators 4:85
15. Tulliani J-M, Bonville P (2005) Ceram Int 31:507
16. Liu D, Lei J, Guo L, Du X, Zeng K (2009) Microporous Mesoporous Mater 117:67
17. Llusar M, Monros G, Roux C, Pozzo J, Sanchez C (2003) J Mater Chem 13:2505
18. Sartori G, Bigi F, Maggi R, Sartorio R, Macquarrie D, Lenarda M, Storaro L, Coluccia S, Martra G (2004) J Catal 222:410
19. Wahab M, Kim I, Ha C (2004) Microporous Mesoporous Mater 69:19
20. Johari K, Saman N, Mat H (2014) J Mater Eng Perform 23:809
21. Teng M, Wang H, Li F, Zhang B (2011) J Colloid Inter Sci 355:23
22. Johari K, Saman N, Mat H (2013) Can J Chem Eng 9999:1
23. Guo L, Li J, Zhang L, Li J, Li Y, Yu C, Shi J, Ruan M, Feng J (2008) J Mater Chem 18:2733
24. Ross S (1972) Inorganic infrared and raman spectra. McGraw-Hill, London
25. Barczak M, Borowski P, Abrowski AD (2009) Colloid Surf A 347:114
26. Kim J, Fang B, Song M, Yu J (2012) Chem Mater 24:2256
27. Wang Y, Yang C, Zibrowius B, Spliethoff B, Linde M, Schüth F (2003) Chem Mater 15:5029
28. Saadeh S, El-Ashgar N (2006) J Islam Univ Gaza 14:37
29. Zhang W, Zhang X, Hua Z, Harish P, Schroeder F, Hermes S, Cadenbach T, Shi J, Fischer R (2007) Chem Mater 19:2663
30. Li C, Liu J, Zhang L, Yang J, Yang Q (2008) Microporous Mesoporous Mater 113:333
31. Fan H, Wuc J, Fan X, Zhang D, Su Z, Yan F, Sun T (2012) Chem Eng J 355:198
32. Hao N, Han L, Yang Y, Wang H, Webley P, Zhao D (2010) Appl Surf Sci 256:5334
33. Fan H, Su Z, Fan X, Guo M, Wang J, Gao S, Sun T (2012) J Sol-Gel Sci Technol 64:418
34. Sivak W, Pollack I, Petoud S, Zamboni W, Zhang J, Beckman E (2008) Acta Biomater 4:852
35. Sing K (1982) Pure Appl Chem 54:2201
36. Traversa E (1995) Sensors Actuators B Chem 23:135

Chapter 41
Humidity Sensing Properties of Tungsten Based Glass Crystalline Materials in the WO_3-ZnO-La_2O_3-Al_2O_3 System

M. Ataalla, Ahmed S. Afify, M. Hassan, A. M. Adam, M. Milanova, and Iskra Piroeva

Abstract Glass crystalline materials from the WO_3-ZnO-La_2O_3-Al_2O_3 system containing high WO_3 concentrations (60–76 mol%) were prepared by controlling the glass crystallization and were then employed as humidity based sensors. According toX-ray analysis, WO_3 separates as a crystalline phase from the amorphous structures with the nominal compositions $76WO_3{\cdot}9.5ZnO{\cdot}9.5La_2O_3{\cdot}5Al_2O_3$ and $60WO_3{\cdot}7.5ZnO{\cdot}7.5La_2O_3{\cdot}25Al_2O_3$ after the heat treatment. Samples were characterized by scanning electron microscopy (SEM) and energy dispersive X-ray spectroscopy (EDS) for elemental analysis. Using the screen printing technique, the synthesized crystalline glass samples were deposited onto interdigidated Pt electrodes; then the sensors were tested in the range from 0.0% to 96% relative humidity (RH) at room temperature. It was observed that the increase in the content of WO_3 leads to improve sensor sensitivity towards RH.

Keywords Glass crystallization · Melt quenching · Relative humidity · Screen-printing · Sensors

M. Ataalla (✉)
Faculty of Engineering and technology, Badr University in Cairo (BUC), Badr City, Egypt

A. S. Afify
Department of Applied Science and Technology (DISAT), Politecnico di Torino, Torino, Italy

M. Hassan
Department of Applied Science and Technology (DISAT), Politecnico di Torino, Torino, Italy

Department of Natural Science, Obour Institute of Engineering and Technology, Cairo, Egypt

A. M. Adam
Physics Department, Sohag University, Sohag, Egypt

M. Milanova
Institute of General and Inorganic Chemistry, Bulgarian Academy of Sciences, Sofia, Bulgaria

I. Piroeva
Academician Rostislaw Kaischew Institute of Physical Chemistry, Bulgarian Academy of Sciences, Sofia, Bulgaria

P. Petkov et al. (eds.), *Advanced Nanotechnologies for Detection and Defence against CBRN Agents*, NATO Science for Peace and Security Series B: Physics and Biophysics, https://doi.org/10.1007/978-94-024-1298-7_41

41.1 Introduction

Humidity is an important factor for operating certain equipment such as high impedance electronic circuits, electrostatic-sensitive components, high-voltage devices, fine mechanics, etc. Nonetheless, moisture is a common ingredient of most manufactured goods and processed materials. Thus, all these applications emphasize the importance of sensing and detecting the level of the relative humidity (RH) [1–3]. WO_3 is the most widely used transition metal element in sensor technology, along with non-transition metal elements like ZnO and SnO_2 based materials [4–6]. As the chemical, physical and sensing characteristics of metal oxide sensors are affected by the method of synthesis, many preparative routes as electrospinning [7], solvothermal [8], modified thermal evaporation [9], precipitation [10], flame spray pyrolysis [11], and sol-gel [12] have been used for the preparation of WO_3 and WO_3-based gas sensing materials. Thus developing new preparative routes as well as compositional variations are two perspective aspects to achieve significantly sensitive and selective gas sensing materials. ZnO is an n-type semiconductor oxide with a large excitation binding energy (60 meV) and wide band gap energy (3.37 eV). Due to its significant structural, optical and catalytic properties, it is often used in many applications [13, 14]. Great attention has been paid to study the sensing properties of ZnO towards RH and different gases such as methanol, ethanol, propyl alcohol, and methane [15–18]. Having in mind this abovementioned research as well as our previous results [19, 20], demonstrating the possibility, by applying melt quenching and crystallization from glasses, to prepare materials from the WO_3-ZnO-Nd_2O_3-Al_2O_3 system for application as gas sensors for RH and ammonia, now we have extended our studies to investigate the WO_3-ZnO-La_2O_3-Al_2O_3 system.

The aim of this study is to synthesize glass crystalline materials from the WO_3-ZnO-La_2O_3-Al_2O_3 system containing high contents of WO_3 by applying controlled glass crystallization methods and to validate their sensitivity towards RH.

41.2 Experimental

41.2.1 Synthesis of Glass Crystalline Materials

Batches with the nominal compositions $76WO_3{\cdot}9.5ZnO{\cdot}9.5La_2O_3{\cdot}5Al_2O_3$ and $60WO_3{\cdot}7.5ZnO{\cdot}7.5La_2O_3{\cdot}25Al_2O_3$ were prepared using reagent grade WO_3, ZnO, La_2O_3 and Al_2O_3 as starting compounds. The homogenized batches from the starting oxides were melted for 20 min at 1240 °C in platinum crucibles in an air atmosphere. The melt was quenched by pouring and pressing between two copper plates (cooling rates 101–102 K/s). The as-quenched samples were examined by X-ray phase analysis with a Bruker D8 Advance diffractometer, using Cu Kα radiation in the $10° < 2\theta < 60°$ range. The glass transition (T_g), crystallization (T_p), and melting (T_m)

temperatures and the thermal stability of the glasses were determined using differential thermal analysis (DTA) (Machine STA, PT1600, TG-DTA/DSC). The as-obtained glasses were subjected to a heat treatment for 6 h at 530 °C, then for 3 h at 550 °C, and finally for 12 h at 560 °C in platinum crucibles in air atmosphere; by this way glass-crystalline specimens were obtained. The phase formation of the glass-crystalline samples was established by X-ray diffraction analysis as above. The glass – crystalline samples were studied by scanning electron microscopy (SEM) and energy dispersive X-ray spectroscopy (EDS). SEM analyses were performed with a JSM 6390 electron microscope (Japan) in conjunction with energy dispersive X-ray spectroscopy (EDS, Oxford INCA Energy 350) equipped with a ultrahigh resolution scanning system (ASID-3D) in the regimes of secondary electron images (SEI) and back scattered electron (BEC) images. Before attempting SEM characterization, the sample must be clean and completely dry. Surface oils or dirt must be removed with solvents such as methanol or acetone. The sample was mounted on a double coated conductive carbon tape that holds the sample firmly to the stage surface and can be used as ground strap from the sample surface to sample holder. The samples were carbon coated (time of coating ~20 s) as the upper carbon layer at that thickness will have little or no effect on the elemental analysis. The accelerating voltage was 20 kV, I ~65 mA. The pressure was on the order of 10^{-4} Pa. The obtained glass and glass – crystalline samples are listed in Table 41.1.

41.2.2 Humidity Sensor Preparation and the Sensing Mechanism

The sensors were prepared and tested as follows:

1. **Preparation of the interdigitated platinum electrodes:** Platinum conducting paste (ESL 5545, from Electro-Science, King of Prussia, PA, USA) was deposited manually by screen-printing technique onto planar α-alumina substrates (ADS-96 R, 96% alumina, Coors Tek, USA, 0.85 × 5 cm) by using a rubber squeegee through a 270 mesh steel screen; after drying overnight, these devices were heated at 980 °C for 20 min with a 2 °C/min heating/cooling ramp to optimize the electrical conductivity of the electrodes, according to the ink's manufacturer recommendations.

Table 41.1 Investigated compositions in the system WO_3-ZnO-La_2O_3-Al_2O_3

Nominal composition	Phases before heat treatment	Sample symbol	Phases after heat treatment	Sample symbol
76WO_3-9.5ZnO-9.5La_2O_3-5Al_2O_3	Glass	A	WO_3 + glass	C
60WO_3-7.5ZnO-7.5La_2O_3-25Al_2O_3	Glass	B	WO_3 + glass	D

2. **Preparation of the screen-printable ink:** The ink was prepared by dispersing the prepared powders in a suitable amount of the organic solvent ethylene glycol monobutyl ether (Emflow 227, Emca-Remex products, England) to reach the appropriate rheological behavior, adherence to the substrate and to achieve the correct thermal shrinkage properties during the process of screen-printing to obtain a good film.
3. **Preparation of the sensing film:** Thereafter, the screen-printable ink was deposited onto the interdigitated platinum electrodes by the screen-printing technique using a rubber squeegee through a 270 mesh steel screen; once these films were dried, the sensors were heated at 500 °C for 1 h with a 2 °C/min heating/cooling ramp. The formed thick film has thicknesses of about 30–40 μm and areas of about 1 cm^2, scotch tests on the fired films revealed a good adhesion onto the substrates.
4. **Testing of the humidity sensors:** The sensors were electrically characterized using a laboratory apparatus made of a thermostated chamber working at 25 °C in which the RH could be varied from 0% to 96%; the experimental details have been reported previously [21]. RH values were measured by means of a commercial humidity and temperature probe (Delta Ohm DO9406, Italy). Each tested sensor was alimented by an external alternating voltage (V = 3.6 V at a frequency of 1 kHz) and then constituted a variable resistance of this electrical circuit. A 2000 Keithley digital multimeter was used to measure the voltage VDC at the output of the circuit. The sensor resistance was determined by substituting them, in the circuit, by known resistances and then plotting a calibrating curve R = f (VDC). The sensor response (SR), expressed in %, was defined as the relative variation of the starting resistance, compared with the resistance measured under gas exposure as in Eq. (41.1):

$$SR(\%) = 100 \times \frac{|R_0 - R_g|}{R_0} \tag{41.1}$$

where R_0 and R_g are the starting resistance (in the absence of the test gas) and the gas-exposed measured resistance of the sensors, respectively.

41.3 Result and Discussion

According to the XRD data shown in Fig. 41.1, X-ray amorphous samples were obtained after quenching of the melt with $76WO_3{\cdot}9.5ZnO{\cdot}9.5La_2O_3{\cdot}5Al_2O_3$ (sample A) and $60WO_3{\cdot}7.5ZnO{\cdot}7.5La_2O_3{\cdot}25Al_2O_3$ (sample B) nominal compositions. The amorphous nature of the as-quenched samples was also confirmed by DTA analysis. The DTA curves of the synthesized glasses are presented in Fig. 41.2.

Glasses are characterized with a hump, corresponding to the glass transition temperature (T_g) followed by exothermic effect connected with the

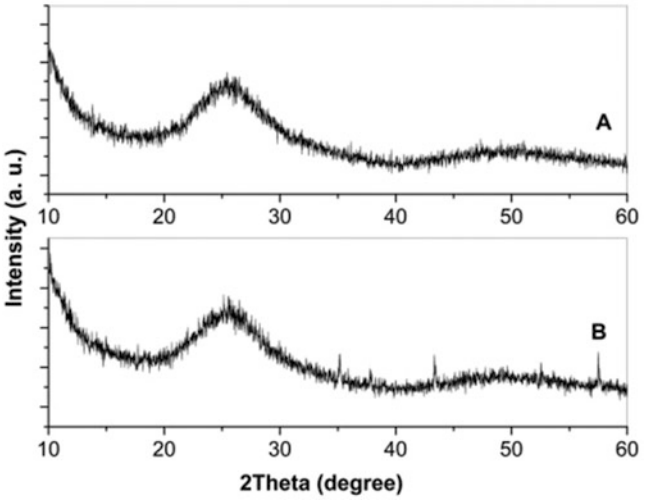

Fig. 41.1 XRD patterns of glass samples obtained by press quenching of the melt with nominal compositions $76WO_3{\cdot}9.5ZnO{\cdot}9.5La_2O_3{\cdot}5Al_2O_3$ (sample A) and $60WO_3{\cdot}7.5ZnO{\cdot}7.5La_2O_3{\cdot}25Al_2O_3$ (sample B)

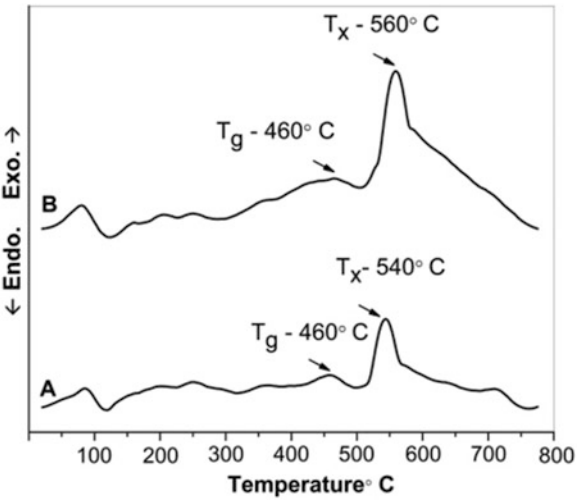

Fig. 41.2 DTA curves of glass samples obtained by press quenching of the melt with nominal compositions $76WO_3{\cdot}9.5ZnO{\cdot}9.5La_2O_3{\cdot}5Al_2O_3$ (sample A) and $60WO_3{\cdot}7.5ZnO{\cdot}7.5La_2O_3{\cdot}25Al_2O_3$ (sample B)

crystallization temperatures of the glasses (T_x). The calculated $\Delta T = T_x\text{-}T_g$ which is 80 °C for the glass sample A and 100 °C for the glass sample B exhibits a good thermal stability of the amorphous specimens obtained. Based on the

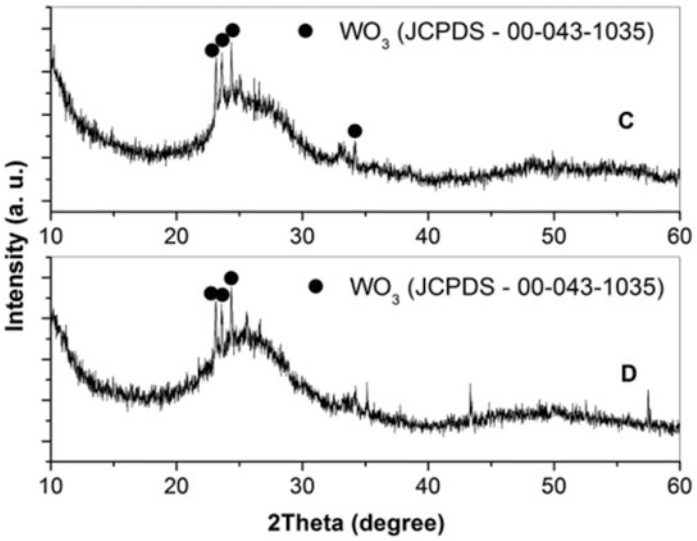

Fig. 41.3 XRD patterns of glass-crystalline samples obtained by heat treatment of the parent glasses with nominal compositions $76WO_3{\cdot}9.5ZnO{\cdot}9.5La_2O_3{\cdot}5Al_2O_3$ (sample C) and $60WO_3{\cdot}7.5ZnO{\cdot}7.5La_2O_3{\cdot}25Al_2O_3$ (sample D)

thermal parameters established, the glasses were subjected to a heat treatment for different times at around the crystallization temperatures T_x.

XRD patterns of the calcined samples are shown in Fig. 41.3. The analysis shows that glass-crystalline specimens, labeled as sample C and as sample D were obtained after the heat treatment from the parent glasses with $76WO_3{\cdot}9.5ZnO{\cdot}9.5La_2O_3{\cdot}5Al_2O_3$ and $60WO_3{\cdot}7.5ZnO{\cdot}7.5La_2O_3{\cdot}25Al_2O_3$ nominal compositions, containing WO_3 as a crystalline phase.

SEM analysis of the glass-crystalline sample C confirmed the XRD data obtained. As can be seen from the SEM image present in Fig. 41.4, the specimen is amorphous in nature. However the EDX elemental analysis of the sample showed that the content of the WO_3 is near 16 mol% which differs much from the initial composition (see Table 41.1). This difference can be regarded as evidence that part of WO_3 crystallizes and separates from the amorphous part of the sample.

Figure 41.5 illustrates the sensors' response of samples C and D towards RH. Sample C shows a significant response towards RH at room temperature starting from 33% RH, while sample D shows a lower sensitivity.

The response times (the time taken by a sensor to achieve 90% of the total resistance change in the case of gas adsorption) and the recovery times (the time necessary to reach 90% of the total resistance changes in the case of gas desorption) are shown in Fig. 41.3 and summarized in Table 41.2. These response and recovery times are quite fast of both samples although, sample D is quite faster than sample C (Fig. 41.6).

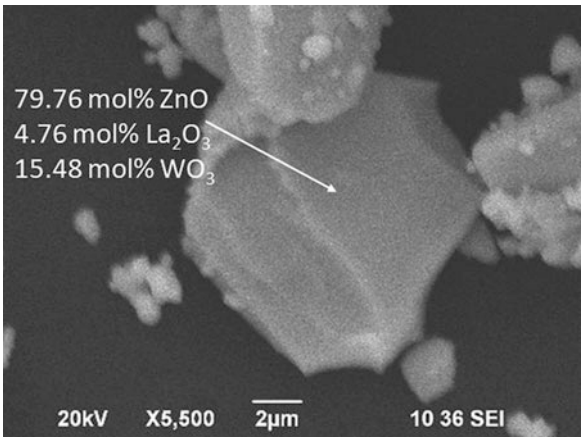

Fig. 41.4 SEM image of a sample, obtained after heat treatment of a parent glass with the nominal composition $76WO_3 \cdot 9.5ZnO \cdot 9.5La_2O_3 \cdot 5Al_2O_3$ (sample C)

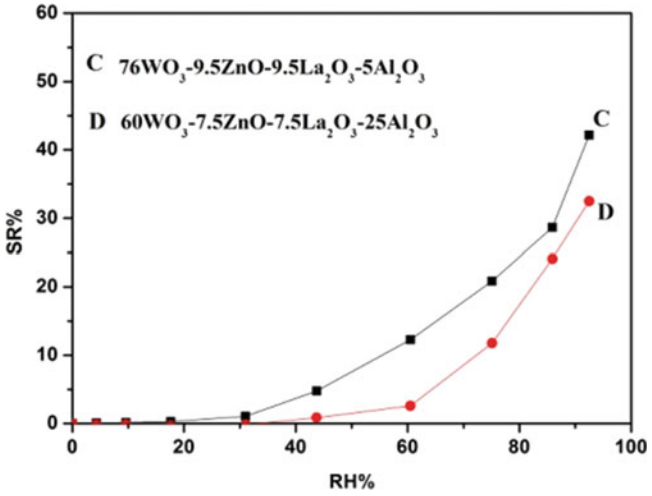

Fig. 41.5 Sensor's response towards relative humidity

Table 41.2 Response and recovery time of samples C and D

Humidity change	**Sample**	**0–60% RH**	**0–75% RH**	**0–95% RH**
Response time (min)	C	4	3.85	3.41
	D	3.92	3.1	3
Humidity change	**Sample**	**60–0% RH**	**75–0% RH**	**95–0% RH**
Recovery time (min)	C	1.61	1.8	1.93
	D	1.36	1.54	1.76

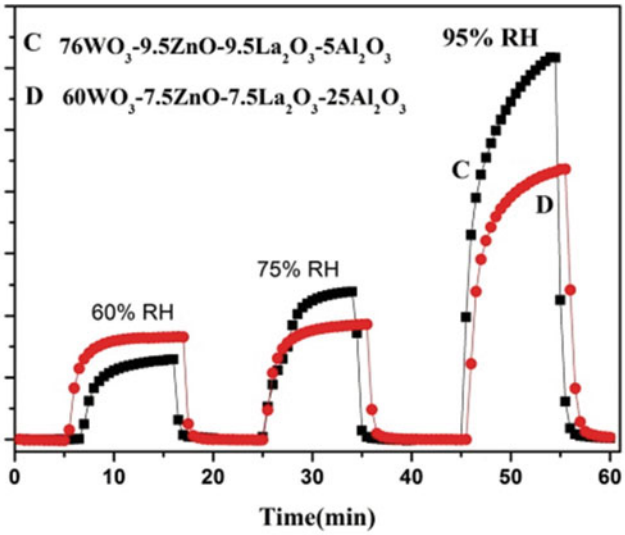

Fig. 41.6 Response and recovery time of the sensors

41.4 Conclusion

A glass crystallization method was used to prepare glass-crystalline samples after heat treatment of the parent glasses with $76WO_3{\cdot}9.5ZnO{\cdot}9.5La_2O3{\cdot}5Al_2O_3$ and $60WO_3{\cdot}7.5ZnO{\cdot}7.5La_2O_3{\cdot}25Al_2O_3$ nominal compositions near T_x. On measuring the sensitivity of samples C and D (glass crystalline samples) towards RH, Sample C shows a significant response towards RH at room temperature starting from 33% RH, while sample D shows a lower sensitivity. The response and recovery times are quite fast for both samples.

Acknowledgments The authors greatly acknowledge Professor Jean Marc Tulliani from department of Applied Science and Technology (DISAT), Politecnico di Torino, Turin, Italy, for working in his laboratory facilities for gas sensors testing and for fruitful discussions and Dr. Amr Mohamed, Chemistry Department, Taibah University, Saudi Arabia, for his valuable comments on the manuscript.

References

1. Zhou X, Zhang J, Jiang T, Wang X, Zhu Z (2007) Sensors Actuators A 135:209
2. Chou KS, Lee TK, Liu FJ (1999) Sensors Actuators B Chem 56:106
3. Patil DY, Seo YK, Hwang YK (2008) Sensors Actuators B Chem 128:374
4. Zheng H, Ou JZ, Strano MS, Kaner RB, Mitchell A, Kalantar-zadeh K (2011) Adv Funct Mater 21:2175
5. Potje-Kamloth K (2008) Chem Rev 108:367

6. Kamali Heidari E, Marzbanrad E, Zamani C, Raissi B (2009) Nanoscale Res Lett 5:370
7. Leng J, XU X, Lv N, Fan H, Zhang T (2011) J Colloid Interface Sci 54:356
8. Liu B, Cai D, Liu Y, Wang D, Wang L, Wang Y (2014) Sensors Actuators B Chem 28:193
9. Ponzoni A, Comini E, Ferroni M, Sberveglieri G (2005) Thin Solid Films 81:490
10. Sriyudthsak M, Supothina S (2006) Sensors Actuators B Chem 113:265
11. Siriwong C, Wetchakun K, Wisitsoraat A, Phanichphant S (2009) IEEE Sens Conf 1:118
12. Kim SJ, Cho PS, Lee JH, Kang CY, Kim JS, Yoon SJ (2008) Ceram Int 34:827
13. Ong HC, Lei DY, Li J, Xu JB (2010) In: Geddes CD (ed) Metal-enhanced fluorescence. Wiley, New York, p 393
14. Hahm J (2010) In: Geddes CD (ed) Metal-enhanced fluorescence. Wiley, New York, p 363
15. Kanan SM, El-Kadri OM, Abu-Yousef IA, Kanan MC (2009) Sensors 9:5158
16. Cheng XI, Zhao H, Huo LK, Gao S, Zhao JG (2004) Sensors Actuators B Chem 102:248
17. Nunes P, Fortunato E, Lopes A, Martins R (2001) J Int Inorg Mater 3:1129
18. Pal E, Hornok V, Kun R, Oszko A, Seemann T, Dékany I, Busse M (2012) J Colloid Interface Sci 100:378
19. Ataalla M, Milanova M, Hassan M, Afify AS, Tulliani JM, Dimitriev Y (2015) Nano-science advances in CBRN agents detection, information and energy security, NATO science for peace and security series A: chemistry and biology, 451
20. Ataalla M, Milanova M, Hassan M, Tulliani JM, Dimitriev Y, Iliev C (2014) J Nanosci Nanotechnol 14:126
21. Tulliani J-M, Bonville P (2005) Ceram Int 31:507

Chapter 42
Green Synthesis of Silver Nanoparticles Using *Lantana Camara* Leaf Extract and Their Use as Mercury(II) Ion Sensor

Didem Demir, Nimet Bölgen, and Ashok Vaseashta

Abstract Silver nanoparticles (AgNPs) were successfully synthesized via a bottom-up approach by using aqueous extract of *lantana camara* (LC) leaves as reducing and stabilizing agent. Characterization studies were done using UV-Vis spectroscopy and Fourier Transform Infrared Spectroscopy (FTIR). The average size, morphology and shape of the nanoparticles were determined by Scanning Electron Microscopy (SEM) and Dynamic Light Scattering (DLS). A light brown color indicated the synthesis of AgNPs, caused by a surface plasmon resonance (SPR) peak at 460 nm. The silver nanoparticles were used to detect mercury (Hg^{2+}) ions. A color change of the AgNPs solution from light brown to cloudy white due to oxidation of Ag^{0} to Ag^{+1} ions was observed. A good selectivity of the AgNPs towards mercury ions in water has been obtained. This method was found to be simple and rapid for detection of Hg^{2+} ions and demonstrated a potential to be used in environmental colorimetric sensor applications.

Keywords Green synthesis · Ag nanoparticles · Colorimetric sensor · Mercury ions

42.1 Introduction

Soil, air and water pollution due to heavy metals such as cadmium, mercury, lead, copper and zinc has been accepted as a global problem because of the adverse effect on humans, plants and animals [1]. Among the heavy metals, mercury is one of the most toxic pollutants in the environment. The presence of mercury in the

D. Demir · N. Bölgen (✉)
Mersin University, Engineering Faculty, Chemical Engineering Department, Mersin, Turkey
e-mail: nimet@mersin.edu.tr

A. Vaseashta
Institute for Advanced Sciences Convergence, and Int'l Clean Water Institute, Herndon, VA, USA

NJCU - State University of New Jersey, NJ, USA

P. Petkov et al. (eds.), *Advanced Nanotechnologies for Detection and Defence against CBRN Agents*, NATO Science for Peace and Security Series B: Physics and Biophysics, https://doi.org/10.1007/978-94-024-1298-7_42

environment may be the result of volcanic eruptions, rock weathering, natural fires, burning of fossil oils, its usage in cosmetics, dental amalgams, cement production, and mercury mining. Long-term exposure to mercury ions, even at very low concentrations, can permanently damage heart, brain, kidneys, lungs, nerves, and the endocrine system [2]. Therefore, the research related to detection and monitoring of these toxic metal ions has attracted significant attention in recent years. Many instrumental methods such as atomic absorption spectroscopy, fluorescence spectrometry and gas chromatography have been reported for detection of mercury ions [3]. However, these methods have disadvantages such as being expensive, needing long measurement times, and requiring complicated sample pretreatment and highly-trained operators. To overcome these limitations, the development of new methods which are fast, easy, simple; and have low cost is a requirement. Silver particles have been developed and used in many applications including the detection of mercury ions, due to their rapid, economic and eco-friendly synthesis procedure [4, 5]. In this study, AgNPs were green synthesized using an aqueous extract of LC leaves. LC is a vigorous growing plant and can be reached easily in most of the time in a year. The synthesis of the AgNPs was determined by UV-Vis and FTIR. The size distribution of AgNPs was demonstrated by the DLS method; their morphology and shape were determined by SEM. An easy, simple and low-cost synthesis method allows to use AgNPs as a colorimetric sensor for detection of mercury ions in aqueous solutions.

42.2 Materials and Methods

42.2.1 Chemicals

LC leaves were collected from the gardens of Mersin University, Turkey. Silver nitrate ($AgNO_3$) was obtained from Sigma-Aldrich, USA. Distilled water was used for all the experiments. All heavy metal solutions ($ZnSO_4{\cdot}7H_2O$, $CrN_3O_9{\cdot}9H_2O$, CdN_2O_6, $HgCl_2$, $FeSO_4$ and PbN_2O_6) were prepared at 1.0 mM by mixing the requisite amount of heavy metal in distilled water.

42.2.2 Preparation of LC Leaf Extract

AgNPs were prepared by an eco-friendly method using an extract solution of LC leaves. The leaves of the freshly collected plant were washed several times with distilled water to remove any dirt. Leaves were dried in an oven at 40 °C for 48 h. and subsequently grounded to a fine powder; 10 g of them were boiled in 100 mL distilled water at 60 °C. After 30 min, the extract was cooled to room temperature, filtered through a cheese cloth and then centrifuged at 45 × 100 rpm for 5 min. The resulting LC extract was kept in a refrigerator at 4 °C until further usage.

42.2.3 Green Synthesis of AgNPs by Using the LC Leaf Extract

For the synthesis of AgNPs, the LC leaf extract was used as a reducing agent for $AgNO_3$ salt to reduce the Ag^{+1} ions to Ag^0. Ten milliliter of the extract was added into 100 ml of 1 mM of $AgNO_3$ solution at room temperature. A magnetic stirrer was used to mix the solution for 60 min. After mixing, the solution was kept in dark condition for 48 h. As a result, the color of the solution was changed from yellow to light brown, indicating the formation of AgNPs. It showed that aqueous silver ions could be reduced by an aqueous extract of LC leaves.

42.2.4 Colorimetric Sensing of Hg^{2+} Ions by AgNPs

Green synthesized AgNPs from LC leaf extract were used as a nano colorimetric sensor probe for the detection of Hg^{2+} in aqueous solution at room temperature (Fig. 42.1). To investigate the sensing ability of AgNPs for different heavy metal ions, selectivity studies were carried out with various metal ions such as $ZnSO_4{\cdot}7H_2O$, $CrN_3O_9{\cdot}9H_2O$, CdN_2O_6, $HgCl_2$, $FeSO_4$ and PbN_2O_6 in aqueous media. The color changes in the AgNPs solution after the addition of various metal ions were examined by using UV-Vis spectroscopy.

42.2.5 Characterization Studies

FTIR (Frontier Spectrometer, Perkin Elmer, USA) was used to determine the chemical composition of the LC leaf extract and the synthesized AgNPs. FTIR analysis was performed with a resolution of 4 cm^{-1} in the wavelength range of

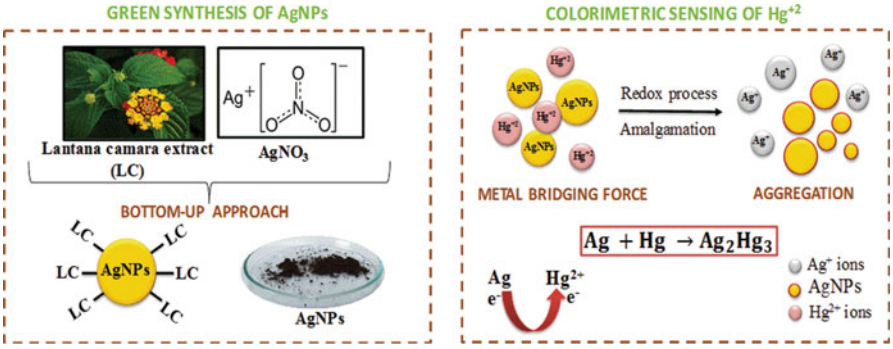

Fig. 42.1 Mechanism of synthesis and colorimetric sensing ability of AgNPs

450–4000 cm^{-1}. The particle size distribution of the synthesized AgNPs was characterized by DLS (Zetasizer Nano ZS90, Malvern, England). The AgNPs were dispersed in distilled water. The surface morphology of the synthesized AgNPs was investigated using SEM (Supra 55, Zeiss, Germany) after coating with platinum. The UV-Vis absorbance of the AgNPs was measured using UV-Vis spectroscopy (Chebios Optimum-One UV-VIS Spectrometer, Italy).

42.3 Results and Discussion

42.3.1 Characterization of AgNPs

The synthesis of AgNPs in aqueous solution of $AgNO_3$ was demonstrated by measuring UV-Vis spectra of the solution in the wavelength range from 300 to 800 nm, after diluting the sample with distilled water (Fig. 42.2a). In the spectrum a broad peak observed at near 460 nm indicates the formation of AgNPs. The transparent color of the silver nitrate solution turned to light brown after addition of the LC extract. The color change of solution was attributed to the excitation of SPR [6].

The FTIR spectrum demonstrates the presence of phenolic compounds in the LC extract, interaction of AgNPs with LC leaf biomolecules and functional groups of the stabilized AgNPs. The FTIR spectra of the LC leaf extract and the synthesized AgNPs are shown in Fig. 42.2b. The broad band at 3305 cm^{-1} in both spectra is characteristic for O-H stretching vibration [7]. The peak at 2190 cm^{-1} is due to the stretching vibration of aliphatic -CH- groups containing compounds present in the LC leaf extract while the sharp absorption band at 1704 cm^{-1} is due to molecules

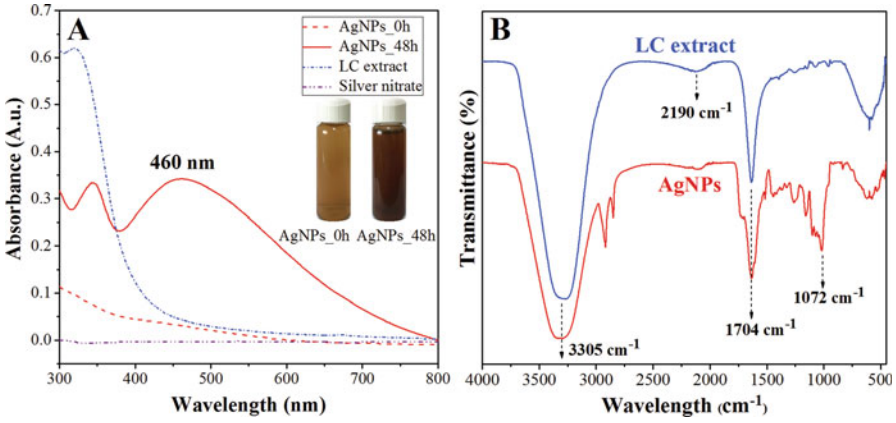

Fig. 42.2 (**a**) UV-Vis absorption spectrum of the LC extract, a silver nitrate solution, and the synthesized AgNPs after 30 min and after 48 h; (**b**) FTIR spectrum of the LC leaf extract and stabilized AgNPs

containing –C=O group present in the LC leaf extract [8]. New peaks are observed in the 900–1400 cm^{-1} region after interaction of LC leaf extract with silver nitrate solution. The strong band at 1072 cm^{-1} is due to ether linkages and suggest the presence of flavanones adsorbed on the surface of metal nanoparticles. The immediate reduction and capping of silver ion into silver nanoparticles may be due to flavonoids and proteins. The flavonoids present in the leaf extract are powerful reducing agents which may play a role in the formation of AgNPs [9].

Dynamic light scattering studies of the colloidal AgNPs were carried out to investigate the average size of the particles in the solution. The size distribution of the synthesized AgNPs is shown in Fig. 42.3a. The average size of the AgNPs was 22.95 nm while the polydispersity index (PDI) of the sample was 0.46, which showed that the synthesized sample was homogeneous and uniform in size.

The shape and morphology of AgNPs were characterized using SEM as demonstrated in Fig. 42.3b. AgNPs were observed as aggregated spherical particles with average particle sizes less than approximately 10 nm. The average particle size of AgNPs obtained by DLS can be larger than the size obtained by SEM, as here the hydrodynamic size of the nanoparticles is measured, as a result of attachment of water on particle surface [10].

42.3.2 Colorimetric Sensing of Hg^{2+} Metal Ions by AgNPs

The ion detection ability of the green synthesized AgNPs was examined separately for a range of metal ions including Zn^{2+}, Cr^{3+}, Cd^{2+}, Hg^{2+}, $Fe^{2+}$and Pb^{2+}. 300 µL of 1×10^{-4} M ion solution was added to 3 mL of AgNPs solution. UV-Vis absorption studies demonstrated that only Hg^{2+} caused a change in color of the solution and showed a change in SPR band intensity of AgNPs (Fig. 42.4). This selectivity can be of advantage for the detection of Hg^{2+} in the presence of other metal ions.

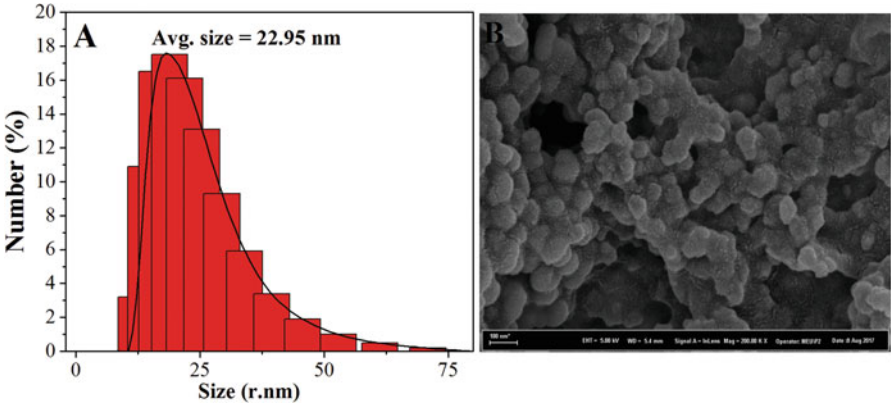

Fig. 42.3 (**a**) Particle size distribution of AgNPs; (**b**) SEM image of AgNPs

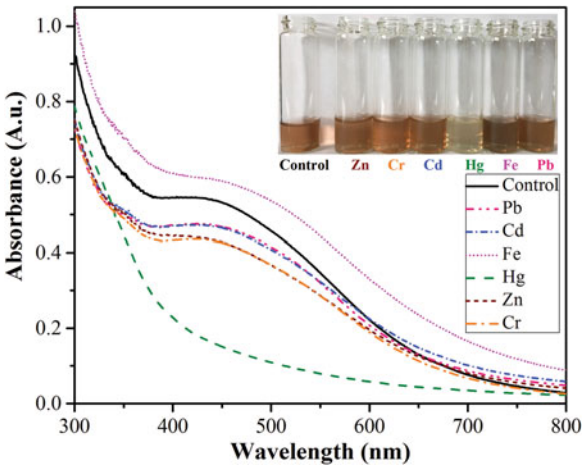

Fig. 42.4 UV-Vis absorption spectra of *green* synthesized AgNPs in the presence of heavy metal ions

42.4 Conclusion

A one step green synthesis of AgNPs was achieved by mixing $AgNO_3$ solution with LC leaf extract. The extract acted as a reducing agent. The biosynthesized nanoparticles were evaluated for colorimetric detection of heavy metal ions. The selective sensitivity of the AgNPs for the detection of Hg^{2+} ions were probed by changes in the SPR resonance. This selectivity demonstrated the potential use of AgNPs for colorimetric detection of Hg^{2+} in the presence of other metal ions.

References

1. Cheon JY, Park WH (2016) International Journal of Molecular Sciences, Green synthesis of silver nanoparticles stabilized with mussel-inspired protein and colorimetric sensing of lead(II) and copper(II) ions. Int. J. Mol. Sci. 17:1–10
2. Tchounwou PB, Yedjou CG, Patlolla AK, Sutton DJ (2012) Heavy metals toxicity and the environment. NIH Public Access 101:133–164
3. Ahmed MH, Hasan N, Mohiuddin S (2014) Silver nanoparticles: green synthesis,characterization, and their usage in determination of mercury contamination in seafoods. ISRN Nanotechnol 2014:1–5
4. Annadhasan M, Muthukumarasamyvel T, Sankar Babu VR, Rajendiran N (2014) Green synthesized silver and gold nanoparticles for colorimetric detection of Hg2+, Pb2+, and Mn2 + in aqueous medium. ACS Sustain Chem Eng 2:887–896
5. Lokhande C, Shinde NM, Shelke A, Babar PT, Kim JH (2017) Reliable and reproducible colorimetric detection of mercury ions (Hg2+) using green synthesized optically active silver nanoparticles containing thin film on flexible plastic substrate. J Solid State Electrochem. 21:2747–2751
6. Balashanmugam P, Kalaichelvan PT (2015) Biosynthesis characterization of silver nanoparticles using Cassia roxburghii DC. aqueous extract, and coated on cotton cloth for effective antibacterial activity. Int J Nanomedicine 10:87–97

7. Ihsan M, Niaz A, Rahim A, Zaman MI, Arain MB, Sirajuddin TS, Najeeba M (2015) Biologically synthesized silver nanoparticle-based colorimetric sensor for the selective detection of Zn2+. RSC Advances 5:91158–91165
8. Dash SS, Bag BG, Hota P (2015) Lantana camara Linn leaf extract mediated green synthesis of gold nanoparticles and study of its catalytic activity. Appl Nanosci 5:343–350
9. Anandalakshmi K, Venugobal J, Ramasamy V (2016) Characterization of silver nan particles by green synthesis method using Pedalium murex leaf extract and their antibacterial activity. Appl Nanosci 6:399–408
10. Mohanta YK, Panda SK, Biswas K, Tamang A, Bandyopadhyay J, De D, Mohanta D, Bastia AK (2016) Biogenic synthesis of silver nano-particles from Cassia fistula (Linn.): in vitro assessment of their antioxidant, antimicrobial and cytotoxic activities. IET Nanobiotechnol 10:438–444

Chapter 43
Highly Ordered AAO Layers for Various Sensor Applications

S. Kozhukharov, Ch. Girginov, and O. Kostadinova

Abstract Automation is applied in continuously extending fields of application in the modern communities. In this respect, sensors are indispensable elements of systems for automatic regulation. Besides, the use of multitudes of sensor elements enables statistical data acquisition from large time and long distance monitoring. Consequently, the requirements for application of multitudes of sensor elements impose a need for elaboration of advanced sensor element production. In this context anodized aluminum oxide (AAO) layers enable the elaboration of relatively simple, large scale technology for reliable and durable sensor elements. The present review is devoted to a summary of the basic concepts related to the elaboration of reliable and durable sensor elements on the basis of anodized aluminum. Furthermore, various examples are provided regarding the recent research activities in this field.

Keywords Anodization · Sensors · Anodized aluminium oxide · Relative humidity

43.1 Introduction

The anodization is relatively simple procedure that enables formation of highly ordered oxide layers. Anodized aluminium oxide (AAO) self-assembled monolayers (SAM) [1, 2] have various possible industrial applications. This method can be used for precise texturing of aluminium roll surfaces for ink-printing on paper and plastic packaging materials [3–5], and even for flexible solar cell production [6]. Besides, these layers can successfully be used for large series of metal oxide semiconductor (MOS), metal dielectric semiconductor (MDS),

S. Kozhukharov · C. Girginov
University of Chemical Technology and Metallurgy, Sofia, Bulgaria

O. Kostadinova (✉)
Section "Solid-State Electrolytes", Institute of Electrochemistry and Energy Systems – BAS, Sofia, Bulgaria
e-mail: ofeliya.kostadinova@iees.bas.bg

P. Petkov et al. (eds.), *Advanced Nanotechnologies for Detection and Defence against CBRN Agents*, NATO Science for Peace and Security Series B: Physics and Biophysics, https://doi.org/10.1007/978-94-024-1298-7_43

and metal oxide semiconductor field effect (MOSFE) high performance transistors and integrated micro-schemes, based on these electronic elements [7, 8].

The AAO pore formation is an object of interest for many years. Abdel-Karim and El-Raghy [1] summarized the basic steps in the theoretical base of this process. According to them, the basic concepts for pore initiation by barrier layer breakthroughs, followed by further pore growth by local oxide dissolution were proposed by Baumann in 1939. Afterwards, this concept was further developed by Keller in 1953, who proposed pore formation by enhanced oxide dissolution caused by local temperature rises. These concepts are completed by Akahori in 1961, who suggests that these temperature increases could be sufficient to promote simultaneous electrolyte evaporation and partial Al-melting followed by formation of new oxide beneath the pores.

Stępniowski and Salerno [2] describe the correlation between the applied process conditions (i.e. preliminary surface treatment, applied voltage or current density, temperature, duration, electrolyte composition, etc.) and the resulting AAO pores morphology and ordering (e.g. pores depth and diameter, average distance between neighboring pores, etc.). Later in the same chapter, the authors propose this method for template-assisted electrochemical fabrication of metallic nanowires, giving examples for Al, Ag, Ni, Bi, Co, Fe, Pt, Pd, Sn, Zn, and even metallic mixtures. Considering the self-assembling capabilities of AAOs during their formation, Kumeria [9] and Santos [10] propose the use of AAOs as optical diffraction grids for optical sensor construction. A schematic view of a highly ordered AAO film in a H_2SO_4 electrolyte is presented in Fig. 43.1 [11].

The most remarkable advantage of the anodization process is the relatively easy control of pore morphology (diameter and depth) and distribution, which has been demonstrated by various authors [1, 2, 12–15]. Besides, in a previous work [16], it was demonstrated that the formation of AAO layers with a comb-like topology is also possible via reaching the breakdown potential. This approach is successfully used for formation of quasi-periodic quantum dots arrays [17].

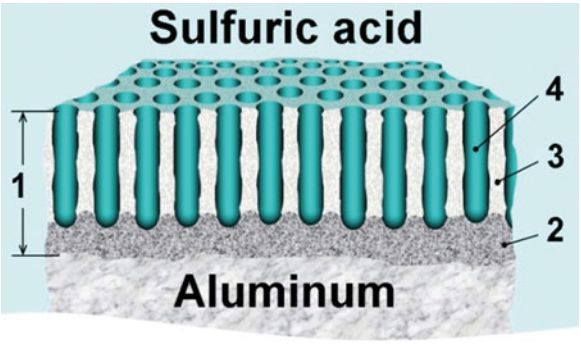

Fig. 43.1 Illustration of the formation of porous oxide films on pure Al surfaces after anodization in an acidic medium *1* – anodised aluminium oxide layer, *2* – thin dense part of the layer, *3* – thick porous part of the layer, *4* – channel shape pores [11]

On the basis of the above mentioned facts, the present brief review aims to summarize the possibilities for sensor element design and production on the basis of aluminium anodization.

43.2 Basic Concepts

In general, the term "sensor element" comprises all the electronic components which initiate or modify the parameters of electric signals passing through them, according to the conditions of their environment [18]. Hence, the sensor elements can be divided into active and passive sensors, regarding whether these elements generate or modify the measurable signal. In the former case, the sensors usually serve as galvanic elements, whereas in the latter case, their ohmic resistance and/or the capacitive resistance changes, modifying the electric signal parameters [19]. In all cases, the sensor elements should provide a reliable, measurable and linear correlation between the change of the measurable environment parameter (input variable) and the electrical signal characteristics (output variable). In this sense, the sensor elements should possess: (1) an *acceptable deviation* of the output variable values; (2) a short *response delay* time; (3) a high *sensitivity*; (4) a large *detection range* (with a definitely linear correlation between input and output values) [18–20]; (5) a low *output signal hysteresis* and (6) a significant difference between the maximal and minimal output signal values (*i.e. max/min output signal range*). An example for sensor response characteristics is shown in Fig. 43.2.

Another important feature of sensor elements is *selectivity* regarding the compounds which are object of detection. In this sense, anodization provides possibilities for elaboration of highly ordered porous "honey comb" interface structures able to adsorb only one type of molecules, resulting in high sensor selectivity.

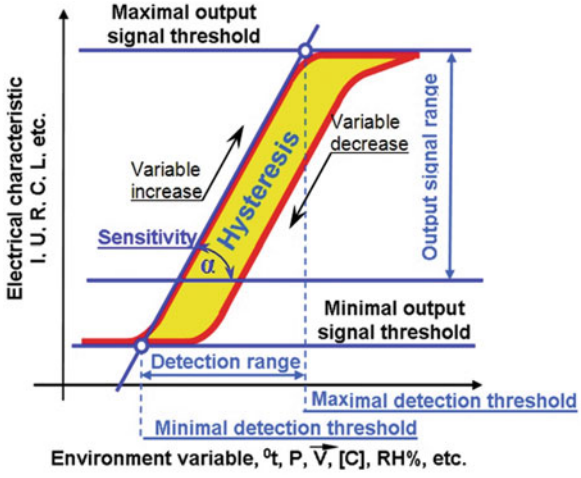

Fig. 43.2 Schematic illustration of the correlation between the input and output characteristics of a sensor element

43.2.1 Chemical sensors

In general terms, chemical sensors are based on chemical conversion reactions between an active compound from the sensor element and the compound from the environment, which is object of detection. The functional principle of this group of sensors is based on heterogeneous chemical conversions on the AAO interface relying on adsorption and desorption processes. Thus, the sensing mechanism is multistage and includes (i) adsorption, (ii) chemical conversion, (iii) desorption. The chemical reactions should be reversible, in order to guarantee long term reliable service. Otherwise, the sensor elements can only serve as replaceable critical concentration detectors for emergency equipment. Various chemical gas-phase detection [10, 21–25] and liquid phase [26] sensors are developed.

43.2.1.1 Gas Phase Chemical Sensors

These sensors can be used in various fields of the human activities, like energy production, transport, environment monitoring, etc. as illustrated in Fig. 43.3.

In this aspect, the AAO layers can be easily modified by incorporation of various chemically active compounds, and particularly metals and transition elements. Various examples for incorporation of Fe [27], Ag [28], Cu [29, 30], Co [31–33], Ni [34], mixed Ni-Cu systems [35] have been demonstrated.

43.2.1.2 Liquid Phase Chemical Sensors

The basic fields of their applications are related to detection of heavy metals or organic contaminants in drinking and industrial water. Heavy metal detection is important for the industrial sector, because it enables to quantify the corrosion rate of

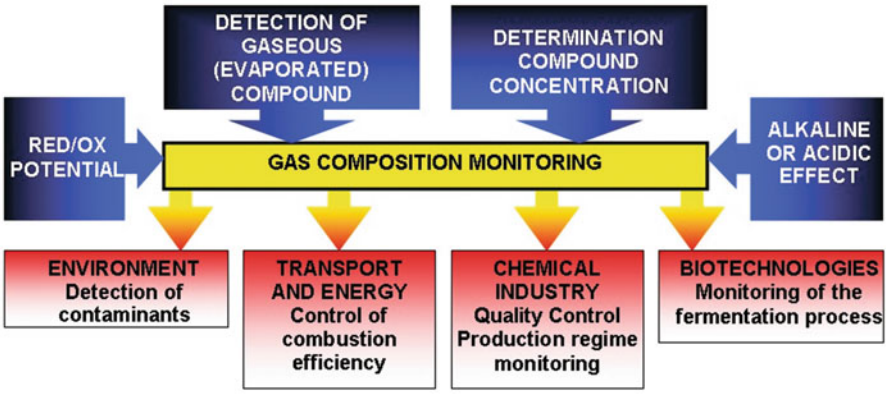

Fig. 43.3 Fields of applications of gas-phase chemical sensors

water delivery pipelines, heat exchange, and cooling equipment. Organic contaminants are basic objects of monitoring in the cases of drinking water. Acceptable organic compound contents in the drinking water are defined by *Chemical Oxygen Demand* (COD) and *Biological Oxygen Demand* (BOD) [36, 37]. The latter criterion is related to the occurrence of potentially pathogenic microorganisms in the water sources. Furthermore, Navaza et al. [38] describe membrane indicator electrodes as an entire class of sensors for biomedical analysis.

In this sense, aluminium anodization provides possibilities for the creation of semi-permeable membranes, after metallic substrate removal usually by dissolution. In this aspect, Wooten et al. propose multilayered $SiO_2 - Al_2O_3 - SiO_2$ [39] porous membranes, suitable for this purpose. Such membranes with exactly defined porosity can be successfully used for elaboration of indicator electrodes for water quality analysis.

43.2.2 Physical Sensors

This group of sensor elements is based on physical interactions between the sensor element and its environment, and can be used for determination of parameters (input variables) like temperature, pressure, mechanical tensions, etc. Nevertheless, the present brief review is focussed only on sensors for relative humidity and chemical compounds determination.

43.2.2.1 Humidity Sensors: The Relative Humidity (RH)

RH affects various areas of human activities, revealing generally detrimental effects, causing corrosion [40] or being an appropriate medium for the development of various microorganisms [41, 42] which are able to deteriorate various nutrition [43] and pharmaceutical [44] products, or even harmful for the human health [45]. At last, high levels of humidity favor destruction in both electrical conductors [46] and insulation materials [47–49], thus affecting branches as high voltage energy supply, microelectronics, automation and communications. Obviously, it damages composition, structure and properties of various hygroscopic materials, causing remarkable economic losses when such materials are employed. Nevertheless, the humidity possesses beneficial effects in some cases, such as greenhouse agricultural [50, 59] and antibiotics production [51]. Some branches of chemical industry, as the catalyzed steam-reforming of hydrocarbons [52], and storage of explosive materials [53, 54] also require elevated levels of humidity. All of the mentioned above branches of human activity emphasize the tremendous importance of humidity measurement and control. Table 43.1 summarizes the human activity branches affected by humidity.

The remarkable importance of the RH levels has generated intensive research activities for elaboration of advanced humidity sensors on the basis of highly ordered

Table 43.1 Human activity branches affected by humidity

No	Detrimental effects	Beneficial effects
1.	Human health	Greenhouse plants growth
2.	Transport vehicles corrosion	Fungal antibiotics production
3.	Building constructions deterioration	Storage of explosive soil fertilizers,
4.	Microelectronic devices shortcircuits	
5.	High voltage delivery systems breakdowns	
6.	Undesirable chemical products hydratation	
7.	Automatic control systems failures	
8.	Nutrition products deterioration	
9.	Pharmaceutical products decomposition	

AAO layers with elevated adsorption capabilities [55–58]. In this case, the AAO films favour water vapour adsorption and subsequent capillary condensation. The condensed thin water layers serve as conductive pathways which close the electric circuit between additively deposited electrodes (usually Pt) [59, 60].

Another possible construction is by two parallel Al plates with AAO films deposited face to face [55]. In this case, the sensors serve as electric capacitors, the capacitance of which varies with the quantity of adsorbed water. In the former concept, the measurable output signal is the change of the electrical conductivity (or resistance, respectively), whereas the latter type of sensors change their capacitance. In comparison to the conductivity based sensors, the capacitive humidity sensor elements enable more precise RH value determination, but require modulated high frequency AC sources.

43.2.2.2 Optical Sensors and Biosensors

The possibility of self-assembled AAO layers to be used as diffractive gratings proposed by Kumeria et al. [9] and Santos et al. [10] is already successfully used for optical sensors and biosensors. The AAO based optical sensors provide possibilities for DNA and protein analysis, which is of particular interest for biochemical analysis for medical applications.

43.3 Conclusions

The present brief review summarizes the possibilities for sensor element design and production on the basis of aluminium anodization. Besides, some basic concepts and terminology related to the sensor element characterization were mentioned, due to their indispensability, when a new sensor element is being developed. Various examples for chemical and physical sensors for house-hold, industrial, environment monitoring, and biochemical analysis are given, emphasizing the versatility of the

AAO based sensors. The literature analysis in the present brief review results in several basic conclusions:

1. The anodization is a relatively simple procedure that enables the formation of highly anodised aluminium oxide (AAO) self-assembled monolayers (SAM) with various possible industrial applications**.** Although this method is object of interest for many years, the application of the obtained AAO layers was continuously extending during the recent years.
2. Among the basic advantages is the possibility for incorporation of various metals, like Al, Ag, Ni, Bi, Co, Fe, Pt, Pd, Sn, Zn, and even metallic mixtures, which can serve as active compounds of various chemical sensors.
3. Another advantage of the anodization is that the formation of AAO layers with a comb-like topology is also possible via applying of breakdown potentials.
4. Finally, it can be concluded that the anodization method provides possibilities for elaboration of high performance advanced sensor elements with versatile applications.

Acknowledgments The present review work has been performed by the financial support of the Bulgarian National Scientific Fund, Project T 02 – 27.

References

1. Abdel-Karim R, El-Raghy SM (2014) Chapter 7. Fabrication of nanoporous alumina In: Ebothe J, Ahmed W (eds) Nanofabrication using nanomaterials. One Central Press, ISBN:9781910086155, pp 197–218
2. Stępniowski WJ, Salerno M (2014) Chapter 12. Fabrication of nanowires and nanotubes by anodic alumina template-assisted electrodeposition. In: Ahmed W, Ali N (eds) Manufacturing nanostructures. One Central Press, pp 321–357. isbn:9781910086070
3. Smith TM (1975) Label roll package Patent US 3987897 A
4. Cleveland RE Press roll for paper making machines and the method of making same Patent US 2114072 A
5. Self-centering feed rolls for a dowel machine or the like Curt J Patent US 2780253
6. Bocchetta A, Santamaria M, Di Quarto F (2014) Preparation of large area anodic alumina membranes and their application to Thin film fuel cell. J Mater Sci Nanotechnol 1:1–9
7. Vachkov P, Ivanov D (1990) Powerful MOS transistors and their application In: Powerful MOS transistors and their application, Gov. Ed. "Tekhnicka" (Sofia), 15–18
8. Klauk H (2009) Oxide dielectrics: a change of direction. Nat Mater 8:853–854
9. Kumeria T, Santos A, Losic D (2014) Nanoporous anodic alumina platforms: engineered surface chemistry and structure for optical sensing applications. Sensors 14:11878–11918
10. Santos A, Kumeria T, Losic D (2014) Nanoporous anodic alumina: a versatile platform for optical biosensors. Mater Des 7(6):4297–4320
11. Kozhukharov SV (2016) Deposition of environmentally compliant cerium-containing coatings and primers on copper-containing aluminium aircraft alloys. In: Tiwa-ri A, Galanis A, Soucek MD (eds) Biobased and environmental benign coatings. Wiley, Hoboken
12. Wernick S, Pinner R (1972) The surface treatment and finishing on aluminium and its alloys, 4th edn. Robert Draper Ltd, Teddington
13. Masuda H, Hasegwa F, Ono S (1997) Self-ordering of cell arrangement of anodic porous alumina formed in sulfuric acid solution. J Electrochem Soc 144:L127–L130

14. Masuda H, Fukuda K (1995) Ordered metal nanohole arrays made by a two-step replication of honeycomb structures of anodic alumina. Science 268:1466–1468
15. Masuda H, Yada K, Osaka A (1998) Self-ordering of cell configuration of anodic porous alumina with large-size pores in phosphoric acid solution. Jpn J Appl Phys 37:L1340–L1342
16. Ch G, Kozhukharov S (2011) Surface of alumina films after prolonged breakdowns in galvanostatic anodization. Internat J Electrochem 2011:1–5. Article ID 126726
17. Bandyopadhyay S et al (1996) Electrochemically assembled quasi-periodic quantum dot arrays. Nanotechnology 7:360–371
18. Danev S (1993) In: Bases of the automatic regulation, ("MARTILEN" Sofia), 105–107
19. Kozhukharov S, Nenova Z, Nenov T, Ivanov S (2010) Influence of dopants on the performance of humidity sensitive elements by deposition of TiO2 via sol-gel method annual proceedingsof "AnguelKanchev" University of Rousse (Bulgaria) 49(9.1): 33–35
20. Nenova Z, Ivanov S, Nenov T (2011) Sensors for industrial automation. Ex-Express, Gabrovo, pp 89–90
21. Abrego I, Campos A, Bethancourt G, Ching-Prado E (2012) A study of anodization time and voltage effect on the fabrication of self- ordered nano-porous aluminum oxide films: a gas sensor application a gas sensor application. Mater Proceed Res Soc Symp 1449:73–79
22. Varghese OK, Grimes CA (2003) Metal oxide nanoarchitectures for environmental sensing. J Nanosci Nanotechnol 3:277–293
23. Rumiche F, Wang H, Hub W, Indacochea J, Wang M (2008) Anodized aluminum oxide (AAO) nanowell sensors for hydrogen detection. Sensors Actuators B Chem 134:869–877
24. Varghese O, Gong D, Dreschel W, Ong K, Grime C (2003) Ammonia detection using nanoporous alumina resistive and surface acoustic wave sensors. Sensors Actuators B 94:27
25. Ding D, Chen Z, Lu C (2006) Hydrogen sensing of nanoporous palladium films supported by anodic aluminum oxides. Sensors Actuators B Chem 120:182–186
26. Sriram G (2016) Current trends in nanoporous anodized alumina platforms for biosensing applications. J Nanomater 2016:1–24. Article ID 1753574
27. Yongqing S (2000) Electrolytic coloring of aluminum in ferrous sulfate solution. Met Finish 98:61–62
28. Anicai L (1998) Analysis of electrochemical colored aluminum anodic films in AgNO3-based electrolytes by diffuse reflectance spectra. Met Finish 96:10–13
29. Shih HH, Huang YC (2008) Study on the black electrolytic coloring of anodized aluminum in cupric sulfate. J Mater Process Technol 208:24–28
30. Pastore G, Montes S, Paez M, Zagal JH (1989) Electrocolouring of anodized aluminium with copper: effect of porous and barrier oxide film thicknesses. Thin Solid Films 173:299–308
31. Girginov C, Kanazirski I, Dimitrov TS (2012) Electrolytic coloring of anodic alumina in CoSO4 solution. Part one: influence of pretreatment and the AC polarization frequency. Ann Proceeds Univ Rousse (Bulgaria) 51:57–63
32. Girginov C, Kanazirski I, Dimitrov TS (2012) Electrolytic coloring of anodic alumina in CoSO4 solution part two: influence of the aluminum alloy type. Ann Proceeds Univ Rousse (Bulgaria) 51:64–68
33. Girginov Ch KI, Ilcheva V (2013) Electrolytic coloring of porous aluminum oxide films in CoSO4 solution. Bulg Chem Commun 45:52–56
34. Girginov C, Kanazirski A, Zahariev P, Stefchev J (2012) Electrolytic colouring of anodic alumina films in metal ions containing solution, part one: electrolytic colouring in NiSO4 containing solution. Univ Chem Tech Met 47:187–192
35. Kanazirski I, Girginov C, Girginov A (2012) Electrolytic colouring of anodic alumina films in NiSO4, CuSO4 and (NiSO4 + CuSO4) containing electrolytes. Adv Natur Sci 1:45–51
36. Bulgarian National Standard BDS БДС (1977) 17.1.4.02 Опазване на природата. Хидросфера. Показатели за качествата на водите. Метод за определяне на окисляемостта, (it is written only in Bulgarian, http://www.bds-bg.org/bg/standard/?natstandard_document_id=11347) http://www.bds-bg.org/bg/standard/?ics_id=4210

37. Buchauer K A comparison of two titration procedures to determine volatile fatty acids in influents to waste water and sludge treatment processes ISSN 0378-4738 Water SA, 24; Innsburg Austria No 01.01.1998 p 49
38. D'Ocon-Navaza C, Garcia-Saavedra JG, Garcia JCV (1999) Fundamenos y técnicas de análisis bioquímico. International Thompson Publishing, Madrid, pp 143–167
39. Wooten MKC, Koganti VR, Zhou S, Rankin SE, Knutson BL (2016) Synthesis and nano filtration membrane performance of oriented mesoporous silica thin films on macroporous supports. ACS Appl Mater Interfaces 8:21806–21815
40. Davis J (2000) ASM international, corrosion: understanding the basics. American Technical Publishers Ltd, Ohio, pp 6–10. 2. A
41. Kozhukharov S, Nenova Z, Nenov T, Ivanov S, Machkova M (2013) Elucidation of the contribution of modified titania films over the performance of thin film humidity sensors. J Chem Technol Metal 48:142–146
42. Nenova Z, Kozhukharov S, Nenov T, Nedev N, Machkova M (2012) Development of sensing elements for humidity by deposition of Ce-doped SiO2 films prepared via a sol-gel method. Ann Proceed Univ Rousse (Bulgaria) 51(9.1):14–18
43. Idah P, Musa J, Abdullahi M (2010) Effects of storage period on some nutritional properties of orange and tomato. Assumpt Univ-Jour Technol 13:181–185
43. Kiron S, Shirwaikar A, Saritha M (2011) Influence of storage conditions on the potency of amoxicillin dispersible tablets stored in hospital and community pharmacies in different regions of kerala. Asian J Pharm Clin Res 4(3):101–102
45. Arundel V, Sterling E, Biggin J, Sterling T (1986) Indirect health effects of relative humidity in indoor environments. Environ Health Perspect 65:351–361
46. Veleva L, Dzib-Pérez L, González-Sánchez J, Pérez T (2007) Initial stages of indoor atmospheric corrosion of electronics contact metals in humid tropical climate: tin and nickel. Rev Metal 43:101–110
47. Kumazawa T, Oishi M, Todoki M (2002) High-humidity deterioration and internal structure change of epoxy resin for electrical insulation. Dielec Electric Insulat 1(1):133–138
48. Holtzhausen J High voltage insulators, accessible via: http://www.idc-online.com/technical_references/pdfs/electrical_engineering/highvoltage.pdf
49. Suseela P, Rangaswami MV (2012) Variation of relative humidity inside the greenhouse with height, ventilation and ambient climatic parameters. Karnataka J Agric Sci 25(1):100–103
50. Rawson HM, Begg JE (1977) The effect of atmospheric humidity on photosynthesis, transpiration and water-use efficiency of leaves of several plant species. Planta 134:5–10
51. Yang S-S, Ling M-Y (1989) Tetracycline production with sweet potato by solid state fermentation. Biotechnol Bioeng 33:1021–1028
52. Sehested J, Gelten JAP, Helveg S (2006) Sintering of nickel catalysts: effects of time, atmosphere, temperature, nickel-carrier interactions, and dopants. Appl Catal A 309:237–246
53. Ganev R (2010) Explosion accidents with ammonium nitrate. Ann Proceeds Univ Rousse 49 (9.1):95–99
54. Reddy T, Das B, Reddy T, Suresh S (2012) A method to determine total moisture content of Propellant Oxidizer-Ammonium perchlorate (coarse and fine grade) Res J Pharm Biol. Chem Sci 3:168–173
55. Li J, Liu Y, Tang M, Li J, Lin X (2012) Capacitive humidity sensor with a coplanar electrode structure based on anodised porous alumina film. IET Micro Nano Lett 7:1097–1100
56. Ling ZY, Chen SS, Wang JC, Li Y (2008) Fabrication and properties of anodic alumina humidity. Chin Sci Bull 53:183–187
57. Zhang C, Miao J, Wang N (2014) Rapid response relative humidity sensor using anodic aluminum oxide film Patent US 8783101 B2
58. Juhasz L, Mizsei J (2009) A simple humidity sensor with porous alumina and integrated heating. Thin Solid Films 517(22):6198–6201

59. Kozhukharov S, Nenova Z, Nenov T, Nedev N, Machkova M (2015) Humidity sensing elements based on cerium doped titania-silica thin films prepared via a sol-gel method. Sensors Actuators B Chem 210:676–684
60. Nenova Z, Kozhukharov S, Nenov T, Nedev N, Machkova M (2016) Combined influence of titania and silica precursors on the properties of thin film humidity sensing elements prepared via a sol–gel method. Sensors Actuators B Chem 224:143–152

Chapter 44
Individual Bi_2O_3-Functionalized ZnO Microwire for Hydrogen Gas Detection

Vasile Postica, Oleg Lupan, Jorit Gröttrup, and Rainer Adelung

Abstract Individual micro- and nanostructures of metal oxides are known to be highly sensitive to surface phenomena due to their enhanced surface-to-volume ratio. In this work, an individual Bi_2O_3-functionalized ZnO microwire (Bi_2O_3/ZnO MW) with a diameter of ~2.2 μm was integrated into a sensing device using its direct transfer and placement in a focused ion beam (FIB)/scanning electron microscopy (SEM) equipment. The fabricated device was exposed to H_2 gas at room temperature showing a detectable response. The gas response to 1000 ppm is ~28%.

Keywords Hybrid nanocomposite · ZnO · Hydrogen gas sensor · Bi_2O_3

44.1 Introduction

Being one of the most abundant elements on the earth, hydrogen gas (H_2) is one of the most promising clean, sustainable and renewable energy source. H_2 is a highly explosive and flammable gas when the concentration exceeds 4% in air [1]. Therefore, fast and reliable detection of hydrogen gas leakage is very important in order to face safety challenges in the fields where it is widely used. In this context, metal oxides can provide fast and highly sensitive detection for a large variety of oxidizing and reducing gases, including H_2 down to low concentrations (in range of ppm) [2]. SnO_2 and ZnO nanostructures are widely used for resistive detection of H_2 gas [3].

However, in the case of metal oxides nanostructures the elevated temperatures are necessary for a rapid and highly sensitive detection of gases [3]. In the case of individual micro- and nanostructures of metal oxides (ZnO, SnO_2, etc.) the detection

V. Postica (✉) · O. Lupan
Department of Microelectronics and Biomedical Engineering, Technical University of Moldova, Chisinau, Republic of Moldova
e-mail: vasile.postica@mib.utm.md

J. Gröttrup · R. Adelung
Functional Nanomaterials, Institute for Materials Science, Kiel University, Kiel, Germany

P. Petkov et al. (eds.), *Advanced Nanotechnologies for Detection and Defence against CBRN Agents*, NATO Science for Peace and Security Series B: Physics and Biophysics, https://doi.org/10.1007/978-94-024-1298-7_44

of gases at room temperature is possible [4]. This is attributed to the higher surface-to-volume ratio of individual nanostructures, which leads to a higher influence of surface phenomena (adsorption and desorption of gaseous molecules) on the charge carrier transport through the conduction channel [5].

This huge advantage opens new possibilities to fabricate miniature gas sensors on flexible and organic substrates [6]. Other important advantages are the ultra-low power consumption, which is very important for portable and low-power electronics, and the possibility to detect sub-ppm concentrations of gases [6, 7].

In this work, we integrated an individual *p*-type Bi_2O_3-functionalized ZnO MW into a sensor device for room temperature detection of H_2 gas. The hybrid ZnO MW was connected to Au/Cr pads thus forming a two-terminal device by a Pt complex using a FIB/SEM equipment. Experimental results and possible sensing mechanisms are discussed.

44.2 Experimental Section

Bi_2O_3-functionalized ZnO tetrapod (ZnO-T-Bi_2O_3) networks were produced by the flame transport synthesis (FTS) approach, as was reported previously [8]. The ratio of ZnO:Bi used in this study is 20:1. Morphological, optical, structural, chemical and micro-Raman properties of the hybrid networks were reported previously, as well as DFT calculations [8]. Scanning electron microscopy (SEM) and energy dispersive X-ray spectroscopy were performed as was described in recent work [8]. In this work we will mainly focused on room temperature H_2 gas sensing properties of an individual Bi_2O_3-functionalized ZnO MW, which represents a broken arm of a tetrapod.

The device was fabricated using the procedure reported by Lupan et al. in a FIB/SEM system [9]. The release of Bi_2O_3/ZnO MWs from the ZnO-T-Bi_2O_3 networks was realized by sonication in ethanol followed by the transfer to a SiO_2 coated Si (SiO_2/Si) substrate and further dispersion to a lower density [10]. Then, the individual structure was connected to pre-patterned Au/Cr pads on a SiO_2/Si substrate using Pt complex. This procedure allows the connection of nanostructures with diameters down to 30–40 nm [10, 11]. The electrical and gas sensing measurements were performed as reported previously at room temperature [4].

44.3 Results and Discussions

44.3.1 Morphology and Chemical Characterization

Figure 44.1 shows SEM images of ZnO-T-Bi_2O_3 networks, as well as of a single tetrapod arm. It can be observed that the tetrapods are interconnected. The size of tetrapods varies in a wide range from 20 to 100 μm [8]. The shape of the tetrapod

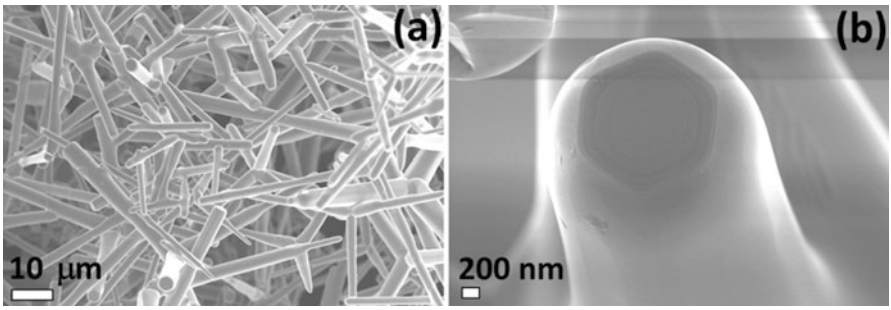

Fig. 44.1 SEM images of (**a**) ZnO-T-Bi_2O_3 networks and (**b**) of a single tetrapod arm

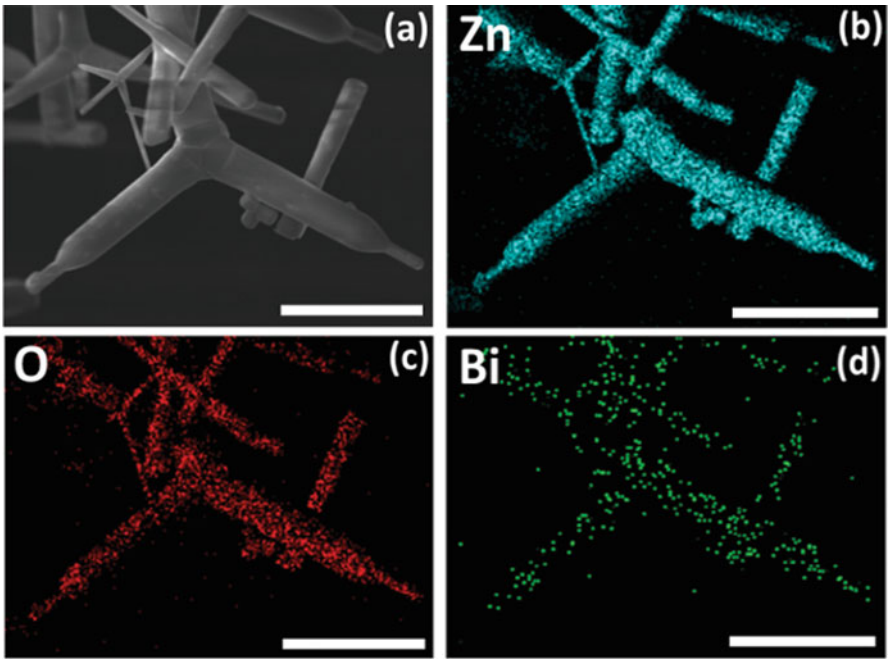

Fig. 44.2 (**a**) SEM image and (**b–d**) elemental mapping of a ZnO-T-Bi_2O_3 network by EDX at high magnification: (**b**) Zn Lα1_2; (**b**) O Kα1; and (**d**) Bi Mα1. The scale bar for all images is 10 μm

arms in the case of ZnO-T networks hybridized with Bi microparticles is cylindrical, compared to the hexagonal shaped arms in pristine ZnO-T networks. A previous study demonstrated that after annealing at 1150 °C for 5 h a crystalline Bi_2O_3 phase was deposited on the surface of ZnO tetrapods, forming a ZnO/Bi_2O_3 core-shell microstructures [8]. Thus, no other particles were observed in the hybrid networks, as in the case of ZnO-T networks hybridized with Al, Sn and Fe metallic microparticles [8, 12]. Figure 44.2 shows the elemental mapping of ZnO-T-Bi_2O_3 tetrapod networks. It can be observed that Bi is well dispersed on the surface of the ZnO tetrapod.

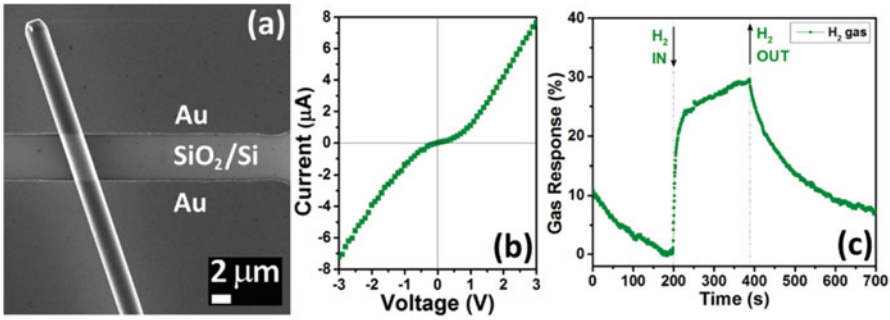

Fig. 44.3 (**a**) SEM image of the fabricated device based on an individual Bi_2O_3-functionalized ZnO MW; (**b**) room temperature current/voltage characteristic of the device; (**c**) Gas response to 1000 ppm H_2 at room temperature

44.3.2 Electrical and H_2 Gas Sensing Properties

Figure 44.3a shows the SEM image of the fabricated device based on an individual Bi_2O_3-functionalized ZnO MW. The diameter of the MW is ~2.2 µm. The gap between the electrodes is ~5 µm. A room temperature (RT) current/voltage (*I/V*) characteristic is presented in Fig. 44.3b, showing the formation of asymmetrical double Schottky barriers at the Au/ZnO interface. This can be explained by the higher work function of Au compared to ZnO [13].

The dynamic gas response to 1000 ppm of H_2 gas at room temperature is presented in Fig. 44.3c. The gas response (S) of ~28% was calculated as:

$$S = \left((R_g - R_a)/R_a\right) \cdot 100\% \tag{44.1}$$

where R_g and R_a are the resistances of the device under exposure to gas and in the air, respectively. The response and recovery time were defined as necessary time to reach and recover 90% of the signal, respectively. The calculated response time is ~150 s, while the recovery time is >400 s. These values are much higher compared to sensors based on networks of metal oxide nanostructures due to the operation at room temperature [3]. However, the obtained values are lower compared to individual Pt-coated ZnO NW reported by Tien et al. [14].

The gas sensing mechanism can be explained based on an ionosorption model and surface reactions [2, 3]. Under exposure to ambient air, oxygen molecules will adsorb on the surface of the hybrid ZnO MW by trapping electrons and forming a surface depletion layer with a higher resistivity compared to the unaffected conductive core (conduction channel) [2, 3]. Therefore, these surface reactions will lead to a resistance increase of the device. Under exposure to H_2 gas the hydrogen molecules will be oxidized to H_2O molecules by the adsorbed O_2 molecules under the release of electrons to the surface of the ZnO [2, 3]. This will lead to a narrowing of the electron depletion region and thus to a decrease in the resistance of the device [2, 3]. More details on the gas sensing mechanism are presented in previous work [8].

44.4 Conclusions

In this work, an individual Bi_2O_3-functionalized ZnO microwire with a diameter of ~2.2 μm was successfully integrated into a sensing device for room temperature detection of hydrogen gas. The device showed a response of ~28% to 1000 ppm of H_2 with a relatively fast response of ~150 s and a reversible signal, which is very important for practical applications. Further investigations are necessary to improve the room temperature gas sensing performances of an individual ZnO MW which are in progress in our group.

Acknowledgments This research was sponsored partially by the German Research Foundation (DFG) under the schemes PAK 902 (AD 183/12-2) and by the STCU within the Grant 6229.

References

1. Katoch A, Abideen ZU, Kim HW, Kim SS (2016) Grain-size-tuned highly H_2-selective chemiresistive sensors based on ZnO–SnO_2 composite nanofibers. ACS Appl Mater Interfaces 8:2486–2494
2. Barsan N, Weimar U (2001) Conduction model of metal oxide gas sensors. J Electroceram 7:143–167
3. Barsan N, Koziej D, Weimar U (2007) Metal oxide-based gas sensor research: how to? Sensors Actuators B Chem 121:18–35
4. Lupan O, Cretu V, Postica V, Ahmadi M, Cuenya BR, Chow L et al (2016) Silver-doped zinc oxide single nanowire multifunctional nanosensor with a significant enhancement in response. Sensors Actuators B Chem 223:893–903
5. Schütt F, Postica V, Adelung R, Lupan O (2017) Single and networked ZnO–CNT hybrid tetrapods for selective room-temperature high-performance ammonia sensors. ACS Appl Mater Interfaces 9:23107–23118
6. Zhang J, Liu X, Neri G, Pinna N (2016) Nanostructured materials for room-temperature gas sensors. Adv Mater 28:795–831
7. Zhang D, Liu Z, Li C, Tang T, Liu X, Han S et al (2004) Detection of NO_2 down to ppb levels using individual and multiple In_2O_3 nanowire devices. Nano Lett 4:1919–1924
8. Postica V, Gröttrup J, Adelung R, Lupan O, Mishra AK, de Leeuw NH et al (2017) Multifunctional materials: a case study of the effects of metal doping on ZnO tetrapods with bismuth and tin oxides. Adv Funct Mater 27:1604676
9. Lupan O, Chai G, Chow L (2007) Fabrication of ZnO nanorod-based hydrogen gas nanosensor. Microelectron J 38:1211–1216
10. Lupan O, Postica V, Cretu V, Wolff N, Duppel V, Kienle L et al (2016) Single and networked CuO nanowires for highly sensitive p-type semiconductor gas sensor applications. Phys Status Solidi (RRL) 10:260–266
11. Lupan O, Postica V, Wolff N, Polonskyi O, Duppel V, Kaidas V et al (2017) Localized synthesis of iron oxide nanowires and fabrication of high performance nanosensors based on a single Fe_2O_3 nanowire. Small 13:1602868
12. Lupan O, Postica V, Gröttrup J, Mishra AK, de Leeuw NH, Carreira JFC et al (2017) Hybridization of zinc oxide tetrapods for selective gas sensing applications. ACS Appl Mater Interfaces 9:4084–4099

13. Lao CS, Liu J, Gao P, Zhang L, Davidovic D, Tummala R et al (2006) ZnO nanobelt/nanowire Schottky diodes formed by dielectrophoresis alignment across Au electrodes. Nano Lett 6:263–266
14. Tien LC, Wang HT, Kang BS, Ren F, Sadik PW, Norton DP et al (2005) Room-temperature hydrogen-selective sensing using single Pt-coated ZnO nanowires at microwatt power levels. Electrochem Solid-State Lett 8:G230–G232

Part X
Applications: Water Treatment, Environment and Health

Chapter 45
Improvement of the Catalytic Activity of Pt through Synergetic Interaction with Co

Perica Paunović, Orce Popovski, Prashant Khadke, Ulrike Krewer, Goran Načevski, Anita Grozdanov, and Aleksandar T. Dimitrov

Abstract This study is concerned with the preparation and characterization of electrocatalysts containing Magneli phases as a support material, and different metallic systems (Co, Pt, and CoPt, Co:Pt = 1:1 wt.), as catalytic phase. The main idea was to reduce the amount of Pt with the addition of Co as a non-noble metal. The studied electrocatalysts were tested for water electrolysis in aqueous electrolytes, i.e. for hydrogen evolution reactions (HER) and for oxygen evolution reactions (OER). They were also tested in PEM fuel cells for oxygen reduction reaction (ORR). The order of activity for HER and OER was the following: CoPt > Pt > Co, and for ORR: CoPt ≈ Pt > Co. Co has been shown as promoter for reducing Pt particles (the most active monometallic phase), so the reduction of the Pt quantity in the metallic phase was compensated by smaller particles. Also, the interaction between the metallic phases increases the intrinsic catalytic activity for all reactions (HER, OER and ORR).

Keywords Magneli phases · Hydrogen evolution · Oxygen evolution · Oxygen reduction · d-band center

P. Paunović (✉) · G. Načevski · A. Grozdanov · A. T. Dimitrov
Faculty of Technology and Metallurgy, University "SS Cyril and Methodius", Skopje, Republic of Macedonia
e-mail: pericap@tmf.ukim.edu.mk

O. Popovski
Military Academy "Mihailo Apostolski", Skopje, Republic of Macedonia

P. Khadke
Max Planck Institute for Dynamics of Complex Technical Systems, Magdeburg, Germany

U. Krewer
Max Planck Institute for Dynamics of Complex Technical Systems, Magdeburg, Germany

Institute of Energy and Process Systems Engineering, TU Braunschweig, Braunschweig, Germany

P. Petkov et al. (eds.), *Advanced Nanotechnologies for Detection and Defence against CBRN Agents*, NATO Science for Peace and Security Series B: Physics and Biophysics, https://doi.org/10.1007/978-94-024-1298-7_45

45.1 Introduction

Considering the exhaustinged and limited reserves of fossil fuels [1], the "hydrogen economy" is pushed as a potential alternative energy supply system instead of the current fossil fuel based system [1–4]. Also, the hydrogen economy and hydrogen as a fuel show several crucial advantages such as: the highest calorific value, high efficiency (>60%) of energy conversion, the possibility to be stored in all aggregate states, the renewable nature allowing a clean energy system without pollutant emission [5]. In all segments of the closed loop of the hydrogen economy, such as hydrogen production, hydrogen storage and conversion to electricity in fuel cells, corresponding electrochemical reactions occur. Thus, an essential role for assuring technical and economic efficiency of a hydrogen economy is taken by the electrode materials involved in the hydrogen electrolysers and fuel cells. The higher the electrode activity, the lower is the energy consumption in electrolysers, and the higher is the conversion efficiency to electricity in fuel cells.

Platinum is the most active electrocatalytic metal and commercially the most used electrode material for hydrogen electrolysers and fuel cells. But, exploitation of Pt will be seriously limited in the near future, due to its low abundance and high price. Worldwide platinum resources are concentrated in only two geological settings – South Africa and Russia [6, 7]. According to Graedel et al. [6], the current Pt resources will be sufficient to supply 500 million fuel cell vehicles for only 15 years. Besides the transportation sector, the need for energy in other sectors such as electricity supply for industry and the domestic sector could not be covered. Similar predictions were given by Lee et al. [8], who calculated that the present resources of Pt will be enough to supply only 20% of the automotive industry. Considering this situation of limited Pt resources and a high percentage of uncovered energy needs, the price of platinum projected on the supply/demand ratio will be incredibly high.

One of the main challenges in modern hydrogen economy is thus to reduce the load of Pt in the electrode materials, or even to completely replace it by other active non-noble electrode materials. One of the approaches has a physical nature and means increasing the real surface area of the catalytic material through decreasing the particle sizes. Result of this approach is the use of nano-scaled catalytic materials. The other approach has a chemical nature and means increasing the intrinsic catalytic activity through alloying the catalytic material with other chemical elements. Strong synergism has been perceived when metals (or their compounds) with dissimilar electronic character have been mixed [9]. In such systems, titania has shown the highest interaction with corresponding catalytic metal having more electrons in the outer shell [10, 11]. Synergism of catalytic activity can also be achieved when metals with similar electronic character are mixed. This phenomenon has been studied by Nørskov and his collaborators [12, 13], who established that the position of the d-band is crucial for determining the affinity of d-metals (Pt, Pd, Ru, Ir, Ni, Co) to the adsorption of H and O. The higher the d-band center regarding to the Fermi level, the better is the interaction of metal–adsorbates. Metals with larger

atomic radii and electronegativity up-shift the d-band center of Pt and improve its adsorptive ability and accelerate the overall electrode reaction. The same effect can be achieved with reducing the particle size of the catalytic material, which lead to a d-band center closer to the Fermi level, and consequently better adsorption of H or O [14, 15].

This research is concerned with reducing the amount of platinum in electrode materials by addition of cobalt and to explain the changes of electrocatalytic activity for hydrogen evolution, oxygen evolution and oxygen reduction reactions, as result of the changes in the structure of the electrocatalytic material.

45.2 Electrocatalysts and Electrodes Preparation

The electrocatalysts studied in this paper are prepared by the sol-gel method using organometallic precursors such as Co-2,4-pentaedionate and Pt-2,4-pentaedionate (Alfa Aesar and Johnson Matthey GmbH). As catalyst support commercial Magneli phases (trade name Ebonex®, Altraverda, UK) were used. Organometallic precursor and catalyst support were dispersed in ethanol separately; after 1 h they were mixed and dispersed together and magnetically stirred with 900 rpm. Evaporation of the solvent (ethanol) lasted until a fine powder of the electrocatalyst was obtained. This material was further thermally treated at 250 °C in a reductive atmosphere to remove organic residues. The prepared electrocatalysts contain 10% metallic phase; the rest is the catalyst support.

For HER and OER testing, gas-diffusion electrodes (GDE, Fig. 45.1a) were prepared from the catalyst powders by hot pressing at 300 °C. GDE consists of two layers: the back layer of carbon black acetylene and PTFE, and the front layer of the catalyst and PTFE [16]. This structure of the GDE provides several functions: (i) it serves as a carrier catalyst, (ii) it ensures a highly-developed three phase

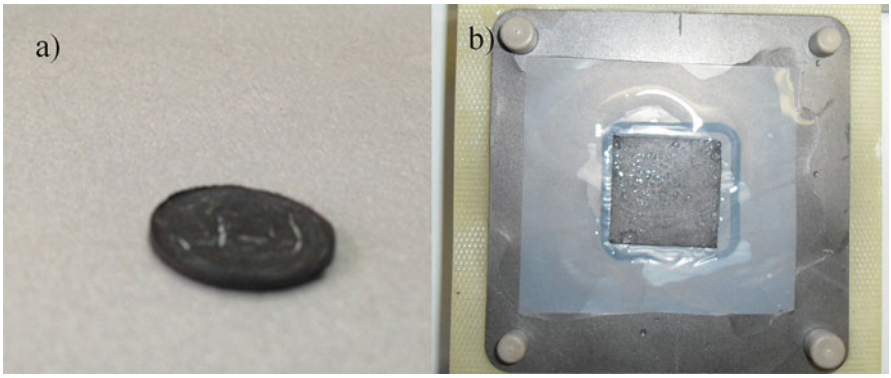

Fig. 45.1 (**a**) Gas-diffusion electrode (GDE) used for HER and OER testing and (**b**) membrane electrode assembly (MEA) for ORR testing

boundary where electron exchange reaction takes place, and (iii) it separates the liquid reactants from the gaseous products (H_2 and O_2) and provides fast transportation of liquid reactants/gaseous products to/from the three phase boundary [17].

ORR testing was performed using an alkaline (anion) exchange membrane (AEM) system. A commercial alkaline membrane from Tokuyama Corp, Japan was used. Both sides of the membrane were coated with the catalytic layers in the so-called membrane electrode assembly (MEA, Fig. 45.1b). For better adherence between the catalytic layers and the membrane, the catalytic layer was coated on carbon paper using anink consisting of 20% vol. solution of the ionomer (Tokuyama Corp) in isopropyl alcohol (IPA) and an corresponding amount of the electrocatalyst to reach 1 $mg{\cdot}cm^{-1}$ of catalytic phase over the electrode surface. The electrodes were merged with the membrane in the MEA system by hot pressing (1.5 bar) at 100 °C for 90 s.

45.3 Electrocatalysts Structure

Structural characterization of the electrocatalysts was performed by means of transmission electron microscopy (TEM) and X-ray diffraction (XRD). A TEM microscope (FEI Tecnai G2 Spirit TWIN) equipped with a LaB_6 cathode was used for microscopic observation, while XRD measurements were performed by a X-ray powder diffractometer Philips APD 15, with CuKa radiation and a constant rate of 0.02°.

In Fig. 45.2 one can see that metallic particles are evenly dispersed on the support material. Uniform dispersion makes all active catalytic centers (metallic particles) for adsorption/desorption processes available, which determines the rate of electrochemical reactions. This intensifies the total electrochemical reaction at a constant intrinsic activity of the metallic phase. The size of the Pt particles in the Pt/Ebonex catalyst is between 5 and 15 nm, while the Co particles in the Co catalyst are in range of 2–3 nm, although in the darker parts of the image particles with sizes of 10–15 nm can be observed. In the bimetallic CoPt/Ebonex catalyst, particles of 2–3 nm can be seen and fewer amounts with sizes of about 5 nm.

XRD spectra are shown in Fig. 45.3. Below each spectrum, the corresponding XRD spectrum of the pure Magneli phases is shown, to distinguish characteristic peaks of the metallic phase and the support material. As can be seen, the Pt/Ebonex catalyst shows two strong and broad peaks characteristic for metallic Pt. The first one corresponds to the 111 crystal orientation, the second one to 200. According to the Scherrer equation [18], the average size of 111 crystallites is 8 nm, that of 200 crystallites 6 nm. The XRD spectrum of monometallic Co/Ebonex electrocatalysts shows characteristic peaks for cubic and hexagonal crystalline Co with sizes near 13 nm. The corresponding weakly pronounced and noisy peaks highlight the low amount of this phase within the catalysts, while the size of the main part of the Co metallic phase is near 2 nm. In the spectrum of the bimetallic CoPt/Ebonex electrocatalyst, one can see a weak but broad peak at $2\theta = 41.8°$, corresponding to the solid state

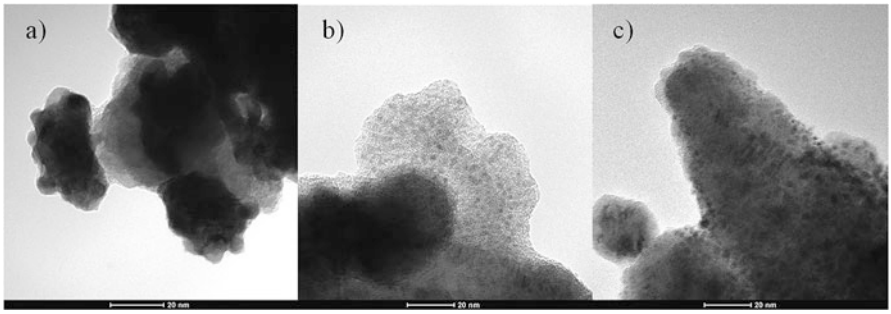

Fig. 45.2 TEM images of the studied electrocatalysts: (**a**) Pt/Ebonex, (**b**) Co/Ebonex, (**c**) CoPt/Ebonex

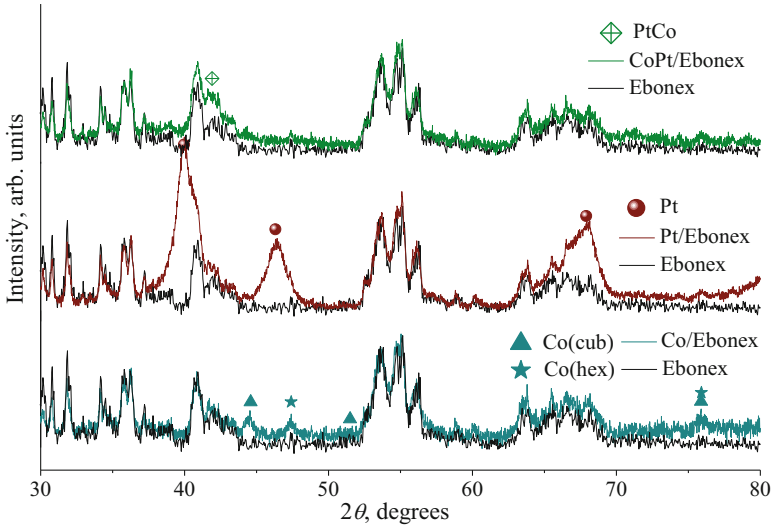

Fig. 45.3 XRD spectra of the studied electrocatalysts

solution of the CoPt alloy. The size of these particles was 2 nm. This suggests that in the presence of cobalt, platinum forms smaller particles. Cobalt is a promoter to reduce the platinum nanoparticle size, as was also observed elsewhere [19, 20].

The results of XRD analysis are in wellgood accordance with those of the TEM analysis.

The specific surface area of the catalysts was determined using measurements of isothermal nitrogen adsorption by a Quantachrome NovaWin (version 11.0). The determined values from the linearized nitrogen adsorption curves are shown in Table 45.1. Pure Ebonex has a value of 4.2 $m^2 \cdot g^{-1}$, while addition of metallic phases increases the surface area related to the catalyst support. In the monometallic systems, addition of Pt insignificantly increases the BET surface area (4.3 $m^2 \cdot g^{-1}$),

Table 45.1 BET surface area of the studied electrocatalysts and the catalyst support

Sample	BET surface area, $m^2 \cdot g^{-1}$
Ebonex	4.2
Co/Ebonex	6.1
Pt/Ebonex	4.3
CoPt/Ebonex	7.6

while addition of Co increases it to 6.1 $m^2 \cdot g^{-1}$. The most developed surface area was shown the bimetallic CoPt/Ebonex catalyst (7.6 $m^2 \cdot g^{-1}$). The results of the BET analysis are in accordance with the particle size analysis by TEM and XRD.

45.4 Electrochemical Characterization

Electrochemical characterization of the studied electrocatalysts was performed by means of cyclic voltammetry in the potential region between the hydrogen and the oxygen evolution reactions. The measurements were performed with two types of electrochemical cells. The first one was an aqueous alkaline three-electrode electrochemical cell, aimed for water electrolysis. A gas-diffusion type of working electrode was used (Fig. 45.1), a platinum wire as a counter electrode, a Hg/HgO reference electrode and 3.5 M solution of KOH (p.a., Merck) as an electrolyte. The cyclic voltammograms of this type of cell are shown in Fig. 45.4a. The second electrochemical cell was a real (two-electrode) alkaline hydrogen fuel cell, using an alkaline membrane (Tokuyama Corp) as a solid electrolyte. The MEA (Fig. 45.1) consisted of a cathode of the studied electrocatalyst and an anode of a commercial Pt/Vulcan XC-72 catalytic layer (60 wt% Pt), merged with the alkaline membrane. The cyclic voltammograms of this type of cell are shown in Fig. 45.4b.

Corresponding cyclic voltammograms (CV) (Fig. 45.4) of the same electrocatalyst for different types of electrochemical cells have similar shapes, but those scanned in the alkaline fuel cell show more pronounced and better shaped peaks for characteristic electrode and surface reactions. The following comments therefore hold for both types of voltammograms.

In the CVs of the Co based electrocatalyst, several characteristic peaks for Co appear. Peak I (−0.98 V vs. Hg/HgO (a) and near 0.09 V vs. NHE (b)) corresponds to the transition of Co(0) to the Co(II) oxidation state. This is a potential region where oxidation of hydrogen surface species still occurs. Peak II corresponds to the Co (II) → Co(III) transition. This peak is less shaped and widespread as result of only few transformations occuring. Also, Co(III) → Co(IV) occurs, which is in accordance with literature data [21, 22]. The oxygen evolution reaction is denoted as peak III. In the reverse polarization, transition of the higher valence states of cobalt to Co (II) occurs, which is observed in peak II'. In both cases this peak is shifted to negative potentials related to peak II, which points on the irreversibility of the Co(II) ⇆ Co(III) transition.

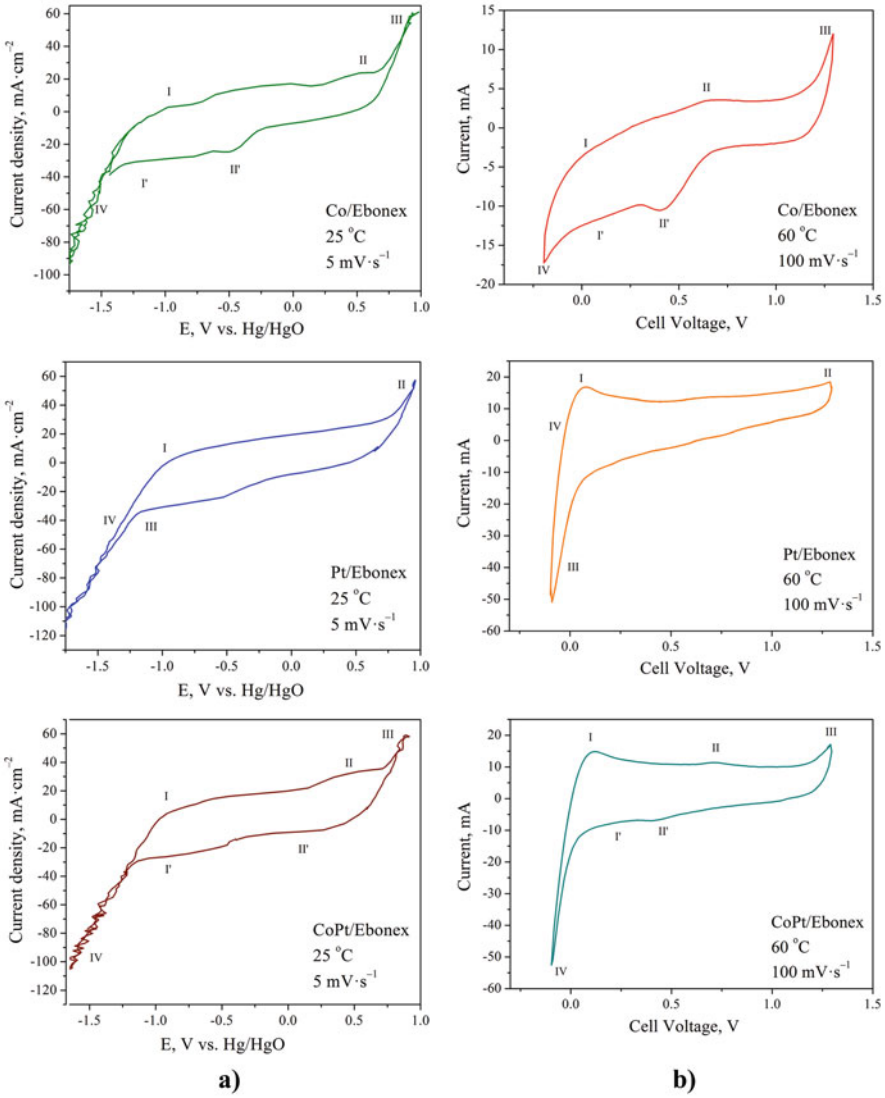

Fig. 45.4 Cyclic voltammograms of the studied electrocatalysts in (**a**) an alkaline hydrogen electrolyser and (**b**) a real alkaline hydrogen fuel cell

The very little shaped peak I' corresponds to the Co(II) → Co(0) transition and to adsorption of hydrogen adatoms on the electrode. Peak IV denotes the hydrogen evolution reaction.

In the CVs of the Pt based electrocatalyst, peak I (−0.96 V vs. Hg/HgO (a) and 0.065 V vs. NHE (b)) denotes the beginning of the covering the electrode surface

with OH^- ions. The adsorption of OH^- ions plays a significant role in the development of surface processes on platinum in an alkaline environment [23]. The covering of platinum with OH^- ions (oxygen-forming species in anodic oxygen evolution reactions denoted with peak II) occurs at a potential close to the hydrogen region. This is the reason why both the anode and cathode parts of the CVs in the area of charge and discharge of the double layer are not parallel to the abscissa [24].

The CVs of the bimetallic CoPt electrocatalyst contain all characteristic peaks observed in the previous spectra of the monometallic Co and Pt electrocatalysts. Adsorption of OH^- ions over the electrode surface starts from peak I (−0.92 V vs. Hg/HgO (a) and 0.1 V vs. NHE (b)). Also, Co(0) → Co(II) transformations occur in the same potential region. The peaks II and II' correspond to the Co(II) ⇆ Co(III) transition. Thhe poorly shaped peak I' denotes the opposite surface reaction of the peak I – desorption of OH^-. The peaks III and IV correspond to oxygen evolution and hydrogen evolution reaction, respectively.

45.5 Electrocatalytic Activity for HER and OER

The electrocatalytic activity of the studied electrodes for HER and OER was observed in the aqueous alkaline three-electrode electrochemical cell described above. Polarization curves for both HER and OER (Fig. 45.5) were obtained by means of steady-state galvanostatic measurements. Converting this curve into a log (i)/η plot in the region of low current densities allows the determinationof the exchange current densities for HER. These values are given in Table 45.2.

Analyzing the electrocatalytic activity for hydrogen evolution in the monometallic systems, one can see that the platinum based catalyst shows a better activity than the Co based. The difference in the overpotential η_{80} for HER at the reference current density of 80 $mA{\cdot}cm^{-2}$ is 50 mV (−445 mV for Co/Ebonex vs. –395 mV for Pt/Ebonex). This order of activity was expected considering the intrinsic activities of pure platinum and pure cobalt. But the bimetallic electrocatalyst shows a considerably better catalytic activity as compared to the monometallic ones, even a 115 mV lower overpotential than that of the monometallic Pt catalyst. This catalyst contains only half of the platinum load as the monometallic Pt based catalyst.

To analyze the reasons for the improvement of the electrocatalytic activity of the bimetallic electrocatalysts, one should consider that the electrocatalytic activity is the sum of: (i) the intrinsic activity, which is the ability of a material to exchange electrons with H^+, to adsorb discharged H adatoms at the electrode surface and to desorb H_2 from the surface and (ii) the surface activity meaning a higher developed surface area of the catalytic material available for the adsorbed species. The smaller the particles size, the higher developed is the surface area. The intrinsic catalytic activity of some materials can be evaluated according to the value of the exchange current density, while the surface activity can be recognized by the specific BET surface area or the particle size.

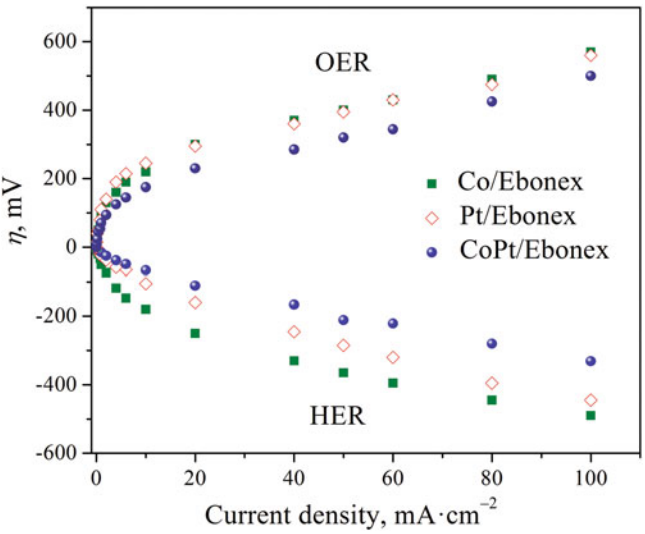

Fig. 45.5 Polarization curves for hydrogen and oxygen evolution reactions

Table 45.2 Overpotential for HER at a reference current density of 80 mA·cm^{-2} and exchange current density i_0 determined from the log(i)/η plot

Sample	η_{80}, mV	i_0, A·cm^{-2}
Co/Ebonex	−445	$1.6 \cdot 10^{-4}$
Pt/Ebonex	−395	$1.8 \cdot 10^{-4}$
CoPt/Ebonex	−280	$1.9 \cdot 10^{-4}$

The comparison of the values of the BET surface area of the Pt/Ebonex and CoPt/Ebonex electrocatalysts (see Table 45.1) show that the bimetallic catalyst has a higher BET value than the monometallic one (7.6 $m^2 \cdot g^{-1}$ vs. 4.3 $m^2 \cdot g^{-1}$). This higher value of the specific surface area is a result of the smaller Pt particles sizes in the bimetallic catalysts, which was shown in the TEM and XRD analysis. In the presence of Co, the size of Pt particles reduces approximately four times (2–3 nm vs. 5–15 nm). Therefore, one can say that the higher surface activity (size effect) contributed to the improvement of the electrocatalytic activity of the bimetallic CoPt based catalyst. Comparing the exchange current densities (see Table 45.2), one can say that the CoPt electrocatalyst has a higher value, which points at an improved intrinsic activity. This improvement of the intrinsic activity can be result of both, hypo-hyper d-interaction between the metallic phase and the Magneli phases, and hyper-hyper d-interaction between Co and Pt. The first interaction can be considered as constant in all catalysts studied, therefore the improvement of the catalytic activity as result of this interaction is the same in all catalysts and included in the presented values of exchange current densities. So, the increase of the exchange current density of the bimetallic CoPt catalyst is result only of the interaction between Co and Pt. As

was mentioned in the introduction, combining Co and Pt shifts the d-band center closer to the Fermi level and consequently improves the adsorption/desorption affinity of the catalytic material to hydrogen or oxygen adatoms. This can be achieved by addition of a metal with a larger atomic radius or by reduction of the Pt particles [13, 14]. In this case, improvement of catalytic activity was caused by the second reason. Namely, in the presence of Co a considerable reduction of the Pt particles was observed.

Finally, the improvement of the overall catalytic activity of the bimetallic CoPt based catalyst with only half the amount of platinum than in the case of the monometallic Pt based catalyst is the result of both intrinsic and surface effect.

The electrocatalytic activity for HER of the electrocatalysts studied and deposited on Ebonex as support material is not so good compared with the same bimetallic systems deposited on multiwalled carbon nanotubes and nano-scaled TiO_2 [20]. For example, the overpotential at the same reference current density of CoPt/ (MWCNTs + TiO_2) was 140 mV, while the overpotential of Pt/(MWCNTs + TiO_2) was 150 mV. The reason for the poor catalytic activity for HER of the studied systems is the very low BET surface area of the catalyst support (Ebonex), only 4.2 $m^2 \cdot g^{-1}$, to be compared with that of MWCNTs of more than 250 $m^2 \cdot g^{-1}$.

The electrocatalytic activity for OER can be seen from the polarization curves shown in Fig. 45.5 (upper curves). The trend of the catalytic activity is similar to that for HER. The monometallic Pt sample shows a slightly better activity than the Co based sample. This low difference is because Co is an appropriate catalyst for OER, considering its transition from metallic to Co(II) and further to the Co(III) oxidation state as was shown in the CVs in Fig. 45.4. In the region of oxygen evolution Co is present as Co(III)oxide, which facilitates the OER. The bimetallic electrocatalyst shows also in the case an improved catalytic activity as compare to the the monometallic ones. The overpotential at the reference current density of 80 $mA \cdot cm^{-2}$ was 490 mV for the Co, 475 mV for the Pt and 425 for thr CoPt based system. The explanation for the improvement of the electrocatalytic activity for OER is the same as in the case of HER, i.e. it is the result of both intrinsic and surface effect.

But, in contrast to the poor catalytic activity for HER, the studied electrocatalysts show a very good activity for OER [25–27]. This is due to active participation of the support material (Magneli phases) in the overall catalytic activity of the electrode material. Namely, Ebonex (Magneli phases) are non-stoichiometric oxides of titanium, and as oxides predestinated for OER. So, in addition to the metallic catalytic phase, also the rest of the electrode material is catalytically active. The surface of the oxide electrode possesses a high energy content and a strong hydrophilicity [28]. As a result, the electrode surface interacts with water molecules and covers itself with OH^- ions, which are responsible for the high electrocatalytic activity for oxygen evolution. They behave as weak acids or bases and exchange protons with the solution. This is the basis of the mechanism by which the inner sites can be active in reactions involving water molecules [29].

One of the key advantages of catalysts deposited on Magneli phases aimed at oxidative electrode reactions is their high chemical stability as compared to similar catalytic systems deposited on carbon. Namely, carbon can be oxidized easily during

the oxidative electrode reaction, especially at the high potentials present during electrolysis, causing the so-called carbon monoxide poisoning of PEM fuel cells or hydrogen electrolysers [30].

45.6 Electrocatalytic Activity for ORR

The testing for ORR was performed in a real (two-electrode) alkaline hydrogen fuel cell (AHFC), using an alkaline membrane (Tokuyama Corp) as a solid electrolyte. The polarization curves of the studied electrocatalysts are shown in Fig. 45.6. The registered potential of the potentiodynamic polarization measurements was the actual voltage of the fuel cell (cell voltage). More precisely, the polarization curves reflect the performance of the fuel cell rather than the OER activity. But, taking into consideration that the other electrode reaction, the hydrogen oxidation reaction (HOR), has a very low overpotential, one can assume that the cell voltage is close to the OER overpotential.

Comparing the activity of the monometallic electrocatalysts on Ebonex, the Pt based sample shows a better activity than the Co based one, which was expected according to the intrinsic activity of the pure metals. But, comparing the monometallic Pt sample and the bimetallic CoPt system, one can see that they show very close catalytic activities for ORR. In some parts of the polarization curves pure platinum shows a better activity, in other parts CoPt. However, the bimetallic catalysts contains only half of the amount of Pt than the monometallic, and its activity for ORR can be considered as a good achievement in comparison to the activity of monometallic Pt catalyst.

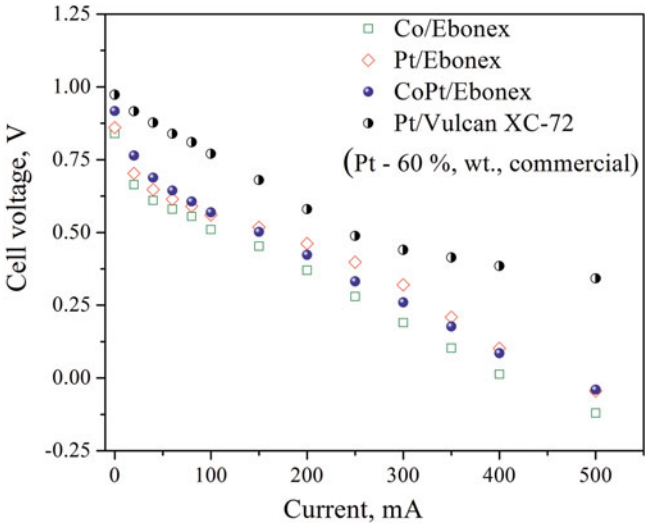

Fig. 45.6 Change of cell voltage with change of current in an alkaline membrane fuel cell for various catalysts at 60 °C

Comparing the activity of the commercial Pt catalysts deposited over Vulcan XC-72 (60 wt% Pt), one can see that the studied samples have much lower activities. The reason of this poor activity compare to the commercial Pt catalyst can be explained as follows: the Pt content in the whole commercial catalyst is 60 wt%, while the content of the metallic phase in the studied electrocatalyst is only 10 wt%. So, to achieve a load of 1 $mg \cdot cm^{-1}$ of the metallic phase over the electrode surface, only one layer of the catalyst is needed in the case of the commercial Pt, while in the case of the studied catalysts this would be too many layers. Therefore, the electrodes with studied catalytic systems become significant three-dimensional structures as compared to the usually thin electrodes. In a two-dimensional electrode the whole amount of the metallic phase is available for electrode reactions, while this is not case in a three-dimensional electrode. So, less than 10 wt.%, of metallic phase are available for electrode reactions, in contrast to the whole 60 wt.%. Pt in the case of a commercial Pt/Vulcan electrode. But with increasing content of the metallic phase, the catalysts deposited on Magneli phases can be considered as very promising electrode material for both OER and HOR in AHFC.

45.7 Conclusion

The results of this research have shown that mixing Co with platinum in an electrocatalytic material for water electrolysis or fuel cells is an appropriate approach for reducing the content of platinum and to reach the same activity or even exceed considerably the activity of catalysts with pure platinum as metallic phase.

The improvement is result of: (i) a surface effect, i.e. reducing the Pt particle size in the presence of Co for four times which increases the real surface area of the catalyst and (ii) intrinsic effects between Co and Pt, i.e. Co reduces Pt particles, which causes a shift of the d-band center closer to the Fermi level and consequently an improvement of the adsorption characteristics toward H, O and other adsorbates.

The studied bimetallic electrocatalytic system deposited on Magneli phases (non-stoichiometric oxides of titanium) are very promising for electrodes on which oxidative reactions occur, especially for the oxygen evolution reaction. There are two main reasons for that: (i) Magneli phases behave not only as catalyst support but also as active electrocatalyst for oxygen evolution and (ii) the oxide nature of the support material which is the dominant fraction in the entire catalyst shows a high chemical stability compared with carbon based support materials which can easily be oxidized and cause the so-called CO poisoning of hydrogen electrolyser or fuel cell and lead to electrode dissolution even for electrolysers.

Acknowledgments This paper has been supported by DAAD, Germany, and most of the research was carried out at the Max Planck Institute for Dynamics of Complex Technical Systems, Magdeburg. Great thanks to the colleagues Maurizio Avella and Gennaro Gentile from the Institute for Chemistry and Technology of Polymers, Napoli, Italy, for their collaboration on TEM observation

and analysis. Also thanks to Elefteria Lefterova from the Institute of Electrochemistry and Energy System within the Bulgarian Academy of Sciences, Sofia, Bulgaria, for useful consultations connected with XRD analysis.

References

1. Sahaym U, Grant Norton M (2003) Advances in the application of nanotechnology in enabling a 'hydrogen economy. J Mater Sci 43:5395
2. O'M Bockris J (1972) A hydrogen Economy. Science 176:1323
3. Paunović P, Popovski O, Dimitrov AT (2011) Hydrogen economy: the role of nano-scaled support material for electrocatalysts aimed for water electrolysis. In: Reithmaier JP et al (eds) Nanotechnological basis for advanced sensors, NATO Science for Peace and Security Series B: Physics and Biophysics. Springer, Dordrecht
4. Mueller-Langer F, Tzimas E, Kaltschmitt M, Peteves S (2007) Techno-economic assessment of hydrogen production processes for the hydrogen economy for the short and medium term. Int J Hydrog Energy 32:3797
5. Barbir F (2005) Fuel cells and hydrogen economy. Chem Ind Chem Eng Q 11:105
6. Gordon RB, Bertram M, Graedel TE (2006) Metal stocks and sustainability. Proc Natl Acad Sci U S A 103:1209
7. Sealy C (2008) The problem with platinum. Mater Today 11:65
8. Lee K, Zhang J, Wang H, Wilkinson DP (2006) Progress in the synthesis of carbon nanotube- and nanofiber-supported Pt electrocatalysts for PEM fuel cell catalysis. J Appl Electrochem 36:507
9. Jakšić MM (1987) Advances in electrocatalysis for hydrogen evolution in the light of the Brewer-Engel valence-bond theory. Int J Hydrogen Energy 12:27
10. Tauster SJ, Fung SC, Garten RL (1978) Strong metal-support interactions. Group 8 noble metals supported on titanium dioxide. J Am Chem Soc 100:170
11. Jaksić JM, Krstajić NV, Vracar LM, Neophytides SG, Labou D, Falaras P, Jaksic MM (2007) Spillover of primary oxides as a dynamic catalytic effect of interactive hypo-d-oxide supports. Electrochim Acta 53:349
12. Norlander P, Nørskov JK, Besenbacher F (1986) Trend in hydrogen heats of solution and vacancy trapping energies in trasnsition metals. J Phys F Met Phys 16:1161
13. Nørskov JK, Bligaard T, Logadottir A, Bahn S, Hansen LB, Bollinger M, Bengaard H, Hammer B, Sljivancanin Z, Mavrikakis M, Xu Y, Dahl S, Jacobsen C (2002) Universality in heterogeneous catalysis. J Catal 209:275
14. Hammer B, Nørskov JB (2000) Theoretical surface science and catalysis – calculations and concepts. In: Gates BC, Knozinger H (eds) Advances in catalysis. Academic, San Diego, p 71
15. Lopez N, Janssens T, Clausen BS, Xu Y, Mavrikakis M, Bligaard T, Nørskov JJ (2004) On the origin of the catalytic activity of gold nanoparticles for low-temperature CO oxidation. J Catal 223:232
16. BG patent Appl. No 38581
17. Paunović P, Popovski O, Radev I (2005) Investigation of cell assemblies prepared out of electrocatalysts aimed for hydrogen evolution. Bull Chem Technol Maced 24:133
18. Cullity CD (1978) Elements of x-ray diffraction. Addison-Wesley, London
19. Slavcheva E, Nikolova V, Petkova T, Lefterova E, Dragieva I, Vitanov T, Budevski E (2005) Electrocatalytic activity of Pt and PtCo deposited on Ebonex by BH reduction. Electrochim Acta 50:5444
20. Paunović P, Radev I, Dimitrov AT, Popovski O, Lefterova E, Slavcheva E, Hadži Jordanov S (2009) New nano-structured and interactive supported composite electrocatalysts for hydrogen evolution with partially replaced platinum loading. Int J Hydrogen Energy 34:866

21. Behl WK, Toni JE (1971) Anodic oxidation of cobalt in potassium hydroxide electrolite. J Electroanal Chem 31:63
22. Spataru N, Terashima C, Tokuhiro K, Sutanto I, Tryk DA, Park S-M, Fujishima A (2003) Electrochemical behaviour of cobalt oxide films deposited at conductive diamond electrodes. J Electrochem Soc 150:E337
23. Othman MR, Riyanto (2012) Electrochemical stability of Cu, Ni, Co, Pt and Ir metals sheet and their composite electrodes in potassium hydroxide solution. Int J Electrochem Sci 7:8408
24. Elezović NR, Babić BM, Vracar LM, Krstajic NV, Serb J (2007) Oxigen reduction at platinum nanoparticles supported on carbon cryogel in alkaline solutions. Chem Soc 72:699
25. García-Mota M, Vojvodic A, Metiu H, Man IC, Su H-Y, Rossmeisl J, Nørskov JK (2011) Tailoring the activity for oxygen evolution electrocatalysis on rutile TiO2 (110) by transition-metal substitution. Chem Cat Chem 3:1607
26. Lyons MEG, Brandon MP (2008) The oxygen evolution reaction on passive oxide covered transition metal electrodes in aqueous alkaline solution. Part 1-Nickel. Int J Electrochem Sci 3:1386
27. Labou D, Slavcheva E, Schnakenberg U, Neophytides S (2008) Performance of laboratory polymer electrolyte membrane hydrogen generator with sputtered iridium oxide anode. J Power Sources 185:1073
28. Hadži Jordanov S (1997) Towards the year 2000: some aspects of the electrochemistry in the last decades of twentieth century. Bull Chem Technol Maced 16:75
29. Boodts JFC, Trasatti S (1989) Hydrogen evolution on iridium oxide cathodes. J Appl Electrochem 19:255
30. Wagner N, Schulze M (2003) Change of electrochemical impedance spectra during CO poisoning of the Pt and Pt–Ru anodes in a membrane fuel cell (PEFC). Electrochim Acta 48:3899

Chapter 46
Antibacterial Coatings for Biomedical Applications

P. Písařík, M. Jelínek, J. Remsa, and J. Mikšovský

Abstract Diamond like carbon (DLC) and Ag-doped DLC (Ag-DLC) films were prepared by dual pulsed laser deposition using graphite and silver targets and two KrF excimer lasers. The silver concentration in the films was varied from 1.1 to 9.3 at. %. The surface topography was analysed by atomic force microscopy. The pure DLC was very smooth, but the roughness increased with rising silver content. Ethylene glycol, diiodomethane and deionized water were used to measure contact angles (CA). The measurements for water showed that the CA of Ag-DLC films (78–98°) was higher than that of the DLC film (77°). In order to understand the influence of incorporated Ag on the wettability, the surface energy and the protein adsorption as an indirect measure of the hemocompatibility were calculated. The surface energy of DLC and Ag-DLC films was same. The hemocompatibility was examined by the adsorption ratio of albumin/fibrinogen as an indirect method and improved with the increase of the Ag concentration. The antibacterial activity of the films were evaluated by bacterial eradication tests with *Staphylococcus aureus* and *Pseudomonas aeruginosa* at different incubation times. DLC and Ag-DLC films demonstrated good results against *Staphylococcus aureus* and *Pseudomonas aeruginosa*, meaning that DLC and Ag-DLC can be useful to produce coatings with antibacterial properties for biomedical devices such as sensors.

Keywords Silver doping · Diamond like carbon · Thin films · Dual pulsed laser deposition · Antibacterial properties

P. Písařík (✉) · M. Jelínek · J. Remsa · J. Mikšovský
Institute of Physics of the Czech Academy of Sciences, Prague, Czech Republic

Faculty of Biomedical Engineering, Czech Technical University in Prague, Kladno, Czech Republic
e-mail: Pisarik@fzu.cz

P. Petkov et al. (eds.), *Advanced Nanotechnologies for Detection and Defence against CBRN Agents*, NATO Science for Peace and Security Series B: Physics and Biophysics, https://doi.org/10.1007/978-94-024-1298-7_46

46.1 Introduction

While the antibacterial effects of silver are known for more than a thousand years, the nanoparticle form is researched for about a hundred years. With the development of nanotechnologies, the attention is again focused on silver nanoparticles, especially for their antibacterial properties. These were tested and verified.

Metal nanoparticles, compared to bigger ones, exhibit higher inhibition effects and potential for a removal of chemical and microbial pollution. The properties of nanoparticles strongly depend on size and shape, because a small size means a higher surface area that can interact with microorganisms. The smaller the particles the higher their catalytic activity [1]. The main trend nowadays is the utilization of nanolayers applied on a specified material surface. Silver nanoparticles are strongly fungicidal, algicidal, and bactericidal even at relatively low dosage, which enables their use in medicine, healthcare, and pharmacology for manufacturing antibacterial materials and disinfectants.

The exact nature of the toxic effect is still discussed, especially if the cause are nanoparticles or silver ions that emerge [2]. Toxic effects of silver on microorganisms are observed not only for silver ions, but also for silver compounds [3]. Some studies show that the decisive factor for silver toxicity is the positive ion charge. Due to electrostatic attraction between a positively charged silver surface and a negatively charged membrane surface the nanoparticle bonds to cell surface [3].

Nanoparticle penetrating cell walls can damage the cell inner structure, but this effect is strongly dependent on the cell species. The silver toxicity on gram-negative bacteria depends on nanoparticle concentration and closely correlates with the semi-permeability of cell membrane [4]. Gram-positive bacteria exhibit higher resistance for silver nanoparticles than gram-negative bacteria, caused by cell wall composition and the presence (or lack) of extracellular polymers [5, 6].

The silver antimicrobial activity is manifesting on several levels. The nanoparticles can damage the cell wall either by itself or by releasing silver ions or by forming reactive oxygen compounds [7]. Silver nanoparticles generate free radicals inside microorganisms, which disrupt the cell function [3]. Silver blocks electron transfer between breathing cycle enzymes and reacts with SH- groups of oxidation enzymes by stopping cell metabolisms, and the cell dies [6, 8].

Incorporation of selected metallic elements (silver) into diamond-like carbon (DLC) has emerged as an innovative approach to add unique functional properties to DLC coatings, thus opening up a range of new potential applications in fields as diverse as sensors, tribology, and biomaterials.

46.2 Experimental

46.2.1 Layers Preparation

Silicon (100) wafers were used as substrates. DLC and Ag-DLC films were prepared by dual PLD using graphite and silver targets and two KrF excimer lasers ($\lambda = 248$ nm, $\tau = 20$ ns) [9, 10]. Both systems were running simultaneously, the fluxes of materials intersected on the substrate. The carbon and silver flows were regulated by the laser repetition rates (atomic silver contents from 1.1 to 9.3 at. %). The number of pulses were adjusted to reach approximately the same layers thickness (100 nm). The base vacuum of the coating system was 5×10^{-4} Pa. The films were deposited in argon ambient (0.25 Pa). More information and the deposition parameters are summarized in Table 46.1 and in [10].

46.2.2 Characterization

Thickness The films thickness was determined using the Alphastep IQ mechanical profilometer (KLA Co.). The alphastep profilometer with a diamond tip (radius 5 μm, 60°) scanned 2 mm film surface [10].

Composition Wavelength dispersive X-ray spectroscopy (WDS). The composition of Ag-DLC thin layers was determined by an electron microprobe using WDS. The WDS was performed using a JEOL 840. The energy of the primary electrons was kept at 5 keV to minimize their penetration depth and the absorption of emitted X-rays. For this energy, the electron spot diameter was estimated to be in the range of 1–2 μm, which gives information at a depth of about 0.5 μm. The accuracy of the measurement of Ag and C using the STRATA program was better than 5% [10].

Morphology Atomic force microscope (AFM) measurements were realized in the dynamic regime with Etalon HA_NC tips (6 nm or higher curvature) on a Solver

Table 46.1 Deposition conditions and silver contents

	Laser 1 – carbon	Laser 2 – silver	
	(LED = 8 J·cm^{-2})	(LED = 5 J·cm^{-2})	WDS
	RR (Hz)	RR (Hz)	SC (at. %)
DLC	45	0	0.00
Ag-DLC-1	45	1	1.07
Ag-DLC-2	45	2	2.44
Ag-DLC-3	45	3	3.49
Ag-DLC-4	45	4	4.90
Ag-DLC-5	45	8	9.34

RR repetition rate, *SC* silver content, *LED* laser energy density

NEXT (NT-MDT) device. Several AFM scans (10×10 μm^2 and 50×50 μm^2) with 2048×2048 digital resolution were performed and quantified in terms of roughness average (S_a) and root mean square (S_q), adapted from ISO 4287/1 (Gwyddion 2.39) [10].

Contact Angle (CA), Surface Free Energy (SFE) The film wettability was measured using distilled water, diiodomethane and ethylene glycol by a contact angle measurement system (DSA100, Krüss Company). The droplet volume was 1.5 ± 0.2 μl. The humidity was $25 \pm 5\%$, the temperature 22 ± 1 °C. The Dropshape3 analysis program was used for contact angle and surface energy analysis, the Laplace method for profile extraction, and the extended Fowkes method for calculations of the disperse and polar parts of the surface free energy [10, 11].
The **fractional polarity** (FP) is a sensitive indicator of the surface energy and gives information about cell adhesion. It is defined as the ratio of the polar component γ^P and the total SFE (polar component γ^P, dispersive component γ^D) [12]

$$FP = \frac{\gamma^P}{\gamma^P + \gamma^D} \tag{46.1}$$

The **interfacial tension** γ_{SL} determines the wetting characteristics and hence, the shear stress generated when the liquid come into contact with the surface [13]. First we calculated total surface energy (γ_{SV}) of the DLC and Ag-DLC films using following expression [14, 15]:

$$\gamma_{LV}(1 + \cos\theta) = 2\sqrt{\gamma_{LV}^{P}}\sqrt{\gamma_{SV}^{P}} + 2\sqrt{\gamma_{LV}^{D}}\sqrt{\gamma_{SV}^{D}} \tag{46.2}$$

where is contact angle, γ_{SV}^{P} and γ_{SV}^{D} are the polar and dispersive components of the surface energy of DLC and Ag-DLC films, and γ_{LV}^{P} and γ_{LV}^{D} the polar and dispersive components of the surface energy of the testing liquids, respectively (Table 46.2) [14, 15]. Because there are two unknowns, γ_{SV}^{P} and γ_{SV}^{D}, in Eq. (46.2), two liquids with the known dispersive and polar components are needed to solve it. In this work, distilled water and diiodomethane were used.

The interfacial tension (γ_{SL}) between the solid surface and biological fluids (blood, fibrinogen, immunoglobulin G and albumin) was calculated using the equation [14, 15]:

$$\gamma_{SL} = \left[\sqrt{\gamma_{LV}^{P}} - \sqrt{\gamma_{SV}^{P}}\right]^2 + \left[\sqrt{\gamma_{LV}^{D}} - \sqrt{\gamma_{SV}^{D}}\right]^2 \tag{46.3}$$

The energetic characteristics (polar and dispersive components of the surface energy) of the biological liquids are shown in Table 46.3 [14, 15].

Antibacterial Properties In the in vitro anti-bacterial tests, the method described in [10] was employed to determine the antibacterial performance against *Pseudomonas aeruginosa* ATCC 27853 (gram-negative) and *Staphylococcus aureus* ATCC 6538

Table 46.2 Surface energy of the testing liquids [14, 15]

Test liquid	γ_{LV}^{D} (mJ·m^{-2})	γ_{LV}^{P} (mJ·m^{-2})	γ_{LV} (mJ·m^{-2})
Distilled water	21.8	51.0	72.8
Diiodomethane	50.8	0.0	50.8
Ethylene glycol	30.9	16.8	47.7

Table 46.3 The surface energy of the biological liquids and plasma proteins [14, 15]

Biological liquid	γ_{LV}^{D} (mJ·m^{-2})	γ_{LV}^{P} (mJ·m^{-2})	γ_{LV} (mJ·m^{-2})
Blood	11.20	36.30	47.50
Fibrinogen	24.70	40.30	65.00
IgG	29.46	35.53	64.99
Albumin	31.38	33.62	65.00

(gram-positive) bacterial strains (Czech Collection of Microorganisms, Brno, Czech Republic). The tested layers (1 × 1 cm^2) were washed with PBS, sterilized in the autoclave and placed into 12-well culture plates. 50 µl of bacterial suspension were placed on the tested layers, covered with glass cover slip and incubated at 35 °C. After 3 h, 450 ml of PBS was added and the bacterial suspension was serially diluted down to 10^{-6} to 10^{-7} in PBS. 1 ml of each diluted sample was spread onto an agar plate (Caso-Agar, Mercoplate®, Merck); the plates were incubated overnight and the number of colony forming units (CFU) was counted using the ImageJ software (National Institutes of Health, Bethesda, MD, USA). The layers were tested in triplicate. A clean Si (100) substrate was used as a control sample. The bactericidal efficacy in % expressing the antibacterial properties of different DLC and Ag-DLC films was estimated using the following formula (46.4), where $\text{Group}_{\text{ref}}$ and $\text{Group}_{\text{exp}}$ stand for the number of live bacteria colonies in the reference group and the experiment group, respectively [10]:

$$\text{Bactericidal Efficacy} = \frac{\text{Group}_{\text{ref}} - \text{Group}_{\text{exp}}}{\text{Group}_{\text{ref}}} \cdot 100\% \tag{46.4}$$

46.3 Results and Discussion

Composition The Ag content varied from 1.1 at.% to ~9.3 at.% (WDS) (Table 46.1), the thickness was 100 ± 30 nm on Si 100 substrates.

Morphology AFM showed the pure DLC to be very smooth (S_a around 0.137 nm and S_q around 0.179 nm); the roughness increases with rising silver content (S_a around 3.87 nm and S_q around 4.94 nm for 9.34 at. %) for 10 × 10 µm^2 scans. For 50 × 50 µm^2

scans the values were slightly higher, as expected, but the trend is the same. The layers with silver contained significantly more droplets than undoped DLC films, with rising silver content the number of the droplets increased and their size rose only a little (Fig. 46.1),

Contact Angle, Surface Free Energy The contact angle values for distilled water are smallest for undoped DLC (76.7°) and highest (97.9°) for 9.3 at. % content of silver (Fig. 46.2). Usually, a hydrophobic surface has a CA higher than 70°, while a hydrophilic surface has a CA value lower than 70°. These results imply that Ag-DLC films are more hydrophobic. For ethylene glycol there is lower CA for doped DLC

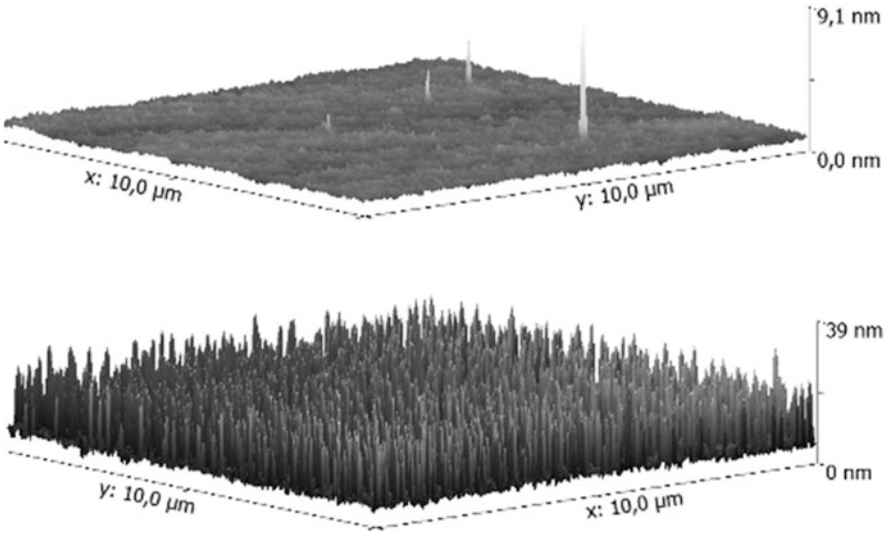

Fig. 46.1 Typical AFM surface of pure DLC (up) and Ag-DLC (down) films

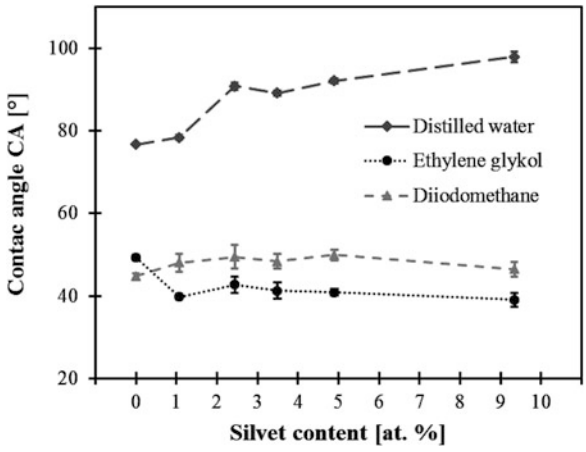

Fig. 46.2 Change of CA with the silver concentrations (Lines are added as a guide for the eye)

(39.1–42.7°) than pure DLC (49.3°). Ag-DLC layers exhibited higher contact angles for diiodomethane (46.5–49.5°) than for pure DLC (44.8°). This is the same trend as in [16, 17]. Calculated SFEs did not change with the silver content. The disperse part is the main component of the surface free energy (Fig. 46.3). Hydrophobicity (higher contact angles and lower SFE) is considered to be one of the properties that could positively affect the antibacterial properties [18].

Fraction Polarity(FP) The cell adhesion is mostly dependent on the polar component and there is practically no change due to dispersive component [19]. Best cellular adhesion (for fibroblast) should be for a fraction polarity of 0.3 [19]. For higher Ag concentrations FP does not change. The highest value of FP was reached by the layer with 1.1 at.% and undoped DLC (Table 46.4).
The calculated **total surface energy** (γ_{SV}) of the DLC and Ag-DLC films, it's polar and dispersive components (γ_{SV}^{P} and γ_{SV}^{D}) determinated from the linear fitting of Eq. (46.3) are show in Table 46.4. The γ_{SV} of the DLC and Ag-DLC films was between 39.19 mJ·m^{-2} (2.4 at.%.) and 43.72 mJ·m^{-2} (1.1 at.%). We did not observe

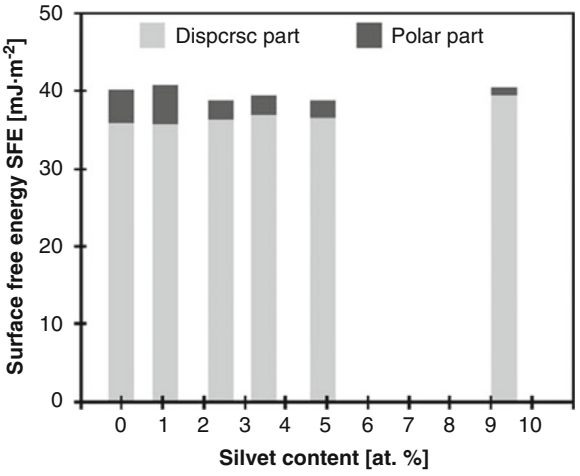

Fig. 46.3 Change of the SFE (polar and disperse component) with the silver concentration

Table 46.4 Calculated fraction polarity and energy components for DLC and Ag-DLC films

Ag	FP	Surface energy (mJ·m^{-2})			γ_{SL} (mJ·m^{-2})					Ratio of A/F
		γ_{SV}^{D}	γ_{SV}^{P}	γ_{SV}	Water	Blood	F	IgG	A	
0.0	0.11	34.66	5.86	40.52	23.77	19.45	16.27	12.75	11.49	0.71
1.1	0.13	39.71	4.01	43.72	29.08	24.92	20.66	16.43	14.90	0.72
2.4	0.06	38.23	0.97	39.19	40.21	33.46	30.25	25.34	23.52	0.77
3.5	0.07	38.95	1.20	40.15	39.01	32.66	29.19	24.32	22.51	0.77
4.9	0.06	39.15	0.67	39.82	42.49	35.57	32.22	27.12	25.22	0.78
9.3	0.03	40.05	0.07	40.12	50.12	42.14	38.93	33.32	31.21	0.80

Ag silver content (at. %), *F* fibrinogen, *A* Albumin

a decrease in the surface energy due to the decrease in SFE as publish in [16]. In our case, SFE was constant and therefore (γ_{SV}) is a constant too.

The calculated **interfacial free energy** (interfacial tension γ_{SL}) between DLC (or Ag-DLC films) and water, blood and plasma proteins (fibrinogen, IgG, albumin) is summarized in Table 46.4, too. The interfacial tension between water and DLC (Ag-DLC) films increased with the silver content in the layer. The interfacial tension increased from 23.8 mJ·m^{-2}(pure DLC) to 50.1 mJ·m^{-2} (Ag-DLC 9.3 at. %). The same trend of results are obtained for the interfacial tension for blood, fibrinogen, IgG and albumin. The results indicate that layers with Ag increased the plasma protein absorption, which in turn may cause decreased blood coagulation [15]. An absorption of albumin in high amounts would inactivate the blood-materials interface, while fibrinogen adsorbed in high amounts would favor platelet adherence and the activation of blood coagulation system. The adsorption ratio of albumin/fibrinogen increased with increasing silver content (Table 46.4).

Antibacterial Properties DLC layers doped with various concentration of silver were tested for their antimicrobial effects against the bacterial strains *Pseudomonas aeruginosa* and *Staphylococcus aureus*. A comparison of their bactericidal efficacy after 3 or 24 h cultivation expressed as percentage of killed cells is present in

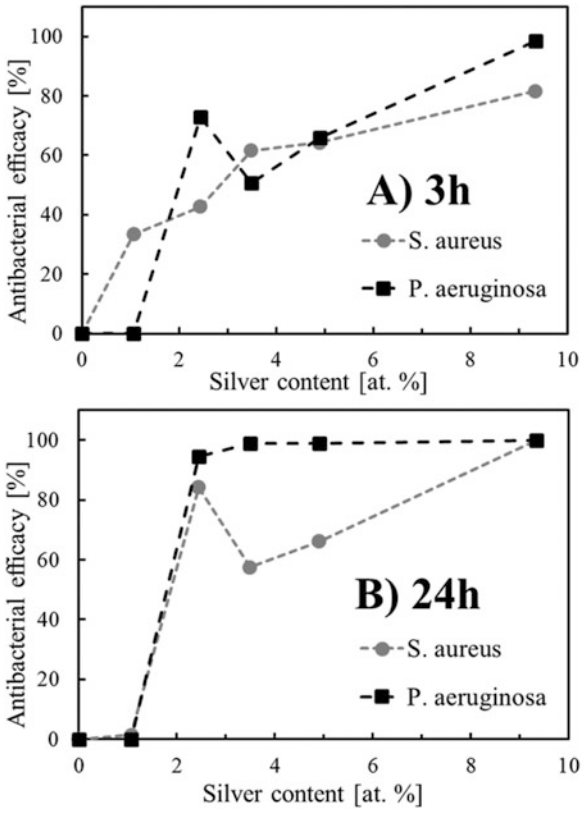

Fig. 46.4 The antibacterial efficiency of Ag-DLC layers after 3 h (**A**) and 24 h (**B**) (Lines are added as a guide for the eye)

Fig. 46.4. The antibacterial efficiency of the films increased with the Ag concentration (Fig. 46.4). The layers with the highest silver content (9.3 at. %) exhibited a antibacterial efficiency of 98.6% for *Pseudomonas aeruginosa*, and 81.6% for *Staphylococcus aureus* after 3 h (Fig. 46.4). For the same samples, the antibacterial efficiency rose after 24 h to roughly 100% for both gram-negative and gram-positive bacteria. Our results demonstrate unequivocally the excellent antibacterial properties of Ag-doped DLC and correspond with [20], but our values of efficiencies are substantially higher.

46.4 Conclusions

Silver doped DLC layers were grown by the dual pulsed laser deposition technology using silver and graphite targets and two lasers. The Ag content increased from 1.1 to 9.3 at. % (WDS). AFM showed the pure DLC to be very smooth but an increasing roughness with rising silver content. The water contact angle rises with increasing silver content, thus the layers become more hydrophobic. The interfacial tension increased from 23.8 (pure DLC) to 50.1 $mJ \cdot m^{-2}$ (Ag-DLC 9.3 at. %). The same trends apply to the interfacial tension for blood, fibrinogen, IgG and albumin. The adsorption ratio of albumin/fibrinogen increased with increasing silver content, which in turn may decrease blood coagulation. The antibacterial effects increased with the Ag concentration, while the maximum antibacterial efficiency of the 9.3 at. % Ag-DLC was 100.0% for *Staphylococcus aureus* and 99.9% for *Pseudomonas aeruginosa* after 24 h. Our results demonstrate that Ag doped DLC films are potentially useful biomaterials, e.g. sensors having both good blood compatibility and antimicrobial characteristics.

Acknowledgments This work has been supported by the Grant Agency of the Czech Technical University in Prague (grant No. SGS16/190/OHK4/2T/17), the Grant Agency of the Czech Republic (grant No. GA15-05864S) and the Ministry of Education, Youth and Sports of the Czech Republic (grant No. LO1409).

References

1. Panyala NR, Peňa-Méndez EM, Havel J (2008) Rewiew: silver or silver nanoparticles: a hazardous threat to the environment and human health? J Appl Biomed 6(3):117–129
2. Navarro E, Baun A, Behra R, Hartmann NB, Filser J, Miao AJ, Quigg A, Santschi PH, Sigg L (2008) Environmental behavior and ecotoxicity of engineered nanoparticles to algae, plants, and fungi. Ecotoxicology 17(5):372–386
3. Kim JS, Kuk E, Yu KN, Kim JH, Park SJ, Lee HJ, Kim SH, Park YK, Park YH, Hwang CY, Kim YK, Lee YS, Jeong DH, Cho MH (2007) Antimicrobial effects of silver nanoparticles. Nanomedicine 3(1):95–101
4. Sondi I, Salopek-Sondi B (2004) Silver nanoparticles as antimicrobial agent: a case study on E. coli as a model for Gram-negative bacteria. J Colloid Interface Sci 275(1):177–182

5. Jung WK, Koo HC, Kim KW, Shin S, Kim SH, Park YH (2008) Antibacterial activity and mechanism of action of the silver ion in Staphylococcus aureus and Escherichia coli. Appl Environ Microbiol 74(7):2171–2178
6. Yang G, Xie J, Hong F, Cao Z, Yang X (2012) Antimicrobial activity of silver nanoparticle impregnated bacterial cellulose membrane: effect of fermentation carbon sources of bacterial cellulose. Carbohydr Polym 87:839–845
7. Choi O, Deng KK, Kim NJ, Ross L Jr, Surampalli RY, Hu Z (2008) The inhibitory effects of silver nanoparticles, silver ions, and silver chloride colloids on microbial growth. Water Res 42 (12):3066–3074
8. Wu B, Wang Y, Lee YH, Horst A, Wang Z, Chen DR, Sureshkumar R, Tang YJ (2010) Comparative eco-toxicities of Nano-ZnO particles under aquatic and aerosol exposure modes. Environ Sci Technol 44(4):1484–1489
9. Písařík P, Jelínek M, Kocourek T, Zezulová M, Remsa J, Jurek K (2014) Chromium-doped diamond-like carbon films deposited by dual-pulsed laser deposition. Appl Phys A Mater Sci Process 117(1):83–88
10. Písařík P, Jelínek M, Remsa J, Mikšovský J, Zemek J, Jurek K, Kubinová Š, Šepitka J (2017) Antibacterial, mechanical and surface properties of Ag-DLC films prepared by dual PLD for medical applications. Mater Sci Eng C Mater Biol Appl 77:955–962
11. Kwok DY, Neumann AW (1999) Contact angle measurement and contact angle interpretation. Adv Colloid Interf Sci 81(3):167–249
12. Dumitrascu N, Topala I, Popa G (2005) Dielectric barrier discharge technique in improving the wettability and adhesion properties of polymer surfaces. IEEE Trans Plasma Sci 33(5):8628221
13. Owens DK, Wendt RC (1969) Estimation of the surface free energy of polymers. J Appl Polym Sci 13(8):1741–1747
14. Topala I, Dumitrascu N, Pohoata V (2007) Influence of plasma treatments on the hemocompatibility of PET and PET + TiO Films. Plasma Chem Plasma Process 27(1):95–112
15. Pandiyaraj KN, Heeg J, Lampka A, Junge F, Barfels T, Wienecke M, Rhee YH, Kim HW (2012) In vitro cyto and blood compatibility of titanium containing diamond-like carbon prepared by hybrid sputtering method. Plasma Sci Technol 14(9):829–836
16. Choi HW, Dauskardt RH, Lee S-C, Lee K-R, Oh KH (2008) Characteristic of silver doped DLC films on surface properties and protein adsorption. Diam Relat Mater 17(3):252–257
17. Lan W, Ou S, Lin M, Ou K, Tsai M (2013) Development of silver-containing diamond-like carbon for biomedical applications. Part I: microstructure characteristics, mechanical properties and antibacterial mechanisms. Ceram Int 39:4099–4104
18. Liu C, Zhao Q, Liu Y, Wang S, Abel EW (2008) Reduction of bacterial adhesion on modified DLC coatings. Colloids Surf B: Biointerfaces 61(2):182–187
19. Ponsonnet L, Reybier K, Jaffrezic N, Comte V, Lagneau C, Lissac M, Martelet C (2003) Relationship between surface properties (roughness, wettability) of titanium and titanium alloys and cell behaviour. Mater Sci Eng C Biomim Mater Sens Syst 23(4):551–560
20. Hatada R, Flege S, Bobrich A, Ensinger W, Dietz C, Baba K, Sawase T, Watamoto T, Matsutani T (2014) Preparation of Ag-containing diamond-like carbon films on the interior surface of tubes by a combined method of plasma source ion implantation and DC sputtering. Appl Surf Sci 310:257–261

Chapter 47
Identification and Evolution of Biocatalysts of Interest

Ioannis V. Pavlidis

Abstract Enzymes are potent biocatalysts for the detection and degradation of chemical warfare agents, due to their activity under mild conditions, the minimization of toxic intermediates, and their high specificity. Despite their numerous advantages in comparison to chemical catalysts, their application is hindered from the difficulty to identify enzymes which are active against a specific agent, as well as to optimize their catalytic activity for a desired process. Recent advances in the field of molecular biology and biotechnology promoted significantly these efforts and pave the way for a vast spectrum of applications, including the biocatalytic processing of chemical warfare agents. Herein, current methods for the identification of enzymes with desired properties are described as well as methods to further evolve the identified enzymes, in order to meet the needs of the desired process. As an example, the application of protein engineering on enzymes active on organohalogen compounds is discussed.

Keywords Protein engineering · Rational design · Directed evolution · De novo design · Organohalogen compounds

47.1 Introduction

Biocatalysis is an established alternative to chemical catalysis for a wide variety of applications, such as organic synthesis of products or building blocks for different industrial branches (such as pharmaceutical, food and cosmetic industry), remediation and sensing. The use of biocatalysts and whole cells for the bioremediation of chemical warfare agents and other pollutants possesses a great potential, as several enzymes have been identified to be able to degrade nerve and blister agents

I. V. Pavlidis (✉)
Enzyme Technology Laboratory, Department of Chemistry, University of Crete, Voutes University Campus, Heraklion 70013, Greece
e-mail: ipavlidis@uoc.gr

P. Petkov et al. (eds.), *Advanced Nanotechnologies for Detection and Defence against CBRN Agents*, NATO Science for Peace and Security Series B: Physics and Biophysics, https://doi.org/10.1007/978-94-024-1298-7_47

[1, 2]. The main advantage of the application of enzymes compared to chemical decontaminants is that biocatalysis, in most cases, is environmentally friendly, while chemical decontaminants like bleach and other antioxidants are toxic, they can generate toxic by-products and they can be aggressive on materials. Moreover, enzymes, in most of their applications, exhibit high specificity and selectivity thus enabling for instance the production of optically pure products. However, the major challenge in biocatalysis is to identify enzymes that fit to the desired processes. For instance, many of the pollutants and warfare agents are synthetic, as a result of anthropogenic activity, and thus nature did not evolve so far any efficient biocatalytic toolbox to degrade them. The same holds for novel active pharmaceutical ingredients. Even if some wild-type enzymes can perform the desired reaction, the efficiency of the process does not grant the application in an economically feasible large scale. Thus, there is a constant need of engineered tailor-made biocatalysts, in order to be able to develop efficient biocatalytic applications. Some of the enzyme features of wild-type enzymes requiring optimization are the substrate scope, the specificity, the catalytic efficiency, the stability, and the elimination of any potential substrate or product inhibition [3]. Several techniques of enzyme identification and protein engineering have been developed the last years to address this demand; together with the advances in the fields of molecular biology and bioinformatics they paved the way for the fourth wave of biocatalysis [4].

47.2 Enzyme Identification

Protein engineering efforts require a template, and in most cases one of the most difficult questions to answer is: "which protein do I use as a scaffold?". This first question is, in most cases, the most important, as the success of the engineering efforts relies on this decision. If there is a known scaffold with minimal activity for the desired reaction, this should be used as a template [5]. In the case that there is no biocatalyst with the desired activity known, there are three major methods of enzyme identification: (i) screening for enzymes in the genome of organisms in contaminated areas, (ii) screening the sequencing data, and (iii) *de novo* design of a biocatalyst.

A well-established approach for enzyme identification is to rely on the evolutionary mechanism of nature and screen for the desired biocatalyst in the environment. In this method, which is widely used in bioremediation processes, samples collected from contaminated areas are screened for microorganisms that can survive in the presence of the contaminant (the compound is added in a specific concentration in the cultivation medium), or use it as sole carbon source (use of minimal medium with the compound of interest being the only one containing carbon). If a microorganism has a catalytic machinery for the desired process, further investigations follow in order to identify which enzymes are involved. A recent successful application of this approach is the identification of a bacterium that degrades poly(ethylene terephthalate) (PET) [6]. As known, the accumulation of PET plastics is a significant challenge of our age, and—as PET is a synthetic material—at that time there was not any

known enzymes active on this polymer. Yoshida and coworkers collected samples from contaminated areas and screened for microorganisms that could grow, using a PET film as the sole carbon source. Thus, they were able to identify a bacterium of the genus *Ideonella* (named *Ideonella sakaiensis* 201-F6) that can feed on PET. By monitoring the transcript levels of genes, they were able to identify two enzymes (hydrolases) that catalyse the release of terephthalic acid from the polymer, which can be further degraded by known metabolic pathways.

The disadvantage of this approach is that only a limited number of microorganisms can grow under laboratory conditions, and the possibility to overlook a potent microorganism is quite high. For this reason, metagenomic approaches are more and more often used, as the recent technological advances on molecular biology facilitated the process. In this approach, DNA is isolated from collected samples, which includes genetic information from the whole population of the microorganisms. This DNA is fractured in smaller pieces and cloned in expression vectors, thus producing a metagenomic library. This library can be either expressed and screened for enzymes that can perform the desired reaction via an activity test, or it can be sequenced, and the genes of interest can be located later using known motifs. The current advances of the sequencing technology produce a vast sequence-space, where the full characterisation of all encoded proteins is not possible. For instance, just one metagenomic project on the human gut flora resulted in 3.3 million nonredundant microbial genes [7]. This sequence-space can be the source of novel enzymatic activities that were not documented so far. Höhne and coworkers used such an approach to identify the first (*R*)-selective amine transaminases [8]. Amine transaminases are a subgroup of pyridoxal phosphate (PLP) dependent enzymes. Höhne et al. developed an algorithm, with which they could sort the sequences of the family to specific substrate selectivity groups, based on motifs they identified. Their suggestion was that the sequences that do not fit to any of the known motifs/groups, should be the "missing" (*R*)-selective amine transaminases. Indeed, once they expressed 17 proteins encoded from the identified sequences, they could observe that all of them were transaminases with (*R*)-selectivity.

The most sophisticated method of identifying enzymes for novel reactions is the *de novo* design. In this approach, an artificial active site, using amino acids that participate in the catalytic mechanism, is designed around the substrate of interest by means of bioinformatics tools, providing the functional groups and the geometry required for the catalysis. Later, other amino acids are added to this structure to facilitate the coordination of the substrate. The implementation of this amino acid set in several protein scaffolds is performed *in silico* (i.e. using a computer), in order to identify the one that provides the optimal geometry. Once the optimal structure is designed, the gene is synthetically generated and is expressed in order to evaluate the prediction. Two of the most prominent examples of *de novo* design are the production of a Kemp eliminase [9] and a Diels-Alderase [10]. Nevertheless, this is a time-intensive method that leads to an output of a low number of proposed enzymes, while the catalytic efficiency of the resulting enzymes is quite low and requires further improvement by means of protein engineering.

47.3 Protein Evolution via Directed Evolution

Usually, the enzymes identified with the aforementioned methods do not meet the criteria for the desired bioprocesses. The most significant challenges to be addressed are the low catalytic efficiency and/or low selectivity, the low stability under process conditions (operational stability), and the possibility of inhibition at higher substrate or product concentrations. Directed evolution approaches are preferred in cases where there are not enough structural or mechanistic information, or the target is not correlated to a specific area of the structure that can be modelled. For instance, the stability of a protein can result from its whole structure and not from specific hot-spots [11]; thus, directed evolution approaches, such as error prone polymerase chain reactions (epPCR; a technique that introduces random mutations during amplification of a given DNA sample), may be more suitable for such a target. The benefit of these approaches is that the libraries produced are not target-oriented, meaning that they can be screened for mutants with improved catalytic behavior for any characteristic of interest. For instance, the same library can be screened for mutants that are more thermostable, and/or for mutants with desired selectivity towards a specific substrate. It is thus understandable that the challenge here is the selection process: a high-throughput assay that allows a fast and accurate selection for the desired characteristic is required; in many cases, the development of the assay is as timely as the screening phase. For instance, the evolution of transaminases was relying for years on chromatographic (HPLC) assays, or even medium-throughput photometric assays [12]. The need for rapid evolution of this class of enzymes led in the recent few years to the development of different high-throughput assays that can assist the selection of the evolved variants even from the expression plate [13, 14].

Nevertheless, random mutagenesis requires a lot of screening effort, without any guarantee that the screening will reveal an improved variant. In the case that the targeted feature is the catalytic activity and selectivity (and in some cases, the inhibition), rational design approaches may be the method of choice, as these features are derived from residues around the active site [15].

47.4 Protein Evolution via Rational Design

47.4.1 Rational Design Approaches for Improved Catalytic Efficiency

The advances in bioinformatics methods have enabled us to predict *in silico* the selectivity as well as the catalytic activity of enzymes. There are several successful examples of rational design. One of the most prominent ones on protein engineering is the evolution of an (*R*)-selective transaminase for the production of Sitagliptin from the companies Merck & Co. and Codexis, despite the facts that a chemical process was already developed and that the compound was already commercialized.

Savile and coworkers were able to enlarge the binding pocket of the enzyme to accommodate Prositagliptin and produce optically pure (*R*)-sitagliptin, in better yield and optically purity compared to the chemical process [16]. Even then, the enzyme was not fitted for an industrial process, and several rounds of directed evolution were performed with further goals (such as stability in the presence of dimethylsulfoxide, high catalytic efficiency at high substrate concentration). In one of our recent works, we were not only able to enlarge the binding pocket of (*S*)-selective amine transaminases by rational design, but, by deciphering the reasons behind the substrate selectivity, we were able to suggest a motif responsible for the acceptance of bulky substrates [17]. Using the motif, we interrogated the sequence-space and were able to identify six novel amine transaminases with the desired substrate selectivity. It is thus understandable that the benefit of the rational design approaches does not only rely on the reduced screening effort needed, but also to the rationalisation of the results that facilitates the design of tailor-made biocatalysts in the future.

47.4.2 Rational Design Approaches for Improved Stability

Although stability is recognised as a global attribute of a protein that is not located in specific areas, there are some rational approaches that can accelerate the evolution of stable variants. The enzymes are catalytic functional once they are properly folded. Elevated temperatures as well as polar organic solvents can lead to protein unfolding. Theory suggests that the unfolding initiates from the most flexible areas, thus if these areas are stabilised, the stability of the enzyme will be increased. Two major methods for enzyme stabilisation via rational design exist: (i) the B-FIT [18] and (ii) the stabilisation by creating new disulfide bonds [19].

The protein databank (PDB, http://www.rcsb.org) provides the static three-dimensional structures of enzymes. However, enzymes in reaction conditions are flexible molecules. PDB data from X-ray crystallography provide the B-factor, a factor that describes the spread of the electron density of an atom. This B-factor is correlated with the flexibility of the atoms and subsequently their amino acids [18]. The B-Fitter is a simple program that averages the B-factors of all atoms of every amino acid of the protein and sorts them in descending order. This allows to target possible “hot-spots” of unfolding. Subsequently these positions are mutated, either to the whole set of natural amino acids, or to a restricted set of amino acids that are expected to provide specific interactions in order to stabilise the amino acid. This method was successfully applied for the evolution of a thermostable lipase [18], but since then the method has been applied to many enzyme classes.

Another method for stabilisation on a molecular level is the introduction of disulfide bonds. The algorithm developed by Dombkowski identifies the pairs of amino acids that can provide a disulfide bond [19, 20]. This takes into account the distance of the amino acids, their angle, as well as the potential energy of a disulfide bond. With these calculations, the platform provides a list with potential disulfide

bonds. Then, the researcher only needs to perform two point mutations to introduce cysteines on the proposed positions and express the enzyme in a host able to express proteins with disulfide bonds. Interestingly, the algorithm predicts not only intramolecular bonds, but also intermolecular one between different chains of the protein. This is important for enzymes that are active as homomultimers, as the intermolecular disulfide bonds stabilize the multimerization process.

47.5 The Example of Enzymes Active Against Halogenated Compounds

Several enzymes classes have been described to be active against chemical warfares, especially against nerve and blister agents [1, 2]. As an example of the evolution of enzyme identification and engineering, a short overview on the enzymes active on halogenated substrates and blister agents is given here.

Haloalkane dehalogenases (EC 3.8.1.5) are enzymes that convert halogenated compounds into alcohols and the respective halides. They were originally identified as crucial enzymes for the bioremediation of environmental pollutants [21, 22], but nowadays several biotechnological applications have been developed, especially by exploiting their enantioselectivity to produce optically pure compounds [23]. These enzymes are used for the decontamination of warfare agents, such as sulfur mustard [1], and for their biosensing [24]. Nowadays we have a good understanding of the catalytic mechanism [25]; therefore the engineering efforts are facilitated. There are three main enzymes mostly used for the degradation of environmental pollutants: DhlA, DhaA and LinB [25]. DhlA was the first enzyme of the class that was characterized, which catalyses the degradation of 1,2-dichloroethane [26]. This enzyme has a cap over the active site that is important for the substrate specificity. Directed evolution experiments increased the activity towards brominated substrates, such as 1,2-dibromoethane and 1-bromobutane [27]. In another work, a *Pseudomonas* strain that could use long chain alcohols as sole carbon source, was genetically modified to be able to grow on 1-chlorohexane [28]. The wild-type DhA variant would not be useful in this case, as it cannot convert this substrate, but Pries and coworkers developed a variant with mutations at the cap domain that could accept this substrate and provide 1-hexanol as carbon source [28]. DhaA is mostly used for its activity towards 1,2,3-trichloropropane. The wild-type enzyme can dehalogenate in position 1, producing 2,3-dichloropropan-1-ol, but the catalytic efficiency is low [25]. Thus, protein engineering was performed and an 32-fold increase was achieved with only five point-mutations [29]. However, this product is still toxic, and thus a further degradation is required. Dvorak and coworkers established an enzymatic cascade of three enzymes, including a variant of DhaA, an haloalcohol dehalogenase and an epoxide hydrolase, that produces glycerol as final product [30]. Wild-type DhaA and LinB are able to degrade sulfur mustard to non-toxic product, while the spontaneous hydrolysis of sulfur mustard leads to a release of toxic intermediates [1].

Another interesting enzyme class are the haloalcohol dehalogenases (also known as halohydrin dehalogenases), which belong to the enzyme class of lyases (EC 4.5.1.-) and catalyze the dehalogenation of halohydrins with a subsequent epoxide formation. If a negatively charged nucleophile is provided, the enzyme catalyses also the epoxide ring opening, resulting to non-reversible dehalogenation [31]. Apart from their application in the degradation of 1,2,3-trichloropropane [30], halohydrin dehalogenases are also used for the detection of azide or cyanide by catalysing the epoxide ring opening reaction on 1,2-epoxybutane [32]. Most of the protein engineering was performed on two well characterized enzymes, HheC and HheA2. Directed evolution via ProSAR was performed on HheC to shift its selectivity from ethyl (*S*)-4-chloro-3-hydroxybutyrate to ethyl (*R*)-4-cyano-3-hydroxybutyrate; after screening more than half a million clones, several variant with the desired selectivity were identified with at least 35 mutations [33]. The variant HheC-2360 carrying 37 mutations not only had a threefold improved turnover number, and an inverted selectivity, but also an increased thermal stability [31].

These are only two of the most studied classes of enzymes active on organohalogen compounds, but there are several other enzyme classes studied that exhibit other selectivities: 2-haloacid dehalogenases that hydrolyses a 2-haloacid to 2-hydroxyacid, fluoroacetate dehalogenases that are able to cleave the strong carbon-fluorine bond, one of the strongest single bonds in organic chemistry and 2-haloacrylate dehalogenase that acts on unsaturated organohalogen compounds [34]. Of course, the *in vivo* solutions are preferred, as there is no need for purification of the biocatalyst. Very recently a bacterial consortium was developed that can dechlorinate trichloroethene to ethene, which uses two vinyl chloride reductive dehalogenases and a trichloroethene reductive dehalogenase for the catabolic pathway [35]. As discussed above, there are numerous solutions for the biocatalytic degradation and sensing of halogenated compounds, and the most suited approach can be selected, according to the characterized enzymes to the date.

47.6 Conclusion

Biocatalytic processes are established in a wide selection of applications. Enzymes are environmentally friendly catalysts that are more appealing from their chemical counterparts, especially due to their selectivity. However, the identification of a suitable enzyme can be a daunting task, and the identified enzyme needs modification to fit to the process conditions. The advances of the last few years in genetics, molecular biology and bioinformatics enable us to develop tailor-made biocatalysts and predict their selectivity. The forth wave of biocatalysis will lead to more sustainable and greener bioprocesses.

References

1. Prokop Z, Opluštil F, DeFrank J, Damborský J (2006) Enzymes fight chemical weapons. Biotechnol J 1:1370–1380
2. Jang YJ, Kim K, Tsay OG, Atwood DA, Churchill DG (2015) Update 1 of: destruction and detection of chemical warfare agents. Chem Rev 115:PR1–PR76
3. Bommarius AS, Blum JK, Abrahamson MJ (2011) Status of protein engineering for biocatalysts: how to design an industrially useful biocatalyst. Curr Opin Chem Biol 15:194–200
4. Bornscheuer UT (2017) The fourth wave of biocatalysis is approaching. Phil Trans R Soc A 376:20170063
5. Preisajovich SG, Tawfik DS (2007) Protein engineers turned evolutionists. Nat Methods 4:991–994
6. Yoshida S, Hiraga K, Takehana T, Taniguchi I, Yamaji H et al (2016) A bacterium that degrades and assimilates poly(ethylene terephthalate). Science 351:1196–1199
7. Qin J, Li R, Raes J, Arumugam M, Burgdorf KS et al (2010) A human gut microbial gene catalogue established by metagenomic sequencing. Nature 464:59–65
8. Höhne M, Schätzle S, Jochens H, Robins K, Bornscheuer UT (2010) Rational assignment of key motifs for function guides in silico enzyme identification. Nature Chem Biol 6:807–813
9. Khersonsky O, Rothlisberger D, Dym O, Albeck S, Jackson CJ, Baker D, Tawfik DS (2010) Evolutionary optimization of computationally designed enzymes: Kemp eliminases of the KE07 series. J Mol Biol 396:1025–1042
10. Siegel JB, Zanghellini A, Lovick HM, Kiss G, Lambert AR et al (2010) Computational design of an enzyme catalyst for a stereoselective bimolecular Diels-Alder reaction. Science 329:309–313
11. Gall MG, Nobili A, Pavlidis IV, Bornscheuer UT (2014) Improved thermostability of a bacillus subtilis esterase by domain exchange. Appl Microbiol Biotechnol 98:1719–1726
12. Schätzle S, Höhne M, Redestad E, Robins K, Bornscheuer UT (2009) Rapid and sensitive kinetic assay for characterization of ω -transaminases. Anal Chem 81:8244–8248
13. Green AP, Turner NJ, O'Reilly E (2014) Chiral amine synthesis using ω -transaminases: an amine donor that displaces equilibria and enables high-throughput screening. Angew Chem Int Ed 53:10714–10717
14. Weiss MS, Pavlidis IV, Vickers C, Höhne M, Bornscheuer UT (2014) Glycine oxidase based high-throughput solid-phase assay for substrate profiling and directed evolution of (R)- and (S)-selective amine transaminases. Anal Chem 86:11847–11853
15. Morley KL, Kazlauskas RJ (2005) Improving enzyme properties: when are closer mutations better? Trends Biotechnol 23:231–237
16. Savile CK, Janey JM, Mundorff EC, Moore JC, Tam S et al (2010) Biocatalytic asymmetric synthesis of chiral amines from ketones applied to sitagliptin manufacture. Science 329:305–309
17. Pavlidis IV, Weiß MS, Genz M, Spurr P, Hanlon SP, Wirz B, Iding H, Bornscheuer UT (2016) Identification of (S)-selective transaminases for the asymmetric synthesis of bulky chiral amines. Nat Chem 8:1076–1082
18. Reetz MT, Soni P, Fernández L, Gumulya Y, Carballeira JD (2010) Increasing the stability of an enzyme toward hostile organic solvents by directed evolution based on iterative saturation mutagenesis using the B-FIT method. Chem Commun 46:8657–8658
19. Dombkowski AA (2003) Disulfide by design™: a computational method for the rational design of disulfide bonds in proteins. Bioinformatics 19:1852–1853
20. Craig DB, Dombkowski AA (2013) Disulfide by design 2.0: a web-based tool for disulfide engineering in proteins. BMC Bioinform 14:346
21. Stucki G, Thüer M (1995) Experiences of a large-scale application of 1,2- dichloroethane degrading microorganisms for groundwater treatment. Environ Sci Technol 29:2339–2345
22. Fetzner S (1998) Bacterial dehalogenation. Appl Microbiol Biotechnol 50:633–635

23. Koudelakova T, Bidmanova S, Dvorak P, Pavelka A, Chaloupkova R, Prokop Z, Damborsky J (2013) Haloalkane dehalogenases: biotechnological applications. Biotechnol J 8:32–45
24. Bidmanova S, Chaloupkova R, Damborsky J, Prokop Z (2010) Development of an enzymatic fiber-optic biosensor for detection of halogenated hydrocarbons. Anal Bioanal Chem 398:1891–1898
25. Nagata Y, Ohtsubo Y, Tsuda M (2015) Properties and biotechnological applications of natural and engineered haloalkane dehalogenases. Appl Microbiol Biotechnol 99:9865–9881
26. Keuning S, Janssen DB, Witholt B (1985) Purification and characterization of hydrolytic haloalkane dehalogenase from Xanthobacter autotrophicus GJ10. J Bacteriol 163:635–639
27. Pikkemaat MG, Janssen DB (2002) Generating segmental mutations in haloalkane dehalogenase: a novel part in the directed evolution toolbox. Nucleic Acids Res 30:e35
28. Pries F, van den Wijngaard AJ, Bos R, Pentenga M, Janssen DB (1994) The role of spontaneous cap domain mutations in haloalkane dehalogenase specificity and evolution. J Biol Chem 269:17490–17494
29. Pavlova M, Klvana M, Prokop Z, Chaloupkova R, Banas P et al (2009) Redesigning dehalogenase access tunnels as a strategy for degrading an anthropogenic substrate. Nat Chem Biol 5:727–733
30. Dvorak P, Bidmanova S, Damborsky J, Prokop Z (2014) Immobilized synthetic pathway for biodegradation of toxic recalcitrant pollutant 1,2,3-trichloropropane. Environ Sci Technol 48:6859–6866
31. Schallmey A, Schallmey M (2016) Recent advances on halohydrin dehalogenases—from enzyme identification to novel biocatalytic applications. Appl Microbiol Biotechnol 100:7827–7839
32. Wan N-W, Liu Z-Q, Xue F, Zheng Y-G (2015) An enzymatic method for determination of azide and cyanide in aqueous phase. J Biotechnol 214:27–32
33. Fox RJ, Davis SC, Mundorff EC, Newman LM, Gavrilovic V et al (2007) Improving catalytic function by ProSAR-driven enzyme evolution. Nat Biotechnol 25:338–344
34. Kurihara T (2011) A mechanistic analysis of enzymatic degradation of organohalogen compounds. Biosci Biotechnol Biochem 75:189–198
35. Yohda M, Ikegami K, Aita Y, Kitajima M, Takechi A et al (2017) Isolation and genomic characterization of a Dehalococcoides strain suggests genomic rearrangement during culture. Sci Rep 7:2230

Chapter 48
Self-Organized Magnetic Nanoparticles in Plant Systems: ESR Detection and Perspectives for Biomedical Applications

T. S. Kavetskyy, R. I. Khalilov, O. O. Voloshanska, L. M. Kropyvnytska, T. M. Beyba, V. A. Serezhenkov, A. N. Nasibova, A. Akbarzadeh, and S. Ya. Voloshanska

Abstract An innovative approach based on the effect of bio-mineralization as a response reaction of cells to decrease their damage upon stress was applied for *Juniperus communis*, the common juniper (in the following JC). Electron spin resonance (ESR) was used as the main experimental tool for detecting paramagnetic species as a result of existence of an antioxidant activity system, represented by superoxide dismutase with manganese, catalase etc., and the formation of superparamagnetic iron oxide nanoparticles (SPIONs). SPIONs are found in the JC shell, while the antioxidant activity due to Mn-containing enzymes is detected in

T. S. Kavetskyy (✉)
Drohobych Ivan Franko State Pedagogical University, Drohobych, Ukraine

The John Paul II Catholic University of Lublin, Lublin, Poland

Joint Ukraine-Azerbaijan International Research and Education Center of Nanobiotechnology and Functional Nanosystems, Baku, Azerbaijan

Joint Ukraine-Azerbaijan International Research and Education Center of Nanobiotechnology and Functional Nanosystems, Drohobych, Ukraine

R. I. Khalilov
Joint Ukraine-Azerbaijan International Research and Education Center of Nanobiotechnology and Functional Nanosystems, Baku, Azerbaijan

Joint Ukraine-Azerbaijan International Research and Education Center of Nanobiotechnology and Functional Nanosystems, Drohobych, Ukraine

Institute of Radiation Problems of NAS Azerbaijan, Baku, AZ, Azerbaijan

Baku State University, AZ, Baku, Azerbaijan

O. O. Voloshanska
Zaporizhzhya State Medical University, Zaporizhzhya, Ukraine

L. M. Kropyvnytska · T. M. Beyba
Drohobych Ivan Franko State Pedagogical University, Drohobych, Ukraine

P. Petkov et al. (eds.), *Advanced Nanotechnologies for Detection and Defence against CBRN Agents*, NATO Science for Peace and Security Series B: Physics and Biophysics, https://doi.org/10.1007/978-94-024-1298-7_48

the seeds. The influence of temperature on the intensity of the ESR signals was also examined. The detected bio-functionality of the JC shell and seeds could be recommended for biomedical applications.

Keywords Electron spin resonance spectroscopy · *Juniperus communis* · Superoxide dismutase · Manganese · Superparamagnetic iron oxide nanoparticles

48.1 Introduction

The influence of physical (stress) factors (e.g. temperature, humidity, strong UV and/or lower level of illumination, radiation, soil salinity, etc.) on plant such as JC forms an antioxidant system with a larger activity than for other plants. Due to the existence of antioxidant enzymes among the many pharmacological effects of JC are antitumor properties, and antioxidant, antitoxic, and anticarious activities. The pharmacological activity of JC could be allocated either to the shell or to the seeds. Also, by adding into compositions of other biologically active dietary supplements (BADS), it is possible to utilize the bio-functionality of the drug for medical purposes. But, if stress factors are influencing the JC bioactivity (this is expected to happen in different seasons), the properties of JC based drugs could be uncontrollable. The present research focuses on resolving this problem by using a

V. A. Serezhenkov
Semenov Institute of Chemical Physics of RAS, Moscow, Russia

A. N. Nasibova
Joint Ukraine-Azerbaijan International Research and Education Center of Nanobiotechnology and Functional Nanosystems, Baku, Azerbaijan

Joint Ukraine-Azerbaijan International Research and Education Center of Nanobiotechnology and Functional Nanosystems, Drohobych, Ukraine

Institute of Radiation Problems of NAS Azerbaijan, Baku, AZ, Azerbaijan

A. Akbarzadeh
Joint Ukraine-Azerbaijan International Research and Education Center of Nanobiotechnology and Functional Nanosystems, Baku, Azerbaijan

Stem Cell Research Center, Tabriz University of Medical Sciences, Tabriz, Iran

Universal Scientific Education and Research Network (USERN), Tabriz, Iran

Joint Ukraine-Azerbaijan International Research and Education Center of Nanobiotechnology and Functional Nanosystems, Drohobych, Ukraine

S. Y. Voloshanska
Drohobych Ivan Franko State Pedagogical University, Drohobych, Ukraine

Joint Ukraine-Azerbaijan International Research and Education Center of Nanobiotechnology and Functional Nanosystems, Baku, Azerbaijan

Joint Ukraine-Azerbaijan International Research and Education Center of Nanobiotechnology and Functional Nanosystems, Drohobych, Ukraine

new approach based on the effect of bio-mineralization as a response reaction of stress-damaged cells, resulting in self-organized magnetic nanoparticles synthesized by a plant system upon stress (so-called "green synthesis") [1–4]. This effect is coupled with electron-transport chain of photosynthesis that leads to a decrease of Fenton's reaction due to the transformation of iron ions (Fe^{2+}, Fe^{3+}) to maghemite and magnetite superparamagnetic iron oxide nanoparticles (SPIONs). Electron spin resonance (ESR) spectroscopy is used in this research as the main experimental tool for detecting the self-organized SPIONs in the JC shell and/or seeds.

48.2 Experimental

The methodology of the present work is based on the application of the above mentioned effect of bio-mineralization of JC samples from the Carpathian region of Ukraine. The ESR spectra of the biomaterials studied were recorded with the aid of an X-range ESR spectrometer ECS-106 (Bruker, Germany) under the following conditions: magnetic field HF-modulation amplitude 0.5 mT, UHF power 20 mW, field center 260 mT, field scanning 290 mT, temperatures 293 and 77 K, and gain 10^4 and 5×10^5, respectively.

48.3 Results and Discussion

Figure 49.1a shows ESR spectra of the JC shell and seeds and their mixture, together with a differential spectrum between seeds and shell as a function of the magnetic field at room temperature. We emphasize two ESR signals registered in the biomaterials. Namely, the ESR signal at $g = 2.01$ is attributed to paramagnetic Mn species [3], characterized by a six-component hyperfine structure, in the Mn-containing enzymes that is found only in the JC seeds. At the same time, the broad ESR signal at $g = 2.28$ is attributed to paramagnetic SPION species [3] only found in the JC shell.

It must be noted here that the SPIONs detected in the investigated material have an important role in the development of pathological conditions and are frequently used for biomedical applications, where their toxic potential is still a major concern [5–14]. The SPIONs have also promising applications in food science [15–17]. These magnetic nanoparticles lead to the appearance of magnetic properties in plant systems and the emergence of ESR signals [3]. Magnetic nanoparticles are present in various natural systems including living organisms of all levels and types of organization. The biogenic generation of nanophase magnetic oxides is associated with physiological processes including a number of pathologies, in particularly, human neurodegenerative diseases, Type 2 diabetes, premature ovarian insufficiency (POI), and hemochromatosis. As a result, the investigation of the mechanisms of formation of iron oxide nanoparticles in living systems is important from a

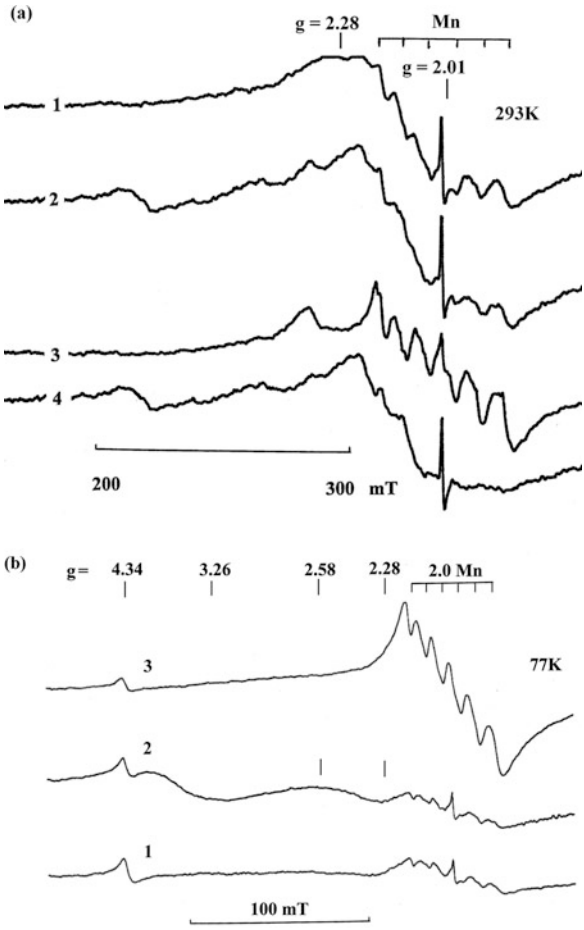

Fig. 48.1 Electron spin resonance spectra of the JC shell, seeds, and a mixture of shell and seeds as a function of magnetic field at temperatures (**a**) 293 K (*1* – mixture of shell and seeds, *2* – shell, *3* – seeds, and *4* – differential spectrum (curve 3 − curve 2)) and (**b**) 77 K (*1* – mixture of shell and seeds, *2* – shell, and *3* – seeds)

fundamental viewpoint and also necessary for the development of novel efficient methods in pharmacy. The appearance of an ESR signal characteristic for magnetic nanoparticles has been found [3, 18] in various plants as a result of effects of external stress factors.

In the present study, the stress factors affecting the JC shell are also directly confirmed by ESR detected SPIONs as a result of bio-mineralization effect under stress. In other words, the JC shell with externally-attained functionalities, resulting in the formation of SPIONs plays a role as protection for the JC seeds. On the other hand, Mn-containing enzymes presenting an antioxidant activity, are normally found in the JC seeds. Therefore, SPIONs in drugs based on the JC shell, and the antioxidant activity detected by enzymes in the case of the JC seeds could be applied for pharmaceutical and biomedical purposes.

Figure 48.1b shows ESR spectra of JC shell and seeds and their mixture as a function of the magnetic field at low temperature. As expected, the measurement

performed at 77 K showed an enhancement of the ESR signal from enzymes ($g = 2.0$) for the JC seeds. At the same time, the intensity of the ESR signal from SPIONs ($g = 2.28$) for the JC shell is reduced at 77 K. Also, the intensity of the broad ESR signal at $g = 3.26$ for the JC shell is found to decrease at low temperature. Note, that in all dried soil samples at room temperature a broad ESR signal with a half-width of 150 mT and a position of the maximum of the low-field component at $g = 3.3$ has been observed [3], while upon lowering the temperature from room to 80 K the intensity of this broad signal was reduced. Registration of the broad ESR signal at $g = 3.3$ in soil samples has been interpreted in [3] to be due to a high content of iron aggregates, among which there could be magnetic nanoparticles (SPIONs) in the soil on which plants grew. As seen in our case for the JC shell, the behavior of the ESR signals at $g = 2.28$ and $g = 3.26$ at 77 K is quite similar, supporting the finding of [3] that these two signals are connected with SPIONs and iron aggregates (containing SPIONs). Besides, a weak signal of Fe^{3+} at $g = 4.3$ (recorded at 80 K in [3]) is also detected for the JC samples at 77 K (Fig. 48.1b). A broad ESR signal with a position of the maximum of the low-field component at $g = 2.58$ is assigned to SPIONs too, as this signal is closest to that at $g = 2.69$ detected for the samples with magnetic nanoparticles in [3].

48.4 Conclusion

An innovative identification method for bioactivity of natural BADS was proposed using the example *Juniperus communis*. The presence of an antioxidant activity system due to the effect of bio-mineralization under stress, represented by Mn-containing enzymes and other enzymes, and the formation of SPIONs in the biomaterials studied has been examined using ESR spectroscopy. The SPIONs are only detected in the JC shell, while the Mn-containing enzymes are only found in the JC seeds. The observed bio-functionality of the JC based shell and seeds could be used for pharmaceutical purposes and biomedical applications.

Acknowledgments T.S. Kavetskyy and S.Ya. Voloshanska acknowledge the Ministry of Education and Science of Ukraine (project No. 0114U002617).

References

1. Khalilov RI, Nasibova AN (2010) The endogenous EPR-detectable iron nanoparticles in plants News Baku Univ 3:35
2. Khalilov RI, Nasibova AN, Gasimov RJ (2011) Magnetic nanoparticles in plants: EPR researches News Baku Univ 4:56
3. Khalilov RI, Nasibova AN, Serezhenkov VA, Ramazanov MA, Kerimov MK, Garibov AA, Vanin AF (2011) Accumulation of magnetic nanoparticles in plants grown on soils of Apsheron peninsula Biophysics 56:316

4. Khalilov RI, Nasibova AN, Youssef N (2015) The use of EPR signals of plants as bioindicative parameters in the study of environmental pollution Int J Pharm Pharm Sci 7:172
5. Ito A, Shinkai M, Honda H, Kobayashi T (2005) Medical application of functionalized magnetic nanoparticles J Biosci Bioeng 100:1
6. Huber DL (2005) Synthesis, properties, and applications of iron nanoparticles Small 1:482
7. Gupta AK, Gupta M (2005) Synthesis and surface engineering of iron oxide nanoparticles for biomedical applications Biomaterials 26:3995
8. Roca AG, Costo R, Rebolledo AF, Veintemillas-Verdaguer S, Tartaj P, Gonzalez-Carreno T, Morales MP, Serna CJ (2009) Progress in the preparation of magnetic nanoparticles for applications in biomedicine J Phys D Appl Phys 42:224002
9. Berry CC (2009) Progress in functionalization of magnetic nanoparticles for applications in biomedicine J Phys D Appl Phys 42:224003
10. Singh N, Jenkins GJS, Asadi R, Doak SH (2010) Potential toxicity of superparamagnetic iron oxide nanoparticles (SPION) Nano Rev 1:5358
11. Soenen SJH, De Cuyper M (2010) Assessing iron oxide nanoparticle toxicity *in vitro*: current status and future prospects Nanomedicine 5:1261
12. Ankamwar B, Lai TC, Huang JH, Liu RS, Hsiao M, Chen CH, Hwu YK (2010) Biocompatibility of Fe_3O_4 nanoparticles evaluated by *in vitro* cytotoxicity assays using normal, glia and breast cancer cells Nanotechnology 21:075102
13. Mahmoudi M, Sant S, Wang B, Laurent S, Sen T (2011) Superparamagnetic iron oxide nanoparticles (SPIONs): development, surface modification and applications in chemotherapy Adv Drug Deliv Rev 63:24
14. Kandasamy G, Maity D (2015) Recent advances in superparamagnetic iron oxide nanoparticles (SPIONs) for *in vitro* and *in vivo* cancer nanotheranostics Int J Pharm 496:191
15. Miller DD (2010) Food nanotechnology: new leverage against iron deficiency Nat Nanotechnol 5:318
16. Hilty FM, Arnold M, Hilbe M, Teleki A, Knijnenburg JTN, Ehrensperger F, Hurrell RF, Pratsinis SE, Langhans W, Zimmermann MB (2010) Iron from nanocompounds containing iron and zinc is highly bioavailable in rats without tissue accumulation Nat Nanotechnol 5:374
17. Zimmermann MB, Hilty FM (2011) Nanocompounds of iron and zinc: their potential in nutrition Nanoscale 3:2390
18. Nasibova AN, Khalilov RI (2016) Preliminary studies on generating metal nanoparticles in pomegranates (Punica Granatum) under stress Int J Dev Res 6:7071

Chapter 49
Nanoparticle Based Decontamination of Bacteria/Pathogens

N. Enaki, T. Paslari, E. Starodub, S. Bizgan, C. Ristoscu, I. N. Mihailescu, and A. Vaseashta

Abstract The decontamination of pathogens (bacteria and yeast fungi) from non-transparent fluids (liquids or gases) using periodical structures like small quartz or glass spheres irradiated by ultraviolet (UV)-C light is proposed. Studies were devoted to the topological effect of individual metamaterial elements which modify UV-C evanescent waves in a contact zone of contaminated fluids and metamaterials, as a function of granule geometry. The efficiency of utilization of metamaterials in decontamination of non-transparent liquids is demonstrated. The decontamination efficiency is assessed both in the dynamic and static regime. Control experiments were performed in the absence of metamaterials and/or UV-C irradiation.

Keywords Pathogen decontamination · Evanescent field · Pulsed light technique · Photonic crystal · Optical fiber · Microsphere · Metamaterial

N. Enaki · E. Starodub · S. Bizgan
Quantum Optics and Kinetic Processes Lab, Institute of Applied Physics of Academy of Sciences of Moldova, Chişinau, Moldova

T. Paslari (✉)
Quantum Optics and Kinetic Processes Lab, Institute of Applied Physics of Academy of Sciences of Moldova, Chişinau, Moldova

Department of Physics and Engineering, Moldova State University, Chisinau, Moldova

C. Ristoscu · I. N. Mihailescu
National Institute for Lasers, Plasma and Radiation Physics, Bucharest, Romania

A. Vaseashta
Institute for Advanced Sciences Convergence, and Int'l Clean Water Institute, Herndon, VA, USA

NJCU - State University of New Jersey, NJ, USA

P. Petkov et al. (eds.), *Advanced Nanotechnologies for Detection and Defence against CBRN Agents*, NATO Science for Peace and Security Series B: Physics and Biophysics, https://doi.org/10.1007/978-94-024-1298-7_49

49.1 Introduction

We propose new decontamination methods of dispersive (non-transparent) infected liquids and gases, based on the potentials offered by periodical optical structures. Classical methods of decontamination using ultraviolet (UV) radiation proposed in the literature are practically impossible to apply in the case of non-transparent fluids. Nanoparticles or ensemble of nanoparticles exhibit a high surface/volume ratio. The collective action property gives us the possibility to use these metamaterials as antibacterial media against pathogens from contaminated gases and liquids [1, 2], and solid media. Nanoparticle application in decontamination of non-transparent fluids using the contact surface of metamaterial is not completely studied and fully understood yet [1]. An important point to note is the evanescent zone with dimension ranging from 100 to 200 nm, which appears around the elements of metamaterials during the propagation of UV-C radiation through periodical optical structures from packed micro- or nanoparticles. The active decontamination zone is built by the UV-C evanescent field in which the contaminated fluids flow. The pathogens which arrive at the surface of microparticles (or nanoparticles) or pass through the evanescent zone are inactivated by UV-C radiation. Using metamaterials, we improved the active decontamination zone of UV radiation. Such a methodology may be used in fiber optic systems in which the contaminated fluids are propagated along with the free space between the fibers [1]. Keeping in mind that using metamaterials formed from nanoparticles, we have a substantial gain in the decontamination contact surface during the propagation of contaminated liquids through the free space between the nanoparticle of meta-materials (or optical fibers), we therefore propose a new decontamination equipment based on these optical metamaterials [3]. The increase of the active decontamination zone of non-transparent fluid strongly depends on the size, shape and structure of each element of the metamaterial. The relative value of the refractive indexes of metamaterial and contaminated liquids becomes a main factor in increasing the penetration depth of UV radiation into the volume of the contaminated fluid flowing between the metamaterial particles (or along the space between the fibers). Another aspect of decontamination using metamaterials is related to the ability to capture the pathogens along the surface of the metamaterial [4, 5] and thereafter their inactivation by evanescent UV radiation. We propose herein a model of metamaterials (periodical optical structures) to inactivate microorganisms present in contaminated gases or liquids.

49.2 Experiment Results and Discussions

The possibility to decontaminate non-transparent liquids using a UV filter based on improving the contact surface with radiation is estimated. The metamaterials with an accessible price on the market consist of SiO_2 spheres with diameters of about

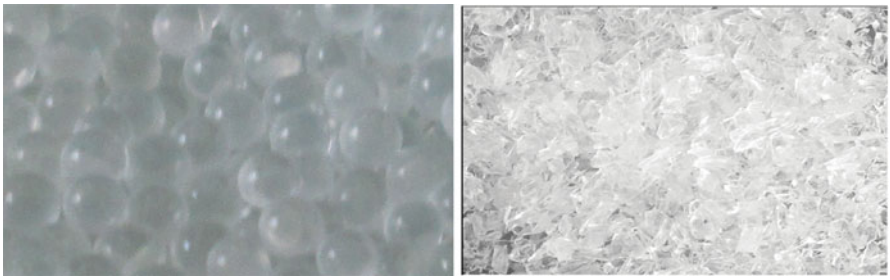

Fig. 49.1 Left: SiO_2 spherical bubbles used in the decontamination core of the reactor, which is focusing the radiation of six UV-C low-pressure mercury lamps. Right: The crushed quartz glass granules

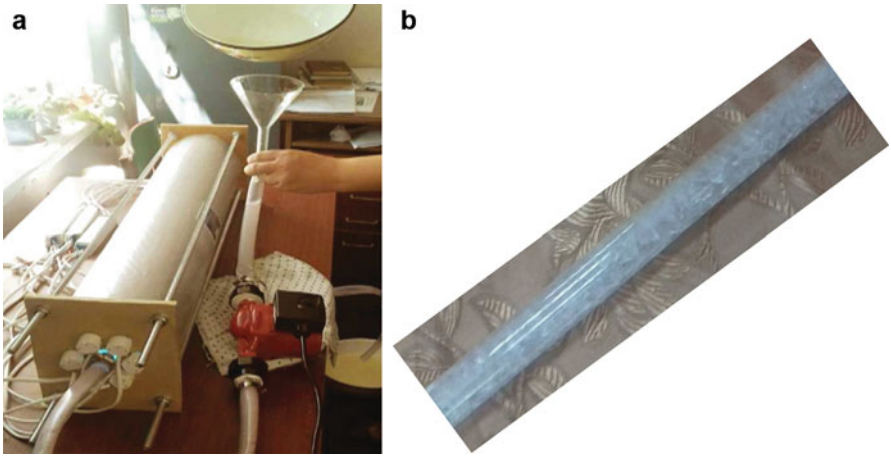

Fig. 49.2 (**a**) Decontamination equipment using metamaterials for inactivation of pathogens in non-transparent fluids. (**b**) The core tube filled with SiO_2 granules

1–3 mm (Fig. 49.1). Elements of the optical metamaterial can disperse the UV-C light and improve the contact zone between radiation and contaminated liquids.

The proposed decontamination equipment using metamaterials is presented in Fig. 49.2a. The radiation of six UV-C (254 nm) lamps is concentrated by the reflective cylinder in the core of the reactor, formed from one quartz tube with a diameter about 3 cm. The light radiation of these lamps is effectively focused and homogeneously distributed along the cylinder axis, with a Gaussian distribution of the intensity of the reflected radiation from a large aluminum surface of the cylinder with a radius of about 15 cm which covers the lamps. The power of each lamp it is about 30 W. The core quartz tube is filled up by the SiO_2 granules. The contaminated fluids can freely flow through the free space between spheres, randomly changing the optical frontiers between these elements and the liquid (or gas) as a function of the concentration of the pathogens in it. The decontamination efficiency is

determined by the contact surface zone between the fluid and the periodical spherical metamaterial, which is proportional to the number of spheres in the core. This UV decontamination reactor may be utilized directly in installations for water, the distribution of central water circuits or in each apartment, in order to avoid biological attacks against our vital necessity in water and air. This equipment may effectively decontaminate the water and air in each apartment in a city.

We present here results of two decontamination experiments. The first of them is connected with the decontamination of *B. coliform*, Intestinal *Enterococci*, *Escherichia coli* (E. coli) bacteria. For this, we took the contaminated water from the nearest reservoir of the "Valea Morilor" lake from Chisinau. The contaminated water was divided into two parts. The first part was treated by our equipment represented in the Fig. 49.2. The pump rotates the contaminated water in intervals from 5 to 10 min. After 24 h, the bacteria from treated and non-treated liquid probes were stimulated for reproductions with a special gel. The multiplication results of bacteria in natural water (a) and treated one in our laboratory (b) are represented in the Fig. 49.3. As follows from experimental results the *E. coli* bacteria practically totally were inactivated from the volume about 1 L of water after 5 min of treatment in the core tube of our reactor. After 10 min of treatment in the decontamination core tube, a total inactivation of bacteria was observed. After flowing along the decontamination cylinder filled up with spherical bubbles of SiO_2 SiO_2(or another metamaterial) the bacteria periodically collapse on the evanescent zone of UV-C radiation of the metamaterial.

Other experiments are linked up with yeast fermentation. By fermentation, the yeast converts carbohydrates to carbon dioxide and alcohols. The fermentation indicators may be used for estimation of the decontamination rate and efficiency of our equipment (Fig. 49.2) in two regimes, dynamic and static. The solution of

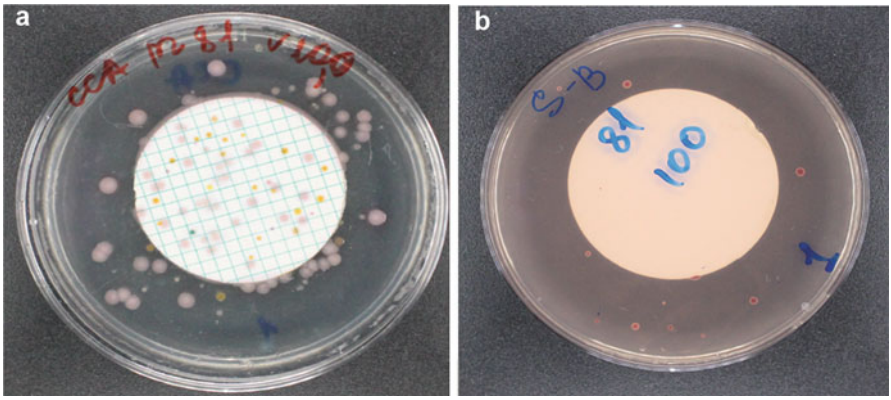

Fig. 49.3 The dynamical regime of decontamination of water. (**a**) probe of natural water: (**b**) The treated probe for 5 min by the proposed decontamination equipment

yeast is non-transparent to UV-C radiation. We used metamaterials consisting of quartz glass granules. After 10 min of treatment in the dynamic regime, when the core tube was filled up with unordered quartz granules (Fig. 49.1b), the fermentation was stopped (Fig. 49.4). Thus, in the experiments yeast treated in our decontaminator in the dynamic regime was efficiently inactivated during the process flowing of liquid through the free space intervals between metamaterial elements (quartz granules), penetrated by the evanescent radiation.

After 1 h of observation the fermentation is active in the untreated solution (Fig. 49.4b), while in the treated yeast solution (1 L) during 10 min of circulating through the core tube filled up by unordered granulated quartz, the fermentation is stopped (Fig. 49.4a). After 5 min of irradiation of yeast solution using unordered granulated quartz a partial inactivation of yeast fungus in the treated solution was observed relative to the control samples.

To demonstrate the efficiency, the same solution of yeast was treated in the core tube without metamaterials, for 10 and 20 min (Fig. 49.5). In both cases the unstopped process of fermentation was observed. The inefficient inactivation of the fungus is related to the non-transparency of the yeast solution for UV radiation.

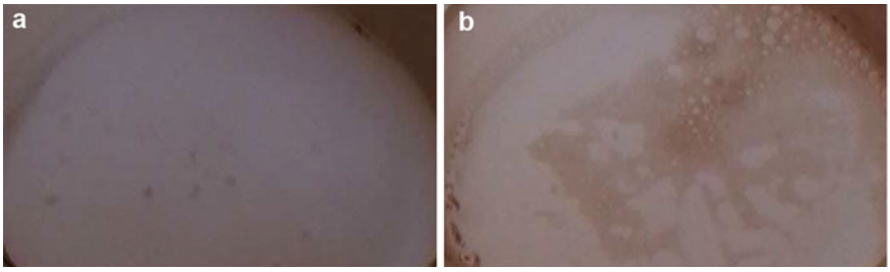

Fig. 49.4 Yeast at 1-h observations. The first portion (**a**) was dynamically treated by our equipment for 10 min while the second (**b**) remained untreated

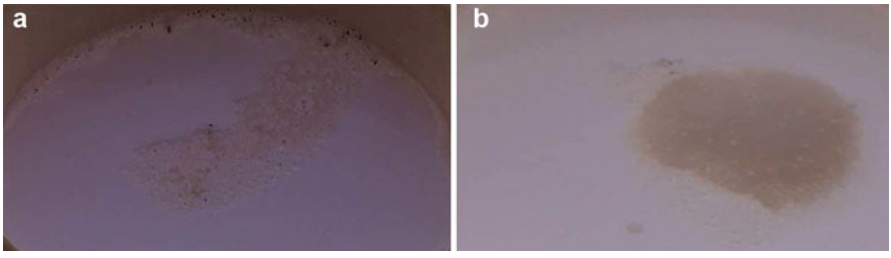

Fig. 49.5 Yeast solution after 1 h's observation. The first portion (**a**) was dynamically treated by our equipment for 10 min and the second (**b**) for 20 min, in both cases without quartz granules in the core tube. As a result of the test, fermentation started in both cases (**a**) and (**b**)

49.3 Conclusions

We demonstrated that using metamaterials, such as photonic crystals, in microspheres or fibers there is a substantial gain in the decontamination of liquids from viruses and bacteria.The increasing of the surface contact of UV radiation with contaminated liquid strongly depends on the refractive index of metamaterial, the liquid volume and the optical properties of viruses and bacteria. The possibility to effectively inactivate with UV-C radiation pathogens from non-transparent fluids (liquids or gases) was further presented.

Acknowledgments This paper was supported by the projects: STCU6140&NATO SPS G4890.

References

1. Enaki NA, Bazgan S, Ciobanu N, Turcan M, Paslari T, Ristoscu C, Vaseashta A, Mihailescu IN (2017) Improvement in ultraviolet based decontamination rate using meta-materials. Appl Surf Sci 417:40–47
2. El-Mashad HM, Pan Z (2015) Food decontamination using nanomaterials. MOJ Food Process Technol 1(2):00011
3. Bazgan S, Ristoscu C, Negut I, Hapenciuc C, Turcan M, Ciobanu N, Mihailescu IN, Enaki N (2015) Propagation of UV radiation through meta-materials and its application in bio-decontamination. Rom Rep Phys 67:1602–1607
4. Ashkin A, Dziedzic JM (1987) Optical trapping and manipulation of viruses and bacteria. Science 235:1517–1520
5. Daly M, Sergides M, Nic Chormaic S (2015) Optical trapping and manipulation of micrometer and sub micrometer particles. Laser Photon Rev 9:309

Chapter 50
Development of Nanostructured Materials with CBRN Agents Sensing Properties

A. Stoilova, A. Georgiev, D. Nazarova, L. Nedelchev, D. Dimov, and P. Petkov

Abstract Azobenzene containing polymers are a class of optical materials extensively investigated in the past decade. Due to their possibility to undergo reversible trans-cis-trans photoisomerization cycles and through their attractive photophysical properties, the azopolymers could be used as storage medium in optical devices, as optical switches and sensors, as responsive surfaces for biomedical applications, in polarization holography, and in photonics. The aim of this paper is to summarize the information available in the scientific literature about the possibility to use these materials not only for optical application but also as sensing platforms for the detection of biological agents listed as category A biological weapons. Furthermore, this review attempts to give the readers insights into the difficulties concerning the detection of biological agents within environmental samples as well as to outline the progress and the weaknesses in the development of sensors based on nanostructured materials to help to combat terrorisms.

Keywords Nanocomposites · Azo polymers · Sensors · CBRN agents diagnostic

50.1 Introduction

The deliberate release of biological agents such as viruses, bacteria or toxins to cause illness or death is defined by the U. S. Center for Disease Control and Prevention (CDC, www.cdc.govas) as bioterrorism. The biological agents are classified into three groups A, B and C based on their infectivity, the mortality they cause, the ease of spread and the likeliness of use. To category A belong the bacteria Francisella tularensis, Clostridium botulinum, Yersinia pestis, *Bacillus anthracis* and also the Variola virus and some RNK viruses causing hemorrhagic fevers. Historically, the

A. Stoilova (✉) · A. Georgiev · P. Petkov
Department of Physics, University of Chemical Technology and Metallurgy, Sofia, Bulgaria

D. Nazarova · L. Nedelchev · D. Dimov
Institute of Optical Materials and Technologies, Bulgarian Academy of Science, Sofia, Bulgaria

P. Petkov et al. (eds.), *Advanced Nanotechnologies for Detection and Defence against CBRN Agents*, NATO Science for Peace and Security Series B: Physics and Biophysics, https://doi.org/10.1007/978-94-024-1298-7_50

pathogenic microorganisms classified as a category A potential bioterrorism agents have killed far more people than the First World War itself. For example, 25 million Europeans died from the bubonic plague alone in the fourteenth century. The pathogenic species from category A could be find actually all around us. They spread through the air, the water and the soil. They are also relatively easy to produce using the common technology available for the production of some antibiotics, for example. As a result they are cheaper than the conventional weapon of mass destruction and also invisible, silent, odourless and stable in environmental samples. All these characteristics make them very attractive to terrorists but not so much to the scientific community from which is expected to develop highly sensitive, rapid, portable and if possible inexpensive sensors for their detection.

This review was generated using references published over the last 20 years. The literature search has been conducted using the database "ScienceDirect" and through the free search engines "PubMed" and "NCBI" by keywords relevant to the topic.

The purpose of this article is to survey the open literature to determine the current state of development of biosensors based on azobenzene containing nanomaterials for the detection of biological agents from category A. The research interest in nanostructured materials as biodefence detection platforms is due to their dimensions comparable to those of the biological molecules [1]. For example quantum dots were used for the detection of Botulinum neurotoxin by means of an optical biosensor, Ln-doped nanoparticles were used for detection of Bacillus anthracis spores using a photoluminescence based sensor, the Variola virus was detected using heterogeneous nanowires [2] (Table 50.1).

50.2 Detection of Biological Agents at the Point of Dissemination

Detection of biological agents or their toxins within soil or water samples is difficult because they usually contain substances that inhibit the detection technique. The target micro-organisms must be isolated, concentrated and/or purified [7]. Typically, after sampling and solubilizing or suspending with phosphate buffered saline, the sample is being transferred to the testing assay. Many of the commercial detection systems use test strips based on the affine chromatography principle. The detection of pathogens within urban aerosols is more difficult. Sampling bioaerosols include impaction, filtration or impingement [8]. In real situations portable cyclones are used for collection of bioaerosols from air into the liquid phase; thereafter the samples obtained are further analysed. Testing for potential biothreat agents in the air is possible at facilities containing approved air or aerosol chambers and wind tunnels.

The most important physical characteristic by which airborne pathogens could be classified is their size. Particles with a diameter in the range 1–5 μm behave in aerosols like gases. Particles larger than 5 μm in diameter settle from the atmosphere and bind to surfaces; particles with a diameter smaller than 1 μm, such as most of the

Table 50.1 A brief summary of the information concerning size range, shape and human's infectious dose of the pathogen species listed to category A [3–6]

Category A biological agents	Size range	Infectious dose for humans
Francisella tularensis-aerobe bacterium, pleomorphic, non-motile, non-spore forming, gram-negative, rod-shaped, responsible for epizootics of tularemia, highly stable in an environmental matrix	0,2–0,7 μm	10–50 organisms (aerosol inoculation)
Clostridium botulinum-anaerobic bacterium, rod-shaped, gram-positive, spore-forming, motile, Botulism causing agent. There are seven types of C. botulinum toxins (A–F). Types A, B, E, and rarely F can cause human botulism	0,1–0,3 μm (aerosolized particles of the botulinum toxins)	0,001 μg/kg body weight by oral exposure
		0,07 μg/kg body weight by inhalation
Bacillus anthracis-aerobic bacterium, gram-positive, rod-shaped, non-motile, resistant to adverse environmental conditions, spore forming, anthrax causing agent	0,95–3,5 μm	8.10^3 to 50.10^3 spores (inhalation)
Yersinia pestis-gram-negative bacterium, rod-shaped, facultative anaerobic organism, non-motile bacillus, causes Bubonic plague	0,5–0,8 μm (width)	100–500 particles
	1–3 μm (length)	
Variola virus	360–270–250 nm	10–100 particles
RNK viruses cause viral hemorrhagic fevers:		
Marburg virus	80 nm (d)	1–10 (ae. o)
Ebola virus	80 nm (d)	1–10 (ae. o)
Lassa virus	80–150 nm (d)	1–10 (ae. o)
Machupo virus	50–300 nm (d)	1–10 (ae. o)

ae.o stands for aerosolized organisms and d for diameter

pathogens belonging to category A, can be collected by processing large volumes of air and passing the air through a filter or impinging the particles from the collected air into a liquid or semisolid sample [9]. The traditional methods of detecting biological agents show high sensitivity and specificity, but these techniques are often slow, expensive and require sample pre-treatment and laboratory conditions for their execution.

50.3 Biosensors for Environmental Monitoring of Biological Agents

To overcome the above mentioned difficulties concerning the biological agent's detection within environmental samples the efforts of the scientific community are focussed on the development of portable and multiplexed nanomaterial-based sensors. Due to the nanoscale interactions providing unique physico-chemical properties and the large surface/volume ratios these materials are well-suited for

application in sensing devices [2]. The fastest growing technology for detection of pathogens in recent years is the biosensor [10]. Several studies report the performance of biosensors for detection of category A bacterial agents. For example Skládal et al. [11] reported an electrochemical immunosensor for rapid and highly sensitive detection of Francisella tularensis. A detection limit of 1000 CFU/mL (colony-forming units per millilitre) was achieved. The required detection time was about 25 min. O'Brien et al. [12] demonstrated an optical bidiffractive grating immunosensing device for direct detection of Francisella tularensis. A detection limit of $3 \cdot 10^4$ CFU/ml was obtained. The required measuring time was 50 min. A novel piezoelectric sensor for direct detection of Francisella tularensis was developed by Pohanka and Skládal. The device exhibited a detection limit of 10^5 CFU/ml. The required measuring time was 5 min after a short pre-cultivation enrichment [11]. For comparison commercial test strips designed for detection of multiple biological warfare agents show a detection limit in the range of 10^5 to 10^6 CFU/ml towards Francisella tularensis. Joint Biological Agent Identification and Diagnostic System is a military, portable, real-time PCR instrument technology (Polymerase chain reaction, or PCR, is a technique used to make many copies of a specific DNA region in vitro) detecting simultaneously up to 32 samples. The assay time takes 30 min, not including sample preparation. The limit of detection reported by the manufacturer is 1000 CFU/ml towards Francisella tularensis [13]. It must be noted that most of the biosensors reported in the scientific literature for detection of Francisella tularensis are research-based prototypes not yet ready for integration into commercial devices.

The biosensor is a small, portable, analytical device made up of a biological recognition element (also called bioreceptor) consisting of biocomponents (nucleic acids, enzymes, anti-bodies, cells etc.) able to detect specific target analytes. Attachment of target molecules on the sensor surface brings about physicochemical changes such as release of heat, flow of electrons, changes in the mass, changes in the absorption spectra which are converted into a measurable signal by a transducer component (converter) and passed to a microprocessor where it is amplified and displayed [14]. In general there are three strategies for immobilization of the biological molecules onto the sensor's surface: binding to a support (physical adsorption or chemical binding), encapsulation or entrapment and cross-linking. The physical adsorption represents a method for reversible immobilization of biomolecules onto support materials which occurs through weak non-specific forces such as van der Waals or Coulomb's forces, hydrophobic interactions and hydrogen bonds. It is a simple method allowing regeneration and reloading of the support material with a high commercial potential due to its low cost. The limitations of this method are related to the too weak bonds between the biomolecules and the substrate leading to leakages [15, 16]. An attractive technique for increasing the immobilization efficiency represents the creation of surface relief gratings into thin films of azobenzene containing polymers. The fabrication of nanostructured materials by photo inscription of surface relief gratings represents a simple, controllable, economical and reproducible method.

50.4 Azo Materials as Sensing Platforms for Detection of CBRN Agents

The azobenzenes are organic compounds which contain azo (-N=N-) chromophore group linked to two aromatic rings. They have two geometrical isomers (trans (E) and cis (Z)) with strong electronic absorption of the -N=N- conjugated π system. The main characteristic UV-VIS absorption bands are at λ_{max} ~440 nm related to the n→π* transition or S1 excited state and at λ_{max} ~340 nm related to the π→π* transition or S_2 excited state [17–19]. The E→Z isomerization can be driven by ultraviolet (UV) light irradiation usually at λ ~365 nm, the reverse Z→E isomerization occurs spontaneously in the dark, under thermal treatment or by exposure to visible (VIS) light (Fig. 50.1).

According to the spectral properties, the nature and the position of the substituents in the aromatic rings azobenzene derivatives can be classified (according to Rau) [20, 21] as: (i) azobenzene derivatives (ABn); (ii) aminoazobenzene derivatives (aAB); (iii) pseudostilbenes (pSB) (Fig. 50.2).

The substitution pattern of the AB molecules determines their photochemical behaviour. The presence of electron withdrawing (EW) groups like -CHO, -CN, $-NO_2$ and electron donating (ED) like $N(R)_2$, -OH, -OR, cause asymmetrical electron ("push-pull") distribution on the molecular backbone and a decrease of the energy of the electron transitions, where the π→π* and n→π* bands are well separated [22].

The azobenzene molecule is of interest because of its colouring properties. The azo dyes represent approximately 60–70% of all dyes used in the food and textile manufacture (Tartrazine, Azorubine, Amaranth, Brilliant Black BN, etc.). Another interesting feature of the azobenzene molecule is the ability to change its spatial arrangement under light irradiation [23]. It is mainly studied for optical application but this characteristic of the azobenzene molecule make it well-suited also for application in bioengineering devices [24–29]. Over the last few years surface relief gratings (SRGs) created on thin films of azobenzene containing polymers are widely investigated as nanostructure for biosensing applications. They offer key advantages for biosensing applications requiring in-situ or portable detection due to their

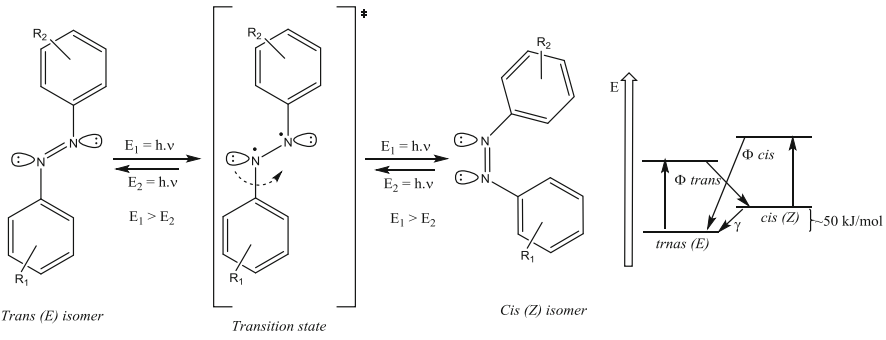

Fig. 50.1 Photoisomerization of azobenzene chromophores

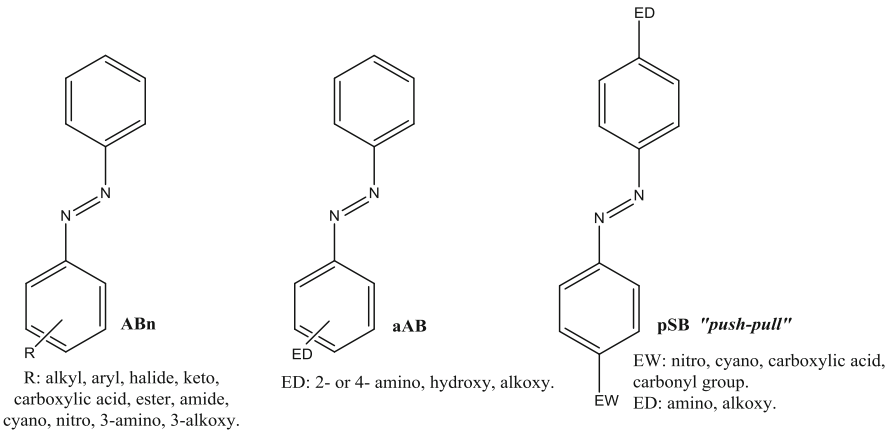

Fig. 50.2 General types of substituted ABs

inherent compact footprint, compatibility with collinear optical formats and easiness of integration with other micro-technological platforms, such as microfluidic [28].

A method of detecting G-type nerve agents based on the colouring properties of azomolecules has been patented by Thoraval and Bovenkamp. The detector material consists of a paper base in which dyes have been incorporated; each dye is sensitive to a particular family of liquid chemical warfare agent droplets. In the presence of specific chemical agent the detector material assumes a characteristic colour [30].

Nair, Escobedo and Sabat have demonstrated a biosensor platform based on inscription of crossed surface relief gratings (CSRGs) with a depth of 75 nm and grating pitch of 550 nm on azopolymer thin films with a thickness of ca. 190 nm by using a solid-state diode-pumped laser (COHERENT, USA, Verdi V5, $\lambda = 532$ nm) with an irradiance of 382 mW/cm^2. The prepared CSRGs were coated with gold, modified with biotin and incubated in a streptavidin solution with different concentrations. The CSRG shows ability to detect local refractive index changes due to the biotin-streptavidin binding events [31].

By photoirradiation the azomolecules deform due to the trans-cis isomerisation. If there are biomolecules on the surface of the thin azopolymer film during the illumination, it deforms along their shapes [32]. This strategy has been successfully used for immobilization of desoxyribonucleic acids, proteins and viruses.

Ikawa et al. [33] reported photoimprint-based immobilization of the Tobacco mosaic virus (TMV) with cylindrical shape and sizes of 18 nm in diameter and ca. 300 nm in length onto azopolymer surface. A droplet of an aqueous solution containing TMV was placed on the surface of a poly{40-[[[2-(methacyloyloxy) ethyl]-ethyl]amino]-4-cyanoazobenzene-co-methy methacrylate} thin film prepared via the spin-coating technique. After drying the droplet, the polymer surface was irradiated with light at a wavelength of 470 nm from blue-light-emitting diodes. Then the surface was washed by an aqueous solution with detergents. The polymer surface was observed at each step by AFM. TMV was shown to embed itself

gradually on the polymer surface during photoirradiation in a time scale of tens of minutes because of the formation of surface grooves complementary to the shape of TMV. The immobilization process is believed to be a noncovalent physical process, because the TMV is completely removed from the azopolymer surface only by washing with surfactants even after 30 min photoirradiation, and because the absorption spectra of the azopolymer were confirmed to be unchanged under these experimental conditions.

50.5 Conclusions

For detection of biothreats at the point of dissemination, expensive equipment with integrated systems for sample collection, preparation and analyzing is needed, now available only to the military of a limited number of countries. The biosensor represents a portable, easy to use, all in one piece of equipment with which sample collection and analysis can speedily be done. One of the scientific factors which currently mitigate the use of biosensors for environmental monitoring of biological agents is the unstable immobilization of the biomolecules. Photoresponsive surfaces such as azobenzene functionalized thin films whose chemical and physical properties can be changed or tuned in an accurate and predictable manner are a promising alternative for switched immobilization/mobilization of biomolecules, such as protein adsorption, cell adhesion, DNA or RNA attachment and so on [32, 34]. However there are limited literature sources reporting the development of biosensors for the detection of category A biological agents using azo polymers as sensing elements. While the success of the nanomaterials as biothreat detection platforms has been demonstrated in the laboratory, factors such as scale-up, device fabrication, systems integration, and interfacing, have yet to be managed.

Acknowledgments This work is financially supported by the National Science Fund of Bulgaria, DN 08/10, 13.12.2016.

References

1. Vaseashta A, Dimova-Malinovska D (2005) Nanostructured and nanoscale devices, sensors and detectors. Sci Technol Adv Mater 6(3–4):312–318
2. Rowland C, Brown C, Delehanty J, Medintz I (2016) Nanomaterial-based sensors for the detection of biological threat agents. Mater Today 19(8):464–477
3. Cooper K, Bandara A, Wang Y, Wang A, Inzana T (2011) Photonic biosensor assays to detect and distinguish subspecies of Francisella tularensis. Sensors 11(3):3004–3019
4. Public Health Agency of Canada. www.publichealth.gc.ca
5. United States Environmental Protection Agency, National Homeland Security Research Center (NHSRC) (2012) Threat and Consequence Assessment Division, Protocol for detection of Bacillus anthracis in environmental samples during the remediation phase of an anthrax event, EPA/600/R-12/577. www.epa.gov/ord

6. Cheng L, Kirkwood L, Stanker L (2012) Current methods for detecting the presence of Botulinum neurotoxins in food and other biological samples. Bioterrorism. InTech, Book chapter 1, p 1–17
7. Gunnell M (2015) The detection and molecular evolution of Francisella tularensis subspecies, dissertation for the degree of Doctor of Philosophy, Department of Microbiology and Molecular Biology, Brigham Young University
8. Silvestri E (2015) Literature review on processing and analytical methods for Francisella tularensis in soil and water, Analytical Office of Research and Development, U. S. National Homeland Security Research Center
9. Lim D, Simpson J, Kearns E, Kramer M (2005) Current and developing technologies for monitoring agents of bioterrorism and biowarfare. Clin Microbiol Rev 18(4):583–607
10. Lazcka O, Campo F, Munoz F (2007) Pathogen detection: a perspective of traditional methods and biosensors. Biosens Bioelectron 22(7):1205–1217
11. Skládal P, Pohanka M, Kupská E, Šafář B (2010) Biosensors for detection of Francisella tularensis and diagnosis of tularemia. Biosensors, Book chapter 7, p 302
12. O'Brien T, Johnson L, Aldrich J, Allen S, Liang L, Plummer AL, Stephen J, Boiarski A (2000) The development of immunoassays to four biological threat agents in a bidiffractive grating biosensor. Biosens Bioelectron 14:815–828
13. Ozanich R, Baird C, Bartolomew R, Colburn H, Straub T, Brucner L (2014) Biodetection technologies for first responders. http://biodetectionresource.pnnl.gov
14. Perumal, Hashim U (2014) Advances in biosensors: principle, architecture and applications. J Appl Biomed 12(1):1–15
15. Mohamada N, Marzukia N, Buanga N, Huyop F, Wahab R (2015) An overview of technologies for immobilization of enzymes and surface analysis techniques for immobilized enzymes. Biotechnol Biotechnol Equip 29(2):205–220
16. Sumitra D, Christena R, Rani Y, Rajaram S (2013) Enzyme immobilization: an overview on techniques and support materials. Biotech 3(1):1–9
17. Dhammika Bandara H, Burdette S (2012) Photoisomerization in different classes of azobenzene. Chem Soc Rev 41(5):1809–1825
18. Yager K, Barrett C (2009) Azobenzene polymers for photonic applications. Smart Light-Responsive Materials, Book chapter 1, pp 1–27
19. Merino E, Ribagorda M (2012) Control over molecular motion using the cis–trans photoisomerization of the azo group. Beilstein J Org Chem 8:1071–1090
20. Rau H (2002) Photoisomerization of azobenzenes, photoreactive organic thin films pp 3–47
21. Rau H (2003) Azo compounds. Photochromism Molecules and Systems, Chapter 1, pp 165–192
22. Georgiev A, Bubev E, Dimov D, Yancheva D, Zhivkov I, Krajčovič J, Vala M, Weiter M, Machkova M (2017) Synthesis, structure, spectral properties and DFT quantum chemical calculations of 4-aminoazobenzene dyes. Effect of intramolecular hydrogen bonding on photoisomerization. Spectrochim Acta A Mol Biomol Spectrosc 175:76–91
23. Rau H (1990) Photoisomerization of azobenzenes. Photochemistry and photophysics, Chapter 4, 2 pp 119–143
24. Rocha L, Păiuş C, Raicu A, Resmerita E, Rusu A, Moleavin I, Hamel M, Branza-Nichita B, Hurduc N (2014) Azobenzene based polymers as photoactive supports and micellar structures for applications in biology. J Photochem Photobiol A Chem 291:16–25
25. Szmigiel A, Switkowski K, Balcerzak E, Szmigiel D (2015) Photoinduced birefringence of azobenzene polymer at blue excitation wavelengths. Appl Phys B 119(2):227–231
26. Oliveira O, Santos D, Balogh D, Zucolotto V, Mendon?a C (2005) Optical storage and surface-relief gratings in azobenzene-containing nanostructured films. Adv Colloid Interf Sci 116:179–192
27. Takahashi M, Okuhara T, Yokohari T, Kobayashi K (2006) Effect of packing on orientation and cis–trans isomerization of azobenzene chromophore in Langmuir–Blodgett film. J Colloid Interface Sci 296(1):212–219

28. Li J, Stachowski M, Zhang Z (2015) Application of responsive polymers in implantable medical devices and biosensors, switchable and responsive surfaces and materials for biomedical applications, pp 259–298
29. Novir S, Hashemianzadeh S (2015) Density functional theory study of new azo dyes with different π-spacers for dye-sensitized solar cells. Spectrochim Acta A Mol Biomol Spectrosc 143:20–34
30. Thoraval D, Bovenkamp J (1992) Paper chemical agent detectors, European Patent EP0334668
31. Nair S, Escobedo C, Sabat R (2017) Crossed surface relief gratings as nanoplasmonic biosensors. ACS Sensors 2(3):379–385
32. Ikawa T, Hoshino F, Matsuyama T, Takahashi H, Watanabe O (2006) Molecular-shape imprinting and immobilization of biomolecules on a polymer containing azo dye. Langmuir 22(6):2747–2753
33. Ikawa T, Kato Y, Yamada T, Shiozawa M, Narita M, Mouri M, Hoshino F, Watanabe O, Tawata M, Shimoyama H (2010) Virus-templated photoimprint on the surface of an azobenzene-containing polymer. Langmuir 26(15):12673–12679
34. Wang G, Zhang J (2012) Photoresponsive molecular switches for biotechnology. J Photochem Photobiol C: Photochem Rev 13(4):299–309

Index

P. Petkov et al. (eds.), *Advanced Nanotechnologies for Detection and Defence against CBRN Agents*, NATO Science for Peace and Security Series B: Physics and Biophysics, https://doi.org/10.1007/978-94-024-1298-7